

Science and social media  
pp. 593, 608–614, & 624

Robots that go to school for  
kids who can't p. 604

Seeking caloric restriction benefits  
without the hunger pp. 620 & 671

# Science

\$15  
11 FEBRUARY 2022  
science.org

AAAS

## DUAL-SCALE LATTICE

Robust, damage-tolerant  
starfish skeletons

pp. 615 & 647





Apply for our exciting research Prize!



**\$25, 000 Grand Prize!**  
**Get published in *Science*!**

The *Science*-PINS Prize is a highly competitive international prize that honors scientists for their excellent contributions to neuromodulation research. For purposes of the Prize, neuromodulation is any form of alteration of nerve activity through the delivery of physical (electrical, magnetic, or optical) stimulation to targeted sites of the nervous system with implications for translational medicine.

For full details, judging criteria and eligibility requirements, visit:

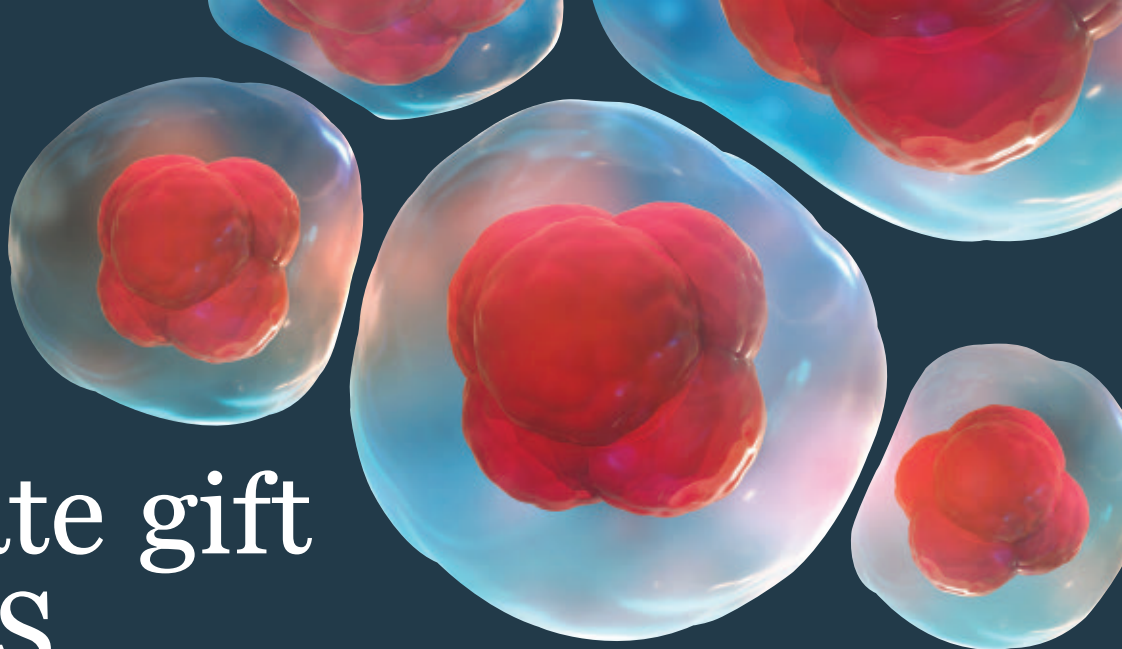
**[www.science.org/pins](http://www.science.org/pins)**

**Submissions Open: 15 December 2021**

**Science**  
AAAS



**Science  
Translational  
Medicine**  
AAAS



# An estate gift to AAAS

Going all the way back to 1848, our founding year, the American Association for the Advancement of Science (AAAS) has been deeply committed to advancing science, engineering and innovation around the world for the benefit of all people.

Today, we are dedicated to advocating for science and scientific evidence to be fully and positively integrated into public policy and for the community to speak with one voice to advance science and engineering in the United States and around the world.

By making AAAS a beneficiary of your will, trust, retirement plan or life insurance policy, you will become a member of our 1848 Society and will help fuel our work on behalf of science and society – including publishing the world’s most promising, innovative research in the *Science* family of journals and engaging in the issues that matter locally, nationally and around the world.

*“As a teacher and instructor, I bear responsibility for the younger generations. If you have extra resources, concentrate them on organizations, like AAAS, that are doing work for all.”*

—Prof. Elisabeth Ervin-Blankenheim, 1848 Society member

If you intend to include AAAS in your estate plans, provide this information to your lawyer or financial adviser:

**Legal Name:** American Association for the Advancement of Science

**Federal Tax ID Number:** 53-0196568

**Address:** 1200 New York Avenue, NW, Washington, DC 20005

If you would like more information on making an estate gift to AAAS, cut out and return the form below or send an email to [philanthropy@aaas.org](mailto:philanthropy@aaas.org). Additional details are also available online at [www.aaas.org/1848Society](http://www.aaas.org/1848Society).

AMERICAN ASSOCIATION FOR THE ADVANCEMENT OF SCIENCE

cut here

Yes, I would like more information about joining the AAAS 1848 Society.

**PLEASE CONTACT ME AT:**

Name: \_\_\_\_\_

Address: \_\_\_\_\_

City: \_\_\_\_\_ State: \_\_\_\_\_ Zip code: \_\_\_\_\_ Country: \_\_\_\_\_

Email: \_\_\_\_\_ Phone: \_\_\_\_\_

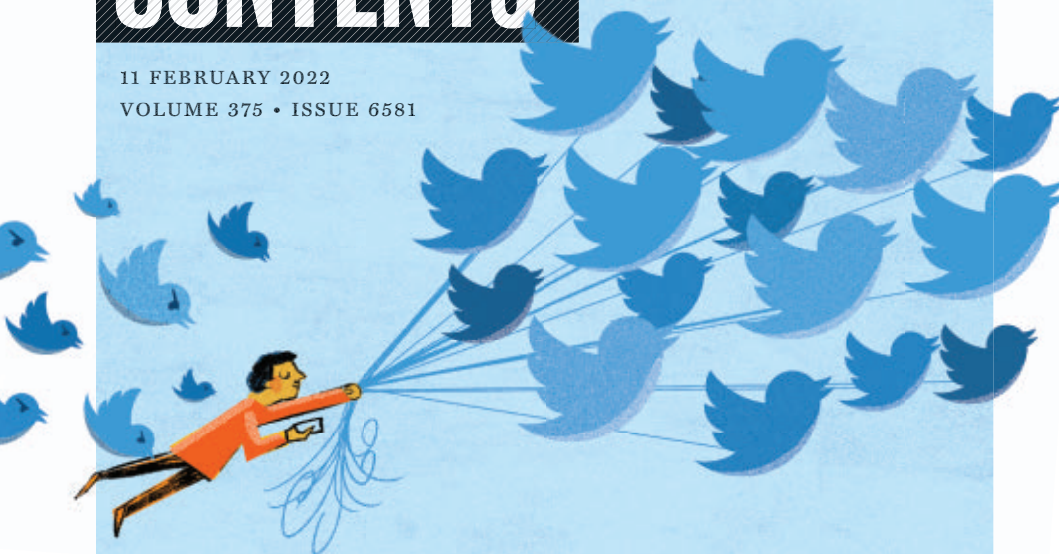
**RETURN THIS FORM TO:**

AAAS Office of Philanthropy and Strategic Partnerships • 1200 New York Avenue, NW • Washington, DC 20005 USA



# CONTENTS

11 FEBRUARY 2022  
VOLUME 375 • ISSUE 6581



## Science and social media

### DEPARTMENTS

#### 593 Editorial

Science and social media *By H. Holden Thorp*

### LETTERS

#### 608 NextGen Voices Social media: Good or evil?

PODCAST

### POLICY FORUM

#### 610 EU and US legislation seek to open up digital platform data

Constraints on data access must be addressed to facilitate research  
*By B. Nonnecke and C. Carlton*

### PERSPECTIVES

#### 613 The chronic growing pains of communicating science online

Scientists have not yet adapted to new information environments  
*By D. Brossard and D. A. Scheufele*  
PODCAST

### BOOKS ET AL.

#### 624 Social media and shared reality

Exacerbated by engagement algorithms, flat Earth theories and other fringe beliefs thrive  
*By J. Golbeck*

#### 602 Massive U.S. innovation bills face difficult road in Congress

Lawmakers must reconcile competing visions for boosting research spending and helping high-tech industries *By J. Mervis*

### FEATURES

#### 604 Dream machine

In a few classrooms, robots attend for children ailing at home. A researcher wants to know how to make the devices better *By A. Katsnelson*

## INSIGHTS

### PERSPECTIVES

#### 615 Starfish grow extraordinary crystals

Biomineralization in a starfish displays morphologically complex features  
*By S. T. Hyde and F. C. Meldrum*  
REPORT p. 647

#### 616 A new model of sex chromosome evolution

A new model, based on the evolution of gene regulation, challenges the classical theory *By P. Muralidhar and C. Veller*  
REPORT p. 663

#### 618 Breaking symmetry for piezoelectricity

Record-breaking piezoelectricity is achieved in oxides with symmetry-breaking defects *By F. Li*  
REPORT p. 653

#### 619 From start to finish— a molecular link in wound repair

p53 mediates epithelial cell migration and leader cell elimination during wound repair *By S. Yun and V. Greco*  
RESEARCH ARTICLE p. 628

#### 620 Caloric restriction has a new player

Reverse translation of a human caloric restriction trial finds an immunometabolic regulator  
*By T. W. Rhoads and R. M. Anderson*  
REPORT p. 671

#### 622 Thomas E. Lovejoy (1941–2021)

Biodiversity pioneer and expert on the Amazon rainforest *By W. F. Laurance*

### BOOKS ET AL.

#### 623 Vivid snapshots of the past

A paleontologist offers an immersive look at pivotal moments in Earth's history  
*By L. Grande*

## NEWS

### IN BRIEF

594 News at a glance

### IN DEPTH

#### 596 U.S. science adviser resigns after bullying charge

Eric Lander's abrupt departure comes as Biden administration pushes research initiatives *By D. Malakoff*

#### 597 Geneticists find clues to unexplained child deaths

Sequencing mysterious cases yields mutations linked to seizures and arrhythmias  
*By K. Servick*

#### 598 A 10,000-year head start for modern humans in Europe?

Tooth and tools suggest moderns and Neanderthals took turns in French cave *By M. Price*  
SCIENCE ADVANCES RESEARCH ARTICLE BY  
L. SLIMAK ET AL. 10.1126/SCIADV.ABJ9496

#### 600 European fusion reactor sets record for sustained energy

World's largest tokamak paves the way for ITER with a capstone run of pulses using power-producing tritium *By D. Clery*

#### 601 An electric jolt strips valuable metals from waste

New method can pull rare earth elements from electronic waste and coal ash *By S. Kean*  
SCIENCE ADVANCES RESEARCH ARTICLE BY  
B. DENG ET AL. 10.1126/SCIADV.ABM3132





## RESEARCH

### IN BRIEF

**625** From *Science* and other journals

### RESEARCH ARTICLES

#### 628 Cell biology

p53 directs leader cell behavior, migration, and clearance during epithelial repair  
*K. Kozyrska et al.*

RESEARCH ARTICLE SUMMARY; FOR FULL TEXT:  
DOI.ORG/10.1126/SCIENCE.ABL8876

PERSPECTIVE p. 619

#### 629 Immunology

CD97 promotes spleen dendritic cell homeostasis through the mechanosensing of red blood cells  
*D. Liu et al.*

RESEARCH ARTICLE SUMMARY; FOR FULL TEXT:  
DOI.ORG/10.1126/SCIENCE.ABI5965

#### 630 Immunology

Marginal zone B cells acquire dendritic cell functions by trogocytosis  
*P. Schriek et al.*

RESEARCH ARTICLE SUMMARY; FOR FULL TEXT:  
DOI.ORG/10.1126/SCIENCE.ABF7470

#### 631 Cell biology

Mechanism of spindle pole organization and instability in human oocytes  
*C. So et al.*

RESEARCH ARTICLE SUMMARY; FOR FULL TEXT:  
DOI.ORG/10.1126/SCIENCE.ABJ3944

#### 632 Neuroscience

Geometry of sequence working memory in macaque prefrontal cortex  
*Y. Xie et al.*

#### 639 Biomedicine

An autonomously swimming biohybrid fish designed with human cardiac biophysics  
*K. Y. Lee et al.*

### REPORTS

#### 647 Materials science

A damage-tolerant, dual-scale, single-crystalline microlattice in the knobby starfish, *Protoreaster nodosus*  
*T. Yang et al.*

PERSPECTIVE p. 615

#### 653 Piezoelectrics

Induced giant piezoelectricity in centrosymmetric oxides  
*D.-S. Park et al.*

PERSPECTIVE p. 618

#### 658 Organic chemistry

Remote steric control for undirected meta-selective C–H activation of arenes  
*B. Ramadoss et al.*

#### 663 Y chromosome origins

Y recombination arrest and degeneration in the absence of sexual dimorphism  
*T. Lenormand and D. Roze*

PERSPECTIVE p. 616

#### 667 Coronavirus

COVID mortality in India: National survey data and health facility deaths  
*P. Jha et al.*

#### 671 Aging

Caloric restriction in humans reveals immunometabolic regulators of health span  
*O. Spadaro et al.*

PERSPECTIVE p. 620

#### 678 Coronavirus

Neutralization of SARS-CoV-2 Omicron by BNT162b2 mRNA vaccine–elicited human sera  
*A. Muik et al.*

#### 681 Spatial epigenomics

Spatial-CUT&Tag: Spatially resolved chromatin modification profiling at the cellular level  
*Y. Deng et al.*

### DEPARTMENTS

#### 591 Editorial

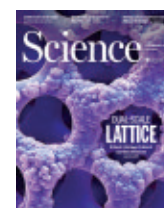
The lessons of Lander  
*By H. Holden Thorp*

#### 690 Working Life

Following my curiosity  
*By Alvina G. Lai*

### ON THE COVER

Artificially colored scanning electron micrograph of a knobby starfish (*Protoreaster nodosus*) skeletal element with small calcite crystals grown on its surface. This overgrowth experiment demonstrates this biomineralized structure's two single-crystalline components—a micrometer-scale periodic lattice and the underlying atomic-scale calcite—that are aligned by their crystal symmetry. This lightweight dual-scale structure exhibits high mechanical efficiency and damage tolerance for enhanced protection. See pages 615 and 647.  
*Image: Ling Li/Virginia Tech*



Science Careers .....687

SCIENCE (ISSN 0036-8075) is published weekly on Friday, except last week in December, by the American Association for the Advancement of Science, 1200 New York Avenue, NW, Washington, DC 20005. Periodicals mail postage (publication No. 484460) paid at Washington, DC, and additional mailing offices. Copyright © 2022 by the American Association for the Advancement of Science. The title SCIENCE is a registered trademark of the AAAS. Domestic individual membership, including subscription (12 months): \$165 (\$74 allocated to subscription). Domestic institutional subscription (51 issues): \$2212; Foreign postage extra: Air assist delivery: \$98. First class, airmail, student, and emeritus rates on request. Canadian rates with GST available upon request. GST #125488122. Publications Mail Agreement Number 1069624. Printed in the U.S.A.

Change of address: Allow 4 weeks, giving old and new addresses and 8-digit account number. Postmaster: Send change of address to AAAS, P.O. Box 96178, Washington, DC 20090-6178. Single-copy sales: \$15 each plus shipping and handling available from backissues.science.org; bulk rate on request. Authorization to reproduce material for internal or personal use under circumstances not falling within the fair use provisions of the Copyright Act can be obtained through the Copyright Clearance Center (CCC), www.copyright.com. The identification code for Science is 0036-8075. Science is indexed in the Reader's Guide to Periodical Literature and in several specialized indexes.

## 15th Edition BBVA Foundation Frontiers of Knowledge Awards

With the collaboration of



The **BBVA Foundation Frontiers of Knowledge Awards** recognize and reward world-class research and artistic creation, prizing contributions of singular impact for their originality and significance. The name of the scheme is intended to denote not only research work that substantially enlarges the scope of our current knowledge – pushing forward the frontiers of the known world – but also the meeting and overlap of different disciplinary areas and the emergence of new fields.

The Frontiers of Knowledge Awards honor fundamental disciplinary or interdisciplinary advances across a broad expanse of the knowledge map of the 21st century.

The BBVA Foundation is assisted in the award process by the **Spanish National Research Council (CSIC)**.

### Categories

---

- 1/ **Basic Sciences (Physics, Chemistry, Mathematics)**
- 2/ **Biology and Biomedicine**
- 3/ **Information and Communication Technologies**
- 4/ **Ecology and Conservation Biology**
- 5/ **Climate Change**
- 6/ **Economics, Finance and Management**
- 7/ **Humanities and Social Sciences**
- 8/ **Music and Opera**

In Humanities and Social Sciences, the award will alternate annually between these two disciplinary domains, with this fifteenth edition dedicated to the Humanities.

### Nomination

---

Nominations are invited from scientific or artistic societies and organizations, public or private R&D centers, university and hospital departments, schools of music, orchestras, and organizations working on or around the issue of climate change, as well as other institutions specified in the call conditions.

### Entry submission

---

The nomination period concludes at **23:00 GMT on June 30, 2022**.

**[www.frontiersofknowledgeawards-fbbva.es](http://www.frontiersofknowledgeawards-fbbva.es)**

**Fundación BBVA**

Plaza de San Nicolás, 4 · 48005 Bilbao  
Paseo de Recoletos, 10 · 28001 Madrid  
**[awards-info@fbbva.es](mailto:awards-info@fbbva.es)**



# The lessons of Lander

Eric Lander's resignation as President Biden's science adviser and director of the Office of Science Technology and Policy (OSTP), amid allegations that he bullied and demeaned subordinates, is the latest disappointment from an administration that has been struggling to guide the nation with sound science and science leadership. Lander's departure now leaves empty the first ever OSTP directorship to be added to the President's Cabinet. This vacancy joins the absence of permanent directors for the Food and Drug Administration (FDA) and the National Institutes of Health (NIH), not to mention a secretary of Health and Human Services (HHS) so disengaged as to appear absent. Let's hope the president appoints the best people—in brilliance and character—into these positions, stops undermining his own workplace policy of respect and dignity, and gets the country back on course to follow the science, as he pledged.

Biden's victory celebration, with signs boasting "The People Have Chosen Science," brought hope to the scientific community. After 4 years of attacks on science by former President Trump and his accomplices, Biden's early days were encouraging. Outstanding appointments were made to Biden's science team, including Alondra Nelson, Jane Lubchenco, Frances Arnold, and Maria Zuber. The new director of the Centers for Disease Control and Prevention (CDC), Rochelle Walensky, was an accomplished physician-scientist who argued for strict adherence to pandemic mitigation measures. But disappointment has built steadily over the past year, beginning with various nominees. There was a long delay in Lander's confirmation for the very reasons that have now brought on the current scandal. There was a protracted search for an FDA commissioner, a vital position during the pandemic. Even after Robert Califf was finally announced as the nominee, he has yet to be confirmed by the full Senate. And months after Francis Collins announced his retirement as NIH director, there is no sign of his replacement.

When it comes to the pandemic, the administration has not been able to get out of its own way. Rapid reversals of messaging on masks and boosters from the CDC have been commonplace, with the agency's director contradicting statements she made before she joined the administration. In two consecutive weeks, Anthony Fauci, the chief medical adviser, made predictions that didn't

happen: first on an airline vaccine mandate that didn't materialize and then on a test requirement for ending quarantine. It's been natural to wonder who's in charge. In his *Science* editorial, Eric Topol laid blame on ineffective leadership by Xavier Becerra, the HHS Secretary, who should be coordinating the nation's pandemic response.

And now, the latest mess. What is troubling about Lander's resignation is that it came under pressure and 2 months after the White House completed the investigation. Firing Lander was clearly not the White House's original intent, contradicting the president's promise to enforce a zero tolerance policy when it comes to treating colleagues disrespectfully. Lander's bullying of OSTP co-workers was initially reported by *Politico*, which obtained a recording of an OSTP staff briefing by White House administrators who conducted the investigation. White

House Press Secretary Jen Psaki confirmed the findings in a press briefing, where she faced understandably tough questions about the administration's approach to appropriate conduct. All Lander was required to do was apologize and hold "brown bags" with staff. Yet this was Biden's inaugural pledge: "If you are ever working with me and I hear you treat another colleague with disrespect, talk down to someone, I promise you I will fire you on the spot. On the spot. No ifs, ands or buts."

Maybe the White House decided to set aside that promise for Lander because he was about to take charge of Biden's recently announced Cancer

Moonshot initiative and testify before Congress about the Advanced Research Projects Agency for Health (ARPA-H), which seeks to redesign the nation's biomedical ecosystem. But Lander should be a lesson for the White House. Legitimate questions about his personal conduct were raised before and during his confirmation hearing. Enthusiasm for his brilliance and political acumen was tempered by accusations that he did not appropriately acknowledge the contributions of Nobel Prize winners Jennifer Doudna and Emmanuelle Charpentier to gene-editing technology. He apologized and then was appointed.

Biden has much work to do to maintain the confidence of the scientific community. It must begin with assembling strong science leadership, and that now includes replacing Lander immediately at the cabinet level. No ifs, ands, or buts.

—H. Holden Thorp



**H. Holden Thorp**  
Editor-in-Chief,  
*Science* journals.  
hthorp@aaas.org;  
@hholdenthorp

**"Biden has  
much work to do  
to maintain  
the confidence  
of the scientific  
community."**

# Rutgers University: R&D with Impact

Committed to research and development driven by  
a relentless pursuit of excellence



**\$907.9**  
million

Research grants and  
sponsored programs

**\$720**  
million

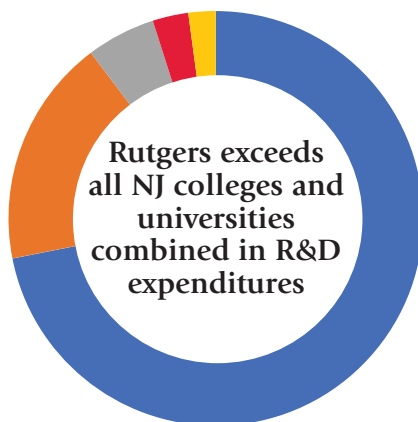
Research and development  
expenditures

**1187**

Active technologies to  
license and market

**1000+**

Companies partner with  
Rutgers researchers



## Top 5 Direct Federal Sponsors of Rutgers Research

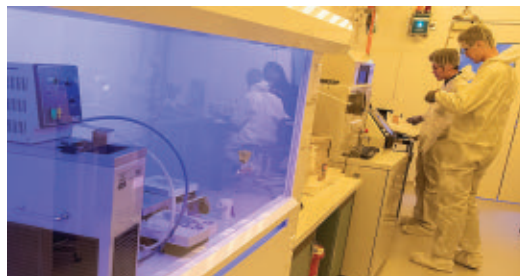
- National Institutes of Health \$229.7M
- National Science Foundation \$56.9M
- U.S. Health Resources and Services Administration \$17.2M
- U.S. Department of Education \$9M
- National Oceanic and Atmospheric Administration \$6.8M



## Recent Outcomes with Global Impact

- Invented COVID-19 diagnostic tests and serving as COVID-19 vaccines clinical trials site
- Pioneering use of underwater gliders for hurricane intensity forecasting
- Lead authorship of Intergovernmental Panel on Climate Change Reports
- Invented clean manufacturing technology for polymers and other monomers
- Co-lead investigator of large-scale urban test site for next-gen Wi-Fi

**Top 100**  
World's Most  
Innovative  
Universities —Reuters



**RUTGERS**  
THE STATE UNIVERSITY  
OF NEW JERSEY

*This is what **Excellence** looks like*  
[excellence.rutgers.edu](http://excellence.rutgers.edu)

Annual data current as of January 2022



# Science and social media

Long before the pandemic, scientists began flocking to social media, sharing ideas, thoughts, and information. But it is undeniable that the pandemic has boosted the visibility and engagement of scientists on many platforms, especially Twitter. Has this been good or bad for science? The answer is both.

On the positive side, social media can be a good way to collaborate on scientific questions quickly and transparently, and along the way, many outstanding scientists have been introduced to the public. It's also a good way for scientists to let off steam when the pressures of hard work and a skeptical public pile up. On the negative side, these wide-open forums allow forces bent on undermining science to cherry-pick the debates. In this week's issue of *Science*, commentaries about "Science and social media" explore these matters, which have become central to the scientific enterprise. As the authors make clear, scientists must give more consideration to the impact and inner workings of social media to use the medium effectively without inadvertently causing misunderstanding and being gamed by hyperalert trolls.

The pandemic has brought these tensions to the fore. For example, Kathleen Hall Jamieson of the University of Pennsylvania's Annenberg School for Communication has pointed out that instead of stating that "masks work," scientists should have been saying "masks help" because they can't completely prevent the spread of COVID-19. Those who communicate science may tend to be drawn to absolutes out of fear of seeming indecisive. However, there's a trade-off. An anti-masker who grudgingly wears a mask in public and catches COVID-19 could gleefully claim that fact as evidence that the scientific consensus is wrong. Though the scientific community should have learned this lesson, the hashtag #MasksWork still screams across Twitter. Similarly, the hashtag #VaccinesWork means to scientists that vaccination induces an immune response that decreases disease severity, but to some of the public, it may mean that vaccination completely prevents infection. Now, antivaxxers are using breakthrough infection cases with the Omicron variant to sow doubt.

Other problems arise when the give-and-take tumult of scientific discussion unfolds in the public eye. Science is an honorably self-correcting process. Interpretations are revised and sometimes experimental results are found to be incorrect, and conclusions are modified. The

system does a good job of converging ever closer to the truth, but the record of these changes, often preserved indefinitely on social media, provides material for agenda-driven naysayers to paint scientists as flip-floppers when they're just doing what scientists are supposed to do.

When conspiracy theories proliferate on social media, particularly about the pandemic, scientists sometimes use humorous posts to scoff at the claims. The highest engagement in my own personal Twitter account occurred when charlatan Scott Atlas (who was an adviser to President Trump) tweeted that many scientists supported the dangerous Great Barrington Declaration, which advocated for letting severe acute respiratory syndrome coronavirus 2 (SARS-CoV-2) spread. I replied to Atlas and said, "No they're not. I would know." The fact that this tweet far outperformed anything else that

I posted on the pandemic—comments backed by authoritative research—reflects how hungry folks are for a break in the tension. Of course, these kinds of exchanges can be taken out of context, which can make scientists appear out of touch with a doubting public.

The overarching problem is that the algorithms used by the social media companies actively discourage authoritative information—disagreement and outlandish statements result in more engagement. This point is discussed compellingly in the Perspective by Brossard and Scheufele. Most scientists don't appreciate how public resistance to facts can be amplified by inanimate algorithms, rather than by living conspiracy theorists, that reinforce what people choose to engage with.

What to do about all of this? At next week's virtual annual meeting (17 to 20 February) of the American Association for the Advancement of Science (the publisher of *Science*), I'll be moderating a discussion among four outstanding scientists and communicators who are on the front lines of these challenges: Jane Lubchenco (White House Office of Science and Technology Policy), Joelle Simpson (Children's National Hospital), Katherine Mack (North Carolina State University), and Kathleen Hall Jamieson (University of Pennsylvania). I'll be asking these leaders what the scientific community should be doing to leverage the power of social media to foster greater understanding of science and more constructive exchange of ideas. Tune in for an enlightening conversation.

—H. Holden Thorp



**H. Holden Thorp**  
Editor-in-Chief,  
*Science* journals.  
hthorp@aaas.org;  
@hholdenthorp

**"...scientists  
must give more  
consideration  
to the...inner  
workings of  
social media..."**

# NEWS

## IN BRIEF

Edited by Jeffrey Brainard

### ASTRONOMY

## Astronomers organize to combat satellite interference

**T**he International Astronomical Union (IAU) announced a new center last week to address the burgeoning constellations of satellites that may interfere with ground-based observations. A U.N. committee also said it would consider the issue—a first step toward international regulations. The constellations, such as SpaceX's Starlink, aim to provide global broadband access, but the sheer number of satellites—2800 now, potentially rising to 50,000—has alarmed professional and amateur stargazers alike.

On 3 February, IAU, which represents professional astronomers, announced the founding of its Centre for the Protection of the Dark and Quiet Sky from Satellite Constellation Interference. The center will gather data, sponsor research on making satellites less reflective and removing their trails from images, and lobby for regulation of satellite operators. Meanwhile, following advocacy by IAU and others, the U.N. Committee on the Peaceful Uses of Outer Space agreed to discuss on 14 February the satellites' impact on astronomy.

### 'Human challenge' ends safely

**COVID-19** | Opening an avenue to test new COVID-19 treatments and vaccines, scientists reported last week they had safely infected healthy young volunteers with SARS-CoV-2. In the unprecedented experiment, known as a human challenge trial, research subjects ages 18 to 29 were inoculated with nose drops containing a very low dose of an early strain of the pandemic coronavirus. Eighteen of 34 who were tracked developed confirmed infections, but none resulted in serious illness, the study investigators reported in a preprint on Research Square. Strikingly, symptoms and detectable virus in the throat developed quickly, by an average of 2 days after inoculation. None of the volunteers had contracted or been vaccinated against

COVID-19, but they would have received medications to treat any serious illness. The organizers of the human challenge study, at Imperial College London and elsewhere, are preparing to launch a follow-up trial, funded by the Wellcome Trust, with the more contagious and pathogenic Delta variant.

### Acquitted professor reinstated

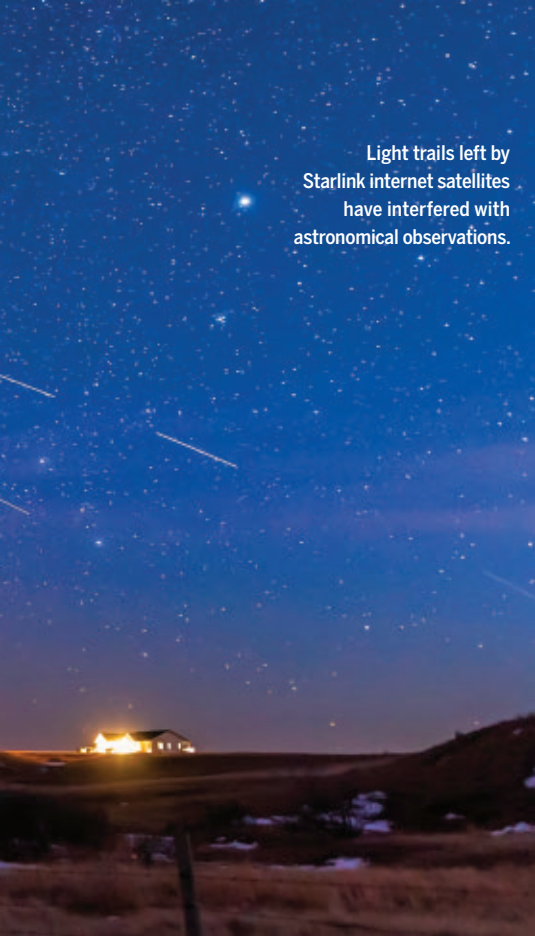
**RESEARCH SECURITY** | Nearly 5 months after being acquitted of charges he lied to U.S. officials about his ties to China, Anming Hu is again a tenured engineering professor at the University of Tennessee, Knoxville. It fired Hu in October 2020, 8 months after his arrest. Hu's case was the first to go to trial under the Department of Justice's 2018 China Initiative, which has brought similar

charges against some two dozen academics and resulted in the recent conviction of Harvard University chemist Charles Lieber. Last month, university officials agreed to help Hu, a Canadian citizen, with his application for permanent U.S. residency, the final sticking point in Hu's bid to be reinstated. The university gave Hu, who returned to campus on 1 February, \$300,000 to resume his research on nanomaterials.

### Cancer Moonshot relaunched

**BIOMEDICINE** | President Joe Biden last week proposed a "reignited" Cancer Moonshot, the research program he led as vice president during former President Barack Obama's administration—but the lack of a price tag has left research advocates





Light trails left by  
Starlink internet satellites  
have interfered with  
astronomical observations.

wondering about its trajectory. Those details could be filled in by the administration's upcoming 2023 budget proposal, expected in March. The new moonshot aims to cut cancer deaths by at least 50% over the next 25 years and to improve support for navigating the medical, financial, and emotional burdens of cancer treatment and survivorship. These actions will "end cancer as we know it," Biden said. The effort would encourage people to get cancer screenings they missed during the COVID-19 pandemic and support research on vaccines and blood tests that screen for multiple cancers. The original moonshot's funding, projected at \$1.8 billion over 7 years, will end in 2023; it has focused on immunotherapies, pediatric cancer treatments, and data sharing.

## CRISPR patent fight heats up

**INTELLECTUAL PROPERTY** | Lawyers for the two sides battling over who invented the genome editor CRISPR traded pointed exchanges at a hearing last week, as one team claimed a key scientist on the other improperly obtained early information on the "guide RNA" molecule that ferries a DNA-cutting enzyme to a target sequence. The lawyer representing the institutions of Jennifer Doudna and Emmanuelle Charpentier, who shared the 2020 Nobel Prize in Chemistry for developing CRISPR, said Feng Zhang of the Broad Institute of

MIT and Harvard was given confidential details on the guide RNA from a collaborator who reviewed the key initial CRISPR paper by Doudna, Charpentier, and colleagues. The lawyer representing the Broad group argued the information was presented publicly and stressed that Zhang's team, not Doudna's and Charpentier's, was the first to make the guide RNA work inside eukaryotic cells. When the U.S. Patent Trial and Appeal Board will rule is unknown.

## Airline ends monkey flights

**RESEARCH ANIMALS** | Kenya Airways has agreed to stop shipping monkeys for research after a truck carrying 100 long-tailed macaques the company had flown from Mauritius to New York City's John F. Kennedy International Airport crashed in Pennsylvania while en route to a quarantine facility. Three of the animals reportedly escaped and were later euthanized; others sat in crates on the road for hours. In a 27 January email to People for the Ethical Treatment of Animals (PETA) obtained by *Science*, Kenya Airways Chair Michael Joseph wrote that he was "horrified" by the accident and that "transport of any wild animals will no longer take place by Kenya Airways" after the current contract for the macaques ends on 28 February. PETA Senior Vice President Kathy Guillermo says another company could jump in to ship monkeys from Mauritius, one of the world's top suppliers of macaques for research.

## U.S. OKs some Iran nuclear work

**NONPROLIFERATION** | Key areas of civilian nuclear cooperation with Iran are back on the table as world powers seek to revive a lapsed nuclear arms control deal. On 4 February, the U.S. Department of State waived sanctions on several projects, including reconfiguring uranium centrifuges at Iran's underground Fordow enrichment site to produce isotopes used in medicine. Under the 2015 agreement, the United States and other nations granted Iran relief from economic sanctions in exchange for curtailing uranium enrichment and plutonium production. Then-President Donald Trump's administration pulled out of the deal in 2018, and 1 year later Iran ramped up enrichment and other proscribed activities. The new sanctions waivers allow China, Russia, and other countries to resume technical discussions on redesigning the Arak heavy water reactor to limit plutonium accumulation in spent fuel, providing uranium fuel for the Tehran Research Reactor, and eventually converting Fordow to an international physics research center.

### THREE Qs

## Archaeology makes amends

Recent discoveries suggest the first people arrived in the Americas at least 23,000 years ago, much earlier than researchers thought only a decade ago. But too often, scientists have not respected their living descendants, say paleogeneticist Jennifer Raff of the University of Kansas, Lawrence—whose book *Origin: A Genetic History of the Americas* was published this week—and archaeologist Joe Watkins, a member of the Choctaw Nation of Oklahoma who is the immediate past president of the Society for American Archaeology. (A longer version of this interview is at <https://scim.ag/3rJJMPT>.)

### Q: In your work on the peopling of the Americas, why has genetics been both vital and controversial?

**Joe Watkins:** Genetics has helped us figure out some of the basic questions.

**Jennifer Raff:** There are major gaps geographically and temporally in the genetic record. I am hopeful as we work in this space in a more ethical way, we can start to recover more genomes. [But] that is really up to the tribes. I don't think we're going to learn the whole picture unless this work is done to build relationships.

### Q: Can scientists do better?

**J.R.:** In the last few years, there have been increasing requirements for [community] engagement as part of ethics statements and increasing scrutiny as part of grant proposals.

**J.W.:** [Efforts] to create ethical guidelines for the field ... may be faltering, but it's progress—at least there are steps.

### Q: How do you address ancient DNA research, which destroys small amounts of human remains?

**J.W.:** [By] bringing in the social and historical concerns of American Indians and understanding the reasons they often feel the way that they do. Too often archaeology and genetics and many of the sciences have jumped in and said, "We need your dead ancestors to give you access to your history." ... We are within the generation that will repair those relationships.

**J.R.:** There are scientists who will say, "If we just hit them with enough data, they'll come around to our way of thinking." But there are other ways to view things, and we should be respectful of these traditional knowledges about history.



Eric Lander speaks to the press in January 2021, shortly after being named White House science adviser by then-President-elect Joe Biden.

## SCIENCE POLICY

# U.S. science adviser resigns after bullying charge

Eric Lander's abrupt departure comes as Biden administration pushes research initiatives

By **David Malakoff**

**A**n axiom of politics is that the higher you rise, the harder you can fall. This week, Eric Lander, the first White House science adviser to be elevated to the president's Cabinet, learned that firsthand. Lander, a prominent geneticist who has a close relationship with President Joe Biden, resigned from his position less than 1 day after a media report revealed a workplace investigation had found "credible evidence" Lander had bullied, disrespected, and demeaned members of his staff at the White House Office of Science and Technology Policy (OSTP).

"I am devastated that I caused hurt to past and present colleagues by the way in which I have spoken to them," Lander wrote in his 7 February resignation letter. "I have sought to push myself and my colleagues to reach our shared goals—including at times challenging and criticizing. But it is clear that things I said, and the way I said them, crossed the line at times into being disrespectful and demeaning, to both men and women." Lander said he would stay until 18 February to allow a smooth transition.

There was little public indication that Lander was under scrutiny until someone

leaked the results of the bullying investigation to *Politico*; even some of OSTP's roughly 140 staffers tell *Science* they were caught by surprise. Research advocates, however, have already begun to speculate about who might replace Lander and what, if anything, his departure will mean for a host of Biden's initiatives, including plans to create a new biomedical research agency and boost green energy and climate science.

Some observers aren't surprised Lander's tenure imploded after less than 275 days. Although he is a brilliant scientist—known for co-leading the public effort to sequence the human genome and founding the Broad Institute of MIT and Harvard, a genomics powerhouse—Lander has a reputation for appearing egocentric, abrasive, and insensitive. He also drew fire for downplaying, in a 2016 *Cell* essay, the role of two female scientists in developing the CRISPR gene-editing technology. (Lander later apologized for the essay.)

Such issues led some to criticize Biden for nominating him—and Lander's manner apparently led to his downfall. According to *Politico* and White House officials, in September 2021, an OSTP attorney, Rachel Wallace, filed a complaint against Lander and "other OSTP leadership," al-

leging they had disparaged staff and demoted Wallace after she criticized such behavior. A 2-month investigation concluded that Wallace's reassignment was not improper and found no evidence of gender-based discrimination. But in a recording of a January White House meeting given to *Politico*, officials described Lander's behavior as "very, very serious" violations of White House policies on creating a "safe and respectful workplace." They required "corrective" actions that included trainings and having Lander meet with staff, and pledged to review the matter in 30 to 45 days.

Three days before *Politico* ran its 7 February bombshell, Lander sent an email apologizing for his behavior to OSTP staff. But it was too little, too late. After the story appeared, pressure grew on the administration to act. At a televised White House press conference, a reporter asked why Biden had not removed Lander, given the president's pledge to fire any appointee who disrespected colleagues, "on the spot, no ifs, ands, or buts." The science committee of the House of Representatives issued a bipartisan request to review the investigation. AAAS (publisher of *Science*) disinvited Lander from speaking at its annual



meeting. Within hours, Lander had submitted his resignation.

That outcome didn't surprise physicist Neal Lane, science adviser to former President Bill Clinton. "He hurt a lot of people," he says. "On top of that, he hurt the president, which is a mortal sin."

Although OSTP is a small office with relatively little clout, observers say Lander deserves credit for helping advance important research policies. He has promoted plans for a new agency to fund high-risk medical research, the Advanced Research Projects Agency for Health. And OSTP has been in the middle of efforts to devise new rules aimed at curbing improper foreign influence in U.S.-funded research.

Some believe any damage to such efforts, including a renewed cancer research "moonshot," will be short-lived. Lander's "behavior is regrettable, but it doesn't mean these programs will grind to a halt," says Mary Woolley, president of the biomedical research advocacy group Research!America. "These big things don't depend on a single person."

"OSTP will get past this," says Chris Fall, former head of OSTP's national security division and now vice president for applied science at MITRE Corp. "The only real source of the [OSTP] director's authority," he notes, is the president. So, "If the president wants something done, it'll happen."

Still, it's not clear whether Lander's replacement will be able to replicate his relationship with Biden. The two men have known each other for decades, and worked together on issues such as cancer research. "Given how much attention science and innovation are getting these days, [that kind of relationship] matters," one lobbyist says.

Observers say one person who might get the OSTP director's job, at least on an interim basis, is marine biologist Jane Lubchenco, who led the National Oceanic and Atmospheric Administration under former President Barack Obama and now handles climate change issues at OSTP. A permanent replacement will need Senate confirmation, and federal rules allow an interim head to serve for some 9 months, so it may be some time before Biden announces a nominee.

In the meantime, Lander's rocky tenure in the White House demonstrates that a key part of the OSTP job is "building relationships and coalitions," the lobbyist says. "At Broad [Lander] could rule his own kingdom. But in the White House you have lots of colleagues who also hold sway ... and his effectiveness was clearly hampered by how he treated other White House officials and his own staff." ■

With reporting by Jocelyn Kaiser and Jeffrey Mervis.

## BIOMEDICINE

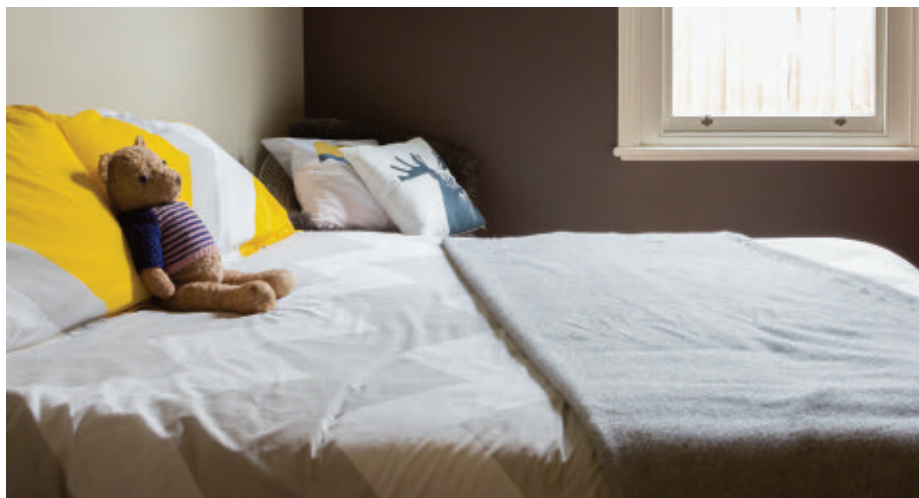
# Geneticists find clues to unexplained child deaths

## Sequencing mysterious cases yields mutations linked to seizures and arrhythmias

By **Kelly Servick**

**I**n 1997, Laura Gould put her 15-month-old daughter, Maria, down for a nap and returned to find her unresponsive. She had died suddenly, with no clues to explain the tragedy besides a fever the night before. When her daughter's body was sent to the medical examiner's office, "I thought they'd call me in an hour and tell me what happened ... like on TV," Gould says. Months later, neither that office nor independent pathologists had an explanation. "I hated ending it with 'the autopsy was inconclusive, go on and live your life

"Having this data is important," says Marco Hefti, a neuropathologist at the University of Iowa Carver College of Medicine who was not involved in the new studies. SUDC is not a single disease, but "a grab bag of different things—and the more of those different things you can pull out, the better for everybody." Neither study can say with certainty that a mutation is responsible for a child's death. But the findings provide a basis for animal studies that could reveal how the genetic changes interfere with vital functions. They might also inform future child death investigations and potentially even screening programs to prevent deaths.



now," she says. "It just didn't really feel like that was an option."

Gould co-founded a nonprofit foundation to support grieving parents, raise research funds, and increase awareness of sudden unexplained death in childhood (SUDC), a term used for children older than 12 months. In the United States, roughly 400 deaths fall into this category each year—about one-quarter as many as are labeled sudden infant death syndrome (SIDS). Two recent genetic analyses, one funded in part by Gould's SUDC Foundation, now suggest potential causes for at least a small fraction of cases: mutations in genes associated with epilepsy, heart arrhythmias, and neurodevelopmental disorders.

Research on SUDC has lagged that on the more common and better known SIDS. Yet, biologically, SIDS and SUDC "may be part of a spectrum," says Ingrid Holm, a medical geneticist at Boston Children's Hospital. In both, death often occurs during sleep, and researchers suspect contributors including undetected heart defects, metabolic disorders, and central nervous system abnormalities. The children who die are roughly 10 times more likely than the average child to have a history of febrile seizures—convulsions that come with fevers in young children, notes neurologist Orrin Devinsky of New York University (NYU) Langone Health.

Following a death, medical examiners routinely take blood or tissue samples and

sometimes order genetic tests to look for dangerous known mutations. With SIDS, studies that sequenced entire exomes—the protein-coding regions of DNA—implicated certain rare genetic mutations. But until now, no whole-exome studies have looked at a large collection of SUDC cases to find genetic clues.

A registry of SUDC cases set up by Gould and Devinsky at the NYU Grossman School of Medicine in 2014 made such a study possible. Their team sequenced the exomes of 124 “trios,” each made up of parents and a child who died suddenly and without explanation between the ages of 11 months and 19 years. The researchers searched for mutations in genes previously associated with cardiac dysfunction or epilepsy. They found variants in eight genes that they think contributed to 11 of the deaths, they reported in the *Proceedings of the National Academy of Sciences* in December 2021.

In seven of those cases, the mutation was *de novo*, meaning neither parent carries it—a finding that bolsters the case that it contributed to death. Six of the variants affected genes involved in calcium signaling—the flow of ions across cellular channels, which regulates diverse processes, including heart contractions and neuron firing.

In a second study, Holm and colleagues explored 352 cases of death in either infants or children. They searched for mutations in 294 genes linked to neurologic conditions, cardiac dysfunction, and conditions that affect metabolism or multiple organ systems. In the 73 cases where DNA from both parents was available, they also looked across the exome for *de novo* variants. “Likely contributory variants” emerged for 37 of the deaths, including six of the 32 deaths in children older than 1 year, the team reported last month in *Genetics in Medicine*. Two of these variants were in genes already associated with rare neurodevelopmental disorders but not with sudden death, suggesting an unrecognized potential consequence of those disorders. Both studies identified mutations in *SCN1A*, a gene known to be involved in epilepsy.

The proportions of deaths with possible explanations in the new studies may seem small, Hefti says, but the approach applied broadly could provide new information to dozens of families in the United States alone. Learning that the potential cause of a child’s death is a *de novo* variant could reassure parents that they’re unlikely to have passed a dangerous mutation to their other children, he says.

In contrast, if a potential genetic cause is inherited, other family members could be tested and take preventive steps if they’re affected, notes Rachel Rabin, a genetic counselor at NYU Langone. For ex-

ample, if parents or siblings carry a disease-linked variation of *SCN1A*, a neurologist can run tests and may prescribe medication if seizures are identified, Rabin says.

Despite the potential value of genetic testing in child or infant death investigations, it’s not always done. “The factors are mostly money, of course,” says Michael Klitschar, a forensic pathologist at Hannover Medical School. Among U.S. medical examiners’ offices, “I would guess that the majority do not do [genetic testing] on every case,” says Kathryn Pinneri, director of Montgomery County Forensic Services in Conroe, Texas, and president of the National Association of Medical Examiners. But declining costs have made it more common in the past 5 years, she says.

The New York City medical examiner’s office investigates unexplained deaths among infants and children using its own panels of genetic tests. Geneticist Yingying Tang, who heads the in-house molecular genetics lab there, says the new study results make her “pretty confident with the cardiac and epilepsy panels I have.” Investigations of pediatric deaths in that office have revealed mutations in several of the genes identified in these studies, she says.

Some parents of children who died suddenly hope genetic analysis will make it possible to screen embryos for a dangerous genetic variant before another pregnancy, says Richard Goldstein, a palliative care pediatrician at Boston Children’s and co-author of the new study. Developing and justifying such screening would require first firming up any causal link between a variant and sudden death. His team plans to delve into the mechanisms of some of the recently identified variants by inserting them into zebrafish to look for differences in behavior or life span.

In principle, some dangerous variants could be added to those routinely screened for in newborns, Devinsky says. “I think that’s where [the field] should probably go.” But in many cases the consequences of a mutation remain obscure, Klitschar notes. Linking a child’s death to a rare mutation in an arrhythmia-related gene doesn’t tell researchers the risk of cardiac arrest in a living baby with the same mutation. Giving all such children implants to correct irregular rhythms might cause more problems than it solves, he says.

Gould, whose daughter’s death remains unexplained, hopes the SUDC registry can help clarify the risk factors. It now includes 292 families, and her team continues to invite parents to participate. “If you want your child’s information to benefit research,” she says, “that opportunity can sometimes be comforting.” ■

## PALEOANTHROPOLOGY

# A 10,000-year head start for modern humans in Europe?

Tooth and tools suggest moderns and Neanderthals took turns in French cave

By Michael Price

A single, broken molar found buried within a windswept rock shelter in southeastern France could push back the first evidence of modern humans in Europe by nearly 10,000 years.

According to an international team, the tooth and dozens of stone tools from the same sedimentary layer belonged to a member of *Homo sapiens* who lived some 54,000 years ago, a time when Neanderthals were thought to have been the sole occupants of Europe. The findings also paint a remarkable picture of the intimacy of modern humans and their Neanderthal neighbors, suggesting they may have traded occupancy of the cave several times—once in as little as a year.

“I found this paper absolutely fascinating,” says Kristin Krueger, a dental paleoanthropologist at Loyola University Chicago. “From what I can tell, this is solid evidence ... that modern humans made it to Europe earlier than thought.”

For others, the excitement is tempered with caution, especially given that the claim relies chiefly on a single modern human tooth. “There are several ‘ifs’ here,” says paleogeneticist Carles Lalueza-Fox of the University of Barcelona. “To make a stronger case, we should have at least more solid skeletal or genetic evidence.”

After arising in Africa, modern humans trekked into the Middle East as early as 180,000 years ago, where they may have first met and mated with the Neanderthals, who already lived in Europe and Asia. (Today, non-Africans carry the legacy of those matings, having inherited about 2% of their DNA from our closest cousins.) But moderns were late arrivals in Europe, where until now the earliest evidence of their remains and artifacts came from Bulgaria’s Bacho Kiro Cave, dated to about 45,000 years old.





In Grotte Mandrin, archaeologists Laure Metz (left) and Ludovic Slimak hold teeth they think belonged to a modern human and a Neanderthal, respectively.

The discoveries that could change that picture come from a rocky overhang known as Grotte Mandrin in the verdant Rhône River Valley. Since 1990, excavations of the cave's floor have delved into 12 sedimentary layers deposited between 80,000 and 35,000 years ago.

In 2006, what archaeologists call layer E yielded a trove of precisely sharpened stone points and animal bones. Six years later, they found a partial molar—a baby tooth. “We spent 15 years excavating this layer,” says Ludovic Slimak, a paleoanthropologist at the University of Toulouse, Jean Jaurès. “We went slowly because it’s very rich and there’s a lot of very little material.”

Slimak and colleagues radiocarbon dated animal bones with butchery marks from layer E to between 57,000 and 52,000 years ago. Luminescence dating of sediments in the layer, which determines when quartz minerals were last exposed to sunlight, returned the same date range. Meanwhile Clément Zanolli, a paleoanthropologist at the University of Bordeaux, analyzed the layer E molar and eight other teeth found in other layers. Although the molar was broken, it retained a telltale part of its cusp called the talonid. The modern human talonid gives their teeth a squarer outline than those of Neanderthals. “[This] tooth is quite square,” Zanolli says, indicating it belonged to a young modern human. In contrast, all the teeth from layers above and below layer E had distinctly Neanderthal characteristics.

Layer E’s stone tools back up the tooth’s identification, Slimak says: They are smaller, more precisely made, and more standardized than the tools from the layers bearing Neanderthal teeth, which resemble Neanderthals’ characteristic Mousterian tools. “With Neanderthal tools, every tool is a creation,” Slimak says. “If you look at 1000 tools, each

will be completely different. But with a *Homo sapiens* industry ... it’s superstandardized, superregular.”

Tools and teeth from the next few layers above layer E suggest Neanderthals at some point reoccupied Grotte Mandrin. Then, in layers dated to about 42,000 years ago, the tools once again appear to have been made by modern humans; they resemble the “proto-Aurignacian” tools found in other modern human sites from the same time period, Slimak says.



This broken baby tooth may be the oldest known modern human fossil in Europe.

Together, that evidence shows modern humans had reached southern France about 54,000 years ago, the researchers report this week in *Science Advances*. The settlers probably came from the east and traveled up the Rhône River Valley from the Mediterranean coast, Slimak says. After modern humans first moved into the shelter, they and Neanderthals took turns for another 10,000 years.

“The authors make a strong case for the dates,” Krueger says. “They provide the stratigraphic sequence, completed over many,

many years of excavation, [and] also use multiple methods for dating each layer.”

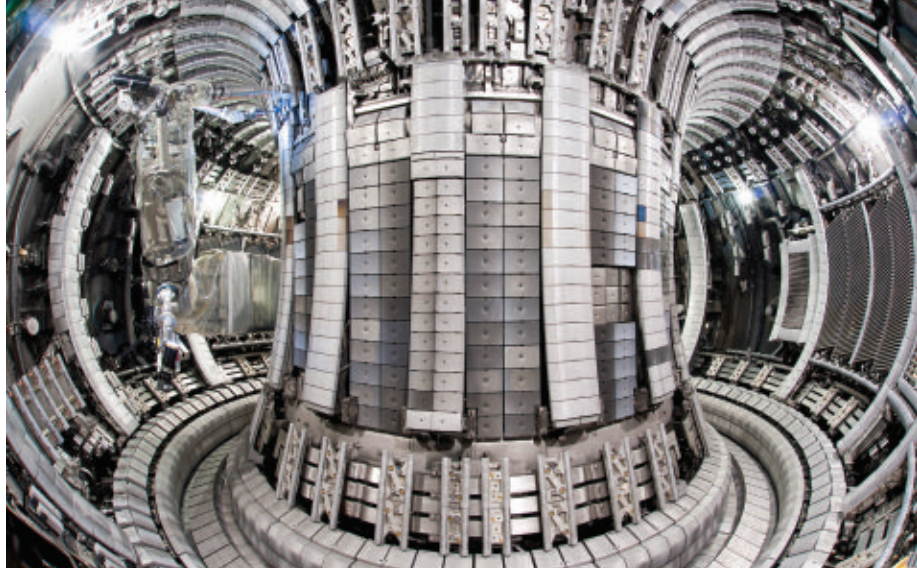
But the layer E molar is key to the argument. Shara Bailey, a dental paleoanthropologist at New York University who developed methods to distinguish modern and Neanderthal teeth, isn’t certain the molar came from a modern human. Too much of it is missing, she says. “It would be so cool if it were true ... but it’s not a slam dunk.”

If members of our species really did make an early appearance in the cave, they may have had close contact with Neanderthals, one intriguing data point suggests. Thin layers of mineral deposits form along the walls of rock shelters like Grotte Mandrin, recording the passage of wet and dry seasons, a bit like tree rings. These mineral layers can trap soot from fires burning inside the caves, offering microscopic records of campfires past. This new technique, known as fulgino-chronology, was first described in 2018 by one of the paper’s co-authors, Ségolène Vandevelde, an archaeologist at the University of Paris-Saclay.

Tiny chunks of mineral fell from the cave wall into each excavated layer. The sequence of soot layers in wall chunks from layer E overlapped with the sequence in chunks from the layer immediately beneath it, which held Neanderthal tools. That suggests only a brief period passed between the formation of the layers and therefore between the exit of the Neanderthals and the entrance of moderns—perhaps no more than a single calendar year. “They probably met at some point, but we cannot say for sure they met in the cave,” Slimak says.

Rachel Wood, a radiocarbon scientist at Australian National University, calls the study “remarkable.” But she isn’t confident the researchers can pinpoint the timing of soot layers from 54,000 years ago to within 1 year given the evidence they’ve presented so far. “Given the uncertainties ... I’d be skeptical about this supporting a short transition between the two [layers].”

The paper’s findings could be revolutionary for our understanding of the transition between the last Neanderthals and the first moderns in Europe, says Francesco d’Errico, an archaeologist also at the University of Bordeaux. But he and others want far more evidence. “If the pattern proposed is confirmed by future discoveries, we will certainly need to change our view of this transition,” he says. “Such a paradigm shift is entirely possible but requires ... more sites and more unequivocal evidence.” ■



## FUSION

# European fusion reactor sets record for sustained energy

World's largest tokamak paves the way for ITER with a capstone run of pulses using power-producing tritium

By **Daniel Clery**

In experiments culminating the 40-year run of the Joint European Torus (JET), the world's largest fusion reactor, researchers announced this week they have smashed the record for producing controlled fusion energy. On 21 December 2021, the U.K.-based JET heated a gas of hydrogen isotopes to 150 million degrees Celsius and held it steady for 5 seconds while nuclei fused together, releasing 59 megajoules (MJ) of energy—roughly twice the kinetic energy of a fully laden semitrailer truck traveling at 160 kilometers per hour. The energy in the pulse is more than 2.5 times the previous record of 22 MJ, set by JET 25 years earlier. “To see shots in which it sustains high power for a full 5 seconds is amazing,” says Steven Cowley, director of the Princeton Plasma Physics Laboratory (PPPL).

JET's achievement doesn't mean fusion-generated electricity will flow into the grid anytime soon, however. Researchers had to put roughly three times as much energy into the gas as the reaction produced. But the result gives them confidence in the design of ITER, a giant fusion reactor under construction in France, which is supposed to pump out at least 10 times as much energy as is fed in. “This is very good news for ITER,” says Alberto Loarte, head of ITER's science division. “It strongly confirms our strategy.”

Fusion has long been promoted as a future green energy source. If the same nuclear re-

action that powers the Sun could be duplicated on Earth, it could provide plentiful energy with small amounts of nuclear waste and no greenhouse gases. But producing net energy has proved elusive. In August 2021, researchers at the National Ignition Facility, which triggers fusion by heating and crushing tiny pellets of fuel with 192 converging laser beams, reported they had gotten to 71% of this break-even mark, closer than anyone else, but only for an instant (*Science*, 20 August 2021, p. 841).

JET and ITER represent a different approach, one that is more suitable for sustained energy production. Both are tokamaks: doughnut-shaped vessels wrapped in a grid of powerful magnets that hold the superhot ionized gas, or plasma, in place and prevent it from touching and melting the vessel walls. Researchers in the 1980s believed JET and a rival machine at PPPL (now dismantled) would quickly reach breakeven. JET got close in 1997, generating a short, 1.5-second burst that reached two-thirds of the input power.

But slow progress spurred researchers in the 1990s to design ITER, a giant tokamak 20 meters wide that holds 10 times as much plasma as JET. A larger plasma volume, models predicted, would maintain fusion conditions longer by making it harder for heat to escape. The \$25 billion ITER, funded by China, the European Union, India, Japan, South Korea, Russia, and the United States, is due to start operation in

The Joint European Torus produced a record 59 megajoules of energy over 5 seconds.

2025 but won't produce large amounts of power until 2035, when it is due to start burning the energy-producing isotopes deuterium and tritium (D-T).

JET's early operation taught ITER's designers a key lesson. JET was lined with carbon because it resists melting. But it turned out to “soak up fuel like a sponge,” says Fernanda Rimini, JET's plasma operations expert. So ITER's designers opted to use the metals beryllium and tungsten.

No one knew how they would perform, however, and JET provided a testbed. Starting in 2006, engineers upgraded its magnets, plasma heating system, and inner wall to make it as ITER-like as possible. When it restarted in 2011, the signs were not good, says Cowley, who was then director of the Culham Centre for Fusion Energy, which runs JET on behalf of the European Union's EuroFusion agency. “We couldn't get into the same [high power] regimes.”

Painstakingly, the JET team worked out what was going on. They found that high energy plasma ions were knocking out tungsten ions from the wall, causing them to radiate energy and bleed heat out of the plasma. Over many years, the team worked out a coping strategy. By injecting a thin layer of gas, such as nitrogen, neon, or argon, close to the vessel wall, they could cool the outermost edge of the plasma and stop ions from hitting the tungsten. “Bit by bit we clawed back performance,” Cowley says.

In September 2021, JET researchers set out to see what their redesigned machine could do. That meant switching fuel, to D-T (*Science*, 5 April 2019, p. 14). Most fusion reactors run on ordinary hydrogen or deuterium, which allows them to explore the behavior of plasmas while avoiding the complications of tritium, which is both radioactive and scarce. But JET staff were itching to test their machine in real power-producing conditions. First, they had to revive the reactor's tritium-handling facilities, not used for 2 decades, which extract unburned tritium and deuterium ions from waste gas after each shot and recycle them.

The recent successes set the stage for ITER and show its designers' gamble on a full metal wall ought to pay off. “This confirms we took the right level of risk,” Loarte says. But for JET, the D-T run is something of a swan song. Joe Milnes, head of JET operations, says the reactor will have one more experimental run, from mid-2022 to the end of 2023, before closing. “It's been the most successful fusion experiment ever,” he says, but it's time “to hand the baton to ITER.” ■

PHOTO: CHRISTOPHER ROUX (CEA-IRFM)/CC BY



## MATERIALS SCIENCE

# An electric jolt strips valuable metals from waste

New method can pull rare earth elements from electronic waste and coal ash

By Sam Kean

**A**s chemists scramble to find ways to reclaim valuable metals from industrial waste and discarded electronics, one team has found a solution that sounds a little like magic: Zap the trash with flashes of electric heat.

Rare earth elements (REEs) present an environmental paradox. On one hand, these dozen or so metals, such as yttrium and neodymium, are vital components of wind turbines and solar panels, and cheap sources of REEs could give those green technologies a huge boost. On the other, mining REEs causes billions of dollars of environmental damage each year. Because the elements occur in low concentrations, mining companies have to chew through tons upon tons of ore, stripping and gutting landscapes. Moreover, REEs are often mixed with radioactive elements, and extracting them creates low-level nuclear waste.

Old electronics and other industrial waste, in contrast, are rich in REEs. But existing recycling methods are inefficient and expensive, and require corrosive chemicals such as concentrated hydrochloric acid. For every environmental problem that REEs could solve, they seemingly introduce two more.

The new process could help break that logjam. This week in *Science Advances*, a team led by organic chemist James Tour of Rice University reports using pulses of electrical heat to make it easier to extract REEs from industrial waste. The technique is roughly twice as efficient as current methods and uses far more benign chemicals.

"It's a very interesting approach," says Amir Sheikhi, a chemical engineer at Pennsylvania State University, University Park, who studies REE extraction. "With a pretty short, high-temperature treatment ... these rare earth elements are set free."

Tour's team tested its process on fly ash, a powdery gray byproduct of burning coal that contains concentrated levels of the REEs originally present in the coal. The researchers mixed the ash with carbon black to improve electrical conductivity, and then placed the mixture in clear quartz tubes 1 to 2 centimeters wide and 5 to 8 centimeters long. Capacitors on the ends of the tubes sent a pulse of current through, causing the tube to flash yellow-white and produce a tiny puff of smoke. The temperature of the

mixed powders spiked to 3000°C within 1 second, then rapidly cooled.

That spike of heat does two things. When coal is burned as fuel, microscopic bits of glass form inside and trap REEs, making them hard to extract. But the bursts of electric heat shock and shatter the glass, freeing the rare earths. Flash heating also induces chemical changes: Phosphates of REEs transform into REE oxides, which are more soluble and easily extractable.

As a result of these changes, Tour's group can use less corrosive solutions to extract the REEs. Tour's team gets by with concentrations of hydrochloric acid 120 times lower

the international REE market (see graphic, left), and Japan, the European Union, and the United States have complained to the World Trade Organization that China uses its near-monopoly to curtail exports and drive up prices. (Japan has since explored measures such as dredging up REE-rich mud from the deep ocean floor, which isn't exactly eco-friendly.) Relying on a foreign supplier for REEs puts countries "at an economic disadvantage if not a natural security disadvantage," says Steven Winston, an independent chemical engineer and former vice president of Idaho National Laboratory who has studied mining waste. Flash heating of waste might open an alternate supply.

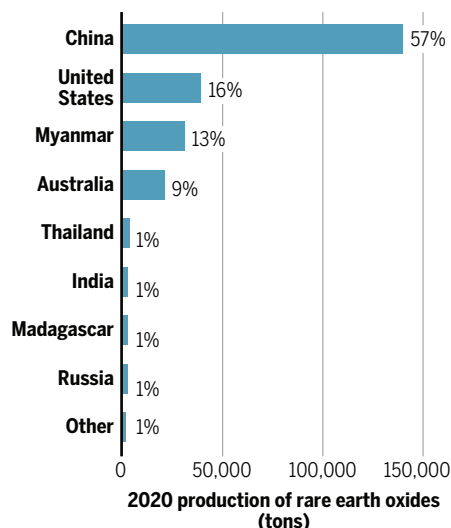
But hurdles remain. After the REEs are extracted, they need to be separated into individual elements for different applications. That "is still a big challenge," says Heileen Hsu-Kim, an environmental engineer at Duke University who studies REE extraction. Companies usually use organic solvents such as kerosene, which themselves cause environmental problems or are difficult to recycle. To address such concerns, Sheikhi's team fashioned biodegradable cellulose into filaments sporting "hairs" with functional groups that selectively bond to and capture neodymium, a vital component in the magnets in wind turbines.

Moreover, Tour's process would need to be massively scaled up to make a difference. Sheikhi points out that "typically, high-temperature processes are expensive." But Tour's team argues that because flash heating is speedy, costs are low, just \$12 per ton of fly ash. As for scaling up, the team previously developed a flash heating process to transform old tires and plastics into graphene (*Science*, 31 January 2020, p. 496), and a spinoff company has already scaled that process up using larger flash heaters.

If Tour's method does work out, there's plenty of industrial waste to have at. Every year, humankind produces 40 million tons of electronic waste, 150 million tons of red mud, and 750 million tons of coal fly ash, much of it piled in giant mounds. Considering that burning coal helped create our current environmental mess, it would be fitting if the spark for green technologies could be extracted from its waste. "We don't need any more coal to be burned for this [recycling] process to work," Tour says. "We have sufficient mountains of this forever." ■

## China's rare earth dominance

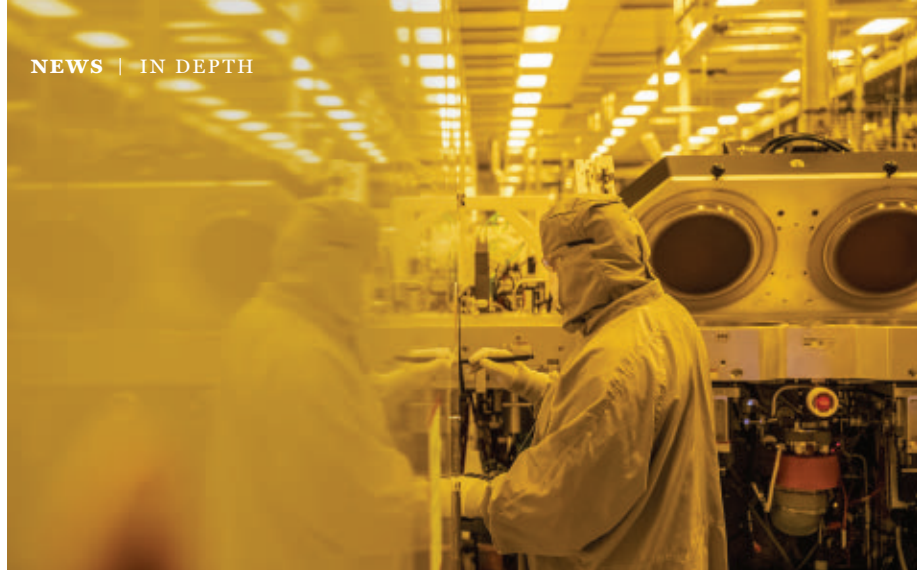
Rare earth elements are vital components of green technologies. Other countries have complained that China uses its market dominance to drive up prices by limiting exports.



than current extraction methods, and still manages to extract twice as much. "It's so dilute," Tour says, "that—well, I wouldn't do it, but I think you could drink [it]."

In addition to fly ash, Tour's team has extracted REEs from so-called red mud—a byproduct of making aluminum—and from electronics. In the latter case, the team gutted an old laptop and ground its circuit board into powder to experiment with.

Many government officials are keen on grabbing REEs from waste, rather than mining them, for economic as well as environmental reasons. China has long dominated



Congress wants to increase U.S. high-tech production such as semiconductor manufacturing, seen at GlobalFoundries in Malta, New York.

## SCIENCE POLICY

# Massive U.S. innovation bills face difficult road in Congress

Lawmakers must reconcile competing visions for boosting research spending and helping high-tech industries

By Jeffrey Mervis

**R**emember when your mother said cramming too much food into your mouth could make you choke? Democrats in the U.S. Congress are about to find out whether that warning also applies to their ability to enact sweeping legislation that aims to double the budgets of the National Science Foundation (NSF) and other key research agencies, pour money into the high-tech industry, prevent “malign foreign influence” on U.S. research, and curb sexual harassment in academic science.

There are two versions of the legislation, both designed to maintain the country’s technological edge over China. Last week, the House of Representatives passed the America COMPETES Act, a bill similar to the U.S. Innovation and Competition Act approved by the Senate in June 2021. Now, ironing out the differences in the massive bills—which are 5200 pages combined and have price tags topping \$250 billion—will test the Democrats’ razor-thin majorities in each body.

Both bills would authorize the government to spend tens of billions of dollars on research. But the numbers are mostly aspirational. Congress would have to approve most of the spending through its annual budget process, and higher education lobbyists fear a repeat of what happened in 2007 and 2010, when lawmakers authorized big hikes in science spending that never materialized.

At NSF, the bills call for adding a technol-

ogy directorate and doubling the agency’s overall budget over 5 years. The Department of Energy’s (DOE’s) Office of Science and its laboratories would get a similar boost, and the Department of Commerce would fund a new network of regional innovation hubs. The nation’s semiconductor industry would receive \$52 billion, mostly to increase manufacturing capacity but also to strengthen microelectronics research facilities.

Both bills call for tightening oversight of collaborations with China and a few other countries seen as exerting a “malign” influence on U.S. research. Scientists with federal grants would be barred from participating in Chinese talent recruitment programs and universities would be required to provide more information about foreign donors. The bills also seek to stamp out sexual harassment in academia, calling for a uniform policy on reporting allegations and findings to federal funding agencies.

There are important policy differences between the two bills, however. The Senate wants NSF’s new technology directorate to focus on 10 key disciplines, such as artificial intelligence and quantum computing, whereas the House asks NSF to combat climate change, reduce economic and social inequality, and build a robust scientific workforce along with advancing strategically important areas.

“The Senate bill implies a trade-off between supporting key technologies to maintain our competitive edge and improving

the quality of life for all Americans,” says a Democratic staffer on the House science committee, which crafted many of the research provisions in the COMPETES bill. “But we think that technology is simply a means to an end, and that you can do both things.”

The House and Senate also differ on how to spread federal research dollars more equitably across the country, including to institutions that enroll large numbers of students from groups underrepresented in science. The Senate bill requires that 20% of the money slated for NSF and DOE be spent in the roughly two dozen states that receive the fewest federal research dollars. In contrast, the House bill avoids any mandatory set-asides, instead creating new programs that target institutions in those have-not states.

The COMPETES Act would also change immigration policy to allow more foreign students to stay after they earn advanced technical degrees at U.S. universities. One provision would exempt them from limits on applying for permanent residency status, and another would create a visa category for budding high-tech entrepreneurs. The Senate bill contains no such changes, and those measures are likely to be opposed by lawmakers who want to limit immigration.

Unlike the Senate bill, the House bill includes several climate change provisions, including a call for the United States to spend \$8 billion to help poorer nations respond to the crisis and \$3 billion to help U.S. solar energy companies become less reliant on components made in China.

The House bill’s sweeping scope is its strength, says Representative Eddie Bernice Johnson (D-TX), chair of the House science committee. “We are making investments to build clean energy ... reinforce our national security, enhance our semiconductor manufacturing capabilities, and so much more,” Johnson said before passage of the bill, which was backed by only one Republican—and opposed by one Democrat.

The science panel’s top Republican, Representative Frank Lucas (OK), explained his party’s opposition during debate on the bill. Democrats, he said, “hijacked good bipartisan bills dealing with U.S. competitiveness and countering the malign influence of China to pass another Democratic wish list that will go nowhere in the Senate.”

Lawmakers from both parties hope to finalize a bill by this spring. President Joe Biden voiced his support, saying: “America can’t afford to wait.” But a full legislative agenda and the upcoming November elections could make it difficult to reach a bipartisan deal. ■



**eppendorf**  
**& Science**  
**PRIZE FOR**  
**NEURO**  
**BIOLOGY**

2021 Winner  
Amber L. Alhadeff, Ph.D.  
Monell Chemical Senses Center, USA  
For research on the gut-brain control  
of hunger circuits



## Tell the World About Your Work!

**Application Deadline**  
June 15, 2022

### **Eppendorf & Science Prize for Neurobiology**

The annual Eppendorf & Science Prize for Neurobiology is an international prize which honors young scientists for their outstanding contributions to neurobiological research based on methods of molecular and cell biology. The winner and finalists are selected by a committee of independent scientists, chaired by *Science's* Senior Editor, Dr. Peter Stern. If you are 35 years of age or younger and doing great research, now is the time to apply for this prize.

### **As the Grand Prize Winner, you could be next to receive**

- > Prize money of US\$25,000
- > Publication of your work in *Science*
- > Full support to attend the Prize Ceremony held in conjunction with the Annual Meeting of the Society for Neuroscience in the USA
- > 10-year AAAS membership and online subscription to *Science*
- > Complimentary products worth US\$1,000 from Eppendorf
- > An invitation to visit Eppendorf in Hamburg, Germany

It's easy to apply! Write a 1,000-word essay and tell the world about your work. Learn more at:

[eppendorf.com/prize](http://eppendorf.com/prize)



## FEATURES

Children test out a robot that can allow ill students to attend school with their classmates.

# DREAM MACHINE

In a few classrooms, robots attend for children ailing at home.  
A researcher wants to know how to make the devices better

In a sunny room at the Boys & Girls Club in Calistoga, a tiny city in California's Napa Valley, Veronica Ahumada is setting up her robot when a bespectacled little boy wanders in to ask what she's doing. Ahumada points to the device—basically a tricked-out tablet on a meter-tall post, mounted onto gyroscopic roller wheels—and he yelps like he's seen a ghost. “She has a robot!” he hollers, bolting out the door.

Soon, about 40 tweens fill the room. Many are Latino like Ahumada, and they are here for after-school child care while their parents work. When she invites them to guess what the robot is for, their ideas bubble over: to play video games! To go to the supermarket! To help people get around! To take orders at a restaurant! To take over the world!

By **Alla Katsnelson**;  
Photography by **Xavier Mascareñas**

Ahumada, who studies health informatics and human-robot interactions at the University of California (UC), Davis, acknowledges each child's suggestion, then explains: “I use these robots for children just like you,” but who can't go to school because they have serious illnesses such as cancer or heart problems. Those children can send the robot instead, she says, and join their classmates virtually, from home. The group falls silent. “Whaaaaaat?” they croon in a collective tune of disbelief.

In fact, rolling robot avatars allow ill children to attend school remotely in a few hundred classrooms across the United States and

a smattering of other countries. The gadgets, called telepresence robots, were designed to allow doctors to conduct rounds from a distance and corporate executives to visit remote facilities. They show a remote user's face and let the user see, listen, and speak as if they were present. Ahumada and a few other researchers think the devices could provide classroom access to a long-overlooked group of children. “We've never in the history of the world had the opportunity for children with these serious medical conditions to go to school with their peers,” Ahumada says.

Children who use the technology have called it life-changing because of the social connections it allows. “It's like I'm actually there—that's why I like it so much,” an 8-year-old told Ahumada. In addition to taking part in lessons as if they were in the



classroom, children can zip around to chat with friends and join their peers for lunch, chorus, or recess.

"There's probably a specific band of kids [for whom] this could be transformational," says Gary Maslow, a pediatric psychiatrist at Duke University who studies how children adapt to chronic illness. But researchers haven't yet proved these tools help academically, socially, or emotionally, he says. And the technology itself has limitations: The robots weren't designed for children and don't work well in schools with spotty Wi-Fi.

Ahumada is "trying to figure out how to overcome those obstacles," says Justin Reich, an expert in educational technology at the Massachusetts Institute of Technology. Aiming to flesh out how best to integrate telepresence robots into classrooms, she and her colleagues have been probing how dozens of children with different illnesses, along with their families, classmates, and teachers, engage with the devices. In 2020, she teamed up with health care roboticist Laurel Riek at UC San Diego to design a machine with features tailored for children, including speakers that can carry sound over a classroom's din, an "arm" for reaching and grasping, and a user interface operable by children with a range of ages and abilities.

She is also planning to join forces with clinicians to pin down whether the benefits that children report in her studies translate into gains in mental health, grades, or other measurable areas. If they do, she says, schools may eventually be required to provide robots, creating a market as well as a vision for the technology. "It's much bigger than I originally imagined," she says.

**OVER THE PAST** 2 years, as the pandemic turned the world inside out, children and families accustomed to attending school, sports, and scouts got a taste of isolation and homebound life. But by Ahumada's count, about 2.5 million U.S. children with serious medical issues already experienced significant stretches of isolation before the pandemic. Teachers tell them not to worry about school and just to focus on getting better—a supportive sentiment, but one that underscores their exile from normalcy. Classmates often don't know why they disappear from school or what their daily life is like.

Ahumada knows the experience well. Congenital heart defects that went undiagnosed until adulthood kept her home for weeks at a time during elementary school. She was too weak to do more than read or doze on the couch in her family's one-bedroom home, waiting for her two brothers to come home with worksheets from her teacher. The days were lonely and achingly boring.

Children whose medical conditions keep

## Making a robot friend

For a robot to stand in effectively for a child in a classroom, it needs to be more than an iPad on wheels. Here are some key features of a child-friendly version of today's telepresence robots.

### 1 Camera

The camera should pan and tilt to move like an eyeball and compensate for the robot's lack of a neck.

### 2 Sound

Speakers should adjust the child's speaking volume based on background noise in the classroom and allow the child to translate typed text to speech. The microphone should pick out single voices and minimize background noise.

### 3 Arm and hand

An extendable arm and hand should be dexterous enough to pick up small objects and squeeze gently enough to avoid breaking them.

### 5 Wi-Fi connectivity

The robot must connect to public and encrypted Wi-Fi, as well as transition seamlessly between routers as the robot moves.

Student at home

**4 Adjustable height**  
Both the screen and arm should be adjustable vertically between sitting and standing position for children of a wide range of ages.

### 6 Agility

The robot should move at a relatively fast walking speed—with wheels that can handle outdoor surfaces.



them out of school are an amorphous group. Some get better and go back to school; others, sadly, succumb to their illness. Still others cycle in and out, as Ahumada did. U.S. public school districts generally provide such children several hours per week of instruction by a visiting teacher. But the system is spotty, and students often fall behind. According to research by Maslow and others, having a chronic illness in childhood puts people at a serious disadvantage. "They are less likely to attend college, half as likely to graduate college, less likely to be employed, and have lower income," he says.

Children stuck at home also miss out on another aspect of school. "Humans have evolved to be social creatures," says Maja Matarić, a roboticist and computer scien-

tist at the University of Southern California. Social development goes hand in hand with cognitive learning, she says, and it benefits from a physical presence in school.

Ahumada was lucky: Her own illness subsided by middle school and her childhood normalized. She went to college and eventually landed a job at Montana's Department of Public Health and Human Services. She soon found herself musing about technology and her solitary childhood. The department was expanding health care access by placing video consoles in clinics it was struggling to staff. Her colleagues expected patients would prefer in-person appointments, but later, when the state reverted to them, some people grumbled about losing the relationship with their distant doctor.



Veronica Ahumada hopes her telepresence research will help children avoid the isolation she felt as a girl, when illness kept her home from school.

If patients can use video to bond with remote doctors, Ahumada thought, perhaps children at home could forge relationships with classmates and teachers the same way. “I wanted to know,” she says, “if it was good enough for physicians, was it good enough for kids? Do we have the technology to completely transform the daily experience of these children?”

Ahumada wanted to study the idea in graduate school, but she struggled to find an adviser. Eventually, she connected with Mark Warschauer at UC Irvine, who investigates how digital technologies can enable learning and social inclusion. His team wasn’t studying remote access for children, he told her—no one he knew of was—but he offered her a spot in his lab.

Colleagues were skeptical, though. One likened research on telepresence robots to “studying TV carts.” Another told her the work would have no impact because “so few” students have illnesses that require them to stay home. Even Warschauer didn’t seem fully convinced, she says, until he saw a Verizon ad from the 2013 Super Bowl, which featured a child maneuvering a robot through school from a hospital bed. “Mark had never seen my idea conceptualized before,” Ahumada says. “We were so excited—we were like, ‘It’s a thing!’”

The device in the ad was manufactured by VGo, a small company that had already been

gun to sell robots to schools for ill students but hadn’t done research to discover how well the devices met their aims. (The company has since been acquired by Vecna Technologies.) Ahumada contacted VGo, which connected her with a school district in Texas that had just purchased several robots. The program had started with a girl in elementary school who was using a robot while undergoing cancer treatment. Her classmates were so grateful their friend could remain among them during her illness that they raised more than \$1000 to help buy another robot for other ill children to use.

Ahumada decided to base her first case study there, using interviews to probe how ill children and their community used the devices. The logistics were complicated. Because the robot captures the classroom on video, families of every student had to consent to its presence. Recruiting robot users was another challenge. Like most families with a seriously ill child, the ones in this district “were just trying to survive,” Warschauer says. “They weren’t thinking about participating in research projects.” But by the end of 2013, Ahumada had completed the study, interviewing five sick students from second to ninth grade about their experiences with the VGo robots, as well as five parents, 10 teachers, 35 classmates, and six school administrators.

The ill students all told Ahumada about

relief the robot brought from social isolation. One child’s mother said she didn’t realize her son was depressed until she saw him blossom with the robot, spending much more time alert and engaged with school. The study also revealed classmates and teachers quickly came to treat the robot not as a moving hunk of plastic and metal, but as the student it represented. Children and adults referred to it by the student’s name, and many classmates went out of their way to help when the robot got stuck. “My research kind of gives me hope for humanity,” Ahumada says. “The majority of kids are so thoughtful.”

Not every experience was positive. A ninth grade girl decided to return the robot because of the unwanted attention it brought—classmates teasingly called her a “vacuum cleaner,” for example. And a fifth grade boy was bullied by a classmate who kept smearing the robot’s lens with ketchup.

**MATARIĆ, TOO**, has explored how the technology works in schools, using robots made by a company called Ohmnilabs. She and her colleagues first had design experts operate a classroom robot remotely, as a child would, to identify technical features that would help children and teachers use them more effectively. These included a signal like raising one’s hand to get a teacher’s attention and a camera that swivels to look at a classmate. A study that gave robots to four



children to use in their classrooms over 2 to 8 weeks also identified the need for a speaker that can regulate the volume of its voice according to whether a child is whispering questions about English homework or being chased on the playground.

All four children found the experience very positive, the researchers saw, but deploying the robots involved extensive coordinating and troubleshooting, as well as navigating school district politics. They weren't ready to use out of the box, Matarić says.

Ahumada's work similarly finds a mix of promise and complexity, as have the few other studies that have looked at telepresence robots used in schools. Since her pilot study in Texas, she has gathered perspectives from 91 children with illnesses across the United States who have used telepresence robots, along with their families, classmates, teachers, and school administrators. The important design needs those interviews revealed identify some of the same features that Matarić pinpointed. But the children's most common demand was for a robotic arm that would allow them to engage with the world—reaching, grabbing, tagging. Children want something that enables “not just seeing and hearing and moving around on your own, but also being able to touch the world and to receive sensations,” Riek says.

The children also voiced values that might appear frivolous but could help them maintain social connections. One child requested a robot feature that's sure to be a design challenge—the ability to do a bunny hop. And 53 of a subset of 82 children Ahumada interviewed described using the robot to play, either with classmates or alone, she and Riek report in a paper under review. One child told Ahumada that using the robot showed their friends they remained the same person they were before they got sick. Peers, too, seek that connection. “Little kids hug the robot because they're so happy to see their friend,” Ahumada says.

**AS THE WORLD** enters the third year of the pandemic, remote attendance through video conferencing platforms has become routine. That change may actually harm the prospects for telepresence robotics in schools, Ahumada says. Video conferencing is cheaper than robots, and teachers now have experience using it. When several schools she works with reopened, they chose to leave students who were remote for medical reasons on video rather than bring back the robots.

The pandemic has also revealed an important limitation of virtual learning, Reich notes. “Teachers have a very hard time managing classes when some people are in person and some people are at a distance,” he says. The difficulty may persist even with

a single remote student on a robot.

But better telepresence technology could help, Reich adds. “I could imagine some future where these things are way better than Zoom.” What if, he wonders, “holding a virtual reality controller, you point your finger at something, and the robot takes its finger and points at it?”

In September 2020, Ahumada and Riek received a \$1.2 million grant from the National Science Foundation to develop a telepresence robot with features specifically designed for remote learning for children. They are starting with a prototype called Stretch, made

ing, and they will modify Stretch to include them. Remote students will test their prototypes and weigh in. “These kids are the pros,” Ahumada says. Long before the pandemic, before many families gave virtual school a thought, “they were already the pioneers.”

Some alterations should be straightforward, such as adding a screen to show the face of the child at home. Other specs will surely require inventing technology. And the researchers want to make the robot's physical presence cool and fun for children, something they can feel proud of as an extension of themselves among their peers. “We want



“Little kids hug the robot because they're so happy to see their friend.”

Veronica Ahumada,  
University of  
California, Davis

by Hello Robot, that was designed for older adults and people with disabilities to use around their home. For now, Stretch lacks a display screen, but it has a retractable arm that moves smoothly up and down a sturdy metal spine. At the end of the arm sits a gripper consisting of two small rubber cups on bendy strips of metal.

In Ahumada's office, a graduate research assistant, Jingjing Xie, explores Stretch's capabilities. Sitting on a chair with the classic board game Trouble at her feet, she uses the robot's controller to bring the arm down to the board and move a yellow peg. It's clumsy, like a claw machine at an arcade, and the gripper's rubber cups can't press the popper that rolls the dice.

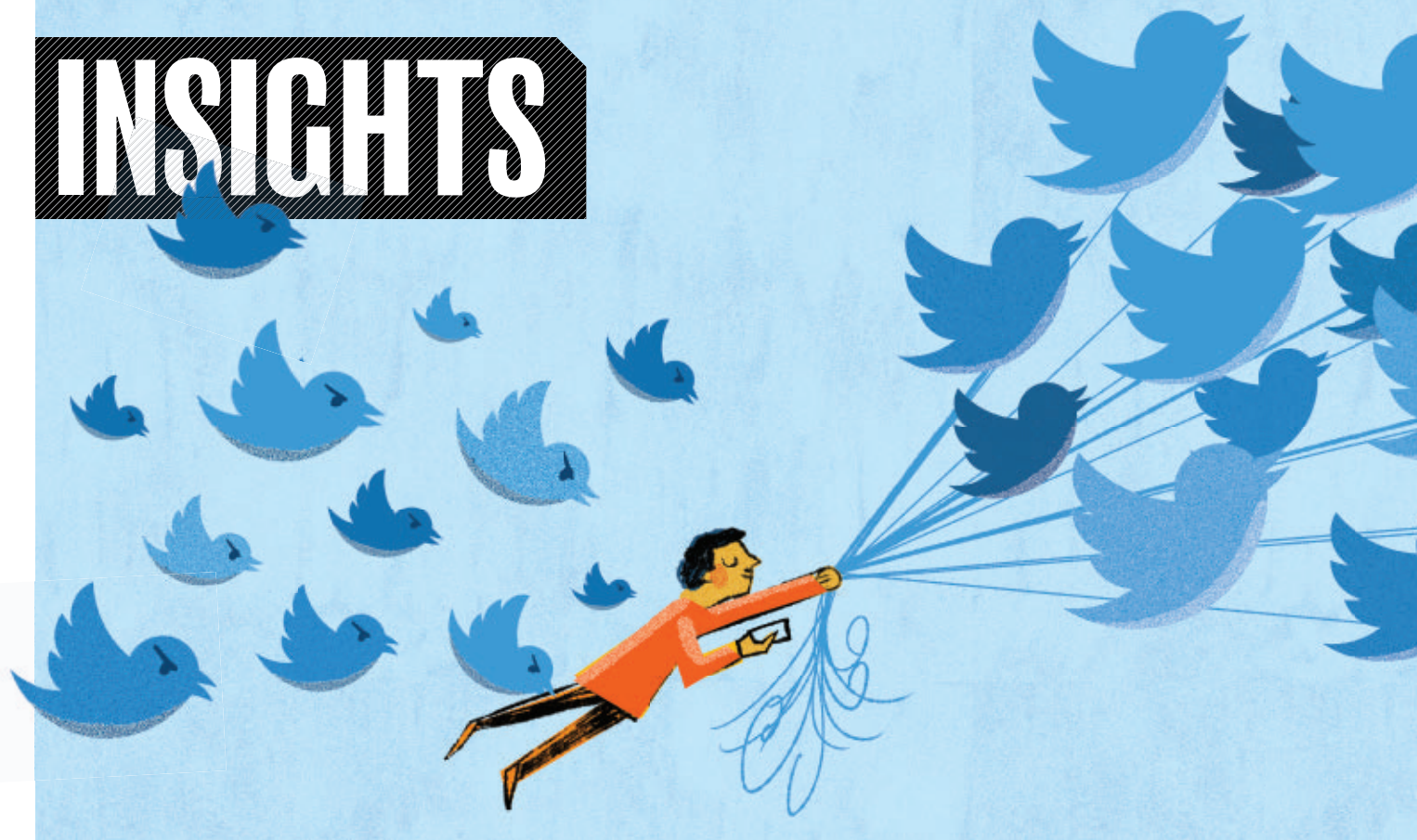
Stretch is a work in progress. Over the next year, based on Ahumada's studies to date, she and Riek will settle on features that a child needs to feel present and engaged in learn-

ing, and they will modify Stretch to include them. Remote students will test their prototypes and weigh in. “These kids are the pros,” Ahumada says. Long before the pandemic, before many families gave virtual school a thought, “they were already the pioneers.”

Still, despite Ahumada's investment in telepresence robots, she would happily abandon them if something more nimble came along. “Today it's robots,” she likes to say, “but tomorrow it could be holograms.” It's all in support of a bigger goal. When she visits classrooms with a robot in play, she sees sick children mentioning their nausea or showing classmates a port for delivering medicine or a scar from a recent surgery. Classmates breezily ask their robot-embodied friends how they are doing. Healthy and sick children form a single community. “If we don't scoot illness away,” she says, “will we be more compassionate?” ■

Alla Katsnelson is a science journalist in Northampton, Massachusetts.

# INSIGHTS



## LETTERS

### NEXTGEN VOICES

## Social media: Good or evil?

We asked young scientists to answer this question in the form of a tweet: **Is social media good or evil when it comes to science communication?** Read a selection of their thoughts below. Follow NextGen Voices on Twitter with hashtag #NextGenSci. —Jennifer Sills

### Good

Early in the pandemic, I had a nightmare: I went to my field's major annual conference but forgot to go to all the parties. Two years into the pandemic, I can definitively say that Twitter is the next best thing. If I can't go to conferences, I can at least have internet friends.

**Caitlin M. Aamodt**

Department of Neurosciences, University of California, San Diego, La Jolla, CA 92037, USA.  
Twitter: @CaitlinAamodt

Social media is a force for good. It levels the playing field (you don't need to be a senior scientist to spread the message); you can reach a broad audience quickly

and effectively; and it's free to everyone (the writer and the readers).

**Prosanta Chakrabarty**

Museum of Natural Science, Department of Biological Sciences, Louisiana State University, Baton Rouge, LA 70803, USA.  
Twitter: @PREAUX\_FISH

My classmates, friends, family, and neighbors don't read *Science* or subscribe to experts' blogs, but they might listen to me.

**Ádám Kun**

Department of Plant Systematics, Ecology, and Theoretical Biology, Eötvös University, Budapest, 1117, Hungary. Email: kunadam@elte.hu

Social media is becoming the go-to venue for science communication. Sharing science

on social media means dealing with nay-sayers, but it also provides the opportunity to engage such people in thoughtful and productive science discussion.

**Ashley Barbara Heim**

Department of Ecology and Evolutionary Biology, Cornell University, Ithaca, NY 14853, USA.  
Email: abh229@cornell.edu

As with any new channel of communication, the signal-to-noise ratio can be very low—if we learn how to listen.

**E. Loren Buhle, Jr.**

DNAexus, Mountain View, CA 94040, USA.  
Email: lorenbuhle@gmail.com

Social media has enabled delivery of information in an economically solvent manner to scientists and the general populace in all parts of the world, making science more accessible and equitable.

**Veerasathpurush Allareddy**

Department of Orthodontics, University of Illinois at Chicago College of Dentistry, Chicago, IL 60612, USA. Email: sath@uic.edu

On social media, scientists have to be clear and succinct, an incentive to eliminate jargon and streamline the message.

**Theresa Oehmke**

Department of Mechanical Engineering, University of New Hampshire, Durham, NH 03824, USA. Twitter: @t\_oehmke





People on social media serve as the best reviewers of our work! #RealTimeReviewer2

#### Khor Waiho

Institute of Tropical Aquaculture and Fisheries,  
Universiti Malaysia Terengganu, Kuala Nerus,  
Terengganu 21030, Malaysia.  
Email: waiho@umt.edu.my

Many current social issues stem from humanity's struggle with nuance. Social media is not known for respecting or encouraging nuance, but science is. And if scientific discussion can add a drop of nuance to the internet, who knows how far the ripples could go.

#### Michael Raitor

Stanford, CA 94305, USA.  
Email: mraitor@stanford.edu

Social media allows me to crowdsource solutions to problems. Troubleshooting programming bugs has never been easier.

#### Ming-Ju Amy Lyu

Center for Excellence in Molecular Plant Sciences,  
Chinese Academy of Sciences, Shanghai, 200031,  
China. Email: lvmj@cemps.ac.cn

Social media platforms can serve as effective science communication if research summaries, outcome measures, and expert advice are sourced from and linked to peer-reviewed journals, scientific

magazines, and websites of reputable research organizations.

#### Sarita Kumari

School of Social Sciences, Devi Ahilya  
Vishwavidyalaya, Indore, Madhya Pradesh 452001,  
India. Email: yogsarita1993@gmail.com

Science relies on the public as much as the public relies on science. Social media empowers scientists with the tools to provide objective scientific discoveries directly to the public, without intermediaries (such as the media) that may be prone to modify the information.

#### Isabel Marín Beltrán

Centro de Ciências do Mar do Algarve, Universidade  
do Algarve, 8005-139 Faro, Portugal.  
Email: imbeltran@ualg.pt

On social media, researchers connect with young viewers directly and share crucial, real-time updates. The scientific community should seize this opportunity to democratize research, give voice to diverse scientists, and encourage the next generation to pursue science.

#### Jiajia Fu

Whittle School and Studios, Washington, DC  
20008, USA. Email: jjnaturalist@gmail.com

Attractive infographics and videos can stimulate the interest of users. Moreover, science communication through social media in different regional languages can quickly reach otherwise overlooked people.

#### Charu Lata

Traditional Knowledge Studies Division, Council  
of Scientific and Industrial Research–National  
Institute of Science Communication & Policy  
Research, New Delhi, Delhi 110067, India.  
Email: charulata@niscair.res.in

Science communication using social media is convenient. In China, scientists from different institutes establish WeChat discussion groups, allowing them to share novel ideas and discuss research progress whenever and wherever possible.

#### Yongsheng Ji

Division of Life Sciences and Medicine,  
University of Science and Technology  
of China, Hefei, Anhui 230026, China.  
Email: jiys2020@ustc.edu.cn

## Evil

A growing number of self-appointed experts peddling misinformation drown out the voices of true scientists, who argue with facts, not opinions.

#### Mpho Diphago Stanley Lekgoathi

Pretoria, Gauteng, South Africa.  
Email: mpho.lekgoathi2@gmail.com

The mental health costs of misunderstandings, attacks, and endless scrolling

are real. Let's hope that new platforms with better incentives emerge.

#### J. Steen Hoyer

Department of Ecology, Evolution, and Natural  
Resources, Rutgers University, New Brunswick, NJ  
08901, USA. Twitter: @jshoyer

Why are we conditioning ourselves to think by digesting large volumes of short, simple snippets? The short-term benefit of a reaction isn't worth the long-term risk: losing the ability, and desire, to think deeply and nonlinearly.

#### Stuart Parker

Montana Bureau of Mines and Geology, Montana  
Technological University, Butte, MT 59701, USA.  
Email: parkstua@isu.edu

Child: A good scientist is smart and hard-working. Grad student: A good scientist is competitive, persistent, lucky. Social media: A good scientist is witty, popular, and attention-seeking. Sometimes I wonder if intelligence and hard work still matter.

#### Anna Uzonyi

Department of Molecular Genetics, Weizmann  
Institute of Science, Rehovot, Central Israel  
7610001, Israel. Email: anna.uzonyi@weizmann.ac.il

A post is not a publication, a retweet is not a citation, and going viral is not verification. #ScrollingIsNotPeerReview

#### Morgan Daly Dedyo

University of Pennsylvania, Philadelphia, PA 19104,  
USA. Email: ddedyo@sas.upenn.edu

Social media platforms build algorithms to display contents that maximize engagement, rewarding sensationalism and soundbites and penalizing more nuanced discourse on complex issues.

#### Edward Lau

University of Colorado School of Medicine, Aurora,  
CO 80010, USA. Twitter: @LauLabColorado

With scientific research, the devil is in the details. With social media, there's a lot of devil with little space for details.

#### Samuel Nathan Kirshner

School of Information Systems and Technology  
Management, University of New South Wales,  
Sydney, NSW 2052, Australia.  
Email: s.kirshner@unsw.edu.au

On social media, experts and non-experts share the same microphone. Because precise scientific language is usually not very appealing, the non-experts' posts are more likely to go viral than the experts' posts, and most readers can't tell the difference.

#### Wagner Eduardo Richter

Department of Chemistry, Federal University of  
Technology–Paraná, Ponta Grossa, Paraná, Brazil.  
Twitter: @richterwe

10.1126/science.abo2409



## POLICY FORUM

### DATA ACCESS

# EU and US legislation seek to open up digital platform data

Constraints on data access must be addressed to facilitate research

By **Brandie Nonnecke<sup>1</sup>** and **Camille Carlton<sup>2</sup>**

**D**espite the potential societal benefits of granting independent researchers access to digital platform data, such as promotion of transparency and accountability, online platform companies have few legal obligations to do so and potentially stronger business incentives not to. Without legally binding mechanisms that provide greater clarity on what and how data can be shared with independent researchers in privacy-preserving ways, platforms are unlikely to share the breadth of data necessary for robust scientific inquiry and public oversight (1). Here, we discuss two notable, legislative efforts aimed at opening up platform data: the Digital Services Act (DSA), recently approved by the European Parliament (2), and the Platform Accountability and Transparency Act (PATA), recently proposed by several US senators (3). Although the legislation could support researchers' access to data, they could also fall short in many ways, highlighting the complex challenges

in mandating data access for independent research and oversight.

As large platforms take on increasingly influential roles in our online social, economic, and political interactions, there is a growing demand for transparency and accountability through mandated data disclosures. Research insights from platform data can help, for example, to understand unintended harms of platform use on vulnerable populations, such as children and marginalized communities; identify coordinated foreign influence campaigns targeting elections; and support public health initiatives, such as documenting the spread of antivaccine misinformation (4).

The "Facebook Papers," leaked by whistleblower Frances Haugen, gave unprecedented insight into that platform's opaque practices (5). But reliance on whistleblowers and leaked data is untenable. Researchers need lawful access to platform data appropriately scoped to advance scientific knowledge and evidence-based policy-making. Yet, how to do this responsibly and in compliance with relevant data privacy laws and regulations remains debated (6).

Platforms have made data available to independent researchers through public application programming interfaces (APIs); how-

ever, because platforms' sharing of data with independent researchers has been primarily voluntary, data access has often been unreliable, inconsistent, and incompatible with research needs (6). For example, research questions that require data unavailable through an API, such as impression data and demographics of those exposed to disinformation campaigns, must rely on research partnerships with a platform or circumvention methods such as web scraping or requesting data directly from users (7). These methods are often not ideal because they pose ethical and legal concerns and may result in collection of data that is limited in terms of scale, quality, and precision (8).

### COMPETING INCENTIVES

Despite the societal benefits, researchers' access to platform data is becoming more difficult. A tension exists between private incentives to retain data for financial, reputational, and privacy reasons and public incentives to access data for scientific research and oversight (1). For example, platforms have pushed back against mandatory data disclosures, emphasizing legal requirements to ensure user privacy and protection of proprietary information (6). Lawmakers have countered that data access is justified because large platforms wield substantial and increasingly monopolistic control over information online, which poses risks to individual rights and collective well-being [see Recitals 53 to 58 of the DSA (2)]. For lawmakers, access to data for empirical research is seen as a necessary step in ensuring transparency and accountability.

Platforms' hesitancy to share data with researchers is not wholly unwarranted. A Facebook-approved research partnership with Cambridge Analytica resulted in scandal, a \$5 billion fine by the US Federal Trade Commission (FTC) for privacy violations, and new requirements in an FTC consent order to implement comprehensive data privacy and security safeguards (9).

In the face of steep fines and unwanted oversight, platforms often justify restrictions on data sharing with independent researchers by claiming that there is a lack of clarity in data privacy legislation and regulatory obligations (10). One of the primary pieces of legislation invoked is the General Data Protection Regulation (GDPR) by the European Union (EU). Platforms claim that the GDPR lacks clear standards for data anonymization and pseudonymization and approved cross-border transfers of personal data (10).

Difficulties faced in the Social Science One initiative are a quintessential example. Despite Facebook's partnership with Social Science One, an initiative that seeks

<sup>1</sup>University of California, Berkeley, CA, USA.

<sup>2</sup>Center for Humane Technology, San Francisco, CA, USA. Email: nonnecke@berkeley.edu



to facilitate academic researchers' access to Facebook data for public-interest research, it took nearly 20 months for researchers to gain access to the data the platform had promised (6). Facebook attributed its delay to the need to establish data privacy mechanisms to maintain GDPR compliance. Researchers used the data for 2 years before Facebook admitted that the data had a serious flaw: It was only representative of approximately half of US users, those who had a detectable political leaning (11). Researchers' trust in future data they receive has been seriously diminished (11).

Researchers trying to collect data outside of API access and formal partnerships have faced fierce opposition. In August 2021, Facebook disabled accounts of researchers behind the NYU Ad Observatory, claiming that the researchers had inappropriately scraped users' data on targeted advertising (8). Although Facebook justified its actions as necessary to ensure data privacy compliance mandated in the FTC consent order, the FTC issued a letter rebuking Facebook's actions and reemphasized that the order "does not bar Facebook from creating exceptions for good-faith research in the public interest. Indeed, the FTC supports efforts to shed light on opaque business practices, especially around surveillance-based advertising" (12).

### LEGAL MANDATES FOR DATA ACCESS

Platforms' resistance to share data demonstrates the need for clarity in how data privacy legislation and regulatory mandates should be interpreted (6, 11). The European Data Protection Supervisor in January 2020 reemphasized that the GDPR seeks to support data access for research and provided additional guidance on data governance for research purposes (13). The European Commission established a "Code of Practice on Disinformation" to support researchers' access to data, and the European Digital Media Observatory is establishing a framework for GDPR-compliant data access (14). Although these efforts are critical, platforms likely will not make data available without binding legal mechanisms. Legislation proposed in the EU and United States that seeks to mandate platform data access for research and oversight could thus be transformative.

### The Digital Services Act

In light of the role played by "very large online platforms" (VLOPs; having at least 45 million active users in the EU) in "facilitating the public debate and economic transactions," the DSA would compel VLOPs to conduct assessments of systemic risks stemming from their services, such as dissemination of illegal content; impacts on fundamental rights; and the "intentional and, oftentimes, coordinated

manipulation of the platform's service, with a foreseeable impact on health, civic discourse, electoral processes, public security, and protection of minors" (2). Once identified, platforms must implement appropriate risk mitigation strategies (2). These assessments and mitigation strategies would be auditable and may require platforms to make data available to a "Digital Services Coordinator," an independent authority established in each member state; to the European Commission; or to "vetted researchers" to support transparency, accountability, and compliance with relevant laws and regulations (2). The Act defines "vetted researchers" as individuals with an affiliation with an academic institution, independence from commercial interests, proven subject or methodological expertise, and the ability to comply with data security and confidentiality requirements (2).

The DSA requires platforms to make three categories of data available through online databases or APIs (2): (i) Data necessary to assess risks and possible harms brought about by the platform's systems; (ii) data on the accuracy, functioning, and testing of algorithmic systems for content moderation, recommender systems, or advertising systems; or (iii) data on processes and outputs of content moderation or of internal complaint-handling systems. In response to increased awareness of the risks of targeted advertising, Article 63 explicitly requires VLOPs to create a public digital ad repository that must include the ad's content; the entity behind the ad; whether it was targeted and, if it was, the parameters used for targeting; and the total number of recipients.

The DSA also stipulates that the European Commission, in consultation with the "European Board for Digital Services" established by the DSA, is tasked with adopting derivative acts that will determine the "technical conditions" for GDPR-compliant data sharing (2). A primary challenge will be to determine how data should be constructed and shared with researchers in ways that are GDPR-compliant while maintaining enough detail to make data useful for research. The DSA provides protections to platforms from having to share data that may pose a security or financial risk, such as trade secrets. Transparency in how VLOPs use this protection will be important to mitigate exploitation.

### Platform Accountability and Transparency Act

PATA is the most comprehensive law proposed in the United States to require large platforms (having more than 25 million monthly users) to make data available to support scientific research and oversight (3). Proposed in December 2021, the Act compels

platforms to make data available to "qualified researchers" through a process intermediated by the National Science Foundation (NSF) and the Platform Accountability and Transparency Office (PATO) to be established within the FTC (3).

The Act defines a "qualified researcher" as university-affiliated and establishes a process by which researchers are granted access to platform data (3). First, all projects must receive ethics approval from the institutional review board at the researcher's affiliated institution, followed by approval from the NSF. Then, in collaboration with the researchers, the NSF determines what platform data and information is necessary to carry out the research. Last, the research project is referred to PATO, which brokers data access between the platform and the researcher. PATO is also responsible for establishing privacy and cybersecurity safeguards for platform data and information provided to researcher(s) (3).

The Act establishes provisions to mitigate potential harms of data sharing and better ensure platforms' compliance. For example, researchers must comply with privacy and cybersecurity provisions and may only use the data for the specified research project. Those who intentionally violate the privacy and cybersecurity provisions will be subject to civil and criminal enforcement (3). Platforms that fail to comply with the Act may face financial penalties and lose immunity protections for user-generated content granted to them in Section 230 of the Communications Decency Act (3).

To support broader access to platform data, the FTC is granted authority to "require platforms to report on or disclose data, metrics, or other information" that will "assist the public, journalists, researchers, the Commission, or other government agencies" in assessing the impact of platforms on consumers, institutions, and society; promoting the advancement of scientific and other research; and ensuring compliance with federal law (3). When possible, the data and information must be made publicly available through a format that is "accessible and understandable to the public," such as a searchable database or API (3). The FTC may also require platforms to disclose the following on an ongoing basis: content that has been "sufficiently disseminated" (an unclear metric to be clarified by the FTC); content originating or spread by major public accounts (having at least 25,000 followers or at least 100,000 monthly viewers); and statistically representative samples of public content (3). The data and content must be accompanied by supporting information, such as dissemination and engagement data, audience characteristics, and whether the content was recommended or amplified by the platform's

algorithms (3). Like the DSA, PATA also compels platforms to report data and information on targeted advertising, such as the use and characteristics of algorithms used and content moderation tactics.

PATA also establishes a process to balance the private interests of platforms with the interests of the public. Researchers are required to submit a prepublication version of the research to PATO, and platforms are given authority to object to publication or release of any analysis that they believe does not comply with federal, state, or local privacy laws or risks disseminating confidential business information or trade secrets. Researchers are given the opportunity to amend their research or appeal. If the platform still objects, PATO makes the final determination. Platforms may thus be limited in their ability to block the release of unfavorable research findings under the guise of legal compliance or protecting trade secrets.

## RECOMMENDATIONS

Although DSA and PATA are promising, several potential constraints merit further attention.

### Broaden the scope

Both Acts have restrictions in scope that, if broadened, would better enable research on a wider breadth of topics from varied epistemological approaches. The DSA and PATA support data access for research but differ in their underlying intentions for doing so. The DSA primarily focuses on data access to support research that informs oversight and compliance with relevant laws and regulations, whereas PATA also seeks to enable general research. By scoping data access to only that which is necessary to ensure oversight and compliance with specific laws and regulations, the data to be made available may have limited usefulness for broader research. Legislation should compel platforms to disclose data for the purpose of advancing scientific knowledge. Research supports greater transparency and empirical understanding of platforms' effects, which is necessary for accountability and oversight.

Transparency is needed in how "vetted/qualified researchers" are selected, and mechanisms should be in place to ensure that certain institutions and disciplines are not disproportionately favored. We recommend expanding the types of researchers who are qualified to access platform data to include nonacademic researchers, such as journalists and others who aim to inform the public about critical matters. These individuals could also be "vetted/qualified" through a formal review process. Unlike the DSA, PATA proactively expands data access beyond academic researchers by creating a safe harbor

for journalists' and other researchers' collection of platform data through web scraping; voluntary donation by users, including through browser extensions and plug-ins; and creation of research accounts. Without this protection, research and public awareness may be stifled out of fear of retaliation.

### Infrastructure and intermediaries

Increasing the availability of platform data will have limited effects if there is not also equity-driven investment in research infrastructure. Research institutions such as the NSF or the European Research Council should increase support for research infrastructure to better ensure that a greater diversity of researchers across institutions and disciplines are equipped to store and analyze data in compliance with the legislation. Otherwise, the requirement that researchers must have the capacity to comply with data security and confidentiality requirements will likely favor larger institutions and disciplines with greater research infrastructure (such as computing power and cybersecurity).

To counter infrastructure constraints, lawmakers should also look to the data intermediary model to enable diverse researchers' access to secure, interoperable, cross-border data. Trusted intermediaries may be able to support development of robust data-sharing ecosystems by working with platforms, researchers, and users to establish data-sharing models that advance public-interest research while ensuring compliance with relevant laws and human rights norms.

### Address methodological challenges

Platform data is often not collected with the intent that it will be used in scientific research. Its structure may be at odds with the goals of scientific inquiry (4). For example, a sample of network data may have characteristics that are wholly different from the entire network itself (15). Moreover, researchers are completely reliant on platforms to provide datasets free from omissions or edits. Any datasets made available to researchers should provide metadata and other contextual information, including how the data was generated and collected, effects of the platform's design (such as recommender system) on the data; how sampling was conducted; and, if applicable, how the data was cleaned, transformed, or modified before being shared. In doing so, data and research insights will be of higher quality and accuracy, better ensuring that any resulting oversight is appropriately scoped and effective—a benefit for both the public and the platforms.

The legislation will require robust anonymization efforts, such as the use of differential privacy, which may diminish the

data's value for researchers (4). To address these challenges, partnerships between lawmakers, platforms, and independent researchers are necessary to better ensure that data are generated, collected, and made available in ways that are of high value for scientific inquiry and public accountability while maintaining legally compliant data privacy and security.

## DEMAND FOR TRANSPARENCY

The European Parliament adopted the DSA during its January 2022 plenary. The Act will now go through subsequent negotiations between the EU Parliament, EU Council, and the EU Commission. PATA's fate is less certain. Although the bill has garnered bipartisan support, it has yet to undergo formal congressional debate. PATA builds on several bills that aimed to make platforms more transparent and accountable. However, it addresses many of the previous bills' shortcomings by providing a comprehensive strategy for how to compel platform data access for research and oversight. As such, PATA's chances of becoming law may be stronger. The emergence of these legislative efforts suggests that as large platforms increasingly play a centralized role in our social, economic, and political interactions, the demand for transparency and accountability mechanisms will continue to grow. ■

## REFERENCES AND NOTES

1. D. M. J. Lazer *et al.*, *Science* **369**, 1060 (2020).
2. European Commission, "The Digital Services Act: Ensuring a Safe and Accountable Online Environment" (2021).
3. "Platform Accountability and Transparency Act" (2021); [www.coons.senate.gov/download/text-pata-117](http://www.coons.senate.gov/download/text-pata-117).
4. D. Lazer *et al.*, *Nature* **595**, 189 (2021).
5. "Facebook Files: 5 things leaked documents reveal," *BBC News*, 24 September 2021.
6. N. Persily, J. A. Tucker, in *Social Media and Democracy: The State of the Field and Prospects for Reform*, N. Persily, J. A. Tucker, Eds. (Cambridge Univ. Press, 2020), p. 313.
7. I. V. Pasquetto *et al.*, *Harvard Kennedy School Misinform. Rev.* **10**, 37016/mr-2020-49 (2020).
8. M. Bobrowsky, "Facebook Disables Access for NYU Research Into Political-Ad Targeting," *The Wall Street Journal*, 4 August 2021.
9. J. J. Simons, N. J. Phillips, C. S. Wilson, "Statement of Chairman Joe Simons and Commissioners Noah Joshua Phillips and Christine S. Wilson In re Facebook, Inc.," Federal Trade Commission (2019).
10. M. Vermeulen, "The keys to the kingdom," Knight First Amendment Institute at Columbia University (2021).
11. D. Alba, "Facebook sent flawed data to misinformation researchers," *The New York Times* 12 September 2021.
12. S. Levine, "Letter from acting director of the Bureau of Consumer Protection Samuel Levine to Facebook," Federal Trade Commission (2021).
13. European Data Protection Supervisor, "A Preliminary Opinion on Data Protection and Scientific Research," European Data Protection Supervisor (2020).
14. European Commission, "European Digital Media Observatory (EDMO)" (2021).
15. A. Gelman, *J. Surv. Stat. Methodol.* **5**, 22 (2016).

## ACKNOWLEDGMENTS

We thank anonymous reviewers for comments. We thank C. Crittenden, D. Lazer, D. Mulligan, N. Persily, J. Reinhardt, and V. Vaidyanath for their initial reviews and guidance.

10.1126/science.abl8537



## PERSPECTIVES

### SCIENCE COMMUNICATION

# The chronic growing pains of communicating science online

Scientists have not yet adapted to new information environments

By **Dominique Brossard**<sup>1,2</sup> and **Dietram A. Scheufele**<sup>1,2</sup>

**A**lmost a decade ago, we wrote, “Without applied research on how to best communicate science online, we risk creating a future where the dynamics of online communication systems have a stronger impact on public views about science than the specific research that we as scientists are trying to communicate” (1). Since then, the footprint of subscription-based news content has slowly shrunk. Meanwhile, microtargeted information increasingly dominates social media, curated and prioritized algorithmically on the basis of audience demographics, an abundance of digital trace data, and other consumer information. Partly as a result, hyperpolarized public attitudes on issues such as COVID-19 vaccines or climate change emerge and grow in separate echo chambers (2). Scientists have been slow to adapt to a shift in power in the science information ecosystem—changes that are not likely to reverse.

The business-as-usual response to this challenge from many parts of the scientific community—especially in science, technology, engineering, and mathematics fields—has been frustrating to those who conduct research on science communication. Many scientists-turned-communicators continue to see online communication environments mostly as tools for resolving information asymmetries between experts and lay audiences (3). As a result, they blog, tweet, and post podcasts and videos to promote public understanding and excitement about sci-

ence. To be fair, this has been driven most recently by a demand from policy-makers and from audiences interested in policy and decision-relevant science during the COVID-19 pandemic.

Unfortunately, social science research suggests that rapidly evolving online information ecologies are likely to be minimally responsive to scientists who upload content—however engaging it may seem—to TikTok or YouTube. In highly contested national and global information environments, the scientific community is just one of many voices competing for attention and public buy-in about a range of issues, from COVID-19 to artificial intelligence to genetic engineering, among other topics. This competition for public attention has produced at least three urgent lessons that the scientific community must face as online information environments rapidly displace traditional, mainstream media.

One challenge is for scientists to break free from informational homophily. Since the early days of the internet, the scientific community has had a very spotty track record of harnessing the full potential of online communication tools to reach beyond an audience that already follows science (4) and meaningfully connect with those who disagree with or feel disconnected from science. This includes conservative-minded people on climate change; religious audiences on tissue engineering and embryonic stem cell research; and Black, Indigenous, and people-of-color communities on the current pandemic, for example (5).

This is not to say that the scientific community has not become more sophisticated in understanding how different audiences find and make sense of information from online sources (6). Nonetheless, even some

of the scientific community’s more ambitious and resource-intensive efforts to communicate science online, such as science series that have been both streamed online and broadcast on television, were heavily favored by audiences that are likely to be receptive to the messages of scientists already (7). And when faced with empirical data showing that they can do better, scientists often argue that “[i]ntangible measures... may matter most” (8) and give in to the inherently unscientific temptation to turn to personal anecdotes as a defense against inconvenient empirical data that tell them how to do better.

Scientists’ homophilic self-sorting online has another, more subtle siloing effect. Social media platforms have provided a temptation for science journalists, scientists, and other science-affiliated actors to follow and retweet each other in an online environment that looks very different from the rest of society. A survey of 2791 US adult Twitter users by the Pew Research Center in 2018 indicated that those most active on this platform are younger (almost a third of Twitter users are under 30 years old), are more likely to identify as Democrats and have at least a college degree, and have higher incomes than US adults overall (9). Most perniciously, this has allowed scientists to live in their own science-centric bubbles on social media platforms, sheltered from often sizeable cross-sections of citizens that feel disconnected from the scientific community. Meanwhile, scientists share each other’s tweets and—when their instincts get the worst of them—ridicule audiences that they see as “against us” on issues like climate change or evolution (3).

Another challenge for the scientific community is ignoring the allure of social media



<sup>1</sup>Department of Life Sciences Communication, University of Wisconsin–Madison, Madison, WI, USA.

<sup>2</sup>Morgridge Institute for Research, Madison, WI, USA. Email: dombrossard@gmail.com

skirmishes. It is debatable whether social media platforms that are designed to monetize outrage and disagreement among users are the most productive channel for convincing skeptical publics that settled science about climate change or vaccines is not up for debate (10). Even worse, when scientists do engage, the fast-moving and often almost real-time back-and-forth on social media can change the way they use and represent evidence. Rules of scientific discourse and the systematic, objective, and transparent evaluation of evidence are fundamentally at odds with the realities of debates in most online spaces (11). Consequently, scientists are at a distinct disadvantage—especially during everything-goes-type social media clashes—as some of the very few participants in public debates whose professional norms and ethics dictate that they prioritize reliable, cumulative evidence over persuasive power (12).

On social media platforms, this can create a temptation for scientists to maximize persuasive appeal and use quotes from prominent scientists or illustrative single-study results as “anecdotal evidence” when trying to correct misleading truth claims. The unscientific nature of using anecdotal data or scientific authority figures is partly driven by 280-character constraints on platforms like Twitter and partly by generations of science communication training programs urging scientists to tell more engaging stories (13). Unfortunately, this arms race over the most effective narratives has its risks. Decades of communication research indicate that anecdotal accounts on social media of breakthrough severe acute respiratory syndrome coronavirus 2 (SARS-CoV-2) infections or severe adverse reactions to COVID-19 vaccines, regardless of how rare both are, will be imprinted in people's memories much more effectively than pages of sound statistical data documenting herd immunity (14).

Preprints as a form of anecdotal evidence have exacerbated the problem. This is a version of a scientific paper that has often not been peer-reviewed by a scientific journal. Designed to make science more transparent and maximize the corrective potential of science, preprints have emerged as a major driver of episodic, single-study media coverage of science. Especially during the COVID-19 pandemic, conversations surrounding individual non-peer-reviewed preprints has made it difficult to extract meaningful signals about reliable, cumulative scientific evidence from the noise of sometimes short-lived findings reported in a preprint. At first glance, a hyperlink to a preprint article (typically posted on an online archive) might seem like good-enough evidence to support a scientist's Tweet calling for people to wear masks, for example.

But winning these short-term Twitter battles using questionable “evidence” that itself might turn out to be wrong is likely to do irreparable long-term damage to the public's perception of science as a reliable way of understanding the world.

Arguably, the greatest challenge that scientists must address as a community stems from a fundamental change in how scientific information gets shared, amplified, and received in online environments. With the emergence of virtually unlimited storage space, rapidly growing computational capacity, and increasingly sophisticated artificial intelligence, the societal balance of power for scientific information has shifted away from legacy media, government agencies, and the scientific community. Now, social media platforms are the central gatekeeper of information and communication about science. The scientific community has been slow to react.

Recent concerns about misinformation are a good illustration of the scientific community's outdated thinking in this space (15). Especially during the COVID-19 pandemic, scientists misconstrued misinformation as a new problem, in terms of both nature and scope, even though empirical evidence for these assumptions is thin, at best (10). This has distracted scientists from a much bigger and more urgent problem for science: What evidence reaches which parts of the audience is increasingly up to automated algorithms curated by social media platforms rather than scientists, journalists, or users of the platforms themselves.

Algorithms that select and tailor content based on an audience member's social context, personal preferences, and a host of digital trace data increasingly determine what scientific information an individual is likely to receive in Google searches, Facebook feeds, and Netflix recommendations (10). For audiences that engage less with credible science content, artificial intelligence, if left unchecked, might eventually slow the stream of reliable information about COVID-19 to a trickle, drowning it out by a surplus of online noise.

At present, there is little that science can do to escape this dilemma. The same profit-driven algorithmic tools that bring science-friendly and curious followers to scientists' Twitter feeds and YouTube channels will increasingly disconnect scientists from the audiences that they need to connect with most urgently. Moving forward, conquering this challenge will require partnerships among the scientific community, social media platforms, and democratic institutions. Scientific logic and access to information are two of the main foundations of enlightened democracies. Distortions to any part of

this delicate relationship will inevitably lead to the downfall of the whole system. This also means that it is far too late for Band-Aid solutions. Of course, the scientific community can try to increase scientific literacy among the electorate (11). Training scientists to better communicate their science can continue. And scientists can become more savvy at gaming Facebook's or Google's algorithms when communicating science, using tools of digital marketing, for instance, to enhance the reach or effectiveness of their communication.

But these responses address the symptoms rather than the underlying problem. The cause is a tectonic shift in the balance of power in science information ecologies. Social media platforms and their underlying algorithms are designed to outperform the ability of science audiences to sift through rapidly growing information streams and to capitalize on their emotional and cognitive weaknesses in doing so (10). No one should be surprised when this happens. When world chess champion Gary Kasparov lost to Big Blue, a supercomputer solely designed by IBM to beat him, no one called for better training for the next generation of chess players, for developing strategies to outsmart supercomputers at chess, or for blaming Kasparov for not understanding what the machine was up to (10). Everyone realized that this was a new age for chess and for computing with no turning back of the clock. The same understanding is now here for scientists. It's a new age for informing public debates with facts and evidence, and some realities have changed for good. ■

## REFERENCES AND NOTES

1. D. Brossard, D. A. Scheufele, *Science* **339**, 40 (2013).
2. D. A. Scheufele, N. M. Krause, *Proc. Natl. Acad. Sci. U.S.A.* **116**, 7662 (2019).
3. N. M. Krause et al., *Am. Sci.* **109**, 226 (2021).
4. D. A. Scheufele, *Environ. Commun.* **12**, 1123 (2018).
5. E. G. Christopherson, E. L. Howell, D. A. Scheufele, K. Viswanath, N. P. West, *Soc. Innov. Rev.* **19**, 48 (2021).
6. National Academies of Sciences, Engineering, and Medicine, *Communicating Science Effectively: A Research Agenda* (The National Academies Press, 2016).
7. H. Akin, D. Brossard, B. W. Hardy, D. A. Scheufele, “Bill Nye can't save the world,” *Slate*, 27 April 2017.
8. N. DeGrasse Tyson, Comment on Akin et al., “Can Bill Nye – or any other science show – really save the world?,” *The Conversation*, 17 April 2017; [https://theconversation.com/can-bill-nye-or-any-other-science-show-really-save-the-world-76630#comment\\_1276757](https://theconversation.com/can-bill-nye-or-any-other-science-show-really-save-the-world-76630#comment_1276757).
9. S. Wojcik, A. Hughes, “Sizing up Twitter users” (Pew Research Center, 2019).
10. D. A. Scheufele, N. M. Krause, I. Freiling, *J. Appl. Res. Mem. Cogn.* **10**, 522 (2021).
11. E. L. Howell, D. Brossard, *Proc. Natl. Acad. Sci. U.S.A.* **118**, e1912436117 (2021).
12. M. F. Dahlstrom, D. A. Scheufele, *PLOS Biol.* **16**, e2006720 (2018).
13. R. Olson, *Houston, We Have a Narrative: Why Science Needs Story* (Univ. Chicago Press, 2015).
14. National Academies of Sciences, Engineering, and Medicine, *Encouraging Adoption of Protective Behaviors to Mitigate the Spread of COVID-19: Strategies for Behavior Change* (The National Academies Press, 2020).
15. N. M. Krause et al., *J. Risk Res.* **23**, 1052 (2020).

10.1126/science.abo0668



# Starfish grow extraordinary crystals

Biom mineralization in a starfish displays morphologically complex features

By **Stephen T. Hyde<sup>1</sup>** and **Fiona C. Meldrum<sup>2</sup>**

**T**he growth and form of crystals in vivo—biomineralization—challenge many ideas about crystalline materials. One typically pictures a crystal as a sterile object with a regular geometric form, but nature frequently challenges this preconception. This is beautifully illustrated by the calcite plates (stereom) of echinoderms, which exhibit complex, sponge-like morphologies and curved surfaces and yet behave as single crystals. Extraordinarily, the stereom of certain species is highly ordered. Observations of the sea urchin *Cidaris rugosa* more than six decades ago (1) identified a stereom reminiscent of one of the three simplest triply periodic minimal surfaces (TPMS), the so-called P surface, with a lattice parameter four orders of magnitude larger than that of calcite. On page 647 of this issue, Yang *et al.* (2) provide a new example of a TPMS at this extreme length scale. Detected in the knobbly starfish *Protoreaster nodosus*, the stereom resembles another simple TPMS, the D surface.

TPMS-related structures have been reported in a variety of living and nonliving systems, from soft liquid crystalline assemblies to hard wing scales and exoskeletons in insects (3). The genesis and stability of TPMS with lattice parameters of up to ~100 nm in vitro can be understood as a relaxed soft membrane assembly, which is the outcome of competing interactions within the molecular constituents of the membranes, e.g., lipids or copolymers (4). The three simplest TPMS geometries are the gyroid (G), diamond (D), and primitive (P), all of which have cubic symmetry (see the figure). Microstructures related to the G and D geometries have been found in biological chitin assemblies, where they far exceed the 100-nm threshold. These form the pho-

tonic crystals responsible for the iridescence of butterfly wings and weevil carapaces (5). The growth of such structures in the wing scales of butterfly pupae is associated with a particular cellular organelle known as the smooth endoplasmic reticulum, which folds to give a convoluted membrane whose form is markedly similar to the G morphology (6). Templating of the growing chitin crystal by a TPMS-like soft membrane is thus a plausible, though unproven, mechanism that explains the formation of these microstructures.

Yang *et al.* investigated the structure of the stereom formed by the starfish *P. nodosus* at angstrom and higher length scales. In con-

morphologies (7), this remains speculative.

Yang *et al.* reveal an extraordinary interplay between the calcite structures at micrometer and angstrom length scales of cubic and rhombohedral symmetries, respectively. Despite its atomic-scale crystallinity, the calcite fractures like glass, unlike the precise cleavage planes exhibited by geological calcite. This can be attributed to the composite structure of biological calcite, in which organic macromolecules are occluded within the crystal lattice. Further, as proposed as early as the 1960s (8), it is now accepted that these calcite biominerals are better described as “mesocrystals,” composed

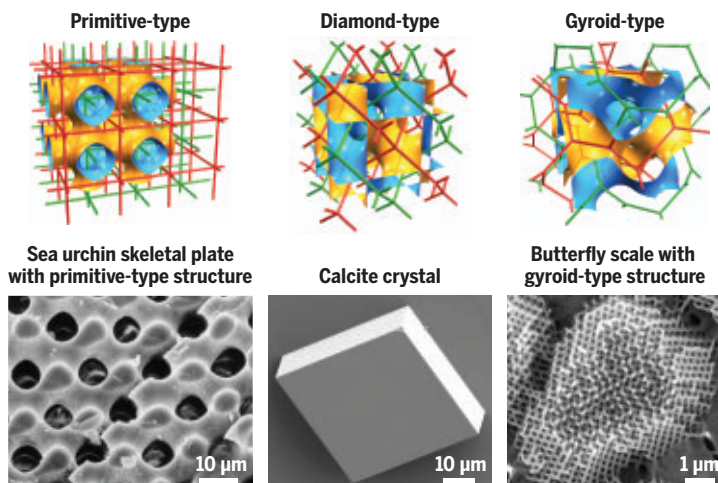
of space-filling arrays of calcite nanoparticles, rather than true single crystals (9). This structure is a direct consequence of the crystallization mechanism, whereby biogenic calcite often forms through an amorphous calcium carbonate (ACC) precursor phase. The shape of the constituent ACC nanoparticles is then preserved within the product calcite. It is also conceivable that the mesocrystal ultrastructure enables the crystal lattice to warp and follow the shape of the skeletal surface in some echinoderms (10).

These findings confirm the extraordinary control that biology achieves over crystallization. Traditional models of biomineralization emphasize the role of soluble macromolecules in directing crystal morphologies. The D-type TPMS can be considered as a network of four-armed tetra-

pods. Calcite crystals with comparable tetrapod morphologies can be generated by using soluble additives. Such a model is consistent with the calcite shells of some dinoflagellates, a type of phytoplankton (11), which are reminiscent of a disordered echinoderm stereom but comprise multiple crystallites. Instead, the echinoderm stereom is templated by an organic matrix that defines its morphology. This has been demonstrated in studies of sea urchin larvae, in which mineralization begins with the formation of a triradial calcite crystal (spicule). Culturing larvae under conditions that change the shape of the organic

## Three simplest triple periodic minimal surfaces

Although triply periodic minimal surfaces (TPMS) have been observed in the natural world, examples of TPMS with large length scales in living organisms are extremely rare. Researchers have now identified a diamond-type TPMS in the calcium carbonate skeletal elements of the knobbly starfish. This raises questions about the mechanisms by which organisms sculpt the morphologies of these biominerals.



trast to the sea-urchin *C. rugosa*, plates of *P. nodosus* resemble the D surface and exhibit a 30-μm lattice parameter, a measurement made on the basis of the types and prevalence of structural defects compared with the ideal D surface. These defects may explain why the structure responds to loading in a way that is reminiscent of soft materials, avoiding brittle fracture commonly associated with calcite. Some of that data suggest microstructural tuning for biological fitness during evolution. However, given the similar defects in mesoporous and amorphous silica grown within synthetic membranes with G

<sup>1</sup>School of Chemistry, University of Sydney, Sydney, New South Wales 2006, Australia. <sup>2</sup>School of Chemistry, University of Leeds, Woodhouse Lane, Leeds, LS2 9JT, UK. Email: stephen.hyde@sydney.edu.au; f.meldrum@leeds.ac.uk

compartment in which the spicule forms, yields spicules with morphologies defined by this modified compartment (12). More recently, the shape of larval spicules in vitro has been engineered by directing the assembly of cultured cells that then generate the three-dimensional environment in which the spicule forms (13).

It has been widely proposed that biomineralization by way of an amorphous precursor phase—which has no preferred geometry—allows the mineral to be molded into complex shapes by templating. However, as seen in both synthetic systems (14) and organisms such as coccoliths (15), it is not a pre-requisite. With the ease of forming crystals that far exceed the length scale of the template, and fairly isotropic crystal morphologies, calcite is a perfect construction material for the stereom, where it can fill a template of any shape without correspondence between the micrometer-scale morphology of the crystal and its crystal lattice.

The ultimate question of what determines the ultrastructure remains open, however. Given that lipids can assemble into G-, D-, and P-TPMS in vitro, and similar assemblies of soft matter are present in butterfly wing scales, it is possible that the calcite grows within a sponge-like membrane that templates the calcite. That case is strengthened by the presence of both P and D morphologies in echinoderms. However, current knowledge does not explain how those structures can form with huge lattice parameters ( $>10\ \mu\text{m}$ ). They may be the result of dynamic and coordinated cellular processes, commonly assumed to control morphologies in living systems. Alternatively, they may result from growth within a porous matrix, analogous to the origin of those structures in synthetic soft materials. ■

#### REFERENCES AND NOTES

1. G. Donnay, D. L. Pawson, *Science* **166**, 1147 (1969).
2. T. Yang *et al.*, *Science* **375**, 647 (2022).
3. S. T. Hyde, S. Schröder-Turk, *Interface Focus* **2**, 529 (2012).
4. S. Hyde *et al.*, *The Language of Shape* (Elsevier Science, 1996).
5. B. D. Wilts, K. Michielsen, J. Kuipers, H. De Raedt, D. G. Stavenga, *Proc. Biol. Sci.* **279**, 2524 (2012).
6. H. T. Ghiradella, M. W. Butler, *J. R. Soc. Interface* **6** (suppl. 2), S243 (2009).
7. L. Han *et al.*, *JUCrJ* **7**, 228 (2020).
8. K. M. Towe, *Science* **157**, 1048 (1967).
9. J. Seto *et al.*, *Proc. Natl. Acad. Sci. U.S.A.* **109**, 3699 (2012).
10. D. M. Raup, in *Physiology of Echinodermata*, R. A. Booloofian, Ed. (Interscience, 1966), pp. 379–395.
11. A. Jantschke, I. Pinkas, A. Schertel, L. Addadi, S. Weiner, *Acta Biomater.* **102**, 427 (2020).
12. K. Okazaki, *Embryologia* (Nagoya) **7**, 21 (1962).
13. C. H. Wu, A. Park, D. Joester, *J. Am. Chem. Soc.* **133**, 1658 (2011).
14. N. B. J. Hetherington *et al.*, *Adv. Funct. Mater.* **21**, 948 (2011).
15. Y. Kadan, F. Tollervy, N. Varsano, J. Mahamid, A. Gal, *Proc. Natl. Acad. Sci. U.S.A.* **118**, e2025670118 (2021).

10.1126/science.abn2717

#### GENETICS

## A new model of sex chromosome evolution

A new model, based on the evolution of gene regulation, challenges the classical theory

By Pavitra Muralidhar<sup>1,2</sup> and Carl Veller<sup>1,2</sup>

In many species, sex is determined by the presence or absence of a particular chromosome. In mammals, for example, males usually carry a Y and an X chromosome and females usually carry two X chromosomes. The sex-specific chromosome is often degenerate—small in size and gene-poor. Until recently, biologists have relied on a classical model to explain the evolution of degenerate sex chromosomes, involving sex differences in selection and the principle that selection acts less efficiently in regions of the genome that do not recombine in gametogenesis (1, 2). However, this model has received little concrete empirical support, and recent observations have called into question its generality (3, 4). On page 663 of this issue, Lenormand and Roze (5) propose a new model for the evolution of degenerate sex chromosomes, based on the evolution of gene regulation.

Theories of sex chromosome evolution start with a pair of chromosomes that differ only in the genetic variant that they carry at a single, sex-determining locus. For simplicity, consider one variant to be dominantly male-determining, defining a “proto-Y chromosome” (see the figure). (Alternatively, the variant could be dominantly female-determining, defining a ZW-female and ZZ-male system, as in birds and butterflies.) Genetic exchange between the proto-Y and proto-X chromosomes, through recombination during sperm formation, homogenizes them. For differences between the proto-Y and proto-X to evolve, recombination must be shut down across a region that includes the sex-determining locus.

The classical theory invokes sexually antagonistic selection to explain this initial recombination shutdown (3, 4). Sexual antagonism occurs when males and females have different fitness optima for some traits—genetic variants that influence these traits and are expressed in both sexes can be beneficial in one sex and costly in the

other. According to the classical theory, first, a male-beneficial variant appears on a chromosome with the male-determining gene, forming a combination that jointly triggers male development and increases male fitness. To preserve this mutually beneficial arrangement, recombination is shut down along a segment of the proto-Y that contains the male-beneficial and male-determining genes, and the segment subsequently spreads to high frequency. Recombination shutdown can be achieved in several ways, the simplest of which is physical inversion of the chromosomal segment. Because selection acts inefficiently in genomic regions that do not recombine, deleterious mutations subsequently accumulate in various genes within the nonrecombining segment of the proto-Y (1, 2). To minimize their negative effects, expression of mutated proto-Y genes is then reduced. This silencing of the proto-Y creates an imbalance in gene expression between XY males and XX females, selecting for mechanisms that correct this imbalance by increasing proto-X expression in males or decreasing proto-X expression in females—a phenomenon called dosage compensation.

This “textbook” theory has received relatively little empirical support (3, 4). A key uncertainty revolves around the causal role of sexual antagonism in the initial shutdown of recombination, which has been demonstrated in some taxa (6, 7) but appears to be absent in others (8, 9). The ambiguous importance of sexual antagonism, together with the discovery of cases where dosage compensation precedes degeneration (10, 11), has led to growing skepticism about the generality of the classical theory.

Lenormand and Roze propose a radically different theory for sex chromosome evolution, with gene regulation playing the starring role. In the simplest version of their model, the expression of each of the many genes on the proto-sex chromosomes is controlled by one “cis-regulator” on the same chromosome as the gene and two “trans-regulators” on distinct chromosomes. Each cis-regulator controls only the copy of the gene to which it is physically linked, whereas the trans-regulators—one male-specific and

<sup>1</sup>Center for Population Biology, University of California, Davis, CA, USA. <sup>2</sup>Department of Evolution and Ecology, University of California, Davis, CA, USA.  
Email: pmuralidhar@ucdavis.edu; cveller@ucdavis.edu



one female-specific—affect expression of both copies of the gene in an individual. The regulators' effects are subject to mutation, causing them to increase or decrease expression of their associated genes. At the same time, the genes can accrue mutations, which are usually deleterious.

A major departure from the classical theory is that, in Lenormand and Roze's model, the initial recombination shutdown around the sex-determining gene does not require sexual antagonism—only luck. By chance, some copies of the male-determining gene will happen to lie on chromosomal tracts with fewer than average deleterious mutations. A recombination shutdown across such a tract would “lock in” a high-fitness stretch of DNA, which would then increase in frequency. This process can repeat, expanding the region across which recombination is shut down.

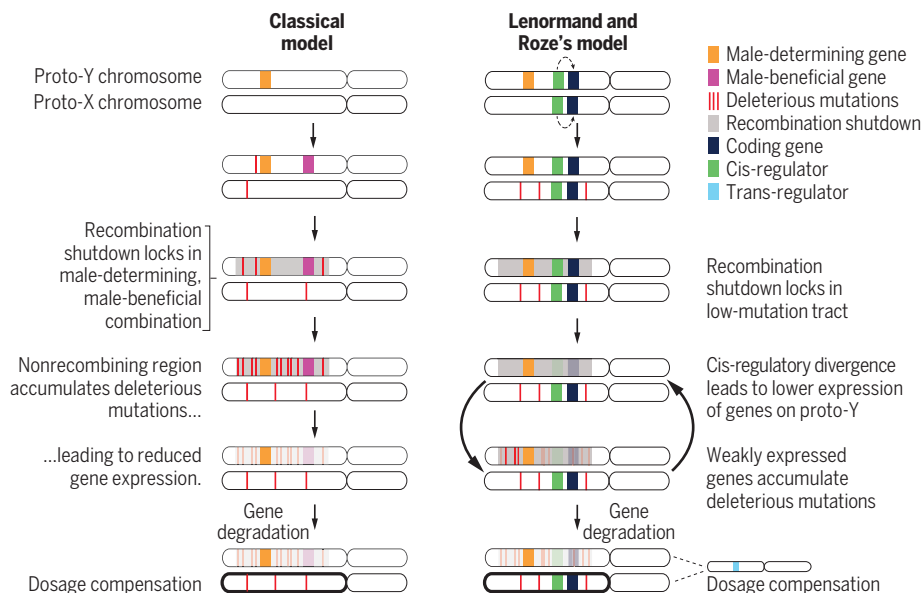
With no genetic exchange between the proto-X and proto-Y chromosomes, proto-X and proto-Y cis-regulators can evolve independently. Lenormand and Roze identify a subtle asymmetry in their evolution. Consider a cis-regulator on the proto-X that has mutated to reduce expression of its associated gene (also on the proto-X). Because that copy of the gene is now weakly expressed, a deleterious mutation in it does not affect fitness as substantially as if the gene were strongly expressed, and so it can sometimes, by chance, spread to appreciable frequency in the population (together with the weak cis-regulator). However, as the mutated gene becomes more common, it is more often paired with another copy of itself in females (who carry two proto-X chromosomes), unmasking its full deleterious effect. This creates a “frequency-dependent” selection that limits the spread of the mutated gene and its weak cis-regulator.

Now consider the case of a weak cis-regulator on the proto-Y. Again, because its gene is weakly expressed, a deleterious mutation in that gene can, by chance, spread to appreciable frequency. However, because the mutated gene is only ever present in males, its deleterious effect is always masked by the homologous gene on the proto-X (which is unlikely to carry the same mutation). Therefore, no frequency-dependent selection checks the spread of the mutated gene (and its weak cis-regulator). Thus, relative to the proto-X, the proto-Y tends to evolve weaker cis-regulators, and this process self-reinforces: Reduced expression of genes on the proto-Y permits more deleterious mutations to accumulate, selecting for even weaker expression to mask these deleterious mutations (12).

Reduced expression of the proto-Y would result in lower-than-optimal sex chromosome expression in XY males. This is where

## Two models of sex chromosome evolution

The classical model (left) is based on sexually antagonistic selection, whereas Lenormand and Roze's new model (right) is based on the regulation of gene expression.



the sex-specific trans-regulators step in: Male-specific trans-regulators increase expression of proto-X and proto-Y genes, returning expression to optimal levels in males. The result is that, on average across their two sex chromosomes, males have weaker cis-regulation and stronger trans-regulation than females. This sex difference in balancing cis- and trans-regulation “locks in” the recombination shutdown on the proto-Y—if recombination were again permitted, strong cis-regulators would recombine from the proto-X onto the proto-Y and, in concert with strong male-specific trans-regulators, push sex chromosome expression in males above its optimum.

Of these two theories for sex chromosome evolution, which is correct? Complicating this question is the substantial scope for overlap between the theories. For example, it is not crucial for the later steps of Lenormand and Roze's model whether the initial recombination shutdown is due to chance or to sexual antagonism (as in the classical theory). Similarly, although their theory does not need selective interference to explain the accumulation of deleterious mutations on the proto-Y, this accumulation is accelerated by interference (12).

Historically, most of our knowledge of sex chromosome evolution has been built on ancient systems like the mammalian X and Y. However, the chronology of events in the early evolution of these sex chromosomes has been substantially obscured by time, making it difficult to use them to empirically distinguish theories of sex chromosome evolution (3, 4). Encouragingly,

attention has recently shifted to young sex chromosome systems, where genetic sex determination has newly evolved (as in many plants) or where the chromosome that determines sex has switched (as in several clades of frogs and fish) (8). These systems enable direct observation of the early steps of sex chromosome evolution, creating opportunities to use experimental methods to test the causal role of sexual antagonism in recombination shutdown (9) and to use molecular and comparative techniques to track the early progression of dosage compensation (10, 11). The coming years will be exciting for sex chromosome biology, as the full theoretical implications of Lenormand and Roze's model are fleshed out and empirical methods that have been developed for young sex chromosome systems are brought to bear on the theory. ■

### REFERENCES AND NOTES

1. B. Charlesworth, *Science* **251**, 1030 (1991).
2. D. Bachtrog, *Genetics* **179**, 1513 (2008).
3. A. E. Wright, R. Dean, F. Zimmer, J. E. Mank, *Nat. Commun.* **7**, 1 (2016).
4. D. Charlesworth, *Philos. Trans. R. Soc. London Ser. B* **372**, 20160456 (2017).
5. T. Lenormand, D. Roze, *Science* **375**, 663 (2022).
6. R. B. Roberts, J. R. Ser, T. D. Kocher, *Science* **326**, 998 (2009).
7. A. E. Wright et al., *Nat. Commun.* **8**, 14251 (2017).
8. S. Ponnika, H. Sigeman, J. K. Abbott, B. Hansson, *Trends Genet.* **34**, 492 (2018).
9. N. Perrin, *Philos. Trans. R. Soc. London Ser.* **376**, 20200094 (2021).
10. A. Muyle et al., *PLoS Biol.* **10**, e1001308 (2012).
11. H. Martin et al., *Genome Biol. Evol.* **11**, 350 (2019).
12. T. Lenormand, F. Fyon, E. Sun, D. Roze, *Curr. Biol.* **30**, 3001 (2020).

## PIEZOELECTRICS

# Breaking symmetry for piezoelectricity

Record-breaking piezoelectricity is achieved in oxides with symmetry-breaking defects

By Fei Li

**P**iezoelectricity, the ability of a material to generate an electric field in response to applied mechanical stress, has been widely used for state-of-the-art electronics, such as medical ultrasound machines, underwater microphones, and vibration and pressure sensors (1, 2). As a basic prerequisite, only materials with a noncentrosymmetric microstructure can potentially be piezoelectric. Thus, the search for piezoelectric materials has been mainly limited to noncentrosymmetric materials. On page

are ferroelectrics (4–10)—materials that have a spontaneous electric polarization. The piezoelectric coefficient ( $d_{33}$ ) is perhaps the most important measure for a piezoelectric material. It quantifies the change of mechanical strain when a piezoelectric material is subject to an electric field and is often expressed in picometers per volt. The piezoelectric coefficient of ferroelectrics is determined by several parameters. Two of these parameters—dielectric permittivity and spontaneous polarization—are what materials scientists focus on. Dielectric permittivity is the measure of how much electric polarization is in-

ultrahigh piezoelectric coefficients ranging from 1000 to 4000 pm/V (9, 10). However, there is a long-standing issue presented in these ferroelectrics—their operational temperature range is greatly limited by Curie temperature. Above this temperature, these materials would go from being ferroelectric to paraelectric and, with this transition, would lose their spontaneous polarization and piezoelectricity. To generate piezoelectricity in ferroelectric materials above the Curie temperature, one of the most promising approaches is to induce polarization for the materials by applying a direct current (DC) electric field.

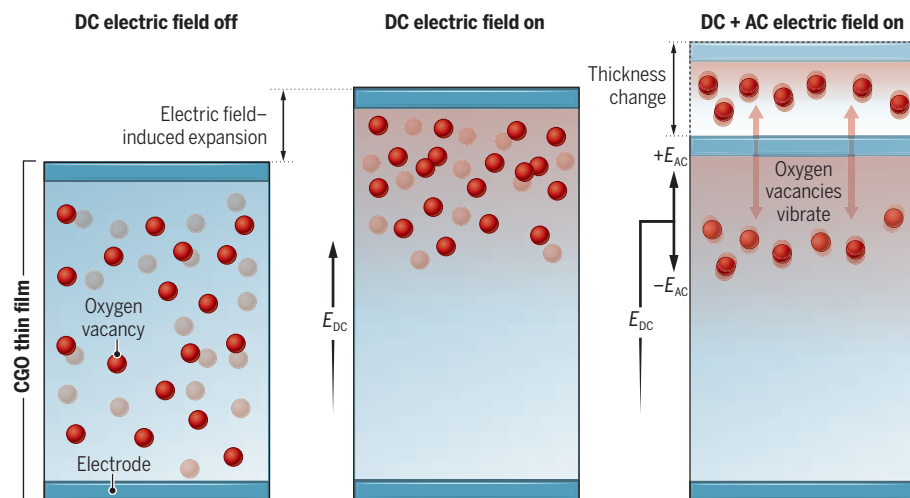
Previous efforts that looked for piezoelectric materials using this DC electric field approach focused on centrosymmetric perovskite oxides. However, because the dielectric permittivity generally decreases as the DC electric field increases for perovskite oxides, there is a limitation to the piezoelectricity induced by a DC electric field, with the current bottleneck around 1500 pm/V (11). Looking beyond perovskites, Park *et al.* used a DC electric field on a thin film of Gd-doped  $\text{CeO}_{2-x}$  (CGO) to induce even higher piezoelectricity. By applying a DC electric field of 1 MV/cm, the authors obtained an ultrahigh piezoelectric coefficient of 200,000 pm/V at a frequency of 10 mHz—about 50 times as high as that of the current best piezoelectric oxides (10).

Park *et al.* discovered that the oxygen vacancies in the CGO thin film can be rearranged by the DC electric field, which leads to symmetry breaking and thus incorporating piezoelectricity in the film (see the figure). They measured the piezoelectric coefficient by applying an alternating current (AC) electric field on top of the DC field. The AC field pushes oxygen vacancies toward the top electrode when it is in the same direction as the DC field, which expands the material, and it does the opposite when it is in the opposite direction of the DC field.

The authors attributed the ultrahigh piezoelectricity of the thin film to the large dielectric permittivity caused by the greatly enhanced defect migration under the DC electric field. Additionally, the authors observed that the redistribution of oxygen vacancies could induce a cubic-to-tetragonal structural transition, which is

## Breaking symmetry aids piezoelectric materials

A direct current (DC) electric field ( $E_{\text{DC}}$ ) induces the redistribution of oxygen vacancies within a Gd-doped  $\text{CeO}_{2-x}$  (CGO) thin film, turning the material piezoelectric. The piezoelectricity is then measured using an additional alternating current (AC) electric field ( $E_{\text{AC}}$ ), which further drives the oxygen vacancies up and down in synchronization with the physical expansion and contraction of the thin film.



653 of this issue, Park *et al.* (3) report a record-breaking piezoelectric performance in a centrosymmetric oxide. Instead of starting with a noncentrosymmetric material, the symmetry of the oxide was broken by inserting oxygen vacancies—a type of point defect—and then manipulating these vacancies with an electric field.

Most high-performance piezoelectrics

induced in a material by an external electric field, and spontaneous electric polarization is the measure of the material's naturally existing polarization in the absence of an external field.

The general approach to enhance the piezoelectric coefficient of ferroelectrics is to enlarge the dielectric permittivity by inducing structural instability. For example, through the design of ferroelectric phase transition and chemical disorder to enhance structural instability,  $\text{Pb}(\text{Mg}_{1/3}\text{Nb}_{2/3})\text{O}_3\text{-PbTiO}_3$  (PMN-PT) and rare earth element-doped PMN-PT crystals can exhibit

Electronic Materials Research Lab, Key Lab of Education Ministry and State Key Laboratory for Mechanical Behavior of Materials, School of Electronic Science and Engineering, Xi'an Jiaotong University, Xi'an 710049, China.  
Email: ful5@xjtu.edu.cn

GRAPHIC: C. BICKEL/SCIENCE



thought to be a critical factor responsible for the large electric field-induced strain observed in the CGO thin film. This is good news for the design of piezoelectric actuators based on thin films.

Notably, Park *et al.* have implemented the same approach to other centrosymmetric systems for inducing piezoelectricity. They showed that by applying a DC electric field to yttria-stabilized zirconia and CGO bulk ceramics, the induced piezoelectric response can be comparable to those piezoelectric materials currently used in microelectromechanical systems.

Park *et al.* show that extremely high piezoelectricity can be achieved in centrosymmetric oxides through the electric field-induced redistribution of oxygen vacancies. Although further research is required to improve the frequency stability of the piezoelectric response and to reduce the dielectric loss for CGO thin films, the strategy of utilizing mobile ions or defects to induce high piezoelectricity in centrosymmetric materials opens a new avenue for designing future advanced piezoelectric materials. Even higher piezoelectricity in ferroelectrics is also possible if this design strategy can be incorporated with other design approaches already in use, such as the manipulation of ferroelectric phase transition (4), domain configuration (12–14), and structural fluctuation at the nanoscale (10). From an application viewpoint, the electric field-biased CGO thin film may not only benefit state-of-the-art piezoelectric devices but also expand the application space for piezoelectric materials, including biocompatible piezoelectric devices and piezoelectric sensors with an operational temperature range above 600°C and a pressure range above 250 MPa (15). ■

## REFERENCES AND NOTES

1. S. Zhang *et al.*, *Prog. Mater. Sci.* **68**, 1 (2015).
2. E. Aksel, J. L. Jones, *Sensors* **10**, 1935 (2010).
3. D.-S. Park *et al.*, *Science* **375**, 653 (2022).
4. B. Jaffe, W. R. Cook Jr., H. Jaffe, *Piezoelectric Ceramics* (Academic Press, 1971).
5. J. Wu, D. Xiao, J. Zhu, *Chem. Rev.* **115**, 2559 (2015).
6. W.-Q. Liao *et al.*, *Science* **363**, 1206 (2019).
7. M. Höfling *et al.*, *Science* **372**, 961 (2021).
8. H. Liu *et al.*, *Science* **369**, 292 (2020).
9. S.-E. Park, T. R. Shrout, *J. Appl. Phys.* **82**, 1804 (1997).
10. F. Li *et al.*, *Science* **364**, 264 (2019).
11. R. E. Newnham, Q. C. Xu, S. Kumar, L. E. Cross, *Ferroelectrics* **102**, 259 (1990).
12. B. Wang, F. Li, L.-Q. Chen, *Adv. Mater.* **33**, 2105071 (2021).
13. S. Wada, K. Yako, H. Kakemoto, T. Tsurumi, T. Kiguchi, *J. Appl. Phys.* **98**, 014109 (2005).
14. K. Wang, J.-F. Li, *Adv. Funct. Mater.* **20**, 1924 (2010).
15. A. J. Bell, T. P. Cornyn, T. J. Stevenson, *APL Mater.* **9**, 010901 (2021).

## ACKNOWLEDGMENTS

This work was supported by the National Natural Science Foundation of China (grant no. 51922083). The author thanks L. Luo for helping design the figures.

10.1126/science.abn2903

## CELL BIOLOGY

# From start to finish—a molecular link in wound repair

p53 mediates epithelial cell migration and leader cell elimination during wound repair

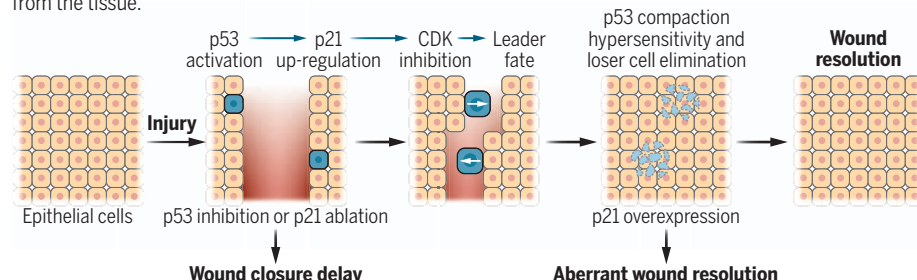
By Sangwon Yun<sup>1</sup> and Valentina Greco<sup>1,2</sup>

During epithelial wound repair, a subset of epithelial cells become “leaders” as the epithelial sheet collectively migrates to close the gap. These leader cells adopt distinct morphological characteristics and up-regulate migratory pathways (1, 2), but the molecular mechanism by which this subset emerges from an otherwise

Under homeostatic conditions, epithelial cells may become motile and move as individuals or groups. These two forms of cell migration play key roles in various biological processes to reorganize a tissue in response to stimuli (6). During collective cell migration, a subset of cells at the leading edge, called leader cells, direct the trajectory of the epithelial sheet. Using Madin-Darby canine kidney (MDCK) cells in culture, Kozyrska *et al.* observed that

## Dual role of p53 in wound repair

Upon epithelial injury, p38 stress kinase-mediated p53 activation leads to p21 expression, which induces cyclin-dependent kinase (CDK) inhibition and the leader cell phenotype. For wound resolution to occur, leader cells become loser cells as a result of p53-mediated compaction hypersensitivity, resulting in their elimination from the tissue.



homogeneous population remained to be elucidated. On page 628 of this issue, Kozyrska *et al.* (3) find that leader cell behavior initiates with the activation of the tumor suppressor and transcription factor p53, which induces p21 expression and attendant cell cycle inhibition. Once the injury is resolved, leader cells are eliminated through p53-dependent crowding hypersensitivity. Classically, p53 becomes activated by cell stressors, including DNA damage, oncogenic expression, and hypoxia (4). In the case of mechanical disruption from wounding, p53 activation occurs through the stress kinase p38 (5). These newly found roles of p53 in leader cell emergence and elimination provide important insight into wound repair.

some of these cells spontaneously lost epithelial morphology and exhibited migratory behavior consistent with that of leader cells in collective migration. Because these spontaneous leader cells tended to be binucleate, the authors sought to determine whether this property was sufficient to elicit the leader cell phenotype and blocked cytokinesis, observing that the resulting binucleate cells became leaders. Because cytokinesis failure causes p53-mediated cell cycle arrest, the authors reasoned and verified that spontaneous leader cells also had significantly higher expression of p53. Indeed, pharmacologic p53 activation was sufficient to provoke leader cell fate. Thus, p53 plays a central role in leader cell emergence and behavior. These findings are surprising given prior studies that describe a role of p53 in inhibiting cancer cell invasiveness and the link between loss of p53 and hallmarks of epithelial-mesenchymal transition, a phenomenon in which epithe-

<sup>1</sup>Department of Genetics, Yale School of Medicine, New Haven, CT, USA. <sup>2</sup>Departments of Cell Biology and Dermatology, Yale Stem Cell Center, Yale Cancer Center, Yale School of Medicine, New Haven, CT, USA. Email: valentina.greco@yale.edu; sangwon.yun@yale.edu

lial cells adopt mesenchymal properties, such as increased migratory capacity (7, 8).

p53 induces expression of p21, causing cell cycle arrest at the G<sub>1</sub>/S checkpoint. Kozyrskaya *et al.* discovered that spontaneous leader cells expressed higher amounts of p21, suggesting that p53 mediates the leader cell phenotype through up-regulation of p21 expression (see the figure). p21 inhibits cyclin-dependent kinases (CDKs), and the authors found that cells inducibly overexpressing p16, a CDK inhibitor structurally unrelated to p21, also began exhibiting leader cell characteristics. Curiously, upon treating leader-follower pairs with CDK1 and CDK2 inhibitors, the authors observed a decrease in migration. This suggests that, although spontaneous leader cell-directed collective cell migration depends upon cell cycle arrest through p53 and p21-mediated CDK inhibition, the ability of leaders to migrate while leading followers requires a disparity in CDK activity.

What is the relevance to injury? Kozyrskaya *et al.* found that epithelial scratch in their cell culture system gave rise to leader cells with increased expression of p53 and p21. These cells underwent cell cycle arrest, whereas cells that became migrating followers had no evidence of cell cycle changes. Activation of p53 along the scratch was caused by activation of the mechanical stress kinase p38. Moreover, inhibiting p53 or ablating p21 delayed the rate of wound closure, indicating that the p53-p21 axis mediates epithelial injury repair, a finding consistent with cutaneous wound repair experiments *in vivo* (9).

Prior work showed that MDCK cells with increased p53 expression become hypersensitive to compaction, resulting in their elimination from the epithelium as “losers” in a form of mechanical cell competition (a process by which cells with higher fitness expand whereas less fit ones are eliminated) (5). Notably, increased p53 expression in this biological context was also due to p38 activation. Kozyrskaya *et al.* found that both spontaneous leaders and scratch-induced leader cells underwent cell death or extrusion as they became compacted by follower cells. Curiously, this appeared to be independent of p21. However, leader cells inducibly overexpressing p21 failed to undergo elimination during wound resolution, instead exhibiting an aberrant morphology that disrupted the repaired epithelium. These findings underscore the dual function of p53 activation in both initiating and concluding wound repair, as well as the importance of mechanical cell competition during this process. The epithelial disruption observed with leader cell retention evokes the loss of cell elimi-

nation by mechanical cell competition that is observed in the context of oncogenic Ras expression in *Drosophila melanogaster* (10). Intriguing questions remain to be addressed about how leader cell induction and elimination through cell competition might differ in a hyperproliferative epithelium, and in the event that inappropriate injury resolution occurs, there may also be important implications for wound repair in tissue harboring cancer-associated mutations.

These discoveries engender new ways of conceptualizing both the process of tissue reorganization and p53 regulation, including the manner by which tissue and cellular context determines how a common signal (p53) may yield different responses. Investigating these molecular regulators will enable further insight into the principles of cell behavior modulation, as well as their applicability to other organismal systems and complex tissues. For example, during wound repair of mouse skin, epithelial cells adjacent to injury become migratory and nonproliferative, suggesting that the same molecular mechanism may apply (11). Collectively, they may offer molecular opportunities for therapeutic intervention, including correcting aberrant wound healing. For example, chronic wounds fail to re-epithelialize owing to various mesenchymal, basement membrane, and inflammatory derangements, including epidermal hyperproliferation without migration (12). In this tissue context, reactivation of epithelial migratory pathways while arresting cell cycling may correct defects in this process. ■

#### REFERENCES AND NOTES

1. M. Poujade *et al.*, *Proc. Natl. Acad. Sci. U.S.A.* **104**, 15988 (2007).
2. R. Mayor, S. Etienne-Manneville, *Nat. Rev. Mol. Cell Biol.* **17**, 97 (2016).
3. K. Kozyrskaya *et al.*, *Science* **375**, 628 (2022).
4. A. Hafner, M. L. Bulyk, A. Jambhekar, G. Lahav, *Nat. Rev. Mol. Cell Biol.* **20**, 199 (2019).
5. L. Wagstaff *et al.*, *Nat. Commun.* **7**, 11373 (2016).
6. P. Friedl, D. Gilmour, *Nat. Rev. Mol. Cell Biol.* **10**, 445 (2009).
7. S. P. Wang *et al.*, *Nat. Cell Biol.* **11**, 694 (2009).
8. C. J. Chang *et al.*, *Nat. Cell Biol.* **13**, 317 (2011).
9. H. N. Antoniadou, T. Galanopoulos, J. Neville-Golden, C. P. Kiritky, S. E. Lynch, *J. Clin. Invest.* **93**, 2206 (1994).
10. R. Levayer, C. Dupont, E. Moreno, *Curr. Biol.* **26**, 670 (2016).
11. S. Park *et al.*, *Nat. Cell Biol.* **19**, 155 (2017).
12. S. A. Eming, P. Martin, M. Tomic-Canic, *Sci. Transl. Med.* **6**, 265sr6 (2014).

#### ACKNOWLEDGMENTS

V.G. and S.Y. are supported by a Howard Hughes Medical Institute Scholar award and NIH grants (1R01AR063663-01, 1R01AR067755-01A1, 1DP1AG066590-01 and R01AR072668). S.Y. is supported by a Medical Scientist Training Program grant from the NIH (T32GM136651).

#### AGING

## Caloric restriction has a new player

Reverse translation of a human caloric restriction trial finds an immunometabolic regulator

By Timothy W. Rhoads<sup>1</sup> and Rozalyn M. Anderson<sup>1,2</sup>

Caloric restriction (CR) has been a cornerstone of aging biology for decades (1). A reduction of energy intake without malnutrition delays aging and the onset of age-associated diseases in multiple species, including nonhuman primates (2). Although there has been interest in CR as a lifestyle recommendation for humans, the real potential lies in understanding the mechanisms and translating them. By identifying critical factors and processes that are causal in the beneficial effects of CR, it could be possible to learn what is creating vulnerability and what might be targeted to change the pace of functional decline. On page 671 of this issue, Spadaro *et al.* (3) profiled adipose tissues from people undergoing CR for 2 years and identified reduced expression of platelet-activating factor acetylhydrolase (PLA2G7). Poised at the intersection of metabolism and immunity, PLA2G7 could be a valuable target for correction of immunometabolic dysfunction.

The importance of immune and inflammatory pathways in aging is well established (4, 5). Multiple diseases and disorders of age bear a signature of dysfunction in these pathways, which are critical for health, repair, and continued fitness after infection or injury. Of particular clinical relevance, these processes are also associated with disease vulnerability in the context of obesity. Metabolic dysfunction is thought to be a key driver of disease vulnerability associated with age and with expanded adipose depots, and there is a highly

<sup>1</sup>Department of Medicine, School of Medicine and Public Health, University of Wisconsin–Madison, Madison, WI, USA. <sup>2</sup>Geriatric Research, Education, and Clinical Center, William S. Middleton Memorial Veterans Hospital, Madison, WI, USA. Email: rozalyn.anderson@wisc.edu



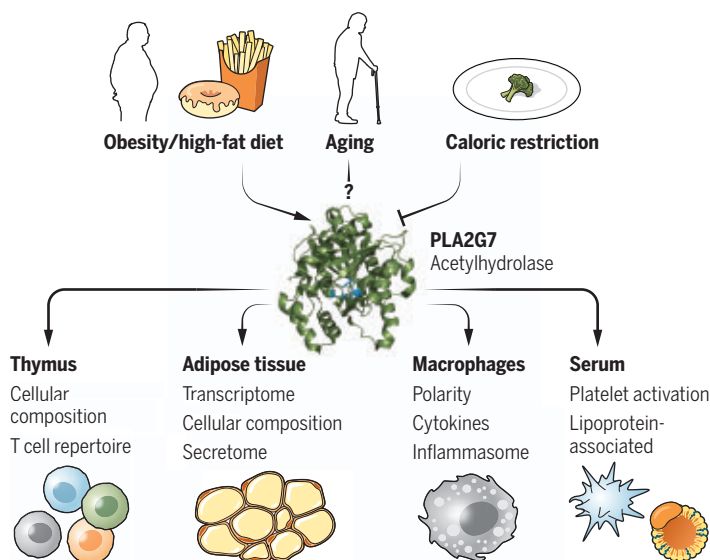
complex inter-relationship between metabolic, immune, and inflammatory pathways (6). Adipose tissue-derived factors are implicated in loss of metabolic integrity and increased inflammatory tone, including factors produced by adipocytes, macrophages, and stromovascular cell types. In mice, CR substantially lowers adiposity and influences the abundance of adipose tissue-derived factors, including adipokines, lipokines, and circulating lipids (7).

Reverse translation is an approach that takes clinical observations and investigates the underlying biology in laboratory models (animals and cell culture). Spadaro *et al.* took advantage of data and specimens captured as part of the CALERIE study (Comprehensive Assessment of Long-term Effects of Reducing Intake of Energy). This clinical trial involved 2 years of dietary intervention, and although the target was 25% CR, the eventual level attained was closer to 14% (8). Notably, many of the features of CR identified in mouse, rat, and non-human primate studies were also evident in humans undergoing CR, including reduced adiposity, improvements in insulin sensitivity, and lower risk markers of cardiovascular disease (9–11). Spadaro *et al.* showed that in humans, CR preserves thymic volume, and that CD4<sup>+</sup> and CD8<sup>+</sup> T cell production is preserved, suggesting that the effects of CR are protective. The thymus is a key tissue for T cell maturation, and shrinkage of the thymus, which begins during middle age, blunts immune surveillance. The authors went on to investigate adipose tissue using gene expression profiles from abdominal subcutaneous depots and found evidence for substantial adipose tissue remodeling with CR, and changes were identified in pathways of metabolism, innate-immune and antigen processing, and inflammation. One gene that was lower in expression in adipose tissue in response to CR was *PLA2G7*.

*PLA2G7* is best known for its role in degrading platelet-activating factor, a phospholipid mediator of platelet aggregation and potent activator of inflammation. In clinical studies, higher circulating amounts of *PLA2G7* have been associated with numerous disorders that have a basis in metabolic, immune, and inflammatory dysfunction, including stroke, chronic obstructive pulmonary disease, autoimmune diseases, cardiovascular diseases, type II diabetes, neuropathy, and some types

## A regulator of immunometabolism

Obesity and high-fat diet stimulate platelet-activating factor acetylhydrolase (*PLA2G7*) expression in mice, whereas caloric restriction in humans attenuates its expression. Through immunometabolic regulation in various tissues, *PLA2G7* influences pathways that contribute to local and systemic metabolic integrity, immune regulation, and inflammation.



of cancer. A causal role for *PLA2G7* in disease onset has not been identified, and it is not yet clear how increased circulating amounts could be predisposing for this host of chronic diseases. Little is known about the biology of *PLA2G7*; it is a secreted enzyme that is physically associated with lipoproteins (particles that transport triacylglycerides and cholesterol in the blood) and is particularly enriched on low-density lipoproteins (LDLs) (12, 13), the particles associated with “bad cholesterol.” *PLA2G7* plays a role in degrading other lipid inflammatory mediators, and its expression is sensitive to differences in composition of circulating lipids (14, 15). In this way, *PLA2G7* could link lipid metabolism and lipid signaling to disease vulnerability.

To understand the basis for the lower expression of *PLA2G7* in adipose tissue in people undergoing CR, Spadaro *et al.* deleted the corresponding gene in mice. This protected mice from high-fat diet-induced obesity. In addition to lower adiposity, increased adipose tissue lipolysis, and reduced hepatic steatosis (fatty liver), the authors demonstrate that mice lacking *Pla2g7* had lower circulating concentrations of proinflammatory cytokines. The absence of *PLA2G7* changed the cellular composition of visceral adipose tissue toward a more healthy disposition, lowering the relative numbers of B cells, T cells, and proinflammatory macrophages. Furthermore, the ability to induce inflammation in adipose tissue-derived macrophages was blunted when *PLA2G7* was genetically disabled. Notably, the connection to lipids was

again observed; macrophages primed with the proinflammatory molecule lipopolysaccharide (LPS) were protected by loss of *PLA2G7*, but only when a lipid ceramide was used as the inflammatory trigger. The loss of *PLA2G7* also protected thymic volume in older mice and preserved thymocyte abundance, both changes that are predicted to be beneficial for immune health. Together, these findings demonstrate clear connections between *PLA2G7*-directed lipid processing and inflammation and suggest that *PLA2G7* plays a role in coordinating metabolic, immune, and inflammatory status (see the figure).

The study by Spadaro *et al.* adds to the evidence linking nutrition to metabolism, immune regulation, and inflammation and provides further support for the idea that lipid-derived molecules are a key mediator in

nutritional modulation of health. The implementation of reverse translation has clearly borne fruit in this work. In taking the leap from observations in humans to experiments with transgenic mouse models, Spadaro *et al.* provide new insight into the biology of *PLA2G7* and its important role in immunometabolic regulation and systemic homeostasis. This work is a nice example of what can be gained by focusing on the mechanisms underlying the beneficial effects of CR. ■

## REFERENCES AND NOTES

1. A. Richardson, *J. Gerontol. A Biol. Sci. Med. Sci.* **76**, 57 (2021).
2. P. Balasubramanian, P. R. Howell, R. M. Anderson, *EBioMedicine* **21**, 37 (2017).
3. O. Spadaro *et al.*, *Science* **375**, 671 (2022).
4. D. Furman *et al.*, *Nat. Med.* **25**, 1822 (2019).
5. A. H. Lee, V. D. Dixit, *Immunity* **53**, 510 (2020).
6. C. R. Kahn, G. Wang, K. Y. Lee, *J. Clin. Invest.* **129**, 3990 (2019).
7. K. N. Miller *et al.*, *Aging Cell* **16**, 497 (2017).
8. E. Ravussin *et al.*, *J. Gerontol. A Biol. Sci. Med. Sci.* **70**, 1097 (2015).
9. J. Most *et al.*, *Am. J. Physiol. Endocrinol. Metab.* **314**, E396 (2018).
10. S. K. Das *et al.*, *Am. J. Clin. Nutr.* **105**, 913 (2017).
11. W. E. Kraus *et al.*, *Lancet Diabetes Endocrinol.* **7**, 673 (2019).
12. L. W. Tjoelker *et al.*, *Nature* **374**, 549 (1995).
13. K. E. Stremmel, D. M. Stafforini, S. M. Prescott, T. M. McIntyre, *J. Biol. Chem.* **266**, 11095 (1991).
14. L. Jackisch *et al.*, *Diabetologia* **61**, 1155 (2018).
15. J. T. Boyd *et al.*, *Nat. Metab.* **3**, 762 (2021).

## ACKNOWLEDGMENTS

The authors are supported by National Institutes of Health grants AG067330, AG057408, AG070686; the Department for Veterans Affairs BX003846; the Simons Foundation; and Impetus Grants.

## RETROSPECTIVE

# Thomas E. Lovejoy (1941–2021)

## Biodiversity pioneer and expert on the Amazon rainforest

By William F. Laurance

**T**homas E. Lovejoy, one of the world's most storied conservation biologists, died on 25 December 2021 at the age of 80. Lovejoy was a renowned expert on biodiversity, tropical forests, and climate change who devoted much of his career to working in the Amazon, the world's largest rainforest. Our natural world, and those who study and protect it, will be poorer for his loss.

Lovejoy was born in New York City in 1941, the only child in a prominent, politically connected family. An avid reader and lover of the outdoors, he attended Millbrook School, a private boarding school in upstate New York, largely because it had a zoo whose wildlife piqued his interest. Later, he enrolled at Yale University, earning his bachelor's degree in biology in 1964 while working as a zoological assistant at the Yale Peabody Museum of Natural History. He then spent a gap year exploring the Nile River region of Nubia in East Africa before commencing a PhD at Yale on the ecology of Amazon forest birds, which he completed in 1969.

After finishing his doctorate, Lovejoy moved to the Washington, DC, area, where he quickly emerged as a new breed of scientist—a “biopolitician” who was just as comfortable rubbing shoulders with leading politicians, celebrities, and billionaires as he was exploring ecosystems as a muddy-kneed field biologist. In a career spanning half a century, Lovejoy held high-level positions with organizations such as the World Wildlife Fund, the Smithsonian Institution, and the United Nations Foundation, among others. He also served as an environmental adviser to Presidents Reagan, Bush Sr., and Clinton and as chief biodiversity adviser to the World Bank, where he helped to strengthen environmental safeguards for World Bank-funded projects.

Lovejoy was in every sense an international scientific leader. He made key contributions to President Carter's *Global 2000 Report* that in 1980 raised urgent concerns about biodiversity loss, population growth, and other environmental threats. He devised

the first debt-for-nature swap (in which a cash-strapped country exchanges part of its foreign debt for a pledge to undertake environmental protection), an innovative financial tool that so far has leveraged more than \$1 billion for nature conservation in at least three dozen nations. He popularized—or, according to some, coined—the iconic modern term “biodiversity.” Perhaps most notably, over the course of his dynamic career, Lovejoy served on scores of boards and advisory panels for scientific, academic, environmental, and philanthropic organizations. This gave him remarkable influence as well as personal



connections to a long string of global movers and shakers.

Of all of Lovejoy's accomplishments, the nearest and dearest to his heart was probably the Biological Dynamics of Forest Fragments Project (BDFFP) in central Amazonia. In concert with Brazilian colleagues, Lovejoy founded the BDFFP in 1979 to study how habitat fragmentation affects Amazonian birds, bats, trees, vines, insects, and other elements of rainforest biodiversity. Today it is one of the world's largest and longest-running ecological experiments, spanning some 1000 km<sup>2</sup>. Along the way, the project has been a scientific and educational windfall, producing nearly 800 technical publications, 180 student theses, and advanced training for more than 700 environmental professionals from across Latin America. The BDFFP's sprawling study area also plays a key role in limiting deforestation associated with rapid road expansion in central Amazonia.

Lovejoy and I got to know each other in

1996 when I was hired as a lead researcher at the BDFFP. At that time, a portion of the project's annual funding came from the Smithsonian Tropical Research Institute in Panama, and Lovejoy occasionally butted heads with the institute's directors, who wanted him to share access to the many wealthy donors and philanthropists that had funded his work over the years. Lovejoy invariably refused, and the resulting clashes could be memorable. These were the only times I ever saw the normally buttoned-down Lovejoy lose his temper.

As a colleague, Lovejoy was charming, politically astute, and brilliant. He was also a natty dresser (after his passing, Lovejoy's daughters discovered that he owned 362 bow ties). Among many personal honors, Lovejoy received the Tyler Prize for Environmental Achievement in 2001, the BBVA Foundation Frontiers of Knowledge Award in Ecology and Conservation Biology (which he and I shared equally) in 2008, and the Blue Planet Prize in 2012. Last year, he was elected to the US National Academy of Sciences in recognition of his seminal contributions to the study of tropical ecosystems and his vital work with Brazilian researcher Carlos Nobre on Amazon tipping points.

Of all of Lovejoy's myriad accomplishments, I believe the BDFFP will be the most enduring and valuable. Over the past four decades, Lovejoy used the project as a living laboratory to introduce innumerable politicians, entertainers, and wealthy patrons to the Amazon rainforest. Prominent visitors such as Al Gore, Tom Cruise, and Walter Cronkite ended their tour of the study area with a stay at Camp 41, the project's best-known field camp, where they enjoyed a captivating evening with a caipirinha (a potent Brazilian cocktail) in one hand and a plate of tambaqui (delectable Amazonian fish) in the other. It was a transformative experience for many visitors, who slept in hammocks under a pristine night sky untarnished by the glare of civilization. On waking, some were lucky enough to discover softball-sized footprints where a curious jaguar had recently stalked through the camp.

Will Lovejoy's singular research project survive without him? In 2018, he helped to establish the Amazon Biodiversity Center, a nongovernmental group in the United States devoted to funding the BDFFP. The Smithsonian Institution will also provide some continuing support. Such monies are uncertain, however, without Lovejoy to lead the fundraising. In my view, the most important way we can honor Tom Lovejoy is to ensure the long-term survival of his extraordinary legacy in the Amazon. ■

10.1126/science.abo1787

Centre for Tropical Environmental and Sustainability Science, College of Science and Engineering,  
James Cook University, Cairns, QLD 4878, Australia.  
Email: bill.laurance@jcu.edu.au



## PALEONTOLOGY

# Vivid snapshots of the past

A paleontologist offers an immersive look at pivotal moments in Earth's history

By **Lance Grande**

**O***therlands* is scientific, in the sense that the author is an award-winning young paleontologist who uses his expertise to reconstruct Earth's history. But it is by no means a textbook. Instead, Thomas Halliday's poetic prose positions the reader as an observer who has gone back in time for a graphic look at 16 of Earth's ecosystems at different times and places, ranging from Australia in the Ediacaran period to Alaska in the Upper Pleistocene.

The book's first chapter places the reader on the northern slope of Alaska 20,000 years ago, when the region was still connected to Siberia. Halliday begins: "Dawn is near breaking in the Alaskan night, where a small herd of horses, four adults and three foals, huddle against the frigid northeasterly wind. By this time, the sun has been gone for well over ten hours, and the air is skin-tighteningly cold." The text continues in this vein, weaving in descriptions of other creatures living along the mammoth steppe and the forests of the Bering land bridge.

"To the roaming horses of the North Slope, and to the cave lions that pursue them, the steppe must seem immovably wide, but when seen at the scale of deep time, permanence is an illusion," writes Halliday, at the chapter's end. "As the ice retreats, all it takes is a drop of rain, and the hard land beneath the stamping hooves will soon give way. All it takes is a flicker, and the aurora dies." Such passages bring this long-extinct ecosystem to life.

In chapter 2, Halliday moves to Kanapoi, Kenya, 4 million years ago, vividly highlighting the sensory experiences of early hominids: "A scream of alarm from a turaco sets a commotion among a troop of *Australopithecus*. Disturbed from chewing on leaves, the hominins scramble to their feet and run to climb lianas to safety..."

The reviewer is at the Negaunee Integrative Research Center, Field Museum, Chicago, IL 60605, USA. Email: lgrande@fieldmuseum.org



The enormous flightless *Garganornis ballmanni* lived in what is now Gargano, Italy, during the late Miocene.

Halliday's next stop is Gargano, Italy, and the Zanclean flood, which occurred 5.33 million years ago. Gargano, we learn, was once an island known for highly endemic fauna, some of which showed signs of gigantism and dwarfism: think enormous geese and tiny deer-like ruminants. Eventually, however, Gargano "found itself below the waves, its unique creatures wiped out."

In Tinguiririca, Chile, 32 million years ago, Halliday paints a portrait of the first grasslands to evolve on the planet and a few of the animals that took advantage of them. On Seymour Island, Antarctica, some 41 million years ago, we observe a climate that was much warmer than it is currently with a much more diverse biota. "Exactly when and where the Antarctic biota died out on Antarctica itself is not known," writes Halliday. "Unlike the early doomed human expeditions to the Antarctic interior, there is no diary, no record of the dates and places of species death."

In chapter 6, Halliday examines the post-Cretaceous biosphere after the Chicxulub asteroid impact, which resulted in the extinction of most terrestrial species. The burning fires and explosive debris obscured the sky so deeply that "after two years of darkness, two years without photosynthesis anywhere worldwide, two years of rain infused with

nitric and sulfuric acid entering the oceans, populations have failed...For three quarters of species on Earth, every male, every female, every adult and every child is dead. It is the winter that lasts a generation."

Other places and times covered in the book include Swabia, Germany, 155 million years ago; Madygen, Kyrgyzstan, 225 million years ago; Moradi, Niger, 253 million years ago; Rhynie, Scotland, 407 million years ago; Yaman-Kasy, Russia, 435 million years ago; Chengjiang, China, 520 million years ago; and the Ediacara Hills of Australia, 550 million years ago.

"The world as it is today is a direct result—not a conclusion or a denouement, but a result—of what has gone before," concludes Halliday. By the same logic, what we do (or do not do) today can

mold our future in profound ways. Halliday states that "this is now undoubtedly a human planet." However, I might emphasize that it is not the planet that is in peril right now, it's us. Species come and go over time, but the planet remains.

Overall, this book is a highly entertaining read for anyone who wishes to be transported back to various points in Earth's history. It is also a novel approach to igniting broader public interest in the field of paleobiology. ■

10.1126/science.abn5448



**Otherlands**

Thomas Halliday  
Random House, 2022.  
416 pp.

## SOCIAL MEDIA

# Social media and shared reality

Exacerbated by engagement algorithms, flat Earth theories and other fringe beliefs thrive

By Jennifer Golbeck

**K**elly Weill's new book, *Off the Edge*, is a deep dive into the world of flat Earth conspiracy theorists—those who believe Earth is a plane or disc-shaped rather than spherical—that brilliantly reveals how people fall into illogical beliefs, reject reason, destroy relationships, and connect with a broad range of conspiracy theories in the social media age. Beautiful, probing, and often empathetic, the book connects the flat Earth movement with other conspiracy theories currently affecting our lives and politics.

Flat Earth theories vary, but the most popular one states that the planet is a disc with a high ice wall around its perimeter; the sun is very small and hovers only about 3000 miles above Earth, illuminating portions of it like a spotlight; there is no such thing as outer space; and gravity may not exist. Adherents believe NASA guards the ice wall and, along with other governments, puts out misinformation to make people believe that Earth is a sphere and space travel is possible.

The reviewer is at the Social Intelligence Lab, University of Maryland, College Park, MD 20742, USA. Email: golbeck@cs.umd.edu

Weill has spent years immersed in the online communities of flat Earthers, attending their conventions and interviewing hundreds of believers. Although their theories and backgrounds differ, Weill has identified a few common traits. First, their initial contact with flat Earth theories often comes at a time when the rest of their lives are not going well. Second, they come to believe in a flat Earth by “doing their own research,” which often entails watching YouTube videos and reading internet forums. One subject profiled in the book, notes Weill, “watched hours of Flat Earth videos over the course of several days and converted before the week was up.”

In fact, social media often introduces flat Earth ideas to would-be believers. YouTube's recommendation engine, for example, is optimized to send people to “engaging” content—that is, media that will keep them on the platform longer. As researchers have long known, more-extreme content—content that makes those consuming it angry, espouses conspiracy theories or extremist views, or contains shocking information or images—is more engaging. Thus, people who begin by watching relatively benign videos can be incrementally directed toward increasingly fringe topics.

**Off the Edge: Flat Earthers, Conspiracy Culture, and Why People Will Believe Anything**

Kelly Weill  
Algonquin Books,  
2022. 256 pp.



Once you believe in one conspiracy theory, it is much easier to start believing in others. The language, tactics, and community that characterize conspiracy groups are similar, as are the social media algorithms that shape what searchers see online. “The flat earth and pro-Trump movements share strands of the same conspiratorial, counter-factual DNA,” notes Weill.

When someone buys into a conspiracy theory, it is hard to change their minds. Information that debunks the theory is often deemed untrustworthy, either because of the source or because believers are primed with superficially compelling counterarguments. Conspiracy theories also separate believers from friends and family, convincing adherents that those who reject the theory cannot be trusted. “Cults and conspiratorial movements are cousins,” observes Weill. “You’re either helping the movement or actively hurting it.”

Toward the end of the book, Weill highlights how easily conspiracy theories can pervade people's worldviews, writing “I would like my old neighbors to stop invoking a fictional cannibalism ring when the diner down the road takes basic health precautions during a pandemic.” As a social media researcher who has spent the past several years studying what goes on in the murky corners of the internet, my heart ached with recognition. A pancake-shaped planet may seem innocuous, but the serious ramifications of conspiracy beliefs are always just below the surface.

Weill is impressively empathetic and respectful of the people she interviews, even as she expresses frustration at the damage conspiracy theories are doing in the world today. She outlines how difficult it is to debunk such theories, given that followers usually do not come to conversations willing to engage, but she is not without hope, highlighting the profound impact social media policies can have in limiting their spread. A 2019 change to YouTube's recommendation algorithm, for example, made flat Earth content much harder to find.

Conspiracy theories and their ramifications have infiltrated our daily lives. *Off the Edge* provides an insightful, human look at what fuels these beliefs and the critical role that social media has played in enticing people into these worlds. ■



Flat Earth theories shared online may seem innocuous, but they can prime users to believe in other conspiracies.

10.1126/science.abn6017



# RESEARCH

IN SCIENCE JOURNALS

Edited by  
Michael Funk

## TOOLS

### Reporting on p53 in living color

**M**any of our insights into the tumor-suppressor properties of the transcription factor p53 have been obtained from cell culture studies because tools in live animals tend to be invasive or are limited by detection issues. Humpton *et al.* generated mice expressing a fluorescent, p53-responsive reporter that overcame both limitations, revealing the dynamics of p53 activity during embryonic development and in the liver after injury in adult mice. —LKF *Sci. Signal.* 15, eabd9099 (2022).

A fluorescent reporter reveals tissue-specific p53 induction in mouse organs.

## AGING

### Searching for caloric restriction mimetics

Moderately decreased food intake that does not cause malnutrition (caloric restriction) has beneficial effects on health span and life span in model organisms. Spadaro *et al.* examined measures

of immune function in humans who restricted caloric intake by about 14% over 2 years and in mice under a more severe 40% restriction (see the Perspective by Rhoads and Anderson). Cellular analyses and transcriptional surveys showed marks of improved thymic function under caloric restriction. Expression of the gene

encoding platelet activating factor acetylhydrolase (*PLA2G7*) was decreased in humans undergoing caloric restriction. Inactivation of the gene in mice decreased inflammation and improved markers of thymic function and some metabolic functions in aging mice. Thus, decreased expression of *PLA2G7* might mediate

some beneficial effects of caloric restriction. —LBR

*Science*, abg7292, this issue p. 671;  
see also abn6576, p. 620

## CORONAVIRUS

### Vaccination protects against Omicron

The Omicron (B.1.1.529) variant of concern has proven more transmissible and infectious than the original severe acute respiratory syndrome coronavirus 2 (SARS-CoV-2) virus. Muik *et al.* investigated whether the BioNTech/Pfizer BNT162b2 messenger RNA (mRNA) vaccine is effective against the Omicron variant. Sera were collected from two groups of clinical trial subjects: those who only received the primary two-dose BNT162b2 vaccine series (spaced 21 days apart) and those who also received a third, “booster” vaccine 6 to 18 months after the second dose. Individuals who received only two doses had a low ability to neutralize the Omicron variant, whereas a third shot of BNT162b2 significantly improved antibody recognition of Omicron. These data suggest that three BNT162b2 mRNA doses are likely required to protect against Omicron-driven COVID-19. —PNK

*Science*, abn7591, this issue p. 678

## SPATIAL EPIGENOMICS

### Close-up on chromatin modifications

Despite recent advances in spatial transcriptomics to map gene expression, it has not been possible to determine the underlying epigenetic mechanisms controlling gene expression and tissue development with high spatial resolution. Deng *et al.* report on a technique called spatial-CUT&Tag for genome-wide profiling of histone modifications pixel by pixel on a frozen tissue section without dissociation. This method resolved spatially distinct and cell-type-specific chromatin modifications in mouse embryonic organogenesis and postnatal brain development. Single-cell epigenomic profiles were derived

from the tissue pixels containing single nuclei. Spatial-CUT&Tag adds a new dimension to spatial biology by enabling the mapping of epigenetic regulations broadly implicated in development and disease. —DJ

*Science*, abg7216, this issue p. 681

## CORONAVIRUS

### Uncounted cases in India

It is apparent that the official number of COVID-19 cases that have accumulated in India is substantially underestimated, but the question is, by how much? In an independent survey of 137,000 adults, Jha *et al.* recorded how many people died from severe acute respiratory syndrome coronavirus 2 (SARS-CoV-2)-related causes. Examining the data for all-cause mortality for the year spanning 2020 to 2021 revealed 26 to 29% excess mortality tracking waves of new variant transmission. Extrapolating to the Indian population, this equates to the deaths of more than 3.2 million people, with the majority occurring during April to June of 2021. —CA

*Science*, abm5154, this issue p. 667

## BIOENGINEERING

### Swimming cardiac cells

Biohybrid organisms, which are devices containing biological components, provide a way to study physiological control mechanisms in living organisms and may inspire robotic solutions to various challenges. Lee *et al.* designed a swimming fish analog using a bilayer construct made of

cardiac cells. These cells generate autonomous, rhythmic, antagonistic muscle movements that are either light induced or self paced, thus exploiting both the mechanoelectrical signaling and automaticity of cardiac cells. The biohybrid fish showed increased performance over previous biohybrids and provided insight into how mechanoelectrical signaling can be used for self-paced muscle actuation. —MSL

*Science*, abh0474, this issue p. 639

## ARCHAEOLOGY

### Early *Homo sapiens* in Europe

Data from Mandrin Cave in southwestern France challenge our understanding of the entry of modern humans into Europe and their interactions with Neanderthals. Previous studies estimated the date of entry as being around 45,000 years ago, followed by the rapid disappearance of Neanderthals. Slimak *et al.* have now discovered alternating strata of Neanderthal and modern human stone tool assemblages. One of these strata, which was dated to 54,000 years ago and has an assemblage of tools resembling one found in the Mediterranean, also has dental remains similar to those of modern humans. These findings suggest that the replacement of Neanderthals in Europe may not have been a single event but one of greater complexity. —MSA

*Sci. Adv.* 10.1126/sciadv.abj9496 (2022).

## IN OTHER JOURNALS

Edited by **Caroline Ash** and **Jesse Smith**

## CONSERVATION

### Solar threat to Florida panthers

**A**dopting alternative energy sources is critical for mitigating climate change, but implementing these new technologies can also create problems for wildlife. The endangered Florida panther (*Puma concolor coryi*) is found only in south Florida, an area with an increasing density of solar energy facilities. Using habitat suitability and least-cost path analyses, Leskova *et al.* evaluated the effects of 45 recently installed and planned solar facilities on panther habitat and movement. The authors found that 20% of the facilities were located within major panther movement corridors, indicating that current measures for the assignment of solar facility permits may not adequately address potential impacts on this endangered species. —BEL  
*J. Appl. Ecol.* 10.1111/1365-2664.14098 (2022).

**Florida panthers (*Puma concolor coryi*) are further endangered by encroaching solar power installations.**

## OPTOELECTRONICS

### Illuminating information transfer

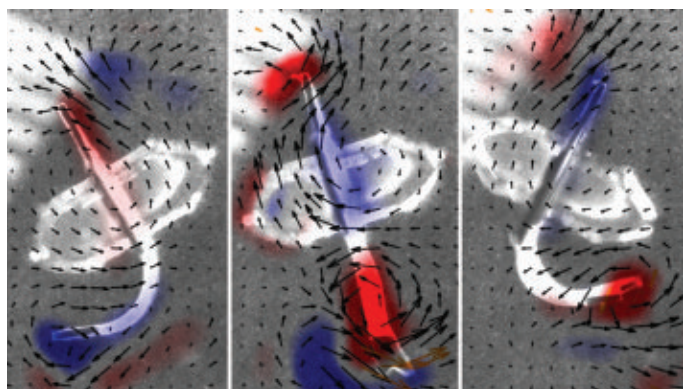
The insatiable demand for increased information capacity in an ever-increasingly connected world puts strains on existing radiofrequency communication channels. The shift to digital lighting with light-emitting diodes (LEDs) and laser diodes has seen not just a decrease in power consumption for lighting applications, but also the possibility to piggyback information transfer on the back of the LED output. Using a combination of three LEDs and five micro-LEDs operating at different wavelengths, Qiu *et al.* demonstrate data-transfer rates exceeding 25 gigabits per second using a standard wavelength division multiplexing encoding method, which exceeds present wi-fi capabilities. This steady progress

implies that li-fi will be able to provide the platform to meet the data rate requirements of the Internet of Things. —ISO  
*Opt. Lett.* 47, 317 (2022).

## NEURODEVELOPMENT

### Glial cells respond to a neurotransmitter

Inhibitory and excitatory neurotransmission is mediated by  $\gamma$ -aminobutyric acid (GABA), depending on context. Oligodendrocytes and their precursors, which go on to build myelin sheaths, can also carry GABA receptors. Pudasaini *et al.* analyzed the function of GABA receptors in oligodendroglial cells of the developing rat brain. Inhibition of GABA receptors in neonatal rats delayed the maturation of oligodendrocytes and drove deficits in myelination. A subset of oligodendroglial cells showed more



**A biohybrid fish swims by exploiting antagonistic contraction of a muscular bilayer of cardiac cells.**

CREDITS: (IMAGE) LE ET AL.; (PHOTO) MARK CONLIN/ALAMY STOCK PHOTO





GWAS analysis solely for coffee and tea preferences, which, however, identified specific genetic variants associated with caffeine metabolism and perception. The authors conclude from these results that whereas taste plays some role in coffee-drinking behavior, caffeine perception was a larger determinant in the preference for black coffee, black tea, and dark chocolate. —LMZ

*Sci. Rep.* **11**, 23845 (2021).

## REGENERATION

### Mice with a special ability

Most adult mammals are unable to regenerate damaged axons, for example, after spinal cord injury. Repair is hindered by the inhibitory environment caused by fibrosis (scarring) at the damage site. Nogueira-Rodrigues *et al.* report that spiny mice (*Acomys cahirinus*), which repair skin and ear without scarring, can astonishingly regenerate spinal axons and lower limb function after complete transection of the spinal cord. The authors found that the activity of several glycosylation pathways was altered in these mice at the injury site. A proteoglycan signature was associated with scarless regeneration, in which  $\beta$ -1,3-N-acetylglucosaminyltransferase 7 ( $\beta$ 3gnt7) was highly expressed. Neurons from *Mus musculus* (used in laboratory experiments) co-cultured with cells overexpressing  $\beta$ 3gnt7 also exhibited increased axon growth in vitro.

rapid proliferation, although the overall numbers of mature cells remained stable. Thus, GABA not only carries neuronal signals but also informs the development of the cells that support and speed up neuronal signals. —PJH

*Dev. Neurobiol.* **82**, 16 (2022).

## HUMAN GENOMICS

### Taste or morning euphoria?

Genetic variants can affect people's preferences for certain foods, such as the perception of bitter flavors. Modification of foods, such as by adding milk and sugar, will offset the naturally bitter flavors of coffee, tea, and chocolate products. Examining genome-wide association study (GWAS) data from about 6000 individuals in the United Kingdom and the

United States, Cornelis and van Dam included information on dietary preferences. Correlations emerged between drinking bitter beverages without modifications and candidate genetic variants associated with taste and behavior. The authors followed up with a



Despite milk and sugar counteracting the bitter flavors in tea, coffee, and chocolate, these additives are not as important to consumers as the caffeine hit.

Further analysis of spiny mice could reveal mechanisms of regeneration that might be translatable to humans. —GKA

*Dev. Cell* **10**, 1016/  
*j.devcel*.2021.12.008 (2022).

## FLOODS

### A shift in kind

Climate change may or may not be affecting the intensity and frequency of floods, but it might have an effect on the factors that cause them. Huang *et al.* examined the history of flooding in the western United States over the past 80 years, finding that although the frequency and magnitude of rain-on-snow-driven floods have decreased, they have increased for floods caused by convective storms. There has also been a temporal shift of snowmelt-driven floods to earlier in the year. The characteristics of floods produced by other mechanisms are generally stable. —HJS

*Geophys. Res. Lett.*  
**10**, 1029/2021GL097022 (2022).

## PHYSICS

### A pressure-induced crossover

In most superconductors, the pairs of electrons that are responsible for superconductivity are large and overlapping. This so-called BCS (Bardeen-Cooper-Schrieffer) limit can be contrasted with the Bose-Einstein condensation (BEC) regime of small pairs. To cross over from the BEC to the BCS regime, experimenters can vary parameters such as carrier density, but finding materials that undergo such a crossover is tricky. Suzuki *et al.* studied the transport properties of the organic compound  $\kappa$ -(BEDT-TTF)<sub>4</sub>Hg<sub>2.89</sub>Br<sub>8</sub> as they subjected the samples to external pressure. The character of the superconducting phase that formed at low temperatures could be varied from the BEC to the BCS limit by increasing the pressure. —JS

*Phys. Rev. X* **12**, 011016 (2022).

ALSO IN *SCIENCE* JOURNALS

Edited by Michael Funk

## CELL BIOLOGY

**The making and removal of a leader**

When epithelia are injured, the remaining cells repair the epithelial sheet by migrating into and closing the open gap. In many epithelia, this happens through a coordinated cell movement driven by specialized cells called leaders. However, it is unclear how epithelial cells become leaders. Kozyska *et al.* reveal that injury activates the damage sensor p53, which then promotes the emergence of leaders through its downstream effector p21 (see the Perspective by Yun and Greco). However, leader cells only live transiently, because cell competition removes them once the gap is closed, restoring epithelial integrity. Localized p53 elevation could drive cell migration in other contexts in which damage has been shown to induce cell migration. —SMH

*Science*, ab18876, this issue p. 628;  
see also abn7411, p. 619

## IMMUNOLOGY

**CD97 helps DCs fight going with the flow**

A subset of conventional dendritic cells (DCs) called cDC2s are found within a blood-exposed region of the spleen. These cells efficiently capture antigens from the blood and present them to T cells. However, how cDC2s sense their location regarding blood flow remains unclear. Liu *et al.* found that in mice, the N-terminal fragment of the G protein-coupled receptor CD97 mechanically senses CD55 expressed on red blood cells. This triggers the  $G\alpha_{13}$  signaling required for correct cDC2 positioning. Deficiencies in the CD55–CD97– $G\alpha_{13}$  pathway result in a loss of cDC2s into the circulation and impaired immune responses to blood-borne bacteria. —STS

*Science*, abi5965, this issue p. 629

## IMMUNOLOGY

**MZ B cells take on “a-gnaw-ther” role**

Marginal zone (MZ) B cells are a subset of lymphoid tissue-resident B cells specializing in the rapid production of polyreactive immunoglobulin M antibodies. Schriek *et al.* found that MZ B cells can also emulate conventional dendritic cells (cDCs), which present antigens to T cells. Complement receptor 2 (CR2) expressed by MZ B cells recognizes complement component 3 (C3) bound to peptide-loaded major histocompatibility complex class II (pMHC II) molecules on the surface of cDCs. MZ B cells can then “nibble” pMHCII–C3 complexes from cDCs and display them on their own membranes in a process called trogocytosis. A ubiquitin ligase, MARCH1, limits the damage to cDCs by regulating the levels of pMHCII–C3 complexes expressed on the surface of cDCs. —STS

*Science*, abf7470, this issue p. 630

## CELL BIOLOGY

**A missing motor in human meiosis**

Chromosomal errors in human eggs are a leading cause of miscarriages and infertility. These errors result from chromosome missegregations during the maturation of oocytes into eggs. Chromosome segregation is driven by the spindle, a macromolecular machinery that pulls chromosomes apart. However, human oocytes often assemble unstable spindles, favoring chromosome missegregations. So *et al.* discovered that human oocyte spindles are unstable because they are deficient in the molecular motor KIFC1, which stabilizes spindles in other mammalian oocytes and in cancer cells. By introducing exogenous KIFC1, the authors were able to increase the fidelity of spindle assembly

and chromosome segregation in human oocytes. —SMH

*Science*, abj3944, this issue p. 631

## NEUROSCIENCE

**How to remember a sequence of events**

How is serial order mentally encoded and stored in memory? Xie *et al.* addressed this question using two-photon calcium imaging to simultaneously record thousands of prefrontal neurons in monkeys performing a delayed visuospatial sequence reproduction task. The animals saw a sequence of three locations and, after a delay, made a saccade to the corresponding locations in the appropriate order. The data obtained using a mathematical decomposition technique support a new and simple type of model: a static population code with distinct and near-orthogonal subspaces for each rank in the sequence, all superimposed in the same overlapping groups of prefrontal neurons. These results open an important and new perspective on understanding sequence representations in the brain. —PRS

*Science*, abm0204, this issue p. 632

## PIEZOELECTRICS

**A surprising way to detect strain**

Piezoelectric materials usually rely on their crystal structure alone to create electrical charge in response to strain. This makes the materials attractive for a variety of sensing applications. Park *et al.* present a different strategy by introducing gadolinium into non-piezoelectric cerium dioxide (see the Perspective by Li). This approach also creates oxygen vacancies that turn the material into one with a frequency-dependent piezoelectric effect under a static electric field. The size of the effect is similar to that of commercial piezoelectric

materials, and the strategy should work more generally for a wide class of materials. —BG

*Science*, abm7497, this issue p. 653;  
see also abn2903, p. 618

## MATERIALS SCIENCE

**Naturally strong but light**

Cellular solids such as foams or honeycombs can exhibit excellent stiffness or toughness with minimal weight. Yang *et al.* examined ossicles, calcareous skeletal elements from the skeletons of knobby starfish (see the Perspective by Hyde and Meldrum). The authors show that the structure consists of a dual-scale microlattice with both an atomic-level calcite and a micro-level diamond-triply periodic minimal surface, as well as gradients in composition and atomic level defects. It is these combined features that enhance the damage tolerance of the ossicles under compression, giving the starfish remarkable specific energy absorption capabilities. —MSL

*Science*, abj9472, this issue p. 647;  
see also abn2717, p. 615

**Y CHROMOSOME ORIGINS**  
**Evolutionary models of the Y chromosome**

A major question in evolutionary genetics is how and why sex chromosomes form from otherwise undifferentiated chromosomes. The sexual antagonism theory posits that antagonistic alleles that benefit males but harm females lie on the same chromosome as an initial male-determining locus, resulting in selection against recombination. Lenormand and Roze have developed a four-step model proposing an alternative evolutionary path (see the Perspective by Muralidhar and Veller). Chance fixation of an inversion leads to recombination arrest on a portion of the Y chromosome. This triggers divergence of X and Y cis-regulators,



selecting for dosage compensation and sexually antagonistic regulatory effects. This sexual antagonism protects inversions from reestablishment of recombination. Thus, expansion of the non-recombining region of sex chromosomes, instrumental in the progressive degeneration of the Y chromosome, does not rely on the recruitment of sexually antagonistic genes. —LMZ

*Science*, abj1813, this issue p. 663;  
see also abn7410, p. 616

## VIRAL DISEASES

### Ebola virus: Hiding in plain sight

The host-pathogen determinants of Ebola virus (EBOV) persistence and recurring disease in immune-privileged organs, including any association with standard-of-care monoclonal antibody-based treatments, remain to be elucidated. Liu *et al.* report frequent EBOV persistence in the brain ventricular system of nonhuman primates that survived acute disease after monoclonal antibody-based treatment. Viral persistence was associated with lethal recrudescence of disease, including severe inflammation in the brain. These findings have implications for long-term follow-up efforts to reduce the individual (disease relapse/recrudescence) and public health (reignition of outbreaks) consequences of viral persistence in survivors of EBOV infection. —OMS

*Sci. Transl. Med.* **14**, eabi5229 (2022).

## CANCER IMMUNOLOGY

### Trouble in the tumor for young T cells

Aging is associated with a decline in adaptive immune responses, but the impact of young age, particularly on immunity against pediatric tumors, is not well understood. Moustaki *et al.* used major histocompatibility complex class I-deficient tumors to demonstrate that, compared with adult mice, the young tumor microenvironment promotes hyperactivation

and terminal differentiation of tumor-specific CD8<sup>+</sup> T cells. Both migratory dendritic cells in lymph nodes and tumor-engulfing myeloid cells were more mature and efficient at presenting antigen to CD8<sup>+</sup> T cells. Despite low mutation rates, solid tumors from pediatric tumors also contained a pool of antigen-experienced T cells, which correlated with the frequency of PD-L1<sup>hi</sup> myeloid cells. These results highlight distinct features of younger tumor microenvironments that could contribute to age-associated differences in tumor immunity and immunotherapy responses. —CO

*Sci. Immunol.* **7**, eabf6136 (2022).

## RESEARCH ARTICLE SUMMARY

## CELL BIOLOGY

## p53 directs leader cell behavior, migration, and clearance during epithelial repair

Kasia Kozyraska<sup>†</sup>, Giulia Pilia<sup>†</sup>, Medhavi Vishwakarma<sup>‡</sup>, Laura Wagstaff<sup>‡</sup>, Maja Goschorska, Silvia Cirillo, Saad Mohamad, Kelli Gallacher, Rafael E. Carazo Salas, Eugenia Piddini\*

**INTRODUCTION:** Layers of epithelial cells protect animals from environmental insults. When the integrity of these tissues is compromised by injury, epithelial cells migrate as a cohesive unit over the exposed area to seal the breach. In some epithelia, collective migration is guided by cells that acquire leader behavior. Leader cells activate specific migratory pathways and drive directed migration of the remaining epithelial cells, which act as follower cells to enable wound closure. How leader cells arise from a seemingly homogeneous population remains unresolved, particularly because only a few cells at the wound edge develop into leader cells. It is also unclear what happens to leader cells once epithelial monolayers are repaired. Understanding the basis of leader cell specification will shed light on the fundamental cellular processes that drive wound healing and will help to identify interventions that could accelerate and improve wound repair.

**RATIONALE:** Madin-Darby canine kidney (MDCK) epithelial cells are a well-characterized model for investigating epithelial repair and leader cell migration. The genetic tractability of these cells and their ease of use for imaging assays allow for in-depth molecular dissection of epithelial cell biology. Prior work has shown that

leader cells have a characteristic flattened morphology and distinct cytoskeletal properties and that they activate specific migratory pathways. In this study, we sought to identify how the leader program is activated in epithelial cells. We took advantage of the fact that in untreated MDCK cultures, a few cells spontaneously display a morphology reminiscent of leader cells and, on contact with neighbor cells with epithelial morphology, lead directed migration. These “spontaneous leaders” behave similarly to leaders observed at the edge of injured MDCK epithelial sheets. We investigated the mechanisms that drive spontaneous leader cell behavior, as an entry point to identify what invokes leader cell specification upon epithelial injury.

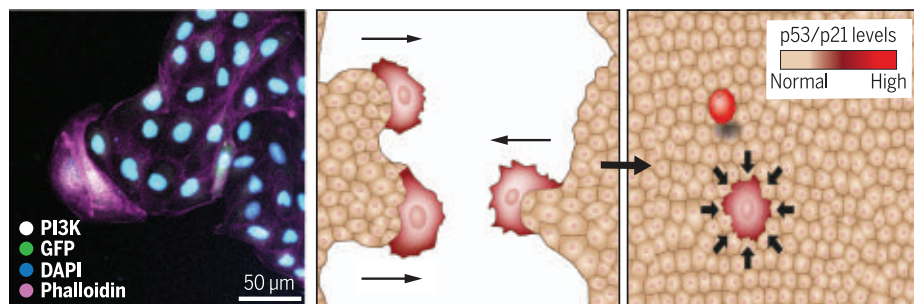
**RESULTS:** We found that spontaneous leaders exhibited elevated cellular tumor antigen p53 levels. Indeed, inducing p53 activation, either by inducing binucleation (which is a common feature among leader cells) or with the DNA-damaging agent mitomycin C (MMC) or the Mdm2 inhibitor nutlin-3, was sufficient to instruct leader behavior. Ablation of p53 by CRISPR mutagenesis strongly inhibited the emergence of leader cells upon MMC treatment, indicating that p53 is necessary for cells to be leaders. Working downstream of p53, we

found that its target gene p21<sup>WAF1/CIP1</sup> (p21) was also elevated in spontaneous leaders. Indeed, p21 elevation and its functional output, cyclin-dependent kinase (CDK) activity inhibition, were sufficient and necessary to induce leader cell behavior. Up-regulating p21 was sufficient to elevate integrin  $\beta$ 1 and phosphoinositide 3-kinase (PI3K), which are known markers of spontaneous leader cells and are required for their migration.

Next, we investigated whether the p53-p21-CDK inhibition pathway that we identified in spontaneous leaders was also responsible for leader behavior upon epithelial injury. We found that scratch-induced leader cells experienced cell cycle delay, consistent with CDK inhibition, and showed high levels of both p53 and p21. Using a live reporter of p53 activity, we showed that injury itself induced p53 elevation at the edge of the damaged epithelium. This induction likely resulted from the mechanical insult, as it was dependent on the stress kinase p38, which activates p53 in response to mechanical stress. We then found that p53 and p21 both promoted cell migration in monolayers undergoing repair. Indeed, activating p53 at the migration front by laser-induced DNA damage accelerated cell migration, an effect that could be rescued by p53 inhibition. Conversely, inhibiting p53 or p21 slowed down migration.

We then followed the fate of leader cells as the injury resolved itself. Prior work has shown that cells with moderate p53 activation are eliminated by mechanical cell competition. Accordingly, we found that, once the epithelium was repaired, leader cells with high p53 activity were cleared by cell competition, undergoing extrusion or apoptosis. Failure to remove leader cells compromised the regular cobblestone-like morphology of the epithelium.

**CONCLUSION:** We have identified p53 as a key determinant of leader-driven cell migration in epithelial repair. p53 activation appeared to instruct leader cell specification and accelerate cell migration by modulating p21 and CDK activity. Upon epithelial repair, p53 induced leader cell elimination by mechanical cell competition, reinstating epithelial integrity. Nonproliferative cells leading collective migration have been previously observed in vivo in various physiological and pathological contexts. The p53-p21-CDK pathway could therefore have broader relevance in leader-driven cell migration. ■



**p53 and p21 induce leader cell behavior and drive migration in epithelial repair.** (Left panel) p21-overexpressing cells [green fluorescent protein (GFP)–negative] lead a colony of wild-type cells (GFP-positive) and direct their collective migration. Cells are immunostained with the leader marker PI3K (white), which is elevated in p21-expressing leaders. Nuclei are counterstained with DAPI (4',6-diamidino-2-phenylindole); phalloidin marks the actin cytoskeleton. (Middle and right panels) Model summarizing the role of p53 in epithelial repair. Upon injury, mechanical damage of epithelial cells induces p53, which, through p21 elevation and CDK inhibition, instructs leader cells to drive cell migration, accelerating epithelial closure. High-p53 leader cells are also “mechanical losers” and are cleared by means of cell competition once the epithelium closes. Removal of leaders contributes to the restoration of tissue integrity.

The list of author affiliations is available in the full article online.

\*Corresponding author. Email: eugenia.piddini@bristol.ac.uk

†These authors contributed equally to this work.

‡These authors contributed equally to this work.

Cite this article as K. Kozyraska et al., *Science* 375, eabl8876 (2022). DOI: 10.1126/science.abl8876

**S** READ THE FULL ARTICLE AT  
<https://doi.org/10.1126/science.abl8876>



## RESEARCH ARTICLE

## CELL BIOLOGY

## p53 directs leader cell behavior, migration, and clearance during epithelial repair

Kasia Kozyrsk<sup>1,2,†,‡</sup>, Giulia Pilia<sup>1,†</sup>, Medhavi Vishwakarma<sup>1,§,¶</sup>, Laura Wagstaff<sup>2,§,¶</sup>, Maja Goschorska<sup>1</sup>, Silvia Cirillo<sup>1</sup>, Saad Mohamad<sup>1</sup>, Kelli Gallacher<sup>1,\*</sup>, Rafael E. Carazo Salas<sup>1</sup>, Eugenia Piddini<sup>1,\*</sup>

Epithelial cells migrate across wounds to repair injured tissue. Leader cells at the front of migrating sheets often drive this process. However, it is unclear how leaders emerge from an apparently homogeneous epithelial cell population. We characterized leaders emerging from epithelial monolayers in cell culture and found that they activated the stress sensor p53, which was sufficient to initiate leader cell behavior. p53 activated the cell cycle inhibitor p21<sup>WAF1/CIP1</sup>, which in turn induced leader behavior through inhibition of cyclin-dependent kinase activity. p53 also induced crowding hypersensitivity in leader cells such that, upon epithelial closure, they were eliminated by cell competition. Thus, mechanically induced p53 directs emergence of a transient population of leader cells that drive migration and ensures their clearance upon epithelial repair.

**W**hen the integrity of an epithelial monolayer is compromised by injury or wounding, epithelial cells extend and migrate over the exposed area to seal the open space. In some epithelia, wound closure is driven by leader cells, which are located at the edge of the epithelial front and guide the collective migration of epithelial sheets (1–8). Follower cells trail behind as mechanically and physically coherent protrusions, advancing gap closure (3, 4, 9). Leader cells have a characteristic flattened morphology and distinct cytoskeletal properties and activate specific migratory pathways (2, 5, 10, 11), however, they originate from the same epithelial cells as follower cells. How leader cells arise from a seemingly homogeneous population of epithelial cells is unclear. Studies have proposed that geometric and mechanical cues at the wound edge may induce asymmetry and that this may be sufficient to instruct the leader cell fate (12–15). However, only a few cells at the wound edge become leaders, suggesting that additional factors are involved.

## p53 elevation induces leader cell behavior

Madin-Darby canine kidney (MDCK) epithelial cells are a well-characterized model for investigating leader cell migration and epithelial re-

pair (2, 9, 10, 14, 15). While imaging colonies of wild-type MDCK cells, we observed the emergence of cells with a flattened morphology, resembling senescent cells (16) (Fig. 1A). Upon contact with colonies of cells with epithelial morphology, these flat cells led the colonies in directed migration (90% of cases,  $n = 112$ ) (Fig. 1, A to C; fig. S1, A and B; and movie S1). Such collectively migrating fingerlike structures have been previously observed in MDCK cells (10) and are reminiscent of leader-driven migration in scratched epithelial monolayers (2, 9, 11). Because these cells appear in the absence of epithelial injury, we named them “spontaneous leaders.”

Leader cells have larger surface area, more frequent binucleation, and lower division rates than do normal epithelial cells (2, 9, 11, 17). Spontaneous leaders shared these features—they divided only in 2.5% of the cases observed ( $n = 89$ ) during the course of our movies (>48 hours) and were often binucleated (fig. S1C). To determine whether binucleation is sufficient to induce leader status, we treated MDCK cells with the myosin inhibitor blebbistatin, which prevents cytokinesis while allowing karyokinesis to proceed (18). To visualize blebbistatin-induced binucleated cells (BBCs), we treated cells expressing nuclear green fluorescent protein (GFP) with blebbistatin and cocultured them with untreated, unlabeled wild-type cells. The resulting BBCs were morphologically similar to spontaneous leaders and led migration, recruiting unlabeled wild-type cells as followers (fig. S1D).

The “tetraploidy checkpoint” triggered upon cytokinesis failure induces cell cycle arrest in a p53-dependent manner (19). Indeed, p53 levels were elevated in BBCs (fig. S1, E and F). To determine p53 levels in spontaneous leaders, we used live imaging to identify and track

spontaneous leaders (Fig. 1D, first three panels) and then located them after fixation. Immunostaining revealed that spontaneous leaders exhibited significantly higher p53 levels than did neighboring nonleader cells (Fig. 1, D, right-most panel, and E).

To determine whether elevated p53 induces the leader cell fate, we treated wild-type MDCK cells expressing nuclear GFP with the DNA-damaging agent mitomycin C (MMC) (20) to stabilize p53 irreversibly (fig. S1G). After extensive washing to prevent MMC carryover, we co-seeded MMC-treated, GFP-labeled cells with untreated, unlabeled wild-type cells (Fig. 2A). MMC treatment was sufficient to induce the formation of migrating “fingers” of untreated follower cells led by MMC-treated cells (Fig. 2, B to D; fig. S1, H and I; and movie S2), suggesting that p53 elevation is sufficient to trigger the leader phenotype.

Aside from p53 activation, MMC causes an extensive DNA damage response and reactive oxygen species activation (21, 22). To activate p53 more specifically and in the absence of DNA damage, we used nutlin-3, an Mdm2 inhibitor that stabilizes p53 (23), at doses that slow down but do not arrest cell proliferation (24) (fig. S1, J and K). We cocultured GFP-labeled wild-type cells with p53 knockout (*p53KO*) cells (24) in the presence of nutlin-3, so that p53 would be elevated only in one population. Under these conditions, p53 activation induced a leader phenotype in wild-type cells, whereas *p53KO* cells behaved as followers (fig. S1, L to O). Thus, p53 elevation is sufficient to instruct the leader cell fate.

To test whether p53 is also required for leader cell migration, we generated MDCK cells that inducibly express the p53 peptide inhibitor GSE-22 (25) in tandem with GFP. GSE-22 expression reduced the frequency but did not abolish the formation of MMC-induced leaders (fig. S2, A to E). Next, we ablated p53 function using CRISPR mutagenesis, generating *p53KO* clones, which we verified functionally (fig. S2, F and G) and by sequencing (fig. S2H). Functional ablation of p53 substantially reduced the incidence of leader behavior in the binucleated cell assay (fig. S2, I and J). It also strongly inhibited the emergence of leaders induced by MMC, which dropped from 80% in wild-type cells to just below 20% in *p53KO* cells (Fig. 2, D and E; fig. S1H; and movie S3). The impairment in leader behavior could also be observed as a reduction in speed, displacement, distance, and persistence of migration for wild-type cells in contact with *p53KO* MMC-treated cells in comparison with those in contact with wild-type MMC-treated cells (Fig. 2, F to I, and fig. S2, K to M). Thus, although a few cells behaving as leaders still remained, the great majority of cells did not display leader migration in the absence of p53, indicating that p53 is an important contributor to leader cell migration.

<sup>1</sup>School of Cellular and Molecular Medicine, University of Bristol, Bristol BS8 1TD, UK. <sup>2</sup>The Wellcome Trust/Cancer Research UK Gurdon Institute and Department of Zoology, University of Cambridge, Cambridge CB2 1QN, UK.

\*Corresponding author. Email: eugenia.piddini@bristol.ac.uk

†These authors contributed equally to this work.

‡Present address: Horizon Discovery Ltd., Cambridge CB25 9TL, UK.

§These authors contributed equally to this work.

¶Present address: Centre for BioSystems Science and Engineering, Indian Institute of Science Bangalore, Karnataka 560012, India.

#Present address: School of Biological Sciences, University of East Anglia, Norwich NR4 7UA, UK.

\*\*Present address: Department of Biology and Biochemistry, University of Bath, Bath BA2 7AY, UK.

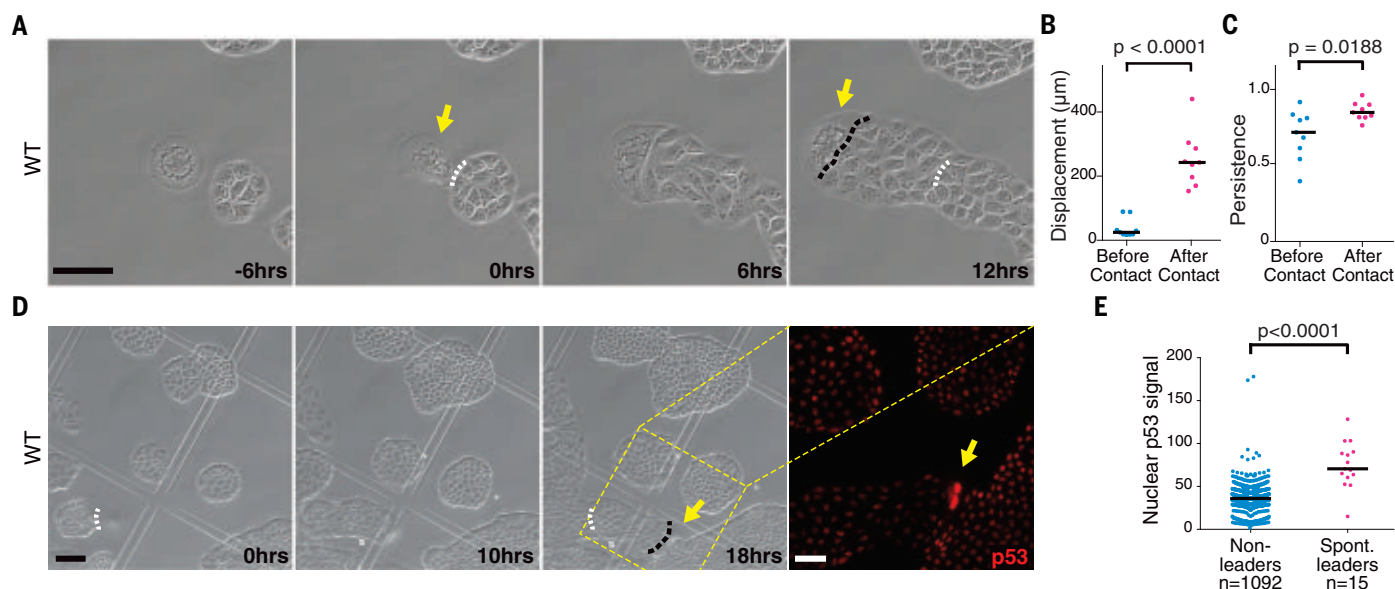


**Fig. 1. Spontaneous leaders elevate p53.** (A) Movie stills of wild-type MDCK cultures showing a spontaneously emerging leader (arrow). (B and C) Displacement (B) and migration persistence (C) of spontaneous leaders before and after contact with follower colonies. (D) Movie stills of a migrating spontaneous leader (arrow), followed by p53 immunostaining (rightmost panel) of the field indicated (dashed yellow lines). (E) Quantification of single-cell nuclear p53 intensity of spontaneous (Spont.) leaders and surrounding nonleaders. The  $n$  values along the  $x$  axis indicate the number of cells. Black

bars in (B), (C), and (E) represent the median. Data are from one representative repeat of three biological replicates (E) or from selected movies of three biological replicates [(B) and (C)].  $P$  values [(B), (C), and (E)] from Mann-Whitney  $U$  test. Here and in subsequent figures, the white dashed line marks the initial contact point, the black dashed line marks the final contact point, the movie sequence scale bars are 100  $\mu\text{m}$ , the confocal image scale bars are 50  $\mu\text{m}$ , and fluorescence values are expressed as arbitrary units.

### p21 promotes the emergence of leader cells downstream of p53

Spontaneous leader cells, BBCs, and MMC-treated cells are all cell cycle arrested, and nutlin-3-treated leaders divide less frequently than untreated controls, suggesting that factors required for the leader phenotype could include p53 effectors involved in cell cycle arrest. The main p53 target gene involved in cell cycle arrest is cyclin-dependent kinase inhibitor 1A (*CDKN1A*), also known as *p21*<sup>WAF1/CIP1</sup> (*p21*) (21, 26). *p21* was indeed up-regulated in spontaneous leaders (Fig. 3, A and B). To determine whether p21 is necessary for leader fate, we generated two *p21* knockout (*p21KO*) clones using CRISPR mutagenesis and verified *p21* disruption functionally (fig. S3A) and by sequencing (fig. S3B). *p21KO* cells treated with MMC were significantly less likely to behave as leaders than were wild-type cells (Fig. 3, C and D; fig. S3C; and movie S4). The impairment in leader behavior could also be observed as a reduction in speed, displacement, distance, and persistence of migration for wild-type cells in contact with *p21KO* MMC-treated cells in comparison with those in contact with wild-type MMC-treated cells (Fig. 3, E to I, and fig. S3, D and E).

To determine whether p21 is sufficient to induce leader cell behavior, we generated a clonal MDCK cell line inducibly overexpressing p21 (*p21OE*). *p21* overexpression resulted in cell cycle arrest, as expected, but also caused

cells to flatten and take on a leader-like morphology (fig. S3, F and G). Upon contact with wild-type cells, *p21OE* cells behaved as leaders (Fig. 4, A to C; fig. S3H; and movie S5, left), indicating that p21 overexpression is sufficient for leader cell behavior. Thus, p53 activation induces leader cells by up-regulating p21.

### p21 promotes the emergence of leader cells through CDK inhibition

Next, we explored how p21 induces leader cell migration. Because p21 is an inhibitor of cyclin-dependent kinase (CDK) activity (26), we asked whether CDK inhibition plays a role in leader cell migration. First, we generated a cell line inducibly overexpressing the CDK inhibitor p16 (27) and found that p16 overexpression also induced leader cell migration (Fig. 4, D and E, and movie S5, right). Given that p21 and p16 are structurally unrelated (28), their common ability to induce leader behavior strongly suggests that leader fate is mediated by inhibition of CDKs, because it would be unlikely that they share additional common targets. Thus, we hypothesized that leader-follower behavior ensues when cells with low CDK activity (leaders) come into contact with cells with relatively high CDK activity (followers). To test this hypothesis, we used small-molecule inhibitors of CDK function. Per our hypothesis, adding CDK inhibitors to migrating leader-follower pairs should stall leader cell migration by turning followers into low-CDK leader-like

cells. Indeed, addition of both the CDK2 inhibitor K0386 and the CDK1 inhibitor RO-3306 stalled spontaneous leader-driven migration (Fig. 4, F and G, and movie S6). Thus, CDK inhibition instructs leader cell behavior. Furthermore, because inhibition of cell cycle progression upon damage can be independent of p53 or p21, the findings may explain the incomplete inhibition of leader behavior upon p53 or p21 loss of function.

### p53 and p21 induce leaders through Rac1, PI3K, and ITG $\beta$ 1 activation

Spontaneous leader cells are known to up-regulate Ras-related C3 botulinum toxin substrate 1 (Rac1), integrin  $\beta$ 1 (ITG $\beta$ 1), and phosphoinositide 3-kinase (PI3K), whose activities are required for cell migration (10). We therefore tested whether these were also up-regulated and required in p53- and p21-induced leaders. Both PI3K and ITG $\beta$ 1 were up-regulated in leaders generated by MMC treatment (fig. S4, A to D) and by nutlin-induced p53 elevation (fig. S4, E to J). Surface levels of ITG $\beta$ 1 were also increased (fig. S4, K and L), suggesting that ITG $\beta$ 1 elevation results in higher integrin activity at the plasma membrane. However, neither PI3K or ITG $\beta$ 1 mRNA was elevated upon MMC treatment (fig. S4, M and N), indicating that their elevation was attributable to posttranscriptional regulation. PI3K and ITG $\beta$ 1 up-regulation was partially mediated by p21, because *p21KO* cells showed reduced PI3K and ITG $\beta$ 1 up-regulation upon treatment with nutlin



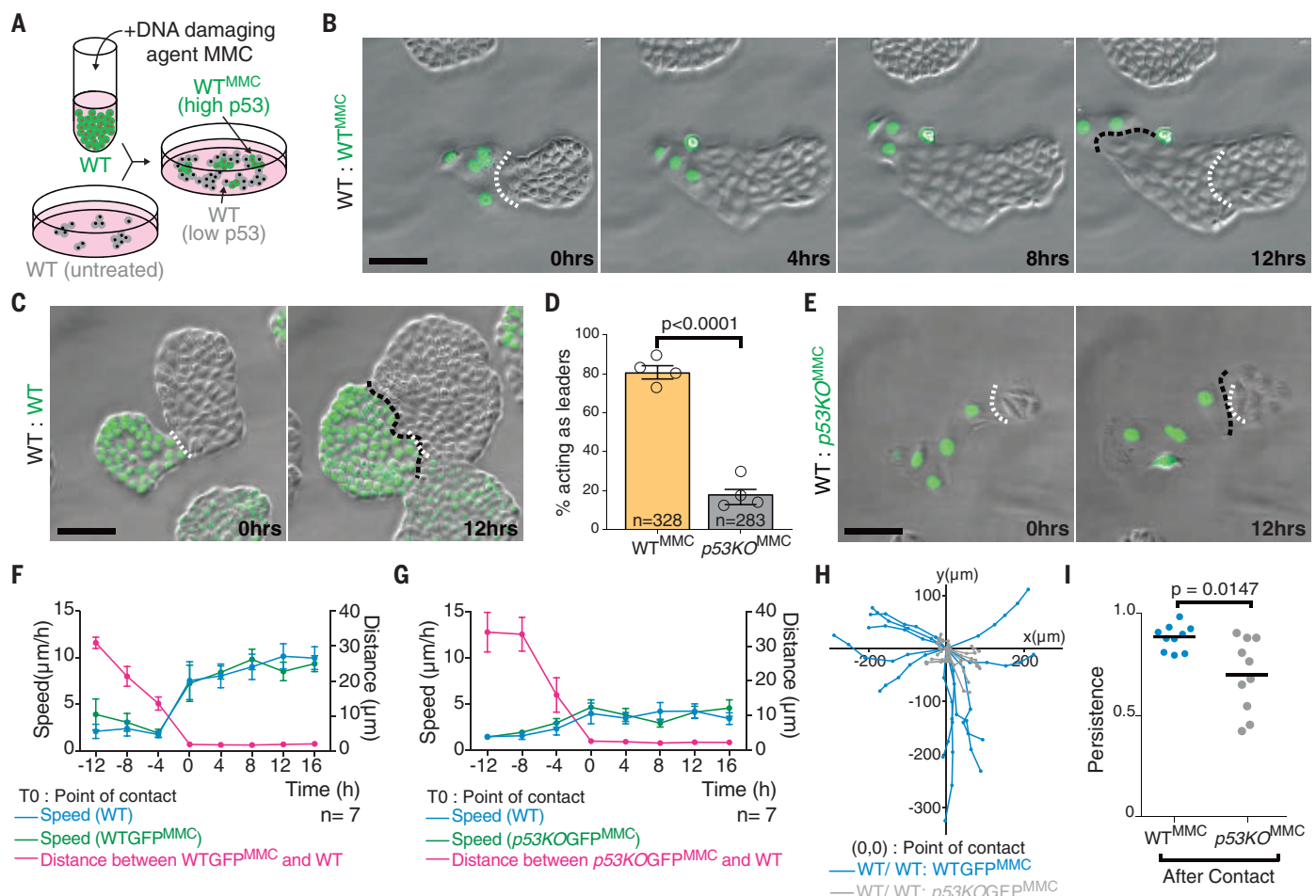


**Fig. 2. p53 instructs leader cell behavior.** (A) Experimental design for coculture of untreated and mitomycin C (MMC)-treated cells. (B) Movie stills of cocultures of MMC-treated GFP-positive wild-type cells and untreated unlabeled wild-type cells. (C) Movie stills from cocultures of untreated unlabeled wild-type cells and untreated wild-type cells expressing nuclear GFP. (D) Percentage of MMC-treated wild-type or p53KO cells acting as leaders. Mean values shown. Here and in subsequent figures, empty circles indicate values obtained in each repetition. (E) Movie stills of cocultures of untreated unlabeled wild-type and MMC-treated GFP-positive p53KO cells. (F and G) Tracking of mean migration

speed of and mean respective distance between pairs of untreated wild-type and MMC-treated wild-type cells (F) or p53KO cells (G). (H) Tracks of wild-type cells upon contact with MMC-treated wild-type (blue) or p53KO (gray) cells. (I) Persistence of migration of wild-type followers upon contact with MMC-treated wild-type or p53KO cells. Black bars indicate median. The  $n$  values along the  $x$  axis in (D) and (F) to (I) indicate the number of contacts. Data are pooled from three biological replicates (D) or from selected movies of three biological replicates [(F) to (I)]. Error bars indicate  $\pm$ SEM in (D), (F), and (G).  $P$  values from logistic regression (D) or Mann-Whitney  $U$  test (I).

(fig. S4, E to J). Induction of leaders by p21 overexpression was also sufficient to up-regulate PI3K and ITG $\beta$ 1 (fig. S4, O to R), which was also up-regulated by addition of the CDK1 inhibitor RO-3306 (fig. S4, S and T). Notably, chemical inhibition of PI3K and Rac1 prevented the active migration of MMC-generated leaders (fig. S5, A and B, and movie S7), indicating that these pathways are also necessary for p53- and p21-mediated leader cell migration. Thus, p53 and p21 induce leader specification by means of elevation of the leader fate effectors PI3K and ITG $\beta$ 1, likely through CDK inhibition.

#### Injury-induced p53 drives collective cell migration during epithelial repair

Because p53- and p21-induced leaders share the same molecular mechanisms as spontaneous

leaders to drive migration, we wondered whether p53, p21, and the resulting CDK inhibition also play a role in the migration of leaders driving epithelial repair. First, we sought to determine the cell cycle status of injury-induced leaders. We generated a cell line expressing the cell cycle reporter FUCCI (fluorescent ubiquitination-based cell cycle indicator) (29) and monitored cell cycle progression in leaders emerging upon epithelial scratch. We found that cells could become leaders in any phase of the cell cycle (fig. S6A). However, they spent more time in the cell cycle phase they were in than did nonleader cells (Fig. 5A). This indicates that leaders tend to experience cell cycle delay and, therefore, likely also CDK inhibition. This delay was not a general feature of migrating cells, because migrating followers led by spontaneous leaders did not cycle more

slowly than nonfollower cells in the same culture (fig. S6B). Thus, a slower cell cycle is not an obligate feature of cells engaging in migration. In addition, scratch-induced leaders showed high levels of both p53 (Fig. 5, B and C) and p21 (fig. S6, C and D). Furthermore, leaders induced by barrier release (fig. S6E) also showed elevated p53 (fig. S6, F and G) and p21 (fig. S6, H and I), suggesting that the p53-p21 pathway is a general driver of leader cell migration in MDCK cells.

We next sought to determine how p53 becomes activated at the edge of the injured epithelial monolayer and hypothesized that mechanical damage, inflicted when epithelia are scratched, could be triggering p53 elevation. To measure p53 activation in live and migrating epithelial sheets, we generated a cell line carrying a live fluorescent p53 reporter consisting of short-lived nuclear localization signal (NLS)-GFP

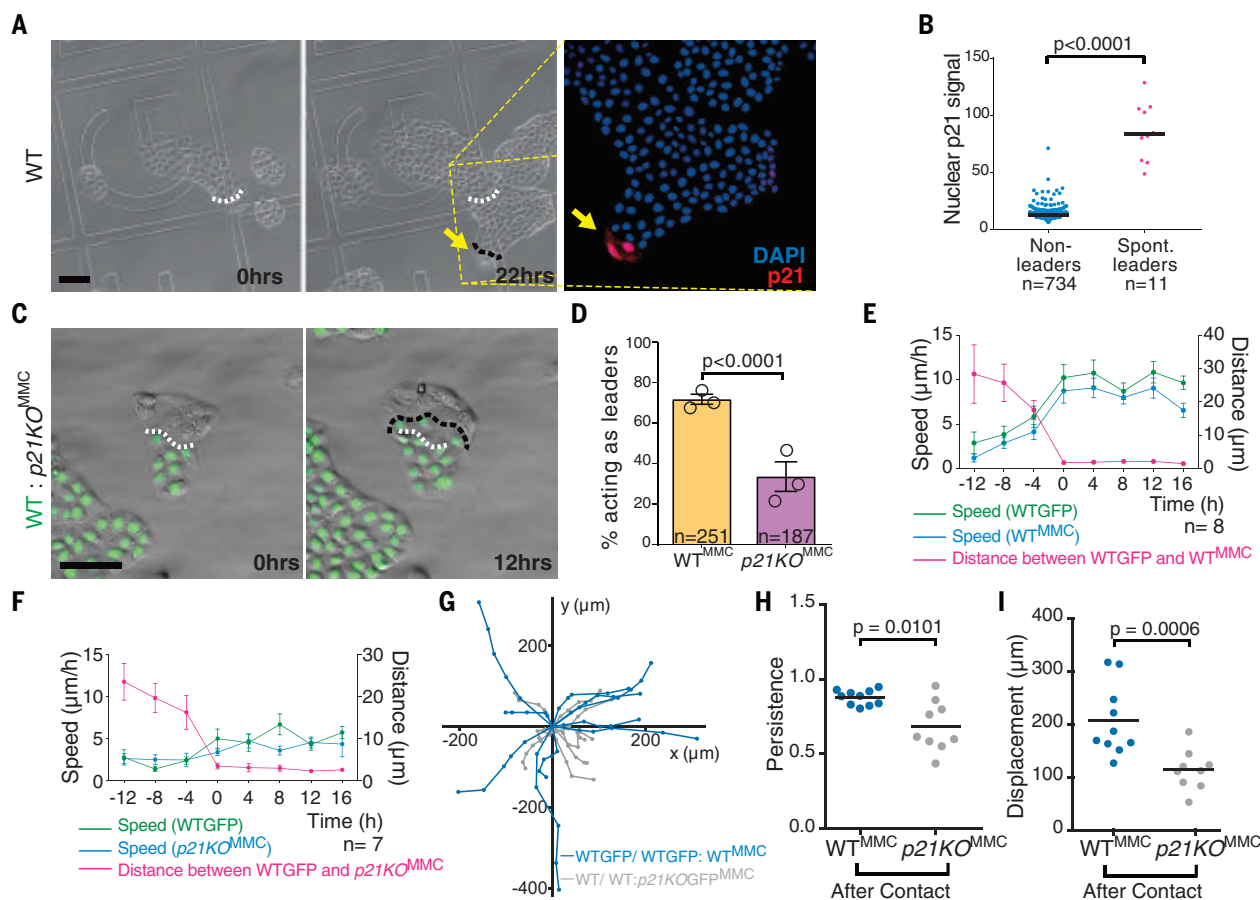


**Fig. 3. The p53 target p21 drives leader cell migration.** (A) Movie stills of a migrating spontaneous leader (arrow), subsequently immunostained for p21 (dashed yellow lines indicate the corresponding field) and (B) corresponding fluorescence intensity quantification. (C) Movie stills of GFP-positive wild-type cells cocultured with MMC-treated *p21KO* cells. (D) Percentage of MMC-treated wild-type or *p21KO* cells acting as leaders. Mean values shown. (E and F) Tracking of mean migration speed of and mean respective distance between pairs of untreated wild-type cells and MMC-treated wild-type cells (E) or *p21KO* cells (F). (G) Tracks of wild-type cell migration upon contact with

MMC-treated wild-type (blue) or *p21KO* cells (gray). (H and I) Persistence of migration (H) and displacement (I) of wild-type colonies upon contact with MMC-treated wild-type or *p21KO* cells. Black bars indicate median in (B), (H), and (I). Error bars indicate  $\pm$ SEM in (D) to (F). The *n* values indicate the number of cells (B) or the number of contacts [(D) to (F)]. Data from one representative repeat of three biological replicates (B), pooled from three biological replicates (D), or from selected movies of three biological replicates [(E) to (I)]. *P* values from Mann-Whitney *U* test [(B), (H), and (I)] or from logistic regression (D).

under the control of p21 promoter sequences that respond to p53 (fig. S6J) (30). We found that scratching induced p53 activity along the scratched epithelial edge (Fig. 5, D, dotted white strip, and E), relative to cells away from the scratch (Fig. 5, D, cells within the yellow dashed line, and E). p53 elevation was not accompanied by detectable DNA damage (fig. S6K), suggesting that p53 was not activated by mechanically induced DNA damage. Instead, p53 activation in edge cells was prevented by inhibition of p38 (Fig. 5, F and G), a stress-related kinase that can activate p53 upon mechanical stress (24, 31). Thus, scratch-induced mechanical insult, through p38, elevates p53, which in turn instructs leader specification to drive epithelial gap closure.

We reasoned that if the p53-p21 pathway plays an active role during repair of injured

MDCK monolayers, then inhibiting p53 should slow down closure of the gap, whereas activating p53 should accelerate epithelial repair. Inhibiting p53 function by GSE-22 overexpression was sufficient to reduce the migration speed of scratched monolayers (Fig. 5, H to J). Ablating *p21* also resulted in slower migration of scratched epithelial sheets relative to wild-type control (Fig. 5K and fig. S6, L and M). To test whether activating p53 can accelerate migration, we used laser-induced DNA damage (32) to elevate p53 specifically in the first row of cells at the edge of the migrating front (Fig. 5L and fig. S6N). DNA damage in edge cells was sufficient to accelerate cell migration, an effect that could be suppressed by p53 inhibition (Fig. 5, M and N, and movie S8). Thus, p53 and its target gene *p21* are the signals activated at the edge of damaged epithelia that instruct leader cell fate.

### Leader cells are eliminated by cell competition upon epithelial repair

p53 elevation in MDCK cells causes mechanical cell competition (24): Cells with high p53 acquire hypersensitivity to cell crowding and behave as “mechanical losers,” undergoing cell extrusion and/or apoptosis when compacted by cells with low p53 (24). Because our data indicate that high p53 is a hallmark of scratch-induced leaders, we wondered whether these leaders might be eliminated upon closure of the epithelial gap, when compacted by follower cells. Both spontaneous leaders (Fig. 6, A and B) and scratch-induced leaders (Fig. 6, C and D, and movie S9) underwent extrusion or death at high rates upon compaction by followers (75.9 and 40%, respectively). This cell elimination was not mediated by p21; p21 ablation did not suppress compaction hypersensitivity in cells



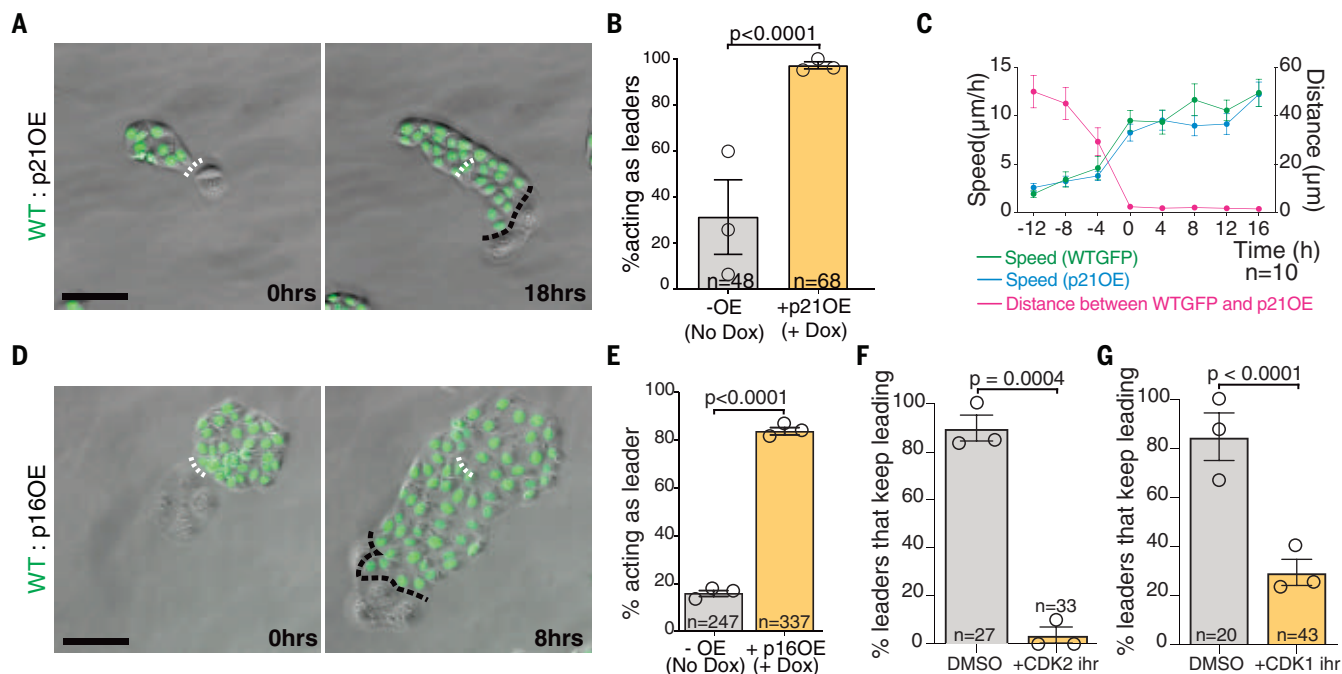


**Fig. 4. CDK inhibition promotes leader cell specification.** (A) Movie stills of cocultures of GFP-positive wild-type cells and cells overexpressing p21 (p21OE). (B) Percentage of p21OE cells acting as leaders. (C) Tracking of mean migration speed of and mean respective distance between pairs of wild-type cells and p21OE cells. (D) Movie stills of cocultures of GFP-positive wild-type cells and cells overexpressing p16 (p16OE). (E) Percentage of p16OE cells acting as leaders. (F and G) Percentage of spontaneous leaders that continue

migrating after addition of DMSO, CDK2 inhibitor K03861 (F), or CDK1 inhibitor RO-3306 (G). Bar charts in (B) and (E) to (G) show mean values. Error bars indicate  $\pm$ SEM in (B), (C), and (E) to (G). The  $n$  values indicate the number of contacts [(B), (C), and (E)] or the number of spontaneous leaders [(F) and (G)]. Data pooled from three biological replicates [(B) and (E) to (G)] or from selected movies of three biological replicates (C).  $P$  values from logistic regression [(B) and (E) to (G)].

with high p53 (Fig. 6E), neither did it rescue their loser status in competition experiments with p53 mutant cells (Fig. 6F and movie S10). In addition, leaders induced by p21 overexpression did not behave as losers in competition experiments with wild-type cells (Fig. 6G), suggesting that p21 is not sufficient for mechanical loser status. Because overexpression of p21 generated leaders that are not mechanical losers, this allowed us to investigate the consequences of failure to clear leader cells upon epithelial gap closure. More than half of the p21-overexpressing cells (56.9% on average in three independent experiments,  $n = 373$ ) displayed an aberrant morphology after the epithelium was repaired, compromising the regular cobblestone-like morphology of the epithelium (Fig. 6H).

## Discussion

Understanding how leader cells emerge in damaged epithelia is important for understanding the process driving wound healing and for identifying interventions that could accelerate and improve wound repair. Our work reveals that p53 is a key cell determinant instructing leader cell fate (Fig. 6, I and J). In damaged epithelia, injury itself causes the emergence of leader cells by mechanically inducing p53 elevation. p53 plays two critical roles in epithelial repair. It initiates leader-

driven epithelial closure, as the juxtaposition of cells with high (leaders) and low (followers) p53 drives directional cell migration across the gap. Once the epithelium has been repaired, p53 induces leader cell clearance by cell competition, reinstating epithelial integrity.

Our work demonstrates that p53 induces leader fate through the transcriptional activation of p21 and that p21, in turn, induces leader fate through inhibition of CDK activity. Cell cycle delay is a feature common to both spontaneous and injury-induced leaders in our system. Nonproliferating cells at the front of collectively migrating cells have been reported in several *in vivo* contexts, such as during cardiomyocyte migration (17), in skin epithelia after wounding (7, 8), in angiogenic sprouting (33), in the migration of often aneuploid cytotrophoblast cells (34), and in metastatic cancer cell migration promoted by radiotherapy-induced senescent cells (35). Our work suggests that developmentally controlled or injury-induced p53, p21, or CDK inhibition may constitute a general mechanism to induce collective leader-driven cell migration.

## Materials and methods

### Antibodies and drugs

For immunofluorescence, we used rabbit anti-p53 (1:750, 9382, RRID:AB\_331476, Cell Signaling Technology), rabbit anti-p21 (1:200, sc-397,

RRID:AB\_632126, Santa Cruz Biotechnology), rat anti-ITG $\beta$ 1 (1:500, AIIB2, RRID:AB\_528306, DSHB), mouse anti-PI3K (1:200, 610045, RRID:AB\_397460, BD Biosciences), rabbit anti- $\gamma$ H2AX (Ser 139) (1:200, 9718, RRID:AB\_561076, Cell Signaling Technology), rabbit anti-cleaved caspase-3 antibody (1:200, 9661, RRID:AB\_2341188, Cell Signaling Technology), mouse anti-ZO-1 (1:500, 33-9100, RRID:AB\_2533147, Thermo Fisher Scientific), and Alexa Fluor conjugated secondary antibodies (1:1000; Thermo Fisher Scientific).

The following treatments and reagents were used: Rac1 inhibitor Z62954982 [100  $\mu$ M in dimethyl sulfoxide (DMSO), 553512, Merck], PI3K inhibitor LY294002 (10  $\mu$ M in DMSO, L9908, Merck), CDK1 inhibitor RO-3306 (10  $\mu$ M in DMSO, SML0569, Sigma-Aldrich), CDK2 inhibitor K0386 (3  $\mu$ M in DMSO, S8100, Selleckchem), nutlin-3 (concentration as specified, in DMSO, CAY10004372, Cambridge Bioscience), p38 inhibitor (10  $\mu$ M in DMSO SB202190, S7067, Calbiochem), mitomycin C (7.5  $\mu$ g/ml in water, M4287, Merck), doxycycline (1  $\mu$ g/ml in water, D9891, Merck), puromycin (0.65  $\mu$ g/ml in water, P9620, Merck), G418 (400  $\mu$ g/ml, 10131035, Thermo Scientific), Hoechst 33342 (3  $\mu$ g/ml in water, H3570, Thermo Fisher Scientific), 4',6-diamidino-2-phenylindole (DAPI; 1  $\mu$ g/ml in water, D3571, Thermo Fisher Scientific).

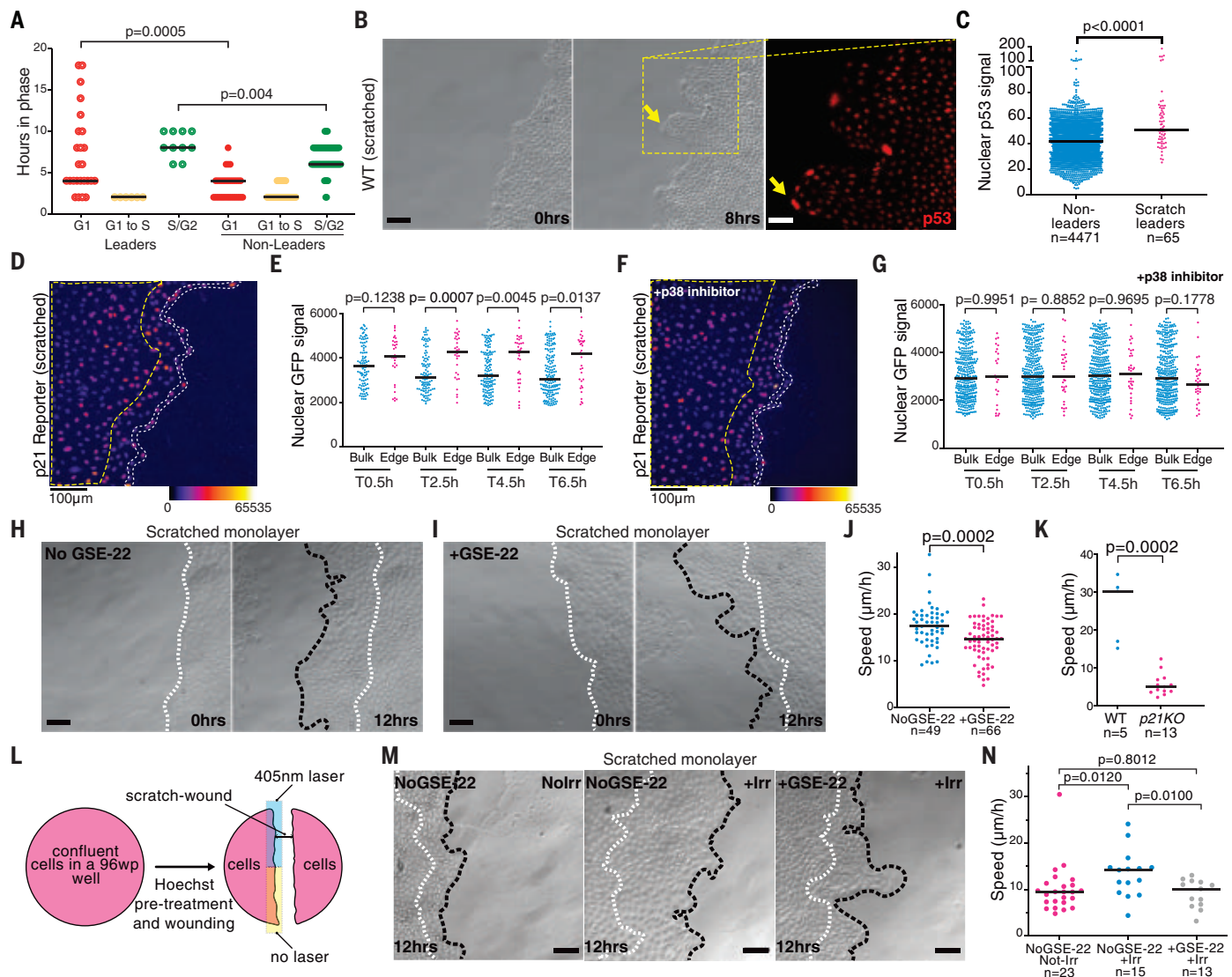


**Fig. 5. Injury-induced p53 elevation drives collective migration in epithelial repair.**

(A) Quantification of cell cycle phase duration in FUCCI-reporter expressing scratch-induced leaders. (B) Movie stills showing emergence of scratch-induced leaders (arrow) from a monolayer of wild-type cells and p53 immunostaining of the indicated field (yellow dashed lines). (C) Quantification of nuclear p53 intensity of scratch-induced leaders and surrounding nonleaders from experiments, as in (B). (D and E) Movie still of cells expressing p21 promoter-driven nuclear GFP after scratching (D) and corresponding quantifications (E). Images are pseudo-colored to reflect signal intensity. Edge cells are within white dotted lines; bulk cells are within the yellow dashed lines. T indicates time elapsed since scratching. (F and G) Movie still of cells expressing p21 promoter-driven nuclear GFP after scratching, as in (D), but in the presence of p38 inhibitor SB202190, and corresponding quantifications (G). (H to J) Movie

stills of uninduced control (H) or cells expressing the p53 inhibitor GSE-22 (I) after scratch and corresponding quantifications of migration speed (J). (K) Quantification of migration speed of wild-type or *p21KO* cells after scratch. (L) Experimental design to induce localized p53 activation at the edge of scratched monolayers. (M and N) Movie stills of control uninduced and nonirradiated (left panel), uninduced and irradiated (middle panel), or GSE-22-expressing and irradiated (right panel) cells after scratching (M) and corresponding quantifications of migration speeds (N). Black bars indicate median in (A), (C), (E), (G), (J) to (K), and (N). The *n* values indicate the number of cells (C) or the number of movies [(J), (K), and (N)]. Data from one representative repeat of three biological replicates [(A), (J), (K), and (N)] or one representative movie of three biological replicates [(E) and (G)]. *P* values from Mann-Whitney *U* test.

#### Cell culture and plasmids

MDCK cells were maintained in Dulbecco's minimum essential medium (21885, Thermo Fisher Scientific) supplemented with 10% fetal bovine serum (FBS; P30-3305, FBS Standard, South America, PAN Biotech) in a humidified incubator at 37°C and 5% CO<sub>2</sub>. Wild-type MDCK cells were obtained from Y. Fujita (Kyoto Univer-

sity); MDCK wild-type GFP-NLS cells have been previously described (24).

MDCK *p53KO* GFP-NLS clones 6 and 14 were generated by infecting a MDCK *p53KO* pool (24) with lentiviral construct pGIPZ-turboGFP-NLS-Puro (24). Selection after infection was carried out in 0.65 μg/ml puromycin. The resulting GFP-NLS-labeled pool was then plated at one

cell per well in 96-well plates. Clones were expanded and verified by immunofluorescence, sequencing, and Western blotting.

MDCK *p21KO* clones G5 and E9 were generated using Cas9 D10A CRISPR technology. Single guide RNAs (sgRNAs) against canine *CDKN1A* were designed manually following published methods (36). Target sequences



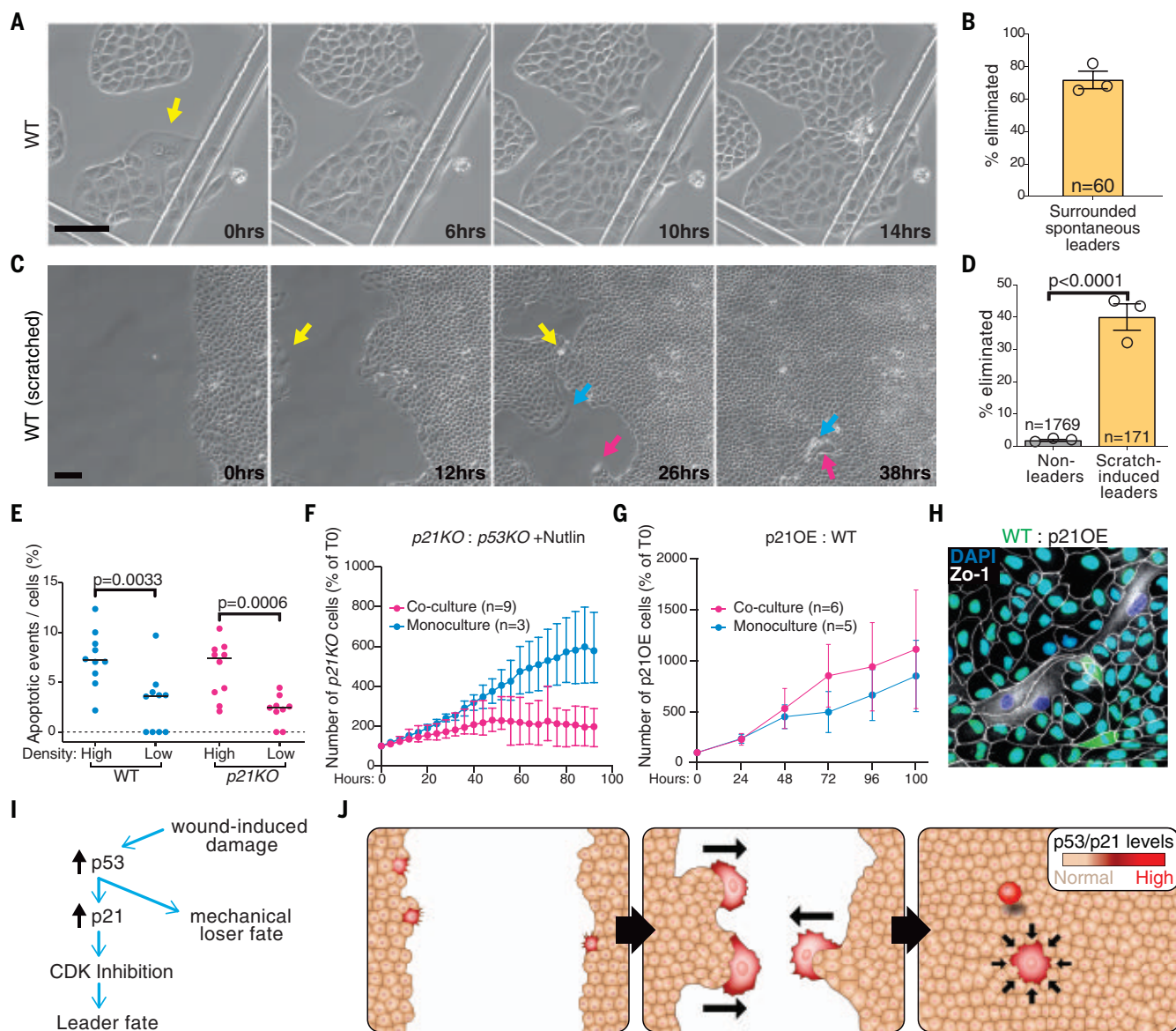


**Fig. 6. Leader cells are eliminated upon epithelial repair.** (A) Movie stills following the fate of a spontaneous leader (arrow). (B) Percentage of spontaneous leaders that are eliminated when surrounded by neighbors. (C) Movie stills of scratch-induced leaders (blue, yellow, and pink arrows point to different leaders over time), showing their elimination at gap closure. (D) Percentage of leader or surrounding nonleader cells eliminated at gap closure. (E) Quantification of apoptotic events (cleaved caspase-3-positive cells) in wild-type or *p21KO* nutlin-3-treated cells grown at low- or high-density and after compaction. (F) Mean number of *p21KO* cells (percentage of initial number/field) in nutlin-3-treated pure cultures (monoculture) or confronted with *p53KO* cells (coculture). (G) Mean number of *p21OE* cells (percentage of initial number/field) in pure cultures (monoculture) or confronted with wild-type cells

(coculture). (H) Confocal imaging of ZO-1 immunostaining of a coculture at confluency of *p21OE* and GFP-positive wild-type cells. (I and J) Diagram and model summarizing the function of p53 and p21 in epithelial repair. Epithelial scratching induces p53 and its target p21, which drives leader cell migration and epithelial closure through CDK inhibition. p53 (but not p21) elevation also induces leader cells to behave as mechanical losers, causing their elimination upon epithelial closure. Bar charts in (B) and (D) show mean values. Black bars indicate median in (E). Error bars indicate  $\pm$ SEM in (F) and (G). The *n* values indicate the number of cells [(B) and (D)] or the number of fields [(F) and (G)]. Data from one representative repeat of three biological replicates [(E) to (G)], pooled from three biological replicates [(B) and (D)], or from one selected field of three biological replicates (H). *P* values from logistic regression (D) or from Mann-Whitney *U* test (E).

used: 5'-CGGCAAGCCTTGCTGCCATG(AGG)-3' and 5'-TGGACAGCGAGCAGCTGCGC(CGG)-3'. sgRNAs were cloned individually into PX461 vectors [RRID:Addgene\_48140 (36)] and co-transfected as a pair into wild-type MDCK cells using Lipofectamine 2000 (Thermo Fisher Scientific). The transfected cells were treated with 11  $\mu$ M nutlin-3 for 6 days to enrich for

non-growth-inhibited *p21KO* cells. The pool was then plated at one cell per well in 96-well plates; the resulting clones were expanded and verified by immunofluorescence and sequencing. For use in the competition experiment, a *p21KO* GFP-positive population was obtained by infecting the *p21KO* G5 clone with a lentiviral construct containing pGIPZ-GFP-NLS-Puro as

described in (24) and selected using 0.65  $\mu$ g/ml puromycin.

To overexpress p21, *p21* cDNA was amplified from a cDNA library obtained from MDCK *scribble* shRNA cells treated with tetracycline to induce *scribble* knockdown, as these cells have been shown to express high levels of p21 (24). The resulting polymerase chain reaction

(PCR) product was introduced into doxycycline-inducible pTRIPZ-RFP-NLS-Puro (24) with a P2A peptide bridging the two proteins to make pTRIPZ-p21-P2A-RFP-NLS-Puro. MDCK wild-type cells were infected with the final construct, selected using 0.65 µg/ml puromycin, and then plated in 96-well plates to isolate single clones that were verified by immunofluorescence. For use in competition experiments, a p21OE GFP-positive population was obtained by infecting a p21OE clone with a lentiviral construct containing pGIPZ-GFP-NLS-Puro, as described in (24), and selecting GFP-positive cells using fluorescence-activated cell sorting (FACS).

To overexpress p16, the human p16 cDNA was amplified from pLenti cytomegalovirus (CMV) p16 Neo (w111-1) (RRID:Addgene\_22260), using a modified forward primer to reintroduce the eight N-terminal amino acids missing when compared with the full-length human p16 sequence (transcript ENST00000304494.9, Ensembl). The resulting PCR product was introduced into doxycycline-inducible pTRIPZ-RFP-NLS-Puro (24) with a P2A peptide bridging the two proteins to make pTRIPZ-p16-P2A-RFP-NLS-Puro. MDCK wild-type cells were infected with the final construct and selected using 0.65 µg/ml puromycin to generate a pool population.

To overexpress the dominant negative GSE-22 peptide (25), amino acids 302 to 381 of canine p53 (homologous to the original rat sequence) were amplified from the MDCK cDNA library used in p21 cloning; a forward primer carrying an adaptor with three start ATG codons and a reverse primer containing three stop codons were used to account for all three reading frames, as was done in the original publication. The resulting PCR product was introduced into doxycycline-inducible pTRIPZ-GFP-NLS-Puro with a P2A peptide bridging the two proteins to make pTRIPZ-GSE-22-P2A-GFP-NLS-Puro. MDCK wild-type cells were infected with the final construct and selected using 0.65 µg/ml puromycin. Clones were selected by FACS, sorting cells with the top 5% GFP intensity on a 96-well plate. p53 inhibition in the clones was verified functionally, by Western blotting, showing absence of p21 induction upon DNA damage.

The MDCK FUCCI cell line was generated by infecting cells with the ready-made IncuCyte Cell Cycle Red/Green Lentivirus Reagent (Sartorius, 4779), according to manufacturer protocols and selected using 0.65 µg/ml puromycin to generate a pool population.

MDCK p21 reporter cell line was generated by transfecting a plasmid containing destabilized turbo GFP downstream of p21 promoter sequences in MDCK cells. The plasmid was generated following a strategy similar to the one described in (30). In short, we obtained a plasmid carrying p21 promoter sequences, described in (30). We amplified the p21 sequences and turbo GFP from pTRIPZ GFP-NLS-Puro

and cloned them upstream of a PEST destabilization signal in pcDNA3.3 d2eGFP (37) (RRID:Addgene\_26821), after excision of CMV promoter, CMV enhancer, and eGFP from the backbone plasmid. Cells transfected with the resulting plasmid were selected using 400 µg/ml G418, and clones were picked on the basis of their brightness by means of FACS. A further round of selection was performed upon nutlin-3 treatment to isolate clones with high post-treatment to pretreatment signal ratio.

#### Mitomycin C (MMC) assays

On day 1, 2500 untreated wild-type MDCK cells (labeled with GFP-NLS or unlabeled, as appropriate) per well were seeded in 24-well plates. On day 2, a second population of MDCK cells was trypsinized, and  $1 \times 10^6$  of these were incubated in suspension in 5 ml complete media containing 7.5 µg/ml MMC for 1 hour at 37°C and 5% CO<sub>2</sub>. Cells were then washed at least three times in complete media (spinning down the cells after each wash) to reduce MMC carryover, and then 10,000 MMC-treated cells or 5000 untreated control cells were plated on top of the pre-seeded untreated population. Live imaging began on day 3; samples were imaged every 2 hours, except for the CDK1 inhibitor experiment where imaging occurred every 45 min. Where applicable, inhibitors were added after leader-follower behavior had emerged, and imaging continued for 4 to 24 more hours.

#### Spontaneous leader assays

Five thousand wild-type MDCK cells were seeded in a 24-well plate or, if immunofluorescence was to be performed at end of live imaging, in a gridded tissue culture plate (µ-Dish 35 mm Grid-500, 81166, ibidi). About 48 hours later, cells with spontaneous leader morphology were selected and imaged every 2 hours. Where applicable, at the end of live imaging, cells were fixed in 4% paraformaldehyde (PFA; 15713-S, Electron Microscopy Sciences) in phosphate-buffered saline (PBS) for 10 min at room temperature (RT).

#### Scratch and barrier release assays

For the scratch assay, 27,000 to 35,000 wild-type, p21KO, GSE-22, or FUCCI MDCK cells were seeded in the middle of a "fence" (Aix Scientifics, <https://aix-scientifics.uk/en/fences.html>) placed in a 24- or directly into a 96-well plate. The fence was removed ~5 hours after seeding, and the culture medium changed. Where indicated, doxycycline-supplemented medium was used to induce GSE-22 expression. About 20 hours later, a P1000 pipette tip was used to generate a scratch-wound through the middle of the now-confluent monolayer, and the culture medium was changed.

For the scratch assay with the p21 reporter cell line, 80,000 to 100,000 cells were seeded

per well on a glass bottom 24-well plate (Sensoplate, 662892, Grenier Bio-One), previously coated with 20 µg/ml fibronectin (F1141, Thermo Fisher Scientific) in PBS for 1 hour at 37°C. Sixteen hours after seeding, the p38 inhibitor was added where indicated, and ~32 hours later the monolayer was scratched, as described above, and imaging was started.

For the barrier release assay, 25,000 to 28,000 wild-type MDCK cells were seeded in each chamber of a two-well silicone insert (ibidi, 80209). Culture medium was added outside of the chambers 5 hours after seeding, and ~20 hours later the barrier was removed.

Imaging was started ~1 hour after scratching or removing the barrier, and images were acquired every 1 to 2 hours. If immunofluorescence was to be performed after live imaging, cells were seeded on optically clear plates (µ-Plate 24 well, 82406, ibidi or CellCarrier-96, 6005550, PerkinElmer).

#### Laser photodamage experiments

On day 1, 25,000 to 30,000 GSE-22 carrying cells per well were plated on an optically clear 96-well plate (CellCarrier-96, 6005550, PerkinElmer). Cells were left to adhere overnight and, where indicated, the culture medium was replaced with doxycycline-supplemented medium to induce GSE-22 expression. On day 2, the cell monolayer was scratched through the middle of each well using a P1000 tip and returned to the 37°C and 5% CO<sub>2</sub> incubator for ~30 min. Cells were then treated in the incubator with 3 µg/ml Hoechst 33342 diluted in complete medium for 10 min and washed three times in complete medium. Irradiation along half of the wound edge was performed using a 20× air objective on a Leica SP8 confocal microscope, which was set up to keep the samples at 37°C and 5% CO<sub>2</sub>; the other half of the wound was not irradiated and served as control. Laser settings used: 40 frames at 100% 405 nm laser with the FRAP booster on. Samples were then live imaged using a Nikon BioStation CT system every 2 hours for at least 24 hours. For γH2AX stainings, samples were fixed and processed 2 to 4 hours after irradiation.

#### Blebbistatin-induced binucleated cell (BBC) generation

On day 1, 5000 unlabeled wild-type MDCK cells were plated per gridded dish (µ-Dish 35 mm Grid-500, 81166, ibidi). Also on day 1, 12,000 GFP-NLS labeled wild-type MDCK cells were incubated with 37.5 µM blebbistatin in DMSO (B0560, Merck) in a 12-well plate. Sixteen hours later, on day 2, cells were washed three times in PBS and left to recover for 4 hours in complete media. Cells were harvested by trypsinization and, after large clumps were removed using a 20-µm filter (04-0042-2315, CellTrics), were plated on the gridded dishes containing unlabeled wild-type MDCK cells. Imaging was started on day 3; cells were imaged every 2 to 4 hours.



### Real-time quantitative reverse-transcription PCR (RT-qPCR)

On day 1, 400,000 MDCK cells per well were seeded in a six-well plate and left to adhere overnight. On day 2, cells were incubated in complete medium containing 7.5 µg/ml MMC for 1 hour at 37°C and 5% CO<sub>2</sub>. After ~16 hours from treatment, cells were lysed and their RNA was extracted with the Quick-RNA Miniprep Kit (Zymo Research, R1054/R1055) according to the supplier instructions. cDNA was retro-transcribed using the SuperScript III Reverse Transcriptase kit (Thermo Fisher, 18080044) as recommended by the supplier. The qPCR was performed in a StepOne Real-Time PCR System (Thermo Fisher) using the QuantiNova SYBR Green PCR Kit (Qiagen, 208056).

The following primers were used: ITGB1 (5'GCGTTGCTGCTGATTGGAA3' and 5'ATTTT-CACCCGTGTCCCAT3'), PI3KCA (5'TGCTG-AACCTATTGGTG3' and 5'TACAGTCCAGA-AGCTCCA3'), and GAPDH (glyceraldehyde 3-phosphate dehydrogenase; 5'AGTCCATCTC-CATCTTCCAG3' and 5'CGTCACGCCACATCT-TCC 3').

The fold change in gene expression was calculated using the comparative Ct method, normalizing to GAPDH.

### Cell competition experiments

Competing mixed MDCK cultures were seeded on the outside of the barrier created by the insertion of “fences” (Aix Scientifics, <https://aix-scientifics.uk/en/fences.html>) in a 24-well plate. Nineteen thousand combined *p53KO:p21KO* GFP-NLS cells mixed at a ratio of 8.5:1 or 8000 combined WT:p21OE GFP-NLS cells mixed at a ratio of 9:1 were used. Two thousand cells of a pure *p21KO* GFP-NLS or *p21OE* GFP-NLS population were seeded in the center of the fence in the same well and served as control monoculture. About 5 hours after plating, fences were removed and the culture medium replaced.

For the *p21OE* experiment, on day 2, *p21* overexpression was induced with doxycycline, and imaging was started on day 3. Images were acquired every 2 hours for an additional 4 or 5 days. Fresh doxycycline-supplemented culture medium was supplied every second day. Live imaging of mixed and pure cultures not supplemented with doxycycline was performed as a control.

For the *p21KO* experiment, on day 3, *p53* elevation was induced with 12 µM nutlin-3, and imaging was started on day 4. Images were acquired every 2 hours for an additional 3 or 4 days. Fresh nutlin-3-supplemented culture medium was supplied every day, with the concentration of nutlin-3 brought to 15 µM from day 5 to compensate for the increased cell number. Time-lapse imaging of mixed and pure cultures treated with DMSO and of treated and untreated *p53KO*:WT GFP-NLS cultures was performed as a control.

### Compaction experiments

Cells were pretreated with 15 µM nutlin-3 or DMSO for 24 hours. Between 95,000 and 125,000 (high density) or 15,000 and 20,000 (low density) MDCK wild-type or *p21KO* cells were then seeded in each of the two compartments of a stretching device (24). In brief, the device is composed of a flexible polydimethylsiloxane (PDMS) membrane (Gel pak PF-60-X4, 150 µm thickness, Teltek) held by a custom-made stretcher (University of Bristol), which, once stretched by 2 cm, provides a 57% greater stretch compared with the resting length. Two cell-seeding chambers are created on the stretched membrane by attaching a silicone insert with two compartments (6.6 mm by 13 mm each), and the PDMS membrane is then coated with 25 µg/ml fibronectin in PBS (F1141, Thermo Fisher Scientific) for 1 hour at 37°C. Low- and high-density cells were seeded side by side on the two chambers of the same membrane and were therefore processed in parallel, minimizing sample-to-sample variability during culture, compaction, and staining.

Once seeded, cells were left to adhere to the membrane for 24 hours and then the stretching was released to induce compaction. Five hours after release, cells were fixed and processed for anti-caspase-3 immunofluorescence.

### Immunofluorescence

Depending on the assay, cells were cultured on glass coverslips, optically clear tissue culture dishes, or PDMS membrane. Cells were fixed in 4% PFA (15713-S, Electron Microscopy Sciences) in PBS for 10 min at RT, quenched for 10 min at RT in 50 mM NH<sub>4</sub>Cl in PBS, and permeabilized for 10 min at RT in 0.1% Triton X-100 in PBS. Samples were blocked for at least 30 min in 2% bovine serum albumin (BSA; A2153, Sigma) 2% FBS in PBS at RT. Both primary and secondary antibodies were diluted in blocking solution diluted 1:1 with PBS. Primary antibody incubations were either a minimum of 1 hour at RT or overnight at 4°C. Following four 5-min washes in PBS, secondary antibodies were incubated for 1 hour at RT then washed four times for 5 min each in PBS. Coverslips were mounted in FluorSave (345789, Merck). Optically clear dishes were either covered with FluorSave and sealed with a coverslip or imaged directly, submerged in PBS. For immunostaining against phosphorylated proteins, the fixing solution was supplemented with PhosSTOP (1 tablet per 10 ml; Sigma), all PBS-based solutions were substituted with tris-buffered saline (TBS)-based ones, and blocking solution was substituted with 5% BSA in TBS.

### Imaging and image analysis

Imaging of fixed samples was done at RT on a Leica SP5 or SP8 confocal microscope using a 63× or 40× oil objective or on the PerkinElmer Opera LX system using a 20× water objective.

Laser photodamage experiments were done on a Leica SP8 confocal microscope set up to keep the samples at 37°C and 5% CO<sub>2</sub> during imaging. All images in the figures are presented as sum projection.

Mean intensities of nuclear p53 and p21 were measured using DAPI as a mask to segment the nuclear volumes in three dimensions using Volocity (PerkinElmer). Mean intensities per cell of ITGB1 and PI3K were measured in FIJI as the integrated density of fluorescence measured on an average intensity projection, multiplied by the number of Z slices and divided by the number of nuclei.

Live imaging was performed on a Nikon BioStation CT system at 37°C and 5% CO<sub>2</sub> using 10× or 4× air objectives with an imaging frequency of 0.25 to 4 hours for all experiments except for the one involving the *p21* reporter cell line; media was changed every 2 to 3 days, unless otherwise stated. For the *p21* reporter experiment, live imaging was performed on a Yokogawa Cell Voyager 7000S at 37°C and 5% CO<sub>2</sub> using a 20× air objective with an imaging frequency of 2 hours.

Particle image velocimetry (PIV) was performed by using a deep learning (DL)-PIV approach. In short, we used the DL-unsupervised optical flow method, described in (38). We trained the pretrained network provided in (38) using 650 video images of MDCK cells in different settings. The network was then applied to a selected subset of movies of migrating MMC-induced leaders or spontaneous leader-follower pairs imaged every 15 min.

Manual cell tracking was done by marking coordinates of cell nuclei over time using MtrackJ plugin in ImageJ. Cells from untreated, MMC-treated, or spontaneous leader-follower pairs were tracked starting from 8 hours (four time points) before to 12 hours (six time points) after contact between cells was established, thereby making coordinate (0,0) a point when the two cells meet. Coordinates of cell tracks were analyzed in Microsoft Excel.

The speed of migration of leader-follower pairs was measured in FIJI by using a custom-made algorithm tracking the position of the colony borders over time (see data and materials availability statement in the acknowledgments). The resulting coordinates were analyzed in Microsoft Excel to calculate the speed of migration and the relative distance between prospective leader and follower colonies. The time of contact between colonies is reported as zero in the graphs.

The fluorescence intensity of *p21* reporter cells was quantified manually by selecting edge (first row at the migrating front) or bulk (from fifth row of the cell monolayer inward) cells and quantifying the mean intensity of each nucleus with Volocity (PerkinElmer). Flat field correction was performed in each image before analysis.

The migration speed of scratched epithelial fronts was measured in FIJI by manually drawing freehand lines outlining the wound edge at the first and final time points. If any wound edges were not parallel to the  $y$  axis, images were adequately rotated. The median  $x$  position for each line was recorded to calculate the median  $x$  displacement in pixels, which was then divided by the duration of the experiment in hours to generate a speed value in pixels per hour and then converted to micrometers per hour. As density affects the speed of migration, we selected only fields with comparable initial density. The initial cell density of the monolayer was obtained by segmenting cells in phase using a custom-made algorithm (see data and materials availability statement).

All graphs were plotted using GraphPad Prism. Figures were made using Adobe Illustrator CS6.

### Statistical analysis

Logistic regression analysis was performed using R, and the reported  $P$  values have been corrected using the false discovery rate method. All other statistical analyses were performed using GraphPad Prism. For the RT-qPCR experiments, the  $P$  values were obtained using the Wilcoxon signed rank test; all the other  $P$  values were obtained using the Mann-Whitney  $U$  test.

Standard guidelines have been followed in providing sufficient methods information for this work, and a Materials Design Analysis Reporting (MDAR) checklist has been provided at submission.

### REFERENCES AND NOTES

1. P. Friedl, D. Gilmour, Collective cell migration in morphogenesis, regeneration and cancer. *Nat. Rev. Mol. Cell Biol.* **10**, 445–457 (2009). doi: [10.1038/nrm2720](https://doi.org/10.1038/nrm2720); pmid: 19546857
2. M. Poujade et al., Collective migration of an epithelial monolayer in response to a model wound. *Proc. Natl. Acad. Sci. U.S.A.* **104**, 15988–15993 (2007). doi: [10.1073/pnas.0705062104](https://doi.org/10.1073/pnas.0705062104); pmid: 17905871
3. S. Begnaud, T. Chen, D. Delacour, R.-M. Mège, B. Ladoux, Mechanics of epithelial tissues during gap closure. *Curr. Opin. Cell Biol.* **42**, 52–62 (2016). doi: [10.1016/j.ceb.2016.04.006](https://doi.org/10.1016/j.ceb.2016.04.006); pmid: 27131272
4. V. Hakim, P. Silberzan, Collective cell migration: A physics perspective. *Rep. Prog. Phys.* **80**, 076601 (2017). doi: [10.1088/1361-6633/aa65ef](https://doi.org/10.1088/1361-6633/aa65ef); pmid: 28282028
5. R. Mayor, S. Etienne-Manneville, The front and rear of collective cell migration. *Nat. Rev. Mol. Cell Biol.* **17**, 97–109 (2016). doi: [10.1038/nrm.2015.14](https://doi.org/10.1038/nrm.2015.14); pmid: 26726037
6. E. Theveneau, C. Linker, Leaders in collective migration: Are front cells really endowed with a particular set of skills? *FI000Res.* **6**, 1899 (2017). doi: [10.12688/fi000research.11889.1](https://doi.org/10.12688/fi000research.11889.1); pmid: 29152225
7. S. Park et al., Tissue-scale coordination of cellular behaviour promotes epidermal wound repair in live mice. *Nat. Cell Biol.* **19**, 155–163 (2017). doi: [10.1038/ncb3472](https://doi.org/10.1038/ncb3472); pmid: 28248302
8. M. Aragona et al., Defining stem cell dynamics and migration during wound healing in mouse skin epidermis. *Nat. Commun.* **8**, 14684–14 (2017). doi: [10.1038/ncomms14684](https://doi.org/10.1038/ncomms14684); pmid: 28248284

9. M. Refay et al., Interplay of RhoA and mechanical forces in collective cell migration driven by leader cells. *Nat. Cell Biol.* **16**, 217–223 (2014). doi: [10.1038/ncb2917](https://doi.org/10.1038/ncb2917); pmid: 24561621
10. N. Yamaguchi, T. Mizutani, K. Kawabata, H. Haga, Leader cells regulate collective cell migration via Rac activation in the downstream signaling of integrin  $\beta 1$  and PI3K. *Sci. Rep.* **5**, 7656 (2015). doi: [10.1038/srep07656](https://doi.org/10.1038/srep07656); pmid: 25563751
11. T. Ormelchenko, J. M. Vasiliev, I. M. Gelfand, H. H. Feder, E. M. Bonder, Rho-dependent formation of epithelial “leader” cells during wound healing. *Proc. Natl. Acad. Sci. U.S.A.* **100**, 10788–10793 (2003). doi: [10.1073/pnas.1834401100](https://doi.org/10.1073/pnas.1834401100); pmid: 12960404
12. S. Mark et al., Physical model of the dynamic instability in an expanding cell culture. *Biophys. J.* **98**, 361–370 (2010). doi: [10.1016/j.bpj.2009.10.022](https://doi.org/10.1016/j.bpj.2009.10.022); pmid: 20141748
13. S. Rausch et al., Polarizing cytoskeletal tension to induce leader cell formation during collective cell migration. *Biointerphases* **8**, 32 (2013). doi: [10.1186/1559-4106-8-32](https://doi.org/10.1186/1559-4106-8-32); pmid: 24706149
14. A. Ravasio et al., Gap geometry dictates epithelial closure efficiency. *Nat. Commun.* **6**, 7683 (2015). doi: [10.1038/ncomms8683](https://doi.org/10.1038/ncomms8683); pmid: 26158873
15. M. Vishwakarma et al., Mechanical interactions among followers determine the emergence of leaders in migrating epithelial cell collectives. *Nat. Commun.* **9**, 3469–12 (2018). doi: [10.1038/s41467-018-05927-6](https://doi.org/10.1038/s41467-018-05927-6); pmid: 30150695
16. J. Campisi, Aging, cellular senescence, and cancer. *Annu. Rev. Physiol.* **75**, 685–705 (2013). doi: [10.1146/annurev-physiol-030212-183653](https://doi.org/10.1146/annurev-physiol-030212-183653); pmid: 23140366
17. J. Cao et al., Tension creates an endoreplication wavefront that leads regeneration of epicardial tissue. *Dev. Cell* **42**, 600–615.e4 (2017). doi: [10.1016/j.devcel.2017.08.024](https://doi.org/10.1016/j.devcel.2017.08.024); pmid: 28950101
18. A. F. Straight et al., Dissecting temporal and spatial control of cytokinesis with a myosin II inhibitor. *Science* **299**, 1743–1747 (2003). doi: [10.1126/science.1081412](https://doi.org/10.1126/science.1081412); pmid: 12637748
19. P. R. Andreassen, O. D. Lohez, F. B. Lacroix, R. L. Margolis, Tetraploid state induces p53-dependent arrest of nontransformed mammalian cells in G1. *Mol. Biol. Cell* **12**, 1315–1328 (2001). doi: [10.1091/mbc.12.5.1315](https://doi.org/10.1091/mbc.12.5.1315); pmid: 11359924
20. M. M. Cohen, M. W. Shaw, Effects of mitomycin C on human chromosomes. *J. Cell Biol.* **23**, 386–395 (1964). doi: [10.1083/jcb.23.2.386](https://doi.org/10.1083/jcb.23.2.386); pmid: 14222823
21. J. S. Lanni, T. Jacks, Characterization of the p53-dependent postmitotic checkpoint following spindle disruption. *Mol. Cell Biol.* **18**, 1055–1064 (1998). doi: [10.1128/MCB.18.2.1055](https://doi.org/10.1128/MCB.18.2.1055); pmid: 94488003
22. J. Y. Park, Y. R. Seo, Enhancement of mitomycin C-induced apoptosis in Nrf2-deficient human colon cancer cells. *Mol. Cell Toxicol.* **6**, 51–56 (2010). doi: [10.1007/s13273-010-0007-4](https://doi.org/10.1007/s13273-010-0007-4)
23. L. T. Vassilev et al., In vivo activation of the p53 pathway by small-molecule antagonists of MDM2. *Science* **303**, 844–848 (2004). doi: [10.1126/science.1092472](https://doi.org/10.1126/science.1092472); pmid: 14704432
24. L. Wagstaff et al., Mechanical cell competition kills cells via induction of lethal p53 levels. *Nat. Commun.* **7**, 11373 (2016). doi: [10.1038/ncomms11373](https://doi.org/10.1038/ncomms11373); pmid: 27109213
25. V. S. Ossoskaya et al., Use of genetic suppressor elements to dissect distinct biological effects of separate p53 domains. *Proc. Natl. Acad. Sci. U.S.A.* **93**, 10309–10314 (1996). doi: [10.1073/pnas.93.19.10309](https://doi.org/10.1073/pnas.93.19.10309); pmid: 8816796
26. V. Dulić et al., p53-dependent inhibition of cyclin-dependent kinase activities in human fibroblasts during radiation-induced G1 arrest. *Cell* **76**, 1013–1023 (1994). doi: [10.1016/0092-8674\(94\)90379-4](https://doi.org/10.1016/0092-8674(94)90379-4); pmid: 8137420
27. M. Serrano, G. J. Hannon, D. Beach, A new regulatory motif in cell-cycle control causing specific inhibition of cyclin D/CDK4. *Nature* **366**, 704–707 (1993). doi: [10.1038/366704a0](https://doi.org/10.1038/366704a0); pmid: 8259215
28. A. Besson, S. F. Dowdy, J. M. Roberts, CDK inhibitors: Cell cycle regulators and beyond. *Dev. Cell* **14**, 159–169 (2008). doi: [10.1016/j.devcel.2008.01.013](https://doi.org/10.1016/j.devcel.2008.01.013); pmid: 18267085
29. A. Sakaue-Sawano et al., Visualizing spatiotemporal dynamics of multicellular cell-cycle progression. *Cell* **132**, 487–498 (2008). doi: [10.1016/j.cell.2007.12.033](https://doi.org/10.1016/j.cell.2007.12.033); pmid: 18267078
30. A. L. Paek, J. C. Liu, A. Loewer, W. C. Forrester, G. Lahav, Cell-to-cell variation in p53 dynamics leads to fractional killing.

- Cell* **165**, 631–642 (2016). doi: [10.1016/j.cell.2016.03.025](https://doi.org/10.1016/j.cell.2016.03.025); pmid: 27062928
31. M. Hofmann et al., Mechanical pressure-induced phosphorylation of p38 mitogen-activated protein kinase in epithelial cells via Src and protein kinase C. *Biochem. Biophys. Res. Commun.* **316**, 673–679 (2004). doi: [10.1016/j.bbrc.2004.02.101](https://doi.org/10.1016/j.bbrc.2004.02.101); pmid: 15033452
32. C. Dinant et al., Activation of multiple DNA repair pathways by sub-nuclear damage induction methods. *J. Cell Sci.* **120**, 2731–2740 (2007). doi: [10.1242/jcs.004523](https://doi.org/10.1242/jcs.004523); pmid: 17646676
33. H. Gerhardt et al., VEGF guides angiogenic sprouting utilizing endothelial tip cell filopodia. *J. Cell Biol.* **161**, 1163–1177 (2003). doi: [10.1083/jcb.200302047](https://doi.org/10.1083/jcb.200302047); pmid: 12810700
34. J. F. Weier et al., Human cytotrophoblasts acquire aneuploidies as they differentiate to an invasive phenotype. *Dev. Biol.* **279**, 420–432 (2005). doi: [10.1016/j.ydbio.2004.12.035](https://doi.org/10.1016/j.ydbio.2004.12.035); pmid: 15733669
35. M. Demaria et al., Cellular senescence promotes adverse effects of chemotherapy and cancer relapse. *Cancer Discov.* **7**, 165–176 (2017). doi: [10.1158/2159-8290.CD-16-0241](https://doi.org/10.1158/2159-8290.CD-16-0241); pmid: 27979832
36. F. A. Ran et al., Genome engineering using the CRISPR-Cas9 system. *Nat. Protoc.* **8**, 2281–2308 (2013). doi: [10.1038/nprot.2013.143](https://doi.org/10.1038/nprot.2013.143); pmid: 24157548
37. L. Warren et al., Highly efficient reprogramming to pluripotency and directed differentiation of human cells with synthetic modified mRNA. *Cell Stem Cell* **7**, 618–630 (2010). doi: [10.1016/j.stem.2010.08.012](https://doi.org/10.1016/j.stem.2010.08.012); pmid: 20888316
38. M. Zhang, M. D. Piggott, Unsupervised learning of particle image velocimetry. *Lect. Notes Comput. Sci.* **12321**, 102–115 (2020). doi: [10.1007/978-3-030-59851-8\\_7](https://doi.org/10.1007/978-3-030-59851-8_7)

### ACKNOWLEDGMENTS

We thank C. Tommasi for input on the project and the Wolfson Bioimaging Facility for access to microscopes and for image analysis support (S. Cross). We thank our anonymous reviewers for constructive feedback and suggestions and Life Science Editors (LSE) for editorial assistance. **Funding:** This work was supported by a Human Frontier Science Program (HFSP) grant RGP0043/2019 to R.E.C.S., a Cambridge Cancer Centre PhD studentship to M.G., a Cancer Research UK Programme Grant to E.P. (A12460), a Cancer Research UK Programme Foundation Award to E.P. (C38607/A26831), and a Royal Society University Research fellowship to E.P. (UF0905080). E.P. is a Wellcome Trust Senior Research Fellow (205010/Z/16/Z). **Author contributions:** E.P. conceived of and led the project. E.P., L.W., G.P., and K.K. designed the experimental strategy. Using protocols developed by L.W., M.G. performed the experiments on BBCs, except for anti-p53 immunostaining of wild-type BBCs (done by L.W.) and quantification of the leader behavior of p53KO BBCs (done by K.K.). M.G. generated GFP-labeled clonal p53KO lines. Experiments involving the p21 reporter cell line were performed by M.V. The mechanical compression experiments were performed by S.C. K.G. performed part of the FUCCI experiments and their analysis. K.K. performed all cloning and generated all cell lines except the FUCCI cell line and the GFP-positive p21KO and p21OE cell lines, which were generated by G.P. S.M. and R.E.C.S. generated the custom-made algorithm for cell segmentation and count in phase. S.M. performed the PIV analyses. Manual and automated cell tracking analyses were performed by M.V. All other experiments and analyses were carried out by K.K. and G.P. The manuscript was prepared by E.P., K.K., and G.P., with input from M.V. **Competing interests:** The authors declare no competing interests. **Data and materials availability:** All data are available in the main text or the supplementary materials. The custom-made algorithms used for image analysis are available on GitHub ([https://bit.ly/Kozyrska\\_Pilia\\_et\\_al2021](https://bit.ly/Kozyrska_Pilia_et_al2021)).

### SUPPLEMENTARY MATERIALS

[science.org/doi/10.1126/science.abl8876](https://science.org/doi/10.1126/science.abl8876)  
Figs. S1 to S6  
MDAR Reproducibility Checklist  
Movies S1 to 10

12 August 2021; accepted 17 December 2021  
10.1126/science.abl8876



## RESEARCH ARTICLE SUMMARY

## IMMUNOLOGY

## CD97 promotes spleen dendritic cell homeostasis through the mechanosensing of red blood cells

Dan Liu, Lihui Duan, Lauren B. Rodda, Erick Lu, Ying Xu, Jinping An, Longhui Qiu, Fengchun Liu, Mark R. Looney, Zhiyong Yang, Christopher D. C. Allen, Zhongmei Li, Alexander Marson, Jason G. Cyster\*

**INTRODUCTION:** Antigen capture and presentation by conventional dendritic cells (cDCs) is crucial for the initiation of adaptive immune responses. These responses often take place inside secondary lymphoid organs. The spleen is the largest secondary lymphoid organ, has an open blood circulation, and fosters T cell and antibody responses against blood-borne pathogens. A major population of cDCs within the spleen, called cDC2s, is situated in a blood-exposed location at the interface of the white pulp and the red pulp, known as the bridging channel. These cDC2s are very efficient at capturing antigens from the blood and presenting them to T cells, but the factors that enable

cDC2s to sense their location with respect to blood flow are not well understood.

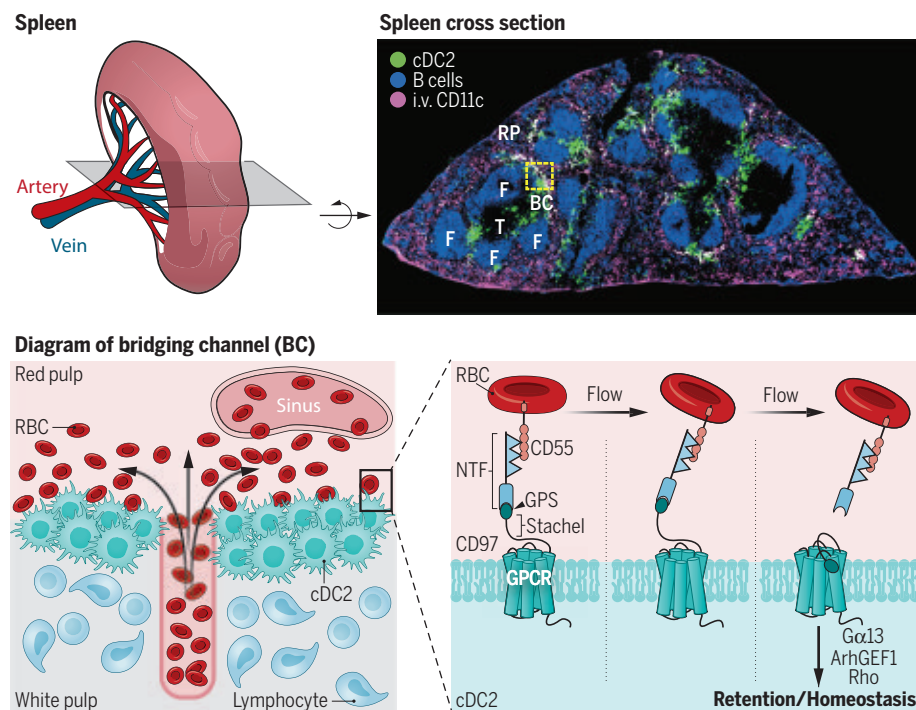
**RATIONALE:** G protein-coupled receptors (GPCRs) that signal through  $G\alpha_{13}$ -containing heterotrimeric G proteins can cause chemorepulsion and thereby help to confine cells in tissue niches. Whether these G proteins and associated GPCRs are involved in cDC positioning and function has been unclear.

**RESULTS:**  $G\alpha_{13}$  and the downstream effector ArhGEF1 were required for cDC2 positioning in blood-exposed regions of the mouse spleen. Using in vivo CRISPR-based screening, we

identified adhesion GPCR family member E5 (Adgre5, or CD97) as a  $G\alpha_{13}$ -coupled receptor needed for splenic cDC2 positioning. In the absence of  $G\alpha_{13}$ , ArhGEF1, or CD97, there was a deficiency of splenic cDC2s but not cDC1s. Intravital two-photon microscopy and spleen transplant experiments showed that this deficiency reflected a loss of splenic cDC2s into the blood circulation. As a member of the adhesion GPCR family, CD97 has a large extracellular domain and is expressed as a noncovalent heterodimer of the extracellular N-terminal fragment (NTF) and the GPCR domain. The CD97 NTF binds CD55 on other cells. CD97 engagement by CD55 on red blood cells (RBCs) under conditions of shear stress led to the removal of the CD97 NTF and the activation of the CD97 GPCR domain. A mutant form of CD97 that could not undergo autoproteolytic cleavage or NTF extraction was not able to restore the cDC2 compartment of CD97 null mice. Deficiency in the CD55-CD97- $G\alpha_{13}$  pathway was associated with a reduced ability to mount T follicular helper cell and antibody responses to modified RBCs and to blood-borne bacteria.

CD97-deficient splenic cDC2s had increased F-actin content and markedly altered gene expression. Gene set enrichment analysis suggested that part of the altered gene expression profile was due to increased activity of the G-actin-repressed Mrtf transcription factors. The transcription factor IRF4 is important for cDC2 homeostasis, and CD97 expression in cDC2s was promoted by IRF4. Overexpression of CD97 could partially restore splenic cDC2s in IRF4-deficient mice.

**CONCLUSION:** Homeostasis of cDC2s within the spleen depends on CD97 mechanosensing of circulating CD55<sup>+</sup> RBCs. This pathway enables cDC2s to sense exposure to blood flow and thereby avoid loss into the blood circulation. We speculate that by leading to activation of Rho, CD97 signaling causes the cell to retract membrane processes from flow-exposed locations. Rho signaling may also enhance integrin-mediated adhesion of cDC2s within the spleen. CD97 signaling allows cDC2s to position at the tissue-blood interface, a location that optimizes antigen capture and enables very rapid immune responses to systemic pathogens. CD97 is widely expressed in the immune system and other tissues, including some tumors and inflamed tissues, and may allow additional cell types to sense their location on the basis of interactions with CD55<sup>+</sup> cells under conditions of fluid flow. ■



**CD97 mechanosensing of CD55<sup>+</sup> RBCs enables splenic cDC2s to position near blood flow.** The spleen is a highly vascularized organ. In a cross-sectional view, B cell follicles (F) and T cell zones (T) highlight white pulp cords that are separated from the red pulp (RP) by cDC2-containing bridging channels (BC; dashed box). Intravenously administered antibody to CD11c labels blood-exposed cDC (labeled cDC2 appear white). Splenic cDC2s in bridging channels are near open-ended terminal arterioles and are exposed to RBCs as they pass into the red pulp. cDC2s express CD97, and the interaction with CD55 on RBCs exerts a pulling force on CD97, causing extraction of the NTF and activation of the GPCR domain. This pathway promotes the retention of blood-exposed cDC2s in the spleen. i.v., intravenous; GPS, GPCR proteolysis site.

The list of author affiliations is available in the full article online.

\*Corresponding author. Email: jason.cyster@ucsf.edu  
Cite this article as D. Liu et al., *Science* 375, eabi5965 (2022). DOI: 10.1126/science.abi5965

**READ THE FULL ARTICLE AT**  
<https://doi.org/10.1126/science.abi5965>

## RESEARCH ARTICLE

## IMMUNOLOGY

# CD97 promotes spleen dendritic cell homeostasis through the mechanosensing of red blood cells

Dan Liu<sup>1,2</sup>, Lihui Duan<sup>1,2</sup>, Lauren B. Rodda<sup>1,2,†</sup>, Erick Lu<sup>1,2,†</sup>, Ying Xu<sup>1,2</sup>, Jinping An<sup>1,2</sup>, Longhui Qiu<sup>3</sup>, Fengchun Liu<sup>3</sup>, Mark R. Looney<sup>3</sup>, Zhiyong Yang<sup>4,5,6,§</sup>, Christopher D. C. Allen<sup>4,5,6</sup>, Zhongmei Li<sup>7</sup>, Alexander Marson<sup>2,3,7</sup>, Jason G. Cyster<sup>1,2,\*</sup>

Dendritic cells (DCs) are crucial for initiating adaptive immune responses. However, the factors that control DC positioning and homeostasis are incompletely understood. We found that type-2 conventional DCs (cDC2s) in the spleen depend on  $G\alpha_{13}$  and adhesion G protein-coupled receptor family member-E5 (Adgre5, or CD97) for positioning in blood-exposed locations. CD97 function required its autoproteolytic cleavage. CD55 is a CD97 ligand, and cDC2 interaction with CD55-expressing red blood cells (RBCs) under shear stress conditions caused extraction of the regulatory CD97 N-terminal fragment. Deficiency in CD55-CD97 signaling led to loss of splenic cDC2s into the circulation and defective lymphocyte responses to blood-borne antigens. Thus, CD97 mechanosensing of RBCs establishes a migration and gene expression program that optimizes the antigen capture and presentation functions of splenic cDC2s.

**S**entinel conventional dendritic cells (cDCs) are stationed in most tissues of the body, where they continually sample their micro-environment for antigens (1, 2). The spleen is a large lymphoid organ involved in surveying the blood for pathogens and clearing defective red blood cells (RBCs) (3). The spleen is unusual in having an open circulation, in which terminal arterioles release blood into the marginal zone (MZ) that surrounds the lymphocyte-rich white pulp, or directly into the macrophage-rich red pulp (4, 5). Two main classes of cDCs are present in the spleen: cDC1s and cDC2s (1, 2). By promoting CD4 T cell activation and T follicular helper cell ( $T_{FH}$ ) cell generation, cDC2s are important for B cell responses. Many splenic cDC2s are positioned in regions of the spleen that connect the T cell zone with the red pulp, which are known as MZ bridging channels. Cells in the outer parts of the bridging channel, the MZ, and the red pulp are directly exposed to blood flow, and this facilitates their encounter with circulating antigens (6–10). cDC2s depend on the chemo-

attractant receptor EBI2 (GPR183) to position in MZ bridging channels (6, 11), and these cDCs are also dependent on IRF4, Notch, and integrins for their homeostasis (1, 2). However, the mechanisms that allow cDC2 exposure to blood flow while ensuring their retention in the spleen are poorly understood. We define a critical role for an adhesion G protein-coupled receptor (GPCR) in sensing passing blood cells and promoting splenic cDC2 homeostasis and function.

## Results

### Splenic cDC2s depend on $G\alpha_{13}$ signaling

Because  $G\alpha_{13}$ -coupled receptors can promote confinement of cells within tissue compartments (12, 13), we asked whether the  $G\alpha_{13}$ -signaling pathway was required for cDC positioning. The Rho guanine nucleotide exchange factor (GEF) ArhGEF1 is an effector of  $G\alpha_{13}$ -containing heterotrimeric G proteins (12). We observed by means of flow cytometry and immunofluorescence microscopy that ArhGEF1-deficient mice suffered a splenic cDC2 deficiency (Fig. 1, A to C, and fig. S1, A and B). cDC2s were identified by use of DCIR2 because this marker stains the majority of splenic cDC2s (fig. S1A) and allows their selective staining in tissue sections. Similar reductions in cDC2s were observed when other markers were used (fig. S1B). Splenic cDC1 frequencies were not significantly affected by ArhGEF1 deficiency (Fig. 1A and fig. S1C). Mixed bone marrow (BM) chimera experiments established that the splenic cDC2 deficiency reflected a cell-intrinsic role for ArhGEF1 (Fig. 1, D to F). Under these competitive conditions, a reduction in cDC1s was also observed (Fig. 1D and fig. S1D). We next determined whether  $G\alpha_{13}$  was required for splenic cDC homeostasis.  $Gna13^{ef/f}$  *CD11c*-Cre mice (referred to as  $Gna13^{cKO}$ ) had a

selective cDC2 deficiency similar to that of *Arhgef1*<sup>−/−</sup> mice (Fig. 1, A to C, and fig. S1, C and E). Deficiency in the gene encoding the related  $G\alpha_{12}$  protein had no effect on cDC frequencies (fig. S1, F and G). Mice lacking both  $G\alpha_{12}$  and ArhGEF1 had the same extent of splenic cDC2 deficiency as that of the single mutants, which is consistent with these molecules acting in the same pathway (Fig. 1, A to C).

Examining the basis for the reduced cDC2 frequencies, we performed intravascular labeling to measure whether cDC2s were not properly positioned in blood-exposed locations (7–9). We used mixed BM chimeras to allow comparison of wild-type (WT) and  $G\alpha_{13}$ -deficient cells in the same mice. These mice showed a reduction in  $Gna13^{cKO}$  cDC2s, whereas the cDC1 compartment remained intact (Fig. 1G and fig. S1H).  $Gna13^{cKO}$  cDC2s remaining in the spleen were less strongly labeled by intravascular antibody (Fig. 1, H and I). By contrast,  $G\alpha_{13}$  deficiency did not alter the labeling of cDC1s (fig. S1I). A possible explanation for the reduced labeling of cDC2s was the loss of mutant cells into the bloodstream. We detected an increased frequency of cDC2s in blood circulation of ArhGEF1- and  $G\alpha_{13}$ -deficient mice (Fig. 1J). Once in blood circulation, cDC2s are rapidly lost, most likely through their capture and clearance by phagocytic cells (9). Investigating other possible causes for the reduction in cDC2s, there was no significant alteration in the frequency of pre-DCs in the BM and spleens of *Arhgef1*<sup>−/−</sup> or  $Gna13^{cKO}$  mice (fig. S1, J and K). Among the splenic cDC2s remaining in  $Gna13^{cKO}$  mice, a greater fraction were actively dividing (fig. S1L). Apoptotic cell frequencies were low in control mice and were similar in  $Gna13^{cKO}$  mice (fig. S1M). Expression of the Notch2-induced surface molecule ESAM (endothelial cell-specific adhesion molecule) (14) was not altered on the cDC2s remaining in  $G\alpha_{13}$ - and ArhGEF1-deficient mice, which suggests that Notch2 signaling was intact (fig. S1N). Thus, the reduced cDC2 frequencies in spleens of ArhGEF1- and  $G\alpha_{13}$ -deficient mice appear to be a consequence of cDC2 loss into blood circulation.

### CD97 functions upstream of $G\alpha_{13}$

The  $G\alpha_{13}$  requirement for splenic cDC2 homeostasis implicated involvement of a GPCR. To search for such a receptor, we used an in vivo CRISPR-based mutagenesis screen of 20 GPCRs abundantly expressed by cDC2s. Only a mutation of the adhesion GPCR family member E5 (Adgre5, also known as CD97) led to a reduction in cDC2s (Fig. 2, A and B). Typical of adhesion GPCRs, CD97 has an extended N-terminal extracellular domain (Fig. 2C) (15–17). This region of CD97 is alternatively spliced and includes three or four epidermal growth factor (EGF) domains and a GPCR autoproteolysis-inducing (GAIN) domain that

<sup>1</sup>Howard Hughes Medical Institute, University of California, San Francisco, San Francisco, CA 94143, USA. <sup>2</sup>Department of Microbiology and Immunology, University of California, San Francisco, San Francisco, CA 94143, USA. <sup>3</sup>Department of Medicine, University of California, San Francisco, San Francisco, CA 94143, USA. <sup>4</sup>Cardiovascular Research Institute, University of California San Francisco, San Francisco, CA 94143, USA. <sup>5</sup>Sandler Asthma Basic Research Center, University of California, San Francisco, San Francisco, CA 94143, USA. <sup>6</sup>Department of Anatomy, University of California, San Francisco, San Francisco, CA 94143, USA. <sup>7</sup>J. David Gladstone Institutes, San Francisco, CA 94158, USA.

\*Corresponding author. Email: jason.cyster@ucsf.edu

<sup>†</sup>Present address: Department of Immunology, University of Washington School of Medicine, Seattle, WA 98109, USA.

<sup>‡</sup>Present address: Gilead Sciences, Foster City, CA 94404, USA.

<sup>§</sup>Present address: Department of Immunology Discovery, Genentech, South San Francisco, CA 94080, USA.



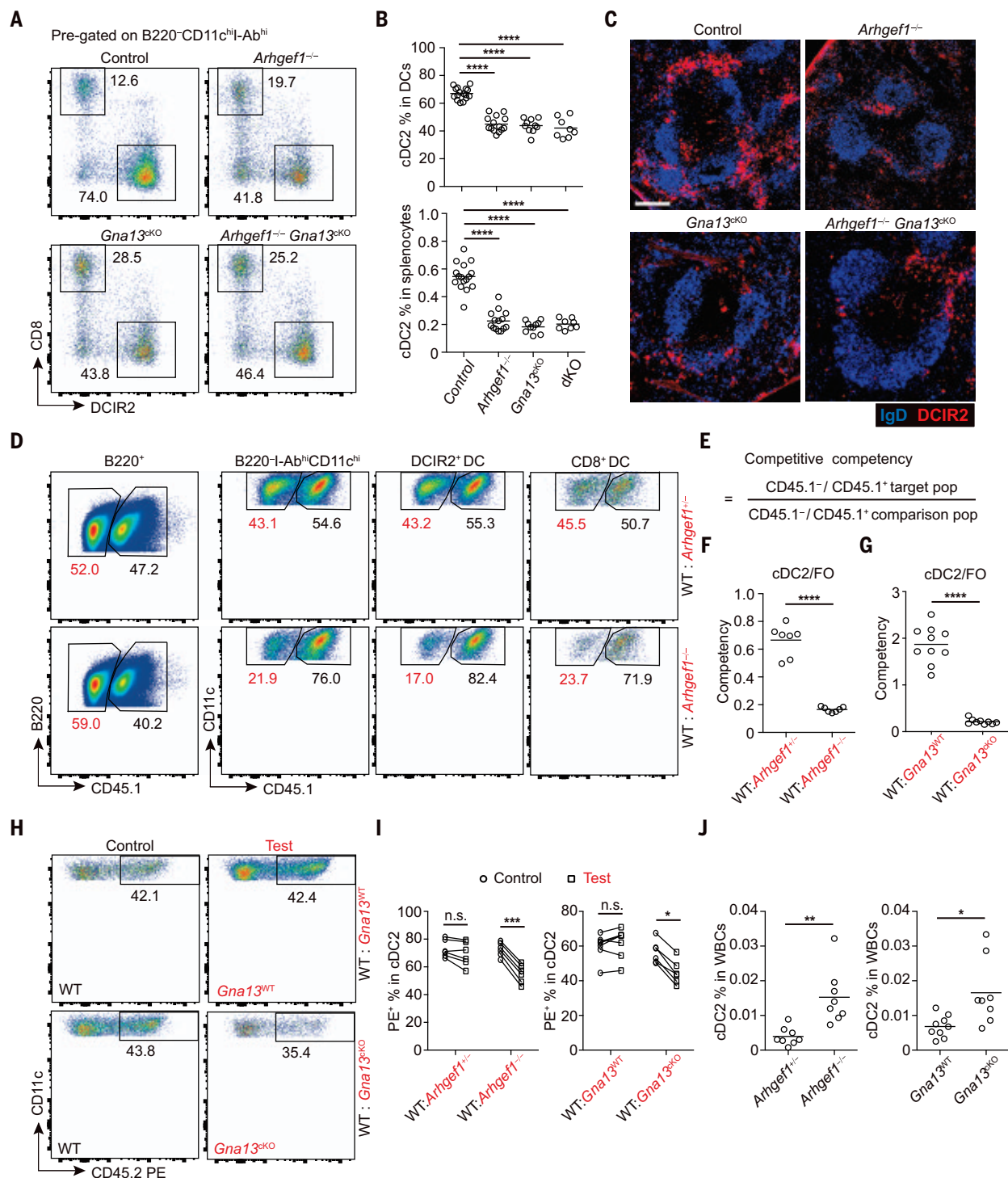
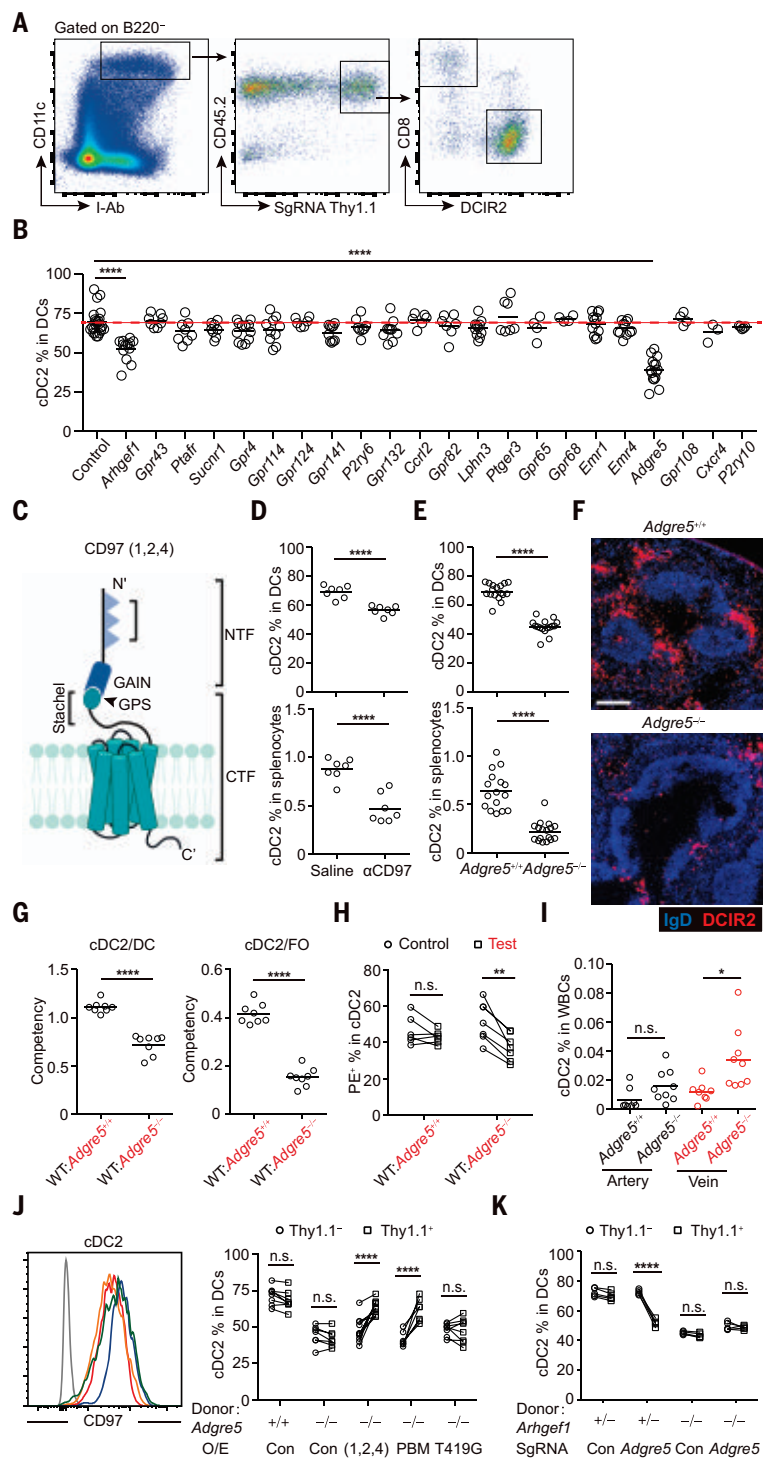


**Fig. 1.  $G\alpha_{13}$ -ArhGEF1 signaling pathway is required in splenic cDC2s.** (A and B) Representative (A) flow cytometry profiles and (B) frequencies of DCIR2<sup>+</sup>CD8<sup>+</sup> cDC2s in (top) total B220<sup>+</sup>CD11c<sup>hi</sup>I-Ab<sup>hi</sup> DCs and (bottom) total splenocytes in *Arhgef1*<sup>-/-</sup>, *Cd11c*-cre *Gna13*<sup>fl/fl</sup> (labeled as *Gna13*<sup>cko</sup>), *Arhgef1*<sup>-/-</sup> *Cd11c*-cre *Gna13*<sup>fl/fl</sup> (labeled as *Arhgef1*<sup>-/-</sup> *Gna13*<sup>cko</sup>) or dKO, and control mice. Data are pooled from three independent experiments. (C) Representative distribution patterns of DCIR2<sup>+</sup> cDC2s (red) relative to B cells [immunoglobulin D (IgD), blue] in spleens of mice of the indicated genotypes. Scale bar, 200  $\mu$ m. Sections are representative of multiple cross sections from at least three mice of each type. (D to F) Mixed (50:50) BM chimeras were made with CD45.1 WT (*Arhgef1*<sup>+/+</sup>) and CD45.2 *Arhgef1*<sup>+/+</sup> or *Arhgef1*<sup>-/-</sup> BM cells. (D) Representative flow cytometry profiles show gating strategies. (E) Equation

for calculating the competitive competencies of CD45.2<sup>+</sup> (gated as CD45.1<sup>-</sup>) population. (F) Plots showing CD45.2<sup>+</sup> competency values in individual chimeras for the cDC2 compartment compared with B220<sup>+</sup> follicular (FO) B cells. (G) Plots showing CD45.2<sup>+</sup> competency values in WT:*Gna13*<sup>WT</sup> and WT:*Gna13*<sup>cko</sup> chimeras for the cDC2 compartment compared with B220<sup>+</sup> follicular (FO) B cells. (H) Flow cytometry profiles and (I) frequencies of in vivo anti-CD45-PE-labeled cDC2s of indicated genotyped cells in (left) WT: *Arhgef1*<sup>-/-</sup> or (right) WT: *Gna13*<sup>cko</sup> and their control mixed BM chimeras. Lines connect data from the same animals. (J) Frequencies of cDC2s in blood of (left) *Arhgef1*<sup>-/-</sup> or (right) *Gna13*<sup>cko</sup> and their control mice. In (D) to (J), data are pooled from two independent experiments. Each symbol represents one mouse, and lines denote means. \**P* < 0.05; \*\**P* < 0.01; \*\*\**P* < 0.001; \*\*\*\**P* < 0.0001.

**Fig. 2. CD97 functions upstream of  $G\alpha_{13}$ -ArhGEF1 in splenic cDC2s.**

(A and B) Cas9-based mutagenesis screen was performed by making chimeras reconstituted with Cas9-expressing BM cells transduced with sgRNA targeting specific genes, with Thy1.1 as a reporter. (A) Gating strategy for the screen. (B) Frequencies of cDC2s in sgRNA-Thy1.1<sup>+</sup> DCs of chimeras with sgRNA targeting the indicated genes. Data are pooled from eight independent experiments. (C) Structural components of the CD97 short isoform. NTF, N-terminal fragment; CTF, C-terminal fragment; GAIN, GPCR autoproteolysis-inducing domain; GPS, GPCR proteolysis site; Stachel, putative tethered agonist peptide. Triangles indicate individual EGF domains. (D) Frequencies of cDC2s in (top) total DCs and (bottom) total splenocytes in WT mice treated with antibody to CD97 or saline. (E) Frequencies of cDC2s in (top) total DCs and (bottom) total splenocytes in *Adgre5*<sup>+/+</sup> or *Adgre5*<sup>-/-</sup> mice. Data are pooled from four independent experiments. (F) Representative distribution of DCIR2<sup>+</sup> cDC2s (red) relative to B cells (IgD, blue) in spleens of *Adgre5*<sup>+/+</sup> or *Adgre5*<sup>-/-</sup> mice. Scale bar, 200  $\mu$ m. Sections are representative of multiple cross sections from at least three mice of each type. (G and H) Mixed (50:50) BM chimeras were made with CD45.1 WT and CD45.2 *Adgre5*<sup>+/+</sup> or *Adgre5*<sup>-/-</sup> BM cells. (G) The plots show CD45.2<sup>+</sup> competency values in individual chimera for the cDC2 compartment compared with (left) total DCs or (right) B220<sup>+</sup> follicular B (FO) cells. (H) Frequencies of in vivo anti-CD45-PE-labeled cDC2s of indicated genotyped cells in mixed BM chimeras. (I) Frequencies of cDC2s in blood of *Adgre5*<sup>-/-</sup> and control mice. Artery means blood was collected from celiac artery near splenic artery. Vein means blood was collected from portal vein after ligation of superior mesenteric vein. (J) BM chimeras were reconstituted with *Adgre5*<sup>+/+</sup> or *Adgre5*<sup>-/-</sup> BM cells transduced with a retroviral construct encoding *Adgre5* (1, 2, 4) or its mutants or empty vector, with Thy1.1 as a reporter. (Left) Representative histogram plots of surface CD97 on Thy1.1<sup>+</sup> cDC2 cells in chimeras reconstituted as indicated. (Right) Color coding of histograms is as labeled in graph. Gray indicates isotype control. Frequencies of cDC2s in Thy1.1<sup>+</sup> or Thy1.1<sup>-</sup> DCs of chimeras reconstituted as indicated. In (G) to (J), data are pooled from two independent experiments. (K) Frequencies of cDC2s in sgRNA-Thy1.1<sup>+</sup> or Thy1.1<sup>-</sup> DCs of chimeras reconstituted with indicated genotyped BM cells transduced with sgRNA targeting *Adgre5* or control. One of two independent experiments with similar results is shown. In (B), (D), (E), (G), and (I), each symbol indicates one mouse, and lines denote means. In (H), (J), and (K), lines connect data from the same animals. \**P* < 0.05; \*\**P* < 0.01; \*\*\*\**P* < 0.0001.



contains the GPCR proteolysis site (GPS). The N-terminal fragment (NTF) of CD97 remains noncovalently bound to the seven-transmembrane part of the receptor after autoproteolytic cleavage (15, 18). CD97 binds several ligands in vitro, including CD55, chondroitin sulfate, Thy1, and integrins  $\alpha_5\beta_1$  and  $\alpha_v\beta_3$  (15, 19). An antibody against CD97 blocks some of these interactions (20). Treatment with this antibody led to a

selective reduction in the splenic cDC2 frequency (Fig. 2D and fig. S2A).

We generated mice lacking CD97 (fig. S2, B and C) and confirmed that CD97 was required for splenic cDC2 but not cDC1 homeostasis (Fig. 2, E and F, and fig. S2, D and E). Peripheral lymph node (pLN) cDC homeostasis was unaffected (fig. S2, F and G), and BM and splenic pre-DC frequencies were normal (fig.

S2H). Mixed BM chimera experiments confirmed the intrinsic requirement for CD97 in cDC2s (Fig. 2G) but not cDC1s (fig. S2, I and J). Intravascular labeling in BM chimeras showed that the CD97-deleted cDC2s remaining in the spleen had reduced blood exposure compared with that of the WT cDC2s in the same animals (Fig. 2H). Mice in which CD97 was deleted had increased frequencies of



cDC2s in blood circulation (fig. S2, K and L). Sampling of blood in the splenic artery and vein revealed that cDC2s were most increased in the vein in accord with cell loss from the spleen and rapid clearance from circulation (Fig. 2I). Splenic cDC2s endogenously expressed long and short CD97 isoforms (fig. S2M). Using retroviral transduction experiments, the full-length isoform and the short isoform that contains EGF domains 1, 2, and 4 could rescue the cDC2 deficiency in mice in which CD97 was deleted (Fig. 2J and fig. S2N). A CD97 mutant lacking a C-terminal PDZ-binding motif (PBM) (21) retained function (Fig. 2J). In vitro studies have suggested that autoproteolytic cleavage of the NTF from the GPCR domain is important for receptor function (21–23). Changing a conserved Thr (T) residue at the +1 position of the CD97 GPS to Gly (G) disrupts autoproteolysis (21). This T419G mutant of CD97 was unable to rescue cDC2 frequencies in mice in which CD97 was deleted, despite being well expressed (Fig. 2J). Thus, autoproteolysis is necessary for in vivo CD97 function in cDC2s.

Further approaches were used to test whether CD97 was acting in the same pathway as  $G\alpha_{13}$  and ArhGEF1. Mutation of CD97 in ArhGEF1-deficient mice did not have any effect, which is consistent with CD97 functioning upstream of  $G\alpha_{13}$  and ArhGEF1 (Fig. 2K). cDC2s from ArhGEF1-,  $G\alpha_{13}$ -, and CD97-deficient mice had highly similar gene expression profiles, further indicating that these molecules are in a common pathway (fig. S3, A to D). This analysis revealed lower expression of F4/80 (Emr1 or Adgre1) in the mutant cDC2s, which was confirmed with flow cytometry (fig. S3E). Analysis of available human spleen cDC gene expression data (24) showed high expression of CD97 by CD1c<sup>+</sup> cDC2s (fig. S3F). Gene set enrichment analysis (GSEA) revealed that human splenic cDC2s were enriched for CD97 pathway-dependent genes compared with CD141<sup>+</sup> cDC1s and were depleted for genes that were up-regulated in CD97-deficient cells (fig. S3G). Thus, the CD97 pathway dependence of splenic cDC2s is most likely conserved in humans.

#### CD55-expressing RBCs activate CD97 on splenic cDC2s

CD55, the decay accelerating factor (DAF) of complement, binds the first two EGF domains of CD97. Treatment of mice with an antibody to CD55 (15) that blocks this binding led to a selective decrease in splenic cDC2 frequencies (Fig. 3A and fig. S4A) and the appearance of cDC2s in blood circulation (Fig. 3B). We generated mice in which CD55 was deleted (fig. S4, B and C) and found reduced frequencies of splenic cDC2s (Fig. 3C and fig. S4D). The frequencies of splenic cDC1s (Fig. S4E), pLN cDCs (fig. S4F), and BM and spleen pre-DCs were not altered (fig. S4G). Like the other mutant strains, CD55-deficient mice had increased

cDC2s in blood (Fig. 3D and fig. S4H). CD55 is widely expressed by hematopoietic and non-hematopoietic cells (15, 19), although it is not expressed by splenic DCs (Fig. 3E and fig. S4I). Staining of spleen sections showed broad CD55 expression, including on endothelial and stromal cells (fig. S4J). However, BM chimera experiments established that CD55 expression by hematopoietic cells and not by radio-resistant stromal cells was needed for cDC2 homeostasis (Fig. 3F). Despite the strong CD55 expression by B cells (Fig. 3E and fig. S4I), when B cells or T cells or all lymphocytes lacked CD55, cDC2 homeostasis remained intact (Fig. 3, G to I, and fig. S4, K and L).

RBCs also strongly express CD55 (Fig. 3J) (19). Because the most prominent loss of cDC2s in the mutant strains is that of blood-exposed cells and given that RBCs constitute ~99.9% of circulating cells (25), we asked whether RBCs could be a sufficient source of CD55 to maintain cDC2 homeostasis. Transfer of purified WT RBCs to hosts in which CD55 was deleted, so that they constituted one-third of the circulating RBCs (Fig. 3K and fig. S4M), was sufficient to substantially restore cDC2 homeostasis (Fig. 3, L and M, and fig. S4N). Transfers of white blood cells (WBCs) did not restore the cDC2 compartment (fig. S4O). Platelets were present in mouse blood at about 5% the frequency of RBCs and also expressed CD55 (fig. S4, P and Q). Mice genetically deficient in platelets or lacking CD55 on platelets maintained a normal splenic cDC2 compartment, however (Fig. 3N and fig. S4, P to S). Thus, RBCs are the dominant source of CD55 needed for splenic cDC2 homeostasis.

Surface levels of CD97 on spleen and blood lymphocytes are increased in mice lacking CD55 (fig. S5, A and B) (26). Modulation of CD97 on lymphocytes is suggested to depend on engagement by CD55 under conditions of shear stress, with the NTF likely being extracted by pulling forces (26). Because the antibody used to detect CD97 is NTF-specific, it provides a measure of the intact heterodimeric form of CD97 (Fig. 2C). When the NTF separates away from the heterodimer, the membrane-associated GPCR domain can no longer be detected. NTF<sup>+</sup> CD97 abundance on splenic cDC2s was elevated in mice in which CD55 was deleted (Fig. 4A). In the CD55-deficient mice reconstituted with WT RBCs, NTF<sup>+</sup> CD97 abundance on cDC2s was reduced (Fig. 4A). Using another approach, we examined the effect of short-term blockade of the CD55-CD97 interaction. In experiments in which mice were treated with the CD55-blocking antibody, NTF<sup>+</sup> CD97 became more strongly elevated on blood-exposed splenic cDC2s (Fig. 4B and fig. S5C). In mice expressing the T419G noncleavable mutant of CD97, blocking CD55 had no effect on CD97 levels on blood-exposed cDC2s (Fig. 4C and fig. S5D). We then tested the impact of stopping

blood flow through the inferior vena cava (IVC) by tying off the vessel for 30 min (movie S1). These mice were injected intravenously with splenocytes immediately before the vessel ligation. Transferred cDC2s and B cells in the region with flow (heart) had reduced NTF<sup>+</sup> CD97 compared with those in the IVC, where flow was stopped (Fig. 4D and fig. S5E). When the same experiment was performed in CD55-deficient mice, there was no difference in NTF<sup>+</sup> CD97 on cDC2s and B cells in regions with or without blood flow (Fig. 4D and fig. S5E). Thus, cDC2s interacting with RBCs in vivo under conditions of shear stress undergo CD55-mediated extraction of the CD97 NTF.

To more directly test whether the CD97 NTF on cDC2s was extracted upon interaction with CD55<sup>+</sup> RBCs under shear stress conditions, we incubated spleen cells with WT or CD55-deleted RBCs. In the absence of shear stress, cDC2s maintained abundant cell-surface NTF<sup>+</sup> CD97. However, under shear stress conditions, NTF<sup>+</sup> CD97 expression by cDC2s was significantly reduced (Fig. 4E). When the added RBCs lacked CD55, shear stress conditions did not lead to any modulation of NTF<sup>+</sup> CD97 (Fig. 4E). The reduction in surface NTF<sup>+</sup> CD97 was matched by a reduction in total NTF<sup>+</sup> CD97, suggesting that the reduced surface levels were not due to CD97 internalization (fig. S5, F and G). When cDC2s expressing the T419G ectodomain cleavage-resistant CD97 mutant were exposed to WT RBCs under shear stress conditions, there was no change in surface NTF<sup>+</sup> CD97 (Fig. 4F). Last, we studied cDC2s expressing CD97 with green fluorescent protein (GFP) fused at the C terminus. Incubation with RBCs under shear stress conditions led to reduced NTF<sup>+</sup> CD97 but did not alter abundance of the CD97 GPCR domain as reported by GFP intensity (fig. S5, H and I). Thus, cDC2 exposure to RBCs under shear stress conditions is sufficient to lead to extraction of the CD97 NTF without changing the abundance of the GPCR domain.

#### CD97 pathway restrains F-actin and actin-regulated transcription

Because Rho is a major regulator of cytoskeletal dynamics, we stained cells from the gene-deficient mouse lines for F-actin content. In every case, cDC2s from mutant mice had increased F-actin compared with that of cDC2s from WT mice (Fig. 5, A and B, and fig. S6, A and B). Blocking antibody treatment also led to an increase in F-actin content on blood-exposed cDC2s (Fig. 5, C and D). Analysis of splenic cDC1s showed a slight increase in F-actin content in *Arhgef1*<sup>-/-</sup> but not *Gna13*<sup>CKO</sup>, *Adgre5*<sup>-/-</sup>, or *Cd55*<sup>-/-</sup> mice (fig. S6, C to F). Mrf1-a is a transcription factor that is kept in an inactive and predominantly cytoplasmic form by binding to G-actin. When G-actin is consumed to form F-actin, Mrf1-a accumulates in the nucleus as an active transcription factor (27, 28).

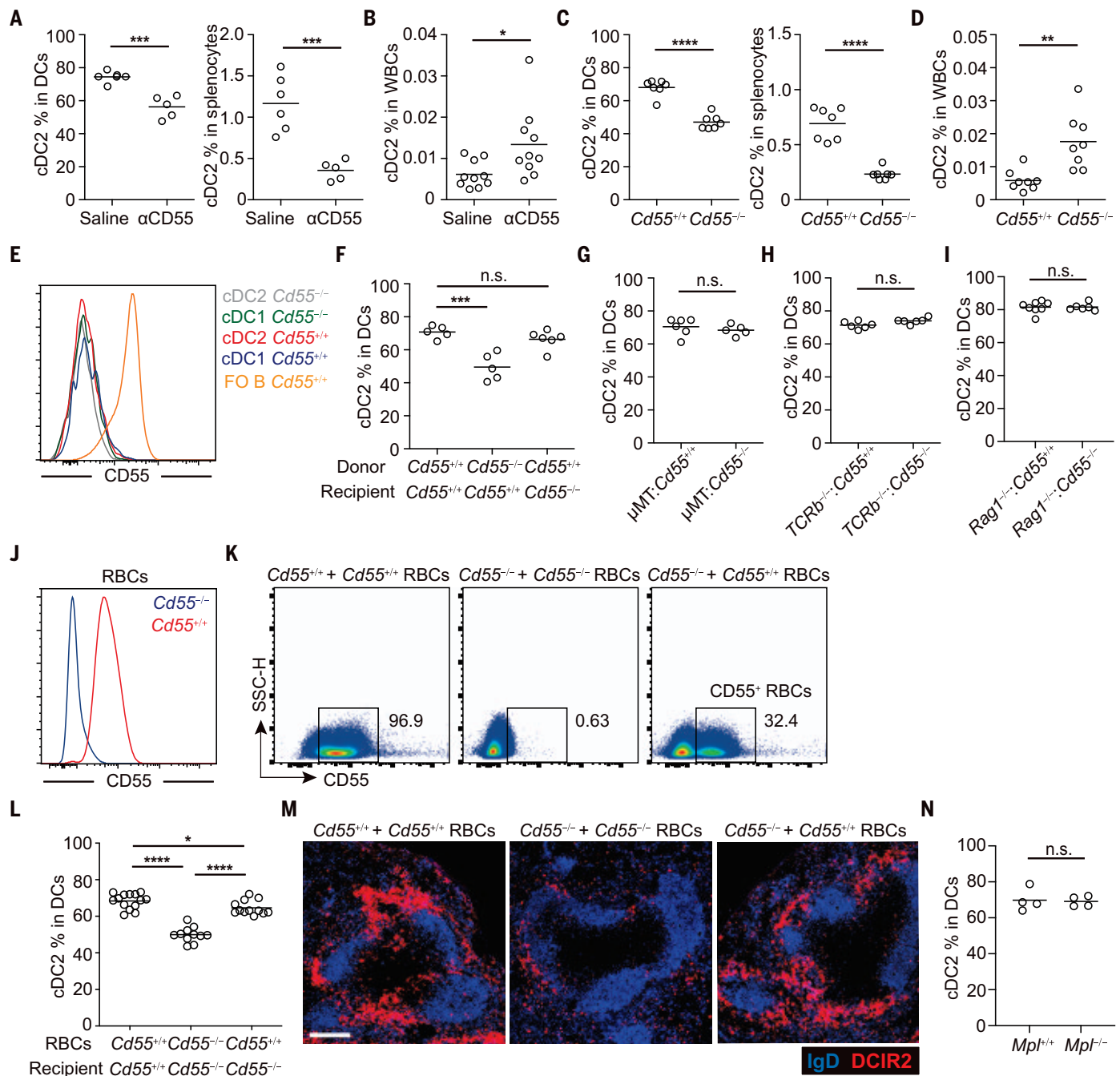


**Fig. 3. CD55 on RBCs is required for splenic cDC2 homeostasis.**

(A) Frequencies of cDC2s in (left) total DCs and (right) total splenocytes in WT mice treated with antibody to CD55 or saline. (B) Frequencies of cDC2s in blood of WT mice 8 hours after treatment with antibody to CD55 or saline. (C) Frequencies of cDC2s in (left) total DCs and (right) total splenocytes in *Cd55*<sup>+/+</sup> or *Cd55*<sup>-/-</sup> mice. (D) Frequencies of cDC2s in blood of *Cd55*<sup>-/-</sup> and control mice. (E) Representative histogram plots of surface CD55 on cDC2s, cDC1s, and B cells in mice with indicated genotype. (F) Frequencies of cDC2s in total DCs in chimeras as indicated. (G) Frequencies of cDC2s in total DCs in chimeras reconstituted with 90% μMT (IgM null) and 10% *Cd55*<sup>+/+</sup> or *Cd55*<sup>-/-</sup> BM cells. (H) Frequencies of cDC2s in total DCs in chimeras reconstituted with 90% *Tcrb*<sup>-/-</sup> and 10% *Cd55*<sup>+/+</sup> or *Cd55*<sup>-/-</sup> BM cells. (I) Frequencies of cDC2s in total DCs in chimeras reconstituted with 90% *Rag1*<sup>-/-</sup> and 10% *Cd55*<sup>+/+</sup> or *Cd55*<sup>-/-</sup>

BM cells. In (A) to (I), data are pooled from two independent experiments. (J) Representative histogram plots of surface CD55 on RBCs in mice with indicated genotype. (K to M) RBC transusions were performed from *Cd55*<sup>-/-</sup> or *Cd55*<sup>+/+</sup> mice into the indicated recipient mice, and analysis was performed after 6 to 8 days. (K) Representative profile of purified *Cd55*<sup>+/+</sup> RBCs or *Cd55*<sup>-/-</sup> RBCs transfused into *Cd55*<sup>-/-</sup> or *Cd55*<sup>+/+</sup> recipients. (L) Frequencies of cDC2s in total DCs in mice with purified RBCs transfused as indicated. Data are pooled from three independent experiments. (M) Distribution of DCIR2<sup>+</sup> cDC2s (red) and B cells (IgD, blue) in spleens as indicated. Scale bar, 200 μm. Representative of multiple cross sections from at least three mice of each type. (N) Frequencies of cDC2s in total DCs in *Mpl*<sup>+/+</sup> or *Mpl*<sup>-/-</sup> mice. Data are pooled from two independent experiments. Each symbol indicates one mouse, and lines denote means.

\**P* < 0.05; \*\**P* < 0.01; \*\*\**P* < 0.001; \*\*\*\**P* < 0.0001.



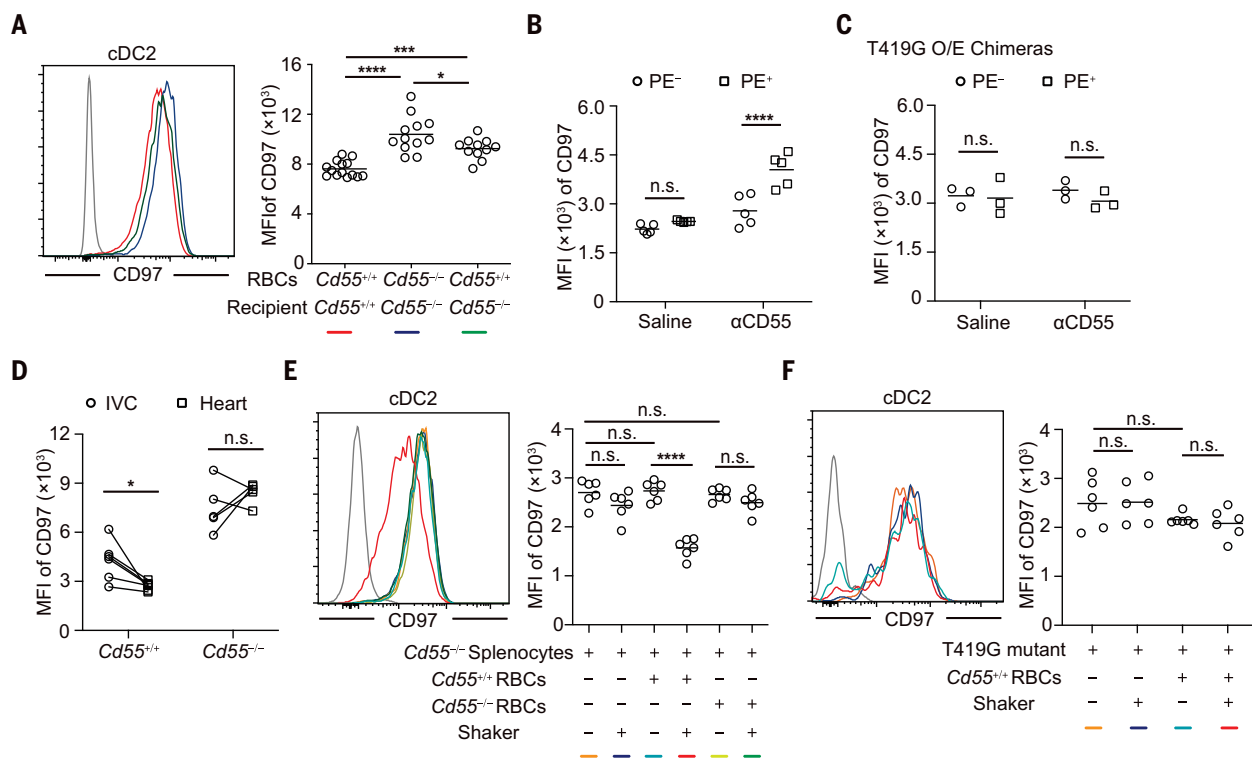


**Fig. 4. CD55-mediated CD97 NTF extraction is dependent on shear stress.**

(A) Representative (left) histogram and (right) geometric mean fluorescence intensity (MFI) of surface CD97 expression on cDC2s in mice with blood transfusion as indicated. Data are pooled from three independent experiments. (B) MFI of surface CD97 on in vivo PE-labeled (PE<sup>+</sup>) and PE-nonlabeled (PE<sup>-</sup>) cDC2s in WT mice that had been treated 8 hours earlier with antibody to CD55 or saline. Data are pooled from two independent experiments. (C) Chimeras were reconstituted with *Adgre5*<sup>-/-</sup> BM transduced with *Adgre5* (1, 2, 4)-T419G mutant, with Thy1.1 as a reporter. MFI of surface CD97 on in vivo PE-labeled (PE<sup>+</sup>) and PE-nonlabeled (PE<sup>-</sup>) Thy1.1<sup>+</sup> cDC2s in chimeras that had been treated 8 hours earlier with antibody to CD55 or saline. One of two independent

experiments with similar results is shown. (D) MFI of surface CD97 expression on transferred *Cd55*<sup>-/-</sup> cDC2s in blood collected from heart and distal ligated IVC of recipients as indicated (movie S1). Data are pooled from two independent experiments. (E and F) Splenocytes from (E) *Cd55*<sup>-/-</sup> mice or (F) CD97 T419G expressing BM chimeras were cocultured for 1 hour at RT with *Cd55*<sup>-/-</sup> or *Cd55*<sup>+/+</sup> RBCs, on a shaker or not. Representative (left) histogram and (right) MFI of surface CD97 expression on cDC2s are shown. Data are pooled from two independent experiments. In (A), (E), and (F), color coding of histograms is as for the graphs, and gray lines indicate isotype control. In (A) to (C), (E), and (F), each symbol indicates one mouse, and lines denote means. In (D), lines connect data from the same animal. \**P* < 0.05; \*\*\*\**P* < 0.001; \*\*\*\*\**P* < 0.0001.

GSEA showed that *Mrtf*-a-dependent genes (29) were up-regulated in *ArhGEF1*- and CD97-deficient cDC2s (Fig. 5E). Many of the *Mrtf*-a-regulated genes encode for cytoskeletal proteins (27, 28), and several such genes were up-regulated in CD97-deficient cDC2s (Fig. 5F). Hematopoietic cells lacking *Mrtf*-a (and the related gene *Mrtf*-b) show poor migratory responses (29, 30). Thus, *Mrtf*-induced gene expression may contribute to altered motility of cDC2s deficient in the CD97 pathway.

#### CD97 pathway restrains splenic cDC2 migration

We next used intravital microscopy to observe splenic cDC migration. We intercrossed *Batf3*<sup>-/-</sup> mice that lack cDCs (fig. S6, G and H) (31) with *CD11c*-YFP (yellow fluorescent protein) reporter mice and *Arhgef1*<sup>-/-</sup> mice. Analysis of tissue sections showed that the majority of *CD11c*-YFP<sup>+</sup> cells in these mice were *DCIR2*<sup>+</sup> cDC2s, and their density was reduced in mice lacking *ArhGEF1* (fig. S6G). Real-time intravital imaging revealed that although most cDC2s showed

little migratory activity, occasional cells were detected that were actively migratory (Fig. 5G and movie S2). Rare cells could also be detected moving into large blood vessels (likely red pulp sinuses), in some cases through active migration (Fig. 5G and movie S3). In other cases, cells appeared to already be detached, rounded up, and in flow within the red pulp at the time of reaching a large vessel (movie S4). Like intravascular DCs in dermal lymphatics (32), intravascular cDC2s often continued to migrate for a period of time before being carried away into the blood flow (Fig. 5G and movies S3 and S4). Despite the overall reduction in cDC2s detectable per frame (fig. S6I), there was an increased frequency of migratory cDC2s in *ArhGEF1*-deficient mice (Fig. 5H and movies S5 to S8). Moreover, an increased frequency of cDC2s was observed moving into large blood vessels and being caught in flow (Fig. 5I and movies S5 to S8). In accord with the imaging data, there was an increased frequency of *ArhGEF1*-deficient *CD11c*-YFP<sup>+</sup> cDC2s in the blood circulation (Fig. 5J).

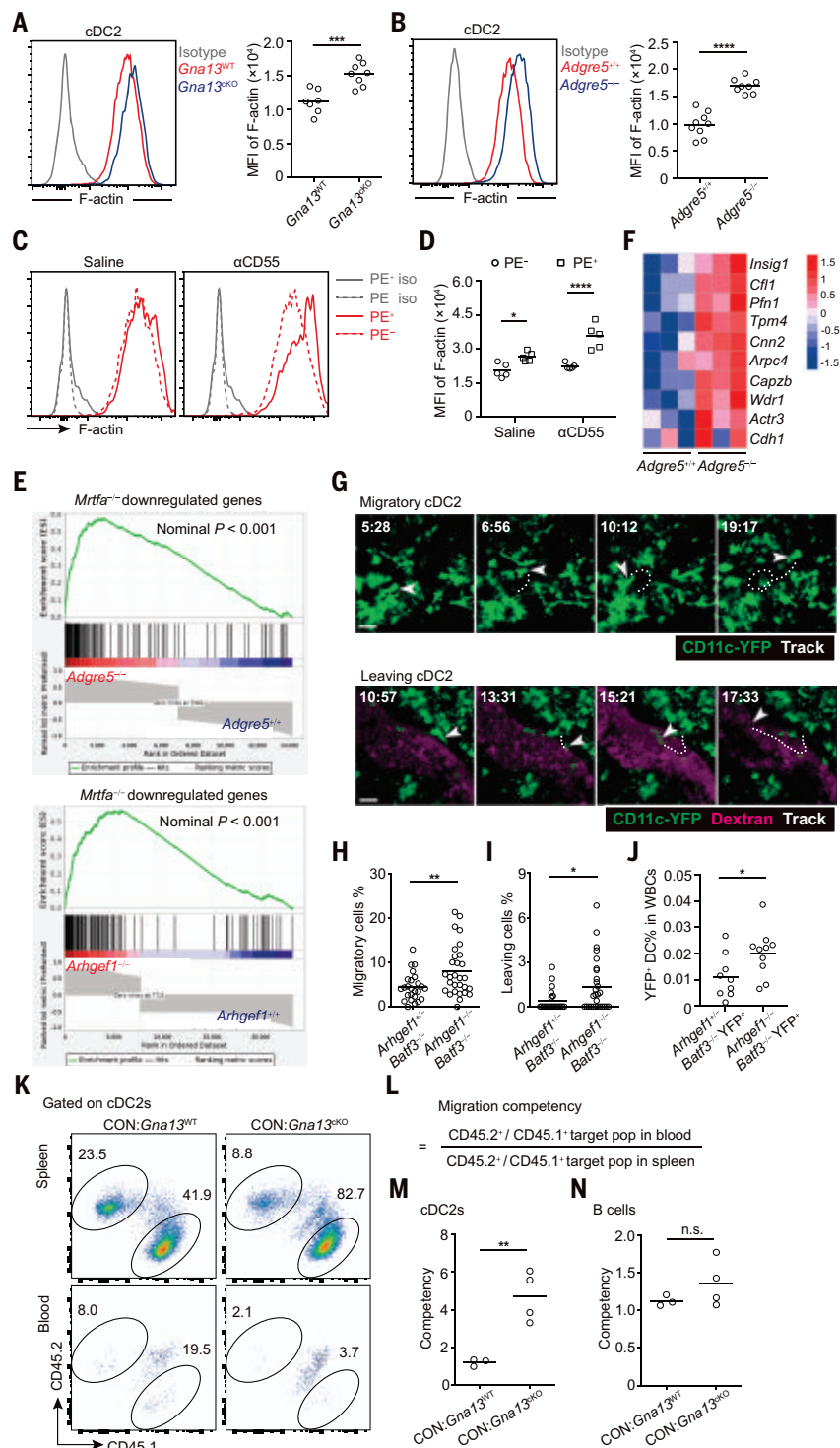
As another approach to test for cDC2 movement from the spleen into the blood, we transplanted spleens from *Gna13*<sup>ckO</sup> or control mixed chimeric mice into WT recipients. Eight to nine hours after the surgery, we examined the recipient blood for donor-derived B cells and cDC2s. The frequency of B cells in the blood closely matched the chimerism in the transplanted spleen, whereas cDC2s in blood were significantly enriched for *Gna13*<sup>ckO</sup> cDC2s (Fig. 5, K to N, and fig. S6J). Thus, *Ga13*-deficient cDC2s have altered migratory behavior that results in their loss from the spleen into the blood circulation.

#### Deficiency in the CD97 pathway alters DC function

To test the impact of deficiency in the CD97 pathway on DC activation and function, we immunized mice with a model systemic antigen, sheep red blood cells (SRBCs). Three hours after immunization, there was a selective defect in antigen acquisition by the CD97-deficient

**Fig. 5. CD97 pathway deficiency leads to increased F-actin and cDC2 motility.**

**(A and B)** Representative (left) histogram and (right) MFI of F-actin in cDC2s from (A) *Gna13*<sup>CKO</sup> or (B) *Adgre5*<sup>-/-</sup> and control mice. Data are pooled from two independent experiments. **(C and D)** Representative (C) histogram and (D) MFI of F-actin expression on in vivo PE-labeled (PE<sup>+</sup>) and PE-nonlabeled (PE<sup>-</sup>) cDC2s in WT mice treated for 8 hours with antibody to CD55 or saline. Data are pooled from two independent experiments. **(E and F)** GSEA of *Mrtfa*<sup>-/-</sup> down-regulated genes compared with *Adgre5*<sup>-/-</sup> or *Arhgef1*<sup>-/-</sup> cDC2 dataset. (E) Enrichment profiles for genes that are down-regulated ( $P_{\text{adj}} < 0.001$ ) in *Mrtfa*<sup>-/-</sup> BMDs (29) compared with (top) *Adgre5*<sup>-/-</sup> and (bottom) *Arhgef1*<sup>-/-</sup> cDC2 datasets. (F) Genes in the core enrichment, presented as a cluster-analyzed heat-map of expression levels of *Adgre5*<sup>+/+</sup> and *Adgre5*<sup>-/-</sup> cDC2s. **(G to I)** The motility of splenic cDC2s was observed with intravital two-photon microscopy in *Arhgef1*<sup>+/+</sup> *Batf3*<sup>-/-</sup> *Cd11c*-YFP and *Arhgef1*<sup>-/-</sup> *Batf3*<sup>-/-</sup> *Cd11c*-YFP chimeras. Dextran-TRITC was used to label large blood vessels. (G) Example of migratory cDC2 and leaving cDC2 (white arrowhead and dashed track, respectively) in *Arhgef1*<sup>+/+</sup> *Batf3*<sup>-/-</sup> *Cd11c*-YFP or *Arhgef1*<sup>-/-</sup> *Batf3*<sup>-/-</sup> *Cd11c*-YFP chimera spleen (movies S2 and S3). Time is indicated in min:sec. Scale bar, 20  $\mu\text{m}$ . (H) Frequencies of migratory cells (cDC2 with a minimum track length of 30  $\mu\text{m}$ ) in chimeras as indicated. (I) Frequencies of "leaving cells" (cDC2 that enter large vessels) in chimeras as indicated (movies S5 to S8). Each symbol indicates one movie in the supplementary materials. Lines denote the means. Data are pooled from five independent experiments. **(J)** Frequencies of YFP<sup>+</sup> DCs in blood of *Arhgef1*<sup>-/-</sup> *Batf3*<sup>-/-</sup> *Cd11c*-YFP and control chimeras. Data are pooled from two independent experiments. **(K to N)** Spleens from CD45.1 WT:CD45.2 *Gna13*<sup>CKO</sup> or CD45.1 WT:CD45.2 *Gna13*<sup>WT</sup> mixed chimeric mice were transplanted into CD45.1/2 WT recipients. The percentages of donor-derived B cells and cDC2s from the recipient blood and transplanted spleens were examined 8 to 9 hours after surgery. (K) Representative flow cytometry profiles show gating strategies. (L) Equation for calculating the migration competencies of CD45.2<sup>+</sup> population into blood. (M) Plots showing CD45.2<sup>+</sup> competency values in individual chimera for cDC2s leaving spleen into blood. (N) Plots showing CD45.2<sup>+</sup> competency values in individual chimera for B cells leaving spleen into blood. Data are pooled from three independent experiments. Each symbol indicates one mouse. Lines denote the means. \* $P < 0.05$ ; \*\* $P < 0.01$ ; \*\*\* $P < 0.001$ ; \*\*\*\* $P < 0.0001$ .



cDC2s (Fig. 6A and fig. S7A). In accord with the reduced antigen capture, CD97-deleted cDC2s showed less efficient activation as assessed from CCR7 and CD86 up-regulation (Fig. 6B and fig. S7B). Similar SRBC-induced cDC2 activation defects were observed in *ArhGEF1*-deficient mice (fig. S7, C to E). Moreover, CD4 T cell proliferation in response to SRBC-associated antigen was reduced in CD97-deleted compared

with WT recipients (fig. S7, F and G). To exclude possible roles for the CD97- $\alpha_{13}$  pathway in other cell types, we performed the same experiment in mice lacking  $\alpha_{13}$  selectively in *CD11c*<sup>+</sup> cells and again observed defective T cell proliferation (Fig. 6, C and D). The responding T cells up-regulated ICOS and PD1 to a lesser degree, suggesting reduced induction of T<sub>FH</sub> cells (Fig. 6E and fig. S7, H and I). Both *Gna13*<sup>CKO</sup>

and CD97-deleted recipient mice also showed a reduced germinal center (GC) response to SRBC-associated antigen (Fig. 6F and fig. S7, J and K). cDC2s have been implicated in the splenic B cell response to heat-killed *Listeria monocytogenes* (HKLM) (33). After immunization with HKLM, CD97-deficient mice mounted a reduced GC response (Fig. 6G). RBC allo-immunization can induce hemolytic transfusion



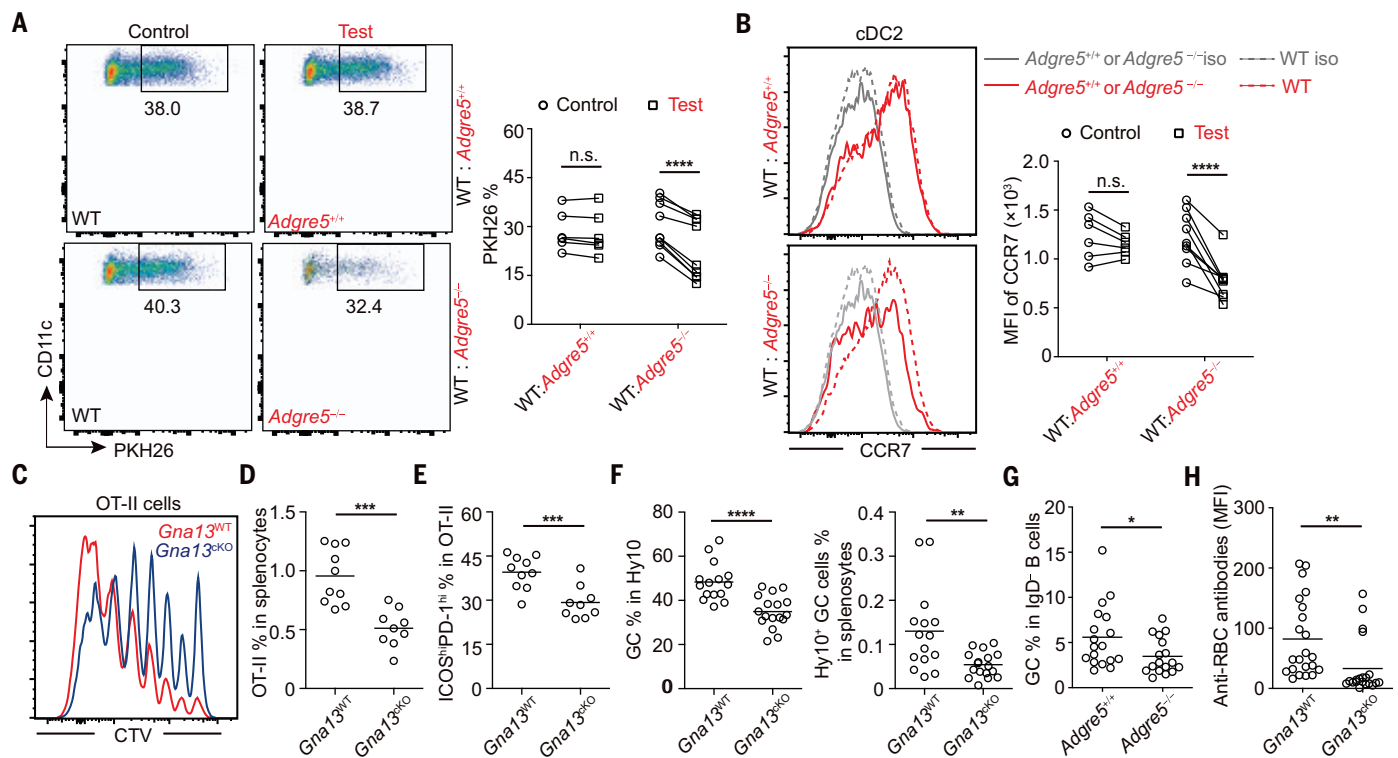


**Fig. 6. Functional defects of CD97 pathway-deficient splenic cDC2s.**

(A and B) Mixed BM chimeras (WT: *Adgre5*<sup>+/+</sup> or WT: *Adgre5*<sup>-/-</sup>) were analyzed 3 hours after PKH26-labeled SRBC injection. (A) Representative (left) flow cytometry plot and (right) frequencies of PKH26 dye-positive cDC2s. (B) Representative (left) histogram and (right) MFI of surface CCR7 expression on cDC2s from chimeras. (C to E) CellTrace Violet (CTV)-labeled OT-II T cells were transferred into *Gna13*<sup>CKO</sup> and *Gna13*<sup>WT</sup> mice. Mice were analyzed 3 days after SRBC-OVA immunization. [(C) and (D)] Representative (C) flow cytometry plot of proliferation and (D) frequencies of OT-II cells in total splenocytes. (E) Frequencies of ICOS<sup>hi</sup>PD-1<sup>hi</sup> T cells among transferred

OT-II T cells. (F) Frequencies of GC B cells in (left) Hy10<sup>+</sup> B cells and (right) frequencies of Hy10<sup>+</sup> GC B cells in splenocytes in *Gna13*<sup>CKO</sup> and control mice. (G) Frequencies of GC B cells in splenic IgD<sup>+</sup>B220<sup>+</sup> B cells in *Adgre5*<sup>-/-</sup> and control mice after HKLM immunization. (H) Antibodies to RBC in the sera of *Gna13*<sup>CKO</sup> and control mice 3 weeks after transfusion of HEL-OVA-conjugated mouse RBCs. In (D) to (H), each symbol indicates one mouse, and lines denote means. Data are pooled from [(A) to (E)] two, (F) three, or [(G) and (H)] four independent experiments. In (A) and (B), lines connect data from the same animal. \**P* < 0.05; \*\**P* < 0.01; \*\*\**P* < 0.001; \*\*\*\**P* < 0.0001.

reactions, potentially resulting in hemolytic diseases and renal failure (7, 34). Using transfers of foreign antigen conjugated mouse RBCs to model RBC allotransfusion, DC *Ga13* deficiency resulted in a reduced allo-RBC antibody response (Fig. 6H).

To determine whether the reduced splenic DC function in CD97 pathway-deficient mice could be explained by the reduced cDC2 frequency or also reflected defects in the function of the remaining cDC2s, we used a BM chimeric approach to generate mice that contained matched frequencies of WT or CD97-deleted cDC2s (fig. S8, A and B). When these mice were immunized with SRBC-associated antigen, control and CD97-deficient chimeric mice showed similarly reduced T cell responses compared with mice with a normally sized cDC2 compartment (fig. S8C). Thus, the reduced cDC2 compartment size appears to be a key contributor to the reduced T cell response in mice lacking the CD97 pathway. Antigen capture capability of WT cDC2s remained intact in mice with a low cDC compartment size (fig. S8D). However, CCR7 up-regulation on WT

cDC2s in these mice was impaired (fig. S8, E and F). Thus, CD97-mediated maintenance of a normally sized cDC2 compartment is necessary for cDC2 function. Moreover, when cDC2 numbers drop, the emptying of the niche leads to functional defects in the remaining cells.

#### *Irf4* acts upstream of CD97

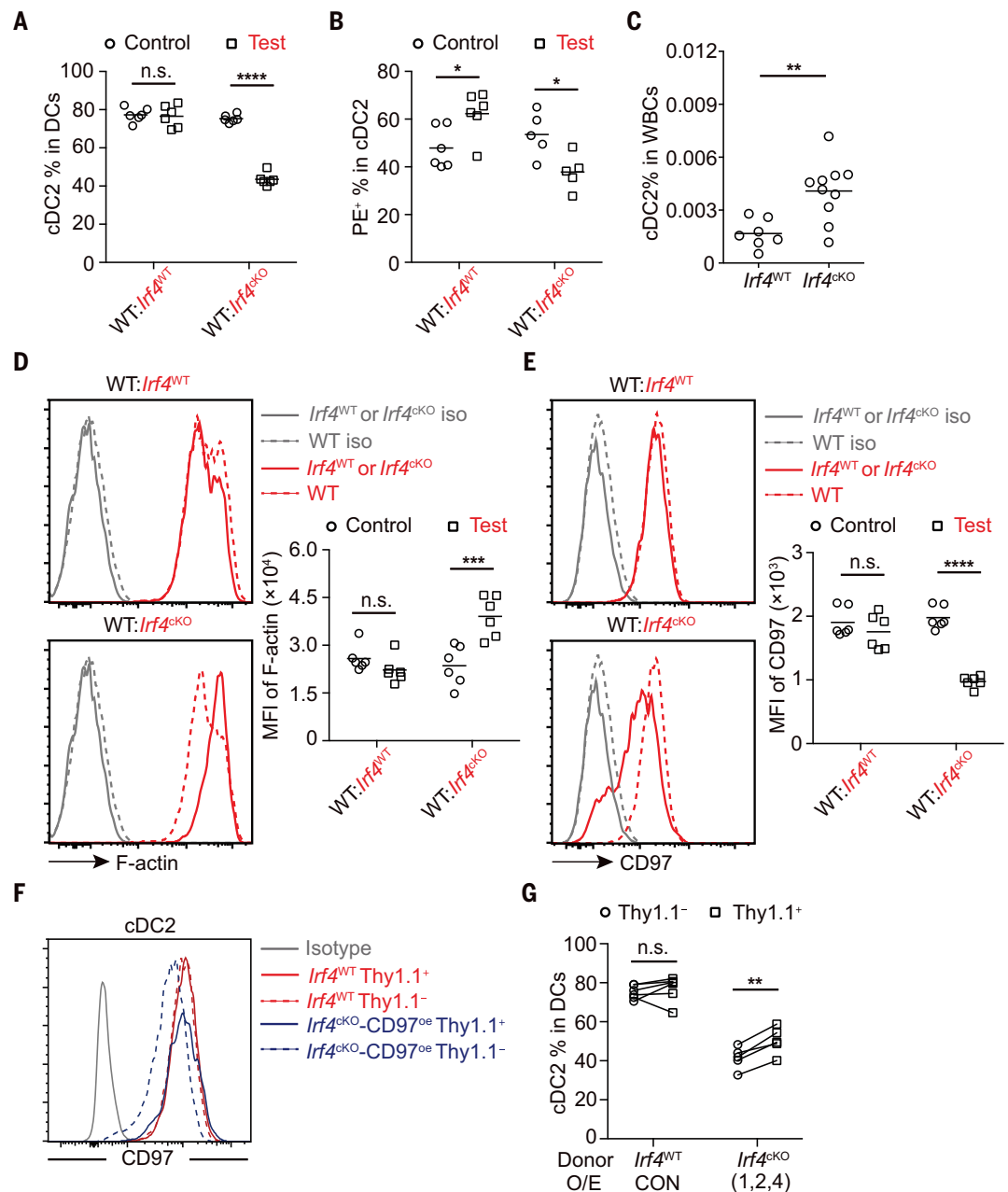
The transcription factor IRF4 has a well-studied but poorly understood role in promoting the normal accumulation and function of cDC2s (2, 7, 35, 36). Splenic cDC2s in mice lacking IRF4 in CD11c<sup>+</sup> cells (referred to as *Irf4*<sup>CKO</sup>) shared many phenotypes with CD97 pathway-deficient cDC2s, including reduced frequency (Fig. 7A), reduced labeling by circulating antibody (Fig. 7B), increased cDC2s in blood (Fig. 7C), increased F-actin (Fig. 7D), and reduced F4/80 expression (fig. S9A). Mice deficient in lymphotoxin β receptor or EBI2 had reduced cDC2 frequencies (6, 9, 37) but exhibited normal F-actin content, F4/80 expression, and CD97 levels (fig. S9, B to E), which suggests that cDC2 deficiency itself does

not cause the changes in these parameters. The abundance of CD97 on the splenic cDC2s remaining in IRF4-deficient mice was ~60% less than on WT cDC2s (Fig. 7E). Analysis of CD97 heterozygous mice showed that they had almost 50% reduced CD97 levels compared with WT cells (fig. S9F), and the cDC2s were slightly reduced in frequency (fig. S9G) and had detectably increased F-actin (fig. S9, H and I), indicating that splenic cDC2s have a dose-sensitive dependence on CD97. Thus, even a partial reduction in CD97 expression in the absence of IRF4 may contribute to the cDC2 deficiency in *Irf4*<sup>CKO</sup> mice.

IRF4 binds the *Adgre5* promoter, as shown in chromatin immunoprecipitation-sequencing analysis (38). RNA-sequencing (RNA-seq) analysis confirmed that IRF4-deficient cDC2s had reduced expression of *Adgre5* (fig. S9J). GSEA showed that up-regulated and down-regulated genes in CD97-deficient cells were strongly enriched in IRF4-regulated genes (fig. S9K). These data are in accord with CD97 acting within the IRF4 gene-expression network. To

**Fig. 7. CD97 action****downstream of *Irf4* in****splenic cDC2s. (A to E) Mixed**

(50:50) BM chimeras were made with CD45.1 WT (*Irf4*<sup>WT</sup>) and CD45.2 *Irf4*<sup>WT</sup> or *Cd11c*-cre *Irf4*<sup>fl/fl</sup> (labeled as *Irf4*<sup>CKO</sup>) BM cells. [(A) and (B)] Frequencies of (A) cDC2s in DCs and (B) in vivo PE-labeled cells in cDC2s in each compartment of the indicated chimeras. (C) Frequencies of cDC2s in blood of *Irf4*<sup>CKO</sup> and control mice. [(D) and (E)] Representative (left) histogram and (right) MFI of (D) F-actin expression and (E) surface CD97 expression on cDC2s in each compartment of the mixed chimeras. (F and G) BM chimeras were reconstituted with *Irf4*<sup>WT</sup> or *Irf4*<sup>CKO</sup> BM cells transduced with Adgre5 (1, 2, 4) or empty vector, with Thy1.1 as a reporter. (F) Representative histogram plots of surface CD97 on Thy1.1<sup>+</sup> and Thy1.1<sup>-</sup> cDC2s and (G) frequencies of cDC2s in Thy1.1<sup>+</sup> or Thy1.1<sup>-</sup> DCs of chimeras reconstituted as indicated. In (A) to (E), each symbol indicates one mouse, and lines denote means. In each summary graph, data are pooled from two independent experiments. In (G), lines connect data from the same animal. \**P* < 0.05; \*\**P* < 0.01; \*\*\**P* < 0.001; \*\*\*\**P* < 0.0001.



further test the contribution of reduced CD97 expression to the *Irf4*<sup>CKO</sup> phenotype, we selectively restored CD97 expression in IRF4-deficient BM chimeric mice. This led to a partial rescue in splenic cDC2s (Fig. 7, F and G). A difference between IRF4 deficiency and CD97 deficiency was the IRF4 requirement for normal accumulation of LN migratory cDC2s (fig. S9L) (39–42) that was not seen for the CD97 pathway (figs. S2G and S4F). IRF4 was not required for CD97 expression by LN migratory cDC2s, although it was needed for normal CD97 expression by LN-resident cDC2s (fig. S9, M and N). Thus, IRF4 is needed for the expression and function of the CD97 pathway in lymphoid tissue cDC2s, and this component of the IRF4 gene expression

program accounts for essential features of the IRF4 requirement of splenic cDC2s.

**Discussion**

Our findings establish a role for an adhesion GPCR in promoting cell retention and function within the spleen. The adhesion GPCR family has 33 members, and the functions of only a small number of them are well understood. In most of these cases, activation occurs in a mechanosensitive manner—for example, through shear force-mediated removal of the NTF (16, 17, 43). The binding of CD97 to CD55 was first shown in vitro in the context of CD97-transfected cells binding RBCs, but the physiological relevance of this binding has

been unclear (20). Our finding that CD97 is needed in splenic cDC2s for engagement by CD55<sup>+</sup> RBCs, cells that cDC2s encounter in regions of blood flow, leads us to propose that the receptor acts in a mechanosensitive manner in cDC2s. We suggest that when cDC2s extend membrane processes into regions of blood flow, they sense their location through the exertion of pulling forces by RBC CD55 on cDC2 CD97. This leads to extraction of the NTF, exposure of the Stachel sequence, and activation of the GPCR domain, triggering a  $G_{i3}$ -dependent membrane retraction pathway. These signals may also promote integrin-mediated adhesion (44, 45). Over time, when this pathway is lacking, not only are cDC2s lost from the spleen, but the remaining



cells up-regulate their F-actin, and Mrf transcription factors become active and drive expression of many cytoskeleton-associated genes. Although our study explains a requirement for splenic cDC2 retention in regions of blood flow, the mechanism used by some cDCs to position in a similar location remains to be defined. We propose that the CD55-CD97-G $\alpha_{13}$ -ArhGEF1 signaling pathway augments the ability of IRF4<sup>+</sup> cDC2s to present blood-borne particulate antigens by promoting cell positioning and cytoskeletal behaviors that facilitate antigen capture and presentation. A number of mechanosensitive pathways have been identified that allow cells to sense exposure to blood flow (43). Our studies add an adhesion GPCR to the mechanosensitive molecular systems used by cells to sense their exposure to blood cells in regions of flow.

## Materials and methods

### Mice

B6 (NCI 556) and B6-Ly5.2 (CD45.1) (NCI 564) mice were purchased from National Cancer Institute at Charles River at age 6 to 8 weeks. *Cd11c-cre* (MGI: 3763248) mice were provided by C. A. Lowell, University of California, San Francisco (UCSF). *Rag1*<sup>-/-</sup> (97848) mice were provided by A. Ma, UCSF. *Mpl*<sup>-/-</sup> mice were provided by M. R. Looney, UCSF. *Irf4*<sup>+/f</sup> mice (MGI: 3664434), *Tcrb*<sup>-/-</sup> mice (MGI:1857256) and CRISPR/Cas9 knock-in mice (026179) were purchased from The Jackson Laboratory. Ov-albumin (OVA)-specific TCR transgenic OT-II mice (MGI: 3046083), hen egg lysozyme (HEL)-specific immunoglobulin heavy chain knockin and light chain transgenic Hy10 mice, *Ebi2*<sup>-/-</sup> mice, and *Ltbr*<sup>-/-</sup> mice were from an internal colony. *Arhgef1*<sup>-/-</sup> mice (46) and *Gna13*<sup>eff</sup> mice (47) were backcrossed to B6/J for 10 generations. *Adgre5*<sup>-/-</sup> mice and *Cd55*<sup>-/-</sup> mice were generated with CRISPR/Cas9 in C57BL/6J background, and the sequences of the guides were 5'-GTAAATGCACACCACTGCA-3' and 5'-GAGTGAGAAATACATGTCA-3' for *Adgre5* and 5'-CTGGCATTAGGAATGTCTGG-3' and 5'-TC-TGTCTTGAAAATGGCCAA-3' for *CD55*. The CRISPR-EZ protocol (48) was followed with the main exception that the electroporation was performed twice. F0 founder mice were bred to C57BL/6J mice for two generations to avoid mosaicism and off-target effects. All mice were maintained under specific-pathogen-free conditions in the Laboratory of Animal Research Center at UCSF, and all animal procedures were approved by the UCSF Institutional Animal Use and Care Committee. For BM chimeras, mice were lethally irradiated by 550 rad  $\gamma$ -irradiation in two doses 3 hours apart and transferred intravenously with BM cells from donors of indicated genotypes. Chimeras were analyzed 5 to 10 weeks after reconstitution. In vivo labeling of blood-exposed cells was with 1  $\mu$ g of PE-conjugated anti-CD45.2 (104, Biolegend) or anti-CD11c (N418, Biolegend)

injected intravenously. Mice were then analyzed after 3 min. For CD97 or CD55 blockade, mice were treated with 40  $\mu$ g of purified anti-CD97 (MAB33734, R&D) or 33  $\mu$ g of purified anti-CD55 (RIKO-3, Biolegend) injected intravenously. Mice were then analyzed 2 days post treatment.

### Retroviral constructs and transductions

Gna13 and Arhgef1 retroviral constructs were made by inserting the murine open reading frame into the MSCV2.2 retroviral vector followed by an IRES and Thy1.1 as an expression marker. *Adgre5* (1,2,X,3,4), *Adgre5* (1,2,4) and its mutants, joined to Thy1.1 by a 2A self-cleaving peptide sequence, were inserted into the pQEF MoMLV retroviral vector that incorporates an EF1 promoter for improved expression (49). *Adgre5* (1,2,4) with a C-terminal GFP fusion, was inserted into the pQEF MoMLV retroviral vector. For the G protein-coupled-receptor screen, single-guide RNA (sgRNA) sequences were cloned into the pTR-MSCV-IRES-Thy1.1 vector. sgRNA sequences were selected using Benchling's CRISPR Guide tool. For BM transduction, donor mice were injected intravenously with 3 mg of 5-fluorouracil (Sigma). BM was collected after 4 to 5 days and cultured with complete DMEM, supplemented with 20 ng/ml of interleukin-3 (IL-3), 50 ng/ml of IL-6, and 100 ng/ml of stem cell factor. BM cells were spin-infected (1000g, 2 hours, 32°C) at day 1 and day 2 and injected into irradiated recipients after the second infection.

### Adoptive transfer and immunizations

For analysis of OVA-specific OTII T cell response,  $2 \times 10^5$  naïve CellTrace violet (CTV)-labeled OTII T cells were intravenously injected into mice and immunized with OVA-conjugated sheep blood cells (SRBCs). For OVA-SRBC conjugation (6), 1 ml of SRBCs was pelleted by centrifugation at 1000g for 5 min. One milliliter of PBS containing 30 mg/ml OVA with 25 mg EDC (1-ethyl-3-(3-dimethylaminopropyl)carbodiimide hydrochloride, ThermoFisher) was added to resuspend the pellet, and incubated for 1 hour on ice. For analysis of GC response,  $1 \times 10^5$  naïve HEL-specific Hy10 B cells were adoptively transferred into recipients and immunized with SRBCs conjugated with low affinity HEL<sup>2x</sup>. For conjugation of SRBC-HEL<sup>2x</sup>, 1 ml of washed SRBCs was resuspended in 0.8 ml of PBS buffer, mixed with 0.1 ml of 0.2 mg/ml HEL<sup>2x</sup> solution and 0.1 ml of 100 mg/ml EDC and incubated for 1 hour on ice. Conjugated SRBCs were washed three times to remove the free HEL<sup>2x</sup>. For the SRBC uptake assay, 1 ml of SRBCs was resuspended with 1 ml of conjugation buffer with 4  $\mu$ l of PKH26 dye for 20 min following the manual instruction. They were then washed three times with PBS. Eighty microliters of PKH26-labeled SRBCs was intravenously injected into each mouse 3 hours prior to analysis. Mice were

immunized intravenously with  $5 \times 10^8$  heat-inactivated *L. monocytogenes* (HKLM, InvivoGen) and analyzed for splenic GC reaction 8 days post immunization.

### Dendritic cell ablation

For DC ablation in *Zbtb46*<sup>DTR/+</sup>, *Adgre5* mixed BM chimeras, mice were injected intravenously with 25 ng of diphtheria toxin (DT, Sigma) per gram of body weight 2 days before transfer of OTII T cells or PKH26 labeled SRBCs. The mice were further treated intraperitoneally with 2.5 ng per gram of body weight DT on the day of cell transfer and 2 days after cell transfer to maintain ablation.

### RBC alloimmunization model

RBCs were collected from C57/B6 mice in Alsever's solution at 4°C. The cells were stored for 12 days before use as human RBC storage for this period has been shown to increase their allogenicity (34). Before transfusion, 1 ml of washed RBCs was added to 0.8 ml of PBS buffer, mixed with 0.1 ml of 0.5 mg/ml HEL-OVA solution and 0.1 ml of 100 mg/ml EDC and incubated for 1 hour on ice. Conjugated RBCs were washed three times to remove free HEL-OVA. Eighty microliters of HEL-OVA conjugated RBCs were intravenously transferred for allo-antibody induction. Twenty-one days later, serum was collected. To identify the presence of allo-antibodies, sera were diluted 1:5 with PBS and incubated with 5  $\mu$ l of HEL-OVA conjugated RBCs or unconjugated RBCs for 30 min on ice. After washing, the RBCs were stained with anti-mouse IgG conjugated with APC for 30 min on ice. The stained samples were washed and the total IgGs were detected by flow cytometry.

### Immunofluorescent staining

Ten-micron cryosections of spleen were fixed by acetone for 10 min, dried for 1 hour, and stained as described before (9). For DCIR2 staining, the tyramide amplification kit was used (TSA Biotin System, Perkin Elmer; Waltham, MA) according to the manual. Images were captured using a Zeiss AxioObserver Z1 inverted microscope with Zeiss AxioCam 506 mono and Zeiss Plan-Apochromat 10X/0.45 objective lens. Images were processed and stitched by Zeiss ZEN 2 (blue edition) software.

### Flow cytometry

Single-cell splenocyte suspensions were washed, blocked with 2.4G2 antibody (Bio X cell), and stained with antibodies of indicated specificities in MACS buffer (PBS+1% FBS). Staining reagents include: BV786-conjugated anti-B220 (RA3-6B2), eFluor450-conjugated anti-CD8a (53-6.7), PerCP/Cy5.5-conjugated anti-MHCII (M5/114.15.2), APC-conjugated anti-DCIR2 (33D1), PE/Cy7-conjugated anti-CD279 (RMP1-30), PE-conjugated anti-CD45.2 (104), biotinylated-conjugated anti-DCIR2 (33D1), biotinylated-conjugated anti-CCR7 (4B12),

BV711-conjugated anti-CD4 (GK1.5), PE-conjugated anti-CD278 (15F9), PE/Cy7-conjugated anti-CD95 (SA367H8), Pacific Blue-conjugated anti-GL7 (GL7), PE-conjugated anti-CD135 (A2F10), APC-conjugated anti-CD172a (P84) and BV605-conjugated anti-CD86 (GL-1) from Biolegend; FITC-conjugated anti-V $\alpha$ 2 TCR (B20.1), streptavidin-BV711 and streptavidin-BV605 from BD Biosciences; PE/Cy7-conjugated anti-CD11c (N418) from Tonbo Bio; PE-conjugated anti-CD55 (REA300) and APC-conjugated anti-CD97 (REA678) from Miltenyibiotec. HEL was conjugated with Alexa Fluor 647 by Alexa Fluor 647 Antibody Labeling Kit (A20186) from Thermo Fisher. All antibodies were used at a 1:200 dilution except for those against CCR7, CD97, and CD55, which were used at a 1:100 dilution. Dead-cell exclusion was based on Fixable Viability Dye eFluor 780 staining (eBioscience) and non-singlet events were excluded with FSC-W/FSC-H characteristics. All data were collected on an LSR II cytometer (BD Biosciences) and analyzed with FlowJo software (TreeStar).

#### EdU labeling and analysis

For short-term EdU labeling, mice were treated intravenously with 1 mg of 5-ethynyl-2'-deoxyuridine (EdU) 45 min before being sacrificed. Cells were stained for incorporated EdU with the Click-iT EdU Alexa Fluor 647 Flow Cytometry Assay Kit (Invitrogen) according to the manufacturer's instructions.

#### Red blood cell enrichment and transfusion

Five hundred microliters of blood was collected retro-orbitally from *Cd55*<sup>-/-</sup> or *Cd55*<sup>+/+</sup> mice into Alsever's solution. The blood was mixed followed by 100g centrifugation for 15 min at room temperature. The platelet-rich plasma and leukocyte-rich buffy coat were removed. Then *Cd55*<sup>-/-</sup> or *Cd55*<sup>+/+</sup> RBCs were intravenously transferred into appropriate mice from which 500  $\mu$ l of blood had previously been removed. For WBC transfer, 500  $\mu$ l of blood from *Cd55*<sup>-/-</sup> or *Cd55*<sup>+/+</sup> mice was lysed by ACK buffer. WBCs were then transferred into recipients with indicated genotypes. Mice were analyzed 6-8 days post blood transfusion.

#### CD97 isoforms detection

cDC2s and cDC1s were enriched by CD11c MicroBeads from Miltenyi Biotec, and then sorted with an Aria III (BD Biosciences). CD97 isoforms were detected by polymerase chain reaction. The following primers were used: P1, 5'-CAGGAGCTGGAACCCAGAAG-3'; P2, 5'-GGTGGCTCTTGGCATATGGT-3'.

#### Shear flow model in vitro

To mimic shear flow in vitro, 900  $\mu$ l of blood were collected from *Cd55*<sup>+/+</sup> or *Cd55*<sup>-/-</sup> mice in 100  $\mu$ l of Alsever's solution, and the blood was mixed followed by 100g centrifugation for 15 min at room temperature to separate RBCs

from the white blood cells. 100  $\mu$ l of the lower RBC fraction was added to 2 $\times$ 10<sup>6</sup> splenocytes from *Cd55*<sup>-/-</sup>, *Cd55*<sup>+/+</sup>, or CD97-mutant mice in 1.5-ml tubes and shaken (Eppendorf-ThermoMixer FL5) at room temperature (RT) at 900 rpm [shear ~12.5 dyne/cm<sup>2</sup> (50)] or not agitated. After 1 hour, cells were harvested, lysed, and analyzed by flow cytometry for CD97 expression.

#### IVC surgery

*Cd55*<sup>+/+</sup> or *Cd55*<sup>-/-</sup> mice were anesthetized with isoflurane. A midline abdominal incision was made to expose the portal vein, the IVC and the aorta. Three 7-0 silk sutures were placed under the three vessels prepared for ligation. Donor *Cd55*<sup>-/-</sup> splenocytes were harvested and stained with CellTrace Violet. Twenty units of heparin was injected retroorbitally. Five minutes later, labeled *Cd55*<sup>-/-</sup> splenocytes were intravenously transferred into recipients. Fifteen seconds later, the portal vein, the IVC and the aorta were ligated. Blood from the distal IVC and heart was collected 30 min after vessel ligation.

#### Mouse spleen transplantation

Mouse spleen transplantation was performed as previously described (51). Donor chimeras CD45.1 WT: CD45.2 *Gna13*<sup>WT</sup> or CD45.1 WT: CD45.2 *Gna13*<sup>cKO</sup> were anesthetized with isoflurane. A midline abdominal incision was made to expose the spleen. The short gastric vein, superior pancreaticoduodenal vein, and left gastric vessels were ligated with 7-0 silk suture. Part of the portal vein connecting with the splenic vein and the abdominal aorta near the celiac trunk were dissected and mobilized. Then 50 units of heparin was injected into the IVC. The portal vein distal to the splenic vein and the aorta above celiac trunk were ligated with a 7-0 suture, respectively. The spleen was perfused with 3 to 4 ml of cold heparinized saline (4°C, 100 U/ml) through the abdominal aorta. The splenic artery–celiac trunk–abdominal aorta patch was prepared by transecting the aorta below the celiac trunk. The splenic vein–portal vein patch was prepared by transecting the portal vein proximal to the liver. The spleen graft was then removed and preserved in cold saline (4°C). For the CD45.1/CD45.2 recipients, the aorta, and the IVC were cross-clamped using two microvascular clips. The splenic artery–celiac trunk–abdominal aorta patch was anastomosed to the recipient aorta and the splenic vein–portal vein patch was anastomosed to the recipient IVC using 11-0 sutures. The microvascular clips were removed to perfuse the donor spleen. The native splenic artery and vein were occluded by 7-0 suture and the recipient native spleen was removed. Finally the abdomen was closed with 6-0 suture. Eight to nine hours later, blood and spleens were collected to analyze the B cell and cDC2 compartments.

#### RNA-seq and GSEA

Spleens were digested with type IV collagenase and deoxyribonuclease I for 10 min and mashed into single cell suspension. DCs were enriched with anti-CD11c microbeads (Miltenyi Biotec) and sorted on an AriaIII from BD Biosciences. Total RNA was purified from sorted cells using the RNeasy Micro kit (Qiagen). RNA quality was assessed with an Agilent 2100 Bioanalyzer. Barcoded sequencing libraries were generated with the Ovation RNA-Seq System V2 (Nugen), a KAPA HyperPrep Kit for Illumina (KAPA Biosystems) and NEXTflex DNA barcodes. Single-end sequencing was performed on an Illumina HiSeq 4000 in the UCSF Center for Advanced Technology. Sequences were aligned to the mm10 genome with STAR. HTseq was used to count the mapped reads of each gene and DESeq2 was used for the gene differential expression analysis. lfcShrink function of DESeq2 is used to calculate the shrunken log2-fold changes. plotMA function of DESeq2 is used to generate the MA plot. Points are colored blue if the adjusted *P* value of shrunken log2-fold change is less than 0.1. Points which fall out of the window are plotted as open triangles pointing either up or down. GSEA analysis was carried out using the GSEA software. *P*<sub>adj</sub> < 0.001 was used as the threshold to define the significantly differentially expressed genes. For each comparison, the rank file was generated with the fcrs-package for subsequent pre-ranked GSEA analysis. The significantly up- or down-regulated genes were compared to the pre-ranked files. GSE77671 was used to compare CD97 regulated genes in mice with splenic human dendritic cells (24). Genes that were down-regulated by *Mrtfa*<sup>-/-</sup> BMDCs cells (29) were used as the test gene sets for enrichment analysis. Raw RNA-seq data are available from the GEO under the accession no. GSE188835.

#### Intravital imaging of DCs in spleen

Splenic DCs were imaged with *Arhgef1*<sup>+/-</sup> *Batf3*<sup>-/-</sup> *Cd11c*-YFP and *Arhgef1*<sup>-/-</sup> *Batf3*<sup>-/-</sup> *Cd11c*-YFP chimeras. In some cases, 0.5 mg of 155-kDa dextran-TRITC in 200  $\mu$ l of PBS was intravenously injected 30 min prior to imaging. The basic setup and procedure for intravital two-photon imaging of mouse spleens were essentially the same as previously described (10). Images were conducted with ZEN2012 (Carl Zeiss) using a 7MP two-photon microscope equipped with a Chameleon laser, Zeiss INDIMO 4 channel GaAsP detector system and W Plan-Apochromat 20X/1.0 objective lens at a *z*-step of 3  $\mu$ m. The imaging depth under the capsule of the spleen was between ~50  $\mu$ m and ~150  $\mu$ m. For video acquisition, a series of images were collected every 20 s. Excitation wavelengths were 830-860 nm. Emission filters were 500 to 550 nm for YFP, and 570-640 nm for TRITC. Off-line analyses were conducted with Imaris software (Bitplane).



Cell count was analyzed with Imaris automatic spot tracking aided by manual verification, and cell migration was analyzed and verified with manual tracking in 3D views. The surface of large blood vessels was created according to dextran-Tritc signaling. Spots and tracks that lasted less than 1 min were excluded from analysis. Migratory cDC2s were defined as cells with at least a 30- $\mu$ m track length across the imaging period. The mean imaging period for both types of chimeras was 45 min (number of movies analyzed: 25 *Arhgef1*<sup>+/-</sup> *Batf3*<sup>-/-</sup> *Cd11c*-YFP and 29 *Arhgef1*<sup>-/-</sup> *Batf3*<sup>-/-</sup> *Cd11c*-YFP). Image sequences were annotated in Adobe PhotoShop when necessary and rendered as movies with Adobe AfterEffect. All movies are played back at 20 frames per second (fps) unless indicated otherwise, and time stamps are minutes:seconds.

### Statistical analysis

Statistical analysis and graphing were performed using Prism 9.0 (GraphPad). Two-tailed Student's *t* tests were used to compare endpoint means of different groups. In grouped analysis, ordinary two-way analysis of variance (ANOVA) was performed and the *P* values indicated are from individual *t* tests with Sidak's multiple test correction. When multiple comparisons were being performed, ordinary one-way ANOVA with Dunnett's multiple comparisons was used.

### REFERENCES AND NOTES

1. S. C. Eisenbarth, Dendritic cell subsets in T cell programming: Location dictates function. *Nat. Rev. Immunol.* **19**, 89–103 (2019). doi: [10.1038/s41577-018-0088-1](#); pmid: [30464294](#)
2. D. A. Anderson 3rd, C. A. Dutertre, F. Ginhoux, K. M. Murphy, Genetic models of human and mouse dendritic cell development and function. *Nat. Rev. Immunol.* **21**, 101–115 (2021). doi: [10.1038/s41577-020-00413-x](#); pmid: [32908299](#)
3. R. E. Mebius, G. Kraal, Structure and function of the spleen. *Nat. Rev. Immunol.* **5**, 606–616 (2005). doi: [10.1038/nri1669](#); pmid: [16056254](#)
4. K. Yamamoto, T. Kobayashi, T. Murakami, Arterial terminals in the rat spleen as demonstrated by scanning electron microscopy of vascular casts. *Scan. Electron Microsc.* **1982**, 455–458 (1982). pmid: [7167761](#)
5. E. E. Schmidt, I. C. MacDonald, A. C. Groom, Comparative aspects of splenic microcirculatory pathways in mammals: The region bordering the white pulp. *Scanning Microsc.* **7**, 613–628 (1993). pmid: [8108677](#)
6. T. Yi, J. G. Cyster, EBI2-mediated bridging channel positioning supports splenic dendritic cell homeostasis and particulate antigen capture. *eLife* **2**, e00757 (2013). doi: [10.7554/eLife.00757](#); pmid: [23682316](#)
7. S. Calabro et al., Differential intrasplenic migration of dendritic cell subsets tailors adaptive immunity. *Cell Rep.* **16**, 2472–2485 (2016). doi: [10.1016/j.celrep.2016.07.076](#); pmid: [27545885](#)
8. E. Lu, E. V. Dang, J. G. McDonald, J. G. Cyster, Distinct oxysterol requirements for positioning naive and activated dendritic cells in the spleen. *Sci. Immunol.* **2**, eaal5237 (2017). doi: [10.1126/sciimmunol.aal5237](#); pmid: [28738017](#)
9. D. Liu, J. Wu, J. An, J. G. Cyster, Requirements for cDC2 positioning in blood-exposed regions of the neonatal and adult spleen. *J. Exp. Med.* **217**, e20192300 (2020). doi: [10.1084/jem.20192300](#); pmid: [32808016](#)
10. T. I. Arnon, R. M. Horton, I. L. Grigorova, J. G. Cyster, Visualization of splenic marginal zone B-cell shuttling and follicular B-cell egress. *Nature* **493**, 684–688 (2013). doi: [10.1038/nature11738](#); pmid: [23263181](#)
11. D. Gatto et al., The chemotactic receptor EBI2 regulates the homeostasis, localization and immunological function of splenic dendritic cells. *Nat. Immunol.* **14**, 446–453 (2013). doi: [10.1038/ni.2555](#); pmid: [23502855](#)

12. T. Wozfeld, N. Wettschureck, S. Offermanns, G(12)/G(13)-mediated signalling in mammalian physiology and disease. *Trends Pharmacol. Sci.* **29**, 582–589 (2008). doi: [10.1016/j.tips.2008.08.002](#); pmid: [18814923](#)
13. E. Lu, J. G. Cyster, G-protein coupled receptors and ligands that organize humoral immune responses. *Immunol. Rev.* **289**, 158–172 (2019). doi: [10.1111/imr.12743](#); pmid: [30977196](#)
14. K. L. Lewis et al., Notch2 receptor signaling controls functional differentiation of dendritic cells in the spleen and intestine. *Immunity* **35**, 780–791 (2011). doi: [10.1016/j.immuni.2011.08.013](#); pmid: [22018469](#)
15. T. Langenhan, G. Aust, J. Hamann, Sticky signaling—Adhesion class G protein-coupled receptors take the stage. *Sci. Signal.* **6**, re3 (2013). doi: [10.1126/scisignal.2003825](#); pmid: [23695165](#)
16. R. H. Purcell, R. A. Hall, Adhesion G protein-coupled receptors as drug targets. *Annu. Rev. Pharmacol. Toxicol.* **58**, 429–449 (2018). doi: [10.1146/annurev-pharmtox-010617-052933](#); pmid: [28968187](#)
17. A. Vizurraga, R. Adhikari, J. Yeung, M. Yu, G. G. Tall, Mechanisms of adhesion G protein-coupled receptor activation. *J. Biol. Chem.* **295**, 14065–14083 (2020). doi: [10.1074/jbc.REV120.007423](#); pmid: [32763969](#)
18. J. C. Leemans et al., The epidermal growth factor-seven transmembrane (EGF-TM7) receptor CD97 is required for neutrophil migration and host defense. *J. Immunol.* **172**, 1125–1131 (2004). doi: [10.4049/jimmunol.172.2.1125](#); pmid: [14707087](#)
19. S. H. Dho, J. C. Lim, L. K. Kim, Beyond the role of CD55 as a complement component. *Immune Netw.* **18**, e11 (2018). doi: [10.4110/in.2018.18.e11](#); pmid: [29503741](#)
20. J. Hamann, B. Vogel, G. M. van Schijndel, R. A. van Lier, The seven-span transmembrane receptor CD97 has a cellular ligand (CD55, DAF). *J. Exp. Med.* **184**, 1185–1189 (1996). doi: [10.1084/jem.184.3.1185](#); pmid: [9064337](#)
21. D. Hilbig et al., Mechano-dependent phosphorylation of the PDZ-binding motif of CD97/ADGRE5 modulates cellular detachment. *Cell Rep.* **24**, 1986–1995 (2018). doi: [10.1016/j.celrep.2018.07.071](#); pmid: [30134161](#)
22. C. C. Hsiao et al., CD97 inhibits cell migration in human fibrosarcoma cells by modulating TIMP-2/MT1- MMP/MMP-2 activity—Role of GPS autoproteolysis and functional cooperation between the N- and C-terminal fragments. *FEBS J.* **281**, 4878–4891 (2014). doi: [10.1111/febs.13027](#); pmid: [25174588](#)
23. I. Liebscher et al., A tethered agonist within the ectodomain activates the adhesion G protein-coupled receptors GPR126 and GPR133. *Cell Rep.* **9**, 2018–2026 (2014). doi: [10.1016/j.celrep.2014.11.036](#); pmid: [25533341](#)
24. G. F. Heidkamp et al., Human lymphoid organ dendritic cell identity is predominantly dictated by ontogeny, not tissue microenvironment. *Sci. Immunol.* **1**, eaai7677 (2016). doi: [10.1126/sciimmunol.aai7677](#); pmid: [28783692](#)
25. E. S. Russell, S. E. Bernstein, in *Biology of the Laboratory Mouse*, E. L. Green, Ed. (Dover Publications, 1966), vol. 2, chap. 17.
26. O. N. Karpus et al., Shear stress-dependent downregulation of the adhesion G protein-coupled receptor CD97 on circulating leukocytes upon contact with its ligand CD55. *J. Immunol.* **190**, 3740–3748 (2013). doi: [10.4049/jimmunol.1202192](#); pmid: [23447688](#)
27. G. Posern, R. Treisman, Actin' together: Serum response factor, its cofactors and the link to signal transduction. *Trends Cell Biol.* **16**, 588–596 (2006). doi: [10.1016/j.tcb.2006.09.008](#); pmid: [17035020](#)
28. D. Gau, P. Roy, SRF'ing and SAP'ing - the role of MRTF proteins in cell migration. *J. Cell Sci.* **131**, jcs218222 (2018). doi: [10.1242/jcs.218222](#); pmid: [30309957](#)
29. C. Guenther et al., A  $\beta$ 2-integrin/MRTF-A/SRF pathway regulates dendritic cell gene expression, adhesion, and traction force generation. *Front. Immunol.* **10**, 1138 (2019). doi: [10.3389/fimmu.2019.01138](#); pmid: [31191527](#)
30. P. Costello et al., MRTF-SRF signaling is required for seeding of HSC/PS in bone marrow during development. *Blood* **125**, 1244–1255 (2015). doi: [10.1182/blood-2014-08-595603](#); pmid: [25573994](#)
31. K. Hildner et al., Batf3 deficiency reveals a critical role for CD8 $\alpha^+$  dendritic cells in cytotoxic T cell immunity. *Science* **322**, 1097–1100 (2008). doi: [10.1126/science.1164206](#); pmid: [19008445](#)
32. J. Arasa, V. Collado-Diaz, C. Halin, Structure and immune function of afferent lymphatics and their mechanistic

contribution to dendritic cell and T cell trafficking. *Cells* **10**, 1269 (2021). doi: [10.3390/cells10051269](#); pmid: [34065513](#)

33. C. G. Briseño et al., Notch2-dependent DC2s mediate splenic germinal center responses. *Proc. Natl. Acad. Sci. U.S.A.* **115**, 10726–10731 (2018). doi: [10.1073/pnas.1809925115](#); pmid: [30279176](#)
34. J. E. Hendrickson, E. A. Hod, S. L. Spitalnik, C. D. Hillyer, J. C. Zimring, Storage of murine red blood cells enhances alloantibody responses to an erythroid-specific model antigen. *Transfusion* **50**, 642–648 (2010). doi: [10.1111/j.1537-2995.2009.02481.x](#); pmid: [19906034](#)
35. E. K. Persson et al., IRF4 transcription-factor-dependent CD103<sup>+</sup>CD11b<sup>+</sup> dendritic cells drive mucosal T helper 17 cell differentiation. *Immunity* **38**, 958–969 (2013). doi: [10.1016/j.immuni.2013.03.009](#); pmid: [23664832](#)
36. J. Li, E. Lu, T. Yi, J. G. Cyster, EBI2 augments Tfh cell fate by promoting interaction with IL-2-quenching dendritic cells. *Nature* **533**, 110–114 (2016). doi: [10.1038/nature17947](#); pmid: [27147029](#)
37. K. Kabashima et al., Intrinsic lymphotoxin-beta receptor requirement for homeostasis of lymphoid tissue dendritic cells. *Immunity* **22**, 439–450 (2005). doi: [10.1016/j.immuni.2005.02.007](#); pmid: [15845449](#)
38. ENCODE Project Consortium, An integrated encyclopedia of DNA elements in the human genome. *Nature* **489**, 57–74 (2012). doi: [10.1038/nature11247](#); pmid: [22955616](#)
39. S. Bajiña, K. Roach, S. Turner, J. Paul, S. Kovats, IRF4 promotes cutaneous dendritic cell migration to lymph nodes during homeostasis and inflammation. *J. Immunol.* **189**, 3368–3377 (2012). doi: [10.4049/jimmunol.1102613](#); pmid: [22933627](#)
40. Y. Gao et al., Control of T helper 2 responses by transcription factor IRF4-dependent dendritic cells. *Immunity* **39**, 722–732 (2013). doi: [10.1016/j.immuni.2013.08.028](#); pmid: [24076050](#)
41. R. Tussiwand et al., Klf4 expression in conventional dendritic cells is required for T helper 2 cell responses. *Immunity* **42**, 916–928 (2015). doi: [10.1016/j.immuni.2015.04.017](#); pmid: [25992862](#)
42. J. K. Krishnaswamy et al., Migratory CD11b<sup>+</sup> conventional dendritic cells induce T follicular helper cell-dependent antibody responses. *Sci. Immunol.* **2**, eaam9169 (2017). doi: [10.1126/sciimmunol.aam9169](#); pmid: [29196450](#)
43. N. Scholz, K. R. Monk, R. J. Kittel, T. Langenhan, Adhesion GPCRs as a putative class of metabotropic mechanosensors. *Handb. Exp. Pharmacol.* **234**, 221–247 (2016). doi: [10.1007/978-3-319-41523-9\\_10](#); pmid: [27832490](#)
44. C. Laudanna, J. J. Campbell, E. C. Butcher, Role of Rho in chemoattractant-activated leukocyte adhesion through integrins. *Science* **271**, 981–983 (1996). doi: [10.1126/science.271.5251.981](#); pmid: [8584934](#)
45. J. Yeung et al., GPR56/ADGRG1 is a platelet collagen-responsive GPCR and hemostatic sensor of shear force. *Proc. Natl. Acad. Sci. U.S.A.* **117**, 28275–28286 (2020). doi: [10.1073/pnas.2008921117](#); pmid: [33097663](#)
46. S. A. Francis, X. Shen, J. B. Young, P. Kaul, D. J. Lerner, Rho GEF Lsc is required for normal polarization, migration, and adhesion of formyl-peptide-stimulated neutrophils. *Blood* **107**, 1627–1635 (2006). doi: [10.1182/blood-2005-03-1164](#); pmid: [16263795](#)
47. K. M. Ruppel et al., Essential role for G $\alpha_{13}$  in endothelial cells during embryonic development. *Proc. Natl. Acad. Sci. U.S.A.* **102**, 8281–8286 (2005). doi: [10.1073/pnas.0503326102](#); pmid: [15919816](#)
48. S. Chen, B. Lee, A. Y. Lee, A. J. Modzelewski, L. He, Highly efficient mouse genome editing by CRISPR ribonucleoprotein electroporation of zygotes. *J. Biol. Chem.* **291**, 14457–14467 (2016). doi: [10.1074/jbc.M116.733154](#); pmid: [27151215](#)
49. Z. Yang, C. D. C. Allen, Expression of exogenous genes in murine primary B cells and B cell lines using retroviral vectors. *Methods Mol. Biol.* **1707**, 39–49 (2018). doi: [10.1007/978-1-4939-7474-0\\_3](#); pmid: [29388098](#)
50. K. Ley, E. Lundgren, E. Berger, K. E. Arfors, Shear-dependent inhibition of granulocyte adhesion to cultured endothelium by dextran sulfate. *Blood* **73**, 1324–1330 (1989). doi: [10.1182/blood.V73.5.1324.1324](#); pmid: [2467707](#)
51. J. J. Wang et al., A mouse model of vascularized heterotopic spleen transplantation for studying spleen cell biology and transplant immunity. *J. Vis. Exp.* (148): (2019). doi: [10.3791/59616](#); pmid: [31259895](#)

### ACKNOWLEDGMENTS

We thank S. Coughlin for *ArhGEF1*- and *Gna13*-deficient mice and R. Brink for HEL<sup>2x</sup>. We thank M. De Giovanni for advice regarding



imaging analysis, J. Muppidi and X. Piao for helpful discussions, and N. Carey for advice on statistical analysis. **Funding:** D.L. was supported by a Cancer Research Institute Irvington Fellowship and by funds from the UCSF Helen Diller Family Comprehensive Cancer Center. E.L. was supported by NSF grant 1144247. A.M. holds a Career Award for Medical Scientists from the Burroughs Wellcome Fund and a Lloyd J. Old STAR award from the Cancer Research Institute, is an investigator at the Chan Zuckerberg Biohub, and received funds from Parker Institute for Cancer Immunotherapy and the Innovative Genomics Institute. Z.Y. and C.D.C.A. were supported by funds from The Sandler Asthma Basic Research Center. J.G.C. is an investigator of the Howard Hughes Medical Institute. This work was supported in part by NIH grant A1040098 to J.G.C. **Author contributions:** D.L. and J.G.C. conceived the project, designed the experiments, interpreted the results, and wrote the manuscript. D.L. conducted the

experiments. L.D. analyzed the RNA-seq data. L.B.R. made initial observations in ArhGEF1-deficient mice. E.L. performed RNA-seq of ArhGEF1-deficient cDC2s. Y.X. performed molecular biology experiments. J.A. genotyped mice. L.Q. and M.R.L. performed spleen transplantation and IVC ligation from the UCSF microsurgery core. F.L. and M.R.L. performed surgery to collect blood from splenic artery and vein. Z.Y. and C.D.C.A. provided the pQEF vector. Z.L., Y.X., and A.M. generated the CD97-deleted and CD55-deleted mouse lines. **Competing interests:** J.G.C. is an advisor for MiroBio and Be Biopharma and owns stock in ALX Oncology. A.M. is a compensated cofounder, member of the boards of directors, and a member of the scientific advisory boards of Spotlight Therapeutics and Arsenal Biosciences. A.M. owns stock in Arsenal Biosciences, Spotlight Therapeutics, Merck, and PACT Pharma; A.M. is an investor in and informal advisor to Offline Ventures. **Data and materials availability:** GSE77671 was used to

compare CD97-regulated genes in mice with splenic human dendritic cells. Raw RNA-seq data have been deposited at GEO, accession no. is GSE188835. All other data are available in the main text or the supplementary materials.

#### SUPPLEMENTARY MATERIALS

[science.org/doi/10.1126/science.abi5965](https://science.org/doi/10.1126/science.abi5965)

Figs. S1 to S9

MDAR Reproducibility Checklist

Movies S1 to S8

21 March 2021; resubmitted 15 September 2021

Accepted 23 December 2021

10.1126/science.abi5965



**AAAS.ORG/COMMUNITY**



AAAS' Member Community is a one-stop destination for scientists and STEM enthusiasts alike. It's "Where Science Gets Social": a community where facts matter, ideas are big and there's always a reason to come hang out, share, discuss and explore.

**Member  
COMMUNITY**  
AAAS

AMERICAN ASSOCIATION FOR THE ADVANCEMENT OF SCIENCE

## RESEARCH ARTICLE SUMMARY

## IMMUNOLOGY

## Marginal zone B cells acquire dendritic cell functions by trogocytosis

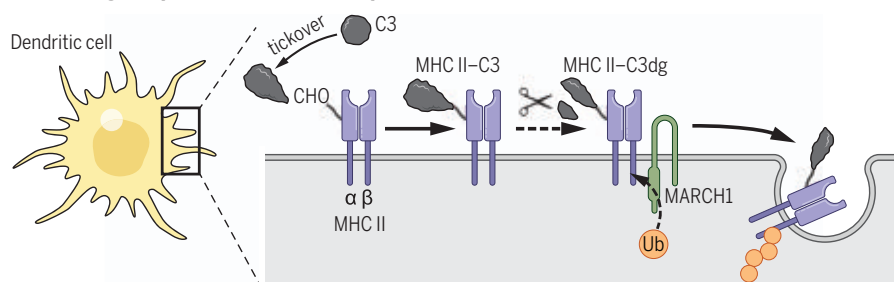
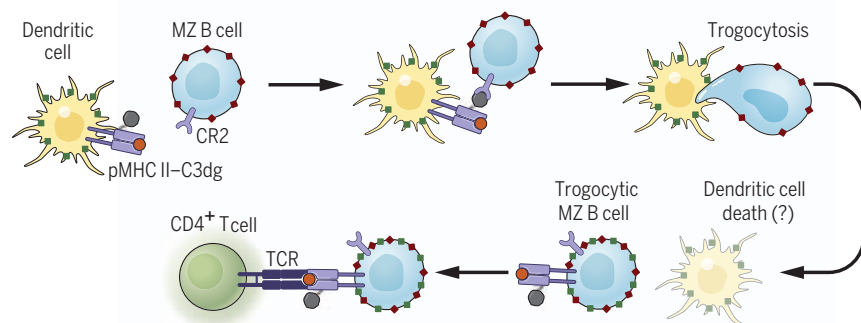
Patrick Schriek, Alan C. Ching, Nagaraj S. Moily, Jessica Moffat, Lynette Beattie, Thiago M. Steiner, Laine M. Hosking, Joshua M. Thurman, V. Michael Holers, Satoshi Ishido, Mireille H. Lahoud, Irina Caminschi, William R. Heath, Justine D. Mintern\*, Jose A. Villadangos\*

**INTRODUCTION:** Effective immunity is multi-layered, requiring the cooperation of various types of molecules and cells. Some types are components of the fast-responding innate arm of the immune system, like the molecules that constitute the complement system and marginal zone (MZ) B cells. Other types of molecules and cells participate in adaptive immune responses that provide long-term protection. These include conventional dendritic cells (cDCs) and major histocompatibility complex class II (MHC II) molecules. This study describes molecular linkages between complement and MHC II molecules that enable MZ B cells and cDCs to carry

out cooperatively immunological functions that neither cell type can perform on its own.

**RATIONALE:** The initiation of adaptive immunity against infections requires cDCs to detect, capture, degrade, and present pathogen antigens. cDCs use their MHC II molecules to bind and display peptide fragments derived from these antigens. Recognition of the resulting pMHC II complexes by the antigen receptor of T cells elicits adaptive immune responses and, eventually, the establishment of protective immunological memory against the infectious agent. MZ B cells are specialized in the

## MHC II–C3dg complex formation and ubiquitination at the surface of cDCs

MZ B cells trogocytose from cDC pMHC II–C3 complexes for antigen presentation to CD4<sup>+</sup> T cells

**Marginal zone B cells trogocytose dendritic cells, acquiring peptide-loaded MHC II molecules bound to complement C3 for antigen presentation to CD4<sup>+</sup> T cells.** Activated complement C3 binds MHC II on conventional dendritic cells (cDCs). The complexes are processed into MHC II–C3dg and either internalized via MARCH1-mediated ubiquitination or recognized by the complement receptor 2 (CR2) of marginal zone (MZ) B cells. The latter enables MZ B cells to trogocytose and display on their own membrane cDC receptors. Trogocytic MZ B cells expand their capacity to stimulate helper CD4<sup>+</sup> T cells using antigen-loaded MHC II molecules generated by cDCs. Excessive trogocytosis eliminates cDCs, but MARCH1 prevents this by limiting the number of MHC II–C3dg complexes on cDCs.

production of polyreactive antibodies that protect newborns and infants from different types of microorganisms. In some instances, MZ B cells require “help” from T cells to perform this function, which they obtain by displaying pMHC II complexes. This suggests that MZ B cells may be able to emulate the antigen-presenting activity of cDCs.

**RESULTS:** Complement component 3 (C3) is an abundant serum protein that constitutively adopts a reactive form in the absence of pathogens by a mechanism known as tickover. We determined that C3 binds to pMHC II exposed on the surface of mouse and human cDCs, forming a covalent bond with the carbohydrate moiety of the MHC II  $\alpha$  chain. Because C3 can damage healthy cells, it is converted to inactive C3dg while still bound to pMHC II. These pMHC II–C3dg complexes are recognized by complement receptor 2 (CR2), which is highly expressed by MZ B cells. Interaction between CR2 and C3dg triggers the transfer of pMHC II–C3dg complexes, along with associated cDC membrane and additional proteins embedded in the membrane, from cDCs to MZ B cells—a process termed trogocytosis. The trogocytic MZ B cells are thus able to present pMHC II complexes to T cells they do not generate themselves but acquire from cDCs.

Although trogocytosis is beneficial for MZ B cell function, it must be limited to prevent excessive damage and elimination of the trogocytosed cDCs. This takes place through an evolutionarily conserved mechanism, namely pMHC II–C3dg ubiquitination by a highly specialized ubiquitin ligase, MARCH1, embedded in the cDC plasma membrane. The ubiquitinated pMHC II–C3dg complexes are endocytosed and degraded intracellularly, reducing the number exposed on the cDC surface in the steady state.

**CONCLUSION:** Our results describe how C3 and MHC II interact and how this interaction enables MZ B cells and cDCs to cooperatively carry out functions they cannot perform individually. We demonstrate how an evolutionarily conserved mechanism for the constitutive elimination of potentially damaging C3 has been co-opted by cDCs to tag pMHC II complexes for capture by MZ B cells via trogocytosis. This mechanism expands the range of antigens that MZ B cells can present to T lymphocytes. The beneficial and deleterious consequences of trogocytosis are balanced by MARCH1 ubiquitination. ■

The list of author affiliations is available in the full article online.

\*Corresponding author. Email: jmintern@unimelb.edu.au (J.D.M.); jvilladangos@unimelb.edu.au (J.A.V.)  
Cite this article as P. Schriek et al., *Science* 375, eabf7470 (2022). DOI: 10.1126/science.abf7470

**S READ THE FULL ARTICLE AT**  
<https://doi.org/10.1126/science.abf7470>



## RESEARCH ARTICLE

## IMMUNOLOGY

## Marginal zone B cells acquire dendritic cell functions by trogocytosis

Patrick Schriek<sup>1</sup>, Alan C. Ching<sup>1</sup>, Nagaraj S. Moily<sup>1</sup>, Jessica Moffat<sup>1</sup>, Lynette Beattie<sup>2</sup>, Thiago M. Steiner<sup>2</sup>, Laine M. Hosking<sup>3</sup>, Joshua M. Thurman<sup>4</sup>, V. Michael Holers<sup>4</sup>, Satoshi Ishido<sup>5</sup>, Mireille H. Lahoud<sup>6</sup>, Irina Caminschi<sup>6</sup>, William R. Heath<sup>2</sup>, Justine D. Mintern<sup>1\*</sup>, Jose A. Villadangos<sup>1,2\*</sup>

Marginal zone (MZ) B cells produce broad-spectrum antibodies that protect against infection early in life. In some instances, antibody production requires MZ B cells to display pathogen antigens bound to major histocompatibility complex class II (MHC II) molecules to T cells. We describe the trogocytic acquisition of these molecules from conventional dendritic cells (cDCs). Complement component 3 (C3) binds to murine and human MHC II on cDCs. MZ B cells recognize C3 with complement receptor 2 (CR2) and trogocytose the MHC II–C3 complexes, which become exposed on their cell surface. The ubiquitin ligase MARCH1 limits the number of MHC II–C3 complexes displayed on cDCs to prevent their elimination through excessive trogocytosis. Capture of C3 by MHC II thus enables the transfer of cDC-like properties to MZ B cells.

Effective immunity requires orchestrated cooperation of multiple molecular and cellular components to maintain homeostasis and respond to infections. Although major histocompatibility complex class II (MHC II) molecules and complement component 3 (C3) are ancient centerpieces of adaptive and innate immunity, respectively, no interaction between these two components has previously been described.

The primary role of MHC II is to bind peptides derived from protein antigens (Ag) encountered by antigen-presenting cells (APCs) (1). The resulting peptide-loaded MHC II (pMHC II) complexes are displayed on the APC plasma membrane and detected by CD4<sup>+</sup> T cells, initiating adaptive immune responses. All APCs ubiquitinate the cytosolic tail of MHC II using the membrane ubiquitin ligase MARCH1 (membrane-associated RING-CH-type finger 1, encoded by *March1*) (2). Ubiquitination reduces the surface expression and half-life of pMHC II complexes by promoting their delivery to lysosomes, where they are degraded (2). Both MARCH1 and the single MHC II

β-chain residue ubiquitinated by MARCH1, Lys<sup>225</sup>, have been conserved through evolution, but their role in Ag presentation remains elusive (2–4), raising questions as to whether MHC II ubiquitination by MARCH1 plays other functions.

The complement system comprises >30 soluble and membrane proteins that undergo a cascade of activation upon pathogen encounter (5). Its pivotal component is C3, which can be activated by the classical, lectin, or alternative pathways (fig. S1A). This third pathway occurs at low levels in the absence of pathogens in what is known as tickover. Activated C3 binds covalently to carbohydrates on bacterial cell walls (6). This is followed by recruitment of other complement components that mediate lysis or phagocytosis of bacteria (fig. S1A) (5). C3 can also bind to the plasma membrane of normal host cells during and, via tickover, in the absence of infection (6). Deposited C3 is recognized by surface receptors and serum proteases that cleave it into the inactive forms C3dg and C3d, which remain attached to the cell membrane (fig. S1, B and C, and table S1), thereby preventing cell damage. Activation of C3 by tickover primes the complement system to respond rapidly to infection, but whether this pathway plays other immunoregulatory roles in the steady state is unclear (7).

Here, we show that C3 activated by tickover specifically binds the carbohydrate of murine and human MHC II glycoproteins. The resulting complexes are recognized by complement receptor 2 (CR2), expressed by marginal zone (MZ) B cells, triggering the trogocytic transfer of pMHC II and other membrane proteins from conventional dendritic cells (cDCs) to MZ B cells. This mechanism enables MZ B cells to

present pMHC II complexes generated by cDCs. Excessive trogocytosis causes cDC elimination, but MARCH1 ubiquitination prevents this outcome by limiting the accumulation of MHC II–C3 complexes.

#### *March1*<sup>−/−</sup> mice have reduced numbers of splenic cDCs

Relative to wild-type controls, the spleens of *March1*<sup>−/−</sup> mice exhibited reduced numbers of the two major cDC subsets, cDC1s and cDC2s, with no alteration in the number of plasmacytoid DCs (pDCs), B cells, or T cells (Fig. 1, A and B, and fig. S2, A to C). By contrast, cDC numbers in lymph nodes and the thymus were not altered (fig. S2D). The expression of characteristic cDC markers was comparable between wild-type and *March1*<sup>−/−</sup> cDCs with the exception of the MARCH1 substrates MHC II and CD86 (fig. S2E).

#### *March1*<sup>−/−</sup> mice have enriched numbers of MZ B cells displaying cDC proteins

A splenic CD11c<sup>int</sup>CD24<sup>+</sup>CD8<sup>int</sup> population that was present in low numbers in wild-type mice comprised >20% of CD11c<sup>+</sup> cells in their *March1*<sup>−/−</sup> counterparts (Fig. 2A). These cells displayed several surface markers characteristic of cDC1s, cDC2s, or both, although mostly at lower levels than cDCs (Fig. 2B). They also expressed B cell molecules at levels similar to B cells but did not express markers characteristic of other cell populations (Fig. 2B). No equivalent cell type was found in lymph nodes or thymus (fig. S3A). The transcriptome of CD11c<sup>int</sup>CD24<sup>+</sup>CD8<sup>int</sup> cells was similar to those of wild-type or *March1*<sup>−/−</sup> B cells (Fig. 2C), with high expression of B cell receptor (BCR)–signaling and B cell–activation genes (Fig. 2D) and no expression of cDC genes (Fig. 2E). This suggested that CD11c<sup>int</sup>CD24<sup>+</sup>CD8<sup>int</sup> cells were B cells that displayed cDC surface proteins but did not transcribe the corresponding genes. Additional immunophenotyping revealed that the majority of these cells were MZ B cells (8) (Fig. 2F).

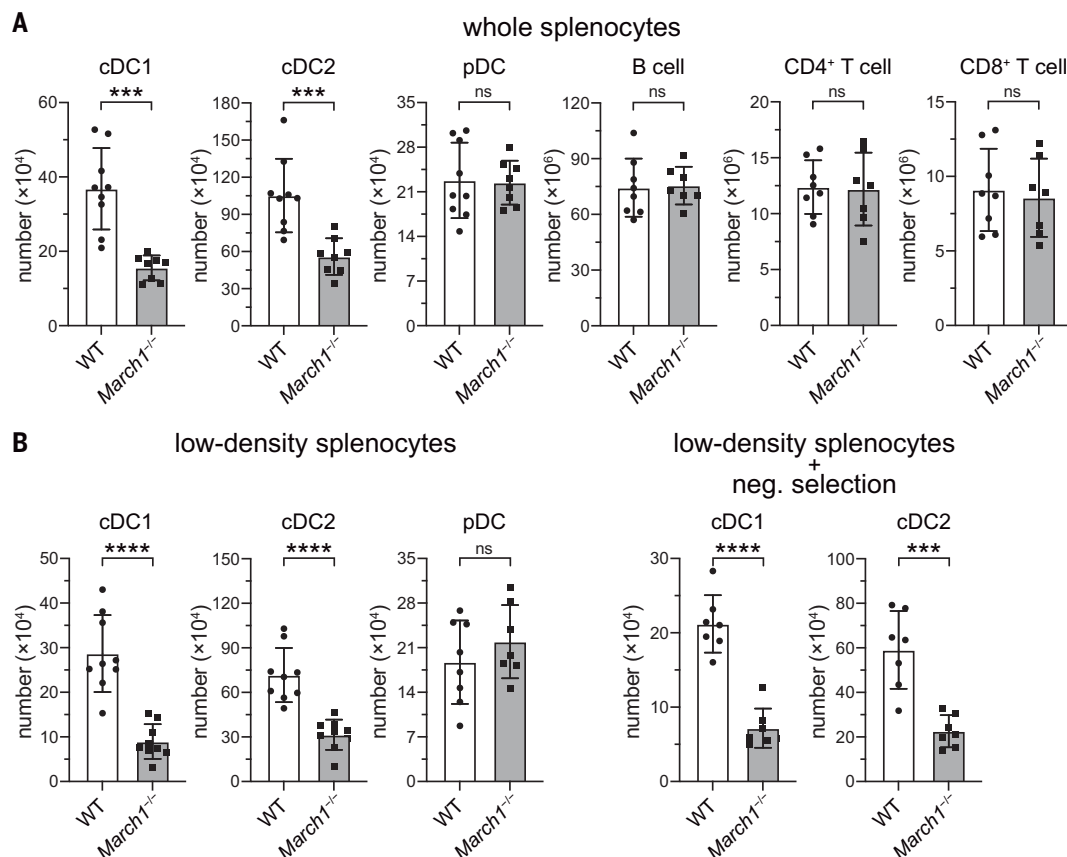
#### MZ B cells trogocytose plasma membrane from cDCs in a MARCH1-dependent manner

We tested the hypothesis that MZ B cells displayed cDC membrane proteins as a result of trogocytosis (9–11) and the absence of MARCH1-promoted plasma membrane transfer between the two cell types (fig. S3B). Indeed, B cells incubated with cDCs trogocytosed fluorescently labeled plasma membrane (Fig. 3A) and surface receptors (Fig. 3B) from cDCs. Trogocytosis was more prominent if cDCs were *March1*<sup>−/−</sup> than if they were wild-type, even though the two cDC groups were similarly labeled with fluorescent membrane dye (fig. S3C) and expressed similar levels of the surface receptors acquired by the B cells (fig. S2E). Membrane transfer between cDCs and B cells was monodirectional, as little

<sup>1</sup>Department of Biochemistry and Pharmacology, Bio21 Molecular Science and Biotechnology Institute, University of Melbourne, Parkville, VIC 3010, Australia. <sup>2</sup>Department of Microbiology and Immunology, Peter Doherty Institute for Infection and Immunity, University of Melbourne, Parkville, VIC 3010, Australia. <sup>3</sup>Department of Allergy and Immunology, Royal Children's Hospital, Parkville, VIC 3052, Australia. <sup>4</sup>Division of Rheumatology, University of Colorado School of Medicine, Aurora, CO 80045, USA. <sup>5</sup>Department of Microbiology, Hyogo College of Medicine, 1-1 Mukogawa-cho, Nishinomiya 663-8501, Japan. <sup>6</sup>Monash Biomedicine Discovery Institute and Department of Biochemistry and Molecular Biology, Monash University, Clayton, VIC 3800, Australia.

\*Corresponding author. Email: jmintern@unimelb.edu.au (J.D.M.); j.villadangos@unimelb.edu.au (J.A.V.)

**Fig. 1. Mice deficient in MARCH1 E3 ubiquitin ligase have reduced numbers of splenic cDCs.** (A and B) Numbers of the indicated wild-type (WT) and *March1*<sup>-/-</sup> cell types in whole splenocytes (A) or low-density splenocyte preparations (B) before (left) and after (right) depletion of non-cDCs. Graphs display data pooled from three independent experiments, with each symbol representing an individual mouse ( $n = 2$  or 3 per experiment); bars denote mean  $\pm$  SD. \*\*\* $P < 0.0002$ , \*\*\*\* $P < 0.0001$  [independent-samples  $t$  test with Welch's correction (no assumption of equal variances), two-tailed  $P$  value (95% CI)]; ns, not significant.



transfer was observed from B cells to cDCs (fig. S3D). MZ B cells were more trogocytic than their follicular (FO) counterparts (Fig. 3C). Furthermore, B cells did not trogocytose *March1*<sup>-/-</sup> macrophage, neutrophil, or T cell membranes (fig. S3E). Thus, B cells—particularly MZ B cells—specifically acquire cDC plasma membrane and surface proteins via trogocytosis, and MARCH1 deficiency makes cDC membranes more susceptible to trogocytic transfer.

#### MARCH1 controls the amount of C3 that accumulates on the surface of cDCs

Trogocytosis is mediated by surface receptors (9), so we hypothesized that MARCH1 regulates the expression of a receptor that mediates trogocytosis. The only receptors known to increase in expression in *March1*<sup>-/-</sup> cDCs are MHC II and CD86 (fig. S2E) (2), but a recent plasma membrane proteome analysis showed that the surface of *March1*<sup>-/-</sup> cDCs is also highly enriched in C3 (12). Because C3 is inaccessible to cytosolic ubiquitination by MARCH1, we sought to characterize the mechanism that caused its accumulation on the cell surface before investigating its potential role in trogocytosis.

First, we confirmed that C3 is present on wild-type cDC1s and cDC2s and is overexpressed on their *March1*<sup>-/-</sup> counterparts (Fig. 4A and fig. S4A). Analysis of C3-deficient mice

demonstrated the specificity of this detection (Fig. 4A). MARCH1 is active in all hematopoietic APCs, where it keeps surface MHC II expression at intermediate to low levels (12). We observed an increase in C3 deposition on both professional and “atypical” APCs from the spleen, lymph nodes, and thymus but not on T cells (Fig. 4B). C3 binding to cDCs was not caused by enzymatic tissue digestion because it was also observed in cell suspensions prepared by mechanical disruption (fig. S4B). Furthermore, when wild-type and *March1*<sup>-/-</sup>  $\times$  *C3*<sup>-/-</sup> spleens were pooled before cell purification, the mutant cDCs remained negative for C3 expression (fig. S4C).

In mixed-bone marrow (BM) chimeric mice where 1:1 wild-type and *March1*<sup>-/-</sup> BM was used to reconstitute *C3*<sup>-/-</sup> recipients, neither wild-type nor *March1*<sup>-/-</sup> cDCs displayed C3 (Fig. 4C). This indicated that C3 was captured from the extracellular environment, as expected, because it is produced mainly by liver cells (13). If the recipient chimeric mice were wild-type, the cDCs generated from the *March1*<sup>-/-</sup> BM displayed higher surface expression of C3 than their wild-type counterparts (Fig. 4C), which implies that the effect of the mutation was cell-intrinsic. Thus, C3 is secreted into circulation by nonhematopoietic cells and is deposited on all APCs. If the cells do not express MARCH1, C3

deposition increases by as much as a factor of 20 in the case of cDC1s.

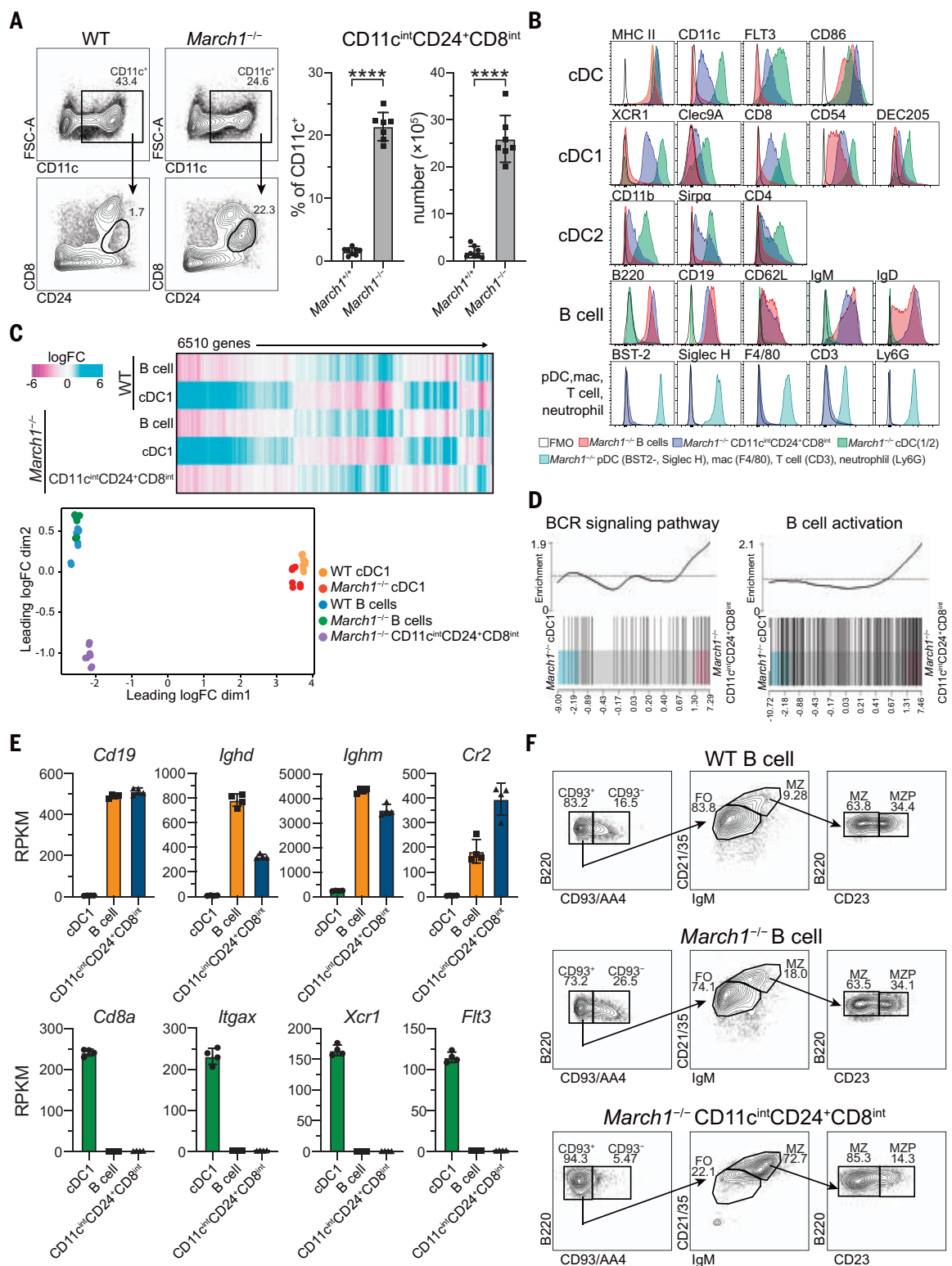
#### C3 activated by tickover binds to MHC II

Proteomic analysis of the *March1*<sup>-/-</sup> cDC plasma membrane (12) (table S2) indicated that the C3 species found on the cDC surface is one or both of its inactivated forms (i.e., C3dg or C3d) (fig. S1B and table S1). Analysis of wild-type, *March1*<sup>-/-</sup>, and *C3*<sup>-/-</sup> cDC lysates by immunoblot identified several molecular species of C3 that were only detected in *March1*<sup>-/-</sup> cDCs (Fig. 5A, fig. S1B, and table S1). The most prominent species had a molecular weight of ~70 kDa and was absent from the serum. We hypothesized that this species corresponded to C3dg or C3d covalently bound to MHC II  $\alpha$  or  $\beta$ .

The cDCs of mice deficient in both MARCH1 and MHC II (*March1*<sup>-/-</sup>  $\times$  *H2-Aa*<sup>-/-</sup>) showed elevated CD86 expression (fig. S4D), indicating that the absence of MHC II did not prevent surface accumulation of MARCH1 substrates. However, C3 was barely detectable on the surface of these cells (Fig. 5B) or on cDCs that only lacked MHC II expression (fig. S4E). Furthermore, the cDCs of knock-in mice—in which the only MHC II ubiquitination site, Lys<sup>225</sup> of the  $\beta$  chain, has been replaced with Arg (MHC IIKR<sup>KI/KI</sup> mice) (3, 14)—expressed similarly high levels of C3 relative to *March1*<sup>-/-</sup>

## Fig. 2. MARCH1-deficient mice harbor MZ B cells expressing cDC surface proteins.

(A) Left: Representative flow cytometry plots of CD24 versus CD8 expression in CD11c<sup>+</sup> wild-type and *March1*<sup>-/-</sup> low-density splenocytes. Right: Frequencies and total numbers of CD11c<sup>int</sup>CD24<sup>+</sup>CD8<sup>int</sup> cells. Graphs display data pooled from three independent experiments, with each symbol representing an individual mouse (*n* = 2 or 3 per experiment); bars denote mean ± SD. \*\*\*\**P* < 0.0001 [independent-samples *t* test with Welch's correction (no assumption of equal variances), two-tailed *P* value (95% CI)]. (B) Flow cytometry analysis of the indicated surface molecules on splenic CD11c<sup>int</sup>CD24<sup>+</sup>CD8<sup>int</sup> cells (blue), cDCs (green), or B cells (red) of *March1*<sup>-/-</sup> mice. Histograms are representative of at least two independent experiments with two or three individual mice per experiment. (C to E) RNA-seq of sort-purified CD11c<sup>int</sup>CD24<sup>+</sup>CD8<sup>int</sup> cells from *March1*<sup>-/-</sup> mice and B cells and cDC1s from wild-type and *March1*<sup>-/-</sup> mice. (C) Top: Heat-map showing 6510 differentially expressed genes across the five groups. Bottom: Two-dimensional scaling plot of the top 500 differentially expressed genes. (D) Barcode plots showing enrichment of genes in the B cell receptor signaling pathway (BioCarta) (left) and B cell activation (GO:0042113) (right) based on gene set analysis comparing *March1*<sup>-/-</sup> CD11c<sup>int</sup>CD24<sup>+</sup>CD8<sup>int</sup> cells and cDC1s. (E) Reads per kilobase million (RPKM) for genes encoding characteristic B cell (top) or cDC1 (bottom) surface markers in *March1*<sup>-/-</sup> cDC1s, B cells, and CD11c<sup>int</sup>CD24<sup>+</sup>CD8<sup>int</sup> cells. For RNA-seq analysis in (C) to (E), mRNAs from sort-purified cells of four biological replicates with pooled spleens from five mice were sequenced in technical replicates. (F) Representative gating strategy for the identification of splenic follicular (FO), MZ, and progenitor MZ (MZP) B cells, based on the surface expression of B220, CD93, IgM, CD21/35, and CD23 (all gated on CD19<sup>+</sup> alive cells), in whole splenocyte preparations of wild-type and *March1*<sup>-/-</sup> mice (top and middle rows) or among the CD11c<sup>int</sup>CD24<sup>+</sup>CD8<sup>int</sup> cells from low-density splenocytes of *March1*<sup>-/-</sup> mice (bottom). Data are from at least two independent experiments with two or three individual mice per experiment.



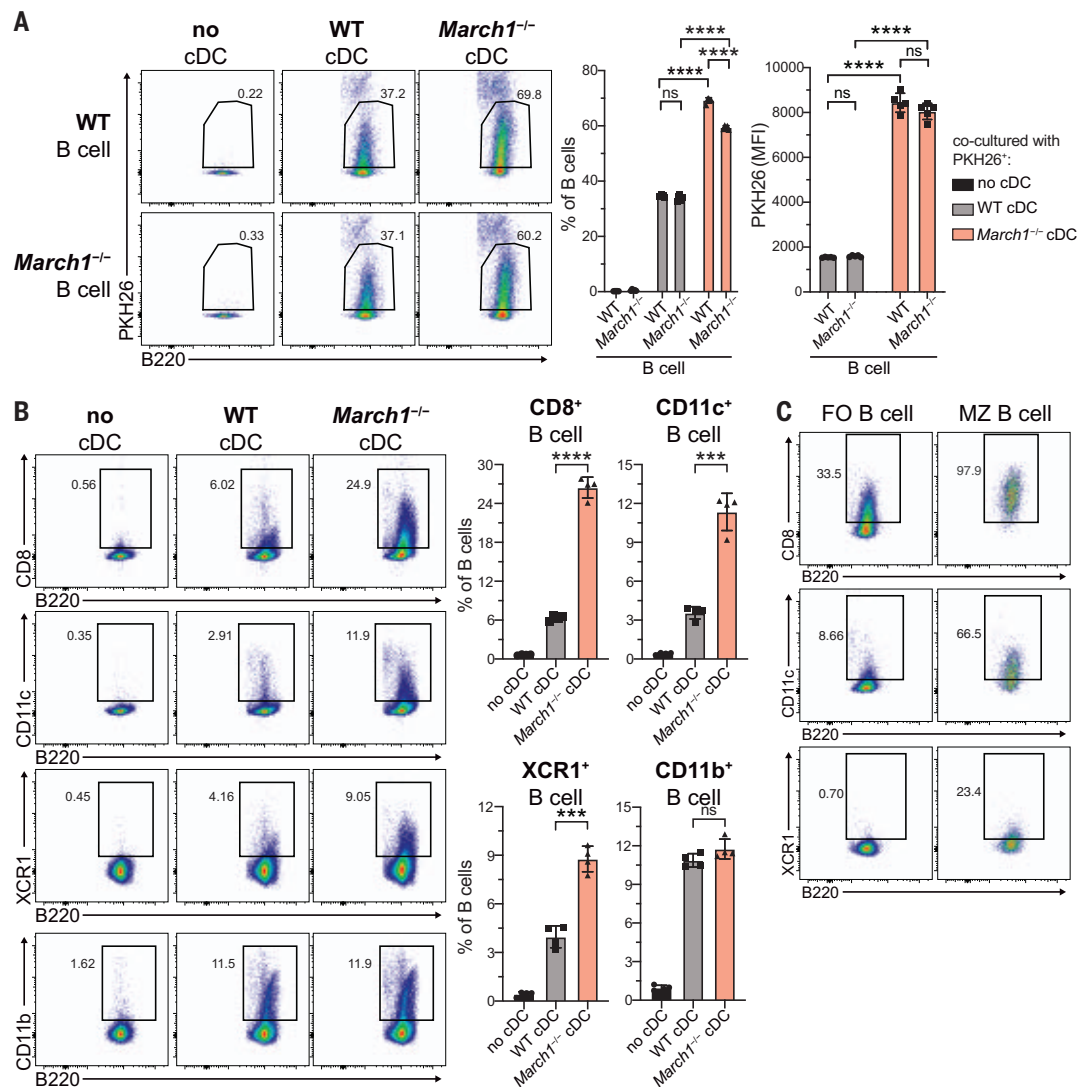
(F) Representative gating strategy for the identification of splenic follicular (FO), MZ, and progenitor MZ (MZP) B cells, based on the surface expression of B220, CD93, IgM, CD21/35, and CD23 (all gated on CD19<sup>+</sup> alive cells), in whole splenocyte preparations of wild-type and *March1*<sup>-/-</sup> mice (top and middle rows) or among the CD11c<sup>int</sup>CD24<sup>+</sup>CD8<sup>int</sup> cells from low-density splenocytes of *March1*<sup>-/-</sup> mice (bottom). Data are from at least two independent experiments with two or three individual mice per experiment.



**Fig. 3. MZ B cells trogocytose cDC plasma membrane in vitro.**

(A) Left: Trogocytic acquisition of cDC membrane, fluorescently labeled with PKH26, by wild-type and *March1*<sup>-/-</sup> B cells after in vitro incubation with PKH26-stained wild-type or *March1*<sup>-/-</sup> cDCs. Right: Frequency of PKH26<sup>+</sup> B cells and the mean fluorescence intensity (MFI) value of their PKH26 fluorescence after coculturing.

(B) As in (A), but measuring the indicated cDC proteins. (C) As in (B), but displaying separately FO and MZ B cells (as identified in Fig. 2F). Graphs in (A) and (B) display data pooled from two independent experiments, with each data point ( $n = 2$  or 3 per experiment) representing a measurement of a technical replicate; bars denote mean  $\pm$  SD. \*\*\* $P < 0.0002$ , \*\*\*\* $P < 0.0001$  [Welch's analysis of variance (ANOVA) test (no assumption of equal variances) followed by pairwise comparison (A) or by Games-Howell multiple-comparisons test (B), adjusted  $P$  value (95% CI)]. Plots in (C) are representative of at least two independent experiments with two or three individual mice per experiment.



cDCs (Fig. 5B), even though MARCH1 is functional in these cells as shown by their wild-type expression of CD86 (fig. S4F).

To confirm the formation of MHC II-C3 complexes in cDCs, we immunoprecipitated MHC II or C3 from wild-type, *March1*<sup>-/-</sup>, *March1*<sup>-/-</sup>  $\times$  *C3*<sup>-/-</sup>, MHC IIK<sup>KI/KI</sup>, *C3*<sup>-/-</sup>, and *H2-Aa*<sup>-/-</sup> cDCs and detected MHC II $\alpha$ , MHC II $\beta$ , and C3 by immunoblot. Two ~70-kDa proteins recognized by anti-I-A $\alpha$  and anti-C3 but not by anti-I-A $\beta$  antibodies were identified in immunoprecipitates from *March1*<sup>-/-</sup> and MHC IIK<sup>KI/KI</sup> cells, but not from *C3*<sup>-/-</sup> cells (Fig. 5, C and D). Mass spectrometry analysis of this protein confirmed that it contained C3d/C3dg peptides (table S3). Accumulation of C3 on cDC1s was accompanied by increased expression of complement regulators involved in conversion of C3b to C3dg, namely CR1/CR2, complement decay-accelerating factor (DAF), and factor H (fig. S4G). Thus, activated C3 binds to I-A $\alpha$ ; it is then processed, generat-

ing I-A $\alpha$ -C3dg and I-A $\alpha$ -C3d complexes, which accumulate on the surface of APCs (fig. S1D). For simplicity, we henceforth use the term “C3dg” to refer to both C3d and C3dg isoforms.

A comparison of C3 levels on the surface of cDCs expressing wild-type, MHC II K225R mutant molecule, or no MHC II at all (*H2-Aa*<sup>-/-</sup>) indicated that virtually all C3 was associated with MHC II (Fig. 5B and fig. S4E). This suggested that some feature in the MHC II $\alpha$  glycoprotein made it a target for activated C3. Activated C3 displays little protein conformation specificity but reacts preferentially with mannose (6), so we explored the possibility that C3dg might be bound to the MHC II $\alpha$  carbohydrate. Indeed, when MHC II $\alpha$  immunoprecipitated from *March1*<sup>-/-</sup> cDCs was deglycosylated with PNGase F, the MHC II $\alpha$ -C3dg complex was not detectable (Fig. 5E). This was accompanied by a change in free I-A $\alpha$  mobility in SDS-polyacrylamide gel electropho-

resis due to the loss of the carbohydrate group (Fig. 5E).

#### Binding of C3 to MHC II is conserved in mice and humans

To test whether C3 binding to MHC II was a peculiarity of C57BL/6 mice, we measured C3 on cDCs of *March1*<sup>-/-</sup> mice backcrossed to BALB/c (H-2<sup>d</sup> haplotype) or C3H (H-2<sup>k</sup> haplotype) mice. High levels of C3 were present on cDCs of all three strains (fig. S5A). We also detected C3 on human blood DCs (fig. S5, B and C), with highest expression on cDC2s followed by pDCs and cDC1s (Fig. 6). To determine whether C3 binding required MHC II expression, we assessed DCs in parallel from two human donors with a 362A>T mutation in RFXANK, which causes impaired MHC II transcription (15) and a lack of MHC II at the cell surface (fig. S5B). All MHC II-deficient DCs showed reduced C3 expression (Fig. 6). Thus, like MHC II ubiquitination by MARCH1, constitutive C3

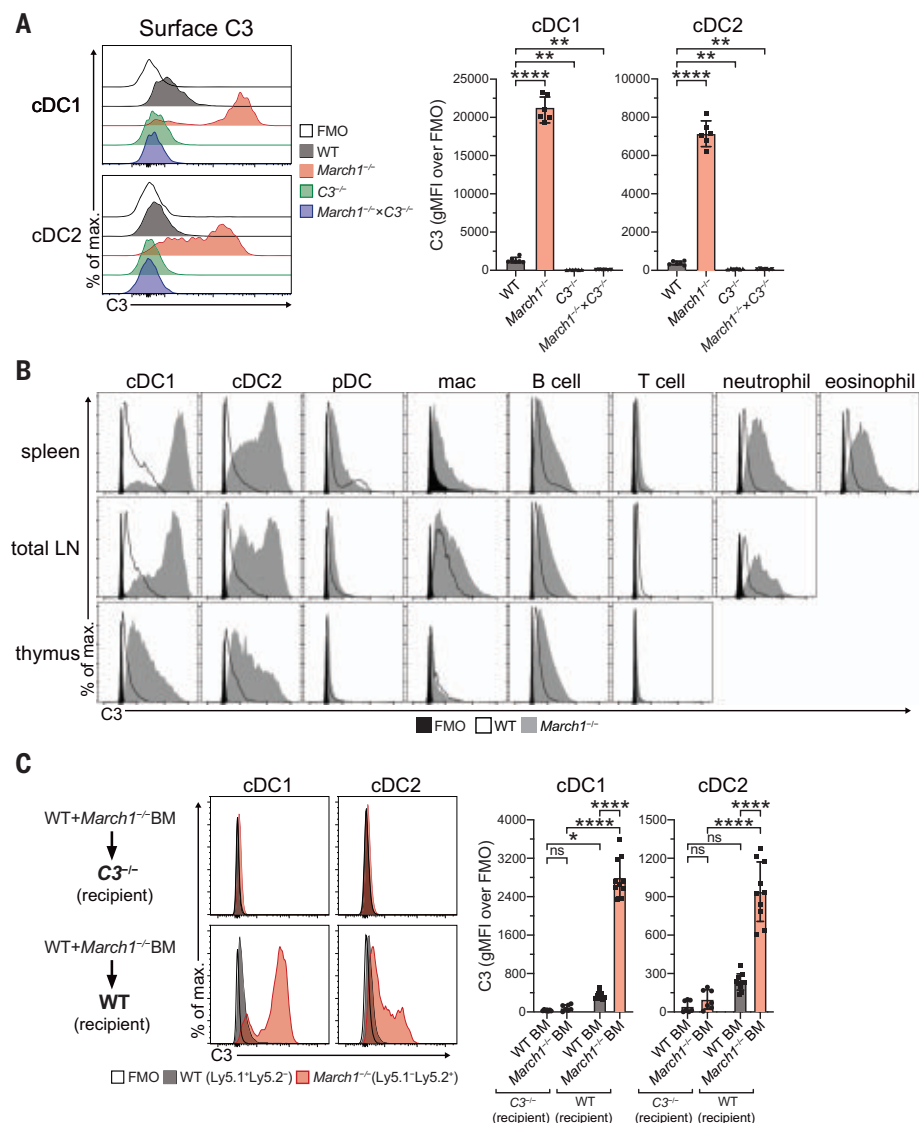


**Fig. 4. Complement C3 deposition on the surface of splenic cDCs.** (A) Representative flow cytometry histograms (left) and bar graphs with MFI values (right) of C3 surface expression on splenic cDC1s and cDC2s purified from the indicated mice. (B) Representative histograms of flow cytometry analysis of C3 surface levels on the indicated cell types in spleen, lymph nodes (LN), and thymus of wild-type or *March1*<sup>-/-</sup> mice. Histograms are representative of at least two independent experiments with two or three individual mice per experiment. (C) Representative flow cytometry histograms (left) and bar graphs with MFI values (right) of C3 surface expression on wild-type and *March1*<sup>-/-</sup> cDC1s and cDC2s from mixed-BM chimeras where wild-type or *C3*<sup>-/-</sup> recipient mice were reconstituted with a 1:1 mix of wild-type and *March1*<sup>-/-</sup> BM. Graphs in (A) and (C) display data pooled from a minimum of two independent experiments, with each symbol representing an individual mouse ( $n = 3$  to 5 per experiment); bars denote mean  $\pm$  SD. \* $P < 0.0332$ , \*\* $P < 0.002$ , \*\*\*\* $P < 0.0001$  [Welch's ANOVA test (no assumption of equal variances) followed by Games-Howell multiple-comparisons test (A) or by pairwise comparison (C), adjusted  $P$  value (95% CI)].

binding to MHC II has been conserved through evolution.

#### CR2 drives B cell trogocytosis of cDC membranes containing MHC II–C3 complexes

Analysis in vitro confirmed that high surface MHC II–C3 expression on MHC IIKR<sup>KI/KI</sup> cDCs was necessary and sufficient to induce B cell

trogocytosis (Fig. 7A and fig. S6A). C3dg is the ligand for complement receptor 2 (CR2, also known as CD21), which is expressed only by B cells (5). CR2-deficient B cells lacked the capacity to trogocytose more membrane from C3-decorated cDCs than from wild-type cDCs (Fig. 7A and fig. S6A). Furthermore, MZ B cells express higher levels of CR2 than FO B cells

(Fig. 2F), and virtually all MZ B cells trogocytosed cDC membrane containing MHC II–C3dg complexes (fig. S6B).

We next tested the validity of the conclusions from our in vitro analyses in vivo. *March1*<sup>-/-</sup> and MHC IIKR<sup>KI/KI</sup> mice accumulated trogocytic (CD8<sup>+</sup>CD11c<sup>+</sup>) B cells in their spleens in a MHC II- and C3-dependent manner (Fig. 7B). Wild-type spleens contained a small number of CD8<sup>+</sup>CD11c<sup>+</sup> MZ B cells, but these were absent from *C3*<sup>-/-</sup> spleens (Fig. 7C and fig. S6C); hence, trogocytosis occurred constitutively in wild-type mice. Although lymph node cDCs also displayed MHC II–C3 complexes (Fig. 4B), few trogocytic B cells were detected in lymph nodes (fig. S6D), as expected because mouse lymph nodes lack MZ B cells (8). The number of splenic cDCs decreased in all mice where cDCs had enriched C3 surface expression (Fig. 7D) and B cells expressed CR2 (Fig. 7E), in lockstep with the increase in trogocytic MZ B cells. The spleens of mice deficient in C3 did not contain more cDCs than those of wild-type mice (fig. S6E); this finding suggests that the limited amount of trogocytosis occurring in wild-type mice is insufficient to affect cDC homeostasis.

To further assess whether cDC number reduction and trogocytosis were directly correlated, we produced mixed-BM chimeras where wild-type or *C3*<sup>-/-</sup> recipient mice were reconstituted with 1:1 wild-type and *March1*<sup>-/-</sup> BM. In wild-type recipient mice, both wild-type and *March1*<sup>-/-</sup> B cells displayed higher trogocytic activity, but only *March1*<sup>-/-</sup> cDCs were reduced in numbers. Neither of these events were observed in *C3*-deficient recipients (Fig. 7F). Thus, the loss of cDCs required the accumulation of MHC II–C3 complexes but was caused by CR2-dependent MZ B cell trogocytosis (fig. S7).

#### Trogocytic MZ B cells present pMHC II generated by cDCs

Because the primary mediator of trogocytic cDC membrane transfer to B cells was CR2 recognition of MHC II–C3dg complexes, we wondered whether the complexes found on splenic B cells (Fig. 4B) were in fact acquired from cDCs. In mixed-BM chimeras where wild-type recipient mice were reconstituted with a 1:1 mix of wild-type and *Cr2*<sup>-/-</sup> BM, all B cells, and in particular MZ B cells, displayed more C3 if they expressed CR2 than if they did not (Fig. 8A). This suggested that although some of the MHC II–C3 complexes displayed by B cells probably formed on the B cells themselves, most were acquired from cDCs. This is supported by the absence of C3 detection on B cells of mice where MHC II–C3 complexes could not be generated (i.e., *H2-Aa*<sup>-/-</sup>) or lacked CR2 expression (Fig. 8B), which indicates that virtually all C3 (bound to MHC II) on the B cell surface was acquired by trogocytosis of cDCs. These results also confirmed that

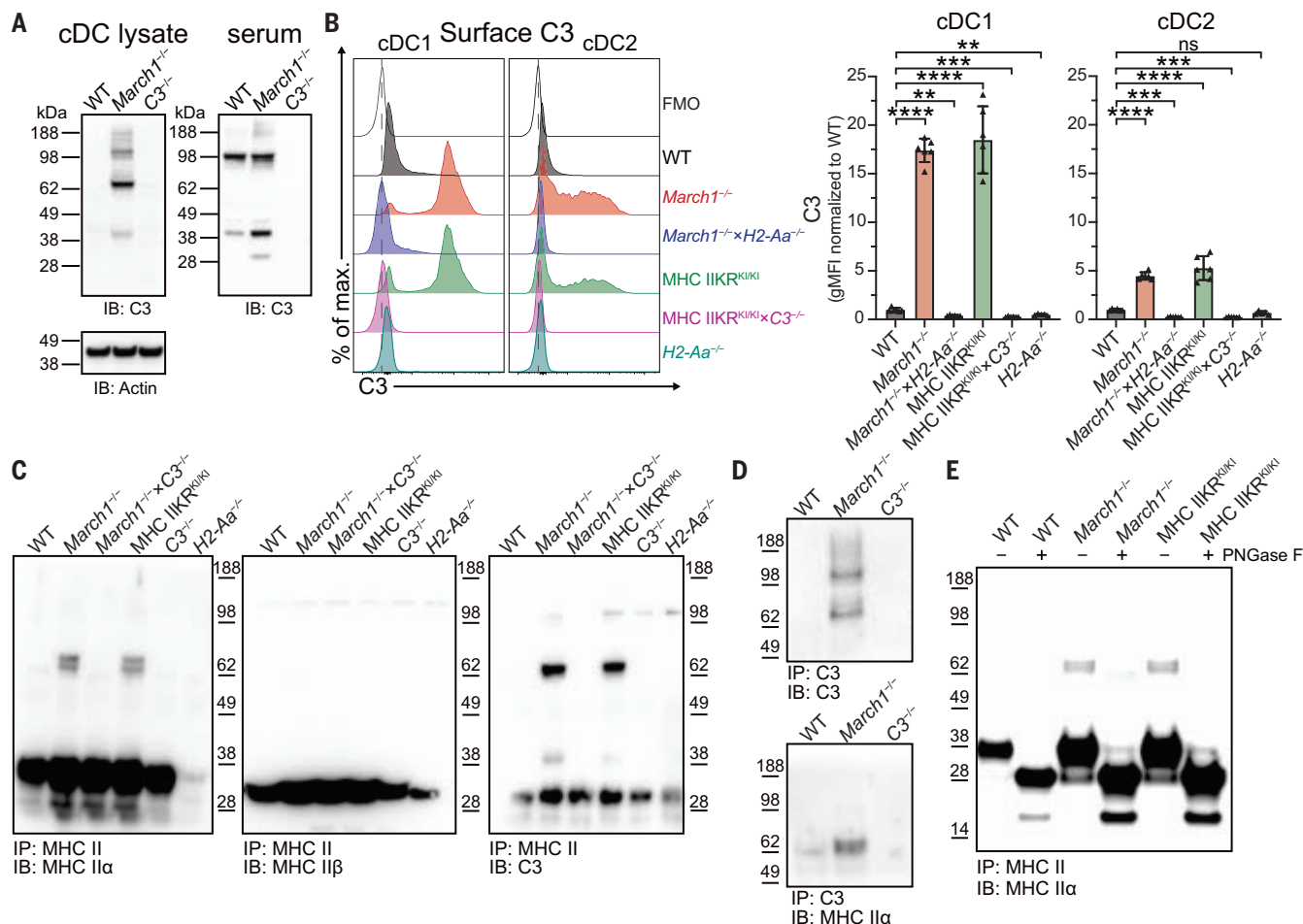


**Fig. 5. C3 binds covalently to the MHC IIα carbohydrate on the surface of cDCs.** (A) Immunoblot (IB) of C3 from lysates of splenic cDCs and serum of wild-type, *March1*<sup>-/-</sup>, or *C3*<sup>-/-</sup> mice. (B) Representative flow cytometry histograms (left) and bar graphs with MFI values (right) of C3 surface expression on splenic cDC1s and cDC2s of the indicated wild-type and mutant mice. Graphs display normalized data pooled from two independent experiments, with each symbol representing an individual mouse ( $n = 3$  per experiment); bars denote mean  $\pm$  SD.  $**P < 0.002$ ,  $***P < 0.0002$ ,  $****P < 0.0001$  [Welch's ANOVA test (no assumption of equal variances) followed by Games-Howell multiple-comparisons test, adjusted  $P$  value (95% CI)]. (C) IB analysis of

MHC II immunoprecipitates (IPs) obtained from lysates of cDC1s of the indicated wild-type or mutant mice, using Abs against MHC IIα, MHC IIβ, or C3. (D) IB detection of MHC IIα in IPs of C3 obtained from cDC1 lysates of the indicated wild-type or mutant mice. (E) IB analysis of MHC II IPs obtained from cDC1 lysates of the indicated wild-type or mutant mice after treatment with (+) or without (-) PNGase F and subsequent detection of MHC IIα. All immunoblots in (C) to (E) derive from separate gels and membranes for each immunoblot (instead of sequential detection) and are representative of at least three independent experiments, each lane loaded with IPs from cell lysate of  $2.5 \times 10^5$  purified splenic cDCs.

MZ B cell trogocytosis occurs constitutively in wild-type mice.

Finally, we tested whether trogocytosis enabled MZ B cells to “hijack” cDC Ag-presenting functions by acquiring pMHC II complexes generated by cDCs. First, we assessed MZ B cell presentation of the model Ag, I-Ea<sub>46-72</sub> (IEp) (16), after cDC1-targeted immunization. Wild-type, MHC IIKR<sup>KI/KI</sup>, and MHC IIKR<sup>KI/KI</sup> × *C3*<sup>-/-</sup> mice were immunized with an Ag consisting of IEp fused to either an isotype control monoclonal antibody (mAb) or a mAb that recognizes Clec9A, a cDC1 receptor (17). Presentation of IEp bound to MHC II (I-A<sup>b</sup>) was measured with a mAb (Yae) that specifically recognizes this complex (16) (Fig. 8C). In wild-type mice immunized with the

mAb that binds Clec9A, only cDC1s, not cDC2s or B cells, presented IEp (Fig. 8D). Additionally, no presentation occurred after immunization with the isotype control mAb (Fig. 8D). Immunization of MHC IIKR<sup>KI/KI</sup> and MHC IIKR<sup>KI/KI</sup> × *C3*<sup>-/-</sup> mice with the isotype control mAb led to low presentation of IEp by all four cell types (Fig. 8D), which is likely due to their increased MHC II surface expression. However, immunization with Clec9A-targeted mAb led to a much higher IEp presentation by cDC1s. This was the case in both MHC IIKR<sup>KI/KI</sup> and MHC IIKR<sup>KI/KI</sup> × *C3*<sup>-/-</sup> mice, implying that presentation of IEp by cDC1 was C3-independent (Fig. 8D). By contrast, presentation of the epitope by MZ B cells was C3-dependent (Fig. 8D). This indicated that

C3-mediated trogocytosis enabled MZ B cells to display in vivo pMHC II complexes they cannot generate on their own but can acquire from cDC1s. To assess whether acquired pMHC II complexes could be recognized by T cells, we immunized wild-type, MHC IIKR<sup>KI/KI</sup>, and MHC IIKR<sup>KI/KI</sup> × *C3*<sup>-/-</sup> mice with Clec9A mAb conjugated to the model Ag ovalbumin (OVA). We purified splenic FO and MZ B cells and incubated them in vitro with I-A<sup>b</sup>-OVA<sub>323-339</sub>-specific transgenic T cells (OT-II). Only MHC IIKR<sup>KI/KI</sup> MZ and, to a lesser extent, FO B cells presented the antigen and hence stimulated OT-II cells (Fig. 8E).

## Discussion

We have described two intersections between the innate and adaptive immune systems. The



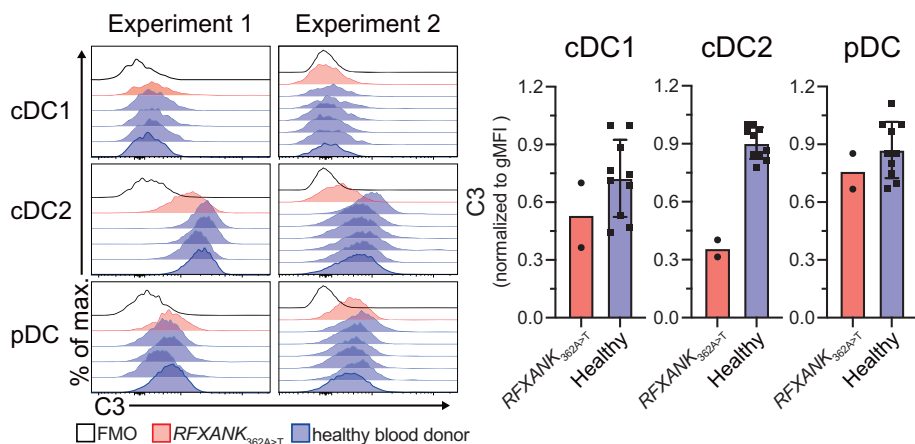


**Fig. 6. MHC II-dependent C3 deposition on human blood dendritic cells.** Representative flow cytometry histograms (left) and bar graphs with MFI values (right) of C3 surface expression on human blood DCs of healthy donors and two MHC II-deficient (*RFXANK*<sub>362A>T</sub>) patients. Graphs display pooled data (normalized to highest geometric MFI values) from the two experiments, with each symbol representing an individual blood sample; bars denote mean  $\pm$  SD.

first is cellular and features cDCs and MZ B cells. The main role of cDCs is to present Ag to T cells and initiate adaptive immunity (18). Interactions between cDCs and B cells are less well characterized (19). MZ B cells produce multi-specific Abs that protect infants whose adaptive immune systems have not yet generated the full spectrum of memory B cells that differentiate from the FO B cell repertoire (20). This activity is considered to be T cell-independent. MZ B cells also engage in T cell-dependent immunity (8), but this requires Ag presentation, and it remains unclear whether MZ B cells are efficient APCs. Here, we demonstrated that MZ B cells are constitutively in contact with cDCs and acquire pMHC II complexes from them using C3- and CR2-dependent trogocytosis.

The second interaction between innate and adaptive immunity we have described occurs at the molecular level. Activation of C3 by tickover (in the absence of pathogen) “pre-charges” the complement system to respond to infection (7). However, activated C3 can bind to healthy cells and cause autoimmunity, and several mechanisms are in place to inactivate it (6). We showed that C3 activated by tickover binds to the MHC II $\alpha$  carbohydrate. C3 is then converted to C3dg, and the resulting MHC II–C3dg complexes are ubiquitinated, internalized, and degraded (fig. S1D). Formation and ubiquitination of these complexes are independent processes conserved in mice and humans. Their role may be to prevent C3-driven host cell damage. We have not observed overt inflammation or autoimmunity in mice deficient in MHC II ubiquitination (21), but such disorders often do not manifest spontaneously in laboratory mice.

The MHC II carbohydrate appears to have a property that makes it prone to C3 binding and is not found in other glycoproteins; possibly this

consists of a high mannose content (6). Because the proportion of MHC II molecules bound to C3 at any given time is small, only some molecules may carry the required carbohydrate. It is plausible that mannose removal is incomplete in a fraction of MHC II molecules passing through the Golgi complex, causing microheterogeneity as previously observed (22). Moreover, the size of this fraction may vary among cells as a result of differential expression of glycosidases (23), which would explain why cells with similar levels of surface MHC II (e.g., cDC1s, cDC2s, and B cells) displayed different amounts of C3.

Recognition of C3dg by CR2 was sufficient to trigger the trogocytic acquisition of cDC membrane by MZ B cells. The mechanism of trogocytosis is poorly understood (11). It can be driven by a single receptor-ligand interaction, as demonstrated here between C3dg on cDCs and CR2 on B cells, but it is unclear whether this interaction simply increases cell-cell adhesion or triggers active membrane transfer. Regardless, we showed that B cell trogocytosis of cDC1s occurs in wild-type mice and enables MZ B cells to present pMHC II complexes generated by cDC1s. These results help to explain how MZ B cells may modulate T cell-dependent responses. In addition, trogocytic B cells acquired other cDC receptors that may expand the range of MZ B cell functions—for instance, capture of Ag recognized by SIGN-R1, Clec9A, and other receptors (17, 19, 24). MZ B cells transport Ag to B cell follicles to increase the efficiency of recognition by Ag-specific FO B cells (25). Trogocytic acquisition of DC receptors may expand their capacity for Ag capture and dissemination.

Notwithstanding the benefits trogocytosis may confer on MZ B cells, we have shown that this process must be limited to prevent cDC

elimination. This notion is supported by the following observations: (i) Reductions in cDCs were only observed in mice where all three molecular components required for trogocytosis—MHC II, C3, and CR2—were present; (ii) cDCs were lost from the spleen, where MZ B cells are present, but not from lymph nodes, where MZ B cells are absent, even though cDCs displayed similar amounts of MHC II–C3 complexes in both locations; (iii) in mice that contained both *March1*<sup>−/−</sup> cDCs, which could act as a source of trogocytosed membrane, and wild-type cDCs, which could not, only the mutant cDCs were lost. We propose that wild-type cDCs can tolerate trogocytic sequestration of a small amount of plasma membrane but their mutant counterparts cannot repair the damage caused by enhanced trogocytosis and die by “trogoptosis” (26) (fig. S7). Reductions in cDCs may contribute to the described defects in T cell priming in *March1*<sup>−/−</sup> or MHC IIKR<sup>KI/KI</sup> mice (3, 14).

MHC II ubiquitination by MARCH1 plays two important roles: to enhance the removal of surface MHC II–C3 complexes on all APCs, and, as described here, to limit MZ B cell trogocytosis and elimination of cDCs. It is conceivable that these two functions, more than the regulation of MHC II antigen presentation, have been the major drivers for the conservation of MHC II ubiquitination through evolution.

## Materials and methods

### Mice

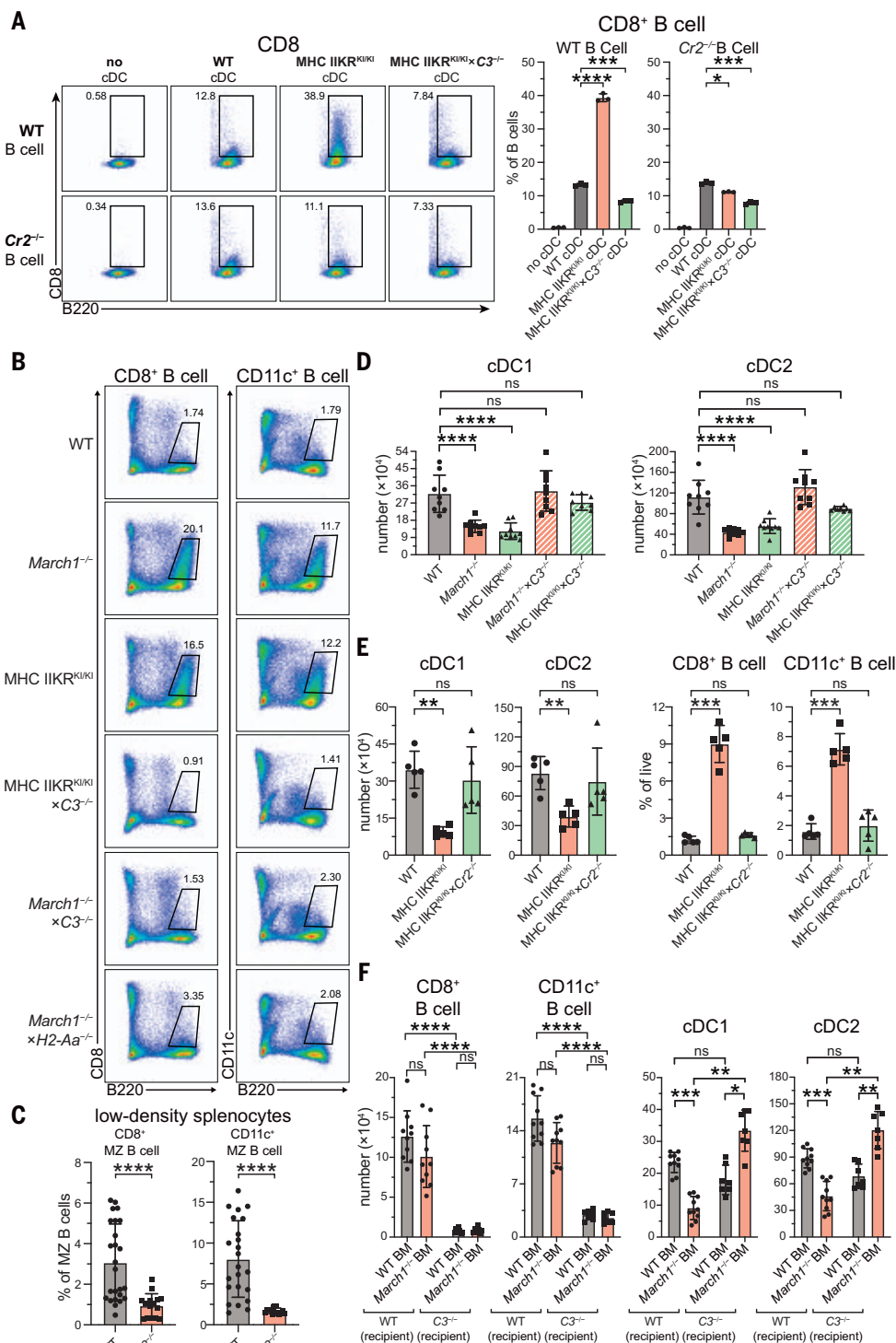
Experimental wild-type C57BL/6, BALB/c, or C3H, and mutant *March*<sup>−/−</sup> (27), *C3*<sup>−/−</sup> (28) (The Jackson Laboratory 129S4-C3tm1Crr/J; #0036410), MHC IIKR<sup>KI/KI</sup> (14), *H2-Aa*<sup>−/−</sup> (29), and *Cr2*<sup>−/−</sup> (30) [The Jackson Laboratory 129S7(NOD)-Cr2tm1Hmo/J; #008225] mice were bred and maintained in specific pathogen-free conditions in the Melbourne Bioresources Platform at the Bio21 Molecular Science and Biotechnology Institute, Victoria, Australia. Analyses were undertaken with male and female mice aged 7 to 14 weeks and performed in accordance with the Institutional Animal Care and Use Committee guidelines of the University of Melbourne and the National Health and Medical Research Council of Australia, approved by the Animal Ethics Committee at the University of Melbourne (#1714238 and #1513472).

### Isolation of primary murine cells and analysis by flow cytometry

Whole splenocyte suspensions were generated through digestion of finely chopped spleens with 0.1% DNase I (Roche) and collagenase type III (1 mg/ml; Worthington) followed by lysis of red blood cells through incubation with 168 mM ammonium chloride (5 min at room temperature). cDCs were purified from whole splenocyte suspensions as described (31). In brief, low-density splenocytes were

**Fig. 7. B cell trogocytosis of cDC membrane is MHC II-, C3-, and CR2-dependent. (A)** Trogocytic acquisition of CD8

**dependent. (A)** Trogocytic acquisition of CD8 from cDCs by wild-type or *Cr2*<sup>-/-</sup> B cells after their incubation with wild-type or mutant cDCs as indicated, with bar graphs (right) representing the percentage of CD8<sup>+</sup> B cells, determined as shown in the flow cytometry plots (left). Each data point represents the measurement of a technical replicate (*n* = 3), displayed as mean ± SD. \**P* < 0.0332, \*\*\**P* < 0.0002, \*\*\*\**P* < 0.0001 [Welch's ANOVA test (no assumption of equal variances) followed by Games-Howell multiple-comparisons test, adjusted *P* value (95% CI)]. **(B)** Representative B220 versus CD8 and CD11c plots of flow cytometry analysis of low-density splenocytes from the indicated wild-type or mutant mice, showing the proportion of trogocytic (CD8<sup>+</sup> and CD11c<sup>+</sup>) B cells. Plots are representative of at least two independent experiments with two or three individual mice per experiment. **(C)** Frequency of trogocytic MZ B cells among low-density splenocytes of wild-type or *C3*<sup>-/-</sup> mice. **(D)** Number of splenic cDC1s and cDC2s in the indicated wild-type or mutant mice. **(E)** Number of cDC1s and cDC2s (left) and frequency of trogocytic B cells (right) identified as shown in (B) in the indicated wild-type or mutant mice. **(F)** Number of wild-type or *March1*<sup>-/-</sup> trogocytic B cells, cDC1s, and cDC2s present in the spleens of mixed-BM chimeras (wild-type or *C3*<sup>-/-</sup> recipient mice), reconstituted with a 1:1 mix of wild-type and *March1*<sup>-/-</sup> BM. Graphs in (C) to (F) display data pooled from six (C) or two [(D) to (F)] independent experiments, with each symbol representing an individual mouse (*n* = 2 to 5 per experiment); bars denote mean ± SD. \**P* < 0.0332, \*\**P* < 0.002, \*\*\**P* < 0.0002, \*\*\*\**P* < 0.0001 [independent-samples *t* test with Welch's correction (no assumption of equal variances) in (C), Welch's ANOVA test (no assumption of equal variances) followed by Games-Howell multiple-comparisons test in (D) and (E), or followed by pairwise comparison in (F), two-tailed (C), or adjusted [(D) to (F)] *P* value (all 95% CI)].



enriched by density gradient centrifugation (at 2237g) with 1.077 g/cm<sup>3</sup> Nycodenz (Axis shield) and subsequent negative depletion using rat mAbs against CD3 (KT3-1.1), Thy1 (T24/31.7), Ly-76 (Ter119), B220 (RA3-6B2), and Ly-6C/G (RB6-8C5) and BioMag anti-rat IgG-coupled magnetic beads (20 µl/10<sup>6</sup> cells, Qiagen), resulting in 75 to 90% purity. Similarly, cDCs from total lymph nodes were enriched

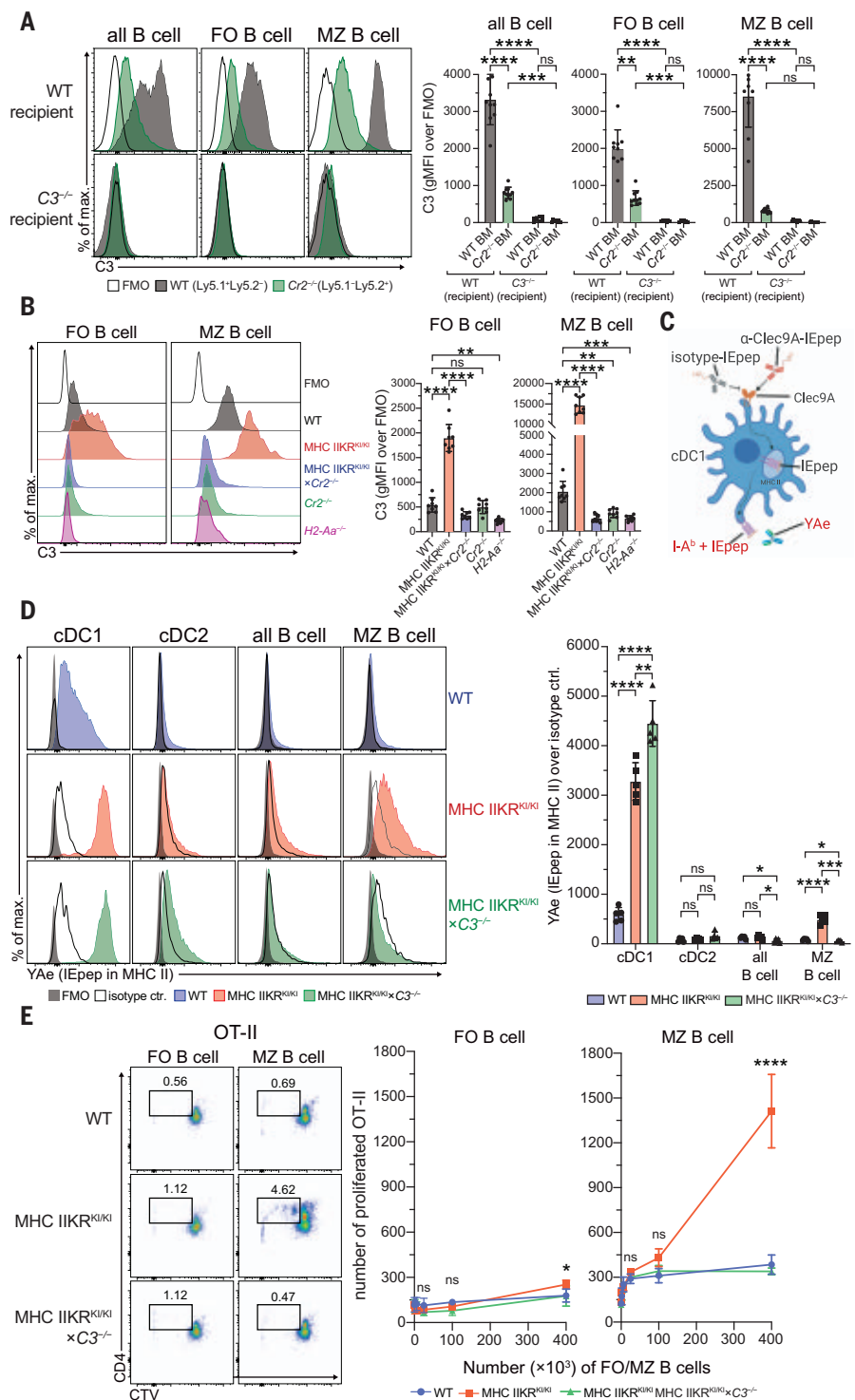
through enzymatic digestion [0.1% DNase I and collagenase type III (1 mg/ml)] and Nycodenz (1.077 g/cm<sup>3</sup>, Axis shield) gradient centrifugation (at 2237g). Splenic B cells were isolated from whole-splenocyte suspensions through gradient centrifugation (at 2237g) with Ficoll-Paque Plus (GE Healthcare) and subsequent negative depletion using FITC-conjugated mAb against CD4 (GK1.5, 1.6 µg/

ml), Ly76 (TER119, 1.6  $\mu\text{g/ml}$ ), and CD43 (S7, 1.6  $\mu\text{g/ml}$ ) and magnetic anti-FITC MicroBeads (2  $\mu\text{l}/10^6$  cells, Miltenyi Biotec), resulting in 95 to 98% purity.

For flow cytometry analysis, purified murine cells were washed in EDTA-BSS with 2% (v/v) FCS, Fc receptor-blocked (1:50, Miltenyi Biotec), and incubated with mAb for the detection of surface markers (table S4). All

### Fig. 8. MZ B cells present pMHC II complexes trogocytosed from cDC1s in vivo. (A and B)

Representative flow cytometry histograms (left) and bar graphs with MFI values (right) of C3 surface expression on wild-type or  $Cr2^{-/-}$  total, FO, or MZ B cells of mixed-BM chimera mice (wild-type or  $C3^{-/-}$  recipients), reconstituted with a 1:1 mix of wild-type and  $Cr2^{-/-}$  BM (A) or on FO and MZ B cells of the indicated wild-type or mutant mice (B). Bar graphs display data pooled from two independent experiments, with each symbol representing an individual mouse ( $n = 4$  or 5 per experiment); bars denote mean  $\pm$  SD.  $**P < 0.002$ ,  $***P < 0.0002$ ,  $****P < 0.0001$  [Welch's ANOVA test (no assumption of equal variances) followed by pairwise comparison (A) or by Games-Howell multiple-comparisons test (B), adjusted  $P$  value (95% CI)]. (C) Cartoon representing the capture of anti-Clec9A mAb fused to the I-E peptide (I-E<sub>46-72</sub>) by cDC1s, followed by intracellular processing and presentation of I-E peptide by MHC II (I-A<sup>b</sup>) and detection of the complex on the cell surface with YAE mAb. (D) Left: Surface expression of I-A<sup>b</sup> + IEep (YAE) on splenic cDC1s, cDC2s, total B cells, and MZ B cells of the indicated wild-type or mutant mice immunized with anti-Clec9A-IEep or control isotype-IEep mAb. Right: Bar graphs with MFI values of YAE surface expression; data pooled from two independent experiments, with each symbol representing an individual mouse ( $n = 2$  or 3 per experiment), displayed as means  $\pm$  SD.  $*P < 0.0332$ ,  $**P < 0.002$ ,  $***P < 0.0002$ ,  $****P < 0.0001$  [Welch's ANOVA test (no assumption of equal variances) followed by pairwise comparison within each group (cell type),  $P$  value (all 95% CI)]. (E) Proliferation of OT-II cells incubated with increasing numbers of sort-purified FO or MZ B cells from the indicated wild-type or mutant mice immunized with anti-Clec9A mAb conjugated with OVA. Left: Dividing OT-II cells, gated as shown in the representative flow cytometry plots. Right: Numbers of proliferated OT-II cells pooled from two independent experiments, with each symbol representing a technical replicate ( $n = 3$  per experiment), displayed as means  $\pm$  SD.  $*P < 0.0332$ ,  $****P < 0.0001$  (one-way ANOVA followed by Bonferroni's multiple-comparisons test).



fluorescence-minus-one (FMO) controls correspond to cells that were stained with mAbs for the detection of lineage markers but not for the indicated molecule. Cell surface C3 was detected using biotinylated anti-C3 mAbs clone 11H9 (Novus Biological), clone 3d29 [kindly provided by V. M. Holers and J. M. Thurman, School of Medicine, University of Colorado, Denver, Anschutz Medical Campus (32)], or

polyclonal Abs (pAbs) HP8012 (Hycult) and 55500 (MP Biomedical) (table S4) with subsequent incubation with BV605-, APC-, or APCy7-conjugated streptavidin. All FMO controls for C3 surface staining correspond to cells that were incubated with mAbs for the detection of lineage markers, including streptavidin-BV605/APC-Cy7/APC but no biotinylated anti-C3 Abs. All staining steps were

performed on ice (30 min) and isotype-matched control Abs were used where required. Cells were analyzed using a LSRFortessa flow cytometer (BD Biosciences) in the Melbourne Cytometry Platform (University of Melbourne) and FlowJo software (Tree Star) with exclusion of cell doublets and dead cells, in all cases identified on the basis of forward and side scatter (FSC and SSC) and propidium iodide (PI) staining (fig. S2).



Enumeration of cells via flow cytometry was performed using a defined number of Sphero blank calibration beads (BD Biosciences).

B cells were identified as CD19<sup>+</sup>B220<sup>+</sup>, CD4<sup>+</sup>T cells as CD3<sup>+</sup>CD4<sup>+</sup>, CD8<sup>+</sup>T cells as CD3<sup>+</sup>CD8<sup>+</sup>, pDCs as MHC II<sup>+</sup>CD11c<sup>+</sup>BST-2<sup>+</sup>Siglec H<sup>+</sup>, and cDCs as CD11c<sup>+</sup>MHC II<sup>+</sup>, with further discrimination of cDC1s as CD11b<sup>−</sup>CD8<sup>+</sup> and cDC2s as CD11b<sup>+</sup>CD8<sup>−</sup> (fig. S2). Macrophages were identified as F4/80<sup>+</sup>CD64<sup>+</sup>, neutrophils as B220<sup>−</sup>CD3<sup>−</sup>CD4<sup>−</sup>CD8<sup>−</sup>CD11c<sup>lo-int</sup>CD11b<sup>hi</sup>Ly6G<sup>+</sup>, and eosinophils as B220<sup>−</sup>CD3<sup>−</sup>CD4<sup>−</sup>CD8<sup>−</sup>CD11c<sup>lo-int</sup>CD11b<sup>hi</sup>Ly6G<sup>+</sup>SSC-H<sup>hi</sup>Ly6C<sup>lo-int</sup> (33).

#### Isolation of human blood DCs and analysis by flow cytometry

Blood samples from healthy donors ( $n = 10$ , male and female,  $45.8 \pm 15.9$  years of age) were obtained as buffy coats from the Australian Red Cross Lifeblood, Victoria, Australia, with written and informed consent from the donors and ethics approval from the University of Melbourne Human Research and Ethics Committee (#1035100). Whole blood samples from MHC II-deficient patients ( $n = 2$ , male, 11 and 15 years of age) were collected by staff of the Royal Children's Hospital, Victoria, Australia, with written and informed consent from the donors and ethics approval from the Royal Children's Hospital Research Ethics Committee (#33146) after receiving regular intravenous immunoglobulin (IVIg) infusions. Peripheral blood mononuclear cells (PBMCs) from both healthy donors as well as from MHC II-deficient patients were enriched using centrifugation (at 2237g) with Ficoll-Paque Plus (GE Healthcare). DCs were purified from PBMCs with the Pan-DC Enrichment Kit (Miltenyi Biotec) according to the manufacturer's instructions. In brief,  $10^8$  cells were stained with mAb to block FcR and incubated with a depletion Ab cocktail and magnetic microbeads to deplete Ab-labeled cells using LS magnetic columns and MidiMACS magnet (both Miltenyi Biotec). This resulted in 5 to 10% purity of cDCs (CD11c<sup>+</sup>HLA-DR<sup>+</sup>). For flow cytometry analysis, purified human DCs were washed in EDTA-BSS with 2% (v/v) FCS and incubated with mAb against CD1c (L161), CD11c (3.9), CD141 (M80), HLA-DR (LN3), CD123 (6H6), or lineage (lin) mAb cocktail against CD3, CD14, CD16, CD19, CD20, and CD56 (OKT3, M5E2, 3G8, HIB19, 2H7, and HCD56). cDC1s were identified as lin<sup>−</sup>CD11c<sup>int-hi</sup>CD123<sup>−</sup>CD141<sup>+</sup>CD1c<sup>−</sup>, cDC2s as lin<sup>−</sup>CD11c<sup>int-hi</sup>CD123<sup>−</sup>CD141<sup>−</sup>CD1c<sup>+</sup>, and pDCs as lin<sup>−</sup>CD11c<sup>int-hi</sup>CD11b<sup>−</sup>CD123<sup>+</sup> (fig. S5B). Cells were incubated with whole rabbit serum and cell surface C3 detected using biotinylated anti-C3-specific rabbit pAb (Abcam, ab48342) with subsequent incubation with APC-conjugated streptavidin, including appropriate controls to ensure specificity (fig. S5C). Cells were analyzed using an LSRFortessa (BD Biosciences) and FlowJo software (Tree Star) with exclusion of

cell doublets and dead cells in all cases identified on the basis of FSC and SSC and staining with PI.

#### RNA sequencing and transcriptomic analysis

Splenic cDC1s, B cells, and CD11c<sup>int</sup>CD24<sup>+</sup>CD8<sup>int</sup> cells from four biological replicates with pooled spleens from five wild-type or *March11<sup>−/−</sup>* mice per replicate were sorted (95 to 99% purity) with the Influx Cell Sorter (BD Biosciences) at Murdoch Children's Research Institute, Royal Children's Hospital, Victoria, Australia. Genomic DNA was removed and total RNA extracted using the RNeasy Mini Kit (Qiagen). RNA quality was assessed via Agilent Bioanalyzer 2100 using the Agilent RNA 6000 Nano Kit (Agilent Technologies) and rRNA depletion and library preparation were performed according to manufacturer protocols (TruSeq, Illumina) at the Australian Genome Research Facility (AGRF), Victoria, Australia. Whole-transcriptome sequencing was undertaken using Illumina Hi Seq 2500 (Illumina, San Diego, CA) at the AGRF in replicates on two lanes. All 100-base pair single-end reads were mapped to the reference mouse genome (GRCm38/mm10) using STAR aligner (version 2.7) (34), and gene-wise counts were obtained using Subread package (v1.6.2) (35). Differential expression analysis of RNA sequencing data was carried out in Galaxy/Australia (usegalaxy.org.au, Melbourne Bioinformatics) (36) using the differential expression tool (Trinity assembly) (37, 38) and in RStudio (version 1.1.447)/R (version 3.6.1) using the edgeR (version 3.26.6) (39) and limma (version 3.40.2) (40) packages. Gene counts were converted to log<sub>2</sub> counts per million and normalized using the trimmed mean of M-values normalization method in edgeR (41). Precision weights were applied with the "voom" function (42) of the limma package, and a linear model was fitted to each gene correcting for inter-replicate variation. Empirical Bayes-moderated *t* statistics were used to assess differences in gene expression and determine *P* values. Differences in expression levels were evaluated using a linear model on replicates, with samples compared across the different groups. Genes were corrected for multiple testing, and genes having a false discovery rate (FDR) of <0.05 using the decideTest function (43) in limma were considered significant. Gene set analysis was performed using the fast implementation of rotation gene set testing (44) (FRY in limma) for B cell signatures—GO:0042113 for B cell activation and BCR signaling pathway (Biocarta) from the Molecular Signatures Database (org.Mm.db version 3.12.0). RNA-seq data from this study were deposited in GEO under accession number 185597.

#### In vitro trogocytosis assay

In vitro trogocytosis assays were carried out as described (9), excluding Ag priming. In brief,

$2 \times 10^5$  B cells and  $3 \times 10^5$  cDCs purified from spleens were cocultured in RPMI media supplemented with 10% (v/v) FCS (Sigma),  $1 \times$  GlutaMAX (Gibco), penicillin (100 U/ml), streptomycin (100 µg/ml; Media Preparation Unit, Peter Doherty Institute, Victoria, Australia), and 50 µM β-mercaptoethanol (Life Technologies) in 96-well U-bottom cell culture plates for 2 hours at 37°C after quick centrifugation at 150g to promote cell contact. In some experiments, either cDCs or B cells were stained with PKH26 Red Fluorescent Cell Linker according to the manufacturer's instructions (Sigma Aldrich). After incubation, cells were washed in EDTA-BSS with 2% (v/v) FCS to disrupt intercellular clusters and analyzed by flow cytometry as described above.

#### Mixed-bone marrow chimeric mice

Bone marrow (BM) was harvested from tibia and femur of donor mice (wild-type, *March11<sup>−/−</sup>*, and *Ct2<sup>−/−</sup>*), and recipient mice (wild-type and *C3<sup>−/−</sup>*) were irradiated twice at 550 cGy (rad), 3 hours apart, before intravenously injected with 50:50 mixed BM cells. Recipient mice were intraperitoneally injected with anti-Thy1 (clone T24) to eliminate radio-resistant host T cells the day after irradiation. Mice were reconstituted for at least 8 weeks before use.

#### Immunoblotting, immunoprecipitation, and PNGase F treatment of MHC II and C3

cDCs purified from Flt3L-expanded mice (45) were lysed on ice in 1% (v/v) IGEPAL CA-630 (Sigma-Aldrich), 50 mM Tris (pH 7.5; Astral Scientific), 5 mM magnesium chloride (Chem-Supply), and cOmplete protease inhibitor cocktail (Roche) at a concentration of  $10^7$  cells/ml, and nuclei were removed by centrifugation at 14,000g at 4°C. For immunoprecipitation of MHC II and C3, lysates were precleared twice by incubation with uncoupled protein G-sepharose beads (Walter and Eliza Hall Institute, WEHI) in the presence of normal rabbit serum. To immunoprecipitate MHC II or C3, protein G-sepharose beads were precoupled with anti-I-A/I-E (clone M5/115) mAb (10 µg per  $10^7$  cells) or anti-C3dg (clone 3d29) mAb (5 µg per  $10^7$  cells) and added to the lysate. To eluate MHC II/C3 from protein G-sepharose beads for immunoblot analysis, beads were incubated in 3× SDS (reducing) sample buffer at 95°C. For deglycosylation of MHC II molecules, treatment with PNGase F was carried out according to manufacturer's instructions (New England BioLabs). In brief, washed protein G-sepharose beads with mAb-bound MHC II molecules were incubated with denaturing buffer followed by incubation with 500 U of PNGase F in  $1 \times$  GlycoBuffer containing 1% NP-40.

For analysis of MHC II and C3 by immunoblotting, serum samples, whole-cell lysates or immunoprecipitates from equal cell numbers were separated on a precast NuPAGE gel (4 to

12% Bis-Tris Plus) and transferred to iBlot 2 PVDF membranes with an iBlot 2 system according to manufacturer's instructions (all Invitrogen). Samples were probed for C3 with anti-C3 pAb from rabbit serum (HP8012, Hycult) or MHC II with anti-I-A $\alpha$ - or anti-I-A $\beta$ -specific pAb from rabbit serum JV1 and JV2 (WEHI antibody facility) followed by HRP-coupled secondary antibodies with the appropriate species reactivities. Chemiluminescence was measured using the ECL Select Western Blotting reagent (Amersham GE Healthcare), acquired on a ChemiDoc MP imaging system (Bio-Rad) and ImageJ.

### Mass spectrometry

Immunoprecipitated MHC II was analyzed using a precast NuPAGE gel (4 to 12% Bis-Tris Plus, Invitrogen) and stained using Coomassie Brilliant Blue R-250 (Bio-Rad). Bands of interest were excised and subjected to reduction, alkylation, and trypsin digestion before mass spectrometry (MS) as described (46). In brief, excised gel samples were destained in 50 mM ammonium bicarbonate dissolved in 50% (v/v) acetonitrile, reduced with 10 mM dithiothreitol (DTT), and then alkylized with 55 mM iodoacetamide. Air-dried gel pieces were incubated with trypsin (15 ng/ $\mu$ l, Promega) in 25 mM ammonium bicarbonate for ~16 hours at 37°C and peptides were extracted through incubation with 0.1% (v/v) formic acid in 60% acetonitrile.

Mass spectrometry and data analysis were carried out at the WEHI Proteomic Laboratory (Webb laboratory), Victoria, Australia. Extracted peptides were separated by reverse-phase chromatography on a 1.9- $\mu$ m C18 fused silica column (I.D. 75  $\mu$ m, O.D. 360  $\mu$ m  $\times$  25 cm length) packed into an emitter tip (Ion Opticks, Australia), using a nano-flow HPLC (M-class, Waters). The HPLC was coupled to an Impact II UHR-QqTOF mass spectrometer (Bruker) using a CaptiveSpray source and nanoBooster at 0.20 bar using acetonitrile. Peptides were loaded directly onto the column at a constant flow rate of 400 nl/min with buffer A (99.9% Milli-Q water, 0.1% formic acid) and eluted with a 90-min linear gradient from 2 to 34% buffer B (99.9% acetonitrile, 0.1% formic acid). Mass spectra were acquired in a data-dependent manner including an automatic switch between MS and MS/MS scans using a 1.5-s duty cycle and 4-Hz MS1 spectra rate followed by MS/MS scans at 8 to 20 Hz dependent on precursor intensity for the remainder of the cycle. MS spectra were acquired within a mass range of 200 to 2000  $m/z$ . Peptide fragmentation was performed using collision-induced dissociation (CID).

All raw files were analyzed by MaxQuant (1.6.5) software using the integrated Andromeda search engine. Experiment type was set as TIMS-DDA with no modification to default settings. Data were searched against the mouse Uniprot Reference Proteome with isoforms and

a separate reverse decoy database using a strict trypsin specificity allowing up to two missed cleavages. The minimum required peptide length was seven amino acids.

### Immunization with IEp/OVA-conjugated Clec9A mAb for YAE detection and ex vivo antigen presentation assay

IEp (Ea<sub>52-68</sub>)-loaded I-Ab surface expression, as detected by biotinylated YAE mAb (16) (Thermo Fisher), was analyzed at the surface of cDCs and B cells after intravenous injection of mice with 0.5  $\mu$ g of anti-Clec9A-IEp (clone 10B4) (47) or isotype-IEp mAb. The IEa epitope (I-Ea<sub>46-72</sub>) was cloned in-frame with the heavy chain C terminal region of the Clec9A mAb (clone 10B4) or isotype mAb via alanine linkers. After 22 to 24 hours, splenic cDCs and B cells were examined for IEp (Ea<sub>52-68</sub>)-loaded I-Ab surface expression by flow cytometry using biotinylated YAE mAb and streptavidin-PE. FMO controls for YAE surface staining correspond to cells that were incubated with mAb for the detection of lineage markers, including streptavidin-PE but not biotinylated YAE mAb.

For ex vivo antigen presentation assays, mice were intravenously injected with 1  $\mu$ g of Clec9A-OVA mAb. After 22 to 24 hours, spleen MZ and follicular (FO) B cells were sorted to purity. OT-II cells were purified from lymph nodes and labeled with 2  $\mu$ M CellTrace Violet (CTV), and  $5 \times 10^4$  cells per well were cultured with isolated FO or MZ B cells in U-bottom 96-well plates for 90 hours. Proliferated OT-II cells were determined by flow cytometry as the number of CD4<sup>+</sup>TCRV $\alpha$ 2<sup>+</sup> cells that had undergone CTV dilution.

### REFERENCES AND NOTES

- J. A. Villadangos, Presentation of antigens by MHC class II molecules: Getting the most out of them. *Mol. Immunol.* **38**, 329–346 (2001). doi: [10.1016/S0161-5890\(01\)00069-4](#); pmid: [11684289](#)
- H. Liu, J. D. Mintern, J. A. Villadangos, MARCH ligases in immunity. *Curr. Opin. Immunol.* **58**, 38–43 (2019). doi: [10.1016/j.coi.2019.03.001](#); pmid: [31063934](#)
- K. R. Wilson et al., MARCH1-mediated ubiquitination of MHC II impacts the MHC I antigen presentation pathway. *PLOS ONE* **13**, e0200540 (2018). doi: [10.1371/journal.pone.0200540](#); pmid: [30001419](#)
- H. J. Kim et al., Ubiquitination of MHC Class II by March-I Regulates Dendritic Cell Fitness. *J. Immunol.* **206**, 494–504 (2021). doi: [10.4049/jimmunol.2000975](#); pmid: [33318291](#)
- V. M. Holers, Complement and its receptors: New insights into human disease. *Annu. Rev. Immunol.* **32**, 433–459 (2014). doi: [10.1146/annurev-immunol-032713-120154](#); pmid: [24499275](#)
- M. K. Pangburn, V. P. Ferreira, C. Cortes, Discrimination between host and pathogens by the complement system. *Vaccine* **26** (Suppl 8), I15–I21 (2008). doi: [10.1016/j.vaccine.2008.11.023](#); pmid: [19388159](#)
- F. Bexborn, P. O. Andersson, H. Chen, B. Nilsson, K. N. Ekdahl, The tick-over theory revisited: Formation and regulation of the soluble alternative complement C3 convertase (C<sub>3</sub>(H<sub>2</sub>O)Bb). *Mol. Immunol.* **45**, 2370–2379 (2008). doi: [10.1016/j.molimm.2007.11.003](#); pmid: [18096230](#)
- A. Cerutti, M. Cols, I. Puga, Marginal zone B cells: Virtues of innate-like antibody-producing lymphocytes. *Nat. Rev. Immunol.* **13**, 118–132 (2013). doi: [10.1038/nri3383](#); pmid: [23348416](#)

- S. Daubeuf, A.-L. Puaux, E. Joly, D. Hudrisier, A simple trogocytosis-based method to detect, quantify, characterize and purify antigen-specific live lymphocytes by flow cytometry, via their capture of membrane fragments from antigen-presenting cells. *Nat. Protoc.* **1**, 2536–2542 (2006). doi: [10.1038/nprot.2006.400](#); pmid: [17406507](#)
- E. Joly, D. Hudrisier, What is trogocytosis and what is its purpose? *Nat. Immunol.* **4**, 815–815 (2003). doi: [10.1038/nri0903-815](#); pmid: [12942076](#)
- D. M. Davis, Intercellular transfer of cell-surface proteins is common and can affect many stages of an immune response. *Nat. Rev. Immunol.* **7**, 238–243 (2007). doi: [10.1038/nri2020](#); pmid: [17290299](#)
- P. Schriek et al., Physiological substrates and ontogeny-specific expression of the ubiquitin ligases MARCH1 and MARCH8. *Curr. Res. Immunol.* **2**, 218–228 (2021). doi: [10.1016/j.crimmu.2021.10.004](#)
- Z. Zhou, M.-J. Xu, B. Gao, Hepatocytes: A key cell type for innate immunity. *Cell. Mol. Immunol.* **13**, 301–315 (2016). doi: [10.1038/cmi.2015.97](#); pmid: [26685902](#)
- M. Ohmura-Hoshino et al., Cutting edge: Requirement of MARCH-I-mediated MHC II ubiquitination for the maintenance of conventional dendritic cells. *J. Immunol.* **183**, 6893–6897 (2009). doi: [10.4049/jimmunol.0902178](#); pmid: [19917682](#)
- W. Wisniewski et al., Novel mutations in the RFXANK gene: RFX complex containing in-vitro-generated RFXANK mutant binds the promoter without transactivating MHC II. *Immunogenetics* **54**, 747–755 (2003). doi: [10.1007/s00251-002-0521-1](#); pmid: [12618906](#)
- Rudenski AYU, S. Rath, P. Preston-Hurlburt, D. B. Murphy, C. A. Janeway Jr., On the complexity of self. *Nature* **353**, 660–662 (1991). doi: [10.1038/353660a0](#); pmid: [1656278](#)
- I. Caminschi et al., The dendritic cell subtype-restricted C-type lectin Clec9A is a target for vaccine enhancement. *Blood* **112**, 3264–3273 (2008). doi: [10.1182/blood-2008-05-155176](#); pmid: [18669894](#)
- J. Banchereau, R. M. Steinman, Dendritic cells and the control of immunity. *Nature* **392**, 245–252 (1998). doi: [10.1038/32588](#); pmid: [9521319](#)
- W. R. Heath, Y. Kato, T. M. Steiner, I. Caminschi, Antigen presentation by dendritic cells for B cell activation. *Curr. Opin. Immunol.* **58**, 44–52 (2019). doi: [10.1016/j.coi.2019.04.003](#); pmid: [31071588](#)
- J. F. Kearney, P. Patel, E. K. Stefanov, R. G. King, Natural antibody repertoires: Development and functional role in inhibiting allergic airway disease. *Annu. Rev. Immunol.* **33**, 475–504 (2015). doi: [10.1146/annurev-immunol-032713-120140](#); pmid: [25622195](#)
- H. Liu et al., Ubiquitination of MHC Class II Is Required for Development of Regulatory but Not Conventional CD4<sup>+</sup> T Cells. *J. Immunol.* **205**, 1207–1216 (2020). doi: [10.4049/jimmunol.1901328](#); pmid: [32747505](#)
- S. J. Swiedler, G. W. Hart, A. L. Tarentino, T. H. Plummer Jr., J. H. Freed, Stable oligosaccharide microheterogeneity at individual glycosylation sites of a murine major histocompatibility antigen derived from a B-cell lymphoma. *J. Biol. Chem.* **258**, 11515–11523 (1983). doi: [10.1016/S0021-9258\(17\)44258-X](#); pmid: [6604728](#)
- S. E. Cullen, C. S. Kindle, D. C. Shreffler, C. Cowing, Differential glycosylation of murine B cell and spleen adherent cell Ia antigens. *J. Immunol.* **127**, 1478–1484 (1981). pmid: [6792276](#)
- S. F. Gonzalez et al., Capture of influenza by medullary dendritic cells via SIGN-R1 is essential for humoral immunity in draining lymph nodes. *Nat. Immunol.* **11**, 427–434 (2010). doi: [10.1038/ni.1856](#); pmid: [20305659](#)
- G. Cinamon, M. A. Zachariah, O. M. Lam, F. W. Foss Jr., J. G. Cyster, Follicular shuttling of marginal zone B cells facilitates antigen transport. *Nat. Immunol.* **9**, 54–62 (2008). doi: [10.1038/ni1542](#); pmid: [18037889](#)
- H. L. Matlung et al., Neutrophils Kill Antibody-Opsonized Cancer Cells by Trogocytosis. *Cell Rep.* **23**, 3946–3959.e6 (2018). doi: [10.1016/j.celrep.2018.05.082](#); pmid: [29949776](#)
- Y. Matsuki et al., Novel regulation of MHC class II function in B cells. *EMBO J.* **26**, 846–854 (2007). doi: [10.1038/sj.emboj.7601556](#); pmid: [17255932](#)
- Q. Shi et al., Complement C3-Deficient Mice Fail to Display Age-Related Hippocampal Decline. *J. Neurosci.* **35**, 13029–13042 (2015). doi: [10.1523/JNEUROSCI.1698-15.2015](#); pmid: [26400934](#)
- F. Köntgen, G. Süss, C. Stewart, M. Steinmetz, H. Bluethmann, Targeted disruption of the MHC class II Aa gene in C57BL/6 mice. *Int. Immunol.* **5**, 957–964 (1993). doi: [10.1093/intimm/5.8.957](#); pmid: [8398989](#)
- H. Molina et al., Markedly impaired humoral immune response in mice deficient in complement receptors 1 and 2. *Proc. Natl.*

- Acad. Sci. U.S.A.* **93**, 3357–3361 (1996). doi: [10.1073/pnas.93.8.3357](https://doi.org/10.1073/pnas.93.8.3357); pmid: [8622941](https://pubmed.ncbi.nlm.nih.gov/8622941/)
31. D. Vremec, K. Shortman, The isolation and identification of murine dendritic cell populations from lymphoid tissues and their production in culture. *Methods Mol. Biol.* **415**, 163–178 (2008). doi: [10.1007/978-1-59745-570-1\\_10](https://doi.org/10.1007/978-1-59745-570-1_10); pmid: [18370154](https://pubmed.ncbi.nlm.nih.gov/18370154/)
  32. J. M. Thurman *et al.*, Detection of complement activation using monoclonal antibodies against C3d. *J. Clin. Invest.* **123**, 2218–2230 (2013). doi: [10.1172/JCI65861](https://doi.org/10.1172/JCI65861); pmid: [23619360](https://pubmed.ncbi.nlm.nih.gov/23619360/)
  33. S. E. Liyanage *et al.*, Flow cytometric analysis of inflammatory and resident myeloid populations in mouse ocular inflammatory models. *Exp. Eye Res.* **151**, 160–170 (2016). doi: [10.1016/j.exer.2016.08.007](https://doi.org/10.1016/j.exer.2016.08.007); pmid: [27544307](https://pubmed.ncbi.nlm.nih.gov/27544307/)
  34. A. Dobin *et al.*, STAR: Ultrafast universal RNA-seq aligner. *Bioinformatics* **29**, 15–21 (2013). doi: [10.1093/bioinformatics/bts635](https://doi.org/10.1093/bioinformatics/bts635); pmid: [23104886](https://pubmed.ncbi.nlm.nih.gov/23104886/)
  35. Y. Liao, G. K. Smyth, W. Shi, The Subread aligner: Fast, accurate and scalable read mapping by seed-and-vote. *Nucleic Acids Res.* **41**, e108–e108 (2013). doi: [10.1093/nar/gkt214](https://doi.org/10.1093/nar/gkt214); pmid: [23558742](https://pubmed.ncbi.nlm.nih.gov/23558742/)
  36. E. Afgan *et al.*, The Galaxy platform for accessible, reproducible and collaborative biomedical analyses: 2018 update. *Nucleic Acids Res.* **46**, W537–W544 (2018). doi: [10.1093/nar/gky379](https://doi.org/10.1093/nar/gky379); pmid: [29790989](https://pubmed.ncbi.nlm.nih.gov/29790989/)
  37. D. Blankenberg, N. Coraor, G. Von Kuster, J. Taylor, A. Nekrutenko, Galaxy Team, Integrating diverse databases into a unified analysis framework: A Galaxy approach. *Database* **2011**, bar011–bar011 (2011). doi: [10.1093/database/bar011](https://doi.org/10.1093/database/bar011); pmid: [21531983](https://pubmed.ncbi.nlm.nih.gov/21531983/)
  38. C. Sloggett, N. Goonasekera, E. Afgan, BioBlend: Automating pipeline analyses within Galaxy and CloudMan. *Bioinformatics* **29**, 1685–1686 (2013). doi: [10.1093/bioinformatics/btt1199](https://doi.org/10.1093/bioinformatics/btt1199); pmid: [23630176](https://pubmed.ncbi.nlm.nih.gov/23630176/)
  39. M. D. Robinson, D. J. McCarthy, G. K. Smyth, edgeR: A Bioconductor package for differential expression analysis of digital gene expression data. *Bioinformatics* **26**, 139–140 (2010). doi: [10.1093/bioinformatics/btp616](https://doi.org/10.1093/bioinformatics/btp616); pmid: [19910308](https://pubmed.ncbi.nlm.nih.gov/19910308/)
  40. M. E. Ritchie *et al.*, limma powers differential expression analyses for RNA-sequencing and microarray studies. *Nucleic Acids Res.* **43**, e47 (2015). doi: [10.1093/nar/gkv007](https://doi.org/10.1093/nar/gkv007); pmid: [25605792](https://pubmed.ncbi.nlm.nih.gov/25605792/)
  41. M. D. Robinson, A. Oshlack, A scaling normalization method for differential expression analysis of RNA-seq data. *Genome Biol.* **11**, R25 (2010). doi: [10.1186/gb-2010-11-3-r25](https://doi.org/10.1186/gb-2010-11-3-r25); pmid: [20196867](https://pubmed.ncbi.nlm.nih.gov/20196867/)
  42. C. W. Law, Y. Chen, W. Shi, G. K. Smyth, voom: Precision weights unlock linear model analysis tools for RNA-seq read counts. *Genome Biol.* **15**, R29 (2014). doi: [10.1186/gb-2014-15-2-r29](https://doi.org/10.1186/gb-2014-15-2-r29); pmid: [24485249](https://pubmed.ncbi.nlm.nih.gov/24485249/)
  43. C. W. Law *et al.*, RNA-seq analysis is easy as 1-2-3 with limma, Glimma and edgeR. *F1000 Res.* **5**, 1408 (2016). doi: [10.12688/f1000research.9005.3](https://doi.org/10.12688/f1000research.9005.3); pmid: [27441086](https://pubmed.ncbi.nlm.nih.gov/27441086/)
  44. D. Wu *et al.*, ROAST: Rotation gene set tests for complex microarray experiments. *Bioinformatics* **26**, 2176–2182 (2010). doi: [10.1093/bioinformatics/btq401](https://doi.org/10.1093/bioinformatics/btq401); pmid: [20610611](https://pubmed.ncbi.nlm.nih.gov/20610611/)
  45. N. Mach *et al.*, Differences in dendritic cells stimulated in vivo by tumors engineered to secrete granulocyte-macrophage colony-stimulating factor or Flt3-ligand. *Cancer Res.* **60**, 3239–3246 (2000). pmid: [10866317](https://pubmed.ncbi.nlm.nih.gov/10866317/)
  46. J. R. Wiśniewski, A. Zougman, N. Nagaraj, M. Mann, Universal sample preparation method for proteome analysis. *Nat. Methods* **6**, 359–362 (2009). doi: [10.1038/nmeth.1322](https://doi.org/10.1038/nmeth.1322); pmid: [19377485](https://pubmed.ncbi.nlm.nih.gov/19377485/)
  47. Y. Kato *et al.*, Display of Native Antigen on cDC1 That Have Spatial Access to Both T and B Cells Underlies Efficient Humoral Vaccination. *J. Immunol.* **205**, 1842–1856 (2020). doi: [10.4049/jimmunol.2000549](https://doi.org/10.4049/jimmunol.2000549); pmid: [32839238](https://pubmed.ncbi.nlm.nih.gov/32839238/)

# ACKNOWLEDGMENTS

We thank S. Choo (Royal Children's Hospital, Melbourne, Australia) for human blood samples; A. I. Webb, L. F. Dagley, and G. Infusini (Advanced Technology and Biology Division, Walter and Eliza Hall Institute of Medical Research, Melbourne, Australia) for the mass spectrometry analyses; and S. Finch for reviewing the statistical analyses. Schematics were created with BioRender.com. **Funding:** National Health and Medical Research Council of Australia 1058193 (J.A.V.), National Health and Medical Research Council of Australia 1016629 (W.R.H., J.A.V.), National Health and Medical Research Council of Australia 1113293 (W.R.H.), Australian Research Council

DP110101383 (J.A.V.), Australian Research Council DP160103134 (J.A.V.), Human Frontier Science Program 0064/2011 (S.I., J.A.V.), National Health Institute R01 DK125823 (J.M.T., V.M.H.), NIH R01DK076690 (J.M.T.), and Australian Research Training Program Scholarship (P.S.). **Author contributions:** Conceptualization: J.A.V. Methodology: J.M.T., P.S., A.C.C., N.S.M., J.M., L.B., T.M.S., L.M.H., V.M.H., S.I., M.H.L., I.C., and W.R.H. Investigation: P.S., A.C.C., N.S.M., J.M., L.B., T.M.S., L.M.H., V.M.H., S.I., M.H.L., I.C., and W.R.H. Visualization: P.S., N.S.M., J.D.M., and J.A.V. Funding acquisition: W.R.H., S.I., and J.A.V. Project administration: J.A.V. Supervision: J.D.M. and J.A.V. Writing—original draft: P.S., J.D.M., and J.A.V. Writing—review and editing: P.S., J.D.M., and J.A.V. **Competing interests:** J.M.T. receives royalties from Alexion Pharmaceuticals Inc. and is a consultant for Q32 Bio Inc., a company developing complement inhibitors. He holds stock and will receive royalty income from Q32 Bio Inc. The authors declare no other competing interests. **Data and materials availability:** RNA-seq data from this study are deposited in GEO under accession number 185597. All other data needed to evaluate the conclusions in this paper are present in the manuscript or the supplementary materials. The *March1*<sup>-/-</sup> and MHC IIK<sup>R<sup>KL</sup>/KL</sup> mice used in this study were obtained from RIKEN Yokohama Institute under the terms of a materials transfer agreement (MTA) with the University of Melbourne. The anti-C3 antibodies were used under the terms of an MTA between the University of Colorado and the University of Melbourne. Patient samples were obtained under the terms of a research collaboration agreement between Melbourne Health and the University of Melbourne. Anti-Clec9A-IEp and anti-Clec9A-OVA mAbs are available upon establishment of an MTA with Monash University.

# SUPPLEMENTARY MATERIALS

[science.org/doi/10.1126/science.abf7470](https://science.org/doi/10.1126/science.abf7470)

Figs. S1 to S7  
Tables S1 to S4

17 November 2020; resubmitted 3 July 2021

Accepted 6 January 2022

[10.1126/science.abf7470](https://doi.org/10.1126/science.abf7470)



## RESEARCH ARTICLE SUMMARY

## CELL BIOLOGY

## Mechanism of spindle pole organization and instability in human oocytes

Chun So, Katerina Menelaou<sup>†</sup>, Julia Uraji<sup>†</sup>, Katarina Harasimov, Anna M. Steyer, K. Bianka Seres, Jonas Bucevičius, Gražvydas Lukinavičius, Wiebke Möbius, Claus Sibold, Andreas Tandler-Schneider, Heike Eckel, Rüdiger Moltrecht, Martyn Blayney, Kay Elder, Melina Schuh\*

**INTRODUCTION:** Many human eggs carry an incorrect number of chromosomes, a condition known as aneuploidy. Aneuploidy in human eggs is the leading cause of aberrant embryonic development, resulting in pregnancy loss and genetic disorders such as Down syndrome. Most aneuploidy results from chromosome segregation errors during the maturation of oocytes into fertilizable eggs. Unlike somatic cells, human oocytes segregate chromosomes with a specialized microtubule spindle that lacks centrosomes. Previous live-imaging studies revealed that human oocytes often assemble spindles with unstable poles, favoring chromosome segregation errors. The causes of high spindle instability in human oocytes were unknown.

**RATIONALE:** Identifying the causes of spindle instability may lead to therapeutic strategies that reduce chromosome segregation errors in human eggs and improve outcomes of assisted reproductive technology. We thus set out to investigate how spindle poles are organized in the absence of centrosomes and why spindles are unstable in human oocytes. To this end, we systematically studied the localization and function of proteins that are required for spindle pole assembly or spindle stability in oocytes of different mammalian species. In stark contrast to human oocytes, the spindles of other mammalian oocytes were stable. We

thus carried out a comparative analysis to investigate whether differences in molecular composition can explain the high degree of spindle instability in human oocytes.

**RESULTS:** Spindle pole assembly requires the bundling of parallel microtubules by microtubule cross-linking proteins as well as stabilization and/or anchoring of microtubule minus ends in the spindle pole region by minus end-binding proteins. We found that the microtubule cross-linking protein NUMA (nuclear mitotic apparatus protein) localized to microtubule minus ends, where it recruited the molecular motor dynein for spindle pole focusing. Depletion of NUMA or inhibition of dynein splayed microtubule minus ends, demonstrating that NUMA and dynein organize the spindle poles in human oocytes.

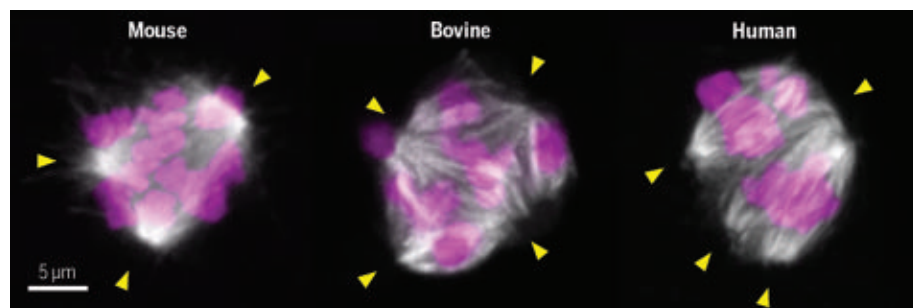
NUMA was similarly enriched at the spindle poles in bovine and porcine oocytes, which naturally lack centrosomes, as well as in mouse oocytes that we artificially depleted of acentriolar microtubule organizing centers (aMTOCs). We thus asked whether spindle instability is a general feature of mammalian oocytes that use NUMA for spindle pole organization. Live imaging, however, revealed that bovine, porcine, and aMTOC-free mouse oocytes did not assemble unstable spindles, indicating that additional mechanisms stabilize spindles in these oocytes.

Using an RNA interference screen of proteins with diverse functions in spindle organization, we identified the molecular motor KIFC1 (kinesin superfamily protein C1) as a spindle-stabilizing factor that is present in other mammalian oocytes but deficient in human oocytes. Depletion of KIFC1 in other mammalian oocytes recapitulated the spindle instability of human oocytes, resulting in spindles with unstable poles and an increase in aneuploidy. To investigate further if the spindle instability in human oocytes was a result of KIFC1 deficiency, we injected recombinant KIFC1 protein into human oocytes and performed live imaging of spindle assembly. Introduction of exogenous KIFC1 stabilized the spindles and reduced chromosome segregation errors, confirming that KIFC1 deficiency contributes to spindle instability in human oocytes.

**CONCLUSION:** Our data reveal notable differences in spindle pole organization in different systems. In somatic cells, two centrosomes act as the main MTOCs and promote bipolar spindle assembly. In mouse oocytes, centrosomes are functionally replaced by aMTOCs. In other mammalian oocytes, including humans, NUMA is enriched at microtubule minus ends. NUMA primarily engages the motor activity of dynein but can also cross-link microtubules itself. These activities allow NUMA to cluster microtubule minus ends, and to thereby organize the spindle poles in the absence of centrosomes or aMTOCs.

Our data also elucidate a cause of spindle instability in human oocytes: Human oocytes are deficient in KIFC1, a key spindle-stabilizing protein in other mammalian oocytes and in cancer cells. KIFC1 stabilizes the spindle poles and prevents their fragmentation. This is likely achieved through the formation of static cross-links along parallel microtubules at the poles and the alignment of antiparallel microtubules in the central region of the spindle. Because human oocytes are deficient in KIFC1, we propose that the deficiency of these activities renders their spindles unstable.

By delivering a defined amount of KIFC1 protein into human oocytes, we were able to reduce spindle instability and the risk of aneuploidy in human oocytes. Thus, our data also reveal a potential method for increasing the fidelity of spindle assembly and chromosome segregation in human oocytes. ■



**Spindle instability in mammalian oocytes.** Depletion of the molecular motor KIFC1 in aMTOC-free mouse oocytes (left) and bovine oocytes (middle) resulted in multipolar spindles (gray) and chromosome (magenta) segregation errors, recapitulating the spindle instability of human oocytes (right), as shown in these immunofluorescence images. Conversely, introduction of exogenous KIFC1 stabilized the spindles in human oocytes, which are naturally deficient in KIFC1. Yellow arrowheads highlight multiple spindle poles.

The list of author affiliations is available in the full article online.

\*Corresponding author. Email: melina.schuh@mpinat.mpg.de

<sup>†</sup>These authors contributed equally to this work.

Cite this article as C. So *et al.*, *Science* 375, eabj3944 (2022). DOI: 10.1126/science.abj3944

**S** READ THE FULL ARTICLE AT  
<https://doi.org/10.1126/science.abj3944>

## RESEARCH ARTICLE

## CELL BIOLOGY

## Mechanism of spindle pole organization and instability in human oocytes

Chun So<sup>1</sup>, Katerina Menelau<sup>1,2†</sup>, Julia Uraj<sup>1,2†</sup>, Katarina Harasimov<sup>1</sup>, Anna M. Steyer<sup>3</sup>, K. Bianka Seres<sup>1,2</sup>, Jonas Bucevičius<sup>4</sup>, Gražvydas Lukinavičius<sup>4</sup>, Wiebke Möbius<sup>3,5</sup>, Claus Sibold<sup>6</sup>, Andreas Tandler-Schneider<sup>6</sup>, Heike Eckel<sup>7</sup>, Rüdiger Moltrecht<sup>7</sup>, Martyn Blayney<sup>2</sup>, Kay Elder<sup>2</sup>, Melina Schuh<sup>1,5\*</sup>

Human oocytes are prone to assembling meiotic spindles with unstable poles, which can favor aneuploidy in human eggs. The underlying causes of spindle instability are unknown. We found that NUMA (nuclear mitotic apparatus protein)-mediated clustering of microtubule minus ends focused the spindle poles in human, bovine, and porcine oocytes and in mouse oocytes depleted of acentriolar microtubule-organizing centers (aMTOCs). However, unlike human oocytes, bovine, porcine, and aMTOC-free mouse oocytes have stable spindles. We identified the molecular motor KIFC1 (kinesin superfamily protein C1) as a spindle-stabilizing protein that is deficient in human oocytes. Depletion of KIFC1 recapitulated spindle instability in bovine and aMTOC-free mouse oocytes, and the introduction of exogenous KIFC1 rescued spindle instability in human oocytes. Thus, the deficiency of KIFC1 contributes to spindle instability in human oocytes.

**A**neuploidy in human eggs is a leading cause of aberrant embryonic development, resulting in miscarriages and genetic disorders such as Down syndrome. Around 25 to 50% of human eggs are aneuploid, and the aneuploidy rate increases with maternal age (1). Until recently, it has remained unclear why human eggs are so prone to aneuploidy, even in young women. Recent studies of meiosis and chromosome segregation in live human oocytes have revealed that human oocytes often assemble highly unstable meiotic spindles during meiosis I (2). Bipolar spindles drive chromosome segregation in mitosis and meiosis, and their correct assembly is a prerequisite for accurate chromosome segregation. In human oocytes, the two spindle poles frequently widen and fragment, forming apolar and multipolar spindle intermediates (2). These unstable spindles often misalign and missegregate chromosomes (2) and have been linked to tridirectional division at anaphase I (3). However, the causes of spindle instability in human oocytes are still unknown. Also, human fertilized eggs (zygotes)

are prone to assembling multipolar spindles and undergo multipolar divisions (4–14). Identifying the causes of spindle instability may lead to therapeutic strategies that reduce chromosome segregation errors in human eggs and improve outcomes of assisted reproductive technology.

Spindle instability is extremely rare in normal mitotic cells, whose aneuploidy rates are much lower (15). Mitotic cells and oocytes assemble spindles differently. In mitosis, two centrosomes act as the main microtubule-organizing centers (MTOCs) (16) and stabilize the two spindle poles (17, 18). By contrast, oocytes of most species, including mammals, lack centrosomes (19–21). How spindle poles are organized in the absence of centrosomes has been studied mostly in nonmammalian oocytes and in mouse oocytes. In nonmammalian oocytes, spindle poles are focused by motor and nonmotor proteins that cross-link microtubules (22–29). In mouse oocytes, canonical centrosomes are functionally replaced by acentriolar MTOCs (aMTOCs) (30). The aMTOCs lack centrioles but contain many other components of centrosomes (31). They form ring-shaped clusters at the two spindle poles and represent major sites of microtubule nucleation and anchoring in mouse oocytes (30, 32–35).

The mechanism of spindle pole organization in nonrodent mammalian oocytes, including humans, cows, and pigs, remains unclear. Unlike mouse oocytes, oocytes from these species lack distinct aMTOC foci at their spindle poles (2, 36). Although studies of these oocytes have reported localization of a few proteins such as  $\gamma$ -tubulin and NUMA (nuclear mitotic apparatus protein) at the spindle poles (2, 37–40),

how these oocytes assemble their spindle poles and control their spindle polarity without centrosomes and aMTOCs remains poorly understood.

## Results

## NUMA organizes the spindle poles in human oocytes

To investigate how spindle poles are organized during meiosis I in human oocytes, we selected eight candidate proteins for analysis. Spindle pole assembly requires the bundling of parallel microtubules by microtubule cross-linking proteins (41, 42). In addition, microtubule minus ends can be anchored to MTOCs (43, 44) and/or stabilized by minus end-binding proteins (41, 42). We analyzed the localization of four minus end-binding proteins [ $\gamma$ -tubulin, CAMSAP3 (calmodulin-regulated spectrin-associated protein 3), KANSL3 (KAT8 regulatory NSL complex subunit 3), and MCRS1 (microspherule protein 1)] and four microtubule cross-linking proteins [ASPM (abnormal spindle-like microcephaly-associated protein), KIF11/EG5 (kinesin superfamily protein 11), NUMA, and TPX2 (targeting protein for Xklp2)] in human oocytes because these proteins associate with the spindle poles in mitotic cells (41, 42) and oocytes from diverse organisms (2, 31, 33, 37–40, 45–53).

As a general microtubule minus end-capping protein (54),  $\gamma$ -tubulin was enriched on microtubules at the spindle poles (fig. S1A), in line with the high abundance of microtubule minus ends at the poles. However,  $\gamma$ -tubulin was not enriched as distinct, micron-sized foci in human oocytes (fig. S1A), consistent with the observation that their spindles lack aMTOCs (2). CAMSAP3, KANSL3, MCRS1, and ASPM showed weak or no spindle localization and were not enriched at the poles (fig. S1A), suggesting that they are unlikely to be important for the organization of spindle poles in human oocytes. Whereas KIF11 and TPX2 were detected both along spindle microtubules and enriched at the poles (fig. S1A), NUMA staining was confined to the extreme region of the poles where minus ends of individual microtubules converge (Fig. 1A and movie S1). Imaging of the spindle in a vertical orientation confirmed that NUMA specifically associated with microtubule minus ends (Fig. 1B), making it a good candidate for organizing microtubule minus ends at the poles in human oocytes.

NUMA was localized at the poles throughout all stages of meiosis (Fig. 1, A and C). It was detected early before spindle bipolarization, suggesting that NUMA is recruited as soon as the poles are forming in human oocytes. Whereas two clusters of NUMA were detected in oocytes undergoing bidirectional anaphase I, three clusters of NUMA were detected in an oocyte undergoing tridirectional anaphase I (Fig. 1D). Thus, NUMA localization is related

<sup>1</sup>Department of Meiosis, Max Planck Institute for Multidisciplinary Sciences, Göttingen, Germany. <sup>2</sup>Bourn Hall Clinic, Cambridge, UK. <sup>3</sup>Electron Microscopy Core Unit, Department of Neurogenetics, Max Planck Institute for Multidisciplinary Sciences, Göttingen, Germany. <sup>4</sup>Chromatin Labeling and Imaging Group, Department of NanoBiophotonics, Max Planck Institute for Multidisciplinary Sciences, Göttingen, Germany. <sup>5</sup>Cluster of Excellence "Multiscale Bioimaging: from Molecular Machines to Networks of Excitable Cells" (MBExC), University of Göttingen, Göttingen, Germany. <sup>6</sup>Fertility Center Berlin, Berlin, Germany. <sup>7</sup>Kinderwunschzentrum Göttingen, Göttingen, Germany.

\*Corresponding author. Email: melina.schuh@mpinat.mpg.de

†These authors contributed equally to this work.

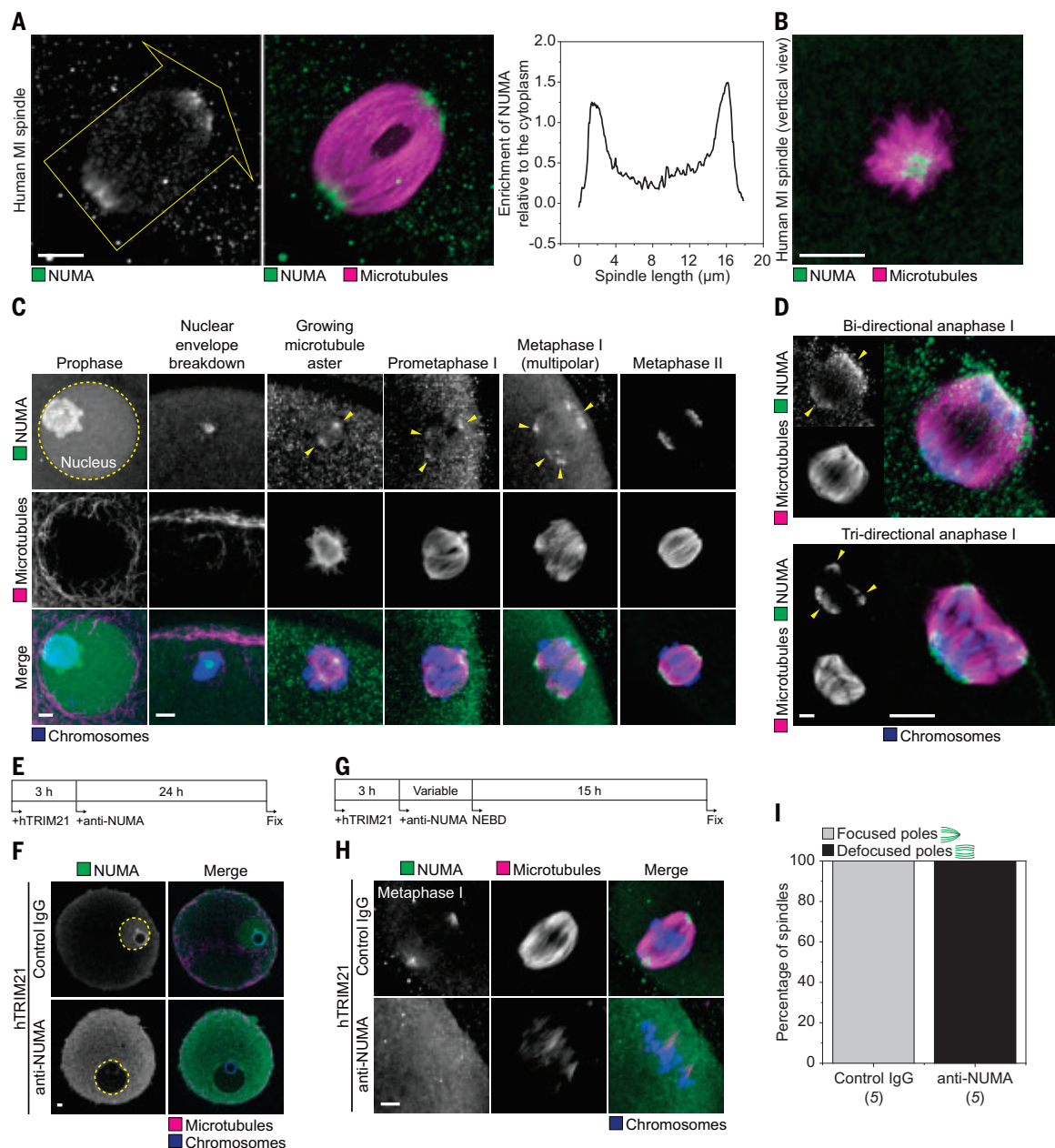


**Fig. 1. NUMA is required for pole focusing in human oocytes.** (A) Immunofluorescence images of a human meiosis I (MI) spindle fixed at 15 hours after NEBD. Green, NUMA; magenta, microtubules ( $\alpha$ -tubulin). The graph is the fluorescence profile of NUMA across the spindle along the direction of the yellow arrow. (B) Immunofluorescence image of a human MI spindle fixed at 15 hours after NEBD, imaged in a vertical orientation. Green, NUMA; magenta, microtubules ( $\alpha$ -tubulin). (C) Immunofluorescence images of human oocytes fixed at different stages of meiosis. Green, NUMA; magenta, microtubules ( $\alpha$ -tubulin), blue, chromosomes (Hoechst). (D) Immunofluorescence images of human oocytes undergoing bidirectional and tridirectional anaphase I. Green, NUMA; magenta, microtubules ( $\alpha$ -tubulin), blue, chromosomes (Hoechst). (E) Schematic diagram of the experiment in (F). (F) Immunofluorescence images of control and NUMA-depleted immature

human oocytes. Green, NUMA; magenta, microtubules ( $\alpha$ -tubulin); blue, chromosomes (Hoechst). Note that the higher cytoplasmic background in the oocyte injected with anti-NUMA in (F) was caused by the injected antibody but not due to perturbation of NUMA entry into the nucleus because the higher cytoplasmic background was consistently detected in the oocyte injected with anti-NUMA after NEBD in (H). (G) Schematic diagram of the experiment in (H). (H) Immunofluorescence images of MI spindles from control and NUMA-depleted human oocytes, fixed at 15 hours after NEBD. Green, NUMA; magenta, microtubules ( $\alpha$ -tubulin); blue, chromosomes (Hoechst). (I) Manual scoring of spindle pole defocusing in control and NUMA-depleted human MI oocytes (Fisher's exact test,  $P < 0.01$ ). The number of oocytes analyzed is specified in italics. Nuclei are outlined by yellow dashed line circles. Yellow arrowheads highlight prominent NUMA clusters. Scale bars are 5  $\mu$ m.

to the organization of spindle poles in human oocytes.

To test directly if NUMA is required for spindle pole organization, we depleted NUMA protein in human oocytes. Many proteins are

synthesized and deposited during oocyte growth, rendering RNA interference (RNAi) of proteins with low turnover inefficient in fully grown oocytes (55). Therefore, we used Trim-Away (56) to trigger acute degradation

of NUMA protein. NUMA was enriched in the nucleus before nuclear envelope breakdown (NEBD) in control oocytes, and this enrichment was lost upon Trim-Away of NUMA (Fig. 1, E and F). After NEBD, NUMA-depleted oocytes



no longer had NUMA at the spindle poles, and the poles became fully defocused (Fig. 1, G to I). Thus, NUMA is required for pole focusing in human oocytes.

***aMTOC-free mouse oocytes assemble spindles that mimic the morphology and organization of spindle poles in human oocytes***

Next, we investigated NUMA localization in bovine and porcine oocytes, which, like human oocytes, naturally lack aMTOCs. NUMA was similarly enriched at the microtubule minus ends in these nonrodent mammalian oocytes (fig. S1, B to E). By contrast, NUMA was hardly enriched at the spindle poles in mouse oocytes but weakly stained aMTOCs (fig. S1, F to I). To confirm that NUMA also marks microtubule minus ends in mouse oocytes, we tracked individual microtubules after depleting specific subpopulations of microtubules to facilitate analysis of the otherwise densely packed spindles. Kinetochore and interpolar microtubules account for most microtubules within the spindle. To enrich for kinetochore and interpolar microtubules, we performed cold treatment to selectively depolymerize non-kinetochore-bound microtubules (57) and acute NDC80/HEC1 depletion to depolymerize kinetochore-bound microtubules (58). Both kinetochore and interpolar microtubules ended at NUMA and aMTOCs (fig. S2 and movies S2 and S3), consistent with the model that NUMA anchors microtubules to aMTOCs in mouse oocytes (33).

Immature human oocytes are not available in large quantities, which makes it challenging to gain mechanistic insights into the organization of spindle poles and the causes of spindle instability during meiosis I. Mouse oocytes with spindles that more closely mimic the morphology and organization of spindle poles in human would be a useful model of human oocytes because mouse oocytes are readily available, progress through meiosis synchronously, and can be manipulated with genetic tools such as follicle RNAi (55). One main difference between mouse oocytes and other mammalian oocytes, including human, is the presence of aMTOCs (2). To ablate aMTOCs in immature mouse oocytes, we used Trim-Away to deplete PCNT (pericentrin), an essential scaffolding component of aMTOCs (59, 60) (fig. S3, A to D). In PCNT-depleted mouse oocytes, aMTOC components such as CEP192 (centrosomal protein of 192 kDa), CDK5RAP2 (CDK5 regulatory subunit-associated protein 2), and  $\gamma$ -tubulin were dispersed in the cytoplasm and no longer formed distinct foci at the spindle poles (fig. S3D), consistent with the successful ablation of aMTOCs (for simplicity, hereafter referred to as aMTOC-free mouse oocytes).

We used complementary approaches to confirm that the spindles assembled in aMTOC-free mouse oocytes mimic the spindles in

human oocytes. Spindle assembly in human oocytes is mediated by chromosomes and the small guanosine triphosphatase Ran (2). In this pathway, a chromosome-centered gradient of Ran-guanosine triphosphate (GTP) promotes microtubule nucleation in the proximity of chromosomes by locally releasing spindle assembly factors from inhibitory binding to importins (61). We found that microtubule nucleation occurred around chromosomes in aMTOC-free mouse oocytes (fig. S3E), similar to human oocytes (2). Dominant negative inhibition with RanT24N prevented microtubule nucleation and spindle assembly in aMTOC-free mouse oocytes (fig. S3, F and G). This is in contrast to wild-type mouse oocytes, in which RanT24N did not prevent microtubule nucleation and spindle assembly (fig. S3, H and I). Thus, spindle assembly in aMTOC-free mouse oocytes, as in human oocytes, is dependent on the Ran pathway. Furthermore, the localization patterns of several minus end-binding proteins and spindle pole-associated proteins were similar in human oocytes and in aMTOC-free mouse oocytes (figs. S1A and S3J). In particular, NUMA was highly enriched at microtubule minus ends in aMTOC-free mouse oocytes (Fig. 2A and fig. S4, A to C), as confirmed by cold treatment, acute NDC80 depletion, and immuno-electron microscopy (Fig. 2B; fig. S4, D to F; and movies S4 to S6). NUMA was enriched at the spindle poles at similar levels in human oocytes and in aMTOC-free mouse oocytes (fig. S4G), and in live imaging, NUMA was localized in a similar pattern in aMTOC-free mouse oocytes to that in human oocytes throughout meiosis (Fig. 1, A and C; fig. S4, H to J; and movie S7). Finally, we used Trim-Away to test whether NUMA is required to organize the spindle poles in aMTOC-free mouse oocytes. In wild-type mouse oocytes, perturbation of NUMA results in hyperfocused spindle poles, which coincides with the aggregation of aMTOCs (32, 33). By contrast, in aMTOC-free mouse oocytes, depletion of NUMA caused defocused spindle poles (Fig. 2, C to E; fig. S5, A to C; and movie S8), similar to those in human oocytes (Fig. 1H). As a result of spindle pole defocusing, the loose packing of spindle microtubules was also reflected by a significant decrease in the microtubule packing index (Fig. 2F), which measures how well microtubules fit into the space of a minimum bounding box surrounding the spindle. Thus, the spindles assembled in aMTOC-free mouse oocytes better mimic the spindles in human oocytes than those in wild-type mouse oocytes.

***NUMA forms a stable scaffold at aMTOC-free spindle poles***

NUMA anchors spindle pole microtubules to centrosomes in somatic cells (44, 62) and to aMTOCs in wild-type mouse oocytes (33), but these stable scaffolds are not present in human

oocytes and in aMTOC-free mouse oocytes. Because NUMA can self-assemble into stable oligomers in vitro (63, 64), we hypothesized that the NUMA enriched at the spindle poles could form a stable scaffold in the absence of aMTOCs.

This hypothesis predicts that NUMA would have a lower turnover in aMTOC-free mouse oocytes compared with wild-type mouse oocytes. To examine the dynamics of NUMA, we photoactivated NUMA at the pole-proximal, pole-distal, and cytoplasmic regions in wild-type and aMTOC-free mouse oocytes, similar to a previous study of  $\gamma$ -tubulin dynamics at the spindle poles in mitotic cells (65). Photoactivation of the pole-proximal region revealed a long-lived NUMA population in aMTOC-free mouse oocytes but not in wild-type mouse oocytes (fig. S5, D to G). By contrast, photoactivation of the pole-distal region revealed a distinct, short-lived NUMA population in both wild-type and aMTOC-free mouse oocytes (fig. S5, D to G). Because NUMA was weakly detected along kinetochore microtubules in both wild-type and aMTOC-free mouse oocytes (figs. S2, D and E; and S4, E and F), we propose that this short-lived population corresponds to the transient, dynamic NUMA cross-links recently reported on kinetochore microtubules (66, 67). Furthermore, photoactivated NUMA in the cytoplasm of aMTOC-free mouse oocytes was only incorporated in the pole-distal region (fig. S5, D to G), providing further support for the low turnover of NUMA at aMTOC-free spindle poles.

In mitotic cells, NUMA at the spindle poles forms insoluble aggregates upon microtubule depolymerization (68–72). To test whether NUMA forms similar cytoplasmic aggregates in aMTOC-free mouse oocytes, we depolymerized spindle microtubules acutely with nocodazole and prolonged cold treatment. However, NUMA did not persist as cytoplasmic foci upon microtubule depolymerization (fig. S5, H and I), suggesting that the associations between NUMA at the spindle poles are predominantly microtubule dependent. Thus, NUMA forms a stable scaffold at aMTOC-free spindle poles in a microtubule-dependent manner.

***NUMA and dynein-dynactin-LIS1 cluster microtubule minus ends at aMTOC-free spindle poles***

We exploited aMTOC-free mouse oocytes to further decipher how the stably associated NUMA organizes the spindle poles. NUMA has been proposed to organize the spindle poles by different mechanisms in different systems, either as a microtubule-cross-linking cargo that is transported to the poles by dynein-dynactin or as an adaptor that recruits dynein-dynactin to microtubule minus ends (25, 73–78).

To understand how NUMA drives pole focusing in the absence of aMTOCs, we depleted endogenous NUMA using follicle RNAi and

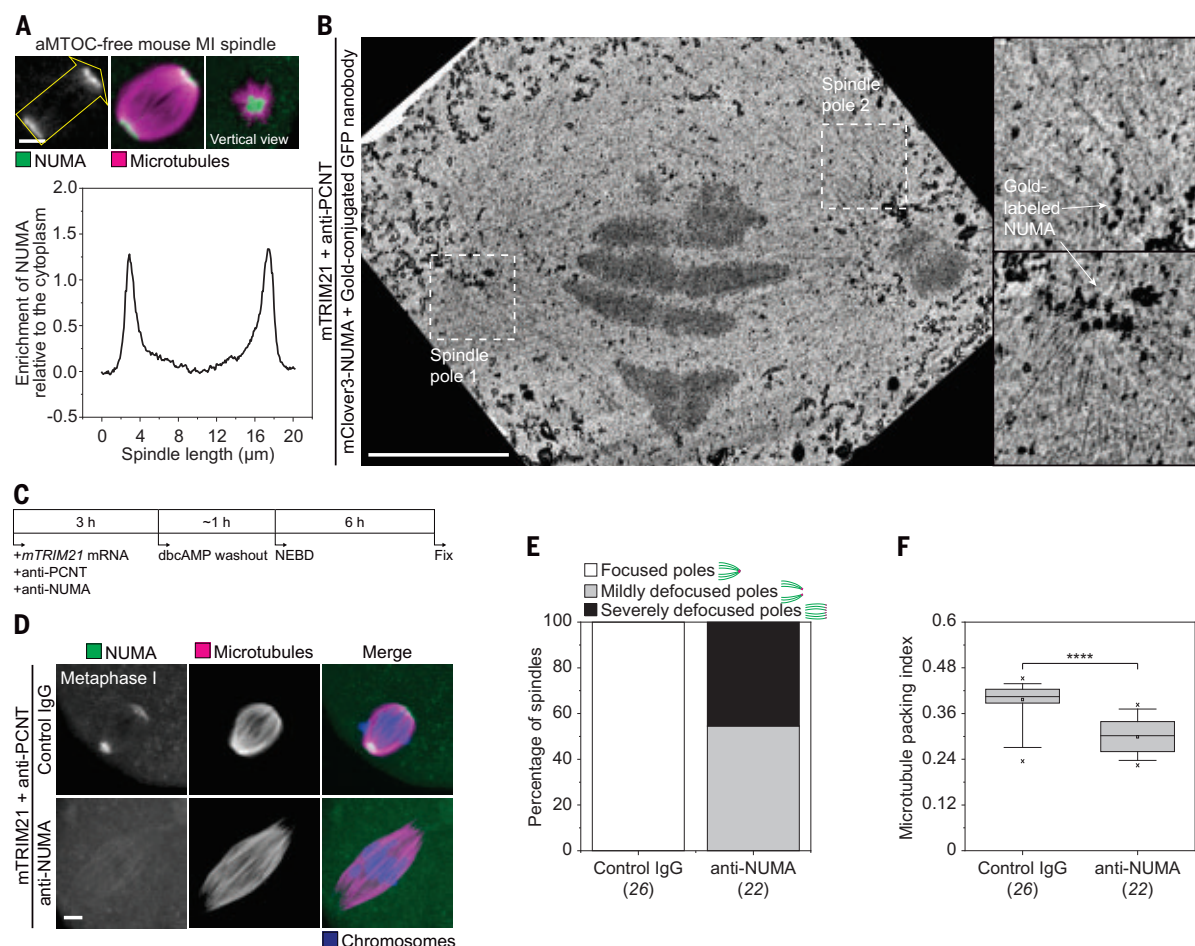


**Fig. 2. aMTOC-free mouse oocytes assemble spindles that mimic the morphology and organization of spindle poles in human oocytes.**

(A) Immunofluorescence images of MI spindles from aMTOC-free mouse oocytes fixed at 7 hours after release. Green, NUMA; magenta, microtubules ( $\alpha$ -tubulin). The graph is the fluorescence profile of NUMA across the spindle along the direction of the yellow arrow. (B) A single focused ion beam–scanning electron microscopy (FIB-SEM) section of a MI spindle from a mClover3-NUMA-expressing aMTOC-free mouse oocyte injected with gold-conjugated green fluorescent protein (GFP) nanobody shortly before fixation at 7 hours

after release. Insets are magnifications of regions marked by the dashed-line boxes. (C) Schematic diagram of the experiment in (D). (D) Immunofluorescence images of MI spindles from control and NUMA-depleted aMTOC-free mouse oocytes fixed at 7 hours after release. Green, NUMA; magenta, microtubules ( $\alpha$ -tubulin); blue, chromosomes (Hoechst). (E and F) Manual scoring (Fisher's exact test,  $P < 0.0001$ ) and automated quantification of spindle pole defocusing in control and NUMA-depleted aMTOC-free mouse MI oocytes. \*\*\*\* $P < 0.0001$ . See Materials and methods for box plot specifications. The number of oocytes analyzed is specified in italics. Scale bars are 5  $\mu$ m.

reexpressed four different NUMA mutants in aMTOC-free mouse oocytes (fig. S6, A to C). NUMA( $\Delta$ N) and NUMA(SpM-4A), which cannot interact with dynein-dynactin (79, 80), bound to microtubule minus ends but failed to rescue pole focusing (fig. S6, D to I). NUMA( $\Delta$ MTBD1), which cannot bind microtubule tips (81, 82), was not enriched at microtubule minus ends and failed to restore pole focusing (fig. S6, J to L). By contrast, NUMA( $\Delta$ MTBD2), which cannot bundle microtubules (83), bound to microtubule minus ends and partially restored pole focusing (fig. S6, J to L). Thus, spindle pole focusing in the absence of aMTOCs depends only partially on NUMA's microtubule cross-linking activity and predominantly on its binding to microtubule minus ends and to dynein-dynactin.

Indeed, NUMA was observed in proximity to dynein-dynactin at the spindle poles in aMTOC-free mouse oocytes (fig. S7, A to D). To examine the roles of dynein-dynactin in NUMA-mediated spindle pole focusing, we performed dominant negative inhibitions. We ectopically expressed the protein fragments P150-CC1, which binds dynein (84) and perturbs its interactions with dynactin's ARP1 filament (fig. S7, E to I), and NUMA-N, which does not oligomerize with endogenous NUMA (fig. S6A) but perturbs the interactions with dynein-dynactin (79). The aMTOC-free mouse oocytes expressing P150-CC1 and NUMA-N displayed similar phenotypes: NUMA remained bound to microtubule minus ends, but spindle poles became defocused (fig. S8, A to H; and movies S9 and S10). Moreover, when we

acutely injected recombinant P150-CC1 and NUMA-N into aMTOC-free mouse metaphase I oocytes, in which NUMA had already stably associated with microtubule minus ends (fig. S5, D and E), spindle poles became defocused (fig. S8, I to P). Thus, NUMA binds microtubule minus ends independently of dynein-dynactin but is insufficient to organize and maintain the spindle poles without dynein-dynactin.

The assembly of fully activated dynein complexes requires an additional cofactor LIS1 (85), which is also expressed in mammalian oocytes (31, 86). Similar to dynein and dynactin, LIS1 localized to the spindle poles in aMTOC-free mouse oocytes (fig. S9, A and B). To test whether LIS1 is also required for pole focusing, we used Trim-Away (fig. S9, C to E). Both

constitutive and acute depletion of LIS1 phenocopied dynein-dynactin inhibition and led to spindle pole defocusing in aMTOC-free mouse oocytes (fig. S9, F to M). To determine if dynein, dynactin, and LIS1 function together, we interfered with individual components, acutely perturbed their poleward transport during metaphase I with nocodazole, and examined their accumulation at kinetochores (87). PI50-CC1-mediated inhibition and LIS1 depletion, but not NUMA depletion, each disrupted the localization of dynein, dynactin, and LIS1 in aMTOC-free mouse oocytes (fig. S10). Thus, stably associated NUMA, together with a dynein-dynactin-LIS1 complex, clusters microtubule minus ends at aMTOC-free spindle poles.

#### ***Dynein-dynactin focuses the spindle poles in human oocytes***

To test whether our findings in aMTOC-free mouse oocytes translate to human oocytes, we first analyzed the localization of dynactin at different stages of meiosis in human oocytes. Dynactin was not recruited during early spindle assembly but localized predominantly to kinetochores and spindle microtubules before the metaphase spindle had assembled (Fig. 3A). At metaphase I and II, dynactin was most prominently detected at the spindle poles (Fig. 3, A and B). Dynactin was in proximity to LIS1 and NUMA at the spindle poles (Fig. 3B), in line with their localization in aMTOC-free mouse oocytes (figs. S7, A and B, and S9, A and B).

We then inhibited dynein-dynactin in human oocytes using PI50-CC1. NUMA remained bound to microtubule minus ends and spindle poles became defocused in dynein-inhibited human oocytes (Fig. 3, C to E), recapitulating our observations in aMTOC-free mouse oocytes (fig. S8, B to D). Thus, dynein-dynactin and possibly LIS1 are required for pole focusing in human oocytes.

#### ***Human oocytes are deficient in the molecular motor KIFC1/HSET***

Next, we asked whether spindle instability is a general feature of mammalian oocytes that lack aMTOCs and use NUMA for spindle pole organization. To this end, we performed live imaging of spindle assembly in bovine, porcine, and aMTOC-free mouse oocytes. These oocytes progressed through similar stages of spindle assembly as human oocytes (figs. S4, H and J, and S11, A and B; and movies S11 and S12). However, unstable spindle poles were observed in only 6% of bovine oocytes, 4.4% of porcine oocytes, and in none of the aMTOC-free mouse oocytes as compared to in 82% of human oocytes (2) (Fig. 3F and fig. S11, C and D). Thus, additional mechanism(s) must stabilize the spindles in nonhuman mammalian oocytes.

When we examined the defocused spindles in human and aMTOC-free mouse oocytes, we noticed that around 40% of the defocused spindles in human oocytes failed to align microtubules within the central region, whereas none of the defocused spindles in aMTOC-free mouse oocytes showed this misalignment (Fig. 3, G and H). Given that multipolar spindles were observed in a similar fraction of untreated human oocytes, but in none of the aMTOC-free mouse oocytes (Fig. 3, F and I), we hypothesized that human oocytes lack a spindle-stabilizing protein that is present in mouse, bovine, and porcine oocytes. Deficiency of this protein would thus lead to spindle instability and misalignment of microtubules within the central region of the human oocyte spindle.

We designed an RNAi screen to identify the protein that protects aMTOC-free mouse oocytes from misalignment of microtubules within the central region of the spindle. Specifically, we codepleted NUMA with one of 20 candidate proteins in aMTOC-free mouse oocytes using follicle RNAi. The candidate proteins included microtubule cross-linking proteins [ASPM, DLG5/HURP (discs large MAGUK scaffold protein 5), and TPX2] (42, 88), proteins related to spindle bipolarization [HAUS6 (HAUS augmin-like complex subunit 6), KIF11/EG5, KIF15/HKLP2 (kinesin superfamily protein 15), and KIFC1/HSET (kinesin superfamily protein C1)] (42, 89, 90), proteins related to microtubule dynamics [KIF2A (kinesin superfamily protein 2A), KIF18A (kinesin superfamily protein 18A), CENPE (centromere-associated protein E), CLASP1 (CLIP-associated protein 1), and CLASP2 (CLIP-associated protein 2)] (91, 92), and proteins related to bridging fibers and the central spindle [RACGAP1/CYK4 (Rac GTPase-activating protein 1), PRC1 (protein regulator of cytokinesis 1), KIF4A (kinesin superfamily protein 4A), KIF12 (kinesin superfamily protein 12), KIF14 (kinesin superfamily protein 14), KIF20A/MKLP2 (kinesin superfamily protein 20A), KIF20B/MPP1 (kinesin superfamily protein 20B), and KIF23/MKLP1 (kinesin superfamily protein 23)] (93, 94). Whereas oocytes codepleted of NUMA and DLG5, TPX2, or HAUS6 did not assemble a spindle, oocytes codepleted of NUMA and all other proteins except one assembled defocused spindles with aligned microtubules within the central region (Fig. 4A). Only oocytes codepleted of NUMA and KIFC1 failed to align microtubules within the central region of the spindle (Fig. 4A). This was further confirmed by an automated analysis of microtubule directionality, which uses pseudocolor to represent variations in the orientation of spindle microtubules (Fig. 4A).

To determine whether KIFC1 is deficient in human oocytes, we examined data from previous proteomics studies on mouse and human

oocytes (95, 96). We noticed that KIFC1 could only be detected in the mouse dataset. However, owing to different depths of proteome coverage for these two studies, we also analyzed *KIFC1* expression using data from previous RNA sequencing (RNA-seq) studies of mammalian oocytes and embryos (97–102). Mouse, bovine, and porcine oocytes had a prominent pool of maternal *KIFC1* messenger RNA (mRNA), which was depleted upon fertilization, and embryonic *KIFC1* mRNA was expressed from the two- to four-cell stage onward (fig. S12A). By contrast, *KIFC1* mRNA was barely detectable in human oocytes and zygotes but was readily expressed from the two- or four-cell stage onward in embryos (fig. S12, A and B). Such discrepancies in gene expression between different mammalian species were not observed for *NUMA* and for the conserved zona pellucida protein *ZP3* (fig. S12C).

We subsequently examined KIFC1 protein levels in oocytes and in asynchronized HeLa cells as a positive control for immunoblot (Fig. 4, B to D). To ensure comparable loading of oocyte lysate from different species, we performed on-blot total protein normalization, which outperformed the sensitivity and linearity of all canonical housekeeping proteins (Fig. 4B and fig. S13, A to G). Although we could readily detect KIFC1 in HeLa cell, mouse oocyte, bovine oocyte, and porcine oocyte lysates (Fig. 4C and fig. S13H), we could not detect KIFC1 in comparable amounts of human oocyte lysate (Fig. 4C). Only after overexposing the entire blot could we detect a very faint smear in the human oocyte lane (Fig. 4C). Thus, human oocytes are deficient in KIFC1.

#### ***Depletion of KIFC1 in aMTOC-free mouse oocytes and in bovine oocytes recapitulates the spindle instability of human oocytes***

To mimic the deficiency of KIFC1 in human oocytes, we depleted KIFC1 in aMTOC-free mouse oocytes and in bovine oocytes using follicle RNAi and Trim-Away, respectively. Around 35% of KIFC1-depleted aMTOC-free mouse oocytes assembled multipolar spindles (Fig. 5, A to C), as confirmed by the significant increase in the number of NUMA clusters per oocyte (Fig. 5D). Moreover, another 30% of KIFC1-depleted aMTOC-free mouse oocytes assembled round spindles with broad poles (Fig. 5, B and C). These spindles closely resembled the “apolar” spindles that have been observed in live human oocytes (2). Quantification of the total volume of NUMA clusters revealed no significant difference between control and KIFC1-depleted oocytes (Fig. 5E), suggesting that these pole defects are caused by the failure of NUMA clusters to coalesce rather than by the de novo assembly of additional NUMA clusters. Similarly, around 60 and 25% of KIFC1-depleted bovine oocytes



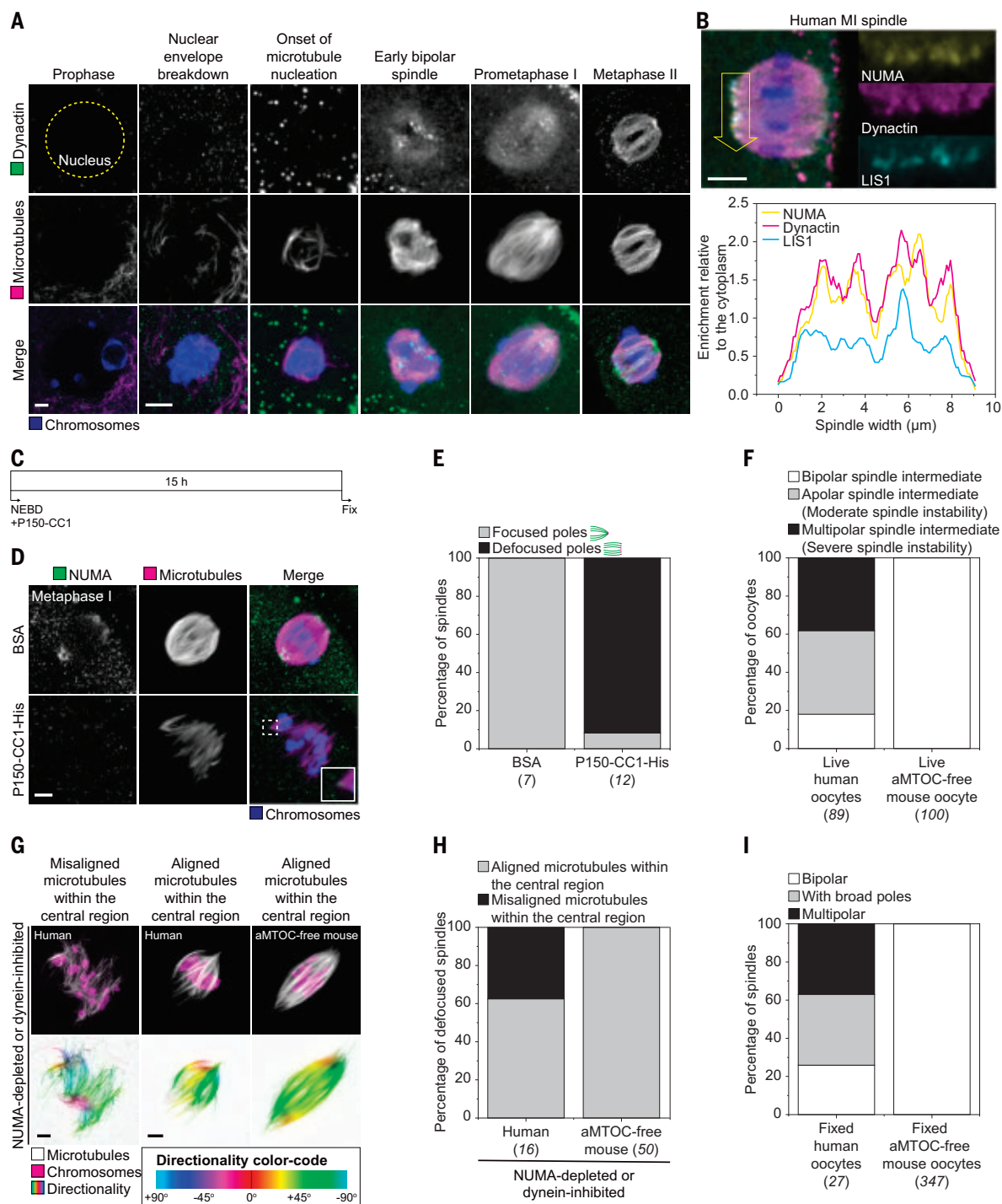


**Fig. 3. Human oocytes focus the spindle poles with dynein-dynactin but lack an additional mechanism that stabilizes the spindles in aMTOC-free mouse oocytes.** (A) Immunofluorescence images of human oocytes fixed at different stages of meiosis. Green, dynactin (P150); magenta, microtubules ( $\alpha$ -tubulin); blue, chromosomes (Hoechst). The nucleus is outlined by a yellow dashed-line circle. (B) Immunofluorescence images of a human MI spindle fixed at 15 hours after NEBD. Yellow, NUMA; magenta, dynactin (P150); cyan, LIS1. The graph is the fluorescence profile of NUMA, dynactin, and LIS1 across the spindle pole along the direction of the yellow arrow. (C) Schematic diagram of the experiment in (D). (D) Immunofluorescence images of MI spindles from human oocytes treated with BSA and P150-CC1-His, fixed at 15 hours after NEBD. Green, NUMA; magenta, microtubules ( $\alpha$ -tubulin); blue, chromosomes (Hoechst). The inset is the magnification of the region

marked by the white dashed-line box. (E) Manual scoring of spindle pole defocusing in control and dynein-inhibited human MI oocytes (Fisher's exact test,  $P < 0.001$ ). (F) Manual scoring of spindle polarity in live human oocytes from (2) and in aMTOC-free mouse oocytes from this study (Fisher's exact test,  $P < 0.0001$ ). (G) Immunofluorescence images of MI spindles from NUMA-depleted or dynein-inhibited human oocytes fixed at 15 hours after NEBD and aMTOC-free mouse oocytes fixed at 7 hours after release. Gray, microtubules ( $\alpha$ -tubulin); magenta, chromosomes (Hoechst); pseudocolor, directionality. (H) Manual scoring of the microtubule organization of the central region of the spindle in NUMA-depleted or dynein-inhibited human and aMTOC-free mouse MI oocytes (Fisher's exact test,  $P < 0.0001$ ). (I) Manual scoring of spindle polarity in fixed human and aMTOC-free mouse MI oocytes (Fisher's exact test,  $P < 0.0001$ ). For (E), (F), (H), and (I), the number of oocytes analyzed is specified in italics. Scale bars are 5  $\mu\text{m}$ .

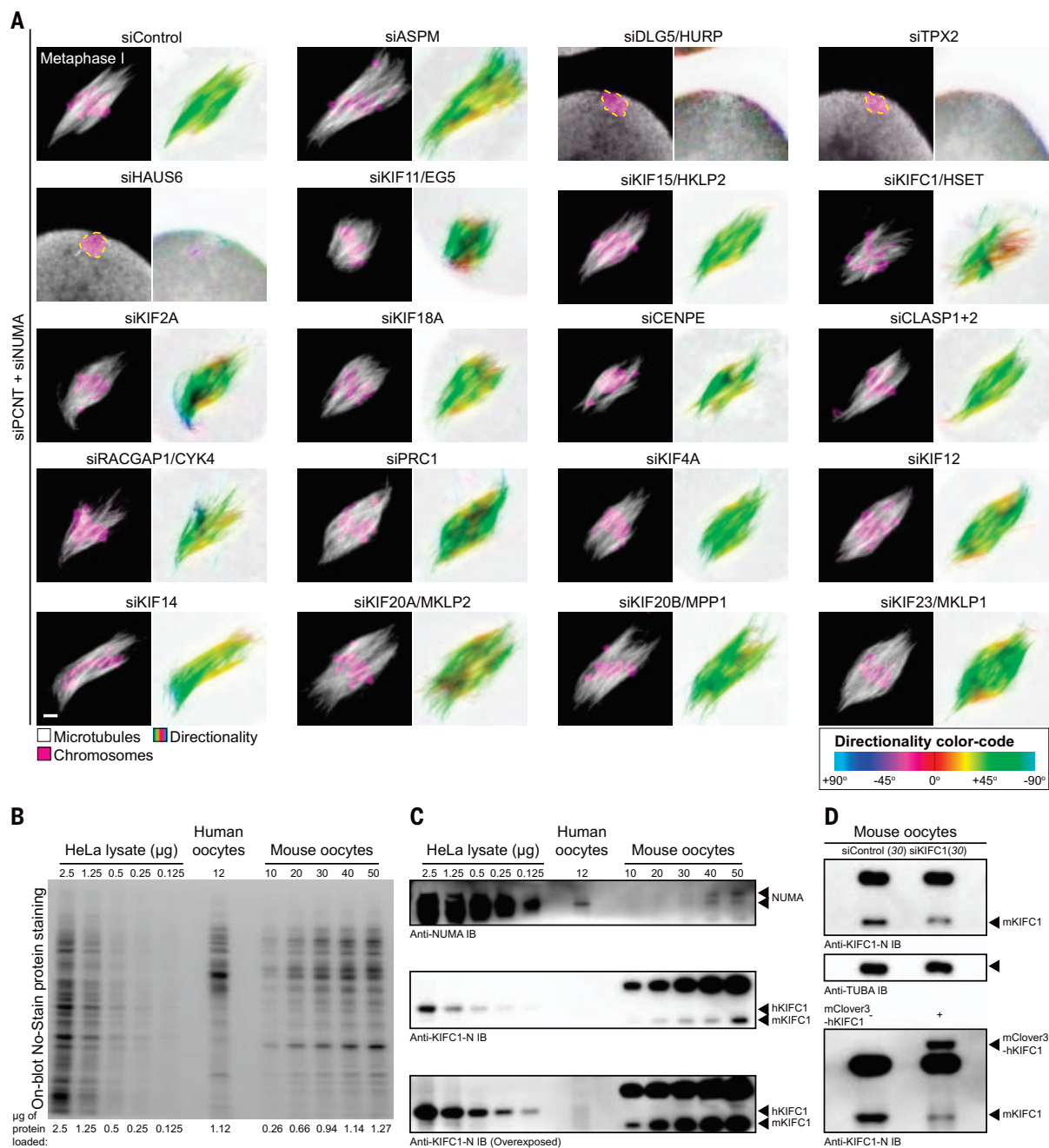


**Fig. 4. Human oocytes are deficient in the molecular motor KIFC1/HSET.**

(A) Immunofluorescence images of MI spindles from aMTOC-free mouse oocytes codepleted of NUMA and one of the 20 candidate proteins, fixed at 7 hours after release. Gray, microtubules ( $\alpha$ -tubulin); magenta, chromosomes (Hoechst); pseudocolor, directionality. For oocytes that did not assemble a spindle, chromosomes are outlined by yellow dashed lines. Scale bars are 5  $\mu$ m. (B) No-Stain protein staining for the blot of HeLa cell, human oocyte, and mouse oocyte lysates. The amount of HeLa cell lysate or the number of oocytes loaded is indicated

above each lane. The corresponding amount of protein loaded is indicated under each lane. (C) Immunoblots of HeLa cell, human oocyte, and mouse oocyte lysates. The two arrows in anti-NUMA IB mark NUMA with and without posttranslational modifications. (D) Immunoblots of control, KIFC1-depleted, and mClover3-KIFC1-expressing mouse oocytes. Human and mouse oocytes were lysed at 15 and 6 hours after NEBD, respectively. Black arrows mark the band corresponding to each protein. The number of oocytes loaded is specified in italics.

assembled multipolar spindles and spindles with broad poles, respectively (Fig. 5, F to H; and fig. S14, A and B). By contrast, codepletion of other members in the kinesin-14 family, KIFC2 and KIFC3, did not result in multipolar spindles and round spindles with broad poles

in aMTOC-free mouse oocytes (fig. S14, C and D). Thus, depletion of KIFC1 recapitulates the spindle instability of human oocytes.

To further investigate spindle assembly in the absence of KIFC1, we performed live imaging in KIFC1-depleted bovine oocytes.

Depletion of KIFC1 resulted in spindle instability in more than 95% of bovine oocytes and an increase in tridirectional division (Fig. 6, A to C; and movies S13 to S15). In human oocytes, 7 to 26% of oocytes underwent tridirectional division (2, 3) (Fig. 6C). By contrast, around

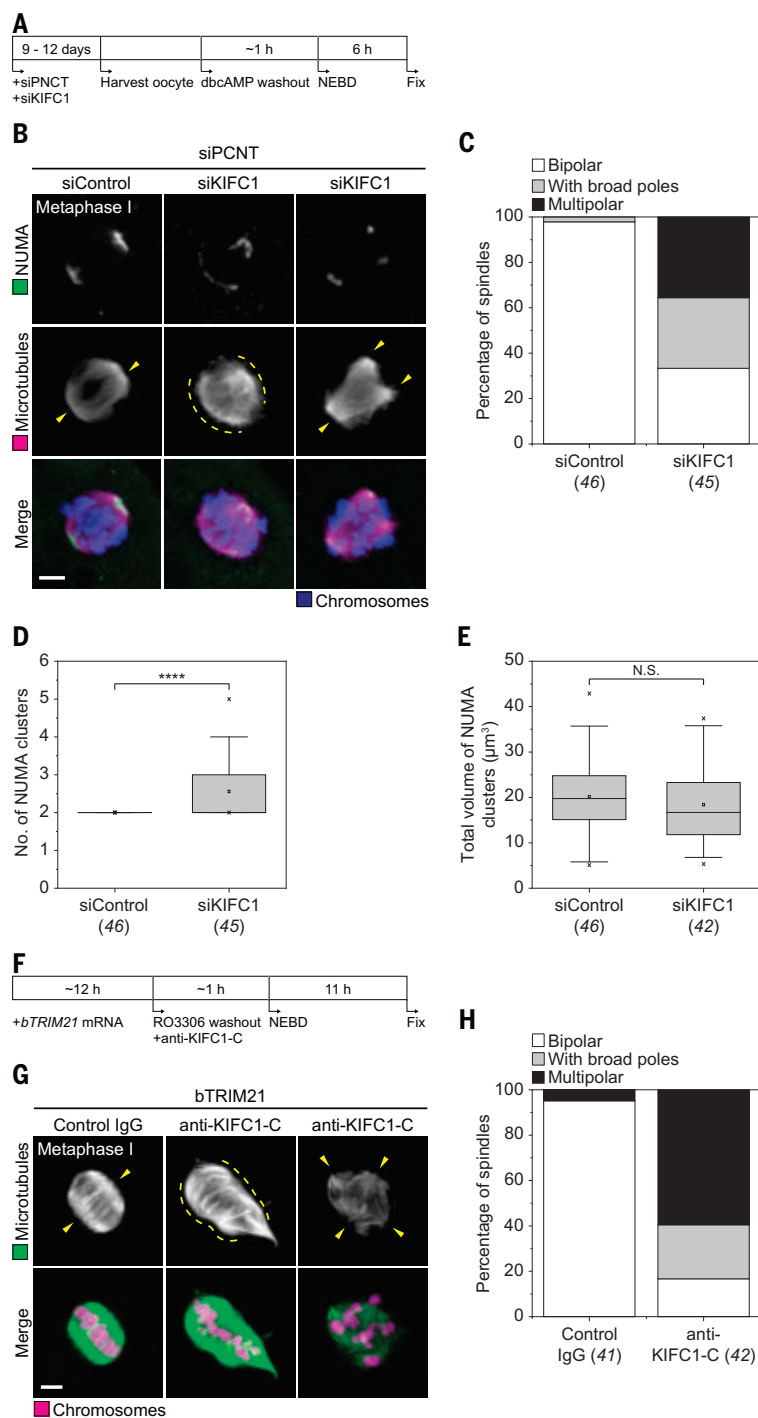


**Fig. 5. Depletion of KIFC1 in aMTOC-free mouse oocytes and in bovine oocytes recapitulates the spindle instability of human oocytes.** (A) Schematic diagram of the experiment in (B). (B) Immunofluorescence images of MI spindles from control and KIFC1-depleted aMTOC-free mouse oocytes, fixed at 7 hours after release. Green, NUMA; magenta, microtubules ( $\alpha$ -tubulin); blue, chromosomes (Hoechst). (C and D) Manual scoring (Fisher's exact test,  $P < 0.0001$ ) and automated quantification of spindle polarity in control and KIFC1-depleted aMTOC-free mouse MI oocytes. \*\*\*\* $P < 0.0001$ . (E) Quantification of the total volume of NUMA clusters in control and KIFC1-depleted aMTOC-free mouse MI oocytes. N.S., not significant. (F) Schematic diagram of the experiment in (G). (G) Immunofluorescence images of MI spindles from control and KIFC1-depleted bovine oocytes, fixed at 12 hours after release. Green, microtubules ( $\alpha$ -tubulin); magenta, chromosomes (Hoechst). (H) Manual scoring of spindle polarity in control and KIFC1-depleted bovine oocytes (Fisher's exact test,  $P < 0.0001$ ). Yellow arrowheads highlight well defined spindle poles. Yellow dashed lines highlight poorly defined spindle poles. The number of oocytes analyzed is specified in italics. See Materials and methods for box plot specifications. Scale bars are 5  $\mu\text{m}$ .

45% of KIFC1-depleted bovine oocytes underwent tridirectional division (Fig. 6C), which was likely because fewer oocytes restored spindle bipolarity at anaphase onset (Fig. 6D). Depletion of KIFC1 also resulted in misaligned chromosomes at anaphase onset and severely lagging chromosomes during anaphase in more than 75% of bovine oocytes (Fig. 6, E and F). In addition, chromosome counts at metaphase II revealed that only 6.5% of KIFC1-depleted bovine oocytes were euploid (Fig. 6G). Thus, depletion of KIFC1 results in spindle instability and promotes aneuploidy in mammalian oocytes that lack aMTOCs.

#### Introducing exogenous KIFC1 rescues spindle instability in human oocytes

To determine if the spindle instability in human oocytes is indeed caused by the deficiency of KIFC1, we purified recombinant mClover3-KIFC1 protein from human embryonic kidney (HEK) 293 cells, injected it into human immature oocytes, and performed live imaging of spindle assembly (Fig. 7, A and B; and movies S16 and S17). Successful delivery of exogenous KIFC1 was confirmed by mClover3 detection in live oocytes and immunofluorescence in fixed oocytes (Fig. 7, C and D). The duration of spindle instability was significantly reduced from around 10.5 hours in noninjected oocytes to around 3.5 hours in mClover3-KIFC1-injected oocytes (Fig. 7E). By contrast, introduction of mClover3-KIFC1 did not significantly alter the time of early spindle bipolarization and anaphase onset (Fig. 7, F and G), implying that KIFC1 is specifically required for spindle stability. Furthermore, introduction of mClover3-KIFC1 increased the frequency of oocytes with aligned chromosomes at anaphase onset from 44 to 75% (Fig. 7H) and the frequency of oocytes with no lagging chromosomes during anaphase from 33 to 63% (Fig. 7I). Thus, introducing exogenous KIFC1 rescues spindle instability and reduces the risk of aneuploidy in human oocytes.

#### KIFC1's cross-linking and sliding activities are required for proper bipolar spindle assembly in the absence of aMTOCs

KIFC1 is dispensable for spindle stability in wild-type mouse oocytes during meiosis I (103, 104). To understand how KIFC1 stabilizes aMTOC-free spindles, we first compared the localization of mClover3-KIFC1 in wild-type and in aMTOC-free mouse oocytes. As expected (103), mClover3-KIFC1 was uniformly localized throughout the spindle in wild-type mouse oocytes (Fig. 8, A to C; and movie S18). By contrast, mClover3-KIFC1 was enriched at the forming spindle before bipolarization, and subsequently at the poles, in aMTOC-free mouse oocytes (Fig. 8, A to C; and movie S18). Fluorescence recovery after photobleaching



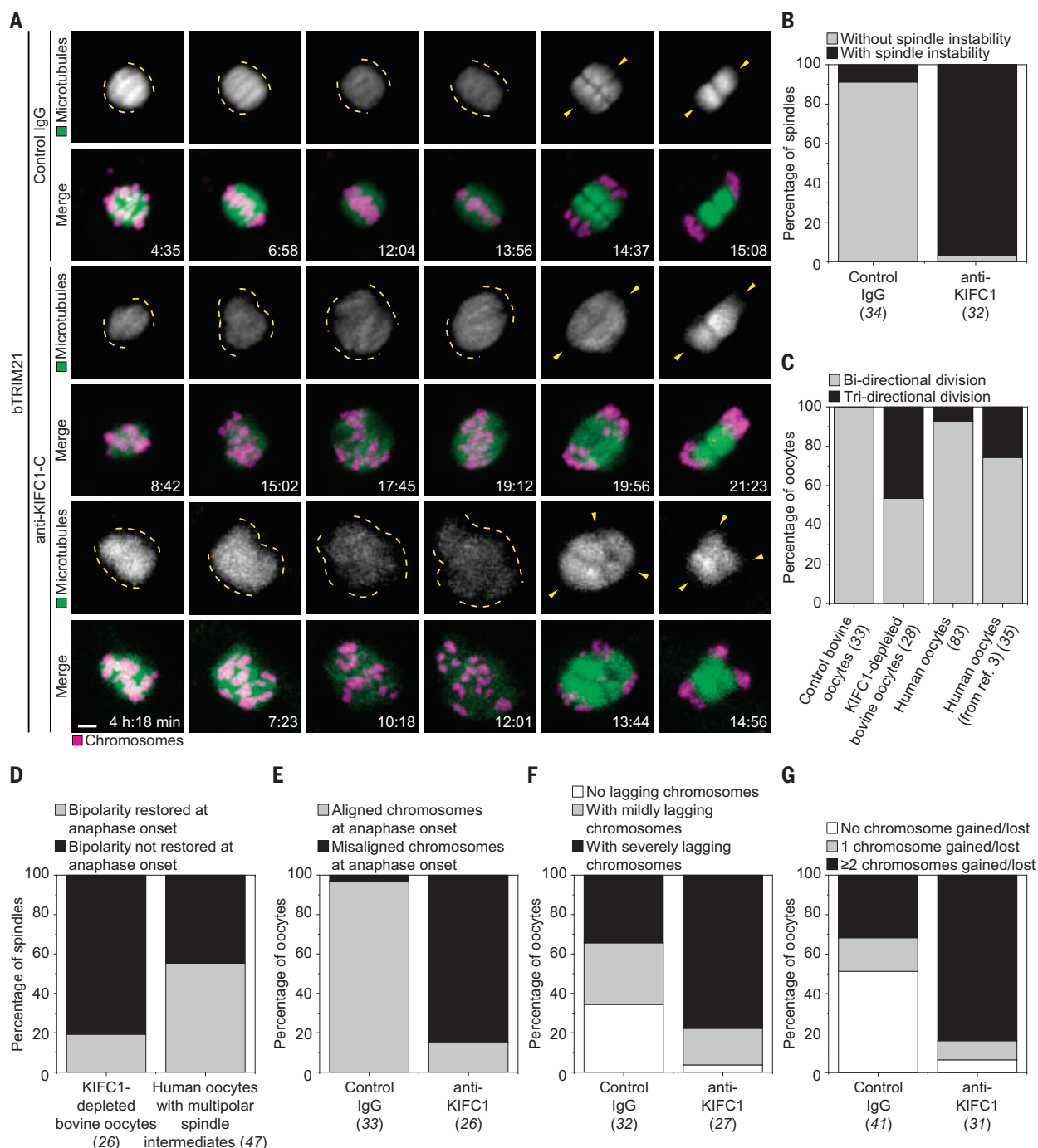


**Fig. 6. Depletion of KIFC1 results in spindle instability and promotes aneuploidy in bovine oocytes.** (A) Still images from time-lapse movies of control and KIFC1-depleted bovine oocytes. Green, microtubules (mClover3-MAP4-MTBD); magenta, chromosomes (H2B-mScarlet). Time is given as hours:minutes after NEBD. (B) Manual scoring of spindle instability in control and KIFC1-depleted bovine oocytes (Fisher's exact test,  $P < 0.0001$ ). (C) Quantification of the directionality of anaphase I in control and KIFC1-depleted bovine oocytes, and in human oocytes from (2, 3). (D) Quantification of spindle bipolarity restoration at

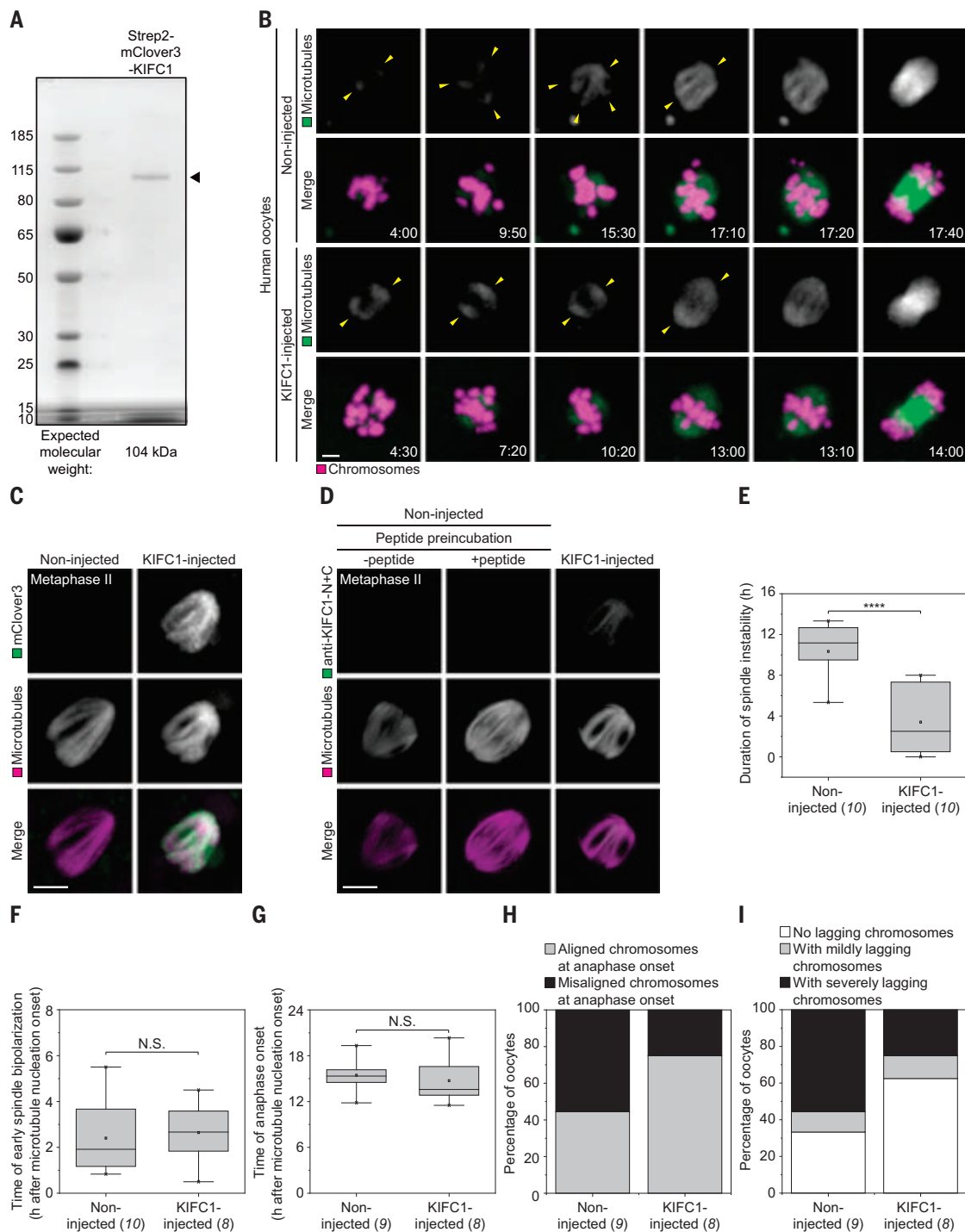
anaphase onset in KIFC1-depleted bovine oocytes and in human oocytes with multipolar spindle intermediates from (2). (E) Quantification of chromosome misalignment at anaphase onset in control and KIFC1-depleted bovine oocytes. (F) Quantification of chromosome missegregation during anaphase in control and KIFC1-depleted bovine oocytes. (G) Quantification of chromosome counts at metaphase II in control and KIFC1-depleted bovine oocytes. Yellow dashed lines highlight spindle poles. Yellow arrowheads highlight directions of anaphase I. The number of oocytes analyzed is specified in italics. Scale bars are 5  $\mu$ m.

analysis revealed that wild-type and aMTOC-free mouse oocytes had a comparable fraction of mobile mClover3-KIFC1, but the turnover of mClover3-KIFC1 at the spindle poles was two times slower in the absence of aMTOCs

(Fig. 8, D to F). By contrast, the absence of aMTOCs did not affect either the turnover of mClover3-KIFC1 in the central region of the spindle or the turnover of the microtubule reporter mScarlet-MAP4-MTBD (fig. S14, E

to G). Thus, the dynamics of KIFC1 at the spindle poles is specifically altered in the absence of aMTOCs, and KIFC1 accumulation at the poles may stabilize aMTOC-free spindles.

**Fig. 7. Introduction of exogenous KIFC1 rescues spindle instability and reduces the risk of aneuploidy in human oocytes.** (A) Coomassie staining for the SDS-polyacrylamide gel electrophoresis (PAGE) of Strep2-mClover3-KIFC1. The black arrow marks the band corresponding to the protein. (B) Still images from time-lapse movies of noninjected and KIFC1-injected human oocytes. Green, microtubules (5-Sir-CTX); magenta, chromosomes (SPY555-DNA). Time is given as hours:minutes after onset of microtubule nucleation. (C) Still images of metaphase II spindles from live noninjected and KIFC1-injected human oocytes. Green, mClover3-KIFC1; magenta, microtubules ( $\alpha$ -tubulin). (D) Immunofluorescence images of metaphase II spindles from noninjected human oocytes stained with nonpreincubated and KIFC1 peptide-preincubated anti-KIFC1-N+C and from KIFC1-injected human oocyte. Green, KIFC1; magenta, microtubules ( $\alpha$ -tubulin). Note that metaphase II spindles in KIFC1-injected human oocytes have thicker microtubule bundles than those in noninjected human oocytes in (C) and (D). (E) Quantification of the duration of spindle instability in non-injected and KIFC1-injected human oocytes. \*\*\*\* $P < 0.0001$ . (F) Quantification of the time of early spindle bipolarization in noninjected and KIFC1-injected human oocytes. N.S., not significant. (G) Quantification of the time of anaphase onset in noninjected and KIFC1-injected human oocytes. N.S., not significant. Note that the onset of microtubule nucleation was chosen as the reference time point because the time gap in between NEBD and the onset of microtubule nucleation varies between oocytes. (H) Quantification of chromosome misalignment at anaphase onset in noninjected and KIFC1-injected human oocytes. (I) Quantification of chromosome missegregation during anaphase in noninjected and KIFC1-injected human oocytes. Yellow arrowheads highlight spindle poles. The number of oocytes analyzed is specified in italics. See Materials and methods for box plot specifications. Scale bars are 5  $\mu$ m.



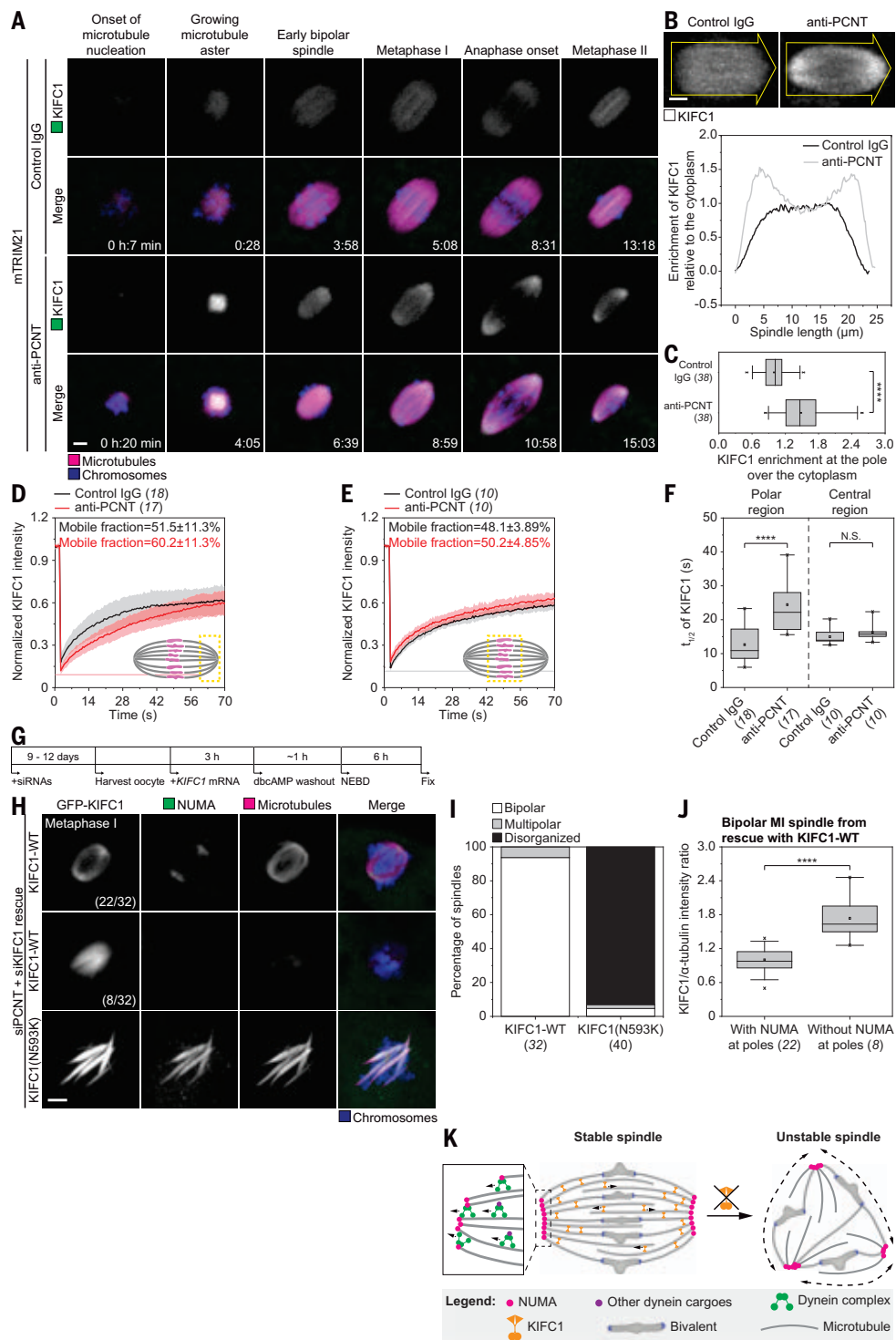
Unlike the other two kinesin-14 family members KIFC2 and KIFC3, KIFC1 distinctively possesses a microtubule-binding domain at its tail (105). This domain, together with the conserved, microtubule-binding motor domain,

allows KIFC1 to organize microtubules through static cross-linking and/or sliding (106). To investigate the requirement of different domains in KIFC1, we expressed a series of truncation mutants in aMTOC-free mouse oocytes

(fig. S14, H and I). The spindle localization of KIFC1 in aMTOC-free mouse oocytes depended predominantly on the tail domain and the stalk but not on its motor domain (fig. S14J). To test whether the motor domain is dispensable for

# Fig. 8. An optimal level of KIFC1's cross-linking and sliding activities is required for proper bipolar spindle assembly in aMTOC-free mouse oocytes.

(A) Still images from time-lapse movies of control and PCNT-depleted mouse oocytes. Green, mClover3-KIFC1; magenta, microtubules (mScarlet-MAP4-MTBD); blue, chromosomes (H2B-miRFP). Time is given as hours:minutes after NEBD. (B) Still images (top) of MI spindles from live control and PCNT-depleted mouse oocytes at 6 hours after NEBD. The graph (bottom) is the fluorescence profile of mClover3-KIFC1 across the spindle along the direction of the yellow arrow. (C) Quantification of mClover3-KIFC1 enrichment at the spindle pole over the cytoplasm in control and PCNT-depleted mouse MI oocytes at 6 hours after NEBD. \*\*\*\* $P < 0.0001$ . (D) Recovery of photobleached mClover3-KIFC1 at the spindle poles in control and PCNT-depleted mouse MI oocytes at 6 hours after NEBD. (E) Recovery of photobleached mClover3-KIFC1 in the central region of the spindle in control and PCNT-depleted mouse MI oocytes at 6 hours after NEBD. Error bars (shaded areas) represent SD. (F) Half-life of mClover3-KIFC1 at different regions of MI spindles from control and PCNT-depleted mouse oocytes. \*\*\*\* $P < 0.0001$ ; N.S., not significant. (G) Schematic diagram of the experiment in (H). (H) Immunofluorescence images of MI spindles from KIFC1-depleted aMTOC-free mouse oocytes rescued with KIFC1-WT and KIFC1(N593K), fixed at 7 hours after release. Gray, GFP-KIFC1; green, NUMA; magenta, microtubules ( $\alpha$ -tubulin); blue, chromosomes (Hoechst). (I) Manual scoring of spindle polarity in aMTOC-free mouse MI oocytes rescued with KIFC1-WT and KIFC1(N593K) (Fisher's exact test,  $P < 0.0001$ ). (J) Quantification of KIFC1 to  $\alpha$ -tubulin intensity ratio in bipolar MI spindles from aMTOC-free mouse oocytes rescued with KIFC1-WT. \*\*\*\* $P < 0.0001$ . (K) Mechanistic model for the organization and instability of aMTOC-free spindle poles in mammalian oocytes. See text for details. The number of oocytes or poles analyzed is specified in italics. See Materials and methods for box plot specifications. Scale bars are 5  $\mu$ m.



KIFC1's functions in aMTOC-free spindles, we depleted endogenous KIFC1 and reexpressed wild-type KIFC1 and KIFC1(N593K), which cross-links microtubules but cannot slide owing to the mutation (Asn<sup>593</sup>→Lys) in its motor domain (107) (Fig. 8G). Whereas almost all aMTOC-free mouse oocytes rescued with wild-type KIFC1 assembled a bipolar spindle, nearly all oocytes rescued with KIFC1(N593K)

assembled disorganized spindles consisting of several misaligned microtubule bundles (Fig. 8, H and I). Thus, static cross-linking is insufficient for restoring bipolar spindle assembly, and KIFC1's sliding activity is required to align cross-linked microtubules into a bipolar spindle. Furthermore, around 25% of oocytes rescued with wild-type KIFC1 assembled bipolar spindles but had poorly focused

poles that lack NUMA (Fig. 8H); quantification of the KIFC1-to- $\alpha$ -tubulin intensity ratio revealed that almost twofold more KIFC1 was loaded onto these spindles (Fig. 8J). Thus, excessive KIFC1 could interfere with NUMA-mediated pole focusing, and an optimal level of KIFC1 activities is required for proper bipolar spindle assembly in the absence of aMTOCs.



## Discussion

Our data elucidate a cause of spindle instability in human oocytes: Human oocytes are deficient in the molecular motor KIFC1, a key spindle-stabilizing factor present in oocytes of other mammalian species. By contrast, most other mammalian and nonmammalian oocytes express KIFC1 to promote proper spindle assembly (22, 23, 103, 108–110). We report that KIFC1 ensures the coalescence of clustered microtubule minus ends into two spindle poles in mammalian oocytes that lack aMTOCs (Fig. 8K). Spindle stabilization is likely achieved through the formation of static cross-links along parallel microtubules at the poles and the alignment of antiparallel microtubules in the central region of the spindle. Because human oocytes are deficient in KIFC1, we propose that the deficiency of these activities renders their spindles unstable.

Our data also reveal notable differences in spindle pole organization in different mammalian oocytes. Whereas aMTOCs dominate the organization of spindle poles in mouse oocytes (30, 32–35), an adaptation in NUMA dynamics can compensate for the absence of aMTOCs in mammalian oocytes. At aMTOC-free spindle poles, NUMA becomes strongly enriched at and stably associated with microtubule minus ends. Owing to its multimodular nature, NUMA can cross-link microtubules at the minus ends and also engage minus end-directed dynein complexes. All of these features allow stably associated NUMA to cluster microtubule minus ends at the spindle poles, replacing the microtubule anchoring function of aMTOCs. In addition to anchoring microtubules, aMTOCs promote microtubule nucleation (30, 32, 35). However, NUMA neither nucleates microtubules nor interacts with microtubule nucleators, in line with the crucial requirement of the Ran pathway for microtubule nucleation in nonrodent mammalian oocytes (2, 36).

Dynein and KIFC1 appear to have similar roles in pole focusing in *Xenopus* egg extracts, *Drosophila* S2 cells, and nonmammalian oocytes (22–25, 29, 109–114). By contrast, perturbation of NUMA-dynein and of KIFC1 result in distinct phenotypes in mammalian oocytes that lack aMTOCs, suggesting that they have nonredundant roles at the spindle poles. Although both dynein and KIFC1 are minus end-directed motors with microtubule cross-linking and sliding activities, their differential roles may be explained by their different distribution on the aMTOC-free spindles in mammalian oocytes. NUMA-dynein is confined at microtubule minus ends and hence acts more locally, whereas KIFC1 localizes throughout the spindle with an enrichment at the polar regions and hence acts more globally.

In normal mitotic cells with two centrosomes, KIFC1 is largely dispensable for bipolar

spindle assembly (107, 115–117). By contrast, mitotic cells with supernumerary centrosomes require KIFC1 to cluster extra centrosomes into two spindle poles, preventing spindle multipolarity (115, 116, 118, 119). Hence, KIFC1 has been proposed as a selective target for treating cancers, where supernumerary centrosomes are frequently observed (120). Here, we demonstrate that KIFC1 also prevents spindle multipolarity in mammalian oocytes that lack aMTOCs. Spindle pole organization in these oocytes may be intrinsically error-prone owing to the absence of additional mechanisms that enforce spindle bipolarity such as those that regulate the number of centrosomes (121) and aMTOCs (34). Thus, KIFC1 is also required to cluster extra spindle poles formed in cancer cells and in mammalian oocytes that lack aMTOCs.

The deficiency of KIFC1 may also render zygotic spindles unstable. Human zygotes have low levels of *KIFC1* mRNA and a high incidence of multipolar spindles (9–13). Spindles are, however, mostly bipolar in human two-cell-stage embryos (13). This sudden reduction in multipolar spindles coincides with a rise in *KIFC1* mRNA from the two-cell stage onward. Indeed, bovine oocytes express KIFC1, and multipolar spindles are rare in bovine zygotes (122–124). Thus, differences in maternal KIFC1 expression may also explain why human zygotes are more prone to assembling multipolar spindles than other mammalian zygotes.

If spindle instability is caused by a general deficiency of KIFC1 in human oocytes, why are spindles in 20% of human oocytes stable (2) and why aren't 80% of human eggs aneuploid? One contributing factor could be heterogeneous KIFC1 expression between individual oocytes. Our immunoblot data show that the average level of KIFC1 in human oocytes is very low. However, as revealed by single-cell RNA-seq of human meiosis I oocytes, there might be individual oocytes expressing a higher level of KIFC1 that could be sufficient to assemble stable spindles. Moreover, human oocytes might have developed additional mechanisms to compensate for the deficiency of KIFC1. Indeed, many human oocytes succeed in forming bipolar spindles shortly before anaphase onset, despite progressing through long phases of spindle instability (2, 3). Furthermore, although most human oocytes with unstable spindles show lagging chromosomes during anaphase (2), only a fraction of lagging chromosomes will eventually lead to aneuploidy (125). Spindle instability also appears to occur more frequently in meiosis I than in meiosis II and the first mitotic division (2, 11–13, 126). This could be because of additional differences in the spindle architecture and the process of spindle assembly. For instance, the kinetics of spindle assembly in meiosis II and the first mitotic division (2 to 4 hours) is much faster than in meiosis I (12 to 16 hours) (2, 12, 13).

Nevertheless, we do not exclude the possibility that in vitro matured oocytes, which are the main source of immature human oocytes available for research, are more prone to spindle instability during meiosis I than oocytes ovulated in vivo.

Our data reveal a cause of the differences in spindle stability between human oocytes and other mammalian oocytes and provide a potential method for reducing chromosome segregation errors in human oocytes. By quantitatively delivering a defined amount of KIFC1 protein into human oocytes, we were able to rescue spindle instability and reduce the risk of aneuploidy in human oocytes. Thus, the deficiency of KIFC1 contributes to spindle instability in human oocytes and the titrated administration of KIFC1 protein has the potential to increase the fidelity of spindle assembly and chromosome segregation in human oocytes.

## Materials and methods

### Preparation and culture of mouse oocytes and follicles

All mice were maintained in a specific pathogen-free environment at the Animal Facility of the Max Planck Institute for Multidisciplinary Sciences according to The Federation of European Laboratory Animal Science Associations guidelines and recommendations.

Oocytes were isolated from ovaries of 8- to 12-week-old FVB/N female mice. Fully grown oocytes of around 75  $\mu\text{m}$  in diameter with a centered nucleus were arrested at prophase in homemade phenol red-free M2 supplemented with 250  $\mu\text{M}$  dibutyryl cyclic AMP (dbcAMP) (Sigma-Aldrich) under paraffin oil (ACROS Organics) at 37°C. To induce resumption of meiosis, oocytes were released into dbcAMP-free M2 at 37°C.

Follicles were mechanically isolated from 10- to 12-day-old (C57BL/6J  $\times$  CBA) F<sub>1</sub> female mice in HEPES-buffered minimal essential medium (MEM) with GlutaMAX (Gibco) supplemented with 5% fetal bovine serum (FBS) (Gibco) and 0.1 $\times$  penicillin G/streptomycin (Sigma-Aldrich). Compact follicles of around 100  $\mu\text{m}$  in diameter with a centered oocyte were cultured in MEM alpha with GlutaMAX and nucleosides (Gibco) supplemented with 5% FBS, 0.03  $\mu\text{g/ml}$  ovine follicle stimulating hormone (National Hormone and Peptide Program), 1 $\times$  insulin/transferrin/sodium selenite (Sigma-Aldrich), and 0.1 $\times$  penicillin G/streptomycin on a 12-mm Transwell-COL collagen-coated 0.4- $\mu\text{m}$  pore polytetrafluoroethylene (PTFE) membrane insert (Corning) at 37°C and 5% CO<sub>2</sub> as previously described (55). Half of the medium surrounding the insert was replaced every 3 days. After 10 to 12 days of culture, in vitro grown oocytes were denuded and matured in modified M2 supplemented with 10% FBS instead of 4 mg/ml bovine serum albumin (BSA).

### Preparation and culture of bovine and porcine oocytes

All ovaries were obtained from local slaughterhouses. Bovine and porcine ovaries were transported in a ThermoFlask to the laboratory within 1 to 3 hours after retrieval and washed extensively with warm 0.9% NaCl. Cumulus-oocyte complexes (COCs) were recovered by aspiration of antral follicles with a 17-gauge needle affixed to a 1-ml syringe. Additionally, 140 µl of 5000 IU/ml heparin (Merck Millipore) was added to every 20 ml of aspirate from bovine ovaries. Bovine and porcine COCs were allowed to sediment and then washed extensively with HEPES-buffered Medium 199 (Sigma-Aldrich) and porcine oocyte/embryo collection medium (POE-CM) (Cosmo Bio), respectively, at 39°C. Only fully grown oocytes with a homogeneous cytoplasm and several layers of compact cumulus cells were selected for experiments. To better synchronize meiotic progression, bovine and porcine oocytes were arrested at prophase in medium supplemented with 10 µM RO-3306 (Sigma-Aldrich) instead of dbcAMP. To induce resumption of meiosis, bovine and porcine oocytes were released into RO-3306-free bovine in vitro maturation (BO-IVM) (IVF Bioscience) and porcine oocyte maturation (POM) (Cosmo Bio) medium, respectively, at 39°C and 5% CO<sub>2</sub>.

### Preparation and culture of human oocytes

The use of unfertilized human oocytes in this study was approved by the UK's National Research Ethics Service under the REC reference 11/EE/0346 (IRAS project ID 84952) and the Ärztekammer Niedersachsen (Ethics Committee of Lower Saxony) under the reference 15/2016. Oocytes were collected from patients who underwent ovarian stimulation for intracytoplasmic sperm injection (ICSI) as part of their assisted reproduction treatment at Bourn Hall Clinic, Kinderwunschzentrum Göttingen, and Fertility Center Berlin. Only oocytes that were immature at the time of ICSI and thus unsuitable for the procedure were used in this study. All patients gave informed consent for their surplus oocyte(s) to be used in this study. Details of all donors were listed in table S1. Care was taken that the donor ages in the control and experimental groups were not substantially different in all experiments. For oocytes collected at Bourn Hall Clinic and Kinderwunschzentrum Göttingen, oocytes were cultured in G-MOPS medium (Vitrolife) supplemented with 10% FBS under paraffin oil at 37°C within 3 to 5 hours after retrieval from ovaries as previously described (2). For oocytes collected at Fertility Center Berlin, oocytes were vitrified with Cryolock (FUJIFILM Irvine Scientific) using Vit Kit-Freeze (FUJIFILM Irvine Scientific). To maximize the survival and developmental rate of vitrified-thawed oocytes, oocytes were thawed in 1 ml of pre-

warmed G-MOPS PLUS (Vitrolife) containing 1 M D-(+)-trehalose (Sigma-Aldrich) at 37°C for 1 min. Oocytes were then transferred to 300 µl of G-MOPS PLUS containing 0.5 M D-(+)-trehalose at room temperature for 3 min, 300 µl of G-MOPS PLUS containing 0.25 M D-(+)-trehalose at room temperature for 5 min, and 300 µl of G-MOPS PLUS at room temperature for 2 min. Recovered oocytes were cultured in G-MOPS supplemented with 10% FBS under paraffin oil at 37°C. For germinal vesicle (GV) oocytes, the time of NEBD was monitored using a Primo Vision EVO+ microscope (Vitrolife) installed inside the incubator. Only GV oocytes that were morphologically normal and underwent NEBD within 24 hours after retrieval from ovaries were used in this study.

### Expression constructs, mRNA synthesis, recombinant protein expression, and purification

To generate constructs for mRNA synthesis, we fused previously published coding sequences with mClover3 (127), mPA-GFP (128), and mScarlet (129) and subcloned them into pGEMHE (130) to obtain H2B-mScarlet (31), mClover3-KIFC1 (OriGene), mScarlet-MAP4-MTBD (31), mClover3-NUMA, and mPA-GFP-NUMA (M. Mancini, unpublished). MBP was subcloned from pET-21a(+)/MBP-His (M. J. Fox Foundation, unpublished) into pET28a(+). pGEMHE-mClover3-KIFC1(Tail), pGEMHE-mClover3-KIFC1(ΔMotor), pGEMHE-mClover3-KIFC1(ΔTail), pGEMHE-mClover3-KIFC1(Motor), pGEMHE-mClover3-KIFC1(N593K), pGEMHE-mClover3-NUMA(ΔN), pGEMHE-mClover3-NUMA(SpM-4A), pGEMHE-mClover3-NUMA(ΔMTBD1), pGEMHE-mClover3-NUMA(ΔMTBD2), pGEMHE-mClover3-NUMA-N, pGEMHE-EGFP-P150(ΔMTBD), pGEMHE-EGFP-P150(ΔABD), and pGEMHE-EGFP-P150-CC1 were constructed from pGEMHE-mClover3-KIFC1, pGEMHE-mClover3-NUMA, and pGEMHE-EGFP-P150 (31) using the Q5 Site-Directed Mutagenesis Kit (NEB). pGEMHE-H2B-mCherry (30), pGEMHE-H2B-miRFP (31), pGEMHE-mClover3-MAP4-MTBD (31), pGEMHE-meGFP-MAP4 (30), pET28a(+)-P150-CC1-His (131), pGEMHE-mCherry-α-tubulin (132), pGEMHE-bTRIM21 (31), HLTV-hTRIM21 (56), and pGEMHE-mTRIM21 (31) were also used. All mRNAs were synthesized and quantified as previously described (133). For protein expression in bacterial cells, NUMA-N was subcloned from pGEMHE-mClover3-NUMA-N into pET28a(+). For protein expression in mammalian cells, mClover3-KIFC1 was subcloned from pGEMHE-mClover3-KIFC1 into pQE-TriSystem-His-Strep2 (Qiagen).

Recombinant His-NUMA-N, P150-CC1-His, and hTRIM21 were expressed in and purified from NiCo21(DE3) (NEB) or OverExpress C41 (DE3) (Sigma-Aldrich) as previously described (133). Briefly, they were first affinity-purified

with ÄKTA pure (GE Healthcare) using HisTrap FF (GE Healthcare), followed by size exclusion chromatography using HiLoad 26/600 Superdex 200 pg (GE Healthcare). Recombinant Strep2-mClover3-KIFC1 was expressed in and purified from HEK 293 cells (85120602; ECACC) as previously described (134).

### Short-interfering RNAs

All short-interfering RNAs (siRNAs) were purchased from Qiagen. The sequences of siRNAs used in this study are listed in table S2. AllStars Negative Control (Qiagen) was used as a control.

### Microinjection of RNAs

Immature mouse oocytes were microinjected with 3.5 pl of mRNAs as previously described (30). *H2B-miRFP* mRNA was microinjected at a needle concentration (final concentration in the microinjection needle) of 28.4 ng/µl, *mClover3-KIFC1* mRNA at 111.1 ng/µl, *mClover3-KIFC1(Tail)* mRNA at 227.2 ng/µl, *mClover3-KIFC1(ΔMotor)* mRNA at 224 ng/µl, *mClover3-KIFC1(ΔTail)* mRNA at 334 ng/µl, *mClover3-KIFC1(Motor)* mRNA at 278.8 ng/µl, *mClover3-MAP4-MTBD* mRNA at 83.5 ng/µl, *mScarlet-MAP4-MTBD* mRNA at 83.5 ng/µl, *MBP* mRNA at 500 ng/µl, *mClover3-NUMA* mRNA at 165.9 ng/µl, *mClover3-NUMA(ΔN)* mRNA at 470.4 ng/µl, *mPA-GFP-NUMA* mRNA at 400 ng/µl, *mClover3-NUMA-N* mRNA at 500 ng/µl, *EGFP-P150(ΔMTBD)* mRNA at 720 ng/µl, *EGFP-P150(ΔABD)* mRNA at 583.8 ng/µl, *EGFP-P150-CC1* mRNA at 448.3 ng/µl, *P150-CC1* mRNA at 500 ng/µl, *mCherry-α-tubulin* mRNA at 250.5 ng/µl, and *mTRIM21* mRNA at 421 ng/µl. Oocytes were allowed to express the mRNAs for 3 to 4 hours before release.

Mouse follicles were microinjected with 3.5 pl of siRNAs at a needle concentration of 2 µM as previously described (55). For rescue experiments, in vitro grown oocytes were microinjected with 3.5 pl of mRNAs. *mClover3-KIFC1* mRNA was microinjected at a needle concentration of 275 ng/µl, *mClover3-KIFC1(N593K)* mRNA at 275 ng/µl, *mClover3-NUMA(SpM-4A)* mRNA at 400 ng/µl, *mClover3-NUMA(ΔMTBD1)* mRNA at 400 ng/µl, and *mClover3-NUMA(ΔMTBD2)* mRNA at 400 ng/µl. Oocytes were allowed to express the mRNAs for 3 to 4 hours before release.

Before microinjection of immature bovine and porcine oocytes, surrounding cumulus cells were stripped with a 135-µm EZ-Tip (CooperSurgical) before microinjection. For live imaging of bovine spindle assembly, oocytes were microinjected with 2 pl of *H2B-mCherry* and *meGFP-MAP4* mRNAs at a needle concentration of 5 and 54 ng/µl, respectively. Oocytes were allowed to express the mRNAs for 3 hours before release. For Trim-Away, bovine oocytes were microinjected with 3.5 pl of *bTRIM21* mRNA at a needle concentration of 1400 ng/µl. Oocytes were allowed to express

the mRNA for 12 hours before release. For live imaging of the spindle assembly with Trim-Away, bovine oocytes were microinjected with 3.5 pl of *H2B-mScarlet*, *mClover3-MAP4-MTBD*, and *bTRIM21* mRNAs at a needle concentration of 0.16, 2.5, and 210.5 ng/μl, respectively. Oocytes were allowed to express the mRNAs for 12 hours before release. For live imaging of porcine spindle assembly, oocytes were microinjected with 2 pl of *H2B-mCherry* and *meGFP-MAP4* mRNAs at a needle concentration of 3 and 30 ng/μl, respectively. Oocytes were allowed to express the mRNAs for 3 hours before release.

#### Microinjection of proteins

For inhibition with RanT24N, immature mouse oocytes were microinjected with 12 pl of recombinant His-RanT24N (Cytoskeleton) at a needle concentration of 2 mg/ml with 0.05% NP-40. Corresponding amount of BSA was microinjected as a control.

For acute inhibition with P150-CC1 and NUMA-N in mouse meiosis I (MI) oocytes, oocytes were microinjected at 7 hours after release with 7 pl of recombinant P150-CC1-His and His-NUMA-N at a needle concentration of 50 and 15 mg/ml, respectively, with 0.1% NP-40. A corresponding amount of BSA was microinjected as a control.

For inhibition with P150-CC1 in human oocytes, oocytes were microinjected immediately after NEBD with 10 to 15 pl of recombinant P150-CC1-His at a needle concentration of 47.85 mg/ml with 0.03% NP-40. A corresponding amount of BSA was microinjected as a control.

For introduction of exogenous KIFC1, recombinant KIFC1 protein was used instead of *KIFC1* mRNA for better control over the final KIFC1 protein level in the oocytes. Immature human oocytes were microinjected with 11 pl of recombinant Strep2-mClover3-KIFC1 at a needle concentration of 0.875 mg/ml with 0.05% NP-40.

#### Trim-Away in mouse, bovine, and human oocytes

Only affinity-purified antibodies were used in this study for Trim-Away-mediated protein depletion (56). Mouse monoclonal anti-NDC80 (sc-515550; Santa Cruz Biotechnology), rabbit polyclonal anti-KIFC1-C (20790-1-AP; Proteintech), mouse monoclonal anti-LIS1 (H00005048-M03; Abnova), rabbit polyclonal anti-NUMA (ab97585; Abcam), and mouse monoclonal anti-PCNT (611814; BD Biosciences) were purified as previously described (133). The control immunoglobulin Gs (IgGs) used were normal mouse IgG (12-371; Millipore) and normal rabbit IgG (12-370; Millipore).

For constitutive Trim-Away in immature mouse oocytes, 3.5 pl of mRNAs and 3.5 pl of antibodies were coinjected as previously de-

scribed (133). All antibodies were microinjected at a needle concentration of 1 to 2 mg/ml with 0.1% NP-40. Target proteins were allowed to be depleted for 3 to 4 hours before the oocytes were released. For acute Trim-Away in mouse MI oocytes, immature oocytes were first microinjected with 3.5 pl of mRNAs and then released after 3 hours. At around 7 hours after release, oocytes were further microinjected with 3.5 pl of antibodies to acutely deplete the target proteins.

For constitutive Trim-Away in immature bovine oocytes, partially stripped oocytes were first microinjected with 3.5 pl of mRNAs and allowed to express the mRNAs for 12 hours. Before release, oocytes were fully stripped and further microinjected with 7 pl of antibodies at a needle concentration of 2.5 mg/ml with 0.05% NP-40.

For constitutive Trim-Away in immature human oocytes, oocytes were first microinjected with 10 to 15 pl of recombinant hTRIM21 at a needle concentration of 4.125 mg/ml with 0.0375% NP-40. After 3 to 4 hours, oocytes were subsequently injected with 12 pl of antibody at a needle concentration of 2.5 mg/ml with 0.03% NP-40.

#### Cold treatment

To selectively depolymerize non-kinetochore-bound microtubules, mouse MI oocytes were incubated on ice for 15 min and immediately fixed as for routine immunofluorescence. To depolymerize all spindle microtubules, mouse MI oocytes were incubated on ice for 1 hour and immediately fixed as for routine immunofluorescence.

#### Nocodazole treatment

Nocodazole (Sigma-Aldrich) was reconstituted in dimethyl sulfoxide (DMSO) (Sigma-Aldrich) as 10 mM stock. To acutely depolymerize spindle microtubules, nocodazole was added to a final concentration of 10 μM at around 7 hours after release.

#### Staining of human oocytes for live imaging of spindle assembly

5-SiR-CTX (135) and 5-SiR-Hoechst (135) were reconstituted in DMSO as 0.9 and 1 mM stock, respectively. SPY555-DNA (Spirochrome) and SPY555-tubulin (Spirochrome) were reconstituted in DMSO following the manufacturer's instructions. 5-SiR-CTX and SPY555-DNA were used in most experiments and present throughout imaging at 15 nM and 1:2000 dilution, respectively. 5-SiR-Hoechst and SPY555-tubulin were also used in some experiments and present throughout imaging at 50 nM and 1:5000 dilution, respectively.

#### Immunofluorescence

To obtain mouse metaphase I spindles, oocytes were incubated at 37°C for around 7 hours after

released into dbcAMP-free medium. To obtain porcine metaphase I and bovine metaphase I and II spindles, oocytes were incubated at 39°C and 5% CO<sub>2</sub> for around 11, 12, and 24 hours, respectively, after being released into RO-3306-free medium. To obtain human metaphase I and II spindles, oocytes were incubated at 37°C for around 15 and 24 hours after NEBD, respectively. Except for meiosis II oocytes in Figs. 6G and 7D, none of the oocytes used for immunofluorescence analyses were subjected to live imaging before fixation.

Oocytes were fixed in 100 mM HEPES (pH 7.0, titrated with KOH), 50 mM EGTA (pH 7.0, titrated with KOH), 10 mM MgSO<sub>4</sub>, 2% methanol-free formaldehyde, and 0.5% Triton X-100 at 37°C for 15 to 60 min. Fixed oocytes were extracted in phosphate-buffered saline (PBS) with 0.5% triton X-100 (PBT) overnight at 4°C and blocked in PBT with 5% BSA (PBT-BSA) overnight at 4°C. All antibody incubations were performed in PBT-BSA at 10 μg/ml overnight at 4°C (for primary antibodies) and at 20 μg/ml for 1 hour at room temperature (for secondary antibodies). Primary antibodies used were human anti-centromere antibody (15-234-0001; Antibodies Incorporated), rabbit anti-ASPM (NB100-2278; Novus Biological), rat anti-α-tubulin (MCA78G; Bio-Rad), rabbit anti-CAMSAP3 (136), rabbit anti-CDK5RAP2 (ABE236; Merck Millipore), rabbit anti-CEP192 (18832-1-AP; Proteintech), rabbit anti-DHC (12345-1-AP; Proteintech), rabbit anti-KIF11 (NB500-181; Novus Biologicals), goat anti-GFP (600-101-215; Rockland Immunochemicals), rabbit anti-γ-tubulin (T3559; Sigma-Aldrich), mouse anti-NDC80 (sc-515550; Santa Cruz Biotechnology), rabbit anti-KANSL3 (HPA035018; Sigma-Aldrich), rabbit anti-KIFC1-N (ab172620; Abcam), rabbit anti-KIFC1-C (20790-1-AP; Proteintech), mouse anti-LIS1 (H00005048-M03; Abnova), rabbit anti-MCRS1 (HPA039057; Sigma-Aldrich), rabbit anti-NUMA (ab97585; Abcam), rabbit anti-NUMA (ab84680; Abcam), mouse anti-P150 (612708; BD Biosciences), mouse anti-PCNT (611814; BD Biosciences), and rabbit anti-TPX2 (NB500-179; Novus Biological). Secondary antibodies used were Alexa Fluor 488-, 594-, or 647-conjugated AffiniPure Fab Fragment anti-goat, anti-rabbit, and anti-rat (Jackson ImmunoResearch Europe), Alexa Fluor 568-conjugated Nano-Secondary anti-mouse IgG1 and anti-mouse IgG2b (ChromoTek), Atto 488-conjugated FluoTag-X2 anti-mouse IgG2a/b (NanoTag Biotechnologies), and Alexa Fluor 488-conjugated anti-human IgG (Molecular Probes). DNA was stained with Hoechst 33342 (Molecular Probes).

#### Optical clearing of bovine and porcine oocytes

Oocytes were fixed, extracted, and blocked as for routine immunofluorescence. Before incubation with primary antibodies, lipid droplets in bovine and porcine oocytes were cleared



with 4000 U/ml lipase from *Candida rugose* (Sigma-Aldrich) in 400 mM NaCl, 50 mM Tris (pH 7.2), 5 mM CaCl<sub>2</sub>, and 0.2% sodium taurocholate supplemented with cOmplete, EDTA-free Protease Inhibitor Cocktail (Roche) at room temperature for 20 to 40 min as previously described (31).

#### Peptide preincubation assay

Oocytes were fixed, extracted, and blocked as for routine immunofluorescence. Mouse monoclonal anti-NDC80 (sc-515550; Santa Cruz Biotechnology), rabbit monoclonal anti-KIFC1-N (ab172620; Abcam) and polyclonal anti-KIFC1-C (20790-1-AP; Proteintech), mouse monoclonal anti-LIS1 (H00005048-M03; Abnova), and rabbit polyclonal anti-NUMA (ab97585; Abcam) were preincubated with recombinant NDC80 (Proteintech), recombinant Strep2-mClover3-KIFC1 (homemade), recombinant LIS1 (Abnova), and recombinant His-NUMA-N (homemade), respectively, before being applied to oocytes as previously described (133).

#### Confocal, super-resolution, and light-sheet microscopy

For confocal imaging, oocytes were imaged in 2  $\mu$ l of medium (for live oocytes) or PBS with 1% polyvinylpyrrolidone and 0.5 mg/ml BSA (for fixed oocytes) under paraffin oil in a 35-mm dish with a no. 1.0 coverslip. Images were acquired with LSM780, LSM800, LSM880, and LSM980 confocal laser scanning microscopes (Zeiss) equipped with an environmental incubator box and a 40 $\times$  C-Apochromat 1.2 NA water-immersion objective. For live imaging, a volume of 50  $\mu$ m by 50  $\mu$ m by 37.5  $\mu$ m or 35  $\mu$ m by 35  $\mu$ m by 37.5  $\mu$ m centered around the chromosomes was typically recorded. Automatic three-dimensional (3D) tracking with a temporal resolution of 5 to 15 min was implemented using a custom-made macro (Zeiss) on LSM800 and MyPiC (137) on LSM880. Super-resolution Airyscan images were acquired using the Airyscan module on LSM880 and LSM980 confocal laser scanning microscopes and processed in ZEN (Zeiss) after acquisition. mClover3, meGFP, mPA-GFP, Alexa Fluor 488, and Atto 488 were excited with a 488-nm laser line and detected at 493 to 571 nm. mCherry, mScarlet, SPY555, and Alexa Fluor 568 were excited with a 561-nm laser line and detected at 571 to 638 nm. Alexa Fluor 594 was excited with a 594-nm laser line and detected at 605 to 638 nm. mRFP, 5-SiR, and Alexa Fluor 647 were excited with a 633-nm laser line and detected at 638 to 700 nm.

For light-sheet imaging, oocytes were imaged in 2 ml of medium under paraffin oil in a multiwell sample holder with four compartments (Viventis Microscopy Sàrl). Images were acquired with LS1 Live (Viventis Microscopy Sàrl) equipped with an environmental incubator box and a 25X 1.1 NA water-dipping

objective. SPY555 was excited with a 561-nm laser line and detected with a 523/20 nm–610/25 nm dual band-pass filter. 5-SiR was excited with a 638-nm laser line and detected with a Chroma ZET405/488/561/640m emission filter.

Images of the control and experimental groups were acquired under identical imaging conditions on the same microscope. For some images, shot noise was reduced with a Gaussian filter. Care was taken that the imaging conditions (laser power, pixel-dwell time, detector gain, and exposure time) did not cause phototoxicity (for live imaging), photobleaching and saturation.

#### Photoactivation

For analyses of fluorescence dissipation, oocytes coexpressing mPA-GFP-NUMA, mScarlet-MAP4-MTBD, and H2B-mRFP were rotated on stage with an unbroken microinjection needle to obtain meiotic spindles parallel to the imaging plane. Rectangular regions of interest (ROIs) were marked and photoactivated using a 405-nm laser line at the maximum power after the fifth time point.

#### Fluorescence recovery after photobleaching

For analyses of fluorescence recovery after photobleaching, oocytes coexpressing mClover3-KIFC1, mScarlet-MAP4-MTBD, and H2B-mRFP or oocytes expressing mCherry- $\alpha$ -tubulin were rotated on stage with an unbroken microinjection needle to obtain meiotic spindles parallel to the imaging plane. Rectangular ROIs were marked and photobleached using a 488- and a 561-nm laser line at the maximum power after the fifth time point.

#### Immuno-electron microscopy and correlative FIB-SEM

For immune-electron microscopy of NUMA, mouse MI oocytes expressing mClover3-NUMA were microinjected with 7  $\mu$ l of 0.167 mg/ml 2-nm Immunogold (Aurion)-conjugated GFP VHH (Chromotek) with 0.1% NP-40. Before fixation in 100 mM HEPES (pH 7.0, titrated with KOH), 50 mM EGTA (pH 7.0, titrated with KOH), 10 mM MgSO<sub>4</sub>, 3% EM-grade glutaraldehyde, and 0.5% methanol-free formaldehyde at 37°C for 1 hour, oocytes were randomly distributed and attached to a high Grid-500 35 mm  $\mu$ -Dish (iBidi) using Cell-Tak Cell and Tissue Adhesive (Corning). To preselect oocytes with optimally oriented spindles, oocytes were stained with Hoechst 33342 and screened on a confocal laser scanning microscope. Before staining for electron microscopy, silver enhancement was performed with R-Gent SE-EM (Aurion).

All of the following processing steps were performed in a microwave (Ted Pella), and oocytes were washed three times with water for 40 s at 250 W in between every staining step. Oocytes were first stained with 2% osmium

tetroxide–1.5% potassium ferrocyanide in 0.1 M phosphate buffer (pH 7.4) for 12 min at 100 W (microwave cycling between on and off every 2 min). Oocytes were then incubated with 1% thiocarbonylhydrazide (Sigma-Aldrich) for 12 min at 100 W (microwave cycling between on and off every 2 min) and stained with 2% osmium tetroxide in water for 12 min at 100 W (microwave cycling between on and off every 2 min). Oocytes were further stained with 1% uranyl acetate in water for 12 min at 100 W (microwave cycling between on and off every 2 min) and 0.02 M lead nitrate–0.03 M aspartic acid (pH 5.5) for 12 min at 100 W (microwave cycling between on and off every 2 min). Oocytes were subsequently dehydrated in a graded ethanol series (10, 30, 50, 75, 90, 100, and 100%) for 40 s at 250 W and infiltrated in a graded series (25, 50, 75, 90, 100, and 100%) of Durcupan resin (Sigma-Aldrich) in ethanol for 3 min at 250 W.

Infiltrated oocytes were embedded with a minimal amount of resin as previously described (138). The polymer coverslip with embedded oocytes on top was cut out of the culture dish using a jigsaw and attached to a SEM stub (Science Services) using silver-filled EPO-TEK EE129-4 adhesive (Electron Microscopy Sciences), and cured overnight at 60°C. Samples were coated with a 10-nm gold layer using the high-vacuum sputter coater EM ACE600 (Leica) at a current of 35 mA. Afterward, samples were placed in the Crossbeam 540 FIB-SEM (Zeiss). To ensure even milling and to protect the surface, a 500-nm platinum layer was deposited on top of the region of interest at a current of 3 nA. Atlas 5 (Atlas 3D, Zeiss) was used to collect the 3D datasets. Preselected oocytes were exposed with a 15-nA current, and a 7-nA current was used to polish the cross-section surface. Images were acquired at 1.5 kV with the energy-selective backscattered (ESB) detector at a grid voltage of 450 V (5 nm pixel size in *x-y*) using 700 pA as the milling current (5 nm *z*-step).

After acquisition, images were first aligned using Linear Stack Alignment with SIFT in Fiji (NIH). Datasets were then cropped, inverted, and smoothed with a Gaussian filter of 1 sigma in Fiji. To better visualize microtubules, datasets were further subjected to Local contrast enhancement (CLAHE) in Fiji. The specific parameters used were 127 for blocksize, 256 for histogram bins, and 1.25 for maximum slope. To obtain a spindle parallel to the imaging plane, the resulting image stacks were rotated and resliced with Interactive Stack Rotation in Fiji.

#### Immunoblotting

Ten to 50 mouse and 12 human, bovine, or porcine MI oocytes (per lane) were extensively washed in protein-free medium and

transferred into 4  $\mu$ l of protein-free medium at around 6, 15, 11, and 10 hours after NEBD, respectively. Then, 12  $\mu$ l of 1.333 $\times$  NuPAGE LDS sample buffer (Thermo Fisher Scientific) with 100 mM dithiothreitol (DTT) was added, and the mixture was immediately snap-frozen in liquid nitrogen. For a positive control, 0.125 to 2.5  $\mu$ g of asynchronized HeLa whole cell lysate (NBP2-10274; Novus Biologicals) was used.

Samples were thawed at 37°C and snap-frozen in liquid nitrogen twice more before being heated at 95°C for 5 min. Samples were resolved on a 17-well NuPAGE 4 to 12% Bis-Tris protein gel of 1.0 mm thickness (Thermo Fisher Scientific) with NuPAGE MOPS SDS Running Buffer (Thermo Fisher Scientific). Proteins were transferred onto a 0.45- $\mu$ m polyvinylidene difluoride (PVDF) membrane with SDS-free Towbin buffer at 200 mA for 2 hours on ice. Blots were stained with No-Stain Protein Labeling Reagent (Thermo Fisher Scientific) before blocking. Blocking and antibody incubations were performed in Tris-buffered saline (TBS) with 5% skim milk and 0.1% tween-20. Primary antibodies used were rat anti- $\alpha$ -tubulin (MCA78G; Bio-Rad), mouse anti- $\beta$ -actin (ab8226; Abcam), mouse anti- $\beta$ -tubulin (T8328; Sigma-Aldrich), rabbit anti- $\gamma$ -tubulin (T3559; Sigma-Aldrich), rabbit anti-GAPDH (ab181602; Abcam), mouse anti-NDC80 (sc-515550; Santa Cruz Biotechnology), rabbit anti-KIFC1-N (ab172620; Abcam), rabbit anti-KIFC1-C (20790-1-AP; Proteintech), mouse anti-LIS1 (H00005048-M03; Abnova), rabbit anti-NUMA (ab97585; Abcam), and rabbit anti-PCNT (ab4448; Abcam). Secondary antibodies used were horseradish peroxidase (HRP)-conjugated anti-mouse (P0447; Dako), anti-rabbit (A9169; Sigma-Aldrich), and anti-rat (sc-2032; Santa Cruz Biotechnology). Blots were developed with SuperSignal West Femto Maximum Sensitivity Substrate (Thermo Fisher Scientific) and documented with Amersham Imager 600 (GE Healthcare). Care was taken that the exposure time did not cause saturation.

### General quantification

Time-lapse movies of live oocytes and images of fixed spindles were analyzed in 3D using Imaris (Bitplane). To determine the timings of meiotic progression, different stages of meiosis were quantified relative to the time of NEBD (for mouse, bovine, and porcine oocytes) or to the time of onset of microtubule nucleation (for human oocytes). NEBD was defined as the time point when the sharp boundary between the nucleus and cytoplasm disappeared in the differential interference contrast image (for mouse oocytes) or when the nucleus started collapsing in the H2B channel (for bovine and porcine oocytes). Onset of microtubule nucleation was defined as the time point when microtubules were first detected outside the

chromosome aggregate. Anaphase onset was defined as the time point before chromosome separation was first observed. To score for chromosome misalignment, chromosomes that failed to congress to the metaphase plate at anaphase onset were classified as misaligned chromosomes. To score for chromosome missegregation, chromosomes that failed to clear the central spindle within 10 or 20 min after anaphase onset were classified as mildly and severely lagging chromosomes, respectively.

In Figs. 1I and 3E and figs. S6 (E, H, and K), S7H, S8 (C, G, K, and O), and S9 (H and L), bipolar spindles, in which ends of all microtubules converged at the poles, were defined as having focused poles. Spindles that had a detectable spindle axis but failed to converge ends of microtubules at the poles were defined as having unfocused poles. For mouse oocytes, unfocused poles were further classified into mildly unfocused poles (with partially separated microtubule ends) and severely unfocused poles (with fully separated microtubule ends).

To score for spindle instability, spindle poles were defined as regions of MAP4 or MAP4-MTBD or  $\alpha$ -tubulin intensity that prominently protruded from the main microtubule mass. In Fig. 3F, spindles with two well-defined poles were scored as bipolar. Round spindles without a detectable spindle axis were scored as apolar. Spindles with more than two well-defined poles were scored as multipolar. In Figs. 3I, 5 (C and H), and 8I and fig. S14D, spindles with two well-defined poles were scored as bipolar. Round spindles with two poorly defined poles were scored as with broad poles. Spindles with more than two well-defined poles were scored as multipolar. Spindles without a barrel shape but that contained several weakly associated microtubule bundles were scored as disorganized. In Figs. 6B and 7E and fig. S11D, spindles that maintained a barrel-shaped bipolar morphology were defined as having no spindle instability. Spindles that lost their initial bipolarity and underwent dynamic remodeling of the poles were defined as having spindle instability.

### Quantification of protein enrichment at the spindle pole over the cytoplasm

Line profiles across half spindles were generated along the spindle axis in ZEN, and mean fluorescence intensities were exported into Excel (Microsoft). The intensity of an equivalent ROI in the cytoplasm of the same oocyte was subtracted to correct for cytoplasmic background. Background-corrected data were then normalized by the minimum intensity of each line profile (cytoplasmic intensity). Enrichment at the spindle pole over the cytoplasm was represented by the maximum intensity of each line profile.

### Automatic quantification of standard deviation of fluorescence intensity within spindle isosurface and microtubule packing index

To reproducibly reconstruct spindles (labeled with anti- $\alpha$ -tubulin) from different immunofluorescence experiments, a previously described MATLAB script (31) was used for automatic surface creation in Imaris. Specific parameters used were: 0.1  $\mu$ m (for microtubule packing index) or 1.0  $\mu$ m [for standard deviation (SD) of fluorescence intensity within spindle isosurface] for smoothing size, no background subtraction, 500 to 750  $\mu$ m<sup>3</sup> and 1000 to 1750  $\mu$ m<sup>3</sup> for minimum and maximum expected total volume of surface object, respectively. SD of fluorescence intensity, volume, and volume of the object-oriented minimum bounding box for the spindle isosurface were exported into Excel. The microtubule packing index was calculated by dividing the volume of the spindle isosurface by the volume of the object-oriented minimum bounding box.

### Manual quantification of volume by 3D reconstruction of NUMA clusters

Manual segmentations were performed using the Surface function of Imaris. For KIFC1 depletion experiments, NUMA clusters (labeled with anti-NUMA) were smoothed with a surface detail of 0.5  $\mu$ m and thresholded after background subtraction with 0.5  $\mu$ m as the diameter of largest sphere that fits into the object. Depending on the cytoplasmic background in each oocyte, a suitable threshold value was selected for segmentation. The volumes of the NUMA clusters' isosurfaces were exported into Excel.

### Quantification of photoactivation experiments

Minor temporal drift was corrected using Rigid registration in Icy (Institut Pasteur). Mean intensities of photoactivated areas over time were exported from Fiji into Excel for further processing. Data were first corrected for cytoplasmic background by subtracting the intensity of the photoactivated area before photoactivation. Background-corrected data were then normalized to the intensity of the first postactivation time point. Plots of intensity against time were fitted to linear functions ( $y = mx + c$ , where  $m$  is the slope and  $c$  is the  $y$  intercept) or one-component exponential functions [ $y = Ae^{(c-x)/\tau}$ , where  $c$  is the offset,  $A$  is the fraction of the component, and  $\tau$  is the time constant] in OriginPro (OriginLab). Half-times of decay ( $t_{1/2}$ ) were calculated by  $-0.5/m$  or  $\tau \times \ln(2)$ .

### Directionality analysis

Directionality of microtubules within spindles were analyzed using OrientationJ in Fiji. The specific parameters used were 9 pixels for local window, Gaussian for gradient, HSB for color survey, orientation for Hue, coherency for

saturation, and original image for brightness. The output images were inverted for better visualization of the results.

### Reanalysis of previously published RNA-seq data

Previously published bulk and single-cell RNA-seq datasets for oocytes and preimplantation embryos from mice (GSE44183) (97), cows (GSE52415) (98), pigs (GSE139512) (101), and humans (GSE44183, GSE101571, GSE133856, and GSE154762) (97, 99, 100, 102) were downloaded from the Gene Expression Omnibus (NIH). To compare gene expression levels between different samples from the same dataset, reads per kilobase of transcript per million reads mapped (RPKM) and fragments per kilobase of transcript per million reads mapped (FPKM) were converted into transcripts per million (TPM). TPM has been shown to better represent transcript abundance at the gene level than RPKM and FPKM because it respects the invariance property and is proportional to the average relative RNA molar concentration of the transcript in a sample (139, 140).

### Quantification of fluorescence recovery after photobleaching experiments

Minor temporal drift was corrected using Rigid registration in Icy. Mean intensities of photobleached areas over time were exported from Fiji into Excel for further processing. Data were first corrected for background by subtracting the intensity of an area outside the oocytes. Background-corrected data were then normalized to the intensity of prebleached time points ( $F_0$ ). Plots of intensity ( $F$ ) against time were fitted to single exponential functions [ $F(t) = c - F_{\infty}e^{-t/\tau}$ , where  $c$  is the offset,  $F_{\infty}$  is the amplitude of maximum intensity recovered after equilibrium, and  $\tau$  is the time constant] in OriginPro. Half-times of maximum recovery ( $t_{1/2}$ ) and mobile fractions were determined by  $\tau \times \ln(2)$  and  $F_{\infty}/(F_0 - F)$  (where  $F$  is the minimum intensity measured immediately after photobleaching), respectively.

### Statistical analysis

No statistical methods were used to predetermine sample size. The experiments were not randomized. The investigators were not blinded to allocation during experiments and outcome assessment. Average (mean) and SD were calculated in Excel. Statistical significance is based on unpaired, two-tailed Student's  $t$  test (for absolute values) and two-tailed Fisher's exact test (for categorical values), which were calculated in Prism (GraphPad), assuming normal distribution and similar variance. All box plots show median (horizontal black line), mean (small black squares), 25th and 75th percentiles (boxes), 5th and 95th percentiles (whiskers), and 1st and 99th percentiles (crosses). All data are from at least two independent experi-

ments.  $P$  values are designated as  $*P < 0.05$ ,  $**P < 0.01$ ,  $***P < 0.001$ , and  $****P < 0.0001$ . Nonsignificant values are indicated as N.S.

### REFERENCES AND NOTES

- J. R. Gruhn *et al.*, Chromosome errors in human eggs shape natural fertility over reproductive life span. *Science* **365**, 1466–1469 (2019). doi: [10.1126/science.aav7321](https://doi.org/10.1126/science.aav7321); pmid: [31604276](https://pubmed.ncbi.nlm.nih.gov/31604276/)
- Z. Holubcová, M. Blayney, K. Elder, M. Schuh, Error-prone chromosome-mediated spindle assembly favors chromosome segregation defects in human oocytes. *Science* **348**, 1143–1147 (2015). doi: [10.1126/science.aaa9529](https://doi.org/10.1126/science.aaa9529); pmid: [26045437](https://pubmed.ncbi.nlm.nih.gov/26045437/)
- J. Haverfield *et al.*, Tri-directional anaphases as a novel chromosome segregation defect in human oocytes. *Hum. Reprod.* **32**, 1293–1303 (2017). doi: [10.1093/humrep/dex083](https://doi.org/10.1093/humrep/dex083); pmid: [28449121](https://pubmed.ncbi.nlm.nih.gov/28449121/)
- A. H. Sathananthan *et al.*, Centrioles in the beginning of human development. *Proc. Natl. Acad. Sci. U.S.A.* **88**, 4806–4810 (1991). doi: [10.1073/pnas.88.11.4806](https://doi.org/10.1073/pnas.88.11.4806); pmid: [2052559](https://pubmed.ncbi.nlm.nih.gov/2052559/)
- M. Plachot, N. Crozet, Fertilization abnormalities in human in-vitro fertilization. *Hum. Reprod.* **7**, 89–94 (1992). doi: [10.1093/humrep/7.suppl.1.89](https://doi.org/10.1093/humrep/7.suppl.1.89); pmid: [1447374](https://pubmed.ncbi.nlm.nih.gov/1447374/)
- H. Balakier, Tripolar human zygotes: The first cell cycle and subsequent development. *Hum. Reprod.* **8**, 1892–1897 (1993). doi: [10.1093/oxfordjournals.humrep.a137955](https://doi.org/10.1093/oxfordjournals.humrep.a137955); pmid: [8288756](https://pubmed.ncbi.nlm.nih.gov/8288756/)
- A. H. Sathananthan *et al.*, The sperm centriole: Its inheritance, replication and perpetuation in early human embryos. *Hum. Reprod.* **11**, 345–356 (1996). doi: [10.1093/HUMREP/11.2.345](https://doi.org/10.1093/HUMREP/11.2.345); pmid: [8671223](https://pubmed.ncbi.nlm.nih.gov/8671223/)
- M. Moornij, L. T. Colombo, L. L. Veeck, Z. Rosenwaks, G. D. Palermo, Sperm integrity is critical for normal mitotic division and early embryonic development. *Mol. Hum. Reprod.* **5**, 836–844 (1999). doi: [10.1093/molehr/5.9.836](https://doi.org/10.1093/molehr/5.9.836); pmid: [10460222](https://pubmed.ncbi.nlm.nih.gov/10460222/)
- Y. F. Gu, G. Lin, C. F. Lu, G. X. Lu, Analysis of the first mitotic spindles in human in vitro fertilized tripolar zygotes after pronuclear removal. *Reprod. Biomed. Online* **19**, 745–754 (2009). doi: [10.1016/j.rbmo.2009.09.013](https://doi.org/10.1016/j.rbmo.2009.09.013); pmid: [20021725](https://pubmed.ncbi.nlm.nih.gov/20021725/)
- Y. Kai, K. Iwata, Y. Iba, Y. Mio, Diagnosis of abnormal human fertilization status based on pronuclear origin and/or centrosome number. *J. Assist. Reprod. Genet.* **32**, 1589–1595 (2015). doi: [10.1007/s10815-015-0568-1](https://doi.org/10.1007/s10815-015-0568-1); pmid: [26395191](https://pubmed.ncbi.nlm.nih.gov/26395191/)
- Y. F. Gu *et al.*, Abnormalities in centrosome number in human embryos and embryonic stem cells. *Mol. Reprod.* **83**, 392–404 (2016). doi: [10.1002/mrd.22633](https://doi.org/10.1002/mrd.22633); pmid: [26946049](https://pubmed.ncbi.nlm.nih.gov/26946049/)
- Y. Kai, H. Moriaki, K. Yumoto, K. Iwata, Y. Mio, Assessment of developmental potential of human single pronucleated zygotes derived from conventional in vitro fertilization. *J. Assist. Reprod. Genet.* **35**, 1377–1384 (2018). doi: [10.1007/s10815-018-1241-2](https://doi.org/10.1007/s10815-018-1241-2); pmid: [29959619](https://pubmed.ncbi.nlm.nih.gov/29959619/)
- E. Ford *et al.*, The first mitotic division of the human embryo is highly error-prone. *bioRxiv* 2020.2007.2017.208744 [Preprint] (2020). doi: [10.1101/2020.07.17.208744](https://doi.org/10.1101/2020.07.17.208744)
- Y. Kai, H. Kawano, N. Yamashita, First mitotic spindle formation is led by sperm centrosome-dependent MTOCs in humans. *Reproduction* **161**, V19–V22 (2021). doi: [10.1530/REP-21-0061](https://doi.org/10.1530/REP-21-0061); pmid: [33843613](https://pubmed.ncbi.nlm.nih.gov/33843613/)
- S. Santaguida, A. Amon, Short- and long-term effects of chromosome mis-segregation and aneuploidy. *Nat. Rev. Mol. Cell Biol.* **16**, 473–485 (2015). doi: [10.1038/nrm4025](https://doi.org/10.1038/nrm4025); pmid: [26204159](https://pubmed.ncbi.nlm.nih.gov/26204159/)
- P. T. Conduit, A. Wainman, J. W. Raff, Centrosome function and assembly in animal cells. *Nat. Rev. Mol. Cell Biol.* **16**, 611–624 (2015). doi: [10.1038/nrm4062](https://doi.org/10.1038/nrm4062); pmid: [26373263](https://pubmed.ncbi.nlm.nih.gov/26373263/)
- P. Meraldi, Centrosomes in spindle organization and chromosome segregation: A mechanistic view. *Chromosome Res.* **24**, 19–34 (2016). doi: [10.1007/s10577-015-9508-2](https://doi.org/10.1007/s10577-015-9508-2); pmid: [26643311](https://pubmed.ncbi.nlm.nih.gov/26643311/)
- H. Maiato, E. Logarinho, Mitotic spindle multipolarity without centrosome amplification. *Nat. Cell Biol.* **16**, 386–394 (2014). doi: [10.1038/ncb2958](https://doi.org/10.1038/ncb2958); pmid: [24914434](https://pubmed.ncbi.nlm.nih.gov/24914434/)
- D. Szollosi, P. Calarco, R. P. Donahue, Absence of centrioles in the first and second meiotic spindles of mouse oocytes. *J. Cell Sci.* **11**, 521–541 (1972). doi: [10.1242/jcs.11.2.521](https://doi.org/10.1242/jcs.11.2.521); pmid: [5076360](https://pubmed.ncbi.nlm.nih.gov/5076360/)
- A. H. Sathananthan, Ultrastructural changes during meiotic maturation in mammalian oocytes: Unique aspects of the human oocyte. *Microsc. Res. Tech.* **27**, 145–164 (1994). doi: [10.1002/jemt.1070270208](https://doi.org/10.1002/jemt.1070270208); pmid: [8123907](https://pubmed.ncbi.nlm.nih.gov/8123907/)
- G. Manandhar, H. Schatten, P. Sutovsky, Centrosome reduction during gametogenesis and its significance. *Biol. Reprod.* **72**, 2–13 (2005). doi: [10.1095/biolreprod.104.031245](https://doi.org/10.1095/biolreprod.104.031245); pmid: [15385423](https://pubmed.ncbi.nlm.nih.gov/15385423/)
- M. Hatsumi, S. A. Endow, Mutants of the microtubule motor protein, nonclaret disjunctional, affect spindle structure and chromosome movement in meiosis and mitosis. *J. Cell Sci.* **101**, 547–559 (1992). doi: [10.1242/jcs.101.3.547](https://doi.org/10.1242/jcs.101.3.547); pmid: [1522143](https://pubmed.ncbi.nlm.nih.gov/1522143/)
- H. J. Matthies, H. B. McDonald, L. S. Goldstein, W. E. Theurkauf, Anastral meiotic spindle morphogenesis: Role of the non-claret disjunctional kinesin-like protein. *J. Cell Biol.* **134**, 455–464 (1996). doi: [10.1083/jcb.134.2.455](https://doi.org/10.1083/jcb.134.2.455); pmid: [8707829](https://pubmed.ncbi.nlm.nih.gov/8707829/)
- R. Heald *et al.*, Self-organization of microtubules into bipolar spindles around artificial centrosomes in *Xenopus* egg extracts. *Nature* **382**, 420–425 (1996). doi: [10.1038/382420a0](https://doi.org/10.1038/382420a0); pmid: [8684481](https://pubmed.ncbi.nlm.nih.gov/8684481/)
- R. Heald, R. Tournebise, A. Habermann, E. Karsenti, A. Hyman, Spindle assembly in *Xenopus* egg extracts: Respective roles of centrosomes and microtubule self-organization. *J. Cell Biol.* **138**, 615–628 (1997). doi: [10.1083/jcb.138.3.615](https://doi.org/10.1083/jcb.138.3.615); pmid: [9245790](https://pubmed.ncbi.nlm.nih.gov/9245790/)
- K. P. McNally, F. J. McNally, The spindle assembly function of *Caenorhabditis elegans* katanin does not require microtubule-severing activity. *Mol. Biol. Cell* **22**, 1550–1560 (2011). doi: [10.1091/mbc.e10-12-0951](https://doi.org/10.1091/mbc.e10-12-0951); pmid: [21372175](https://pubmed.ncbi.nlm.nih.gov/21372175/)
- A. A. Connolly *et al.*, *Caenorhabditis elegans* oocyte meiotic spindle pole assembly requires microtubule severing and the calponin homology domain protein ASPM-1. *Mol. Biol. Cell* **25**, 1298–1311 (2014). doi: [10.1091/mbc.e13-11-0687](https://doi.org/10.1091/mbc.e13-11-0687); pmid: [24554763](https://pubmed.ncbi.nlm.nih.gov/24554763/)
- S. J. Radford, A. M. M. Go, K. S. McKim, Cooperation between kinesin motors promotes spindle symmetry and chromosome organization in oocytes. *Genetics* **205**, 517–527 (2017). doi: [10.1534/genetics.116.194647](https://doi.org/10.1534/genetics.116.194647); pmid: [27932541](https://pubmed.ncbi.nlm.nih.gov/27932541/)
- G. Cavin-Meza, M. M. Kwan, S. M. Wignall, Multiple motors cooperate to establish and maintain acentrosomal spindle bipolarity in *C. elegans* oocyte meiosis. *bioRxiv* 2021.09.09.0549640 [Preprint] (2021); doi: [10.1101/2021.09.09.0549640](https://doi.org/10.1101/2021.09.09.0549640)
- M. Schuh, J. Ellenberg, Self-organization of MTOCs replaces centrosome function during acentrosomal spindle assembly in live mouse oocytes. *Cell* **130**, 484–498 (2007). doi: [10.1016/j.cell.2007.06.025](https://doi.org/10.1016/j.cell.2007.06.025); pmid: [17693257](https://pubmed.ncbi.nlm.nih.gov/17693257/)
- C. So *et al.*, A liquid-like spindle domain promotes acentrosomal spindle assembly in mammalian oocytes. *Science* **364**, eaat9557 (2019). doi: [10.1126/science.aat9557](https://doi.org/10.1126/science.aat9557); pmid: [31249032](https://pubmed.ncbi.nlm.nih.gov/31249032/)
- X. Guo, S. Gao, Pins homolog LGN regulates meiotic spindle organization in mouse oocytes. *Cell Res.* **19**, 838–848 (2009). doi: [10.1038/cr.2009.54](https://doi.org/10.1038/cr.2009.54); pmid: [19434098](https://pubmed.ncbi.nlm.nih.gov/19434098/)
- A. Kolano, S. Brunet, A. D. Silk, D. W. Cleveland, M. H. Verhac, Error-prone mammalian female meiosis from silencing the spindle assembly checkpoint without normal interkinetochore tension. *Proc. Natl. Acad. Sci. U.S.A.* **109**, E1858–E1867 (2012). doi: [10.1073/pnas.1204686109](https://doi.org/10.1073/pnas.1204686109); pmid: [22552228](https://pubmed.ncbi.nlm.nih.gov/22552228/)
- D. Clift, M. Schuh, A three-step MTOC fragmentation mechanism facilitates bipolar spindle assembly in mouse oocytes. *Nat. Commun.* **6**, 7217 (2015). doi: [10.1038/ncomms8217](https://doi.org/10.1038/ncomms8217); pmid: [26147444](https://pubmed.ncbi.nlm.nih.gov/26147444/)
- A. Z. Balboul *et al.*, Haspin kinase regulates microtubule-organizing center clustering and stability through Aurora kinase C in mouse oocytes. *J. Cell Sci.* **129**, 3648–3660 (2016). doi: [10.1242/jcs.189340](https://doi.org/10.1242/jcs.189340); pmid: [27562071](https://pubmed.ncbi.nlm.nih.gov/27562071/)
- Y. H. Kim, I. W. Lee, Y. J. Jo, N. H. Kim, S. Namgoong, Acentriolar microtubule organization centers and Ran-mediated microtubule formation pathways are both required in porcine oocytes. *Mol. Reprod. Dev.* **86**, 972–983 (2019). doi: [10.1002/mrd.23172](https://doi.org/10.1002/mrd.23172); pmid: [31136049](https://pubmed.ncbi.nlm.nih.gov/31136049/)
- J. Lee, T. Miyano, R. M. Moor, Spindle formation and dynamics of  $\gamma$ -tubulin and nuclear mitotic apparatus protein distribution during meiosis in pig and mouse oocytes. *Biol. Reprod.* **62**, 1184–1192 (2000). doi: [10.1095/biolreprod62.5.1184](https://doi.org/10.1095/biolreprod62.5.1184); pmid: [10775165](https://pubmed.ncbi.nlm.nih.gov/10775165/)
- M. R. Shin, N. H. Kim, Maternal gamma ( $\gamma$ )-tubulin is involved in microtubule reorganization during bovine fertilization and parthenogenesis. *Mol. Reprod. Dev.* **64**, 438–445 (2003). doi: [10.1002/mrd.10280](https://doi.org/10.1002/mrd.10280); pmid: [12589656](https://pubmed.ncbi.nlm.nih.gov/12589656/)
- C. Alvarez Sedó, H. Schatten, C. M. Combelles, V. Y. Rawe, The nuclear mitotic apparatus (NuMA) protein: Localization



- and dynamics in human oocytes, fertilization and early embryos. *Mol. Hum. Reprod.* **17**, 392–398 (2011). doi: [10.1093/molehr/gar009](https://doi.org/10.1093/molehr/gar009); pmid: 21297155
40. X. Xu, X. Duan, C. Lu, G. Lin, G. Lu, Dynamic distribution of NuMA and microtubules in human fetal fibroblasts, developing oocytes and somatic cell nuclear transferred embryos. *Hum. Reprod.* **26**, 1052–1060 (2011). doi: [10.1093/humrep/der067](https://doi.org/10.1093/humrep/der067); pmid: 21604448
  41. A. Dammerrmann, A. Desai, K. Oegema, The minus end in sight. *Curr. Biol.* **13**, R614–R624 (2003). doi: [10.1016/S0960-9822\(03\)00530-X](https://doi.org/10.1016/S0960-9822(03)00530-X); pmid: 12906817
  42. M. Martin, A. Akhmanova, Coming into focus: Mechanisms of microtubule minus-end organization. *Trends Cell Biol.* **28**, 574–588 (2018). doi: [10.1016/j.tcb.2018.02.011](https://doi.org/10.1016/j.tcb.2018.02.011); pmid: 29571882
  43. T. Gaglio, M. A. Dionne, D. A. Compton, Mitotic spindle poles are organized by structural and motor proteins in addition to centrosomes. *J. Cell Biol.* **138**, 1055–1066 (1997). doi: [10.1083/jcb.138.5.1055](https://doi.org/10.1083/jcb.138.5.1055); pmid: 9281583
  44. A. D. Silk, A. J. Holland, D. W. Cleveland, Requirements for NuMA in maintenance and establishment of mammalian spindle poles. *J. Cell Biol.* **184**, 677–690 (2009). doi: [10.1083/jcb.200810091](https://doi.org/10.1083/jcb.200810091); pmid: 19255246
  45. J. G. Wakefield, S. Bonaccorsi, M. Gatti, The *Drosophila* protein Asp is involved in microtubule organization during spindle formation and cytokinesis. *J. Cell Biol.* **153**, 637–648 (2001). doi: [10.1083/jcb.153.4.637](https://doi.org/10.1083/jcb.153.4.637); pmid: 11352927
  46. J. D. Bishop, Z. Han, J. M. Schumacher, The *Caenorhabditis elegans* Aurora B kinase AIR-2 phosphorylates and is required for the localization of a BimC kinesin to meiotic and mitotic spindles. *Mol. Biol. Cell* **16**, 742–756 (2005). doi: [10.1091/mbc.e04-08-0682](https://doi.org/10.1091/mbc.e04-08-0682); pmid: 15548597
  47. N. Özlü *et al.*, An essential function of the *C. elegans* ortholog of TPX2 is to localize activated aurora A kinase to mitotic spindles. *Dev. Cell* **9**, 237–248 (2005). doi: [10.1016/j.devcel.2005.07.002](https://doi.org/10.1016/j.devcel.2005.07.002); pmid: 16054030
  48. J. X. Yu, Z. Guan, H. A. Nash, The mushroom body defect gene product is an essential component of the meiosis II spindle apparatus in *Drosophila* oocytes. *Genetics* **173**, 243–253 (2006). doi: [10.1534/genetics.105.051557](https://doi.org/10.1534/genetics.105.051557); pmid: 16510791
  49. S. Brunet *et al.*, Meiotic regulation of TPX2 protein levels governs cell cycle progression in mouse oocytes. *PLOS ONE* **3**, e3338 (2008). doi: [10.1371/journal.pone.0003338](https://doi.org/10.1371/journal.pone.0003338); pmid: 18833336
  50. M. van der Voet *et al.*, NuMA-related LIN-5, ASPM-1, calmodulin and dynein promote meiotic spindle rotation independently of cortical LIN-5/GPR/Ga. *Nat. Cell Biol.* **11**, 269–277 (2009). doi: [10.1038/ncb1834](https://doi.org/10.1038/ncb1834); pmid: 19219036
  51. G. FitzHarris, A shift from kinesin 5-dependent metaphase spindle function during preimplantation development in mouse. *Development* **136**, 2111–2119 (2009). doi: [10.1242/dev.035089](https://doi.org/10.1242/dev.035089); pmid: 19465601
  52. X. L. Xu *et al.*, The microtubule-associated protein ASPM regulates spindle assembly and meiotic progression in mouse oocytes. *PLOS ONE* **7**, e49303 (2012). doi: [10.1371/journal.pone.0049303](https://doi.org/10.1371/journal.pone.0049303); pmid: 23152892
  53. M. F. A. Costa, H. Ohkura, The molecular architecture of the meiotic spindle is remodeled during metaphase arrest in oocytes. *J. Cell Biol.* **218**, 2854–2864 (2019). doi: [10.1083/jcb.201902110](https://doi.org/10.1083/jcb.201902110); pmid: 31278080
  54. J. M. Kollman, A. Merdes, L. Mourey, D. A. Agard, Microtubule nucleation by  $\gamma$ -tubulin complexes. *Nat. Rev. Mol. Cell Biol.* **12**, 709–721 (2011). doi: [10.1038/nrm3209](https://doi.org/10.1038/nrm3209); pmid: 21993292
  55. S. Pfender *et al.*, Live imaging RNAi screen reveals genes essential for meiosis in mammalian oocytes. *Nature* **524**, 239–242 (2015). doi: [10.1038/nature14568](https://doi.org/10.1038/nature14568); pmid: 26147080
  56. D. Clift *et al.*, A method for the acute and rapid degradation of endogenous proteins. *Cell* **171**, 1692–1706.e18 (2017). doi: [10.1016/j.cell.2017.10.033](https://doi.org/10.1016/j.cell.2017.10.033); pmid: 29153837
  57. B. R. Brinkley, J. Cartwright Jr., Cold-labile and cold-stable microtubules in the mitotic spindle of mammalian cells. *Ann. N. Y. Acad. Sci.* **253**, 428–439 (1975). doi: [10.1111/j.1749-6632.1975.tb19218.x](https://doi.org/10.1111/j.1749-6632.1975.tb19218.x); pmid: 1056753
  58. J. G. DeLuca, B. Moree, J. M. Hickey, J. V. Kilmartin, E. D. Salmon, hNuf2 inhibition blocks stable kinetochore-microtubule attachment and induces mitotic cell death in HeLa cells. *J. Cell Biol.* **159**, 549–555 (2002). doi: [10.1083/jcb.200208159](https://doi.org/10.1083/jcb.200208159); pmid: 12438418
  59. W. Ma, M. M. Viveiros, Depletion of pericentrin in mouse oocytes disrupts microtubule organizing center function and meiotic spindle organization. *Mol. Reprod. Dev.* **81**, 1019–1029 (2014). doi: [10.1002/mrd.22422](https://doi.org/10.1002/mrd.22422); pmid: 25266793
  60. C. Baumann, X. Wang, L. Yang, M. M. Viveiros, Error-prone meiotic division and subfertility in mice with oocyte-conditional knockdown of pericentrin. *J. Cell Sci.* **130**, 1251–1262 (2017). doi: [10.1242/jcs.196188](https://doi.org/10.1242/jcs.196188); pmid: 28193732
  61. P. Kalab, R. Heald, The RanGTP gradient – a GPS for the mitotic spindle. *J. Cell Sci.* **121**, 1577–1586 (2008). doi: [10.1242/jcs.005959](https://doi.org/10.1242/jcs.005959); pmid: 18469014
  62. T. Gaglio, A. Saredi, D. A. Compton, NuMA is required for the organization of microtubules into aster-like mitotic arrays. *J. Cell Biol.* **131**, 693–708 (1995). doi: [10.1083/jcb.131.3.693](https://doi.org/10.1083/jcb.131.3.693); pmid: 7593190
  63. A. Saredi, L. Howard, D. A. Compton, Phosphorylation regulates the assembly of NuMA in a mammalian mitotic extract. *J. Cell Sci.* **110**, 1287–1297 (1997). doi: [10.1242/jcs.110.11.1287](https://doi.org/10.1242/jcs.110.11.1287); pmid: 9202389
  64. J. Harborth, J. Wang, C. Gueth-Hallonet, K. Weber, M. Osborn, Self assembly of NuMA: Multiarm oligomers as structural units of a nuclear lattice. *EMBO J.* **18**, 1689–1700 (1999). doi: [10.1093/emboj/18.6.1689](https://doi.org/10.1093/emboj/18.6.1689); pmid: 10075938
  65. N. Lecland, J. Lüders, The dynamics of microtubule minus ends in the human mitotic spindle. *Nat. Cell Biol.* **16**, 770–778 (2014). doi: [10.1038/ncb2996](https://doi.org/10.1038/ncb2996); pmid: 24976384
  66. M. W. Elting, M. Prakash, D. B. Udy, S. Dumont, Mapping load-bearing in the mammalian spindle reveals local kinetochore fiber anchorage that provides mechanical isolation and redundancy. *Curr. Biol.* **27**, 2112–2122.e5 (2017). doi: [10.1016/j.cub.2017.06.018](https://doi.org/10.1016/j.cub.2017.06.018); pmid: 28690110
  67. P. Risteski, M. Jagrić, I. M. Tolić, Sliding of kinetochore fibers along bridging fibers helps center the chromosomes on the spindle. *bioRxiv* 2020.2012.2030.424837 [Preprint] (2021). doi: [10.1101/2020.12.30.424837](https://doi.org/10.1101/2020.12.30.424837)
  68. M. Kallajoki, K. Weber, M. Osborn, A 210 kDa nuclear matrix protein is a functional part of the mitotic spindle: a microinjection study using SPN monoclonal antibodies. *EMBO J.* **10**, 3351–3362 (1991). doi: [10.1002/j.1460-2075.1991.tb04899.x](https://doi.org/10.1002/j.1460-2075.1991.tb04899.x); pmid: 1915296
  69. T. Maekawa, R. Leslie, R. Kuriyama, Identification of a minus end-specific microtubule-associated protein located at the mitotic poles in cultured mammalian cells. *Eur. J. Cell Biol.* **54**, 255–267 (1991). pmid: 1679010
  70. M. A. Dionne, L. Howard, D. A. Compton, NuMA is a component of an insoluble matrix at mitotic spindle poles. *Cell Motil. Cytoskeleton* **42**, 189–203 (1999). doi: [10.1002/\(SICI\)1097-0169\(1999\)42:3<189::AID-CM3>3.0.CO;2-X](https://doi.org/10.1002/(SICI)1097-0169(1999)42:3<189::AID-CM3>3.0.CO;2-X); pmid: 10098933
  71. T. Chinen *et al.*, NuMA assemblies organize microtubule asters to establish spindle bipolarity in acentrosomal human cells. *EMBO J.* **39**, e102378 (2020). doi: [10.15252/embj.2019102378](https://doi.org/10.15252/embj.2019102378); pmid: 31782546
  72. M. Sun *et al.*, NuMA regulates mitotic spindle assembly, structural dynamics and function via phase separation. *Nat. Commun.* **12**, 7157 (2021). doi: [10.1038/s41467-021-27528-6](https://doi.org/10.1038/s41467-021-27528-6); pmid: 34887424
  73. A. Merdes, K. Ramyar, J. D. Vechio, D. W. Cleveland, A complex of NuMA and cytoplasmic dynein is essential for mitotic spindle assembly. *Cell* **87**, 447–458 (1996). doi: [10.1016/S0092-8674\(00\)81365-3](https://doi.org/10.1016/S0092-8674(00)81365-3); pmid: 8898198
  74. A. Merdes, R. Heald, K. Samejima, W. C. Earnshaw, D. W. Cleveland, Formation of spindle poles by dynein/dynactin-dependent transport of NuMA. *J. Cell Biol.* **149**, 851–862 (2000). doi: [10.1083/jcb.149.4.851](https://doi.org/10.1083/jcb.149.4.851); pmid: 10811826
  75. T. Gaglio *et al.*, Opposing motor activities are required for the organization of the mammalian mitotic spindle pole. *J. Cell Biol.* **135**, 399–414 (1996). doi: [10.1083/jcb.135.2.399](https://doi.org/10.1083/jcb.135.2.399); pmid: 8896597
  76. C. L. Hueschen, S. J. Kenny, K. Xu, S. Dumont, NuMA recruits dynein activity to microtubule minus-ends at mitosis. *eLife* **6**, e29328 (2017). doi: [10.7554/eLife.29328](https://doi.org/10.7554/eLife.29328); pmid: 29185983
  77. M. W. Elting, C. L. Hueschen, D. B. Udy, S. Dumont, Force on spindle microtubule minus ends moves chromosomes. *J. Cell Biol.* **206**, 245–256 (2014). doi: [10.1083/jcb.201401091](https://doi.org/10.1083/jcb.201401091); pmid: 25023517
  78. N. Taulet *et al.*, IFT88 controls NuMA enrichment at k-fibers minus-ends to facilitate their re-anchoring into mitotic spindles. *Sci. Rep.* **9**, 10311 (2019). doi: [10.1038/s41598-019-46605-x](https://doi.org/10.1038/s41598-019-46605-x); pmid: 31312011
  79. S. Kotak, C. Busso, P. Gönczy, Cortical dynein is critical for proper spindle positioning in human cells. *J. Cell Biol.* **199**, 97–110 (2012). doi: [10.1083/jcb.201203166](https://doi.org/10.1083/jcb.201203166); pmid: 23027904
  80. M. Okumura, T. Natsume, M. T. Kanemaki, T. Kiyomitsu, Dynein-Dynactin-NuMA clusters generate cortical spindle-pulling forces as a multi-arm ensemble. *eLife* **7**, e36559 (2018). doi: [10.7554/eLife.36559](https://doi.org/10.7554/eLife.36559); pmid: 29848445
  81. L. Haren, A. Merdes, Direct binding of NuMA to tubulin is mediated by a novel sequence motif in the tail domain that bundles and stabilizes microtubules. *J. Cell Sci.* **115**, 1815–1824 (2002). doi: [10.1242/jcs.115.9.1815](https://doi.org/10.1242/jcs.115.9.1815); pmid: 11956313
  82. L. Seldin, A. Muroyama, T. Lechler, NuMA-microtubule interactions are critical for spindle orientation and the morphogenesis of diverse epidermal structures. *eLife* **5**, e12504 (2016). doi: [10.7554/eLife.12504](https://doi.org/10.7554/eLife.12504); pmid: 26765568
  83. S. Gallini *et al.*, NuMA phosphorylation by Aurora-A orchestrates spindle orientation. *Curr. Biol.* **26**, 458–469 (2016). doi: [10.1016/j.cub.2015.12.051](https://doi.org/10.1016/j.cub.2015.12.051); pmid: 26832443
  84. N. J. Quintyne, T. A. Schroer, Distinct cell cycle-dependent roles for dynactin and dynein at centrosomes. *J. Cell Biol.* **159**, 245–254 (2002). doi: [10.1083/jcb.200203089](https://doi.org/10.1083/jcb.200203089); pmid: 12391026
  85. J. T. Canty, A. Yildiz, Activation and regulation of cytoplasmic dynein. *Trends Biochem. Sci.* **45**, 440–453 (2020). doi: [10.1016/j.tibs.2020.02.002](https://doi.org/10.1016/j.tibs.2020.02.002); pmid: 32311337
  86. C. Payne, J. C. St. John, J. Ramalho-Santos, G. Schatten, LIS1 association with dynactin is required for nuclear motility and genomic union in the fertilized mammalian oocyte. *Cell Motil. Cytoskeleton* **56**, 245–251 (2003). doi: [10.1002/cm.10151](https://doi.org/10.1002/cm.10151); pmid: 14584027
  87. R. Gassmann *et al.*, Removal of Spindly from microtubule-attached kinetochores controls spindle checkpoint silencing in human cells. *Genes Dev.* **24**, 957–971 (2010). doi: [10.1101/gad.1886810](https://doi.org/10.1101/gad.1886810); pmid: 20439434
  88. M. Breuer *et al.*, HURP permits MTOC sorting for robust meiotic spindle bipolarity, similar to extra centrosome clustering in cancer cells. *J. Cell Biol.* **191**, 1251–1260 (2010). doi: [10.1083/jcb.201005065](https://doi.org/10.1083/jcb.201005065); pmid: 21173113
  89. R. G. van Heesbeen, M. E. Tanenbaum, R. H. Medema, Balanced activity of three mitotic motors is required for bipolar spindle assembly and chromosome segregation. *Cell Rep.* **8**, 948–956 (2014). doi: [10.1016/j.celrep.2014.07.015](https://doi.org/10.1016/j.celrep.2014.07.015); pmid: 25127142
  90. S. Watanabe, G. Shioi, Y. Furuta, G. Goshima, Intra-spindle microtubule assembly regulates clustering of microtubule-organizing centers during early mouse development. *Cell Rep.* **15**, 54–60 (2016). doi: [10.1016/j.celrep.2016.02.087](https://doi.org/10.1016/j.celrep.2016.02.087); pmid: 27052165
  91. M. Jagrić, P. Risteski, J. Martinčić, A. Milas, I. M. Tolić, Optogenetic control of PRC1 reveals its role in chromosome alignment on the spindle by overlap length-dependent forces. *eLife* **10**, e61170 (2021). doi: [10.7554/eLife.61170](https://doi.org/10.7554/eLife.61170); pmid: 33408356
  92. K. Tsuchiya, G. Goshima, Microtubule-associated proteins promote microtubule generation in the absence of  $\gamma$ -tubulin in human colon cancer cells. *J. Cell Biol.* **220**, e202104114 (2021). doi: [10.1083/jcb.202104114](https://doi.org/10.1083/jcb.202104114); pmid: 34779859
  93. K.-Y. Lee, T. Davies, M. Mishima, Cytokinesis microtubule organisers at a glance. *J. Cell Sci.* **125**, 3495–3500 (2012). doi: [10.1242/jcs.094672](https://doi.org/10.1242/jcs.094672); pmid: 22991411
  94. A. Das *et al.*, Spindle assembly and chromosome segregation requires central spindle proteins in *Drosophila* oocytes. *Genetics* **202**, 61–75 (2016). doi: [10.1534/genetics.115.181081](https://doi.org/10.1534/genetics.115.181081); pmid: 26564158
  95. B. Wang, M. J. Pfeiffer, H. C. Drexler, G. Fuellen, M. Boiani, Proteomic analysis of mouse oocytes identifies PRMT7 as a reprogramming factor that replaces SOX2 in the induction of pluripotent stem cells. *J. Proteome Res.* **15**, 2407–2421 (2016). doi: [10.1021/acs.jproteome.5b01083](https://doi.org/10.1021/acs.jproteome.5b01083); pmid: 27225728
  96. I. Virant-Klun, S. Leicht, C. Hughes, J. Krijgsvel, Identification of maturation-specific proteins by single-cell proteomics of human oocytes. *Mol. Cell. Proteomics* **15**, 2616–2627 (2016). doi: [10.1074/mcp.M115.056887](https://doi.org/10.1074/mcp.M115.056887); pmid: 27215607
  97. Z. Xue *et al.*, Genetic programs in human and mouse early embryos revealed by single-cell RNA sequencing. *Nature* **500**, 593–597 (2013). doi: [10.1038/nature12364](https://doi.org/10.1038/nature12364); pmid: 23892778
  98. A. Graf *et al.*, Fine mapping of genome activation in bovine embryos by RNA sequencing. *Proc. Natl. Acad. Sci. U.S.A.* **111**, 4139–4144 (2014). doi: [10.1073/pnas.1321569111](https://doi.org/10.1073/pnas.1321569111); pmid: 24591639
  99. J. Wu *et al.*, Chromatin analysis in human early development reveals epigenetic transition during ZGA. *Nature* **557**, 256–260 (2018). doi: [10.1038/s41586-018-0080-8](https://doi.org/10.1038/s41586-018-0080-8); pmid: 29720659
  100. L. Leng *et al.*, Single-cell transcriptome analysis of uniparental embryos reveals parent-of-origin effects on

- human preimplantation development. *Cell Stem Cell* **25**, 697–712.e6 (2019). doi: [10.1016/j.stem.2019.09.004](https://doi.org/10.1016/j.stem.2019.09.004); pmid: [31588047](https://pubmed.ncbi.nlm.nih.gov/31588047/)
101. Q. Kong *et al.*, Lineage specification and pluripotency revealed by transcriptome analysis from oocyte to blastocyst in pig. *FASEB J.* **34**, 691–705 (2020). doi: [10.1096/fj.201901818RR](https://doi.org/10.1096/fj.201901818RR); pmid: [31914626](https://pubmed.ncbi.nlm.nih.gov/31914626/)
  102. R. Yan *et al.*, Decoding dynamic epigenetic landscapes in human oocytes using single-cell multi-omics sequencing. *Cell Stem Cell* **28**, 1641–1656.e7 (2021). doi: [10.1016/j.stem.2021.04.012](https://doi.org/10.1016/j.stem.2021.04.012); pmid: [33957080](https://pubmed.ncbi.nlm.nih.gov/33957080/)
  103. I. Bennabi *et al.*, Shifting meiotic to mitotic spindle assembly in oocytes disrupts chromosome alignment. *EMBO Rep.* **19**, 368–381 (2018). doi: [10.15252/embr.201745225](https://doi.org/10.15252/embr.201745225); pmid: [29330318](https://pubmed.ncbi.nlm.nih.gov/29330318/)
  104. V. Mountain *et al.*, The kinesin-related protein, HSET, opposes the activity of Eg5 and cross-links microtubules in the mammalian mitotic spindle. *J. Cell Biol.* **147**, 351–366 (1999). doi: [10.1083/jcb.147.2.351](https://doi.org/10.1083/jcb.147.2.351); pmid: [10525540](https://pubmed.ncbi.nlm.nih.gov/10525540/)
  105. Y. Cao *et al.*, Microtubule minus-end binding protein CAMSAP2 and kinesin-14 motor KIFC3 control dendritic microtubule organization. *Curr. Biol.* **30**, 899–908.e6 (2020). doi: [10.1016/j.cub.2019.12.056](https://doi.org/10.1016/j.cub.2019.12.056); pmid: [32084403](https://pubmed.ncbi.nlm.nih.gov/32084403/)
  106. Z. Y. She, W. X. Yang, Molecular mechanisms of kinesin-14 motors in spindle assembly and chromosome segregation. *J. Cell Sci.* **130**, 2097–2110 (2017). doi: [10.1242/jcs.200261](https://doi.org/10.1242/jcs.200261); pmid: [28668932](https://pubmed.ncbi.nlm.nih.gov/28668932/)
  107. S. Cai, L. N. Weaver, S. C. Ems-McClung, C. E. Walczak, Kinesin-14 family proteins HSET/CTCK2 control spindle length by cross-linking and sliding microtubules. *Mol. Biol. Cell* **20**, 1348–1359 (2009). doi: [10.1091/mbc.e08-09-0971](https://doi.org/10.1091/mbc.e08-09-0971); pmid: [19116309](https://pubmed.ncbi.nlm.nih.gov/19116309/)
  108. C. E. Walczak, S. Verma, T. J. Mitchison, CTCK2: A kinesin-related protein that promotes mitotic spindle assembly in *Xenopus laevis* egg extracts. *J. Cell Biol.* **136**, 859–870 (1997). doi: [10.1083/jcb.136.4.859](https://doi.org/10.1083/jcb.136.4.859); pmid: [9049251](https://pubmed.ncbi.nlm.nih.gov/9049251/)
  109. T. J. Mullen, S. M. Wignall, Interplay between microtubule bundling and sorting factors ensures acentriolar spindle stability during *C. elegans* oocyte meiosis. *PLoS Genet.* **13**, e1006986 (2017). doi: [10.1371/journal.pgen.1006986](https://doi.org/10.1371/journal.pgen.1006986); pmid: [28910277](https://pubmed.ncbi.nlm.nih.gov/28910277/)
  110. C. H. Chuang, A. J. Schlientz, J. Yang, B. Bowerman, Microtubule assembly and pole coalescence: Early steps in *Caenorhabditis elegans* oocyte meiosis I spindle assembly. *Biol. Open* **9**, bio.052308 (2020). doi: [10.1242/bio.052308](https://doi.org/10.1242/bio.052308); pmid: [32493729](https://pubmed.ncbi.nlm.nih.gov/32493729/)
  111. C. E. Walczak, I. Vernos, T. J. Mitchison, E. Karsenti, R. Heald, A model for the proposed roles of different microtubule-based motor proteins in establishing spindle bipolarity. *Curr. Biol.* **8**, 903–913 (1998). doi: [10.1016/S0960-9822\(07\)00370-3](https://doi.org/10.1016/S0960-9822(07)00370-3); pmid: [9707401](https://pubmed.ncbi.nlm.nih.gov/9707401/)
  112. S. Morales-Mulia, J. M. Scholey, Spindle pole organization in *Drosophila* S2 cells by dynein, abnormal spindle protein (Asp), and KLP10A. *Mol. Biol. Cell* **16**, 3176–3186 (2005). doi: [10.1091/mbc.e04-12-1110](https://doi.org/10.1091/mbc.e04-12-1110); pmid: [15888542](https://pubmed.ncbi.nlm.nih.gov/15888542/)
  113. G. Goshima, F. Nédélec, R. D. Vale, Mechanisms for focusing mitotic spindle poles by minus end-directed motor proteins. *J. Cell Biol.* **171**, 229–240 (2005). doi: [10.1083/jcb.200505107](https://doi.org/10.1083/jcb.200505107); pmid: [16247025](https://pubmed.ncbi.nlm.nih.gov/16247025/)
  114. J. Baumbach, Z. A. Novak, J. W. Raff, A. Wainman, Dissecting the function and assembly of acentriolar microtubule organizing centers in *Drosophila* cells in vivo. *PLoS Genet.* **11**, e1005261 (2015). doi: [10.1371/journal.pgen.1005261](https://doi.org/10.1371/journal.pgen.1005261); pmid: [26020779](https://pubmed.ncbi.nlm.nih.gov/26020779/)
  115. M. Kwon *et al.*, Mechanisms to suppress multipolar divisions in cancer cells with extra centrosomes. *Genes Dev.* **22**, 2189–2203 (2008). doi: [10.1101/gad.1700908](https://doi.org/10.1101/gad.1700908); pmid: [18662975](https://pubmed.ncbi.nlm.nih.gov/18662975/)
  116. J. Kleylein-Sohn *et al.*, Acentrosomal spindle organization renders cancer cells dependent on the kinesin HSET. *J. Cell Sci.* **125**, 5391–5402 (2012). doi: [10.1242/jcs.107474](https://doi.org/10.1242/jcs.107474); pmid: [22946058](https://pubmed.ncbi.nlm.nih.gov/22946058/)
  117. N. Kim, K. Song, KIFC1 is essential for bipolar spindle formation and genomic stability in the primary human fibroblast IMR-90 cell. *Cell Struct. Funct.* **38**, 21–30 (2013). doi: [10.1247/csf.12014](https://doi.org/10.1247/csf.12014); pmid: [23318213](https://pubmed.ncbi.nlm.nih.gov/23318213/)
  118. P. L. Chavali *et al.*, A CEP215-HSET complex links centrosomes with spindle poles and drives centrosome clustering in cancer. *Nat. Commun.* **7**, 11005 (2016). doi: [10.1038/ncomms11005](https://doi.org/10.1038/ncomms11005); pmid: [26987684](https://pubmed.ncbi.nlm.nih.gov/26987684/)
  119. B. Vitre *et al.*, IFT proteins interact with HSET to promote supernumerary centrosome clustering in mitosis. *EMBO Rep.* **21**, e49234 (2020). doi: [10.15252/embr.201949234](https://doi.org/10.15252/embr.201949234); pmid: [32270908](https://pubmed.ncbi.nlm.nih.gov/32270908/)
  120. E. A. Nigg, Centrosome aberrations: Cause or consequence of cancer progression? *Nat. Rev. Cancer* **2**, 815–825 (2002). doi: [10.1038/nrc924](https://doi.org/10.1038/nrc924); pmid: [12415252](https://pubmed.ncbi.nlm.nih.gov/12415252/)
  121. J. Fu, I. M. Hagan, D. M. Glover, The centrosome and its duplication cycle. *Cold Spring Harb. Perspect. Biol.* **7**, a015800 (2015). doi: [10.1101/cshperspect.a015800](https://doi.org/10.1101/cshperspect.a015800); pmid: [25646378](https://pubmed.ncbi.nlm.nih.gov/25646378/)
  122. T. Yao *et al.*, Live-cell imaging of nuclear-chromosomal dynamics in bovine in vitro fertilised embryos. *Sci. Rep.* **8**, 7460 (2018). doi: [10.1038/s41598-018-25698-w](https://doi.org/10.1038/s41598-018-25698-w); pmid: [29748644](https://pubmed.ncbi.nlm.nih.gov/29748644/)
  123. T. Cavazza *et al.*, Parental genome unification is highly error-prone in mammalian embryos. *Cell* **184**, 2860–2877.e22 (2021). doi: [10.1016/j.cell.2021.04.013](https://doi.org/10.1016/j.cell.2021.04.013); pmid: [33964210](https://pubmed.ncbi.nlm.nih.gov/33964210/)
  124. I. Schneider, M. de Ruijter-Villani, M. J. Hossain, T. A. E. Stout, J. Ellenberg, Dual spindles assemble in bovine zygotes despite the presence of paternal centrosomes. *J. Cell Biol.* **220**, e202010106 (2021). doi: [10.1083/jcb.202010106](https://doi.org/10.1083/jcb.202010106); pmid: [34550316](https://pubmed.ncbi.nlm.nih.gov/34550316/)
  125. A. I. Mihajlović, J. Haverfield, G. FitzHarris, Distinct classes of lagging chromosome underpin age-related oocyte aneuploidy in mouse. *Dev. Cell* **56**, 2273–2283.e3 (2021). doi: [10.1016/j.devcel.2021.07.022](https://doi.org/10.1016/j.devcel.2021.07.022); pmid: [34428397](https://pubmed.ncbi.nlm.nih.gov/34428397/)
  126. J. Roelofs, G. Tsiavaliaris, Actin-microtubule interplay coordinates spindle assembly in human oocytes. *Nat. Commun.* **10**, 4651 (2019). doi: [10.1038/s41467-019-12674-9](https://doi.org/10.1038/s41467-019-12674-9); pmid: [31604948](https://pubmed.ncbi.nlm.nih.gov/31604948/)
  127. B. T. Bajar *et al.*, Improving brightness and photostability of green and red fluorescent proteins for live cell imaging and FRET reporting. *Sci. Rep.* **6**, 20889 (2016). doi: [10.1038/srep20889](https://doi.org/10.1038/srep20889); pmid: [26879144](https://pubmed.ncbi.nlm.nih.gov/26879144/)
  128. G. H. Patterson, J. Lippincott-Schwartz, A photoactivatable GFP for selective photolabeling of proteins and cells. *Science* **297**, 1873–1877 (2002). doi: [10.1126/science.1074952](https://doi.org/10.1126/science.1074952); pmid: [12228718](https://pubmed.ncbi.nlm.nih.gov/12228718/)
  129. D. S. Bindels *et al.*, mScarlet: A bright monomeric red fluorescent protein for cellular imaging. *Nat. Methods* **14**, 53–56 (2017). doi: [10.1038/nmeth.4074](https://doi.org/10.1038/nmeth.4074); pmid: [27869816](https://pubmed.ncbi.nlm.nih.gov/27869816/)
  130. E. R. Liman, J. Tytgat, P. Hess, Subunit stoichiometry of a mammalian K<sup>+</sup> channel determined by construction of multimeric cDNAs. *Neuron* **9**, 861–871 (1992). doi: [10.1016/0896-6273\(92\)90239-A](https://doi.org/10.1016/0896-6273(92)90239-A); pmid: [1419000](https://pubmed.ncbi.nlm.nih.gov/1419000/)
  131. Q. Zhang *et al.*, Nudel promotes axonal lysosome clearance and endo-lysosome formation via dynein-mediated transport. *Traffic* **10**, 1337–1349 (2009). doi: [10.1111/j.1600-0854.2009.00945.x](https://doi.org/10.1111/j.1600-0854.2009.00945.x); pmid: [19522757](https://pubmed.ncbi.nlm.nih.gov/19522757/)
  132. S. Pfender, V. Kuznetsov, S. Pleiser, E. Kerkhoff, M. Schuh, Spire-type actin nucleators cooperate with Formin-2 to drive asymmetric oocyte division. *Curr. Biol.* **21**, 955–960 (2011). doi: [10.1016/j.cub.2011.04.029](https://doi.org/10.1016/j.cub.2011.04.029); pmid: [21620703](https://pubmed.ncbi.nlm.nih.gov/21620703/)
  133. D. Clift, C. So, W. A. McEwan, L. C. James, M. Schuh, Acute and rapid degradation of endogenous proteins by Trim-Away. *Nat. Protoc.* **13**, 2149–2175 (2018). doi: [10.1038/s41596-018-0028-3](https://doi.org/10.1038/s41596-018-0028-3); pmid: [30250286](https://pubmed.ncbi.nlm.nih.gov/30250286/)
  134. S. Hua, K. Jiang, Expression and purification of microtubule-associated proteins from HEK293T cells for in vitro reconstitution. *Methods Mol. Biol.* **2101**, 19–26 (2020). doi: [10.1007/978-1-0716-0219-5\\_2](https://doi.org/10.1007/978-1-0716-0219-5_2); pmid: [31879895](https://pubmed.ncbi.nlm.nih.gov/31879895/)
  135. J. Bucevičius, G. Kostiuik, R. Gerasimaitė, T. Gilat, G. Lukinavičius, Enhancing the biocompatibility of rhodamine fluorescent probes by a neighbouring group effect. *Chem. Sci.* **11**, 7313–7323 (2020). doi: [10.1039/D0SC02154G](https://doi.org/10.1039/D0SC02154G); pmid: [33777348](https://pubmed.ncbi.nlm.nih.gov/33777348/)
  136. N. Tanaka, W. Meng, S. Nagae, M. Takeichi, Nezha/CAMSAP3 and CAMSAP2 cooperate in epithelial-specific organization of noncentrosomal microtubules. *Proc. Natl. Acad. Sci. U.S.A.* **109**, 20029–20034 (2012). doi: [10.1073/pnas.1218017109](https://doi.org/10.1073/pnas.1218017109); pmid: [23169647](https://pubmed.ncbi.nlm.nih.gov/23169647/)
  137. A. Z. Politi *et al.*, Quantitative mapping of fluorescently tagged cellular proteins using FCS-calibrated four-dimensional imaging. *Nat. Protoc.* **13**, 1445–1464 (2018). doi: [10.1038/nprot.2018.040](https://doi.org/10.1038/nprot.2018.040); pmid: [29844523](https://pubmed.ncbi.nlm.nih.gov/29844523/)
  138. N. L. Schieber *et al.*, Minimal resin embedding of multicellular specimens for targeted FIB-SEM imaging. *Methods Cell Biol.* **140**, 69–83 (2017). doi: [10.1016/bs.mcb.2017.03.005](https://doi.org/10.1016/bs.mcb.2017.03.005); pmid: [28528642](https://pubmed.ncbi.nlm.nih.gov/28528642/)
  139. B. Li, C. N. Dewey, RSEM: Accurate transcript quantification from RNA-Seq data with or without a reference genome. *BMC Bioinformatics* **12**, 323 (2011). doi: [10.1186/1471-2105-12-323](https://doi.org/10.1186/1471-2105-12-323); pmid: [21816040](https://pubmed.ncbi.nlm.nih.gov/21816040/)
  140. G. P. Wagner, K. Kin, V. J. Lynch, Measurement of mRNA abundance using RNA-seq data: RPKM measure is inconsistent among samples. *Theory Biosci.* **131**, 281–285 (2012). doi: [10.1007/s12064-012-0162-3](https://doi.org/10.1007/s12064-012-0162-3); pmid: [22872506](https://pubmed.ncbi.nlm.nih.gov/22872506/)

## ACKNOWLEDGMENTS

We are grateful to the patients who participated in this study. We thank the staff from the Animal Facility and Live-Cell Imaging Facility at the Max Planck Institute for Multidisciplinary Sciences for technical assistance; the clinicians, nursing team, and embryology team at the clinics for their support of this study; L. Abdelhalim, E. Bellou, and L. Wartosch for help with human oocytes; C. Mauksch for help with optimizing thawing of vitrified human oocytes; E. Bellou, T. Cavazza, and M. Daniel for help with bovine and porcine ovaries; T. Ruhwedel for help with sample preparation for electron microscopy; E. Bellou, A. Politi, and F. Xie for helpful discussions; A. Andersen, T. Cavazza, P. Lénárt, and L. Wartosch for critical comments on the manuscript; T. Hiragi, the M. J. Fox Foundation, M. Mancini, and X. Zhu for cDNAs and constructs; and D. A. Compton, E. Nigg, G. Goshima, P. Meraldi, A. McAinsin, M. Takeichi, and R. Uehara for antibodies. **Funding:** The research leading to these results was funded by the Max Planck Society and the DFG under a Leibniz Prize to M.S. (SCHU 3047/1-1) and a grant to W.M. [MO 1084/2-1 (FOR2848, P8)]. C.So is a recipient of the Max Planck Croucher Postdoctoral Fellowship. W.M. and M.S. were supported by the Deutsche Forschungsgemeinschaft (DFG, German Research Foundation) under Germany's Excellence Strategy—EXC 2067/1-390729940. **Author contributions:** C.So and M.S. conceived the study, designed experiments and methods for data analysis; C.So performed all experiments and analyzed the data with the following exceptions: K.M. performed Trim-Away of NUMA in human oocytes; J.H. performed inhibition with P150-CC1 in human oocytes; K.H. performed live imaging of porcine oocytes and optimized live imaging of bovine oocytes; A.M.S. prepared electron microscopy samples with C.So and performed FIB-SEM; K.B.S. optimized Trim-Away of NUMA and inhibition with P150-CC1 in human oocytes; and J.B. and G.L. synthesized 5-SiR-CTX and 5-SiR-Hoechst. C.So and M.S. wrote the manuscript and prepared the figures with input from all authors; W.M. supervised the electron microscopy experiments; C.Si. and A.T.-S. supervised the collection and vitrification of human oocytes at Fertility Center Berlin; H.E. and R.M. supervised the collection of human oocytes at Kinderwunschzentrum Göttingen; M.B. and K.E. supervised the collection of human oocytes at Bourn Hall Clinic; and M.S. supervised the entire study. **Competing interests:** C.So and M.S. filed a patent application (EP21199120.3) based on data presented here. The other authors declare no competing financial interests. **Data and materials availability:** Plasmids are available from M.S. under a material transfer agreement with the Max Planck Society. All data needed to evaluate the conclusions in the paper are present in the main text or the supplementary materials.

## SUPPLEMENTARY MATERIALS

[science.org/doi/10.1126/science.abj3944](https://science.org/doi/10.1126/science.abj3944)

Figs. S1 to S14

Tables S1 and S2

MDAR Reproducibility Checklist

Movies S1 to S18

10 May 2021; resubmitted 2 November 2021

Accepted 11 January 2022

[10.1126/science.abj3944](https://doi.org/10.1126/science.abj3944)



## Pushing the Boundaries of Knowledge

As AAAS's first multidisciplinary, open access journal, *Science Advances* publishes research that reflects the selectivity of high impact, innovative research you expect from the *Science* family of journals, published in an open access format to serve a vast and growing global audience. Check out the latest findings or learn how to submit your research: **[ScienceAdvances.org](https://www.scienceadvances.org)**

Science  
Advances  
AAAS

---

**GOLD OPEN ACCESS, DIGITAL, AND FREE TO ALL READERS**

---



## RESEARCH ARTICLES

## NEUROSCIENCE

# Geometry of sequence working memory in macaque prefrontal cortex

Yang Xie<sup>1†</sup>, Peiyao Hu<sup>1†</sup>, Junru Li<sup>1</sup>, Jingwen Chen<sup>1</sup>, Weibin Song<sup>2</sup>, Xiao-Jing Wang<sup>3</sup>, Tianming Yang<sup>1</sup>, Stanislas Dehaene<sup>4,5</sup>, Shiming Tang<sup>2,6\*</sup>, Bin Min<sup>7\*</sup>, Liping Wang<sup>1\*</sup>

How the brain stores a sequence in memory remains largely unknown. We investigated the neural code underlying sequence working memory using two-photon calcium imaging to record thousands of neurons in the prefrontal cortex of macaque monkeys memorizing and then reproducing a sequence of locations after a delay. We discovered a regular geometrical organization: The high-dimensional neural state space during the delay could be decomposed into a sum of low-dimensional subspaces, each storing the spatial location at a given ordinal rank, which could be generalized to novel sequences and explain monkey behavior. The rank subspaces were distributed across large overlapping neural groups, and the integration of ordinal and spatial information occurred at the collective level rather than within single neurons. Thus, a simple representational geometry underlies sequence working memory.

Episodic experiences in the real or mental world are, by their nature, a succession of events. The ability to remember the ordinal succession of items in a sequence is crucial for various higher-level cognitive functions, including language, episodic memory, and spatial navigation (1). However, how a sequence is represented and stored in memory remains largely unknown. There could be two ways of encoding sequences. First, there may be a repertoire of representations for every sequence encountered—in other words, a separate representation for each sequence. Alternatively, the representation could be factorized, for instance with distinct memory slots for items at different ordinal ranks or by separating the temporal structure from the content items (2, 3).

Such factorized representation is also referred to as a form of disentangling (4). The hypothesis posits that our brain benefits from representing the underlying structure of the world in a disentangled manner because changing the properties in one part of the structure would leave the representation of other parts intact. Thus, disentangling temporal structures from particular events may lead to faster generalization and novel inferences (3, 5, 6).

However, whether and how the neural representations encode abstract temporal structures in sequence working memory (SWM) remains unclear.

At the single-neuron level, it is often proposed that our brain binds information from multiple domains through multiplicative gain modulation (7, 8). One popular hypothesis for SWM is that abstract information about ordinal number could be conjoined with item-specific sensory information through a gain-field mechanism, such that individual prefrontal neurons would be tuned to the product of those two variables (2). Alternatively, the neural codes for sequences may be distributed across a large neural population and bound using matrix or tensor products (9). Recent studies have suggested that abstract information may be represented in high-dimensional neural state space (10, 11). The trajectories within subregions (neural manifolds) of this space can instantiate the hidden organizing structures that underlie, for example, motor movements in motor areas (12) or time and abstract knowledge in the hippocampus and prefrontal cortex (13–16).

To investigate the neural representations of SWM at both the single-neuron and population levels, we asked the following questions: (i) whether low-dimensional manifolds underlie the disentangled representation of temporal structure in SWM, (ii) how neurons integrate neural representations of temporal order and sensory items in SWM, (iii) how single neurons are organized anatomically and functionally to contribute to these manifolds, and (iv) whether we can provide a unified mathematical description of those computations at the single-neuron and population levels. To address these questions, we trained two monkeys to perform a visuospatial delayed

sequence-reproduction task and used two-photon calcium imaging to record neurons in the lateral prefrontal cortex (LPFC).

## Paradigm and behavior

Two macaque monkeys were trained on a delayed spatial sequence-reproduction task (17). On each trial, during the sample period, sequences of two or three spatial locations were visually presented while the monkey fixated on a dot at the center of the screen. Each sequence item was drawn without replacement from one of six spatial locations on a ring. Monkeys had to memorize the sequence over a delay of 2.5 to 4 s and then reproduce it by making sequential saccades to the appropriate locations on screen (Fig. 1A).

Overall, the two monkeys performed the task well: At each rank, the mean percent correct rate was significantly higher than chance (Fig. 1B; all  $P$  values  $< 0.001$ , two-tailed  $t$  test) without any significant spatial bias (see fig. S1 for detailed task performance). Recall accuracy decreased with sequence length (Fig. 1B). Both monkeys showed an advantage for items presented at the start of the sequence (the primacy effect). No recency effect was observed. When an item was recalled at an incorrect serial position, its recall spatial location was likely to lie near the original location (Fig. 1C, left), and its recall order was likely to have been swapped with the neighboring orders. Such transposition errors increased with increasing order (Fig. 1C, right).

## Hypothesis: Disentangled representation of SWM

The factorized model posits that the brain finds the natural decomposition of sequences comprising two generative factors: ordinal information (ranks 1 to 3) and spatial location (six items). Thus, we tested whether the vector space representing the sequence in memory would be a concatenation of multiple independent rank representations, each embedding a representation of the corresponding spatial item. For instance, to represent the sequence [5 2 4], item 5 is bound to rank 1, item 2 is bound to rank 2, and so on.

To measure the neural state, we injected GCaMP6s virus into the LPFCs of the two monkeys to enable two-photon calcium imaging of the LPFC (Fig. 1, D to F, and fig. S2) [monkey 1, 3609 neurons from 20 fields of view (FOVs); monkey 2, 1716 neurons from 13 FOVs]. We focused on neural activity during the late delay period (1 s before the “fixation-off” go signal) while the monkeys maintained length-2 or -3 spatial sequences in memory.

Neurons exhibiting a conjunctive preference for rank and location were immediately apparent (Fig. 1G; see the proportion of conjunctive neurons in different FOVs in fig. S2). Such neurons responded selectively to

<sup>1</sup>Institute of Neuroscience, Key Laboratory of Primate Neurobiology, CAS Center for Excellence in Brain Science and Intelligence Technology, Chinese Academy of Sciences, Shanghai 200031, China. <sup>2</sup>Peking University School of Life Sciences and Peking-Tsinghua Center for Life Sciences, Beijing 100871, China. <sup>3</sup>Center for Neural Science, New York University, New York, NY 10003, USA. <sup>4</sup>Cognitive Neuroimaging Unit, CEA, INSERM, Université Paris-Saclay, NeuroSpin Center, 91191 Gif/Yvette, France. <sup>5</sup>Collège de France, Université Paris Sciences Lettres, 75005 Paris, France. <sup>6</sup>IDG/McGovern Institute for Brain Research at Peking University, Beijing 100871, China. <sup>7</sup>Shanghai Center for Brain Science and Brain-Inspired Technology, Shanghai 200031, China.

\*Corresponding author. Email: liping.wang@ion.ac.cn (L.W.); bin.min@bsbii.cn (B.M.); tangshm@pku.edu.cn (S.T.)

†These authors contributed equally to this work.

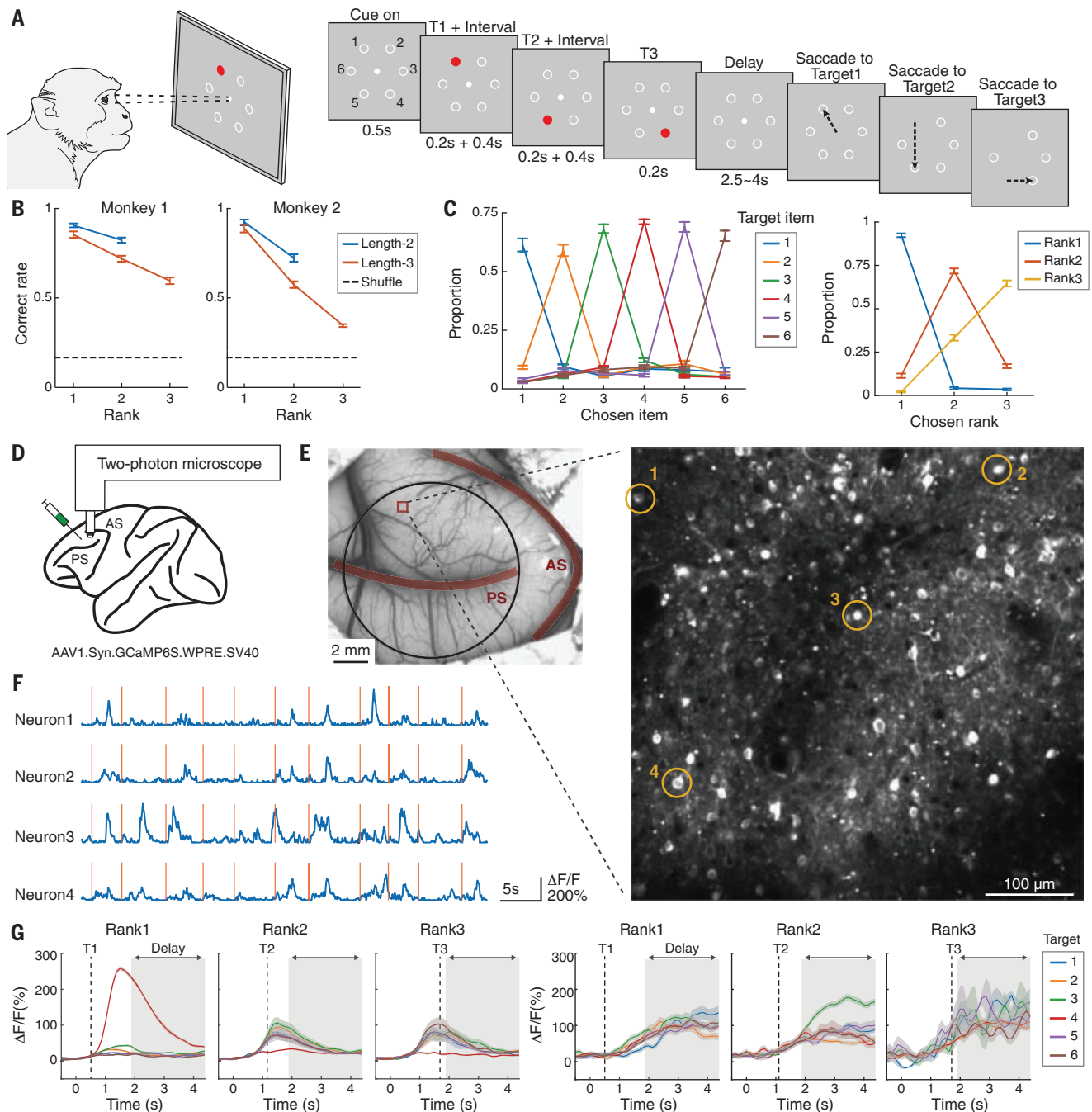


**Fig. 1. Two-photon calcium imaging of macaque LPFCs during a delayed sequence-reproduction task.** (A) Task structure (17). T1, target 1. (B) Behavioral performance averaged across imaging sessions. Performance is shown as a function of ordinal rank in length-2 sequences (blue) and length-3 sequences (red). Error bars represent SEMs. (C) Spatial location (left) and ordinal rank (right) error patterns, averaged across the two monkeys. Location error pattern is shown as a function of spatial location, averaged across different ranks. Rank error pattern is shown as a function of ordinal rank, averaged across different spatial locations. Error bars represent SEMs. (D) Illustration of two-photon calcium imaging of monkey LPFCs (17). AS, arcuate sulcus; PS, principal sulcus. (E) An example FOV, indicated by the red square (left), and its enlargement (right). (F) Normalized calcium traces of four example neurons [yellow circles in (E)].  $\Delta F/F$ , normalized fluorescent intensity. (G) Two example neurons exhibiting the property of conjunctive coding for spatial location and ordinal rank. Traces were aligned to cue onset and pooled across trials according to spatial location and ordinal rank.

particular spatial locations on the ring but also to their ordinal rank in the sequence (first, second, or third). We quantified the influence of spatial item and ordinal rank on the neural responses of single neurons during the late delay period using linear regression, in-

corporating spatial item and ordinal rank as variables (6 items  $\times$  3 ranks = 18 combinations) to fit the calcium signals of individual neurons. We used the regression coefficients to measure each neuron's selectivity to either item or rank variable (17).

### Disentangled representation of SWM by the LPFC neural population

To examine whether the high-dimensional state of LPFC neuron activity reflected a disentangled representation of SWM, we first obtained vector representations in population

states for the 18 location-rank combinations by concatenating the regression coefficients of all neurons from correct trials of monkey 1 (see fig. S3 for monkey 2). We then divided these 18 vectors into three groups along rank and, for each rank, performed a principal components analysis to obtain the axes that captured the major response variance resulting from item changes (fig. S3).

The analysis yielded a highly reliable state-space portrait that captured both the relationship among different rank subspaces and the geometry of spatial representations within each rank subspace (17). First, for length-3 sequences, we found three two-dimensional (2D) subspaces, one for each rank (Fig. 2A). Those subspaces were oriented in a near-orthogonal manner in neural state space, as evident by the large principal angles between them (Fig. 2B). To further quantify the degree of alignment across different rank subspaces, for any two ranks—e.g., rank 1 and rank 2—we calculated the variance accounted for (VAF) ratio by projecting the data from the rank-1 subspace to the rank-2 subspace and computing the remaining data variance after the projection.

If the two rank subspaces are near orthogonal, the projection from one subspace will capture little of the data variance of the other subspace, which results in a low VAF ratio. The result showed low VAF ratios for all cross-subspace pairs. As a control, if the ranks were shuffled while holding item location constant, the orthogonality of the subspaces was lost (fig. S4). Furthermore, neurophysiology reflected behavior: VAF ratios for within-subspace trial pairs, measuring the stability of rank subspace estimation, were high on correct trials (Fig. 2C) but were low for misremembered locations, where rank-2 and -3 subspaces became difficult to estimate (fig. S5).

Next, we explored the neural encoding of location within each rank subspace. At each rank, we found a common geometric ring structure, reminiscent of the ring shape of the spatial items presented to the monkeys (Fig. 2A). This ring structure was not observed during the baseline period when the visual stimuli were not yet present (Fig. 2A; dots located around [0, 0]). The size of the ring in each subspace, reflecting the encoding strength of location information, decreased with ordi-

nal rank. The ring size became smaller, and ring structure was nearly undetectable on error trials (fig. S5).

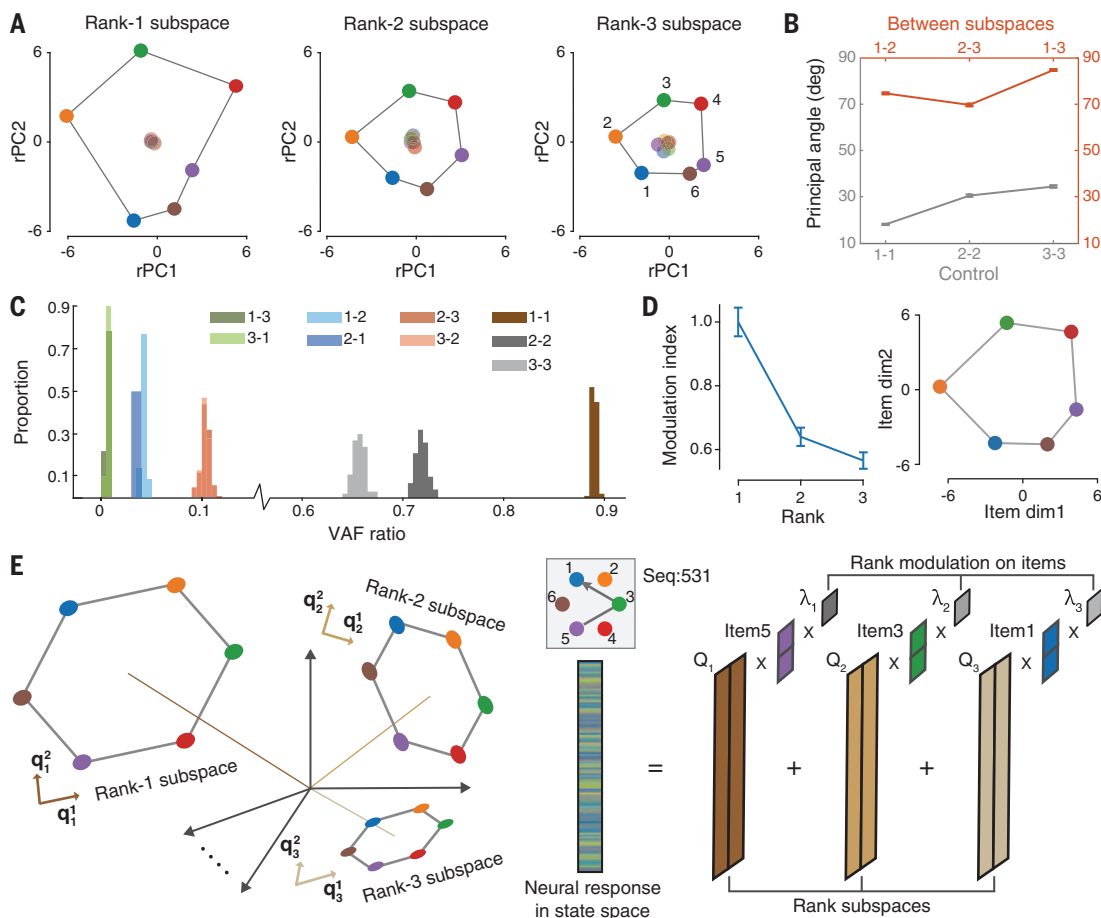
We then quantified how well a simple mathematical model with three rank subspaces, each relying on the same 2D spatial code with a distinct modulation factor, could approximate the full 18-variable regression model at the collective level (Fig. 2D and eqs. S1 and S2). There was a high similarity between the data and the model at each rank (score 0.95 for rank 1, 0.99 for rank 2, and 0.98 for rank 3) (17), which supports the hypothesis of a factorized representation of spatial items at the collective level (Fig. 2E) with an additive combination of vectorial representations of location at each ordinal rank. A similar geometry was observed in the second monkey for length-2 sequences and, to a lesser extent, for length-3 sequences (fig. S3).

### Disentangled rank subspaces at the single-trial level in individual FOVs

The above state-space analysis pools neurons recorded from different FOVs and averages their responses over trials. We investigated

### Fig. 2. Disentangled neural state space representation of SWM.

**(A)** The population response for a given rank-location combination projected to the corresponding rank subspace for monkey 1. Responses were obtained through linear regression of averaged late delay activity (1 s before fixation off). Locations are color coded. The center points were data at the beginning of the sample period. rPC, rotated principal component. **(B)** The principal angle between different rank subspaces (red). As a control, we randomly split trials in half to obtain two separate estimations of each rank subspace and computed their principal angle (gray). deg, degree. **(C)** The VAF ratio with respect to different rank subspace pairs. As a control, we randomly split trials in half to obtain two separate estimations of each rank subspace and computed their VAF ratio. **(D)** Gain modulation approximation of the projected value at difference rank subspaces. These collective variables can be well approximated by a gain modulation model parameterized by a shared spatial layout (right) and a rank modulation vector (left). dim, dimension. **(E)** A graphical summary of SWM representation in neural state space. Three 2D rank subspaces are oriented in a nearly orthogonal manner in neural state space (left). The neural representation of a sequence can be decomposed into a sum of component items in rank subspaces (right).  $q$  and  $Q$ , axes of subspace;  $\lambda$ , rank modulation index.





whether the disentangled representation of sequence memory could be validated at the single-trial level. We tested whether the rank subspaces were abstract enough to generalize to different datasets, including untrained, different-length, or error sequences.

Single-trial decoding methods were used to decode item locations at ranks 1, 2, and 3, respectively (Fig. 3A) (17). Neurons in almost all (30 of 33) FOVs contained item information at rank 1, and neurons in 21 of 33 (64%) FOVs contained item information at other ranks (rank 2 or rank 3) (tables S1 and S2). Figure 3B shows the decoding results for the six items at rank 1, rank 2, and rank 3 from an example FOV located in the dorsolateral prefrontal cortex (monkey 1, FOV4; fig. S2A). At each rank, the corresponding item could be decoded at above-chance levels during the sample, delay, and reproduction periods. During the delay period, the code for the item was stable, with the decoder performing well even when the training and testing times differed. However, the code during the delay period did not generalize to the sample and reproduction periods, which indicates dynamic changes in the neural code. Similar decoding profiles were found in other FOVs in both monkeys (fig. S6, A and B). By examining decoder error patterns during the late delay period (Fig. 3C), we found that most errors were confusions with the neighboring spatial items.

We next visualized the dynamics of the neural code for location by projecting the population activities at each time bin of a trial to the three decoder-based rank subspaces, which were obtained using neural responses during the late delay period (17). The six locations were well separated in the rank subspaces, and, crucially, the ring structure was preserved for all ranks (Fig. 3D). We also investigated the relationships between the three rank subspaces by examining the cross-rank decoding performance and calculating their cross-subspace VAF ratios. The results confirmed the findings from the state-space analysis and showed the minimal cross-rank decoding performance (fig. S6C) and little overlap between the three rank subspaces (fig. S6D), which supports the disentangled representation of sequence memory at the single-trial level.

If sequences are disentangled into a rank-location encoding, the neural subspaces of ordinal rank should generalize to other untrained sequences. We tested this idea using three generalization analyses. First, we used leave-one-sequence-out cross-validation to confirm that the rank subspaces revealed in Fig. 3B remained stable for left-out sequences that were not used during decoder training. The neural subspaces of ordinal ranks (ranks 1 and 2) correctly and stably separated the six spatial

items in the left-out sequences during the delay period (Fig. 3E). Second, we tested whether the rank subspaces transferred to sequences of a different length. The rank-1 and -2 subspaces trained on length-2 sequences successfully generalized to length-3 sequences (Fig. 3F) and vice versa (Fig. 3G). Finally, according to the definition of disentangled representation, rank subspaces are independent and could therefore independently fail. We thus tested whether the decoders, trained on correct trials, generalized to error trials that had a correct response at a given rank. For example, when the response to the sequence [1 3 6] is [2 3 5], the code for rank 2 could be expected to transfer between the correct and error trials, despite the errors at rank 1 and rank 3. Figure 3H shows such successful generalization. However, because of the heterogeneous nature of the LPFC, not all FOVs passed these generalization tests (see fig. S7 and tables S3 to S5 for all FOVs).

### The geometry of SWM explains sequence behavior

Although SWM relies on disentangled representations, the rank subspaces are not perfectly orthogonal. We therefore asked whether the detailed characteristics of these representations could explain classic sequence-reproduction behaviors, such as the primacy and length effects and the transposition gradient shown in Fig. 1 and fig. S1. We first looked at the relationship between ordinal ranks. The VAF ratios between ranks demonstrate a graded and compressive code (Fig. 2C) (18). First, the neural overlap between ranks increased with rank: The VAF ratio between rank 2 and rank 3 was larger than that between rank 1 and rank 2. Second, the overlap was larger for neighboring ranks: VAF ratios between neighboring ranks (rank 1 versus rank 2 and rank 2 versus rank 3) were larger than VAF ratios between distant ranks (rank 1 versus rank 3).

We propose that such compressive coding in the rank dimension is one of the hallmarks of sequence representation in working memory and can explain the monkeys' behavior during sequence recall. First, the larger overlap between adjacent rank subspaces promotes the confusion of locations at consecutive ordinal ranks, leading to the ordinal transposition gradient (Fig. 1C, right) whereby most recall order errors are swaps with the neighboring ranks. Furthermore, the increasing number of transposition errors with rank could potentially arise from the smaller overlap of orders at the beginning of the sequence, resulting in high precision of item information at this stage. Finally, the ring structure in each rank subspace may also explain the frequent confusion of nearby locations (Fig. 1C, left).

### Distributed single-neuron basis of rank subspaces

What is the implementation of rank subspaces at the level of single neurons? Does a single neuron contribute to multiple rank subspaces, and, if so, does it exhibit the same preferred locations across different ranks? For each neuron, we projected the unit vector along its axis onto the different rank subspaces (Fig. 4A). The geometric relationship between a single neuron axis and rank- $r$  subspace was characterized by  $A_r$  and  $\phi_r$ , where  $A_r$  measures the degree of alignment between single neuron axis and rank- $r$  subspace and  $\phi_r$  specifies the spatial item preference of a single neuron in rank- $r$  subspace. We could then ask what proportion of neurons contribute to each subspace, whether single neurons align with multiple subspaces, and, if so, whether they have the same preferred location  $\phi_r$  at different ranks.

The normalized participation ratio (PR) evaluates the fraction of neurons contributing to each subspace (17). A value close to 1 indicates that the corresponding rank subspace is distributed across the entire recorded population, whereas a value close to 0 indicates that it is localized to just a few neurons. Around 38% of neurons contributed to rank 1 (34% for rank 2 and 32% for rank 3; Fig. 4B), which suggests that rank memory is broadly distributed in the LPFC population. The three rank subspaces recruited both overlapping and disjoint neurons (fig. S8A).

Next, for neurons contributing to at least two rank subspaces (see materials and methods for neuron selection criteria), we asked whether their preferred spatial location was the same at different ranks. The difference in preferred location  $\phi_r$  was broadly distributed for all rank pairs and substantially removed from a distribution concentrated around 0 (Fig. 4C and fig. S8B). Thus, the angle  $\phi_r$  varied with rank for many neurons. Figure 4D shows two example neurons, one exhibiting identical spatial tuning but different amplitudes across the three ranks (classical gain modulation; Fig. 4D, left) and the other showing a shift of spatial tuning across the three ranks (tuning to item 6 at rank 1, items 4 to 5 at rank 2, and items 3 to 4 at rank 3; Fig. 4D, right). The angle  $\phi_r$  provided a good summary of the neuron's spatial preference at each rank because the angular difference between ranks predicted the difference in spatial location preference (Fig. 4E; see the angle estimation in fig. S9 and the tuning curves for the 35 neurons that contribute most to each rank subspace in fig. S10). Similar findings were obtained from monkey 2 (figs. S8, S9, and S11).

These results reject a simple model where gain modulation occurs at the level of single neurons, with each neuron having a fixed spatial tuning curve modulated by a different

scalar at each rank (2). Rather, gain modulation is a collective phenomenon that occurs at the neural population level and is best described by matrix rather than scalar multiplication (Fig. 2E and eq. S2). As a result, the memorized content at each ordinal rank is sent in a different direction of neural hyperspace, and the underlying single-neuron tuning curves, characterized by  $\varphi$ , may deviate greatly

from a simple gain modulation profile and exhibit a tuning shift with rank.

### Anatomical organization of the compositional code in the LPFC

Two-photon imaging provided us with the opportunity to examine the spatial anatomical organization of the neural codes and follow it longitudinally across days. We calculated a

spatial clustering index for neurons contributing to each rank subspace (Fig. 5A), as assessed by their alignment  $A_r$ , and compared it with shuffled distributions obtained by randomly permuting the positions of all neurons (17). The rank code showed no significant anatomical clustering at any spatial scale ranging from ~10 to ~500  $\mu\text{m}$  (Fig. 5B). We examined whether neurons with similar

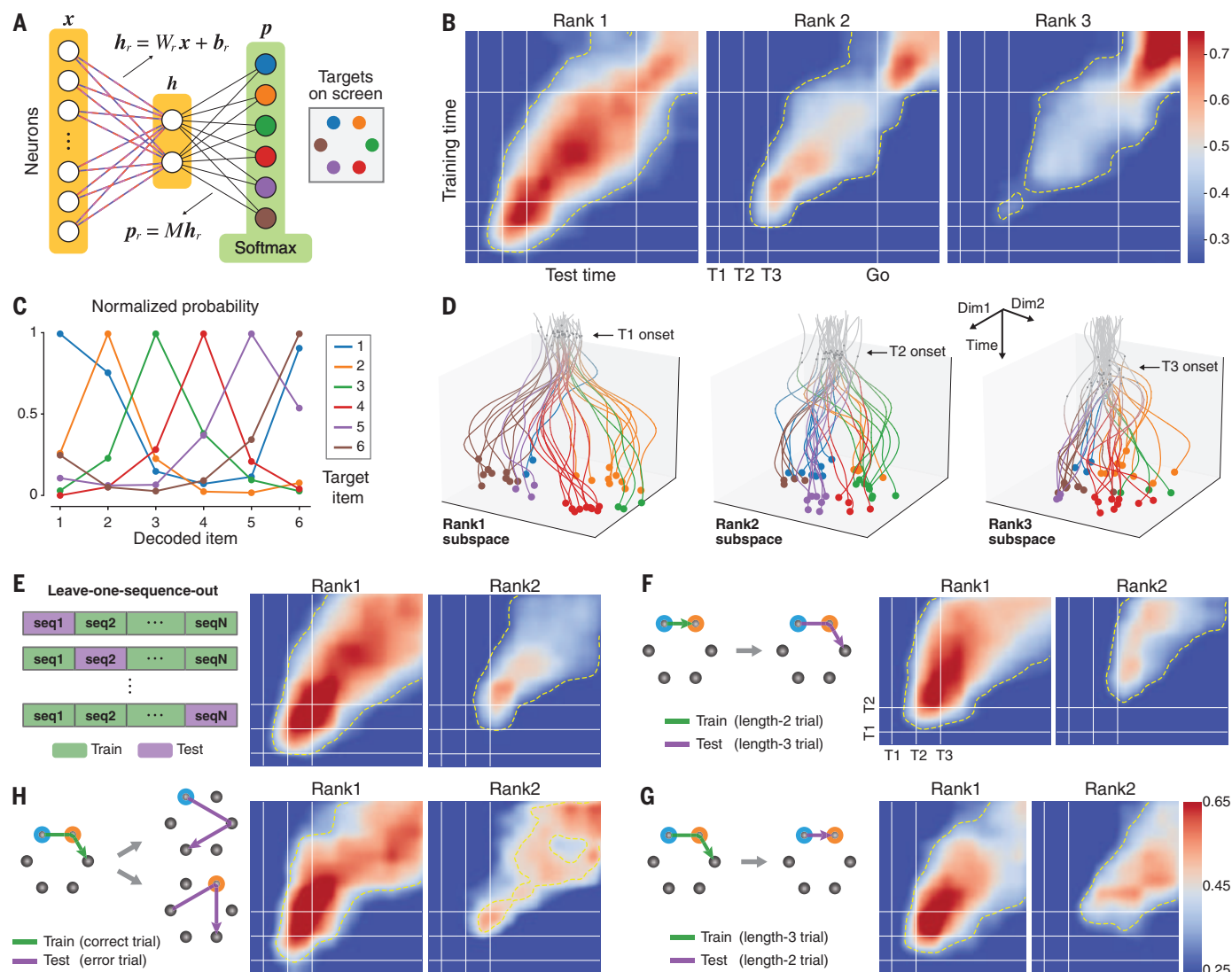


**Fig. 3. Single-trial decoding analysis and compositional generalization test of rank subspace.** (A) The architecture of the decoder (17). Neural activity ( $x$ ) was linearly projected ( $W$ , weight;  $b$ , bias) into a 2D hidden state ( $h$ ), which was classified against target matrix ( $M$ ) to obtain softmax scores ( $p$ ) for all items. Rank-specific variables are indicated by a subscripted  $r$ . (B) Cross-temporal decoding accuracy for spatial locations of each rank in length-3 sequences in an example FOV from monkey 1. Only correct trials were used, and a leave-one-trial-out cross-validation protocol was used. The yellow contours enclose areas of strong decoding performance ( $P < 0.001$ , extreme pixel-based permutation test). T1, T2, and T3 indicate the onset of the first, second, and third targets, respectively. Go indicates fixation point off. Colormap: 0.25 to 0.75. (C) The normalized distribution of decoded locations averaged in the last three time windows of the delay period and across ranks. (D) Sequence trajectories in three decoding-based rank subspaces evolving across

time until the end of delay. Each trajectory was obtained by averaging trials from the same sequence and was colored according to the location of the corresponding rank. (E) Cross-temporal decoding accuracy obtained by leave-one-sequence-out protocol. The correct trials of length-3 sequences were split into test and training sets. The test set contained all the trials for one particular sequence, whereas the training set consisted of the remaining trials for other sequences. Contours,  $P < 0.005$  (extreme pixel-based test). Colormap: 0.25 to 0.65 [same for (E) to (H)]. (F) Cross-length decoding. Decoders trained with trials of the length-3 sequence were tested in trials of length-2 sequence. All the data used for training and testing were correct trials. (G) Cross-length decoding from length-2 sequences to length-3 sequences [similar to (F)]. (H) Decoding location match in error trials. Decoder trained with all the length-3 correct trials was tested in error trials with the correct response at the rank where the decoder was trained.

location tuning were anatomically located closer to each other (Fig. 5C). The location code displayed significant clusters at a scale of  $<150\ \mu\text{m}$  for ranks 1 and 2 (Fig. 5D). A similar anatomical pattern was obtained from other FOVs in both monkeys (fig. S12).

We also examined whether the code in the population of neurons was stable across different recording days. For the same recording FOV, we trained the decoder using data from one recording day and tested it on data from a different day (Fig. 5E). The disentangled rank subspaces generalized well across days (Fig. 5F), indicating the long-term stability of the code embedded in the monkey's LPFC.

## Discussion

Using two-photon calcium imaging in the LPFC of macaque monkeys performing a visuospatial sequence-reproduction task, we revealed the representational geometry of SWM in the LPFC neural state space. Sequence memory relied on a compositional neural code with separate disentangled low-dimensional rank subspaces for every rank, each of which was broadly distributed across the neural population. Rank and item variables were integrated through multiplicative gain modulation at the collective level, but not within single neurons. Furthermore, the rank subspaces were abstract and generalizable to novel and variable-length sequences.

### Disentangled rank representation and gain modulation

How does the brain efficiently learn complex cognitive tasks such as delayed sequence reproduction? One important strategy is to split a complex whole into simpler parts that reflect the underlying structure of a task. In the present study, we explicitly searched for a neural representation with axes that aligned with the generative factors of the model—i.e., the ordinal ranks. We found that the LPFC neural population implements a decomposition into three subspaces that reflect the underlying structure of sequence memory—i.e., three spatial rings, one for each rank (Fig. 2E). The simple 3-by-2 geometrical structure that we observed reflected the 2D spatial content memorized at each rank. Although we showed generalization to left-out trials and sequences (Fig. 3), future research should examine generalization to untrained sequences and new item types (e.g., letters and numbers). If the LPFC neural population geometry is a ubiquitous feature of brain activity that extends beyond the spatial domain, we predict that orthogonal subspaces, one for each ordinal rank, should continue to be observed and may contribute to learning and inference in any task that relies on the temporal structure of ordinal knowledge.

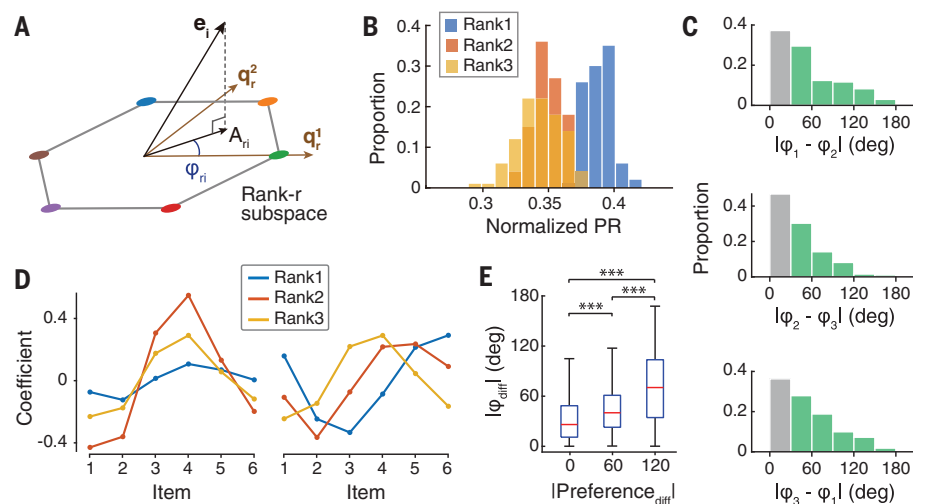


**Fig. 4. Single-neuron basis of rank subspaces.** (A) Illustration of how each single-neuron normalized response vector was projected onto the rank subspaces. (B) Quantification of the degree of localization in neural state space for different rank subspaces for monkey 1. The histogram shows the empirical distribution of normalized PR estimated by bootstrap. (C) Histograms of  $\phi_r$  difference for different rank pairs. A difference of  $<30^\circ$  (gray bar) suggests the same preferred location at two ranks, whereas the larger differences (green bars) indicate different location preferences across ranks. (D) Two example neurons with tuning curves showing classical gain modulation (left) and preference shift (right), respectively. (E) The correspondence of  $\phi_r$  difference (based on  $\phi_r$  extracted from the geometric relationship between single-neuron axis and rank subspaces) and preference difference (based on preference of spatial location extracted from the raw regression coefficients).

Diverse cognitive functions, including coordinate transformation, multimodal integration, place anchoring, abstraction, and attention, are performed through a canonical neural computation of gain modulation (7, 8, 19–21). Accordingly, a previous model had proposed that sequences are encoded through the binding of ordinal and identity information in individual prefrontal neurons tuned to the product of these two variables (2). Our results are close to this gain modulation model but depart from it in a crucial way: In contrast to the predictions of a single-neuron gain modulation, our data suggest that neural gain modulation occurs only at the collective level and is therefore best described by matrix rather than scalar multiplication. This aspect of our results is compatible with models that show how recurrent neural networks can learn vectorial representation of sequences (or even sentences) by implicitly compiling them into a sum of filler-role bindings using tensor products (9). The present data suggest that LPFC neural states implement vector symbolic architectures and tensor-product representations for sequence memory—an idea with a vast number of applications to artificial neural networks.

### Neural mechanisms of classical behavioral effects in serial recall from working memory

Serial recall from working memory is characterized by empirical findings from both behavioral and theoretical perspectives (22, 23),

including not only the quality and quantity of item information maintained but also item-order binding information (e.g., binding errors). Yet, there has previously been no neural evidence providing a mechanistic explanation for most of those behavioral observations. The neural code for SWM that we observed shows that, although the rank subspaces are nearly orthogonal, the sequence representation implements a graded and compressive encoding of rank information, with subspaces showing increasing overlap as rank increases. This neural response profile is consistent with previous findings from single-unit recordings in macaque prefrontal and parietal areas, in which ordinal numbers were represented with the characteristic signature of Weber's law (18). The code property we describe also provides insight into several influential models of sequence memory, such as the slot, resource, and interference model, and can thus explain many behavioral benchmarks of working memory for serial order, including the effects of list length and composition, the primacy effect, the temporal transposition errors, and potentially also working memory capacity (24).

### Converting temporally segregated sensory inputs into spatially overlapping sustained brain activity patterns

Previous mechanistic models of sequence memory have mostly focused on a temporal encoding of sequences supported either by



synfire chains, neural oscillations, or rhythmic fluctuations in neuronal excitability (5, 25–27). All of these models posit that the order of items in a sequence is represented by the timing of neural activity, either by locking to the relative phase of a lower-frequency oscillation (theta, 3 to 8 Hz) (28) or by the replay of a neural trajectory (29, 30). However, it is also widely accepted that attractor states of sustained neural activity play a central role in working memory (31, 32). Neurophysiological studies in nonhuman primates have found that this mechanism could apply to the memory for sequences because the sustained activity of prefrontal cortex neurons maintained both

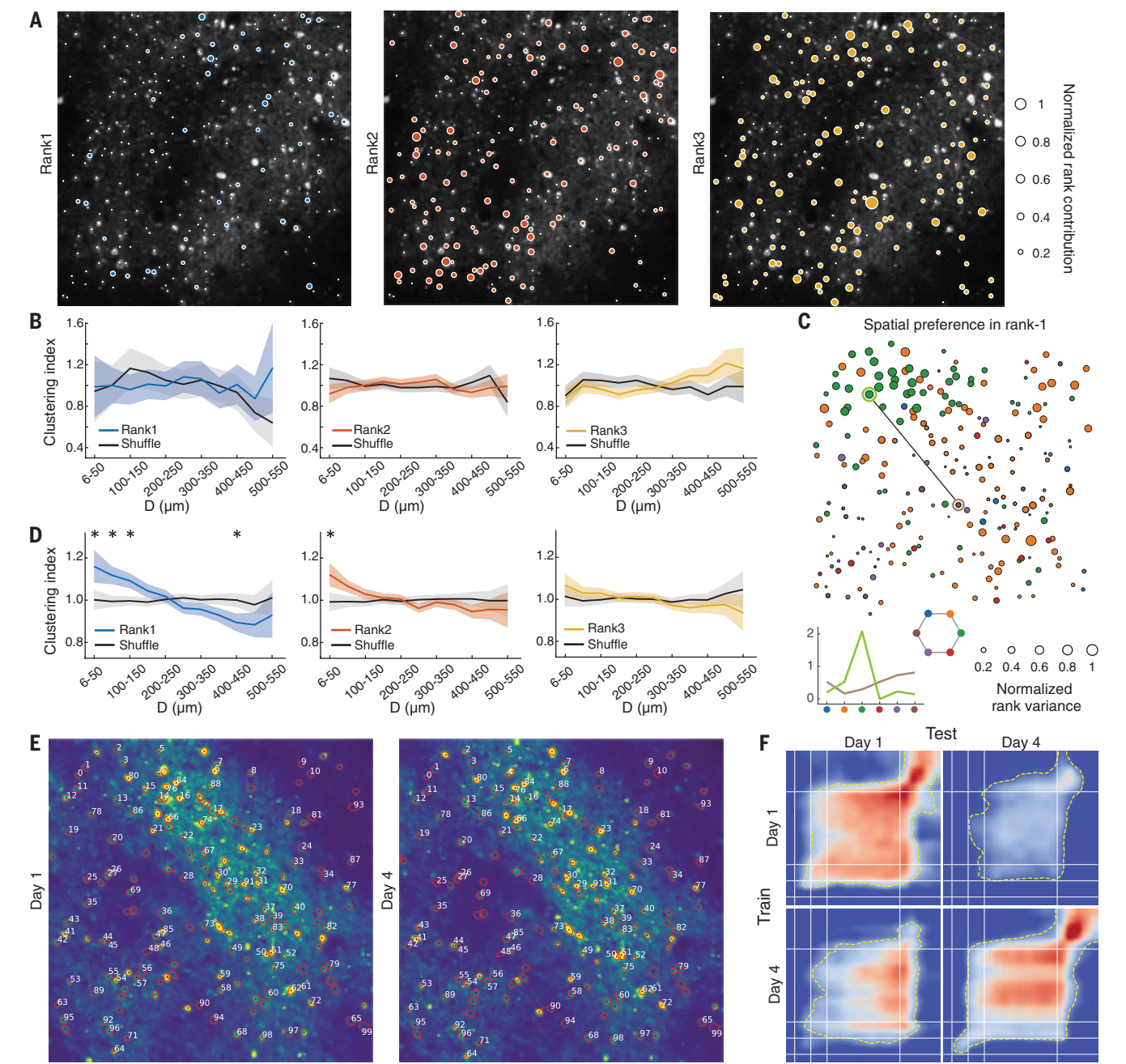


**Fig. 5. Anatomical organization of the compositional code in the LPFC.** (A) The organization of neural alignment with different rank subspaces in an example FOV from monkey 1. Normalized rank contributions (normalized  $A_r^2$  for rank- $r$  subspace) were overlaid with average calcium image. (B) The neurons with similar rank contributions show no spatial clustering in the example FOV. Neurons from the FOV in (A) with substantial rank contribution were collected to calculate the clustering index. Shaded areas represent 95% confidence intervals. (C) Pairwise analysis for one example neuron pair in rank-1 spatial preference map. Neurons were marked by colored circles, with color and size indicating spatial preference and normalized rank variance, respectively. (Bottom) Tuning

curves of the circled neuron pair. (D) Functional clustering for the FOV in (C). The clustering index was based on the average Pearson correlation coefficient across neuron pairs within a particular cortical distance range (17). (E) Comparison of FOVs recorded in the same location across days. 171 regions of interest (ROIs) were identified on both days. The shared indexes of the first 99 ROIs were marked. (F) Cross-day decoding for rank-1 locations in correct, length-3 sequence. In off-diagonal panels, the decoder trained in one day was tested in another day by only using the overlapping neurons. In diagonal panels, decoders were trained with all neurons and tested with the leave-one-trial-out method. Colormap and contour are the same as in Fig. 3G.

item and order information during a working memory delay (33–35). Our data support such a sustained activity mechanism because the geometry of disentangled representations was stable during the delay period (Fig. 3B). Our results suggest that the brain transforms time into space by converting temporally segregated sensory inputs into spatially overlapping sustained brain activity patterns. They do not, however, exclude the simultaneous presence, at a finer time scale, of a temporal code involving phase synchrony or replay.

Seven decades ago, Karl Lashley (36) posulated that serial order is processed by creating and manipulating a spatial pattern of neural activity. He speculated that to control sequential actions, our brain needed to transform temporally segregated sensory experiences into a sustained spatial pattern of brain activity. In agreement with this early intuition, the simple geometrical organization of SWM that we uncovered may provide a fundamental neural mechanism to bridge our understanding of neural circuits and their computational functions.

#### REFERENCES AND NOTES

1. S. Dehaene, F. Meyniel, C. Wacongne, L. Wang, C. Pallier, *Neuron* **88**, 2–19 (2015).
2. M. Botvinick, T. Watanabe, *J. Neurosci.* **27**, 8636–8642 (2007).
3. Y. Liu, R. J. Dolan, Z. Kurth-Nelson, T. E. J. Behrens, *Cell* **178**, 640–652.e14 (2019).
4. Y. Bengio, A. Courville, P. Vincent, *IEEE Trans. Pattern Anal. Mach. Intell.* **35**, 1789–1828 (2013).
5. G. Buzsáki, A. Draguhn, *Science* **304**, 1926–1929 (2004).
6. C. Baldassano et al., *Neuron* **95**, 709–721.e5 (2017).
7. R. A. Andersen, G. K. Eissick, R. M. Siegel, *Science* **230**, 456–458 (1985).
8. A. Pouget, T. J. Sejnowski, *J. Cogn. Neurosci.* **9**, 222–237 (1997).
9. P. Smolensky, *Artif. Intell.* **46**, 159–216 (1990).
10. V. Mante, D. Sussillo, K. V. Shenoy, W. T. Newsome, *Nature* **503**, 78–84 (2013).
11. M. Rigotti et al., *Nature* **497**, 585–590 (2013).
12. M. M. Churchland et al., *Nature* **487**, 51–56 (2012).
13. S. Bernardi et al., *Cell* **183**, 954–967.e21 (2020).
14. E. H. Nieh et al., *Nature* **595**, 80–84 (2021).
15. M. F. Panichello, T. J. Buschman, *Nature* **592**, 601–605 (2021).
16. J. Wang, D. Narain, E. A. Hosseini, M. Jazayeri, *Nat. Neurosci.* **21**, 102–110 (2018).
17. Materials and methods are available as supplementary materials online.
18. A. Nieder, I. Diester, O. Tudusciuc, *Science* **313**, 1431–1435 (2006).
19. J. R. Duhamel, F. Bremmer, S. Ben Hamed, W. Graf, *Nature* **389**, 845–848 (1997).
20. R. Q. Quiroga, L. Reddy, G. Kreiman, C. Koch, I. Fried, *Nature* **435**, 1102–1107 (2005).
21. J. H. Reynolds, D. J. Heeger, *Neuron* **61**, 168–185 (2009).
22. X. Jiang et al., *Curr. Biol.* **28**, 1851–1859.e4 (2018).
23. K. Oberauer et al., *Psychol. Bull.* **144**, 885–958 (2018).
24. M. J. Hurlstone, G. J. Hitch, A. D. Baddeley, *Psychol. Bull.* **140**, 339–373 (2014).
25. J. E. Lisman, O. Jensen, *Neuron* **77**, 1002–1016 (2013).
26. X. J. Wang, *Physiol. Rev.* **90**, 1195–1268 (2010).
27. M. Abeles, G. Hayon, D. Lehmann, *J. Comput. Neurosci.* **17**, 179–201 (2004).
28. M. Siegel, M. R. Warden, E. K. Miller, *Proc. Natl. Acad. Sci. U.S.A.* **106**, 21341–21346 (2009).
29. M. A. Wilson, B. L. McNaughton, *Science* **265**, 676–679 (1994).
30. K. Diba, G. Buzsáki, *Nat. Neurosci.* **10**, 1241–1242 (2007).
31. S. Funahashi, C. J. Bruce, P. S. Goldman-Rakic, *J. Neurophysiol.* **61**, 331–349 (1989).
32. A. Compte, N. Brunel, P. S. Goldman-Rakic, X. J. Wang, *Cereb. Cortex* **10**, 910–923 (2000).
33. P. Barone, J. P. Joseph, *Exp. Brain Res.* **78**, 447–464 (1989).
34. S. Funahashi, M. Inoue, K. Kubota, *Behav. Brain Res.* **84**, 203–223 (1997).
35. Y. Ninokura, H. Mushiaki, J. Tanji, *J. Neurophysiol.* **89**, 2868–2873 (2003).
36. K. S. Lashley, *The Problem of Serial Order in Behavior* (Bobbs-Merrill, 1951).
37. Y. Xie et al., Data repository for ‘Geometry of Sequence Working Memory in Macaque Prefrontal Cortex’, Zenodo (2021); <https://doi.org/10.5281/zenodo.5739376>.
38. P. Hu, Y. Xie, Code for ‘Geometry of Sequence Working Memory in Macaque Prefrontal Cortex’, Zenodo (2021); <https://doi.org/10.5281/zenodo.5746184>.

#### ACKNOWLEDGMENTS

We thank W. Fang for data analysis, Y. Li and H. Jiang for animal surgery, and Peking University Laboratory Animal Center for animal care. **Funding:** This study was supported by National Science and Technology Innovation 2030 Major Program 2021ZD0204102 (L.W. and B.M.), Shanghai Municipal Science and Technology Major Project 2021SHZDZX and 2018SHZDZX05 (L.W.), Strategic Priority Research Programs XDB32070201 (L.W.), Natural Science Foundation of China 11901557 (B.M.), and Natural Science Foundation of China 31730109 and U1909205 (S.T.). **Author contributions:** Conceptualization: Y.X., P.H., X.-J.W., T.Y., S.D., S.T.,

B.M., and L.W. Methodology: Y.X., P.H., J.L., X.-J.W., T.Y., S.D., B.M., and L.W. Investigation: Y.X., W.S., J.C., and S.T. Visualization: Y.X. and P.H. Funding acquisition: S.T. and L.W. Project administration: S.T. and L.W. Supervision: S.T., B.M., and L.W. Writing – original draft: B.M., S.D., and L.W. Writing – review and editing: Y.X., P.H., X.-J.W., T.Y., B.M., S.D., and L.W. **Competing interests:** The authors declare that they have no competing interests. **Data and materials availability:** All data and code used in this study are available on Zenodo (37, 38).

#### SUPPLEMENTARY MATERIALS

science.org/doi/10.1126/science.abm0204  
Materials and Methods  
Figs. S1 to S12  
Tables S1 to S5  
References (39–46)  
MDAR Reproducibility Checklist

24 August 2021; accepted 12 January 2022  
10.1126/science.abm0204

#### BIOMEDICINE

## An autonomously swimming biohybrid fish designed with human cardiac biophysics

Keel Yong Lee<sup>1†</sup>, Sung-Jin Park<sup>1,2†</sup>, David G. Matthews<sup>3</sup>, Sean L. Kim<sup>1</sup>, Carlos Antonio Marquez<sup>1</sup>, John F. Zimmerman<sup>1</sup>, Herdeline Ann M. Ardoña<sup>1‡§</sup>, Andre G. Kleber<sup>4</sup>, George V. Lauder<sup>3</sup>, Kevin Kit Parker<sup>1,5,6\*</sup>

Biohybrid systems have been developed to better understand the design principles and coordination mechanisms of biological systems. We consider whether two functional regulatory features of the heart—mechano-electrical signaling and automaticity—could be transferred to a synthetic analog of another fluid transport system: a swimming fish. By leveraging cardiac mechano-electrical signaling, we recreated reciprocal contraction and relaxation in a muscular bilayer construct where each contraction occurs automatically as a response to the stretching of an antagonistic muscle pair. Further, to entrain this closed-loop actuation cycle, we engineered an electrically autonomous pacing node, which enhanced spontaneous contraction. The biohybrid fish equipped with intrinsic control strategies demonstrated self-sustained body-caudal fin swimming, highlighting the role of feedback mechanisms in muscular pumps such as the heart and muscles.

**C**irculatory systems in living organisms are intricately designed to transport blood throughout the body. Their most basic function is fluid transport, and a diversity of similar fluid pumping mechanisms and designs are found throughout

nature (1). Fluid pumps in vertebrates, considered broadly, range from a human circulatory system with closed vessels within which fluid moves, to oscillatory fluid mechanisms in aquatic species in which fluid is transported along the body to generate propulsive thrust. Inspired by these distinct but similar natural processes, we and others have developed biohybrid analogs of an external fluid pump capable of mimicking the locomotion of aquatic species (2–4). The underlying motivation for developing biohybrid systems capable of reproducing biological behaviors is to better understand the design principles and coordination mechanisms of biological systems, although the performance of these systems has been lacking in comparison to natural fluid transport pumps (4).

A key feature of aquatic species is closed-loop actuation of antagonistic musculature that provides control over the direction of momentum transfer from the body muscles to the

<sup>1</sup>Disease Biophysics Group, John A. Paulson School of Engineering and Applied Sciences, Harvard University, Boston, MA 02134, USA. <sup>2</sup>Biohybrid Systems Group, Coulter Department of Biomedical Engineering, Georgia Institute of Technology and Emory University School of Medicine, Atlanta, GA 30322, USA. <sup>3</sup>Museum of Comparative Zoology, Harvard University, Cambridge, MA 02138, USA. <sup>4</sup>Beth Israel Deaconess Medical Center, Harvard Medical School, Boston, MA 02115, USA. <sup>5</sup>Wyss Institute for Biologically Inspired Engineering, Harvard University, Boston, MA 02115, USA. <sup>6</sup>Harvard Stem Cell Institute, Harvard University, Cambridge, MA 02138, USA.

\*Corresponding author. Email: [kkparker@seas.harvard.edu](mailto:kkparker@seas.harvard.edu)

†These authors contributed equally to this work.

‡Present address: Department of Chemical and Biomolecular Engineering, Henry Samueli School of Engineering, University of California Irvine, CA 92697, USA.

§Present address: Sue and Bill Gross Stem Cell Research Center, University of California, Irvine CA 92697, USA.

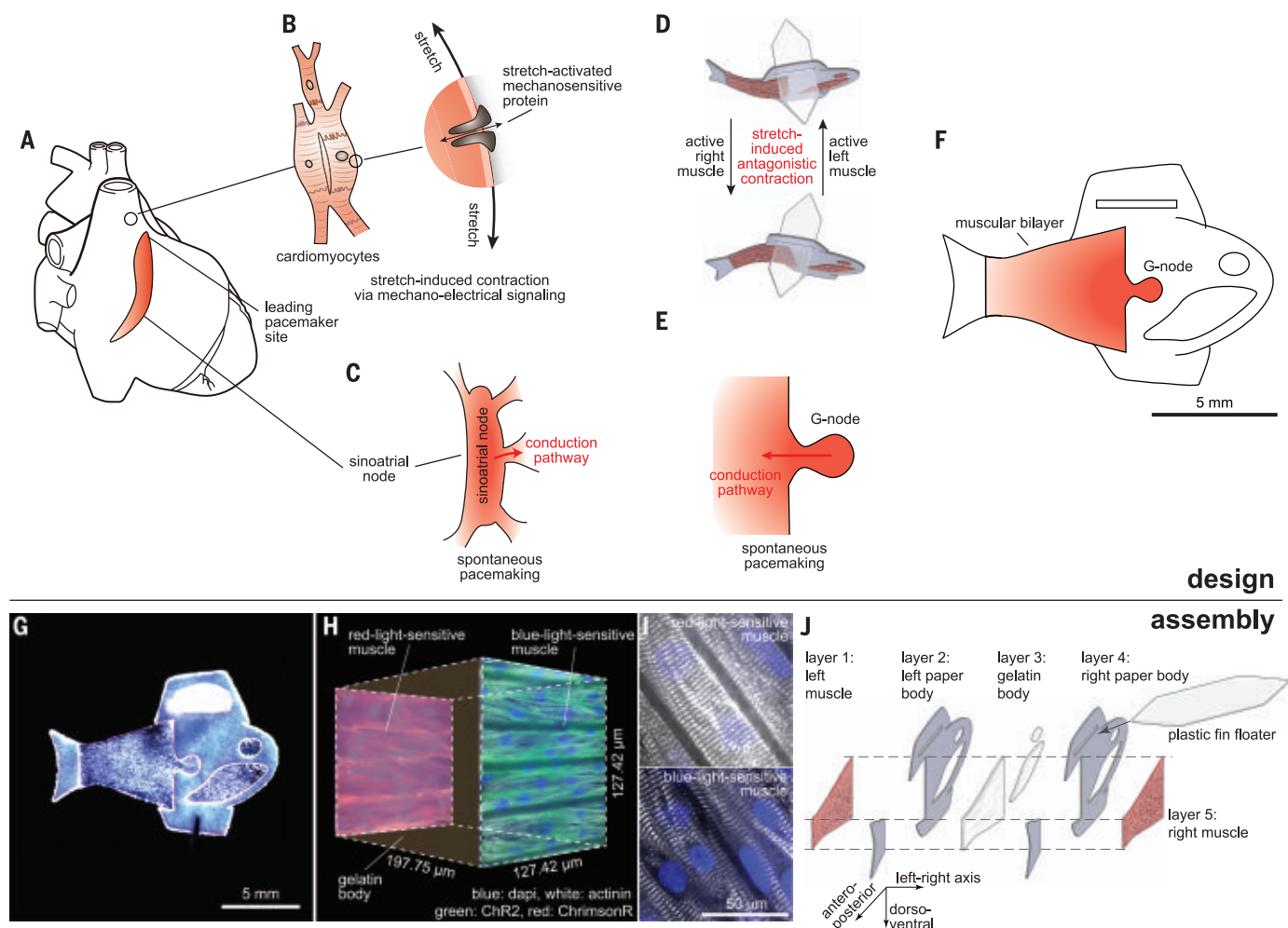


**Fig. 1. Design and assembly of the biohybrid fish.** (A) Intrinsic autonomous muscle control of the heart. (B) Mechano-electrical signaling that adaptively responds to dynamic mechanical pressures by inducing changes in electrophysiology through stretch-activated mechanosensitive proteins. (C) Automaticity of the cardiac sinoatrial node, which is structurally and functionally insulated from the surrounding myocardium and initiates spontaneous electrical activity. (D to F) Autonomously swimming biohybrid fish. (D) Muscular bilayer in which the shortening of contracting muscles on each side directly translates to axial stretching of the opposite side muscle, leading to stretch-induced antagonistic muscle contractions. (E) G-node, where functionally isolated cardiomyocytes (CMs) generate spontaneous muscle activation rhythms. (F) Biohybrid fish

equipped with the muscular bilayer and the G-node. (G) Image of the biohybrid fish made of human stem cell-derived CMs. (H and I) Muscular bilayer construct showing representative (H) mesoarchitecture and (I) microarchitecture. The gelatin posterior body was sandwiched by two muscle tissues expressing either a blue-light-sensitive opsin [ChR2 (green)] or a red-light-sensitive opsin [ChrimsonR (red)]. Representative immunostaining images of both tissues (sarcomeric alpha actinin, gray; nuclei, blue) show that Z-lines of the sarcomeres (the cell force-generating units) are perpendicular to the antero-posterior axis. (J) Five layers of body architecture: the body was symmetrical along the left-right axis but asymmetrical along both the antero-posterior and dorso-ventral axis; this design was chosen to maintain directional body stability against roll and propel the body forward.

fluid, enabling efficient locomotion. Similarly, in the circulatory system, muscles of the heart dynamically respond to physiological demands through internal feedback systems and impart momentum to drive fluid motion. Mechano-electrical signaling and cardiac automaticity play an essential role in regulating the contractile pace and strength in a closed-loop control system (Fig. 1, A to C). Mechano-electrical signaling (5, 6) is hypothesized to regulate intracardiac feedback, which allows cardiomyocytes (CMs) to adaptively respond to dynamic mechanical pressures (7, 8) by inducing changes in electrophysiology through stretch-

activated mechanosensitive proteins (9, 10) (Fig. 1B). Automaticity of the heart stems from the sinoatrial node, which is structurally and functionally insulated from the surrounding myocardium (11–13) and initiates spontaneous electrical activity in the absence of an external stimulus and without direct neural intervention (Fig. 1C).

We reasoned that using principles of cardiac control systems to design a biohybrid platform could result in a fluid pumping system with comparable efficiencies to natural fishlike fluid pumping systems. Leveraging fundamental features of cardiac function allows for autono-

mous self-pacing and independent motion control while providing the basis for a closed-loop design that mimics aquatic swimming systems. We designed, built, and tested a biohybrid fish equipped with an antagonistic muscular bilayer and a geometrically insulated cardiac tissue node (G-node) with human stem cell-derived CMs or neonatal rat ventricular CMs (Fig. 1, D to F) to test the ability of a biohybrid system to control the movement of fluids with biological levels of performance. To integrate mechano-electrical signaling of CMs in a simplified biohybrid platform, we recreated asynchronous muscle contractions (Fig.



1D) based on insect muscles (fig. S1) (14). In insects, each contraction results automatically from a response to the stretching of an antagonistic muscle pair, generating self-sustained muscle contraction cycles. In the muscular bilayer construct of the biohybrid fish (Fig. 1D), CMs are electrically connected within each side and mechanically coupled across sides, so that the shortening of contracting muscles on each side directly translates to axial stretching of the opposite side muscle, leading to antagonistic muscle excitations and contractions. To replicate the electrically insulated structure of a sinoatrial node (Fig. 1C) (15), we functionally isolated a small number of CMs (the source) in the G-node (Fig. 1E) with a single exit pathway that allows for an electrical connection between the G-node and muscle tissues (the sink). This facilitated the activation of large downstream quiescent muscle cells (sink) with a small number of activating CMs (source) by reducing the impedance between source and sink (11–13, 15, 16). Together, the muscular bilayer and G-node in the biohybrid fish (Fig. 1F) enabled the generation of continuous rhythms to regulate its antagonistic muscle pair to produce spontaneous yet coordinated body-caudal fin (BCF) propulsion swimming.

#### Antagonistic contraction of muscular bilayer construct

We developed a muscular bilayer construct by modifying hydrogel-based muscular thin films (16–18). The double-sided micromolded gelatin thin film (200  $\mu\text{m}$  thick) was engineered by sandwiching a gelatin and cross-linker (microbial transglutaminase) mixture between two polydimethylsiloxane stamps with line groove features (25  $\mu\text{m}$  ridge width, 4  $\mu\text{m}$  groove width, and 5  $\mu\text{m}$  groove depth). CMs were then seeded onto both sides of the micromolded gelatin so that they could self-assemble as laminar, anisotropic muscle with engineered cellular alignment, characteristic of the ventricular myocardium (Fig. 1, G and H).

To demonstrate independent activation between the muscular bilayer tissues, we used lentiviral transduction to express blue-light-sensitive (ChR2) (19) and red-light-sensitive (ChrimsonR) (20) ion channels in each muscle layer (Fig. 1, H and I, fig. S2, and movie S1). Alternating blue-and-red light stimulation (15-ms pulses of 450 and 620 nm light, respectively) activated ChR2- and ChrimsonR-expressing muscle layers independently. The shortening of contracting muscles on each side was transduced to produce antagonistic bending stress and oscillate the muscle construct along the longitudinal axis (fig. S3 and movie S2). The contractions and relaxations of muscular bilayer muscles were decoupled at low pacing frequencies (e.g., 1 and 1.5 Hz),

but at higher pacing frequencies (e.g., 2.5 and 3 Hz), the relaxation of one side started to overlap with the subsequent contraction of the other side (fig. S3 and movie S2). The overlapping, fast, active contraction of the opposite-side muscle considerably increased the oscillating speed of the muscular bilayer construct (fig. S3), preventing diastolic stress development that single-layered muscular thin films exhibit at high pacing frequencies (17, 18). These antagonistic muscle contractions in the muscular bilayer construct permitted large peak-to-peak amplitudes over a wide range of pacing frequencies (fig. S3), in contrast to single-layered muscular thin films (17, 18).

#### Integration of the muscular bilayer into biohybrid fish

The muscular bilayer construct was integrated into the biohybrid fish (16) by means of tissue engineering techniques (fig. S4). Inspired by fish musculoskeletal structure (fig. S5), we created an asymmetrical body along both the antero-posterior and dorso-ventral axes while maintaining sagittal symmetry through a five-layered architecture. From left to right (Fig. 1J), the biohybrid fish consists of (i) a layer of aligned muscle tissue made of human stem cell-derived CMs, (ii) a rigid paper layer in the anterior body and caudal fin fabricated by laser ablation, (iii) a compliant gelatin layer in the posterior body cast by means of a three-dimensional elastomer polydimethylsiloxane mold, (iv) a second paper layer, and (v) a second aligned muscle tissue layer for forming the antagonistic muscle pair. The passive component of the biohybrid fish is made up of paper (thickness 190  $\mu\text{m}$ ; Young's modulus 4 GPa; density 1.2 g/ml), the gelatin body (thickness  $192.22 \pm 1.95 \mu\text{m}$ ; Young's modulus 56 kPa; density 1.5 g/ml), and a plastic floater fin (thickness 1 mm; Young's modulus 1.3 GPa; density 0.833 g/ml) was designed to maintain directional body stability and neutral buoyancy while minimizing drag during forward swimming. The large surface area of the floater fin combined with the relatively heavy weight of the hydrogel insert in the anterior ventral portion of the body helped the fish maintain an upright orientation. Neutral buoyancy was achieved by adjusting the size of the plastic floater fin, thereby matching the average density of the biohybrid fish to the media in which it was suspended. The active component of the biohybrid fish consists of a muscular bilayer construct on the flexible posterior gelatin hydrogel body and operates as a single self-propelling system through coordinated contraction of muscle tissues. The final overall design (fig. S6) consists of 73,000 live CMs in a hydrogel-paper composite body 14 mm in length and 25.0 mg of total mass, including 0.36 mg muscle mass (fig. S7).

#### Optogenetically induced BCF propulsion

To characterize system-level kinematics of the muscular bilayer, we controlled antagonistic muscle contractions in the biohybrid fish by external optogenetic stimulation (Fig. 2). We stimulated the muscular bilayers by alternating blue and red light-emitting diode light pulses (Fig. 2A) while the bilayers were submerged in a 37°C Tyrode's salt solution containing glucose. As shown in the video-tracking analysis (Fig. 2, B to H, and movie S3), the biohybrid fish (i) initiated contraction of the muscle tissue on the left side upon red light stimulation and produced a peak oscillation amplitude in the tail (Fig. 2, B, F, and I); (ii) induced contraction of the muscle tissue on the right side after blue light stimulation (180° phase shift between red and blue lights); (iii) recovered its tail at a near-straight position (Fig. 2, C and G) and reached peak thrust production (Fig. 2I); (iv) oscillated its tail with peak amplitude right before a subsequent red light stimulation (Fig. 2, D and I); and (v) rebounded back to a near-straight position (Fig. 2E) generating maximal thrust (Fig. 2I). As shown by the lateral deflection (Fig. 2H), the body curvature (Fig. 2J), and swimming displacement (Fig. 2K), the biohybrid fish generated rhythmic forward thrust reproducing BCF propulsion. The biohybrid fish deformed its posterior body with a single bend while switching between positive and negative posterior body curvature upon light stimulation. The biohybrid fish oscillated its fin instead of generating a bending body wave because optical stimulation induced a simultaneous global muscle contraction. The relatively stiff anterior body and caudal fin resisted deformation from fluid forces. This allowed the biohybrid fish to exhibit asymmetric body deformation in which the largest lateral deflections and curvatures occurred in the posterior body between 0.5 and 0.8 of total length (Fig. 2J), in a manner reminiscent of BCF swimmers (fig. S8).

Antagonistic muscle contractions of the biohybrid fish generated a hydrodynamic signature similar to those of wild-type BCF swimmers—specifically, the water flow in the wake of and around the fish bodies, which we visualized with particle image velocimetry (PIV) (Fig. 2, B to H, fig. S8). The biohybrid fish shed two vortex pairs per tail-beat cycle and one pair per lateral tail excursion (movie S3), one of the key characteristic flow patterns of BCF swimmers (movies S4 to S6). Each lateral tail excursion from bent to near-straight positions induced strong wake flows that formed a visible vortex pair with the opposite rotational direction (Fig. 2, B and C, vortices 1 and 2'; Fig. 2, D and E, vortices 2 and 3'; and Fig. 2, F and G, vortices 3 and 4). When the vortex pair reached the tail from the posterior body, it was shed (Fig. 2D, vortices 1 and

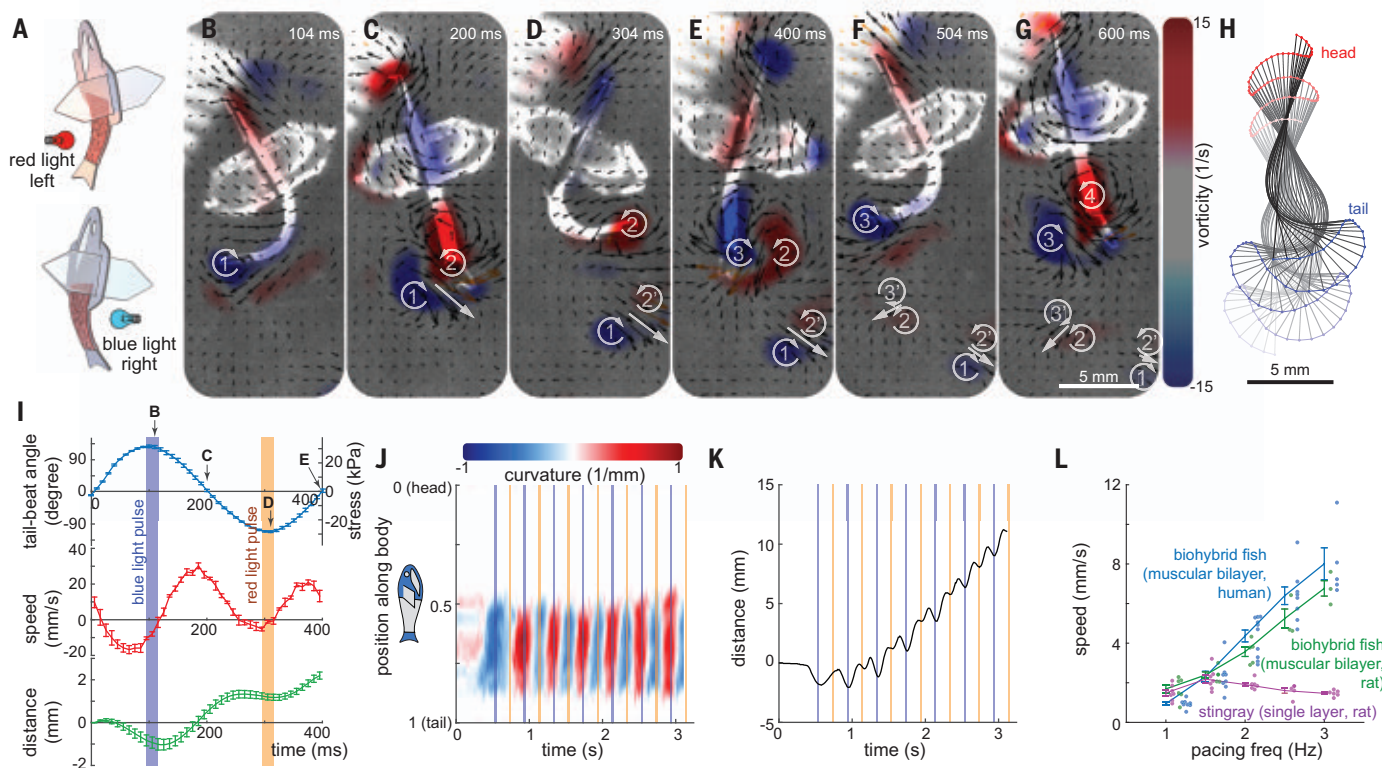


**Fig. 2. Optogenetically induced BCF propulsion.** (A) Upon alternating blue and red light stimulation, the biohybrid fish induces contraction of the ChR2- and ChrimsonR-expressing muscles, respectively. (B to G) Body kinematics and hydrodynamics of the biohybrid fish during one and a half tail-beat cycles. (B and F) Peak contraction of left muscles. (C and G) recovery to straight position. (D) peak contraction of right muscle. (E) recovery to straight position. Left and right muscles work antagonistically against each other, leading to rhythmically sustained body and caudal fin (BCF) propulsion. PIV flow measurements highlight

the shedding of the positive and negative vortex pair at every lateral tail excursion. (H) Corresponding midline kinematics (time step: 50 ms). (I to K) Kinematic analysis of seven strokes; correlation between optogenetic muscle activation and BCF locomotion ( $n = 7$  strokes; data represent mean  $\pm$  SEM). (J) aCurvature of the midline; (K) moving distance. (L) Positive relationship between pacing frequency and moving speed of optogenetically stimulated biohybrid fish [ $n = 31$  videos from seven stingrays (3); 27 videos from six rat fish; and 54 videos from 12 human fish.] Data represent mean  $\pm$  SEM).

2'; Fig. 2F, vortices 2 and 3') and continuously moved away from the fish body under its own momentum (Fig. 2, D to G, vortices 1 and 2'; and Fig. 2, F and G, vortices 2 and 3').

The inclusion of a muscular bilayer architecture improved the high-frequency swimming of the biohybrid fish. Our optogenetically controlled biohybrid fish (6.4-mm-long muscle tissue body) responded up to 3 to 4 Hz (fig. S9 and movie S7), maintained a large tail-beat amplitude and angle, and exhibited a positive pacing frequency and tail beat angular-speed relationship (fig. S9). The biohybrid fish made of human stem cell-derived CMs (movie S7) and primary neonatal rat ventricular CMs (fig. S10 and movie S8) exhibited increased swimming speeds with increasing pacing frequencies (Fig. 2L) reminiscent of the force-frequency relationship of the heart. By contrast, a previous biohybrid stingray (3) exhibited reduced swimming speeds at high pacing frequencies as it had single-layered muscle and lacked antagonistic muscle contractions. The

upper limit of optogenetic pacing frequency that induces a 1:1 stimulus response is also affected by body dimensions: a longer-bodied fish (8.2 mm; fig. S6C) exhibited oscillatory motion up to 2 Hz, but not at 2.5- and 3-Hz stimulation (movie S9).

#### Autonomous BCF propulsion

We tested whether reconstructing antagonistic muscle contractions with CMs could sustain spontaneous rhythmic contractions by means of mechanoelectrical signaling (Fig. 3A). Spontaneous activation and contraction on one side of the 49-day-old biohybrid fish led to a subsequent antagonistic contraction on the opposite side through mechanical coupling between muscle tissues (Fig. 3B and movies S10 and S11). These spontaneous antagonistic contractions led to alternating bending motions of the posterior body (Fig. 3, C to E), resulting in rhythmically sustained forward displacement (Fig. 3D) as shown in optogenetically triggered body-caudal fin propulsions (Fig. 2).

Notably, biohybrid fish with a larger tail-beat angle had a higher probability to induce a subsequent muscle contraction (Fig. 3F), suggesting that the lengthening of one muscle layer caused by a shortening of the other muscle layer directly induced subsequent contractions through cardiac mechanoelectrical signaling. We treated the biohybrid fish with stretch-activated ion channel inhibitors [streptomycin (21) and gadolinium ( $Gd^{3+}$ ) (22) (movies S12 and S13). We observed that these inhibitors disrupted antagonistic contractions in the biohybrid fish by breaking the positive relationship between peak tail-beat angle and probability of antagonistic contractions (Fig. 3F and fig. S11). Further, frequency-domain analysis showed that the spontaneous frequencies of streptomycin- and  $Gd^{3+}$ -treated muscular bilayer tissues were not harmonic (fig. S12). Stretched-activated ion channel inhibition decreased swimming speeds (Fig. 3G), which demonstrated that mechanoelectrical signaling mediates self-sustainable

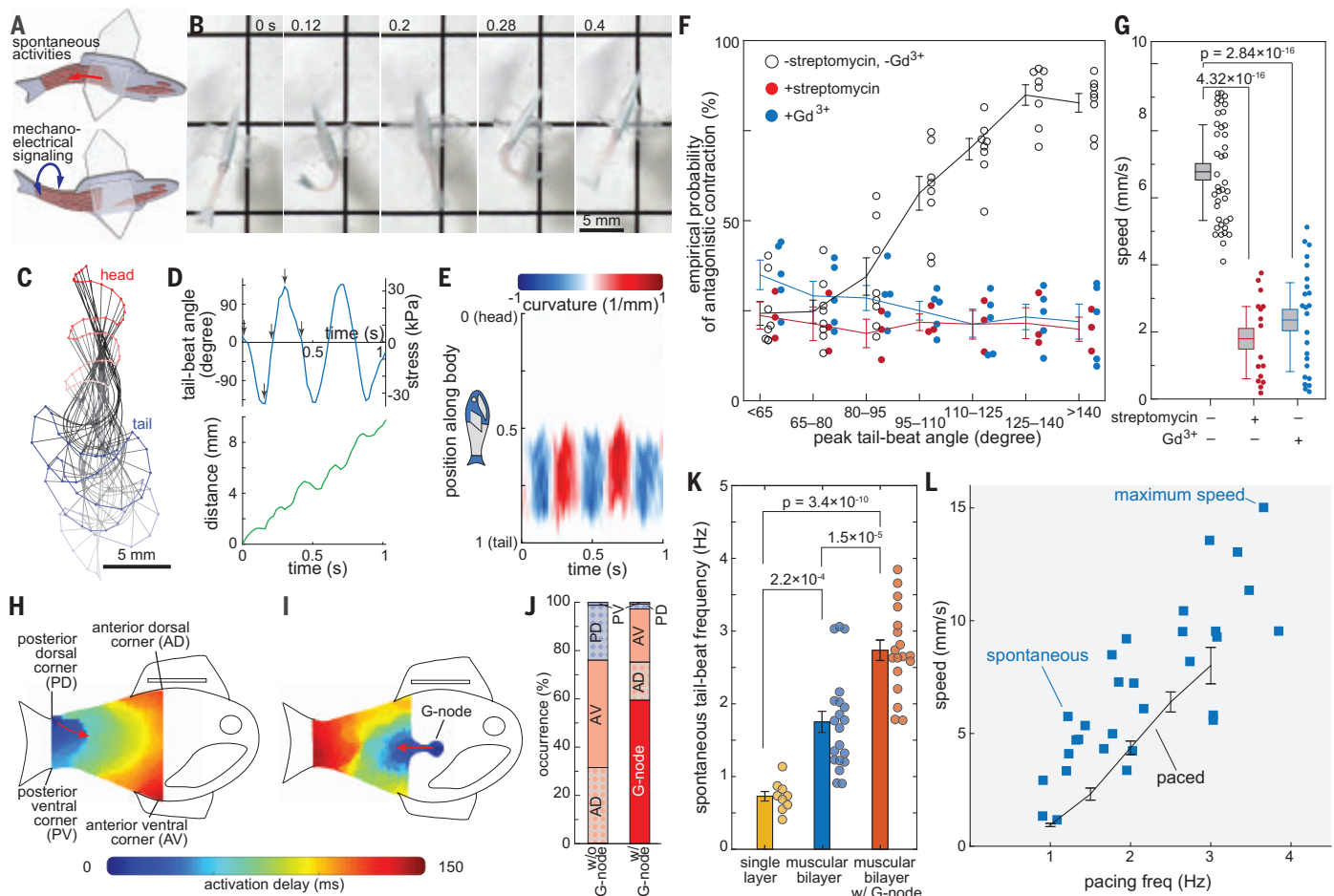


**Fig. 3. Autonomous BCF propulsion.** (A to G) Mechano-electrical signaling of the muscular bilayer. (A) Spontaneous activation of one-side muscle induces consecutive contraction of the opposite-side muscle through mechanoelectrical signaling between muscular bilayer tissues. (B) Representative time lapse images of consecutive antagonistic muscle contraction of 49-day-old biohybrid fish. (C) Midline kinematics (time step: 100 ms). (D) Correlation between spontaneous muscle activation and the moving distance. (E) Curvature of the midline during five consecutive left and right muscle strokes. (F) Empirical probability of antagonistic contraction and (G) moving speed of self-paced biohybrid fish treated with stretch-activated channel blockers, 250  $\mu\text{M}$  streptomycin ( $n = 4$  biohybrid fish) and 100  $\mu\text{M}$  Gd<sup>3+</sup> ( $n = 5$  biohybrid fish) (box plot: center line, box limits, and whiskers indicates mean, SEM, and the first and third quartiles, respectively). The treatment of stretch-activated channel blockers, streptomycin and Gd<sup>3+</sup>

reduced the chance of antagonistic muscle contraction as well as the swimming speed of the biohybrid fish. (H to L) Geometrically insulated node (G-node). Activation pattern of biohybrid fish (H) without G-node and (I) with G-node. (J) Probability of muscle activation sites. Spontaneous muscle activation from G-node dominates spontaneous activation from the corners ( $n = 6$  biologically independent samples without G-node and 5 samples with G-node). (K) Tail-beat frequency of biohybrid fish equipped with single-layer ( $n = 9$  videos from nine fish), muscular bilayer ( $n = 20$  videos from 14 fish), and muscular bilayer with G-node ( $n = 18$  videos from five fish). Significance was determined by the Tukey-Kramer honestly significant difference test. (L) Positive relationship between pacing frequency and moving speed of autonomously swimming biohybrid fish ( $n = 30$  videos from 19 autonomously swimming biohybrid fish and 54 videos from optogenetically swimming biohybrid fish). Data represent mean  $\pm$  SEM.

spontaneous rhythmic contractions in muscular bilayers.

We tested whether reconstructing a geometrically distinct and electrically insulated node could initiate spontaneous electrical activity as a result of the automaticity of CMs in the absence of an external stimulus. Inspired by the partial electrical insulation of a sinoatrial node (15), we created the G-node (Fig. 1E), where a small number of CMs are structurally and functionally isolated with a single exit pathway. The G-node is electrically coupled by gap junctions (12, 23) to muscle tissues and facilitates progressive activation of large quiescent neighboring muscle cells (sink) by a

small number of activating CMs (source). The geometrical design of both the G-node and the sink is crucial in determining the leading muscle activation site, because the electrical current being exchanged between individual CMs of different membrane potentials can be reflected at the tissue edges (12, 16). Thus, we hypothesized that the reflection of intracellular currents at the perimeter of the G-node would synchronize the spontaneous activity and initiate coordinated pacemaking from the G-node.

To decouple the effect of antagonistic muscle contractions from muscle activation at

the G-node, we mechanically restricted muscle movement with laboratory tape on a glass slide and determined muscle activation through calcium imaging (24). CMs in the G-node and four corners [anterior ventral corner (AV), anterior dorsal corner (AD), posterior ventral corner (PV), and posterior dorsal corner (PD) (figs. S13 and S14)] of the muscle tissue overcame source-sink mismatch and initiated muscle activation (Fig. 3, H and I, figs. S13 and S14, and movies S14 and S15). As we hypothesized, the G-node predominantly activated the muscle construct over the other four corners of the muscle tissue (Fig. 3, I and J,



and figs. S13 and S14). Comparing two G-node sizes showed that a larger G-node containing ~1700 cells increased the probability of initial muscular activation at the G-node compared with the smaller G-node with a pointed node (~600 cells) (fig. S13 and movie S15), suggesting that a group of geometrically distinct CMs are needed to initiate muscular activation. Additionally, rounding the sink's corners decreased the probability of activation at the corners (fig. S14A) by increasing the number of downstream cells at each respective corner (fig. S15), but the G-node's corner design did not affect the probability of activation at the G-node (fig. S14B), which indicates that acute angles in small source tissue such as the G-node are not critical in determining the activation site. Rather, this suggests that a larger perimeter-to-area ratio of the G-node synchronized electrical interaction between the geometrically distinct CMs through reflections of electrotonic currents and produced a relatively fast and synchronized activation over the sink tissue. Acute angled anterior corners of the fish body increased the probability of activation at the anterior side (Fig. 3J) by decreasing the number of downstream cells (fig. S15), thus allowing cells on the anterior side (G-node and anterior corners AD and AV) to predominantly initiate spontaneous activation waves (60% from the G-node and 97% from all anterior sides; Fig. 3J).

However, upon removing the restrictions on muscle movement, the G-node primarily acted as a secondary mechanism for controlling contractions. Only when the antagonistic muscle contractions were minimal would the G-node initiate sequential local muscle activation and contraction, leading to undulatory locomotion (fig. S16A and movie S17). However, in subsequent muscle contractions the biohybrid fish predominantly exhibited simultaneous global contractions and oscillatory locomotion with minimal body wave propagations, caused by mechano-electrical signaling of the muscular bilayer (Fig. 3E, fig. S16, B and C, and movie S16). Although G-nodes are located on both sides of the body, one dominant G-node controlled initiation of muscle contraction as a secondary pacemaker (movie S17). Because of the G-node's role as a secondary pacing mechanism of antagonistic contractions, the biohybrid fish equipped with a G-node had significantly increased spontaneous contractile frequencies (Fig. 3K) while maintaining similar body kinematics (fig. S16) and a positive frequency–swimming speed relationship similar to those of externally stimulated fish (Fig. 3L). As a result, our G-node-equipped biohybrid fish demonstrated increased maximum swimming speeds of more than one body length per second (15 mm/s; movie S11).

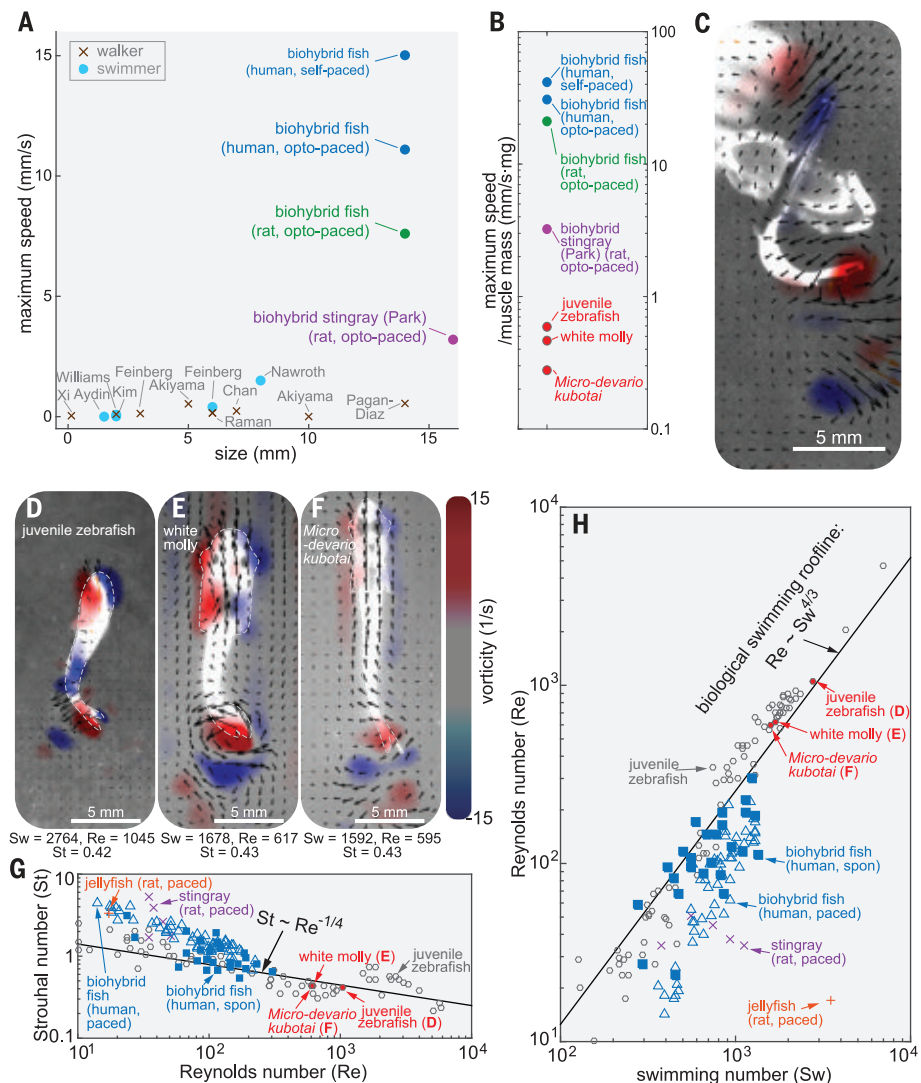


**Fig. 4. Comparison of swimming performance between biohybrid and aquatic swimmers.** (A and B) Comparison of swimming performance in biohybrid walkers and swimmers. (A) locomotion speed (2, 3, 25–35) and (B) speed per unit muscle mass. PIV analysis of (C) biohybrid fish [body length ( $l_b$ ): 14 mm]; (D) wild-type juvenile zebrafish ( $l_b$ : 12 mm); (E) white molly ( $l_b$ : 19 mm); and (F) *M. kubotai* ( $l_b$ : 20 mm). (G and H) Scaling analysis of biohybrid fish and wild-type swimmers with (G)  $Re$ - $St$  and (H)  $Sw$ - $Re$  ( $n = 30$  movies from 19 biohybrid fish).

Although these G-node-entrained, mechano-electrical signaling-sustained, cyclic antagonistic muscle contractions are autonomous, optogenetic stimulation can be used for on-demand locomotion control. Antagonistic muscle contractions became coupled with optical pacing within fewer than three sequential light pulses (movie S18). Further, optogenetic stimulation can also be used to inhibit autonomous locomotion; pausing immediately after a pulsed stimulation can stop muscle contractions for an extended period (50 s; movie S19). Prolonged continuous optogenetic stimulation stops muscle contractions and autonomous locomotion (movie S20). External stimulation reinitiates autonomous, antagonistic muscle

contractions by activating mechano-electrical signaling (movie S21).

#### Advanced performance of the biohybrid fish

Our autonomously swimming biohybrid fish (15.0 mm/s; movie S11) outperformed the locomotory speed of previous biohybrid muscular systems (2, 3, 25–35) [5 to 27 times the speed of the biohybrid stingray (3) and the biohybrid skeletal muscle biorobot] (32) (Fig. 4A), highlighting the role of feedback mechanisms in developing biohybrid systems. Moreover, when considering the ratio of muscle mass to the total weight for the biohybrid fish (1.4%; fig. S7) and biohybrid stingray (9.7%) (3), the biohybrid fish demonstrated faster

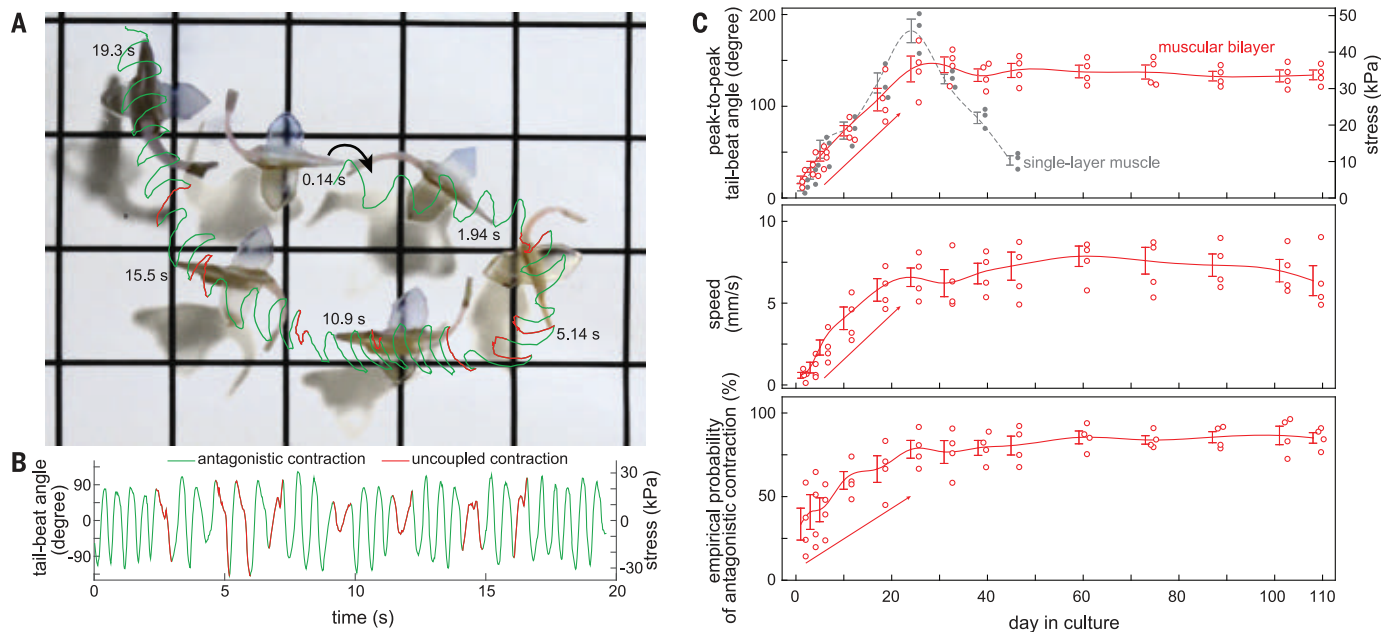


**Fig. 5. Long-term swimming performance analysis.** (A) Trajectory (grids, 1 cm) and (B) corresponding tail-beat angle of 108-day-old biohybrid fish with 79% antagonistic contractions. (C) Swimming performance for 108 days ( $n = 4$  fish). Biohybrid fish equipped with the muscular bilayer exhibited enhanced

contracting amplitude, maximum swimming speed, and muscle coordination for the first month and maintained their performance for at least 108 days, whereas fish made with the single-layer muscle exhibited decreased contracting amplitude after 28 days. ( $n = 4$  fish; data represent mean  $\pm$  SEM).

swimming speeds per unit muscle mass by an order of magnitude (13 times the maximum swimming speed of the biohybrid stingray) (3) (Fig. 4B).

The swimming performance of the biohybrid fish resembles that of wild-type BCF swimmers with similar body lengths (juvenile zebrafish, juvenile white molly, and *Microdevario kubotai*) (Fig. 4, C to F, fig. S8, and movies S4 to S6). Similar to the biohybrid fish, each of these species moves by shedding a pair of reverse-sign vortices when their tails reach maximum lateral excursion (Fig. 4, C to F). The strength of these vortices between the biohybrid and wild-type fish were comparable (Fig. 4, C to F). Rather than forming a continuous chaotic chain of wakes, both the biohybrid and wild-type fish maintain stable vortex pairs with minimal vortex interactions (Fig. 4, C to F). The stable wake pattern is a typical characteristic of juvenile zebrafish locomotion at relatively high Strouhal numbers ( $St$ ) and relatively low Reynolds numbers ( $Re < 5000$ ) (36), where viscous forces cannot be neglected and the lateral velocity of wake flows are relatively high. In this flow regime, the swimming speed is nearly proportional to the tail-beat frequency (37). Thus, the juvenile zebrafish, white molly, and *M. kubotai* had faster tail-beat frequencies (16.7, 7.5, and 7.7 Hz, which were 4.6, 2.1, and 2.1 times as high as that of the biohybrid fish) and showed proportionally increased swimming speeds of 59.7, 25.1, and 21.3 mm/s, respectively (4.0, 1.7, and 1.5 times as high as that of the biohybrid fish). Although

muscle function in wild-type fish encompasses more than locomotion, when considering the ratio of total muscle mass to the total weight of biohybrid fish (1.4%; fig. S7) compared with wild-type fish (80%) (38), the maximum swimming speed per unit muscle mass of biohybrid fish exceeded those of wild-type fish by a factor of 70 to 150 (Fig. 4B).

#### Efficiency of the biohybrid fish

To analyze the efficiency of the biohybrid fish, we used scaling and dimensional analysis. Wild-type swimmers achieved energetically favorable locomotion through convergent evolution and were found to hew to the two scaling relationships  $St \sim Re^{-1/4}$  and  $Re \sim Sw^{-1/4}$  in the low  $Re$  and high  $St$  flow regime (37) (Fig. 4, G and H). The Strouhal number  $St = fA/U$  ( $f$ , tail-beat frequency;  $A$ , tail-beat amplitude;  $U$ , forward speed) represents the ratio of the lateral oscillation amplitude to swimming distance per lateral tail excursion, the swimming number  $Sw = 2\pi fAL/\nu$  ( $L$ , characteristic body length of the swimmer;  $\nu$ , fluid viscosity) represents input kinematics, and the Reynolds number  $Re = UL/\nu$  compares inertial to viscous forces and is a function of swimming speed. Compared with the biohybrid stingray (3), our biohybrid fish operates much closer to these average scaling relationships of wild-type swimmers. Moreover, the biohybrid fish swimming at high tail-beat frequencies (high  $St$  and  $Sw$ ) performed comparably to wild-type swimmers (Fig. 4, G and H).

The performance of the biohybrid fish is very sensitive to muscle kinematics and coordination. Some biohybrid fish accelerated by increasing tail-beat amplitude (figs. S17 and S18A and movie S22), which is similar to the acceleration of wild-type fish (39). This positive relationship between swimming speed and tail-beat amplitude during accelerative locomotion contrasts with the constant tail-beat amplitude regardless of swimming speed during steady locomotion (fig. S9B). Although  $St$ ,  $Sw$ , and  $Re$  numbers increase with its swimming speed (fig. S18, B and C) in the accelerative locomotion, the biohybrid fish exhibited a considerable decrease in propulsive efficiency as its speed increases as shown by the deviation from the optimal  $St$ - $Re$  and  $Re$ - $Sw$  relationships of aquatic swimmers (fig. S18, B and C). The inhibition of muscle coordination with a stretch-activated ion channel blocker,  $Gd^{3+}$ , also led to a drastic reduction of 80.8% in  $Re$  and 40.6% in  $Sw$  and the deviation from optimal  $St$ - $Re$  and  $Re$ - $Sw$  relationships of aquatic swimmers (figs. S12 and S18, D to F, and movie S12), which demonstrate that muscular coordination is necessary to achieve effective and efficient swimming.

#### Long-term performance of the biohybrid fish

Given the autonomous antagonistic muscle contractions of the biohybrid fish, we questioned whether this spontaneous activity would improve its long-term performance. The biohybrid fish maintained spontaneous activity for 108 days [16 to 18 times the length

of the biohybrid stingray (6 days) (3) and the skeletal muscle-based biohybrid actuator (7 days) (40)], equivalent to 38 million beats (Fig. 5, A and B, and movies S23 and S24). Further, its locomotion could also be controlled by external optogenetic stimulation (movie S24) throughout this time. The autonomously swimming biohybrid fish also increased muscle contraction amplitude, maximum swimming speed, and muscle coordination for the first month before maintaining its swimming performance over 108 days (Fig. 5C). By contrast, biohybrid fish equipped with single-layered muscle showed deteriorating tail-beat amplitude within the first month (Fig. 5C and movie S25). These data demonstrate the potential of muscular bilayer systems and mechanoelectrical signaling as a means to promote maturation of in vitro muscle tissues.

## Discussion

We integrated two functional design features of the heart—mechanoelectrical signaling and automaticity—into a biohybrid platform and recreated an autonomously actuating cardiac muscular system in the form of a biohybrid fish. This fish is a closed-loop system in which muscle contraction-induced bending is used as a feedback input to the endogenous mechanosensors—stretch-activated ion channels—in the muscles. These channels respond to this feedback input and induce muscle activation and contraction, producing self-sustainable rhythmic BCF propulsion. The self-driven spontaneous contractions in our muscular bilayer induced coordinated global tissue-level contractions with comparable efficiencies to wild-type fish. Alternatively, integrated optogenetic control enabled overriding of internal control mechanisms to stop and control asynchronous muscle contractions. There are few, if any, closed-loop mechanical fish robots that are free-swimming; fish robots also typically require numerous actuators and sensors to control fin movements, and these are difficult to engineer at smaller size scales (millimeters to centimeters scale) (41). However, integration of the cardiac activation system as an embedded mechanism of both sensing and control enabled the generation of fishlike locomotion at such smaller scales (42). The use of biological muscle actuators with intrinsic closed-loop control simplifies the construction compared with current mechanical robotic systems and provides control beyond existing biohybrid systems.

Additionally, our muscular bilayer construct provides a platform for studying tissue-level cardiac biophysics. We demonstrate that dynamic axial stretching can induce excitations and contractions on a beat-by-beat basis in engineered human stem cell-derived CM tissues by contributing to antagonistic muscle contractions. We found that antagonistic

contractions are sensitive to streptomycin and  $Gd^{3+}$ , which indicates that mechanoelectrical signaling by means of stretch-activated ion channels is one of the essential mechanisms that mediate antagonistic contractions. Notably, in normal myocardium where CMs are mechanically and electrically coupled, mechanoelectrical signaling contributes to synchronizing local ventricular repolarization and protects against cell-to-cell repolarizations and contractile heterogeneities across the heart (43). By contrast, in our muscular bilayer where antagonistic muscle pairs are mechanically coupled yet electrically decoupled across sides, mechanoelectrical signaling generates stretch-induced depolarizations on a beat-by-beat basis. The stretch-induced excitations and contractions were also observed in quiescent single CMs and in a resting ventricular myocardium (10), but these observations were restricted to the ectopic responses of CMs to acute mechanical stimulation, which induced re-entrant arrhythmias. Our muscular bilayer construct is the first to demonstrate that the mechanoelectrical signaling of CMs could induce self-sustaining muscle excitations and contractions for extended periods (108 days, equivalent to 38 million beats). These findings are aligned with the growing appreciation for cardiac stretch-activated channels and mechanoelectrical signaling mechanisms as targets of heart rhythm management (10, 44). The longevity of the autonomously moving fish system also raises the question of whether a feedback between repetitive electrical and mechanical activity and the regulation of its molecular elements through altered gene expression or other basic cellular processes is correlated.

The G-node, an isolated cluster of cells connected through a single conducting exit pathway, initiated spontaneous activation waves by reducing the impedance between source and sink. G-node integration improved locomotion speeds by enhancing the pacing frequency. This increased frequency in the presence of the G-node is reminiscent of entrainment in re-entry cycles in which the focus shortens the re-entry cycle (45). Another possible underlying mechanism of the increased frequency is that the G-node produced regular contractions and consequently induced stronger and more rapid contractions of the muscular bilayer, which could enhance the dynamics of antagonistic, asynchronous muscle contractions. The G-node functionality as a node of automaticity in the biohybrid fish suggests that, functionally, a pacemaker may be defined by its geometry and source-sink relationships as well as its ion channel expression.

Taken together, the technology described here may represent foundational work toward the goal of creating autonomous systems capable of homeostatic regulation and adaptive

behavioral control. Our results suggest an opportunity to revisit long-standing assumptions of how the heart works in biomimetic systems, which may allow a more granular analysis of structure-function relationships in cardiovascular physiology.

## REFERENCES AND NOTES

1. S. Vogel, *Vital Circuits: On Pumps, Pipes, and the Workings of Circulatory Systems* (Oxford Univ. Press, 1992).
2. J. C. Nawroth et al., *Nat. Biotechnol.* **30**, 792–797 (2012).
3. S. J. Park et al., *Science* **353**, 158–162 (2016).
4. L. Ricotti et al., *Sci. Robot.* **2**, eaag0495 (2017).
5. H. E. ter Keurs, *Pflügers Arch.* **462**, 165–175 (2011).
6. T. A. Quinn, P. Kohl, *Physiol. Rev.* **101**, 37–92 (2021).
7. T. A. Quinn, P. Kohl, U. Ravens, *Prog. Biophys. Mol. Biol.* **115**, 71–75 (2014).
8. B. E. Dabiri, H. Lee, K. K. Parker, *Prog. Biophys. Mol. Biol.* **110**, 196–203 (2012).
9. O. Friedrich, S. Wagner, A. R. Battle, S. Schürmann, B. Martinac, *Prog. Biophys. Mol. Biol.* **110**, 226–238 (2012).
10. T. A. Quinn, H. Jin, P. Lee, P. Kohl, *Circ. Arrhythm. Electrophysiol.* **10**, e004777 (2017).
11. S. D. Unudurthi, R. M. Wolf, T. J. Hund, *Front. Physiol.* **5**, 446 (2014).
12. A. G. Kléber, Y. Rudy, *Physiol. Rev.* **84**, 431–488 (2004).
13. S. Rohr, J. P. Kucera, V. G. Fast, A. G. Kléber, *Science* **275**, 841–844 (1997).
14. B. Bullard, A. Pastore, *J. Muscle Res. Cell Motil.* **32**, 303–313 (2011).
15. R. W. Joyner, F. J. van Capelle, *Biophys. J.* **50**, 1157–1164 (1986).
16. Materials and methods are available as supplementary materials.
17. S. J. Park et al., *Circulation* **140**, 390–404 (2019).
18. M. L. McCain, A. Agarwal, H. W. Nesmith, A. P. Nesmith, K. K. Parker, *Biomaterials* **35**, 5462–5471 (2014).
19. E. S. Boyden, F. Zhang, E. Bamberg, G. Nagel, K. Deisseroth, *Nat. Neurosci.* **8**, 1263–1268 (2005).
20. N. C. Klapoetke et al., *Nat. Methods* **11**, 338–346 (2014).
21. F. Gannier, E. White, A. Lacapagnie, D. Garnier, J. Y. Le Guennec, *Cardiovasc. Res.* **28**, 1193–1198 (1994).
22. X. C. Yang, F. Sachs, *Science* **243**, 1068–1071 (1989).
23. A. G. Kléber, Q. Jin, *Biophys. Rev.* **2**, 031301 (2021).
24. K. Y. Lee et al., Optical stimulation for independent activation of muscles: Matlab and Labview, Zenodo (2021); doi:10.5281/zenodo.5618323.
25. A. W. Feinberg et al., *Science* **317**, 1366–1370 (2007).
26. J. Xi, J. J. Schmidt, C. D. Montemagno, *Nat. Mater.* **4**, 180–184 (2005).
27. C. Ovetkovic et al., *Proc. Natl. Acad. Sci. U.S.A.* **111**, 10125–10130 (2014).
28. V. Chan et al., *Sci. Rep.* **2**, 857 (2012).
29. J. Kim et al., *Lab Chip* **7**, 1504–1508 (2007).
30. Y. Akiyama, T. Hoshino, K. Iwabuchi, K. Morishima, *PLOS ONE* **7**, e38274 (2012).
31. Y. Akiyama et al., *Biomed. Microdevices* **14**, 979–986 (2012).
32. G. J. Pagan-Diaz et al., *Adv. Funct. Mater.* **28**, 1801145 (2018).
33. R. Raman et al., *Proc. Natl. Acad. Sci. U.S.A.* **113**, 3497–3502 (2016).
34. B. J. Williams, S. V. Anand, J. Rajagopalan, M. T. Saif, *Nat. Commun.* **5**, 3081 (2014).
35. O. Aydin et al., *Proc. Natl. Acad. Sci. U.S.A.* **116**, 19841–19847 (2019).
36. G. K. Taylor, R. L. Nudds, A. L. Thomas, *Nature* **425**, 707–711 (2003).
37. M. Gazzola, M. Argentina, L. Mahadevan, *Nat. Phys.* **10**, 758–761 (2014).
38. H. E. Jackson, P. W. Ingham, *Mech. Dev.* **130**, 447–457 (2013).
39. T. N. Wise, M. A. B. Schwalbe, E. D. Tytell, *J. Exp. Biol.* **221**, jeb.190892 (2018).
40. Y. Morimoto, H. Onoe, S. Takeuchi, *Sci. Robot.* **3**, eaat4440 (2018).
41. R. Du, Z. Li, K. Youcef-Toumi, P. Valdivia y Alvarado, in *Robot Fish: Bio-inspired Fishlike Underwater Robots*, R. Du, Z. Li, K. Youcef-Toumi, P. Valdivia y Alvarado, Eds. (Springer, 2015), pp. 1–24.
42. G. V. Lauder, J. L. Tangorra, in *Robot Fish: Bio-inspired Fishlike Underwater Robots*, R. Du, Z. Li, K. Youcef-Toumi, P. Valdivia y Alvarado, Eds. (Springer, 2015), pp. 25–49.
43. T. Ophthof, V. M. Meijborg, C. N. Belterman, R. Coronel, *Cardiovasc. Res.* **108**, 181–187 (2015).
44. T. A. Quinn, *Cardiovasc. Res.* **108**, 1–3 (2015).
45. J. Almendral, R. Caulier-Cisterna, J. L. Rojo-Alvarez, *Pacing Clin. Electrophysiol.* **36**, 508–532 (2013).

## ACKNOWLEDGMENTS

We thank M. Rosnach for photography and illustrations.

**Funding:** this work was funded by the Harvard Paulson School of Engineering and Applied Sciences, the Wyss Institute for



Biologically Inspired Engineering, National Institutes of Health National Center for Advancing Translational Sciences grant UH3TR000522, and National Science Foundation Materials Research Science and Engineering Center grant DMR-1420570. K.K.P. was sponsored by National Institutes of Health National Center for Advancing Translational Sciences grant 1-UG3-HL-141798-01. S.-J.P. was funded by the Georgia Institute of Technology and Emory University School of Medicine. G.V.L. was funded by the Office of Naval Research (T. McKenna, Program Manager, ONR 341), grant N00014-15-1-2234, and the National Science Foundation, grant 1830881. H.A.M.A. would like to thank the American Chemical Society for their generous support through the Irving S. Sigal Postdoctoral Fellowship. The views and conclusions contained in this document are those of the authors and should not be interpreted as representing the official policies, either expressed or implied, of the National Institutes of Health, the National Science Foundation, or the US Government. This work was performed in part at the Harvard Center for Nanoscale Systems, a member of the National

Nanotechnology Infrastructure Network, which is supported by the National Science Foundation under award ECS-0335765. The Center for Nanoscale Systems is part of Harvard University. **Author contributions:** K.Y.L. and S.-J.P. conceived and designed the study, developed a geometrically insulated cardiac tissue node-integrated muscular bilayer construct, designed and performed performance experiments, analyzed data, organized figures, and wrote the paper. K.K.P. conceived and designed the study, developed the idea of a geometrically insulated cardiac tissue node and muscular bilayer, and supervised the project. A.G.K. and G.V.L. contributed to the concept of a geometrically insulated cardiac tissue node and muscular bilayer, respectively. D.M. and G.V.L. contributed to the PIV experiments of both biohybrid and wild-type fish. S.L.K. designed optogenetic tools and edited the manuscript. C.M. assisted the fabrication of the biohybrid fish. S.L.K., J.Z., and H.A.M.A. performed primary neonatal rat ventricular harvest for the biohybrid fish optimization. All authors contributed to the preparation of the manuscript. **Competing interests:** K.Y.L., S.-J.P., A.G.K., V.T., and K.K.P. are inventors on a patent filed by Harvard

University, U.S. Provisional Patent Application No. 63/299,920, based on the results described in this manuscript. The remaining authors declare no competing interests. **Data and materials availability:** All data are available in the main text or the supplementary materials. Code and scripts are available at Zenodo (24)

#### SUPPLEMENTARY MATERIALS

science.org/doi/10.1126/science.abh0474  
Materials and Methods  
Figs. S1 to S19  
References (46–48)  
MDAR Reproducibility Checklist  
Movies S1 to S25

16 February 2021; accepted 14 January 2022  
10.1126/science.abh0474

## REPORTS

### MATERIALS SCIENCE

# A damage-tolerant, dual-scale, single-crystalline microlattice in the knobby starfish, *Protoreaster nodosus*

Ting Yang<sup>1†</sup>, Hongshun Chen<sup>1†</sup>, Zian Jia<sup>1</sup>, Zhifei Deng<sup>1</sup>, Liuni Chen<sup>1</sup>, Emily M. Peterman<sup>2</sup>, James C. Weaver<sup>3</sup>, Ling Li<sup>1\*</sup>

Cellular solids (e.g., foams and honeycombs) are widely found in natural and engineering systems because of their high mechanical efficiency and tailorable properties. While these materials are often based on polycrystalline or amorphous constituents, here we report an unusual dual-scale, single-crystalline microlattice found in the biomineralized skeleton of the knobby starfish, *Protoreaster nodosus*. This structure has a diamond-triply periodic minimal surface geometry (lattice constant, approximately 30 micrometers), the [111] direction of which is aligned with the c-axis of the constituent calcite at the atomic scale. This dual-scale crystallographically coaligned microlattice, which exhibits lattice-level structural gradients and dislocations, combined with the atomic-level conchoidal fracture behavior of biogenic calcite, substantially enhances the damage tolerance of this hierarchical biological microlattice, thus providing important insights for designing synthetic architected cellular solids.

**W**eight reduction is often considered a primary goal when developing structural materials, which in turn reduces material usage, energy consumption, and environmental impact. One effective solution is through the introduction of porosity to create cellular solids (1). Conventional cellular solids include honeycombs and open- and closed-cell foams with three-dimensional (3D) stochastic porosities (1). Recently, architected cellular materials, enabled by developments in computational design and additive

manufacturing, further extend the mechanical property space of conventional cellular solids while enabling unusual physical properties such as negative Poisson's ratio and negative stiffness (2). Current synthetic architected cellular structures are exclusively based on either polycrystalline or amorphous materials at the atomic scale (2). These synthetic architected lattice materials often exhibit catastrophic failure, especially for those with ceramic and glassy constituents. To address some of these performance limitations, and by leveraging the advantages of size effects and hierarchical design strategies, recent studies have demonstrated that ceramic nanolattices can exhibit high energy absorption capabilities (2–5). The strength of these materials, however, is usually limited by their feature sizes, such as the wall thickness in hollow nanolattices, which is maintained in the sub-100-nm range to achieve high relative strength and recoverability (2–5).

Widely found in the shallow waters of the tropical Indo-Pacific, the knobby starfish, *Protoreaster nodosus*, is characterized by its hard, pointy protrusions or “knobs” arranged radially along its aboral (dorsal) surface (Fig. 1, A to C). Upon removal of the overlying soft tissue, a well-organized assembly of the calcareous skeletal elements (ossicles) can be revealed with optical microscopy (Fig. 1B and fig. S1) or microcomputed tomography ( $\mu$ -CT; Fig. 1C, figs. S2 and S3, and movie S1). Scanning electron microscopy (SEM) reveals that these millimeter-sized ossicles exhibit a porous lattice-like structure (Fig. 1, D and E), which is so ordered that atomic terrace-like morphologies can be observed on the ossicle surfaces (yellow arrows, Fig. 1E). Furthermore, imaging of the fractured surfaces demonstrates that the periodic microlattice structure fully extends into the ossicle interiors (Fig. 1F and fig. S4).

To determine the lattice structure and symmetry, we performed quantitative 3D analysis on a representative high-resolution  $\mu$ -CT volume ( $243 \times 243 \times 243 \mu\text{m}^3$ ) extracted from a single ossicle (Fig. 1G and movie S2). The skeletonized lattice network demonstrates the periodic arrangement of the tetrahedron units with a branch length ( $l$ ) of  $15.5 \pm 2.5 \mu\text{m}$  (5499 measurements in total) (Fig. 1H, fig. S5, movie S3, and materials and methods). The corresponding 3D fast Fourier transform (3D-FFT) reveals that the most intense reflections result from the cubic “ $Fd\bar{3}m$ ” symmetry, such as the  $\{111\}$  and  $\{220\}$  families, confirming the diamond microlattice structure in these ossicles (Fig. 1I, figs. S6 to S8, and movie S4) (6). Measurement of the reciprocal lattice constants from the 3D-FFT data reveals a lattice constant ( $a$ ) of  $34.0 \pm 5.9 \mu\text{m}$ , which is in excellent correspondence with the real-space measurements ( $a = 4l/\sqrt{3}$  for a diamond lattice). In addition to the standard “ $Fd\bar{3}m$ ” reflections, “symmetry-forbidden” intensity spots corresponding to the  $\{HKL\}$  planes with  $H + K + L = 4n + 2$  (where  $n$  is an integer) were also observed, for example, the  $\{002\}$  family (circled in green, Fig. 1I and

<sup>1</sup>Department of Mechanical Engineering, Virginia Polytechnic Institute and State University, Blacksburg, VA 24061, USA.

<sup>2</sup>Earth and Oceanographic Science, Bowdoin College, Brunswick, ME 04011, USA. <sup>3</sup>Wyss Institute for Biologically Inspired Engineering, Harvard University, Cambridge, MA 02138, USA.

\*Corresponding author. Email: lingli@vt.edu

†These authors contributed equally to this work.

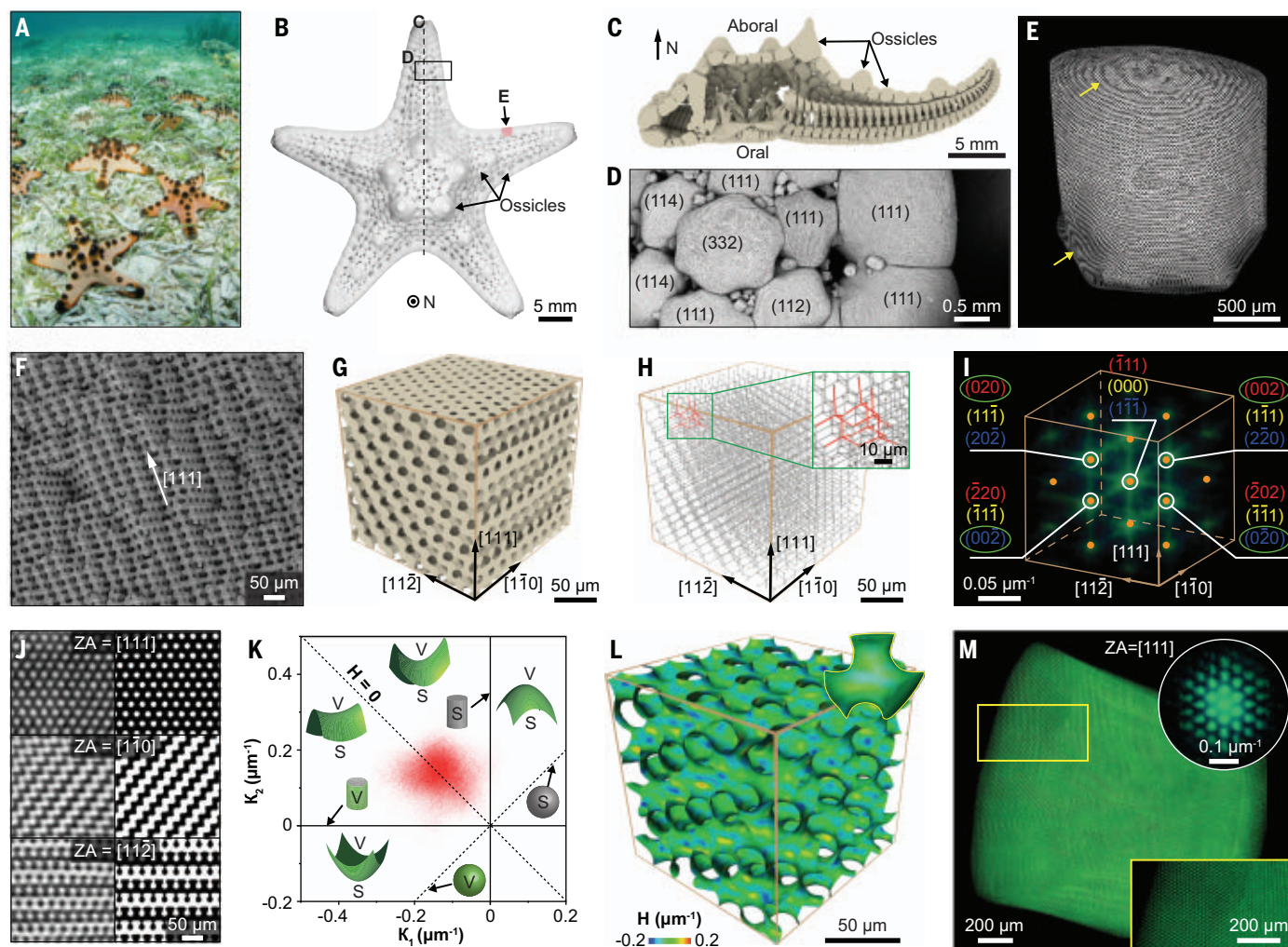


**Fig. 1. Diamond-TPMS microlattice in the ossicles of *P. nodosus*.** (A) Photo of live *P. nodosus*. (B) Skeleton of *P. nodosus* with its superficial soft tissue removed (aboral view). (C)  $\mu$ -CT reconstruction of the skeleton showing the aboral and oral layers of ossicles along the normal direction (defined as the oral-aboral direction). The dashed line in (B) denotes the location of this cross-sectional cut. (D and E) SEM images showing the ossicles' highly ordered lattice structure. The lattice directions of selected ossicles are labeled in (D). The yellow arrows in (E) highlight the terrace-like morphology formed by the {111} lattice planes on the ossicle surface. (F) SEM image of an ossicle's fracture surface. (G and H) 3D rendering (G) and its corresponding skeletonized connectivity diagram (H) of a representative ossicle volume with the orthogonal edges along the [111], [110], and [112]

directions. The inset in (H) highlights the tetrahedral units of a diamond lattice. (I) Corresponding 3D-FFT pattern with diffraction spots denoted by orange dots. Some spots are overlapping, representing multiple crystal planes, as designated by the blue, yellow, and red indices. (J) Comparison of the cross-sectional patterns between the ossicle (left) and a simulated diamond-TPMS structure (right) along the (111), (110), and (112) lattice planes. (K) Interfacial shape distribution map (i.e.,  $\kappa_2$  versus  $\kappa_1$ ) of an ossicle volume. The inset schematics illustrate the representative interface shapes in the different regions. S, solid; V, void. (L) Contour map of the mean curvature  $H$  on the ossicle's diamond-TPMS structure. (M) Projection image of the reconstructed volume in transparent mode and corresponding 3D-FFT pattern (inset) of an intact ossicle along the zone axis (ZA) of [111].

figs. S6 and S7) (7). In contrast to atomic diamond crystals, the presence of these symmetry-forbidden reflections results from the branches connecting neighboring nodes in the diamond lattice structure (see the materials and methods) (7, 8).

The surface morphology of the ossicles' diamond microlattice exhibits marked resemblance to a standard diamond-triply periodic minimal surface (TPMS) structure when viewed normal to low-index planes such as the (111), (110), and (112) (Fig. 1J). From the synchrotron  $\mu$ -CT

data, we quantified the minimum and maximum principal curvatures (i.e.,  $\kappa_1$  and  $\kappa_2$ , respectively) of the microlattice surface and represented their distributions in an interfacial shape distribution plot (Fig. 1K).  $\kappa_1$  and  $\kappa_2$  and are estimated as  $-0.135 \pm 0.050 \mu\text{m}^{-1}$  and  $0.137 \pm 0.043 \mu\text{m}^{-1}$ , respectively. The corresponding mean curvature [ $H = (\kappa_1 + \kappa_2)/2$ ] is  $0.001 \pm 0.032 \mu\text{m}^{-1}$ , which explains the convergence of data points on the line  $\kappa_1 + \kappa_2 = 0$  in Fig. 1K. The contour plot of  $H$  mapped onto the original structure shown in Fig. 1L further

reveals the uniform distribution of nearly zero  $H$  values. Although the existence of periodic minimal surfaces in echinoderm skeletal elements has been broadly accepted in the literature (9), to the best of our knowledge, the present study represents the first quantitative confirmation of a mineralized biological diamond-TPMS structure in nature.

This diamond-TPMS microlattice fully comprises the entire volume of each ossicle, making it possible to "index" specific lattice planes of their outer surfaces (Fig. 1D and fig. S9). As



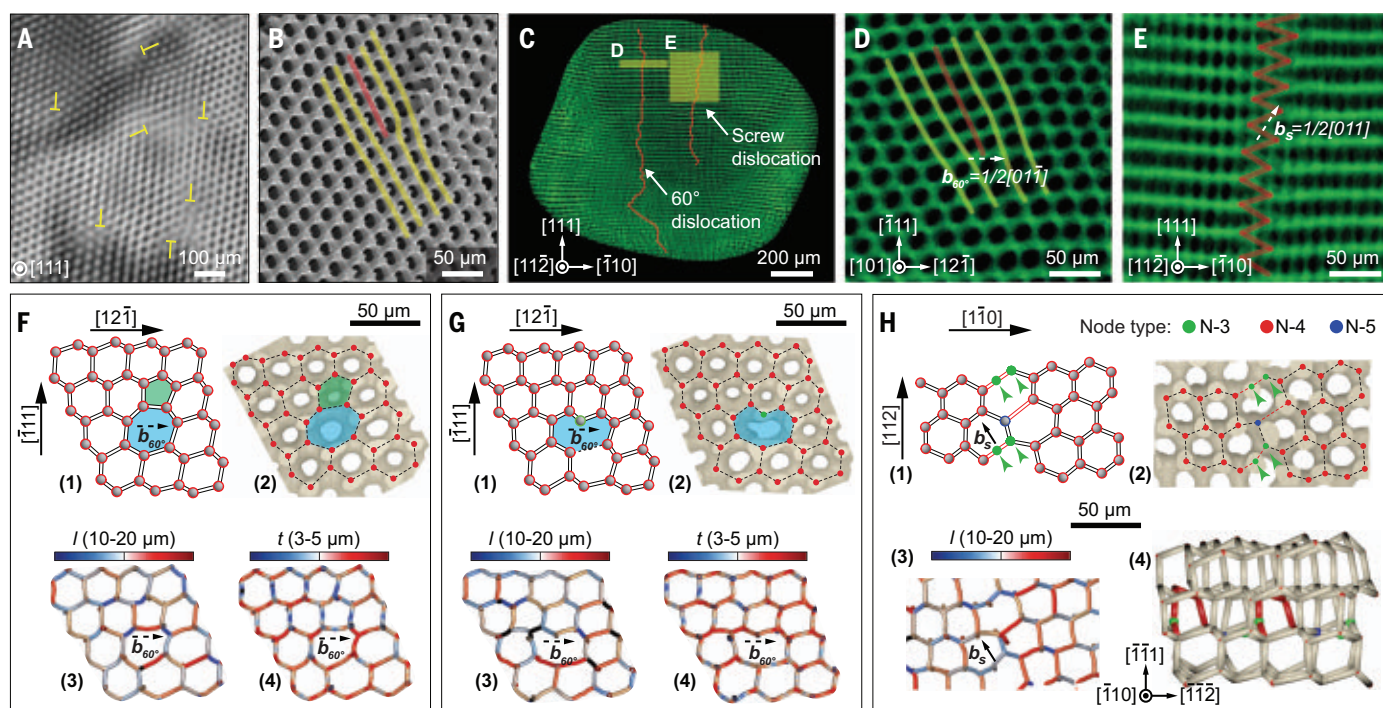


**Fig. 2. Lattice dislocations in the ossicle's diamond-TPMS structure.**

(A)  $\mu$ -CT reconstruction slice along the  $[111]$  plane, with dislocation-like defects highlighted. (B) SEM image of a dislocation-like defect on the fracture surface of an ossicle. (C) Reconstructed volume of an ossicle with representative  $60^\circ$  and screw dislocations highlighted. (D and E) Magnified views of  $60^\circ$  (D) and screw dislocations (E) extracted from (C). (F and G)  $60^\circ$  glide (F) and shuffle dislocations (G) in the ossicles: (1) 2D models, (2)  $\mu$ -CT reconstructions of the dislocation core structures, and corresponding maps of (3) branch length  $l$  and

(4) thickness  $t$ . The five-node ring in F(2) is shaded in green and the seven-node ring in F(2) and the eight-node ring in G(2) are shaded in cyan. Burgers vector  $b_{60^\circ} = 1/2[01\bar{1}]$ . (H) Shuffle screw dislocation with kinks: (1) 2D model, (2)  $\mu$ -CT reconstruction of the observed dislocation core structure, (3) map of branch length  $l$ , and (4) corresponding 3D connectivity diagram from an individual ossicle. The branches in the Burgers circuit are colored in red. Burgers vector  $b_s = 1/2[011]$ . The N3, N4, and N5 nodes are colored in green, red, and blue for (F) to (H), respectively.

shown in Fig. 1D, the normal directions of the ossicles are primarily oriented along the  $[111]$  direction of the diamond microlattice. The  $\mu$ -CT projection images and corresponding 3D-FFT patterns further demonstrate that the diamond microlattice structure is conserved in ossicles from both the aboral and oral sides (Fig. 1M, figs. S10 and S11, and movie S5), and the lattice constant is 29.2 to 34.2  $\mu\text{m}$  (corresponding to a branch length  $l$  of 12.6 to 14.8  $\mu\text{m}$ ) (fig. S12 and table S1). By using a customized cellular network analysis algorithm (10, 11), we further show that structural parameters such as branch length and thickness exhibit spatial variations within individual ossicles, as demonstrated in figs. S13 to S17 and tables S2 and S3.

Defects such as dislocations are ubiquitous in atomic crystals and play significant roles in controlling material properties (12). We investigated the structural defects at the lattice level within ossicles and compared them with known classes of defects in atomic crystals with the cubic diamond symmetry (e.g., diamond and silicon) (12). Careful examination of the  $\mu$ -CT slices and SEM images of fractured ossicle surfaces reveal the presence of dislocation-like

lattice defects (Fig. 2, A and B). In addition, we identified two prominent dislocation types in the ossicles, namely  $60^\circ$  dislocations and screw dislocations (Fig. 2, C to H), which are also the primary dislocation types found in atomic diamond crystals (12–15). For the  $60^\circ$  dislocation, the Burgers vector ( $b_{60^\circ}$ ) and the dislocation line direction ( $\xi_{60^\circ}$ ) are oriented along different  $\langle 110 \rangle$  directions (e.g.,  $b_{60^\circ} = 1/2[01\bar{1}]$ ,  $\xi_{60^\circ} = [\bar{1}0\bar{1}]$ ), making a  $60^\circ$  angle between  $b_{60^\circ}$  and  $\xi_{60^\circ}$  (13, 14). Similar to atomic diamond crystal structures, because of the presence of two inequivalent families of  $\{111\}$  planes, the glide set and shuffle set, two types of  $60^\circ$  dislocations are observed, the G-type and the S-type, respectively, depending on where the inserted extra plane terminates (Fig. 2, F and G) (14, 15). In addition, the branches on the “compressive” and “tensile” sides of the  $60^\circ$  dislocation cores have reduced and increased lengths, respectively, whereas the branch thickness remains relatively uniform (Fig. 2, F and G). For the screw dislocations, the Burgers vector ( $b_s$ ) and the dislocation line direction ( $\xi_s$ ) are along the same  $\langle 110 \rangle$  direction (e.g.,  $b_s = 1/2[011]$ ,  $\xi_s = [011]$ ), which form the classic zig-zag-like pattern of screw dislocations when

viewed normal to a  $(11\bar{2})$  plane (Fig. 2E). Although the core structure of the screw dislocations exhibits multiple different configurations in atomic diamond crystals (13, 16), our analysis reveals that the dislocation core in the ossicles' diamond microlattice resembles an undissociated screw dislocation in the shuffle set with kinks (Fig. 2H) (17, 18). Further structural analyses of dislocations in ossicles are shown in figs. S18 to S23.

At the whole-ossicle level, the microlattice dislocation density is estimated to be in the range of 100 to 1200  $\text{cm}^{-2}$ , corresponding to a normalized density of 0.001 to 0.011 (measurement based on eight ossicles randomly chosen from both aboral and oral sides; see also table S4, fig. S24, and materials and methods). This result is considerably higher than the dislocation density in natural and synthetic single-crystalline diamonds, which is typically  $<10^{-6}$  (19, 20). Beyond the ossicle example described here, lattice dislocations are frequently encountered in other highly periodic biological materials, ranging from the spiral-like comb geometries of stingless honey bees (21) to the damage-tolerant microlaminate architecture of bivalve nacre (22, 23).



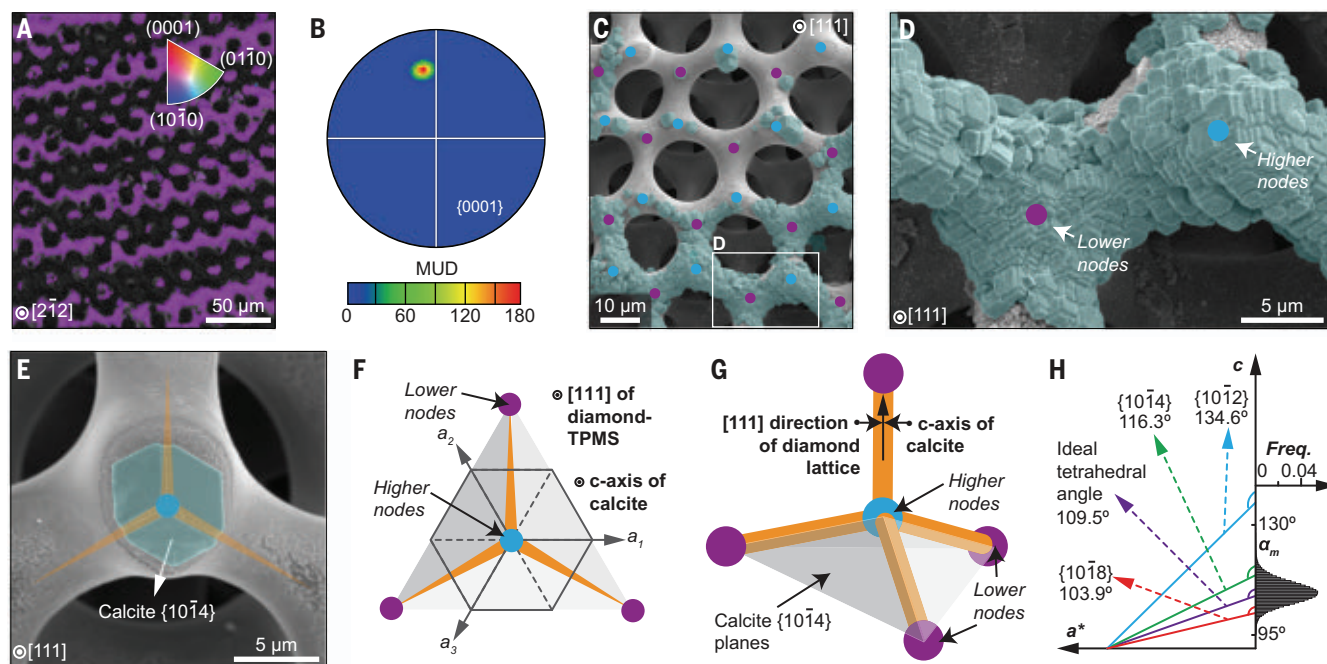


**Fig. 3. Dual-scale single-crystalline diamond-TPMS lattice.** (A and B) Electron backscatter diffraction orientation map (A) and corresponding {0001} pole figure (B) of calcite for a polished ossicle surface. (C and D) SEM images of the ossicle lattice with epitaxially overgrown calcite crystals (shaded in light blue) when viewed along the (111) plane of the diamond-TPMS lattice. The purple and cyan dots represent the lower and higher nodes on the (111) plane, characterized by their concave and convex surfaces,

respectively. (E) Coalignment of a single overgrown calcite crystal and the branch orientations of the diamond lattice. (F and G) 2D (F) and 3D (G) illustrations of the crystallographic coalignment at atomic and lattice length scales. (H) Comparison between the crystallographic angles of the {10 $\bar{1}$ 2}, {10 $\bar{1}$ 4}, and {10 $\bar{1}$ 8} planes with respect to the c-axis of calcite, the ideal tetrahedral angle (109.5°), and the measured interbranch angle distribution ( $\alpha_m$ ).

Previous studies have demonstrated that individual echinoderm ossicles largely diffract as single-crystal calcite (9) despite the presence of intracrystalline organic occlusions, doping of the calcite with magnesium ions, and a mesocrystalline structure in which the calcite shows a nanoparticulate ultrastructure (24). On the basis of these observations, we further explored the potential relationship between the diamond-TPMS microlattice and the underlying atomic-level ordering of the constituent calcite. As expected, crystallographic mapping from electron backscatter diffraction data on ossicles from *P. nodosus* confirms its single-crystal-like nature at the atomic scale (Fig. 3, A and B, and fig. S25). Moreover, to further investigate its multiscale crystallographic relationship, we used the epitaxial overgrowth strategy to induce the formation of synthetic calcite crystals on the ossicle surfaces (see the materials and methods) (25–27). As shown in Fig. 3, C to E, the overgrown calcite crystals (shaded in light blue) still retain the rhombohedral symmetry of calcite, inheriting the crystallographic orientation of the underlying ossicles. When viewed along the [111] direction of the diamond-TPMS microlattice, the overgrown calcite crystals exhibit a threefold symmetry, confirming that the c-axis of the calcite is

oriented along the [111] direction of the diamond-TPMS microlattice (Fig. 3E). Moreover, the edges formed by two adjacent {10 $\bar{1}$ 4} planes of the calcite are aligned with the branches connected with the “higher nodes” in the (111) plane of the diamond microlattice (Fig. 3, F and G). This observation demonstrates that the in-plane threefold symmetry of calcite (space group,  $R\bar{3}c$ ) is aligned with that of the diamond microlattice in the [111] direction. Last, the common edges formed by adjacent {10 $\bar{1}$ 4} planes of calcite crystals intersect with the c-axis at an angle of 116.3°, which is close to the measured interbranch angle within the ossicles ( $\alpha_m = 110.9 \pm 10.2^\circ$ ) and the ideal tetrahedral angle in a diamond lattice (109.5°) (Fig. 3H and fig. S26). On the basis of these observations, the dual-scale coordination observed in the diamond-TPMS structure is likely influenced by the crystal symmetry of the constituent calcite during microlattice formation, which may be further modulated by the mineral’s interactions with macromolecules secreted by the bounding sclerocyte cells (25–27). Although speculative at this point, this proposed mechanism is functionally analogous to the organic template-modulated, directionally specific attachment of mineral particles and crystallization

processes observed in other branched calcitic biomineralized structures, including sea urchin larval spicules and calcareous sponge spicules (25–28).

The diamond-TPMS microlattice also exhibits long-range variations of structural parameters at the ossicle level, such as branch length and thickness (figs. S14 to S17 and table S3). Figure 4A represents an extreme example of this structural gradient in which the branch thickness increases from 4.7 to 7.3  $\mu\text{m}$  toward the ossicle surface over a distance of about six unit cells despite a relatively uniform branch length. Such structural gradients give rise to mechanical property gradients, which were quantified by a micromechanical model based on the Timoshenko beam theory (figs. S27 and S28, table S5, and materials and methods). From these studies, it was found that the normalized modulus ( $E_{\text{Ossicle}}^{\text{111, Iso}}/E_{\text{Calcite}}^{\text{Iso}}$ ) and strength ( $\sigma_{\text{Ossicle}}^{\text{111, Iso}}/\sigma_{\text{Calcite}}^{\text{T, Iso}}$ ) in the [111] direction of the diamond microlattice are strongly correlated with  $\eta(l_1/l_m)$  and  $\lambda(t_1/t_m)$  (Fig. 4B, figs. S29 to S31, and table S6). Here,  $E_{\text{Calcite}}^{\text{Iso}}$  and  $\sigma_{\text{Calcite}}^{\text{T, Iso}}$  represent the equivalent isotropic modulus and tensile strength of the solid calcite, respectively (see the materials and methods);  $l_1$  and  $t_1$  are the length and thickness of the branch in the [111] direction, respectively; and  $l_m$  and  $t_m$  are

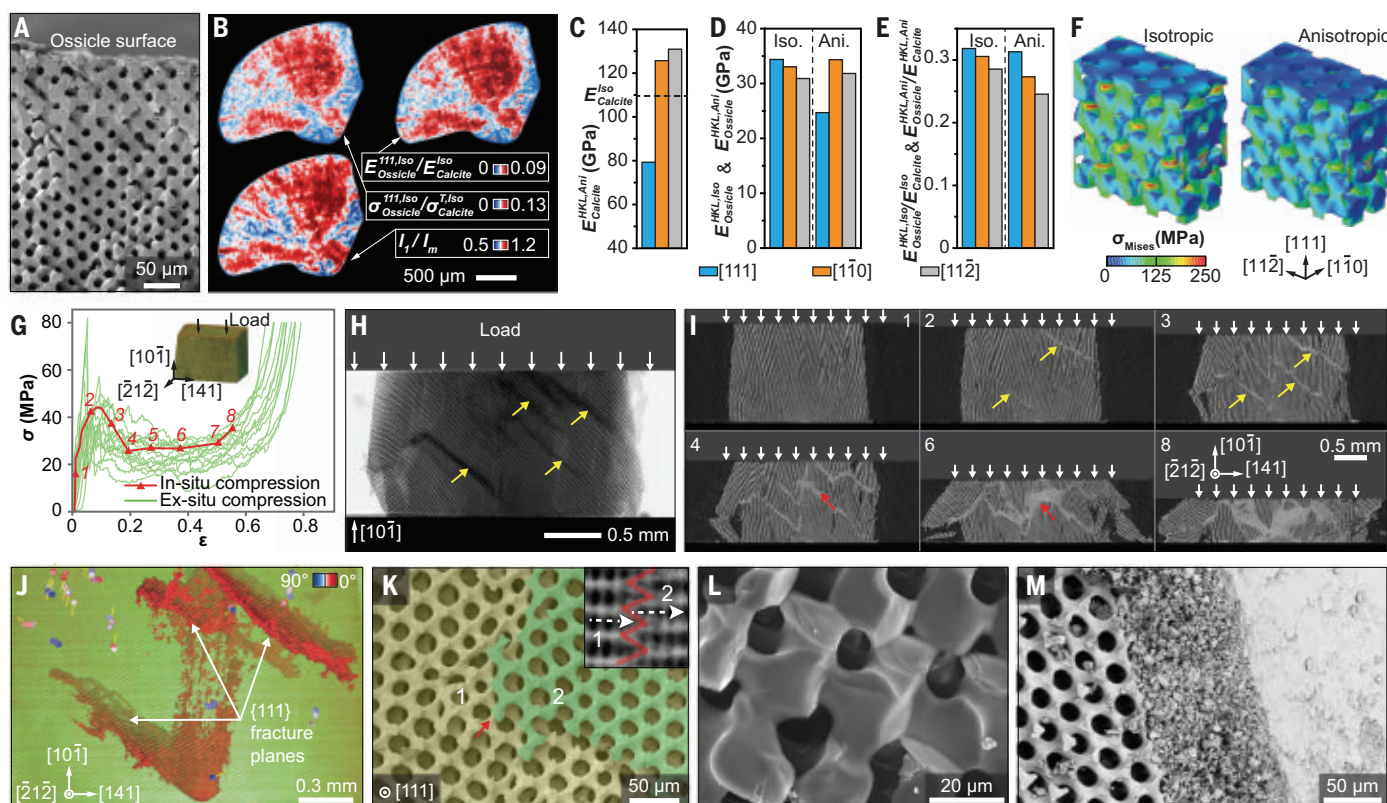


**Fig. 4. Mechanical properties of the ossicle's diamond-TPMS microlattice.**

(A) SEM image of a fractured ossicle showing the local increase in branch thickness toward the outer ossicle surface. (B) Spatial variations of normalized stiffness ( $E_{\text{Ossicle}}^{\text{III, Iso}}/E_{\text{Calcite}}^{\text{III, Iso}}$ ), strength ( $\sigma_{\text{Ossicle}}^{\text{III, Iso}}/\sigma_{\text{Calcite}}^{\text{III, Iso}}$ ), and corresponding branch length ratio ( $\eta = l_t/l_m$ ) for a representative ossicle. (C) Anisotropic moduli ( $E_{\text{Calcite}}^{\text{HKL, Ani}}$ ) and equivalent isotropic modulus ( $E_{\text{Calcite}}^{\text{Iso}}$ ) of the solid calcite. (D and E) Moduli ( $E_{\text{Ossicle}}^{\text{HKL, Ani}}$  and  $E_{\text{Ossicle}}^{\text{HKL, Ani}}$ ) (D) and corresponding normalized moduli ( $E_{\text{Ossicle}}^{\text{HKL, Ani}}/E_{\text{Calcite}}^{\text{HKL, Ani}}$  and  $E_{\text{Ossicle}}^{\text{HKL, Ani}}/E_{\text{Calcite}}^{\text{HKL, Ani}}$ ) (E) of the ossicle diamond-TPMS lattice calculated using the isotropic and anisotropic properties of calcite. The values in (C) and (D) were calculated in three orthogonal directions of the diamond lattice ([111], [110], and [112]). (F) von Mises stress contour plots (compression along the [111] direction) with isotropic and anisotropic material properties. (G) Stress ( $\sigma$ )–strain ( $\epsilon$ )

curves of both ex situ and in situ compression tests. Inset: volumetric reconstruction of a representative in situ test sample. (H) Projection image of an ossicle sample under in situ compression, with damage bands denoted by yellow arrows ( $\epsilon = 0.11$ ). (I) Sequential cross-sectional slices of the reconstructed data showing the deformation and fracture evolution within the sample. The yellow and red arrows denote the slip-like damage bands and the densified regions, respectively. (J) 3D rendering of the sample with the damage bands colored in red and dislocations with Burgers vectors indicated in yellow arrows. (K) SEM image of a fracture surface deviated by a dislocation (denoted by the red arrow). The regions shaded in green and yellow represent two adjacent (111) fractured planes. (L) Conchoidal fracture of the ossicle's biogenic calcite. (M) SEM image of damage localization and densifications during indentation.

the average length and thickness of the branches in non-[111] directions, respectively. It is conceivable that a larger  $\eta$  or a lower  $\lambda$  represents relatively shorter or thicker inclined branches (i.e., non-[111] branches) that have higher bending stiffness, which results in a higher stiffness of the local diamond microlattice (fig. S31). The local increase in mechanical performance in the upper portion of this ossicle (no. 7) may contribute to its resistance against external loads along the aboral to oral direction (Fig. 4B and fig. S29).

Although the theoretical analysis above permits the investigation of long-range mechanical heterogeneity within the ossicles, it ignores the important effects of the mechanical anisotropy of calcite and the crystallographic coalignment between atomic and lattice scales. Calcite is a highly anisotropic material with a lower stiff-

ness along the  $c$ -axis than along the  $a$ -axes (table S7) (29). To accommodate these differences in crystal mechanical anisotropy, we developed a finite element model that incorporates the crystallographic coalignment deduced above and the full stiffness matrix of calcite (see the materials and methods). This approach allows us to estimate the effective Young's moduli of the solid calcite along the diamond lattice directions of [111], [110], and [112] (denoted as  $E_{\text{Calcite}}^{\text{III, Ani}}$ ,  $E_{\text{Calcite}}^{\text{IIO, Ani}}$ , and  $E_{\text{Calcite}}^{\text{II2, Ani}}$ , respectively) as 79.6, 126.8, and 130.8 GPa, respectively (Fig. 4C, fig. S32, and tables S6 and S7). This result again confirms the softness of calcite along the  $c$ -axis or the [111] lattice direction. However, the [111] direction is the stiffest for a diamond-TPMS lattice based on isotropic materials among other orientations, as evident from our modeling results and from previous studies

(Fig. 4D and fig. S33) (30). These results suggest that the alignment of the stiff [111] direction of the diamond-TPMS microlattice with the  $c$ -axis of calcite in the ossicles of *P. nodosus* represents an interesting strategy to compensate for the material-level compliance. Indeed, when the anisotropic properties of calcite are used in simulations, the increase in the normalized modulus of the diamond-TPMS structure is highest along the [111] direction (Fig. 4, D and E, and fig. S33), which leads to a more uniform stress distribution compared with isotropic material properties (Fig. 4F and fig. S34).

Because of the inherent brittleness of ceramic materials, synthetic ceramic foams and the recently developed architected ceramic lattices often suffer from catastrophic failure when the applied load exceeds a critical value (1, 3).



Because calcite is a brittle mineral, and biogenic calcite also fractures upon critical loading (3I), we further investigated the ossicle's fracture behavior and energy dissipation mechanisms using a series of experimental approaches. Uniaxial compression tests on cube-shaped specimens cut from individual ossicles (edge length, ~2 mm) reveal the graceful failure behavior of ossicles as demonstrated by the large stress plateau after reaching the failure strength ( $\sigma_p = 46.48 \pm 15.14$  MPa;  $n = 14$ ) (Fig. 4G). This behavior leads to an energy absorption ( $W_c$ ) of  $14.25 \pm 2.50$  MJ/m<sup>3</sup> and thus a substantial specific energy absorption ( $W_v/\rho$ ) of  $9.76 \pm 1.59$  kJ/kg, outperforming many synthetic ceramic or even metallic foams (figs. S35 and S36).

It is interesting that the calcitic diamond-TPMS structure in these ossicles exhibits a large stress plateau upon compression because this behavior is typically only observed in polymeric and metallic foams (I). We next used synchrotron in situ mechanical testing to track, visualize, and analyze the deformation processes in 3D. Upon loading, the ossicle samples developed slip-like damage bands at initial yielding (yellow arrows, Fig. 4H), and the sequential cross-sectional slices of the reconstructed data demonstrate that the co-parallel damage bands undergo local densification and increase in bandwidth (red arrows, Fig. 4I and figs. S37 and S38). In these representative data, the applied load is in the  $[101]$  direction of the diamond microlattice, and the damage bands are in the  $(11\bar{1})$  plane (Fig. 4I and fig. S38). The preferred failure along the  $\{111\}$  planes is expected in the diamond-TPMS microlattice because the  $\{111\}$  planes contain the highest 2D cross-sectional porosity, and thus the lowest solid fraction, which leads to the highest local stress for crack initiation and the subsequent formation of damage bands along these planes (figs. S39 and S40). However, unlike synthetic architected ceramic lattices, in which damage bands fully propagate to the sample surface, the damage bands in ossicles are often deviated and constrained within the specimen (Fig. 4, H and I). Furthermore, a correlative crystal lattice analysis of both undeformed and deformed volumes suggests that the damage bands do not propagate to the regions with a high density of dislocations (Fig. 4J). When encountering a lattice dislocation, the  $\{111\}$  damage band has to “jump” from one  $\{111\}$  to another  $\{111\}$  plane for further crack propagation (Fig. 4K). This mechanism is similar to the “pinning” behavior of slips by pre-existing dislocations in metals, which is responsible for their well-known strain-hardening behavior (I2).

The biogenic ossicle calcite, despite its single-crystalline nature, does not undergo cleavage fracture along the  $\{10\bar{1}4\}$  planes as in its geological counterpart (24). Instead, it behaves

as a glassy material, exhibiting a distinctive noncleavage “conchoidal” fracture pattern (Fig. 4L) (24, 3I). This behavior leads to continuous fragmentation of the calcitic lattices into micro- and nanoscopic pieces during the densification process within the damage bands (Fig. 4M), with continued loading leading to particle compaction, rotation, and friction, further contributing to enhanced energy absorption (3I–33).

In the present study, we describe a natural ceramic architected microlattice structure in the calcitic skeletal system of the knobby starfish, *P. nodosus* that exhibits exquisite crystallographic registration for both its atomic-scale calcite and its microscale diamond-TPMS lattice. This unique dual-scale microlattice offers multiple effective strategies to achieve high stiffness, strength, and damage tolerance, including crystallographic coalignment, lattice geometric gradients, and suppression of cleavage fracture through microlattice dislocations. It should be noted, however, that some of the structural features described here, such as the crystallographic coalignment or the microlattice-level defects, may not have necessarily evolved for increased mechanical performance, but rather may simply be a by-product of the complex process of skeletal formation in echinoderms. Nevertheless, the engineering lessons learned here emphasize the importance of hierarchical structural and crystallographic design for single-crystalline materials to achieve improved mechanical performance. Future studies focused on investigating the in vivo formation mechanisms of these complex and highly periodic microstructures would be of great value to the materials science community. These biological microlattices are produced by the synthesis of transient amorphous precursor phases under ambient conditions rather than through energy-intensive processes such as sintering and chemical vapor deposition, which are commonly used for the production of engineering cellular solids.

## REFERENCES AND NOTES

1. L. J. Gibson, M. F. Ashby, *Cellular Solids: Structure and Properties* (Cambridge Univ. Press, 1999).
2. T. A. Schaedler, W. B. Carter, *Annu. Rev. Mater. Res.* **46**, 187–210 (2016).
3. L. R. Meza, S. Das, J. R. Greer, *Science* **345**, 1322–1326 (2014).
4. L. R. Meza et al., *Proc. Natl. Acad. Sci. U.S.A.* **112**, 11502–11507 (2015).
5. L. R. Bauer et al., *Adv. Mater.* **29**, 1701850 (2017).
6. T. Hahn, “The 230 space group,” in *International Tables for Crystallography Volume A: Space-Group Symmetry* (Springer, 2006), pp. 112–717.
7. P. Coppens, *X-Ray Charge Densities and Chemical Bonding* (Oxford Science, 1997).
8. B. Dawson, *Proc. R. Soc. London Ser. A* **298**, 264–288 (1967).
9. G. Donnay, D. L. Pawson, *Science* **166**, 1147–1150 (1969).
10. T. Yang, Z. Wu, H. Chen, Y. Zhu, L. Li, *Acta Biomater.* **107**, 204–217 (2020).
11. H. Chen et al., *Acta Biomater.* **107**, 218–231 (2020).

12. P. M. Anderson, J. P. Hirth, J. Lothe, *Theory of Dislocations* (Cambridge Univ. Press, 2017).
13. J. Hornstra, *J. Phys. Chem. Solids* **5**, 129–141 (1958).
14. A. Blumenau, M. Heggge, C. Fall, R. Jones, T. Frauenheim, *Phys. Rev. B* **65**, 205205 (2002).
15. L. Pizzagalli, J. Godet, S. Brochard, *Phys. Rev. Lett.* **103**, 065505 (2009).
16. L. Pizzagalli, P. Beauchamp, J. Rabier, *Philos. Mag.* **83**, 1191–1204 (2003).
17. L. Pizzagalli, A. Pedersen, A. Arnaldsson, H. Jónsson, P. Beauchamp, *Phys. Rev. B* **77**, 064106 (2008).
18. A. Pedersen, L. Pizzagalli, H. Jónsson, *J. Phys. Condens. Matter* **21**, 084210 (2009).
19. N. Sumida, A. Lang, *Philos. Mag. A* **43**, 1277–1287 (1981).
20. J. Isberg et al., *Science* **297**, 1670–1672 (2002).
21. S. S. S. Cardoso et al., *J. R. Soc. Interface* **17**, 20200187 (2020).
22. J. H. Cartwright, A. G. Checa, B. Escribano, C. I. Sainz-Díaz, *Proc. Natl. Acad. Sci. U.S.A.* **106**, 10499–10504 (2009).
23. M. Beliaev, D. Zollner, A. Pacureanu, P. Zaslansky, I. Zlotnikov, *Nat. Phys.* **17**, 410–415 (2021).
24. J. Seto et al., *Proc. Natl. Acad. Sci. U.S.A.* **109**, 3699–3704 (2012).
25. J. Aizenberg, S. Albeck, S. Weiner, L. Addadi, *J. Cryst. Growth* **142**, 156–164 (1994).
26. K. Okazaki, S. Inoue, *Dev. Growth Differ.* **18**, 413–434 (1976).
27. R. T. Knapp, C.-H. Wu, K. C. Mobilia, D. Joester, *J. Am. Chem. Soc.* **134**, 17908–17911 (2012).
28. J. J. De Yoreo et al., *Science* **349**, aaa6760 (2015).
29. L.-F. Zhu et al., *J. Mech. Behav. Biomed. Mater.* **20**, 296–304 (2013).
30. I. Maskery et al., *Mater. Des.* **155**, 220–232 (2018).
31. Z. Deng et al., *Nat. Commun.* **11**, 5678 (2020).
32. X. Li, Z.-H. Xu, R. Wang, *Nano Lett.* **6**, 2301–2304 (2006).
33. L. Li, C. Ortiz, *Nat. Mater.* **13**, 501–507 (2014).

## ACKNOWLEDGMENTS

We thank P. M. Dove for helpful discussions, P. D. Shevchenko and F. De Carlo for help with collecting the synchrotron-based  $\mu$ -CT data and performing in situ mechanical tests, S. McCartney and Y.-P. Yu at the Nanoscale Characterization and Fabrication Laboratory (NCFL) for assistance in electron microscopy, and R. Mueller and R. Wang for their kind help in performing the laboratory x-ray  $\mu$ -CT measurements. **Funding:** This work was supported by the National Science Foundation (DMR-1942865 and CMMI-1825646), the Air Force Office of Scientific Research (FA9550-19-1-0033), and the Institute for Critical Technology and Applied Science (ICTAS) and Department of Mechanical Engineering at Virginia Tech. This research used resources of the Advanced Photon Source, a US Department of Energy (DOE) Office of Science User Facility operated for the DOE Office of Science by Argonne National Laboratory under contract no. DE-AC02-06CH11357. The SEM facility at Bowdoin College was supported by NSF MRI grant no. 1509963 to E. Peterman and R. Beane. **Author contributions:** Conceptualization: L.L.; Funding acquisition: L.L.; Investigation: T.Y., H.C., Z.J., Z.D., L.C., E.M.P.; Methodology: L.L., T.Y., H.C., Z.J., Z.D., J.C.W.; Project administration: L.L.; Supervision: L.L.; Visualization: T.Y., H.C., L.L.; Writing – original draft: H.C., T.Y., L.L.; Writing – review and editing: L.L., H.C., T.Y., Z.J., Z.D., L.C., E.M.P., J.C.W. **Competing interests:** The authors declare no competing interests. **Data and materials availability:** All data are available in the main text or the supplementary materials.

## SUPPLEMENTARY MATERIALS

science.org/doi/10.1126/science.abj9472  
Materials and Methods  
Supplementary Text  
Figs. S1 to S40  
Tables S1 to S7  
Captions for Movies S1 to S5  
References (34–55)  
Movies S1 to S5

15 June 2021; accepted 7 January 2022  
10.1126/science.abj9472



## PIEZOELECTRICS

## Induced giant piezoelectricity in centrosymmetric oxides

D.-S. Park<sup>1,2\*</sup>, M. Hadad<sup>2</sup>, L. M. Riemer<sup>1</sup>, R. Ignatans<sup>3</sup>, D. Spirito<sup>4</sup>, V. Esposito<sup>5</sup>, V. Tileli<sup>3</sup>, N. Gauquelin<sup>6,7</sup>, D. Chezganov<sup>6,7</sup>, D. Jannis<sup>6,7</sup>, J. Verbeeck<sup>6,7</sup>, S. Gorfman<sup>4</sup>, N. Pryds<sup>5</sup>, P. Muralt<sup>2</sup>, D. Damjanovic<sup>1\*</sup>

Piezoelectrics are materials that linearly deform in response to an applied electric field. As a fundamental prerequisite, piezoelectric materials must have a noncentrosymmetric crystal structure. For more than a century, this has remained a major obstacle for finding piezoelectric materials. We circumvented this limitation by breaking the crystallographic symmetry and inducing large and sustainable piezoelectric effects in centrosymmetric materials by the electric field–induced rearrangement of oxygen vacancies. Our results show the generation of extraordinarily large piezoelectric responses [with piezoelectric strain coefficients ( $d_{33}$ ) of  $\sim 200,000$  picometers per volt at millihertz frequencies] in cubic fluorite gadolinium-doped  $\text{CeO}_{2-x}$  films, which are two orders of magnitude larger than the responses observed in the presently best-known lead-based piezoelectric relaxor–ferroelectric oxide at kilohertz frequencies. These findings provide opportunities to design piezoelectric materials from environmentally friendly centrosymmetric ones.

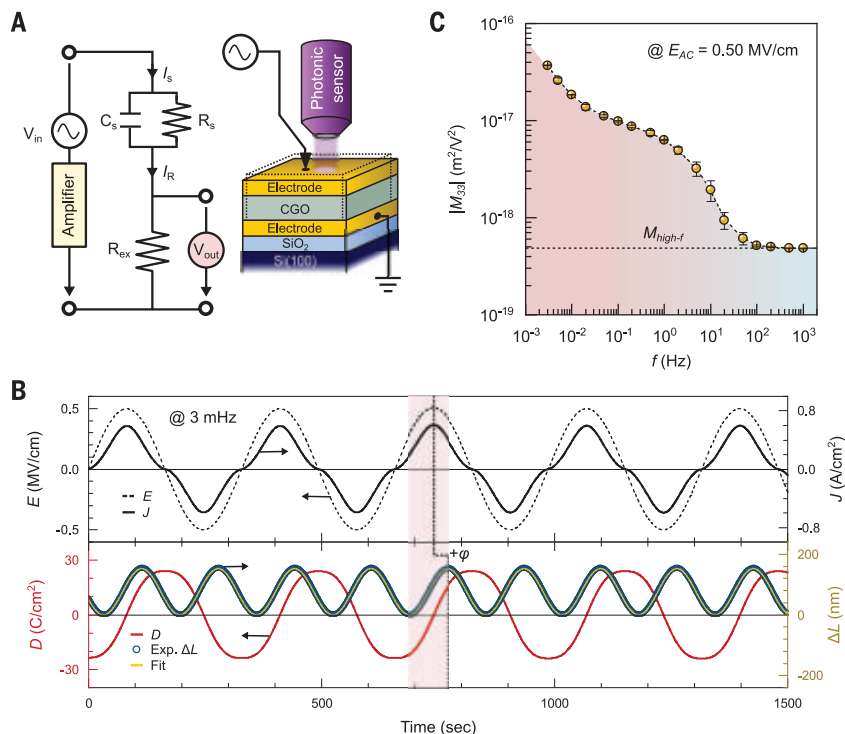
The fundamental principle of electrostriction and piezoelectric effects stems from small deformations of the crystal unit cell by an applied electric field. The latter effect also provides charge separation under mechanical pressure (1). The associated displacements of atoms are in the picometer range, so atoms remain confined around their original crystallographic sites. Piezoelectricity is of high technological and industrial importance and is used in a vast number of applications, such as medical devices, actuators,

and sensors (2). Motivations to augment the piezoelectric response, which requires materials with a noncentrosymmetric structure, are therefore compelling. Among piezoelectric materials, perovskite-type oxides are the most widely used and exhibit excellent piezoelectric responses. Several routes to achieve the highest electromechanical response in these materials have been pursued, including control of the material's structural instability at specific chemical compositions (e.g., morphotropic phase boundary) and associated polarization

rotation and domain engineering (3), chemical disorder (4), and nanocomposite structures (5). All of these strategies demonstrate the possibility for improving the piezoelectric response within an order of magnitude with respect to that of the industrial standard,  $\text{Pb}(\text{Zr,Ti})\text{O}_3$  (PZT) (6).

The piezoelectric effect can be induced in centrosymmetric materials by applying a direct electric field that breaks the inversion symmetry (7, 8). This approach has been revived recently by applying asymmetric electrodes on centrosymmetric samples, creating different Schottky barriers at the electrodes (9). This approach has the potential to widen the number of prospective electromechanical materials beyond the traditionally dominating ferroelectric lead-based perovskites, but the resulting response is still one to two orders of magnitude lower than that of PZT. Another attempt to induce the effect suggests using the electric field–assisted exchange

**Fig. 1. Electric field–induced electrostrictive responses of CGO film.** (A) Schematics of the experimental setup, which combines electrical and electromechanical measurements for the CGO samples. The equivalent circuit shows the voltage source,  $V_{in}$ ; the voltage amplifier; the CGO capacitor,  $C_s$ , with resistance,  $R_s$ ; an external resistor,  $R_{ex}$ ; the current,  $I_R$ , flowing through  $R_{ex}$  and the sample; and the output voltage,  $V_{out}$ , across  $R_{ex}$ . (B) Electrical and electromechanical outputs: (i) the applied  $E_{AC} = 0.5$  MV/cm at  $f = 3$  mHz (dashed line), (ii) the corresponding  $J$  (solid line), (iii) the derived charge density  $D$  (red solid line), and (iv) the concurrently measured second harmonic electromechanical response  $\Delta L$  of the samples (blue circle in lower panel). The measured  $\Delta L$  in time was fitted by  $\Delta L = L_0 \sin^2(\omega t + \phi)$  as depicted by the solid yellow line. (C) Frequency-dependent  $M_{33}$  of the CGO film, excited by  $E_{AC} = 0.5$  MV/cm.



of oxygen with the ambient atmosphere in oxygen-nonstoichiometric fluorite structures (Y-doped  $\text{ZrO}_2$  or  $\text{Re}^{+3}$ -doped  $\text{CeO}_2$ , where Re is a rare earth element) (10). The oxygen exchange (release) results in chemical expansion of the films, leading to bending of thin materials and thus the strain–electrical field ( $x$  versus  $E$ ) relationship, which mimics the piezoelectric effect. The strains achieved are comparable to those in PZT. The field-induced motion of charge carriers takes place over a long range (size of the sample), and the effect is large only at high temperatures ( $>500^\circ\text{C}$ ) and low frequencies (below  $\sim 1$  Hz), where ionic diffusion is sufficiently large. Additionally, some fluorite oxides (e.g., doped  $\text{CeO}_2$ ) were reported to exhibit electrostrictive coefficients that are about two orders of magnitude higher than expected values from phenomenological relations between electrostrictive coefficient and elastic and dielectric susceptibilities (11). The origin of this large electrostriction has not yet been entirely elu-

cidated, but the electric field–induced mechanical deformation is certainly related to the presence and short-range motion of oxygen vacancies (12–14).

We demonstrate a paradigm shift for achieving large, electric field–induced piezoelectricity in centrosymmetric materials. We show that for Gd-doped  $\text{CeO}_{2-x}$  (CGO) films, which have a cubic fluorite centrosymmetric structure, we can achieve very high values of the electric field–induced piezoelectric strain ( $x \sim 26\%$ ) and apparent longitudinal piezoelectric coefficients ( $d_{33}$  of  $\sim 200,000$  pm/V). This latter value, measured in the millihertz range, is two to three orders of magnitude larger than that observed in the best piezoelectric perovskite oxides—e.g.,  $\text{Pb}(\text{Mg}_{1/3}\text{Nb}_{2/3})\text{O}_3$ – $\text{PbTiO}_3$  with  $d_{33} \approx 2000$  pm/V (3). Notably, and relevant for applications, the induced effect is comparable to that in the best PZT thin films ( $\sim 100$  pm/V) in the kilohertz range (15). We argue that the change in the strain mechanism from the short-range lattice or ionic defect-

based mechanism above 10 Hz to the one at low frequencies, is based on distinct actions of the long-range migration of ions (oxygen vacancies,  $\text{V}_\text{O}$ ) and electrons. Our results show that the electric field–induced redistribution of mobile charges in the films leads to crystal phase transition, associated with chemical expansion, and material heterogeneity. These combined effects result in giant piezoelectric and electrostrictive responses and point toward a previously unknown electromechanical mechanism in centrosymmetric fluorites and materials with large ionic and electronic conductivity in general.

We deposited polycrystalline  $(\text{Gd}_{0.2}\text{Ce}_{0.8})\text{O}_{2-x}$  films on  $\text{Al}/\text{SiO}_2/\text{Si}(100)$  substrate at room temperature by sputter deposition (Fig. 1A). The CGO films had thicknesses in the range of  $\sim 1.25$  to  $\sim 1.8$   $\mu\text{m}$  (fig. S1) (16). The electrostrictive strain for a sample of length  $L$  is defined as

$$x = \Delta L/L = ME^2 \quad (1)$$

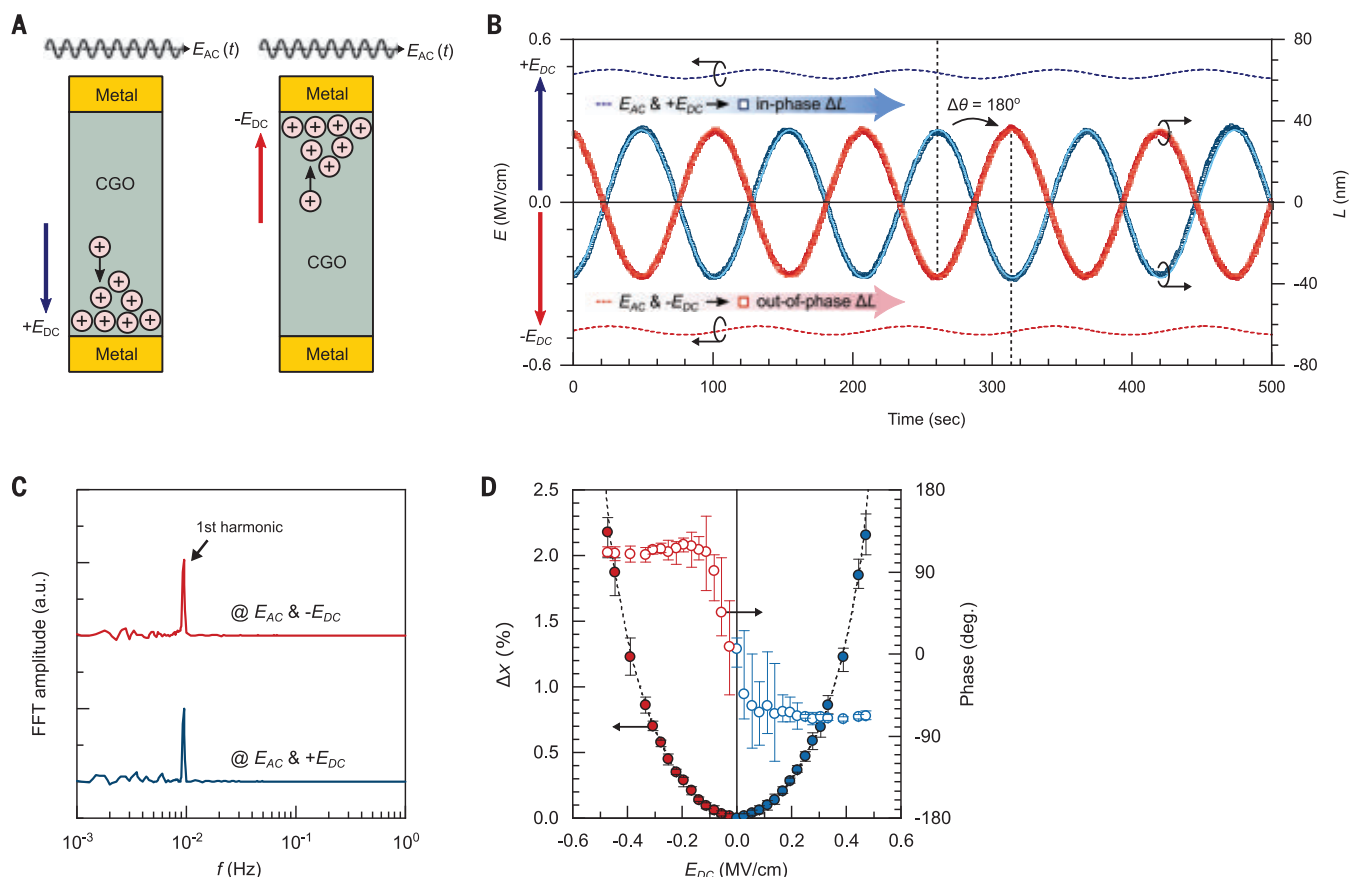


**Fig. 2. The induced piezoelectric displacements in CGO films.** (A) A schematic for the electric field application to CGO film in out-of-plane capacitor geometry, which is simultaneously composed of a small driving AC field ( $E_{AC}$ ) and a large static DC field ( $E_{DC}$ ). The induced in-phase strain ( $x_{33}$ ) in the film is determined by the polarity of the applied DC bias. (B) Time-resolved first harmonic electromechanical displacements of the CGO film, measured at  $\sim 10$  mHz (9.4 mHz) and excited by  $E_{AC} = 15.71$  kV/cm under  $E_{DC} = \pm 0.47$  MV/cm.

The polarity of the DC field switches the sign of the piezoelectric coefficient. The measured  $\Delta L$  in time was fitted by the first-order sine function,  $\Delta L = L_0 \sin(\omega t - \phi)$ , as depicted by the solid red and blue lines. (C) The corresponding fast Fourier transform (FFT) amplitude spectra of the generated first harmonic displacements as a function of frequency. a.u., arbitrary units. (D) Variations in the  $x_{33}$  and response phase angle of the film as a function of DC field while applying a constant  $E_{AC}$  (15.71 kV/cm).

where  $x$  is the out-of-plane strain of the film,  $\Delta L$  is the thickness change,  $M$  is the corresponding electrostrictive coefficient, and  $E$  is the alternated electric field (AC, alternating current) applied between the film's top and bottom electrodes.  $E = E_{AC}(t) = E_{AC}\sin(2\pi ft)$ , where  $f$  is the frequency and  $t$  is time. We used two different top electrodes, Al (~150 nm) and Pt (~150 nm)/Cr (~20 nm) layers, to study the effect of asymmetric electrodes on the polarization (fig. S2C). Electrical (current density  $J$  versus electric field  $E$ ) and electro-mechanical (strain  $x$  versus  $E$ ) measurements on the films were performed on out-of-plane capacitor geometry. We measured the strain  $x$  using a contactless fiber-optic method (16). We confirmed the electromechanical displacements using another setup with direct contact measurements (supplementary text, section 1). All of the instrumental artifacts and external effects (e.g., bending and Joule heating effects) have negligible influence, and thus the dominant contribution to the induced strain is originated only from the electromechanical response of the films (figs. S2 and S3).

We show the measured  $\Delta L$  with the second harmonic response and an offset as obtained

from  $[\sin(2\pi ft)]^2 = \frac{1}{2}[1 - \cos(4\pi ft)]$  (Fig. 1B). We measured the electric current density  $J$  through the film simultaneously with the change in the length  $\Delta L$  and charge density  $D = \int J dt$  (Fig. 1B; supplementary text, section 2; and fig. S4B) (16). We performed measurements of electrostriction across a range of frequencies from 3 mHz to 1 kHz. The electrostrictive coefficient  $M$ , which we determined using Eq. 1, shows a notably complex frequency dependence (Fig. 1C). This clearly indicates that at least three different contributions to the electrostriction exist in these samples (Fig. 1C and fig. S4). We suggest that the strong rate-dependent contributions to strain can be attributed to the existence of mobile ionic species ( $V_O$ ) in the CGO film, as implied by a similar behavior in the AC conductivity (figs. S4 and S5).

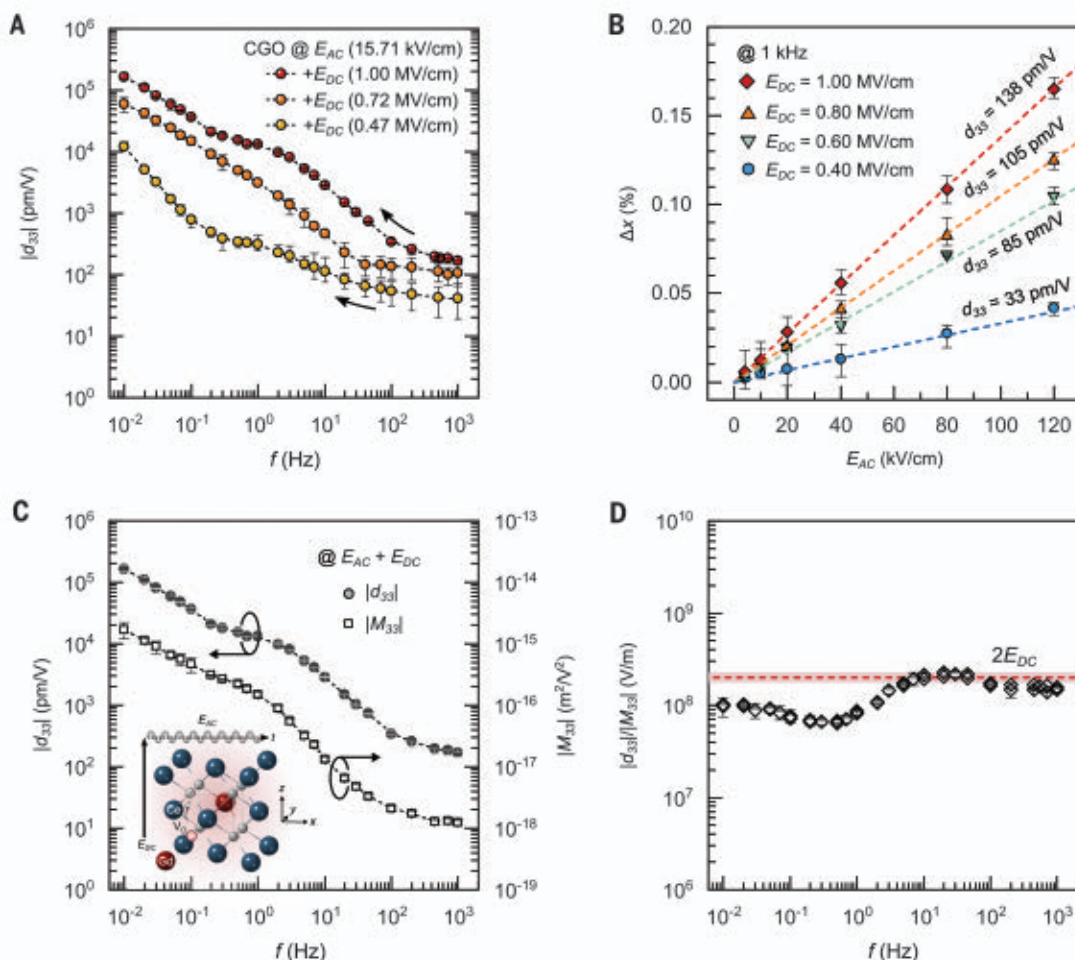
The inversion symmetry in CGO can be broken by applying an electric field bias  $E_{DC}$  (DC, direct current), leading to asymmetric charge distribution and induced polarization  $P_{ind}$  in the material (Fig. 2A) (1). We can explain this by replacing field  $E$  in Eq. 1 with  $E = E(t)_{AC} + E_{DC}$

$$x = ME_{DC}^2 + ME_{AC}^2 + (2ME_{DC})E_{AC} \quad (2)$$

The first and second term describe electrostrictive deformations, and the third term is the symmetry-breaking term with the field-induced piezoelectric coefficient,  $d_{ind} = 2ME_{DC}$ .

The CGO has a centrosymmetric cubic fluorite structure in the ground state and is not piezoelectric. However, we observed the piezoelectric displacement term ( $d_{ind} = 2ME_{DC}$ ) in our CGO films upon application of electric field bias (Fig. 2B) for  $E_{DC} = \pm 0.47$  MV/cm and  $E_{AC} = 15.71$  kV/cm. We observe a clear presence of the first harmonic deformation as well as a  $180^\circ$  phase shift when changing the sign of  $E_{DC}$ , which correspond to the induced piezoelectric effect. In this case, we do not observe the electrostrictive displacements (second harmonic) (Fig. 2, B and C) because of a very small amplitude of  $E_{AC}$  (compared with  $E_{AC}$  in Fig. 1A). Once the  $E_{AC}$  is comparable to or higher than  $E_{DC}$ , we observed an asymmetric response comprising both the first and the second harmonics (fig. S6). Measuring the piezoelectric strain of the CGO sample as a function of  $E_{DC}$  (in the range of  $\pm 0.47$  MV/cm) while keeping the same electric field  $E_{AC}$  (15.71 kV/cm) at 10 mHz clearly shows that the applied  $E_{DC}$  tunes the piezoelectric AC

**Fig. 3. Frequency-dependent piezoelectric susceptibility of CGO film.** (A) The first harmonic electromechanical susceptibility  $|d_{33}|$  of the CGO film as a function of  $f$  (10 mHz  $\leq f \leq 1$  kHz), excited by a constant driving AC field ( $E_{AC} = 15.71$  kV/cm) and different static DC fields ( $E_{DC} = +0.47$ ,  $+0.72$ , and  $+1.00$  MV/cm). (B) Linear piezoelectric strain of the CGO film as a function of  $E_{AC}$  with various  $E_{DC}$ , measured at 1 kHz. (C)  $|d_{33}|$  and  $|M_{33}|$  of the film, simultaneously measured by applying a combined electric field,  $E_{AC} = 15.71$  kV/cm and  $E_{DC} = +1.00$  MV/cm, in the frequency range from 10 mHz to 1 kHz. The inset describes the field-enforced defect dynamics, polarization reorientation, and the following permittivity variations in CGO. (D) Ratios of  $|d_{33}|$  to  $|M_{33}|$  as a function of  $f$ , expected to be  $2E_{DC}$  in the relation of  $d_{ind} = 2M_{ind}E_{DC}$ .





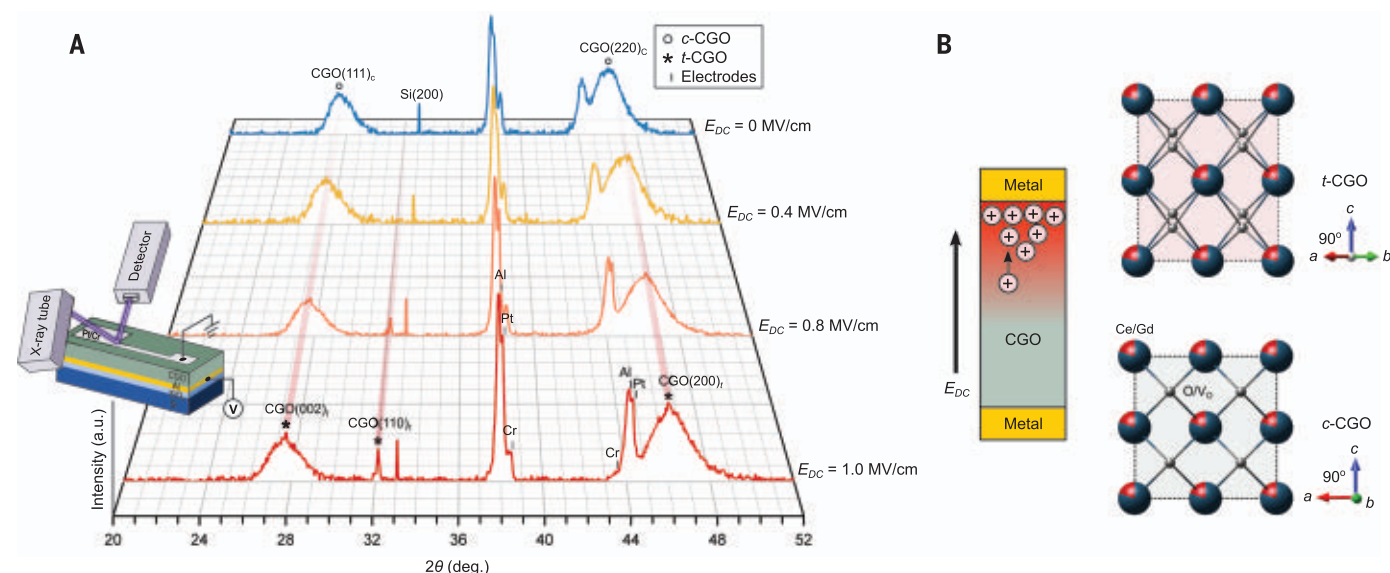


**Fig. 4. Effect of  $V_O$  redistribution in centrosymmetric fluorite CGO film.**

(A) XRD  $2\theta$  patterns of the polycrystalline CGO film under various in situ  $E_{DC}$  applications (0, 0.4, 0.8, and 1.0 MV/cm). Schematic shows the in situ XRD measurement setup using a laboratory-source x-ray ( $\lambda = 1.54056 \text{ \AA}$ ) and top electrode area ( $\sim 10\%$ ) at the surface, which was connected to the applied

electric fields. Under  $E_{DC} \geq 0.8 \text{ MV/cm}$ , diffraction peaks were visible at  $2\theta = 28.3^\circ$ ,  $32.6^\circ$ , and  $46.9^\circ$ , which are assigned to (002), (110), and (200) reflections of a tetragonal phase of CGO, respectively. (B) Schematics for the phase transition of CGO from cubic to tetragonal phase through the field-induced redistribution of mobile positively charged  $V_O$  (+).

strain, reaching values of up to 2.15% ( $d_{ind} \sim 13,700 \text{ pm/V}$ ) (Fig. 2D). The nonlinear dependence of the AC strain on  $E_{DC}$  (Fig. 2D) reflects the fundamental nature of the electrostriction coupling to polarization and not directly to the field. Furthermore, the on-off control of piezoelectricity and electrostriction and the tuning of the electromechanical response can be sustained for at least several hours without any sign of degradation (figs. S7 and S8).

We show the piezoelectric coefficients of the CGO sample, determined as a function of frequency (from 10 mHz to 1 kHz), for different fields  $E_{DC}$ —e.g., 0.47, 0.72, and 1.00 MV/cm (Fig. 3A). The results are notable when compared with the frequency-independent response in conventional piezoelectric materials (e.g., PZT) and a bismuth titanate-based ceramic (fig. S9). First, the piezoelectric coefficient reaches giant values at low frequencies, approaching  $\sim 200,000 \text{ pm/V}$  with increasing  $E_{DC}$ . For comparison, the piezoelectric coefficient in the best commercial single crystals of  $\text{Pb}(\text{Mg}_{1/3}\text{Nb}_{2/3})\text{O}_3\text{-PbTiO}_3$  (PMN-PT) is  $\sim 2000 \text{ pm/V}$  and is  $\sim 200$  to  $500 \text{ pm/V}$  in PZT ceramics (3). Notably, the values around  $100 \text{ pm/V}$ , measured at 1 kHz in our films, are comparable to those of PZT thin films (15). This is the frequency range of interest for many actuator applications. We observed clear high- $f$  (1 kHz) piezoelectric responses for the CGO film with a linear relation following  $x = d_{ind}E_{AC}$ , whereas the  $d_{ind}$  varies with applied  $E_{DC}$ , as expected (Fig. 3B).

Further insight into the electric field-induced piezoelectric response of the CGO can be ob-

tained from the piezoelectric term of Eq. 2, from which one can derive

$$d_{ind} = 2ME_{DC} = 2\epsilon QP_{ind} \quad (3)$$

where  $\epsilon$  is the dielectric permittivity;  $Q$  is the polarization-related electrostrictive constant,  $x = QP_{ind}^2$  (17);  $P_{ind} = \epsilon E_{DC}$  is the induced polarization; and  $M = \epsilon^2 Q$ . Equation 3 generally holds very well for centrosymmetric materials—for example, for perovskite relaxors (7) and Schottky barrier-induced piezoelectric effect (9). We show the simultaneously measured piezoelectric and electrostrictive coefficients over a wide frequency range (Fig. 3C). The ratio of  $|d|/|M|$  is expected from Eq. 3 to be equal to  $2E_{DC}$ . We see a good agreement ( $|d|/|M| \approx 2E_{DC}$ ) for  $f \geq 10 \text{ Hz}$  (Fig. 3D), whereas the ratio is lower at low frequencies ( $f \leq 1 \text{ Hz}$ ). Consequently, these data indicate the presence of a rate-dependent mechanism that is triggered by the application of  $E_{DC}$  and that is assisted by the application of quasi-static  $E_{AC}$  at low frequencies. The relationship  $d_{ind} = 2\epsilon QP_{ind}$  is considered fundamental and always holds (1, 17) where the polarization response is controlled by small oscillations of ions and electrons near their equilibrium lattice sites. Our results show that good agreement between the calculated and the measured  $M$  and  $d$  values holds over the frequency range where apparent polarization and permittivity ( $\epsilon_{ij} = \frac{\partial P_i}{\partial E_j}$ ) are dominated by the rate-dependent migration of  $V_O^{\bullet}$  (supplementary text, section 3, and figs. S10

and S11) (16). The introduction of aliovalent dopants, e.g.,  $\text{Gd}^{3+}$  in  $\text{CeO}_2$ , produces negative charges and requires 1/2 oxygen vacancy for maintaining charge neutrality; in Kröger-Vink notation (18), this can be written as  $\text{Ce}_{0.8-2y}^{\times}\text{Ce}_{2y}^{\bullet}(\text{Gd}_{\text{Ce}}^{\times})_{0.2}\text{O}_{1.9-y}(\text{V}_O^{\bullet})_{0.1+y}$ , where  $(\text{Gd}_{\text{Ce}}^{\times}) = 2(\text{V}_O^{\bullet})$ . The additional oxygen vacancies ( $y$ ) produced during preparation and charge compensated by  $\text{Ce}^{+3}$  are arguably more mobile than those associated with Gd (14, 19), at least at weaker fields. Notably, both the motion of  $V_O^{\bullet}$  and polarons hopping from  $\text{Ce}^{+3}$  to  $\text{Ce}^{+4}$  have a substantial effect on local lattice strain through chemical expansion as well as on polarization (20). From symmetry arguments, only those defects that are simultaneously electric and elastic dipoles can contribute to the piezoelectric effect (21). We observed evidence for charge transport in the electrical conductivity of the CGO films typical for hopping-like ion conduction below 1 kHz. The ionic conductivity greatly increases by applying higher fields (both  $E_{AC}$  and  $E_{DC}$ ) (fig. S4C and fig. S12). The conductivity seems to contribute to the giant apparent dielectric permittivity ( $|\epsilon_r| \sim 10^9$ ) of the system when  $f \rightarrow 0$ . Therefore, the defect migration is enhanced by the static  $E_{DC}$  field and the quasi-static  $E_{AC}$  and contributes substantially to the large permittivity, leading to exceptionally large  $M$  and  $d$  at low frequencies. Notably, the approach for CGO with an electric field is generally also valid for other systems with centrosymmetric fluorite structures in films and bulk. We also show that piezoelectric response can be induced in a YSZ film, YSZ

and CGO ceramics, as well as CGO films prepared by a different deposition technique (figs. S13 to S15). The obtained piezoelectric coefficients of 10 to 100 pm/V in the frequency range of  $f = 1$  Hz to 1 kHz are comparable to those presently used in microelectromechanical systems (MEMS) device applications with materials based on (Al,Sc)N and PZT (15), which indicates the strength of the proposed methodology.

To understand the relationship between the rearrangement of oxygen defects and the associated large low-frequency strain in the CGO films, we conducted in situ x-ray diffraction (XRD) measurements under the application of different  $E_{DC}$  electric fields. In these experiments, we directly observed partial transformation of initial highly strained cubic-like CGO [ $a_{(C)} = b_{(C)} = c_{(C)} = 5.61$  Å,  $\alpha = \beta = \gamma = 90^\circ$  for  $Z = 4$ , where  $Z$  is the number of formula units in the unit cell] into a tetragonal phase [ $a_{(T)} = b_{(T)} = 3.94$  Å,  $c_{(T)} = 6.42$  Å,  $\alpha = \beta = \gamma = 90^\circ$  for  $Z = 2$ ]. For example, there was a gradual appearance of the peak at  $2\theta \sim 32^\circ$  when the applied electric field (0 to 1 MV/cm) was gradually increased (Fig. 4A; fig. S16; and supplementary text, section 4) (16). During the transformation, the base plane of the CGO unit cell shrinks by  $-0.73\%$ , and the  $c$  axis expands by  $+14.39\%$ , which results in a volume increase of  $+12.73\%$  (supplementary text, section 4). These results explain and support the large positive strain observed along the electric field, applied along the crystallographic [001] direction, as well as the large compressive stress observed in the film plane. A similar electric field-induced phase transition has been reported in Y-doped ZrO<sub>2</sub> (YSZ) at  $550^\circ\text{C}$  (22). However, in our case, the effect was observed at room temperature and the resulting strains are much larger than the one reported in (22). In analogy to YSZ, the phase transition occurs because two oxygen sublattices are rearranged along the  $c$  direction in that two oxygen atoms move up and the others two move down while keeping a rotation symmetry of 2. The vertical spacings between O sites remain at  $c/2$ , resulting in a screw axis  $4_2$  along with  $c$ . This alternating shifting of O columns leads to a large expansion of the  $c$  axis. In YSZ, this mechanism was found to be triggered by a high V<sub>O</sub> concentration (23, 24), whereas in ceria it is believed to also be associated with a high Ce' (Ce<sup>3+</sup>) concentration because in both cases (oxygen vacancy formation and the following change of host cation radii) the Coulombic attraction in the ionic matter is reduced (20).

These experimental results together with our measured dielectric data (fig. S12) indicate that a field-driven defect redistribution in the film is accompanied by a partial phase transition from a cubic to a tetragonal phase accompanied with a large volumetric increase.

These results are supported by the recent work of Zhu *et al.* (25), which showed experimentally and theoretically that oxygen vacancies play an essential role in the stabilization of the tetragonal phase in ceria. This suggests that the same mechanism is likely to occur in Gd-doped CeO<sub>2</sub>, which may be even more susceptible to phase transition owing to a higher level of oxygen vacancies, leading to an electric field-driven tetragonal phase. The field-induced heterogeneity in the material is probably accompanied by Maxwell-Wagner dielectric and electromechanical effects (26), which, together with phase transition and chemical expansion (20), contribute to the field-induced strain and polarization. On the basis of the above results, the emergent piezoelectric behavior in Gd-doped ceria depends directly on the rate-dependent V<sub>O</sub> motion on different scales (fig. S17). The selection of different aliovalent dopants and codoping, which can stabilize and control the presence of oxygen vacancies within an oxide material, could be an important strategy to generate sustainable large piezoelectricity using a similar working mechanism as demonstrated here.

We show the possibility of generating extraordinarily high piezoelectricity in intrinsically centrosymmetric nonstoichiometric oxides (fluorites) by the electric field-induced redistribution of mobile V<sub>O</sub>. Our results show giant low-frequency piezoelectricity (up to  $d_{33} \sim 200,000$  pm/V) in CGO films, induced by the concurrent application of alternating and static electric fields. Furthermore, we show a direct way to achieve selective electromechanical conversion in centrosymmetric materials—i.e., either pure and large electrostriction, pure and giant piezoelectricity, or mixed response under controlled electric fields. Controlling chemical expansion, phase transitions, diffusion, and redistribution of mobile ionic species in centrosymmetric ionic materials by electric field is a phenomenological concept with aims to induce large electromechanical conversion, which can be extended to other material systems. Our findings provide a paradigm shift in piezoelectricity by utilizing centrosymmetric materials with large ionic mobility, which opens up a path for a wide range of potential electromechanical, environmentally friendly, and biocompatible materials for applications in actuators and sensors.

## REFERENCES AND NOTES

1. R. E. Newnham, *Properties of Materials: Anisotropy, Symmetry, Structure* (Oxford Univ. Press, 2005).
2. J. Holterman, P. Groen, *An Introduction to Piezoelectric Materials and Components* (Applied Piezo, 2012).
3. S.-E. Park, T. R. Shrout, *J. Appl. Phys.* **82**, 1804–1811 (1997).
4. F. Li *et al.*, *Science* **364**, 264–268 (2019).
5. H. Liu *et al.*, *Science* **369**, 292–297 (2020).
6. B. Jaffe, W. R. Cook, H. L. Jaffe, *Piezoelectric Ceramics* (Academic Press, 1971).

7. J. Kuwata, K. Uchino, Sh. Nomura, *Jpn. J. Appl. Phys.* **19**, 2099–2103 (1980).
8. B. Khanbabaee *et al.*, *Appl. Phys. Lett.* **109**, 222901 (2016).
9. M.-M. Yang *et al.*, *Nature* **584**, 377–381 (2020).
10. J. G. Swallow *et al.*, *Nat. Mater.* **16**, 749–754 (2017).
11. R. Korobko *et al.*, *Adv. Mater.* **24**, 5857–5861 (2012).
12. A. Kossyov *et al.*, *Phys. Rev. B* **87**, 054101 (2013).
13. R. Schmitt *et al.*, *Chem. Soc. Rev.* **49**, 554–592 (2020).
14. M. Hadad, H. Ashraf, G. Mohanty, C. Sandu, P. Murali, *Acta Mater.* **118**, 1–7 (2016).
15. N. Setter *et al.*, *J. Appl. Phys.* **100**, 051606 (2006).
16. Materials and methods are available as supplementary materials online.
17. R. E. Newnham, V. Sundar, R. Yimnirun, J. Su, Q. M. Zhang, *J. Phys. Chem. B* **101**, 10141–10150 (1997).
18. F. A. Kröger, H. J. Vink, *Solid State Phys.* **3**, 307–435 (1956).
19. J. Faber, C. Geoffroy, A. Roux, A. Sylvestre, P. Abélard, *Appl. Phys. A* **49**, 225–232 (1989).
20. D. Marrocchelli, S. R. Bishop, H. L. Tuller, B. Yildiz, *Adv. Funct. Mater.* **22**, 1958–1965 (2012).
21. A. S. Nowick, W. R. Heller, *Adv. Phys.* **14**, 101–166 (1965).
22. A. Lai, C. A. Schuh, *Phys. Rev. Lett.* **126**, 015701 (2021).
23. B. D. C. Bell, S. T. Murphy, P. A. Burr, R. W. Grimes, M. R. Wenman, *J. Appl. Phys.* **117**, 084901 (2015).
24. H. Ikeno *et al.*, *J. Phys. Condens. Matter* **25**, 165505 (2013).
25. H. Zhu *et al.*, *Nat. Commun.* **9**, 5063 (2018).
26. G. S. Radchenko, A. V. Turik, *Phys. Solid State* **45**, 1759–1762 (2003).

## ACKNOWLEDGMENTS

D.-S.P. and D.D. acknowledge M. Yang and M. Alexe in the Department of Physics, University of Warwick, for their supporting measurements during this work. W. H. Bi in the Department of Physics, EPFL, and C.-J. Choi from Chonbuk National University are thanked for technical support. The authors thank I. Lubomirsky from the Weizmann Institute of Technology for helpful discussions during the project period. **Funding:** D.-S.P., V.E., N.P., P.M., and D.D. acknowledge the European Commission for project Biowings H2020 Fetopen 2018-2022 (grant no. 80127). N.P. acknowledges funding from the Villum Fonden for the NEED project (grant no. 00027993) and the Danish Council for Independent Research Technology and Production Sciences for the DFF-Research Project 3 (grant no. 00069B). S.G. acknowledges funding from the Israel Science Foundation (research grant 1561/18 and equipment grant 2247/18). This project has received funding from the European Union's Horizon 2020 research and innovation program under grant no. 823717 – ESTEEM3. D.C. acknowledges TOP/BOF funding of the University of Antwerp. M.H. and P.M. acknowledge funding from the Swiss National Science Foundation (grant nos. 200020-162664/1 and 200021-143424/1). **Author contributions:** D.-S.P., P.M., and D.D. conceived the idea and designed this work. D.-S.P. and M.H. deposited films and prepared samples. D.-S.P. and D.D. performed electromechanical measurements and analyzed results. D.-S.P. and P.M. modeled and calculated electric field-induced V<sub>O</sub> migration in CGO. L.M.R. contributed technical support for measurements. R.I., V.T., N.G., D.C., D.J., and J.V. performed transmission electron microscopy measurements. V.E. and N.P. supplied ceramic samples. D.-S.P., D.S., and S.G. performed XRD measurements and analyzed the data. All authors discussed results. The manuscript was written by D.-S.P. and D.D. with contributions from N.P. and P.M. **Competing interests:** The authors declare no competing interests. **Data and materials availability:** All data are available in the main text or the supplementary materials.

## SUPPLEMENTARY MATERIALS

science.org/doi/10.1126/science.abm7497  
Materials and Methods  
Supplementary Text  
Figs. S1 to S17  
References (27–40)

11 October 2021; accepted 20 December 2021  
10.1126/science.abm7497

## ORGANIC CHEMISTRY

Remote steric control for undirected *meta*-selective C–H activation of arenesBoobalan Ramadoss<sup>†</sup>, Yushu Jin<sup>†</sup>, Sobi Asako<sup>\*</sup>, Laurean Ilies<sup>\*</sup>

Regioselective functionalization of arenes remains a challenging problem in organic synthesis. Steric interactions are often used to block sites adjacent to a given substituent, but they do not distinguish the remaining remote sites. We report a strategy based on remote steric control, whereby a roof-like ligand protects the distant *para* site in addition to the *ortho* sites, and thereby enables selective activation of *meta* carbon-hydrogen (C–H) bonds in the absence of *ortho* or *para* substituents. We demonstrate this concept for iridium-catalyzed *meta*-selective borylation of various monosubstituted arenes, including complex drug molecules. This strategy has the potential to expand the toolbox of C–H bond functionalization to previously nondifferentiable reaction sites.

Direct functionalization of arenes is integral to the synthesis of pharmaceuticals, agrochemicals, and a wide variety of fine chemicals and polymers (1–4). However, controlling regioselectivity in this process remains challenging, particularly in the case of functionalizing electron-rich monosubstituted arenes at the *meta* position (5, 6). Transition metal-catalyzed C–H activation methods have the potential to provide a general solution to this problem (7–9), and to date, regiocontrol has typically been achieved by taking advantage of directing groups (10) or by electronically or sterically biasing the substrate. The steric control strategy is successful in blocking proximal sites (Fig. 1A, a) (11, 12), but differentiation of remote positions such as *meta* and *para* is difficult. A very bulky catalyst can block both the *ortho* and *meta* C–H sites and enable *para* functionalization (Fig. 1A, b) (13, 14), but *meta*-selective activation of a simple monosubstituted arene in the presence of reactive *para* C–H bonds (Fig. 1A, c) has been elusive. Bifunctional ligands that bind a donor or acceptor group on the substrate through attractive interactions such as hydrogen bonding, Lewis acid-base interactions, or ion pairing have been used for *meta* functionalization (15–17), but this strategy requires specialized groups attached to the substrate. Other strategies (18–26) that have been used for remote functionalization also require specialized directing groups installed on the substrate. We present here a strategy based on remote steric control, whereby a roof-like ligand blocks a *para* site (Fig. 1B) to achieve *meta*-selective C–H activation in the presence of *ortho* and *para* C–H bonds. Thus, a spirobipyridine ligand (**L12**) in combination with an iridium catalyst can borylate mono-

substituted arenes selectively at the otherwise featureless *meta* C–H sites, with regioselectivity as high as >20:1 (Fig. 1C). Moreover, whereas sterically demanding ligands typically lower the activity of the catalyst, the roof design induces remote steric bias without affecting the coordination sphere of the metal catalyst; as shown for the reaction of a protected phenol (**10**), the spirobipyridine ligand is more active (84% yield) than the typically used bipyridine ligand, dtbpy (4,4'-di-*tert*-butyl-2,2'-bipyridine, 24% yield). Under these reaction conditions, compounds such as alkylbenzenes, anilines, protected phenol, aryl ethers, and arylsilanes were selectively *meta*-borylated.

Bipyridine derivatives are privileged ligands in transition-metal catalysis (27); for example, they are the ligand of choice in iridium-catalyzed C–H borylation (28). Commonly used bipyridine compounds such as dtbpy enable high reactivity (29), but control of regioselectivity is poor. There have been efforts to attach substrate recognition units to the bipyridine core to achieve regioselectivity, but donor or acceptor groups on the substrate, such as carbonyl, pyridine, or ammonium, are required (15–17). The iridium catalyst is typically sensitive to steric bias, and the steric control strategies **a** and **b** depicted in Fig. 1A have been previously applied (11, 13, 14). To achieve the remote steric control strategy **c**, we envisioned the exploitation of the unexplored space perpendicular to the coordination plane of the bipyridine ligand, and we designed a spirobipyridine compound that possesses a bridging C(sp<sup>3</sup>) carbon, which allows construction of a “steric roof” that is expected to block the *para* site and achieve *meta* selectivity.

The key features of the ligand design are described in Fig. 2 for the iridium-catalyzed borylation of *tert*-butylbenzene (**1a**). We chose this substrate because the *tert*-butyl group is a standard steric marker in organic synthesis, and it lacks functionality that may electronically interact with the catalyst. The Ir catalyst coordinated by the standard dtbpy ligand was

highly reactive, and as expected, we obtained a mixture of *meta* (**2a**, 40%), *para* (**4a**, 20%), and diborylated (**3a**, 41%) products. The *meta* selectivity (4.0:1) was enhanced by diborylation because, for steric reasons, only the *meta* product **2a** can further react to give **3a**. Rigidifying the plane of bipyridine (**L1**) did not affect the selectivity (3.1:1), whereas an unsubstituted spirobipyridine compound (**L2**) gave a larger amount of diborylated **3a**, resulting in a slightly higher selectivity (6.8:1). The selectivity was largely unaffected when a phenyl substituent (**L3**) was introduced into the fluorene ring. A pyridyl group (**L4**) greatly decreased the reactivity, possibly because of competitive coordination or ligand borylation (30). An improvement in selectivity was observed when we increased the size of the substituents on the fluorene ring, as predicted by our “steric roof” model. Thus, groups such as 3,5-dimethylphenyl (**L5**), 3,5-di-*tert*-butylphenyl (**L6**), 2,6-dimethylphenyl (**L7**), 2,4,6-trimethylphenyl (**L8**), and 9-anthracenyl (**L9**) gave 7.7:1 to 9.1:1 *meta* selectivity; notably, for **L7**, **L8**, and **L9**, diborylation was greatly retarded (2%, 7%, and 3%, respectively), which proves that the *meta* selectivity is genuine and not artificially enhanced by diborylation. A spirobipyridine ligand bearing a substituted *N*-carbazolyl group (**L10**) was less selective. The problem of conformational flexibility for these groups was solved by using a more rigid Bpin group (**L12**), where the boronic ester group aligns in a planar fashion with the fluorene group (see fig. S3 for the x-ray structure of the ligand). By using **L12**, we achieved high *meta* selectivity (12:1) while keeping diborylation low (7%). Changing the borylating reagent to pinacolborane (HBpin) (see table S2 for details on the optimization of the reaction conditions), the reaction using ligand **L12** gave the borylated product with high yield (84%) and high *meta* selectivity (23:1) while diborylation was kept low (9%). Recovery of the starting material accounted for the remaining mass balance. Modification of the boronic ester group (**L13**) gave a similar result. The use of a bulky triphenylsilyl group (**L11**) gave moderate selectivity, probably because of its rotational flexibility.

Using ligand **L12**, we next explored the iridium-catalyzed borylation of a variety of monosubstituted arenes such as alkylbenzenes, substituted anilines, protected phenol, and ethers to achieve high to moderate *meta* selectivity, according to the size of the substituent on the arene (Fig. 3). These electron-rich arene substrates typically give *ortho/para* selectivity under electrophilic aromatic substitution conditions (31) and *meta/para* selectivity under catalytic C–H bond activation conditions (7–9, 28). Therefore, *meta*-selective functionalization is of great synthetic interest, especially because the boronic ester group can be readily converted to various functionalities

RIKEN Center for Sustainable Resource Science, 2-1 Hirosawa, Wako, Saitama 351-0198, Japan.

<sup>\*</sup>Corresponding author. Email: sobi.asako@riken.jp (S.A.); laurean.ilies@riken.jp (L.I.)

<sup>†</sup>These authors contributed equally to this work.



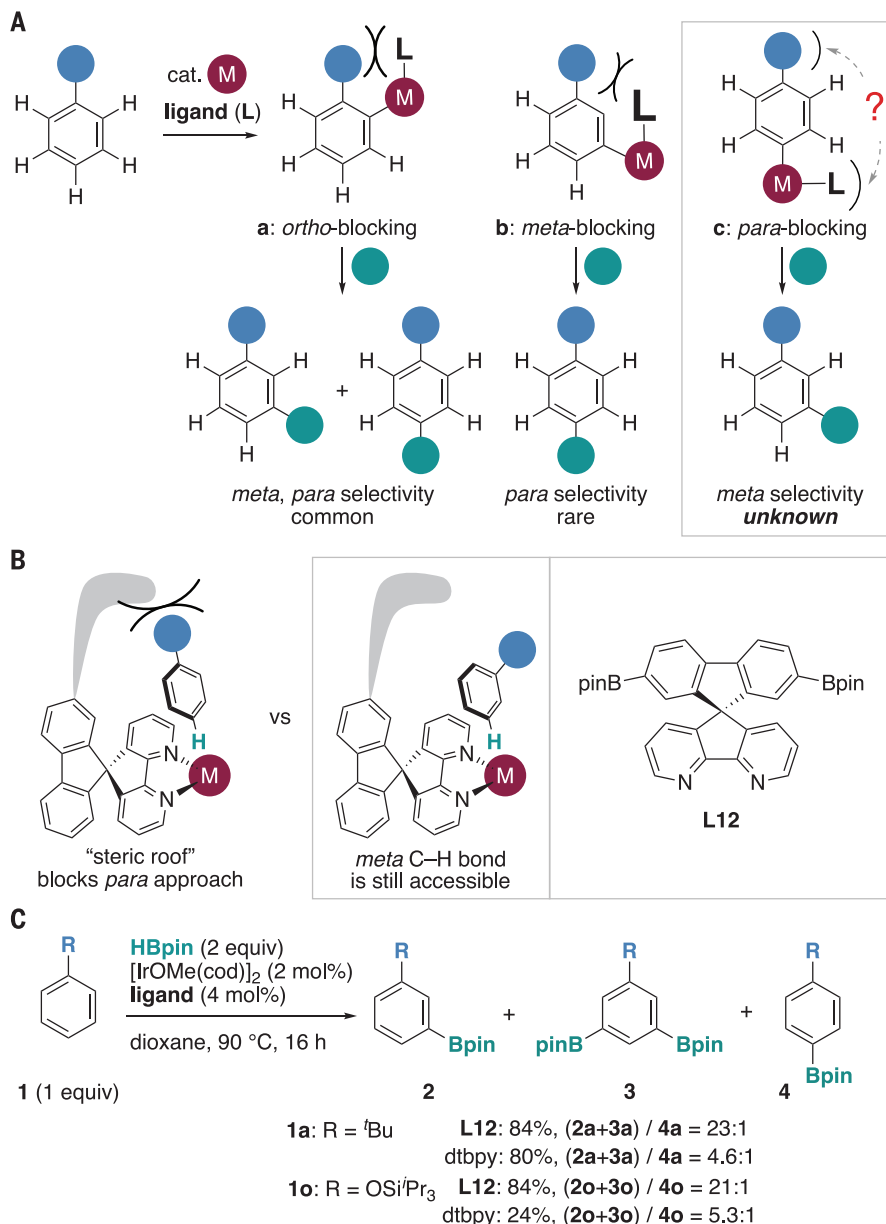


**Fig. 1. Steric control for undirected regioselective C–H activation.** (A) Strategies for sterically induced regiocontrol. M, transition metal; L, ligand. (B) The design of a “steric roof” ligand for remote regiocontrol. pin, pinacolate. (C) *Meta*-selective borylation of *tert*-butylbenzene and triisopropyl(phenoxysilane). R, organic group; cod, 1,5-cyclooctadiene; dtbpy, 4,4′-di-*tert*-butyl-2,2′-bipyridine; Me, methyl; *t*Bu, *tert*-butyl; *i*Pr, isopropyl.

(fig. S2). Alkylarenes bearing a bulky substituent such as *tert*-butyl (**1a**) or adamantyl (**1b**) reacted with high *meta* selectivity (23:1 and 29:1, respectively). A smaller secondary alkyl group such as isopropyl (**1c**) or cyclohexyl (**1d**) also gave high selectivity (15:1 and 14:1, respectively), whereas substrates bearing small groups such as ethyl (**1e**) and methyl (**1f**) reacted with moderate *meta* selectivity (7.3:1 and 5.0:1, respectively). For these substrates, steric control is strongly indicated because of (i) the lack of functionality that might electronically interact with the catalyst and (ii) the direct correlation between the substrate size and selectivity (see also the mechanistic discussion, Fig. 4). The merits of remote regiocontrol, which does not lower the activity of the catalyst, are illustrated by the reaction of sterically demanding 1,3-di-

*tert*-butylbenzene (**1g**), which was unreactive under steric control using bulky ligands (**13**) but could be borylated in moderate yield using our catalyst.

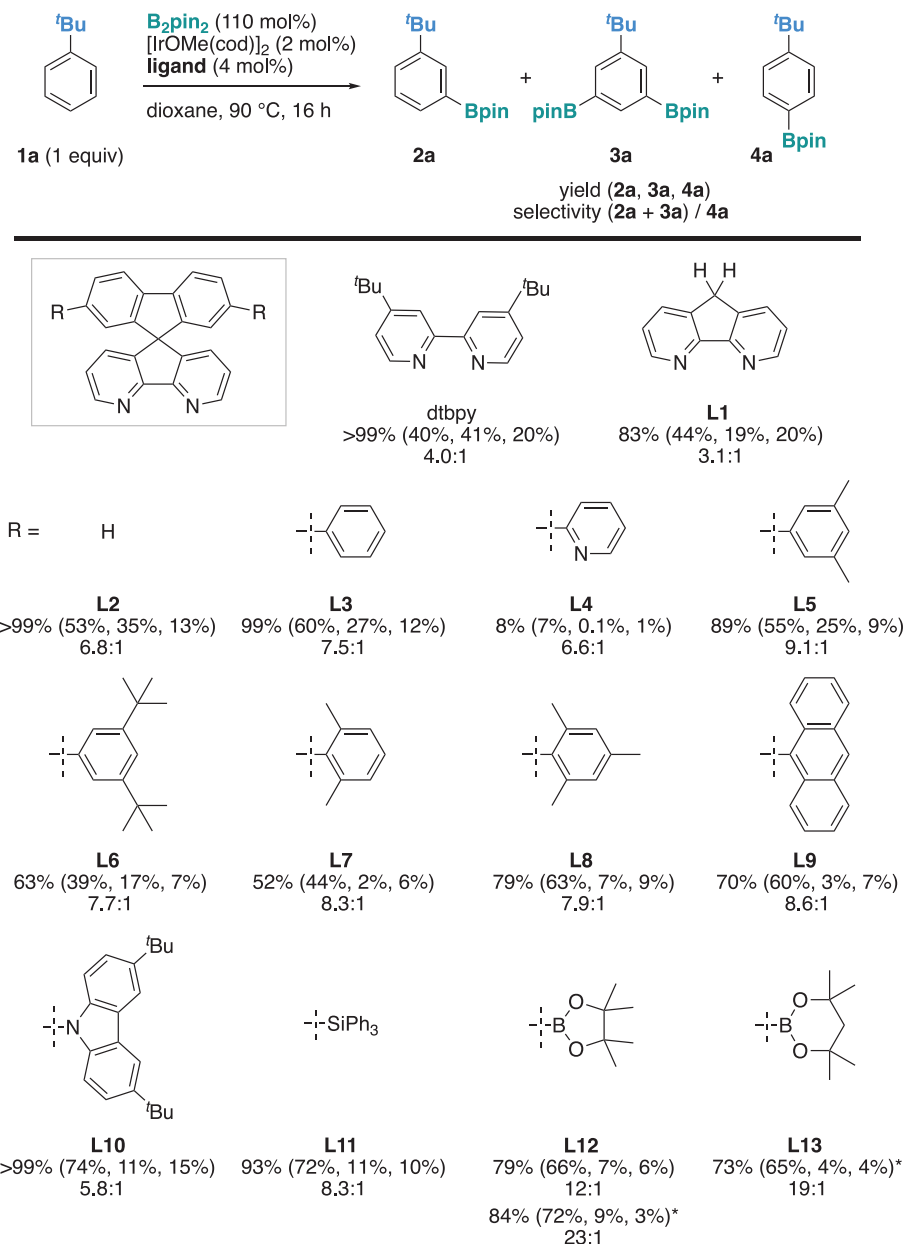
Anilines, compounds of paramount importance for the chemical industry, can also be borylated with high *meta* selectivity, and the selectivity was correlated with the size of the *N*-substituents. Thus, *N,N*-disubstituted anilines bearing bulky groups such as isopropyl (**1h**), cyclohexyl (**1i**), or isobutyl (**1j**) gave the *meta*-borylated products with selectivity higher than 20:1, reaching as high as 45:1 for **1j**. *N,N*-Dibutylaniline (**1k**) also reacted with high selectivity (18:1). The reaction of less sterically congested anilines such as *N*-phenylpyrrolidine (**1l**) and *N,N*-dimethylaniline (**1m**) proceeded with moderate selectivity (13:1 and 11:1, respec-

tively). A diarylamine protected with a silyl group (**1n**) reacted with high yield and high *meta* selectivity (36:1), and selectively at the less hindered phenyl ring. Electron-rich arenes such as anilines are typically less reactive under iridium-catalyzed borylation conditions (28), but our roof ligand enabled the reaction of a stoichiometric amount of these substrates in good yields. For comparison, using dtbpy as the ligand under otherwise identical conditions, **1k** reacted in 5% yield.

Other monosubstituted arenes also reacted with *meta* selectivity. A phenol protected with an easily removable triisopropylsilyl group (**1o**) reacted with high yield and selectivity (21:1), enabling straightforward access to synthetically challenging *meta*-substituted phenols (32) (see also fig. S2). Isopropyl phenyl ether (**1p**) reacted

**Fig. 2. Key structural features of the ligand.**

Reactions were conducted with *tert*-butylbenzene (**1a**, 0.20 mmol), B<sub>2</sub>pin<sub>2</sub> (0.22 mmol), [IrOMe(cod)]<sub>2</sub> (2 mol%), and ligand (4 mol%) in dioxane (1.5 ml) at 90°C for 16 hours. The yield and selectivity were determined using gas chromatography in the presence of hexadecane as an internal standard, after calibration (see supplementary materials). Ph, phenyl. \*HBpin (0.40 mmol) and dioxane (2.0 ml) were used.



with a good yield but moderate selectivity (8.1:1). Phenylsilane (**1q**) reacted with high yield and high *meta* selectivity (18:1). A mesitylene substituent (**1r**) decreased both yield and selectivity, possibly because of unproductive interaction with the roof substituents on the ligand. Electron-deficient monosubstituted arenes such as pivalophenone (**1s**) and diethyl phenylphosphonate (**1t**) reacted with moderate *meta* selectivity. The electron-withdrawing group in these substrates accelerates the oxidative addition of the *para* C–H bond, but the roof ligand overrides the electronic effect and enhances *meta* selectivity. An unsymmetrically *ortho*-disubstituted arene (**1u**) reacted with moderate selectivity at the C–H bond *meta* to the bulkier group, which shows that the ligand can differentiate between the size of the two

groups. Several less successful substrates are shown in fig. S1.

Late-stage functionalization of complex molecules is important for medicinal chemistry because it enables the streamlined creation of new chemical space for the development of new drugs. We tested our reaction for several commercially available drug molecules containing various functionalities. Caramiphen (**1v**), an anticholinergic drug used for the treatment of Parkinson's disease, was *meta*-borylated with high yield and selectivity (20:1). Borylation of this compound at the *para* position (*para/meta* = 5.7:1) was previously reported (13). Pirfenidone (**1w**), an *N*-phenylpyridinone derivative used for the treatment of idiopathic pulmonary fibrosis, was borylated in low yield but with high *meta* selectivity. Although there

is interest in the development of pirfenidone derivatives to increase potency and reduce side effects, the only report (33) on derivatives functionalized at the phenyl group required multiple steps, using the Ullmann coupling of the NH precursor with *para*-substituted aryl bromides. Methylphenidate is a stimulant drug used mostly for the treatment of attention deficit-hyperactivity disorder. After protection of the piperidine's nitrogen, **1x** was borylated with high yield and *meta* selectivity [**2x**, 74%; **3x**, 18%; **4x**, 8% as determined using <sup>1</sup>H nuclear magnetic resonance (NMR) spectroscopy, **2x** isolated in 50% yield]. The structure of product **2x** was confirmed by x-ray crystallography (fig. S4). Medicinally relevant compounds **2v** to **2x** could be isolated as the analytically pure *meta* isomer by gel permeation chromatography.

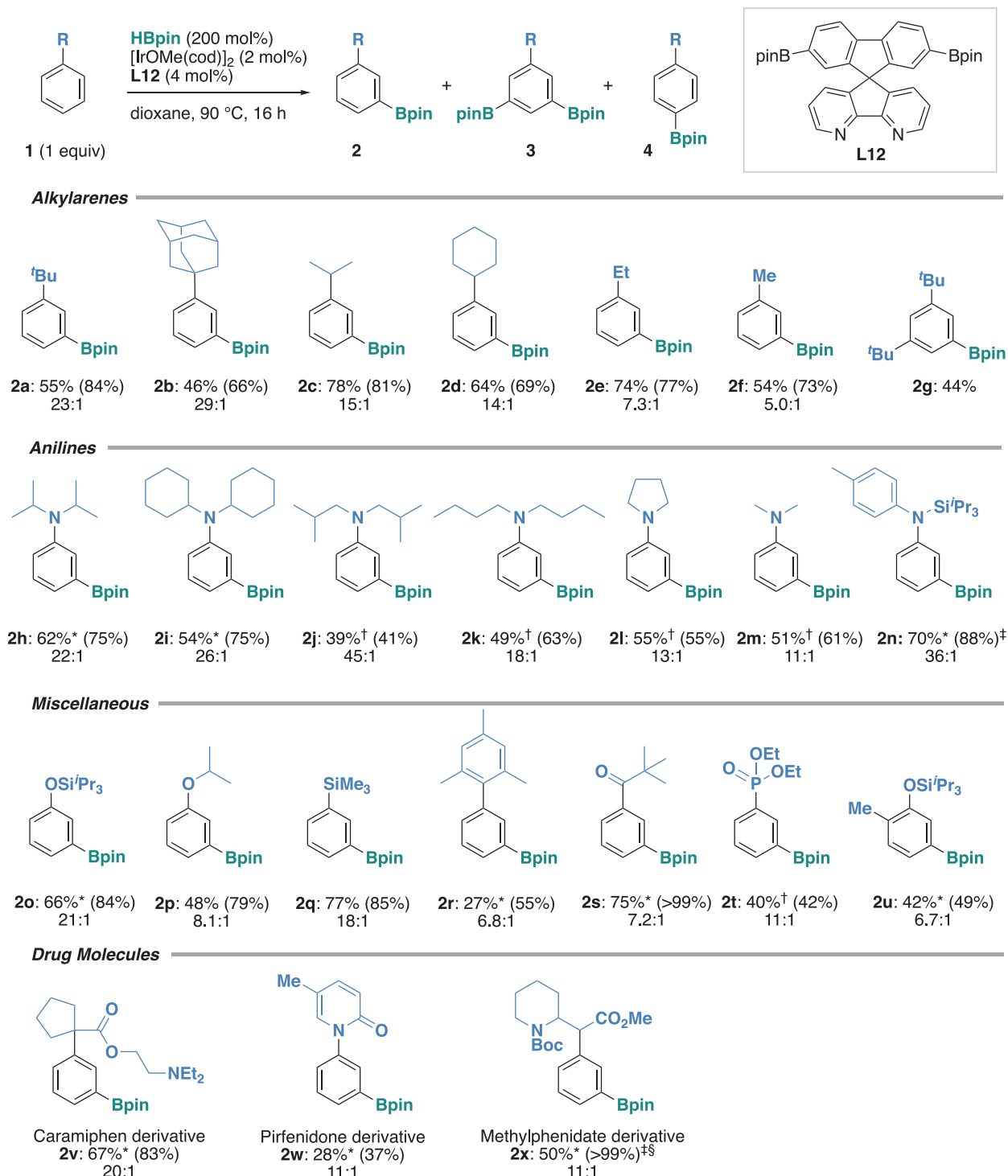


**Fig. 3. Reaction scope.** Reactions were conducted with substrate **1** (0.20 mmol), HBpin (0.40 mmol), [IrOMe(cod)]<sub>2</sub> (2 mol%), and L12 (4 mol%) in dioxane at 90 °C for 16 hours. The yield was determined by isolation (see supplementary materials); the total reaction yield, estimated using gas chromatography or <sup>1</sup>H NMR spectroscopy in the presence of an internal

standard, is shown in parentheses. The selectivity, expressed as (2 + 3)/4, was determined using gas chromatography or <sup>1</sup>H NMR. \*Isolated as single *meta* isomer **2** by gel permeation chromatography. †Isolated as a mixture of **2** and **4**. ‡The reaction was conducted on a 0.1-mmol scale. §B<sub>2</sub>pin<sub>2</sub> (110 mol%) was used instead of HBpin. Et, ethyl; Boc, *tert*-butoxycarbonyl.

An important feature of our reaction is the versatility of the introduced boronic ester group, which can be readily functionalized. For a demonstration, we chose protected phenol **2o** because of the importance of phenol deri-

vatives in organic chemistry (32) and the difficulty in direct *meta* functionalization of phenol. Compound **2o**, which was readily synthesized in high yield and with high *meta* selectivity by borylation of protected phenol **1o** under our

conditions (Fig. 3), could be transformed to a variety of *meta*-substituted phenols such as resorcinol (**5**), *meta*-iodophenol (**6**), *meta*-(1-piperidinyl)phenol (**7**, as the silyl ether), 3-deuteriophenol (**8**, as the silyl ether), and



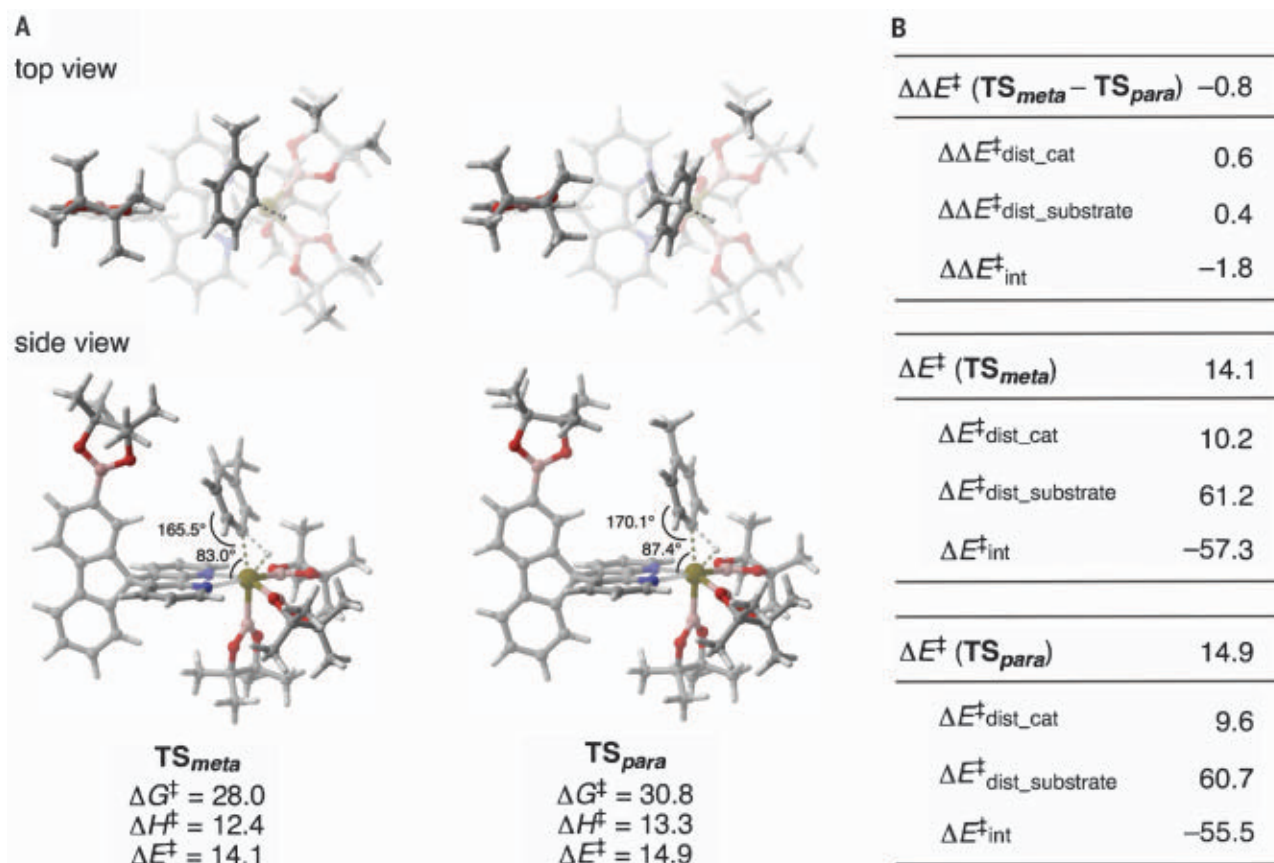


**Fig. 4. Computational study.** (A) Relative Gibbs energies ( $\Delta G^\ddagger$ ), enthalpies ( $\Delta H^\ddagger$ ), and electronic energies ( $\Delta E^\ddagger$ ) calculated at the M06/SDD:6-311+G(d,p)/B3LYP-D3/SDD:6-31+G(d,p)<sub>1,4</sub>-dioxane(SMD) level of theory are given (in kcal/mol) for the reaction of toluene with a simplified ligand model. (B) Distortion/interaction analysis at the B3LYP-D3/SDD:6-31+G(d,p)<sub>1,4</sub>-dioxane(SMD) level of theory.

meta-arylated phenols (**9** and **10**) (fig. S2). Synthesis of *meta*-substituted phenols is not trivial, and there are no efficient direct methods to selectively *meta*-functionalize phenols, a typical trap question for undergraduate organic chemistry students. To date, the most used gateway to these products has been a *meta*-halogenated phenol such as **6**, which in turn cannot be directly synthesized from phenol and requires indirect, often tedious, synthetic routes.

Density functional theory calculations using toluene as the substrate and a simplified ligand model bearing one Bpin substituent revealed that this ligand indeed favors the *meta* transition state [ $\Delta G^\ddagger$ (TS<sub>meta</sub>) = 28.0 kcal/mol] over the *para* transition state [ $\Delta G^\ddagger$ (TS<sub>para</sub>) = 30.8 kcal/mol] by 2.8 kcal/mol in Gibbs free energy (Fig. 4). To investigate the reasons for this difference, we performed a distortion/interaction analysis (34, 35) (Fig. 4B) in which the activation energy ( $\Delta E^\ddagger$ ) of the C–H bond cleavage was partitioned into the energy to distort the catalyst and substrate to the transition state geometry ( $\Delta E^\ddagger_{\text{dist}}$ ) and the energy of interaction between the distorted fragments ( $\Delta E^\ddagger_{\text{int}}$ ). The analysis suggests that the observed selectivity can be ascribed to the larger in-

teraction energy in the *meta* transition state [ $\Delta\Delta E^\ddagger_{\text{int}}(\text{meta} - \text{para}) = -1.8$  kcal/mol], which results from the larger steric hindrance between the substrate and the catalyst in the *para* transition state, tilting the arene substrate away from the ligand ( $\angle \text{IrC}^{\text{meta}}_{\text{ortho}} = 165.5^\circ$  versus  $\angle \text{IrC}^{\text{para}}_{\text{ortho}} = 170.1^\circ$ ;  $\angle \text{C}^{\text{bpy}}_{\text{IrC}^{\text{meta}}} = 83.0^\circ$  versus  $\angle \text{C}^{\text{bpy}}_{\text{IrC}^{\text{para}}} = 87.4^\circ$ ).

This remote steric control strategy has the potential to be applied to a variety of transition metal-catalyzed C–H functionalization reactions (36, 37), and the ligand design can be tuned on demand to fit a substrate in different orientations to achieve different selectivities. Considering the prevalence of bipyridine ligands in transition metal catalysis, we expect that the spirobipyridine scaffold will also enable reactivity and selectivity in various other catalytic reactions.

#### REFERENCES AND NOTES

1. J. Wencel-Delord, F. Glorius, *Nat. Chem.* **5**, 369–375 (2013).
2. J. F. Hartwig, *J. Am. Chem. Soc.* **138**, 2–24 (2016).
3. I. A. Stepek, K. Itami, *ACS Mater. Lett.* **2**, 951–974 (2020).
4. D. J. Abrams, P. A. Provencher, E. J. Sorensen, *Chem. Soc. Rev.* **47**, 8925–8967 (2018).
5. J. Hicks, P. Vasko, A. Heilmann, J. M. Goicoechea, S. Aldridge, *Angew. Chem. Int. Ed.* **59**, 20376–20380 (2020).
6. S. Kurumada, K. Sugita, R. Nakano, M. Yamashita, *Angew. Chem. Int. Ed.* **59**, 20381–20384 (2020).

7. G. Dyker, Ed., *Handbook of C–H Transformations* (Wiley-VCH, 2005).
8. P. H. Dixneuf, H. Doucet, Eds., *Topics in Organometallic Chemistry: C–H Bond Activation and Catalytic Functionalization* (Springer, 2016).
9. J.-Q. Yu, Ed., *Science of Synthesis: Catalytic Transformations via C–H Activation*, Vols. 1 and 2 (Thieme, 2016).
10. S. Murai et al., *Nature* **366**, 529–531 (1993).
11. J.-Y. Cho, C. N. Iverson, M. R. Smith III, *J. Am. Chem. Soc.* **122**, 12868–12869 (2000).
12. C. Cheng, J. F. Hartwig, *Science* **343**, 853–857 (2014).
13. Y. Saito, Y. Segawa, K. Itami, *J. Am. Chem. Soc.* **137**, 5193–5198 (2015).
14. B. E. Haines, Y. Saito, Y. Segawa, K. Itami, D. G. Musaev, *ACS Catal.* **6**, 7536–7546 (2016).
15. Y. Kuroda, Y. Nakao, *Chem. Lett.* **48**, 1092–1100 (2019).
16. Y. Kunitobu, T. Torigoe, *Org. Biomol. Chem.* **18**, 4126–4134 (2020).
17. S. K. Sinha et al., *Chem. Rev.* **1c00220** (2021).
18. T. Truong, O. Daugulis, *Angew. Chem. Int. Ed.* **51**, 11677–11679 (2012).
19. M. T. Mihai, G. R. Genov, R. J. Phipps, *Chem. Soc. Rev.* **47**, 149–171 (2018).
20. J. Wang, G. Dong, *Chem. Rev.* **119**, 7478–7528 (2019).
21. G. Meng et al., *J. Am. Chem. Soc.* **142**, 10571–10591 (2020).
22. K. Korvorapun, R. C. Samanta, T. Rogge, L. Ackermann, *Synthesis* **53**, 2911–2934 (2021).
23. U. Dutta, S. Maiti, T. Bhattacharya, D. Maiti, *Science* **372**, eabd5992 (2021).
24. S. Rej, A. Das, N. Chatani, *Coord. Chem. Rev.* **431**, 213683 (2021).
25. R. Ali, R. Siddiqui, *Adv. Synth. Catal.* **363**, 1290–1316 (2021).
26. C. Haldar, M. E. Hoque, J. Chaturvedi, M. M. M. Hassan, B. Chattopadhyay, *Chem. Commun.* **57**, 13059–13074 (2021).

27. C. Kaes, A. Katz, M. W. Hosseini, *Chem. Rev.* **100**, 3553–3590 (2000).
28. I. A. I. Mkhali, J. H. Barnard, T. B. Marder, J. M. Murphy, J. F. Hartwig, *Chem. Rev.* **110**, 890–931 (2010).
29. T. Ishiyama, J. Takagi, J. F. Hartwig, N. Miyaura, *Angew. Chem. Int. Ed.* **41**, 3056–3058 (2002).
30. O. Kuleshova, S. Asako, L. Iles, *ACS Catal.* **11**, 5968–5973 (2021).
31. R. M. Roberts, A. A. Khalaf, *Friedel-Crafts Alkylation Chemistry. A Century of Discovery* (Dekker, 1984).
32. H. Fiege et al., Phenol Derivatives. In *Ullmann's Encyclopedia of Industrial Chemistry* (Wiley, 2000).
33. Z. Ma et al., *Bioorg. Med. Chem. Lett.* **24**, 220–223 (2014).
34. K. Morokuma, K. Kitaura, in *Chemical Applications of Atomic and Molecular Electrostatic Potentials*, P. Politzer, D. G. Truhlar, Eds. (Plenum, 1981), pp. 215–242.
35. F. M. Bickelhaupt, K. N. Houk, *Angew. Chem. Int. Ed.* **56**, 10070–10086 (2017).
36. N. Kuhl, M. N. Hopkinson, J. Wencel-Delord, F. Glorius, *Angew. Chem. Int. Ed.* **51**, 10236–10254 (2012).

37. P. Wedi, M. van Gemmeren, *Angew. Chem. Int. Ed.* **57**, 13016–13027 (2018).

# ACKNOWLEDGMENTS

We thank the Research Center for Computational Science, Okazaki, Japan, and the RIKEN HOKUSAI BigWaterfall for providing computational time; D. Hashizume and K. Adachi (Materials Characterization Support Team, CEMS, RIKEN, Japan) for x-ray crystallography; and Z. Hou and M. Takimoto (CSRS, RIKEN, Japan) for generously allowing us to use the mass spectrometer. **Funding:** Japan Society for the Promotion of Science (JSPS) KAKENHI Grant-in-Aid for Scientific Research on Innovative Areas no. 20H04830 (L.I.) RIKEN Incentive Research Project grant (S.A.). **Author contributions:** S.A. designed the spirobpy ligand; S.A. and L.I. conceived of and designed the experiments, and L.I. directed the research. B.R. and Y.J. performed the experiments. S.A. performed the computational studies. S.A. and L.I. wrote the manuscript. All authors contributed to discussions. **Competing interests:** The authors declare that

they have no competing interests. **Data and materials availability:** Metrical parameters for the structure of **L12** and **2x** are available free of charge from the Cambridge Crystallographic Data Centre ([www.ccdc.cam.ac.uk/](http://www.ccdc.cam.ac.uk/)) under reference numbers CCDC 2112082 and CCDC 2111841. All other data are available in the main text or the supplementary materials.

# SUPPLEMENTARY MATERIALS

[science.org/doi/10.1126/science.abm7599](https://science.org/doi/10.1126/science.abm7599)  
Materials and Methods  
Supplementary Text  
Spectral Data  
Simulation Data  
Figs. S1 to S101  
Tables S1 to S5  
References (38–70)

11 October 2021; accepted 11 January 2022  
10.1126/science.abm7599

## Y CHROMOSOME ORIGINS

# Y recombination arrest and degeneration in the absence of sexual dimorphism

Thomas Lenormand<sup>1\*</sup> and Denis Roze<sup>2,3</sup>

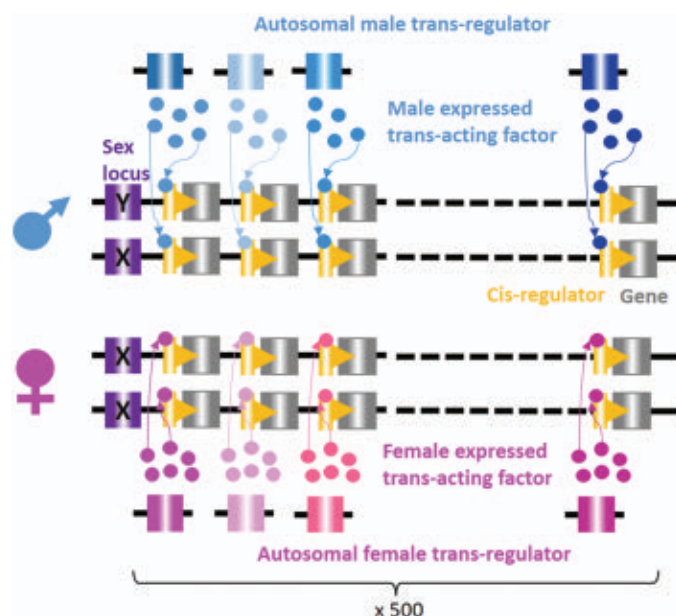
Current theory proposes that degenerated sex chromosomes—such as the mammalian Y—evolve through three steps: (i) recombination arrest, linking male-beneficial alleles to the Y chromosome; (ii) Y degeneration, resulting from the inefficacy of selection in the absence of recombination; and (iii) dosage compensation, correcting the resulting low expression of X-linked genes in males. We investigate a model of sex chromosome evolution that incorporates the coevolution of cis and trans regulators of gene expression. We show that the early emergence of dosage compensation favors the maintenance of Y-linked inversions by creating sex-antagonistic regulatory effects. This is followed by degeneration of these nonrecombining inversions caused by regulatory divergence between the X and Y chromosomes. In contrast to current theory, the whole process occurs without any selective pressure related to sexual dimorphism.

Many species have chromosomal sex-determination systems (1). In XX/XY systems, as in mammals, males are heterogametic (XY). In ZZ/ZW systems, as in birds, females are heterogametic (ZW). We mention only XY systems below, but all arguments are equally applicable to ZW systems. Y chromosomes are often non-recombining and have degenerated through the loss of most of the genes present on ancestral autosomes. In several chiasmate species, such as mammals or birds, suppression of recombination involves successive events, each affecting Y subregions of different sizes, called strata (2). These strata are detected on the basis of different degrees of sequence divergence from the homologous X regions (2).

After the establishment of a sex-determining locus on an autosome, current theory (3–5) proposes that Y chromosomes evolve through three steps: First, sex chromosomes evolve

recombination suppression because selection favors linkage between sex-determining and

**Fig. 1. An overview of the simulated genome evolving sex chromosomes.** A chromosome pair carries the sex locus at one end with two alleles (purple, X; light purple, Y) determining two sexes (XX, female; XY, male). This chromosome carries 500 coding genes, each with a cis-regulatory region. Each cis regulator interacts with a trans acting factor. This trans acting factor is not on the sex chromosomes but is expressed from a pair of autosomal trans regulators, which differ in males and females. See main text for other assumptions of the model.



sexually antagonistic genes (6–9). These sexually antagonistic genes occur when trait optima differ between the sexes, driving the evolution of sexual dimorphism. In the second step, the absence of recombination reduces the efficacy of natural selection by causing “selective interference.” Such interference leads to an accumulation of deleterious mutations on the Y chromosome and genetic degeneration (10). Finally, dosage compensation evolves to restore optimal gene expression in males, whose Y-linked genes have lowered expression due to degeneration, and possibly in females if dosage compensation mechanisms alter expression in that sex (7, 11, 12). The compensation process involves various mechanisms in different species, and compensation is not always complete for all X-linked genes (13–15).

This theory has been explored over the past ~50 years, both empirically and theoretically (3–6, 16). Empirical support for the first step

<sup>1</sup>CEFE, Univ. Montpellier, CNRS, EPHE, IRD, Montpellier, France. <sup>2</sup>CNRS, IRL 3614, Roscoff, France. <sup>3</sup>Sorbonne Université, Station Biologique de Roscoff, Roscoff, France.  
\*Corresponding author. Email: [thomas.lenormand@cefe.cnrs.fr](mailto:thomas.lenormand@cefe.cnrs.fr)

is equivocal—despite decades of investigation, decisive evidence for a causal role of sexually antagonistic loci on recombination arrest is lacking (16–19). The second step is difficult to reconcile with the observation of small degenerated strata (16), within which selective interference should be minimal. Lastly, the causal ordering of events has also been challenged by observations of the early evolution of partial dosage compensation in young sex chromosomes (20–24).

Theoretically, each step suffers from limitations (25). However, an important global limitation is that each step has generally been considered independently from the others, resulting in a piecemeal set of models lacking integration. In particular, changes in gene regulation have not been consistently studied throughout sex chromosome evolution. Yet, such changes can influence the evolution of sex-limited expression, contribute to compensatory adaptive silencing, and are pivotal for the evolution of dosage compensation.

We propose that the joint evolution of regulatory changes and accumulation of deleterious mutations can transform an autosome into a degenerated sex chromosome with dosage compensation. We use individual-based stochastic simulations assuming a population of  $N_{\text{pop}}$  diploid individuals, with XY males and XX females (25) (Fig. 1). We consider the evolution of a pair of autosomes carrying hundreds of genes subject to partially recessive deleterious mutations, with one homolog that has recently acquired a sex-determining locus. Gene expression is controlled by cis-regulatory sequences (affecting expression only on the same chromosome as themselves) interacting with trans regulators that can affect the gene copies on both homologs (26). All of these elements can mutate. To allow for dosage compensation on a gene-by-gene basis while keeping the model symmetric for males and females, we assume that each gene is controlled by one male- and one female-expressed trans regulator (25) (Fig. 1). As in (27), we assume that each gene's overall expression level is under stabilizing selection around an optimal level and that the relative expression of the two copies of each gene determines the dominance level of a deleterious mutation occurring in the coding gene. For instance, a deleterious mutation occurring in a less expressed gene copy is assumed to be less harmful than one in a more highly expressed copy (25).

We then assume that mutations occur that suppress recombination on a segment of the Y. For simplicity, we refer to these mutations as inversions, although they could correspond to other mechanisms causing recombination arrest (25). Inversions of any size can occur; but we follow only those on the Y that include

the sex-determining locus, which will necessarily be confined to males and cause recombination arrest. We assume that inversions can add up, such that new inversions can occur on chromosomes carrying a previous inversion and thus extend the nonrecombining part of the Y. Finally, we assume that reversions restoring recombination can occur, and for simplicity, that such reversions cancel only the most recent inversion (25).

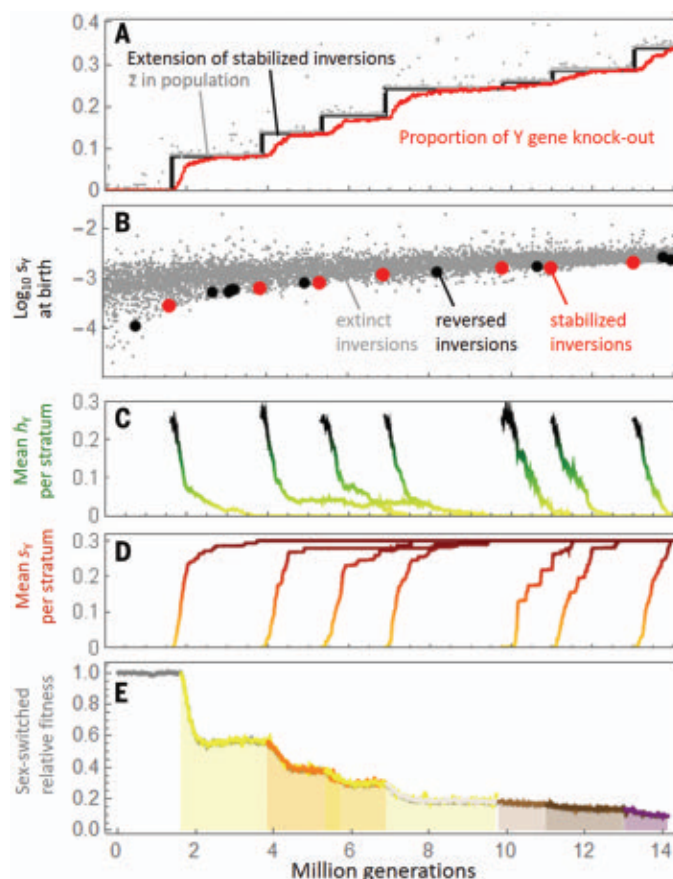
To understand the dynamics of sex chromosome evolution in our model, first consider the case where the cis and trans regulators do not mutate. In this case, all inversions on

the Y are eventually reversed and lost. This occurs in two steps: First, an inversion appears on a given Y and “freezes” a segment of the chromosome. If by chance this Y carries relatively few or milder deleterious mutations, this “lucky” inversion has a selective advantage. Consequently, it tends to fix among Y chromosomes, causing recombination suppression in this portion of the sex chromosomes. Larger inversions are overrepresented among these lucky inversions, as they contain more genes and exhibit a larger fitness variance (25) (fig. S1A). Once fixed, these Y chromosomes start accumulating deleterious

**Fig. 2. Example of a typical Y degeneration process.** The Y progressively degenerates by the accumulation of inversions, which accumulate deleterious mutations, evolve dosage compensation with sex-antagonistic fitness effects, and become immune to reversions.

(A) The black stairplot shows the extension of each successive stratum of the Y (expressed as the fraction of the physical length of the Y), corresponding to stabilized inversions. Gray dots, average fraction of the physical length of the nonrecombining Y in the population. Red, proportion of Y genes that are silenced and knocked out (i.e., they accumulated deleterious mutation effects up to the maximal value  $s_{\text{max}}$ ; here,  $s_{\text{max}} = 0.3$ ). At this time scale, silencing and degeneration appear simultaneous, but silencing is slightly ahead.

(B)  $\text{Log}_{10}$  plot of the average effect of deleterious mutations carried by inversions when they first arise in the population (averaged over the different genes within the inversion). Gray dots, random subsample of inversions that are lost before fixing in the population; black dots, inversions that reach fixation but are lost after the occurrence of a reversion; red dots, inversions that reach fixation and become stabilized strata on the Y. (C) Mean dominance of deleterious mutations on each stabilized inversion (noted  $h_Y$ ). Initial dominance of deleterious mutations is assumed to be 0.25 (25). Fig. S7 shows the detailed dynamics of  $h_Y$  at a smaller time scale. (D) Accumulation of deleterious mutations on each stabilized inversion (the maximum effect  $s_{\text{max}}$  is set to 0.3 for all genes). (E) Fitness that the Y carrying the stabilized inversions would have on average, if expressed in a female (relative to the actual average fitness of males). The different colors highlight the occurrence of the successive strata. The average fitness of males that would carry two X chromosomes at that time is indicated in gray, but yields very similar values and is therefore almost indistinguishable. This simulation considers a population of  $N_{\text{pop}} = 10^4$  individuals, an intensity of stabilizing selection on dosage  $I = 0.1$ , and a mean effect of deleterious mutations  $s_{\text{mean}} = 0.05$ . See (25) for other parameter values.





mutations as a result of selective interference. Fitness declines faster for larger inversions because of stronger selective interference (fig. S1B). When the marginal fitness of the inversion becomes lower than the fitness of the corresponding chromosomal segment on the X, reversions are selectively favored and spread, which restores recombination. Thus, Y-specific inversions are short lived and maintained only transiently in the population in the absence of regulatory mutations (fig. S1C). These periods of recombination suppression do not last long enough to lead to Y chromosome degeneration.

A radically different four-step process emerges when the regulatory sequences can mutate and evolve (Fig. 2). The first step starts, as before, with the fixation of a lucky inversion on the Y. However, once the inversion stops recombination, the X and Y cis regulators start evolving independently; this is step two. This creates a positive feedback loop that causes rapid degeneration of Y-linked alleles (27); by chance, some genes on the Y become slightly less expressed than their X-linked allelic counterparts and accumulate more deleterious mutations (because lower expression makes mutations more recessive), selecting for a further reduction of expression of these Y-linked genes. This process can work on individual genes irrespective of the size of the non-recombining region created by the inversion (27), and the subsequent degeneration does not involve selective interference. However, like in the absence of regulator evolution, recombination arrest also triggers the accumulation of deleterious mutations by selective interference, especially if the inversion includes many genes.

The key step is the third, in which inversions are stabilized in the long term, even when they become entirely degenerated (Fig. 3 and fig. S5). Cis-regulator divergence and degeneration in step 2 cause a departure from optimal expression levels in males. Assuming that gene expression is under stabilizing selection, this causes divergence in sex-specific trans regulators, which evolve to maintain optimal expression in both sexes. For instance, if a Y cis regulator mutates, causing lower expression, this will favor a stronger allele of the male trans regulator, to maintain optimal expression levels. The divergence of X- and Y-linked cis regulators and the divergence of sex-limited trans regulators automatically generate sexually antagonistic fitness effects: X cis-regulators that recombine onto the Y would result in overexpression in males (as a result of mismatches with male trans regulators); similarly, Y cis regulators recombined onto the X would cause underexpression in females. Hence, if a reversion occurs, the reestablished recombination between X and Y would likely reduce offspring fitness by creating a mismatch

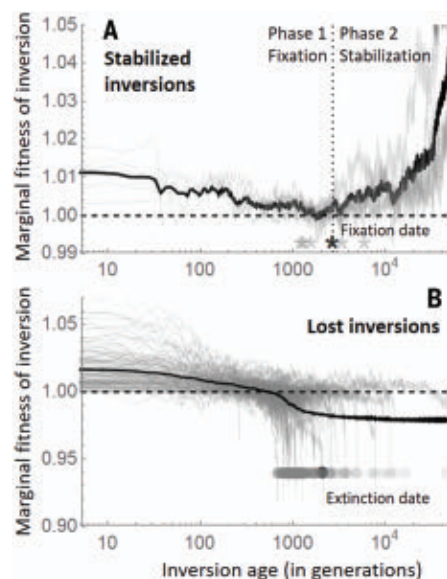


**Fig. 3. Fitness trajectories of stabilized and lost inversions.** The x axis shows inversion age, i.e., the number of generations since the appearance of the inversion (in log scale). The y axis indicates marginal fitness of the inversion relative to the same chromosomal segment on the X if it was in a male, noted  $W_{\text{margX}}$  (25). After fixation, this measures the sexually antagonistic effect of nascent dosage compensation. The marginal fitness of the inversion relative to the same chromosomal segment among Y chromosomes not carrying the inversion, noted  $W_{\text{margY}}$  (25), yields indistinguishable results before the inversion fixes ( $W_{\text{margY}}$  cannot be computed after the inversion fixes, as all Y chromosomes carry the inversion). Gray, individual trajectories; black, average values. (A) Inversions that are stabilized as first Y strata, collected over 10 evolutionary replicates after 1 million generations. Their fixation date is indicated by an asterisk at the bottom. (B) Top 15 longest-lived inversions before stabilization of the first stratum, collected over 10 evolutionary replicates and simulated over 1 million generations. Their extinction date is indicated by a gray disk at the bottom (and the average extinction date by the black disk). The time-averaged fitness at time  $t$  (in black) is computed over all inversions, counting their last achieved fitness if they are extinct at  $t$ . The dashed line indicates value 1.

between cis and trans regulators. This sexually antagonistic effect caused by nascent dosage compensation protects diverging inversions from reversion. This is the ultimate cause of Y recombination suppression in our model (25). However, suppose dosage compensation does not evolve quickly enough. In such a case, recombination can be restored: Af-

ter a reversion, a new recombinant Y can be produced that carries a nondegenerated part of the X without causing strong cis and trans-regulator mismatch in males. This new Y can then replace the previous nonrecombining degenerated Y, which restores recombination on the part of the Y derived from the reversion.

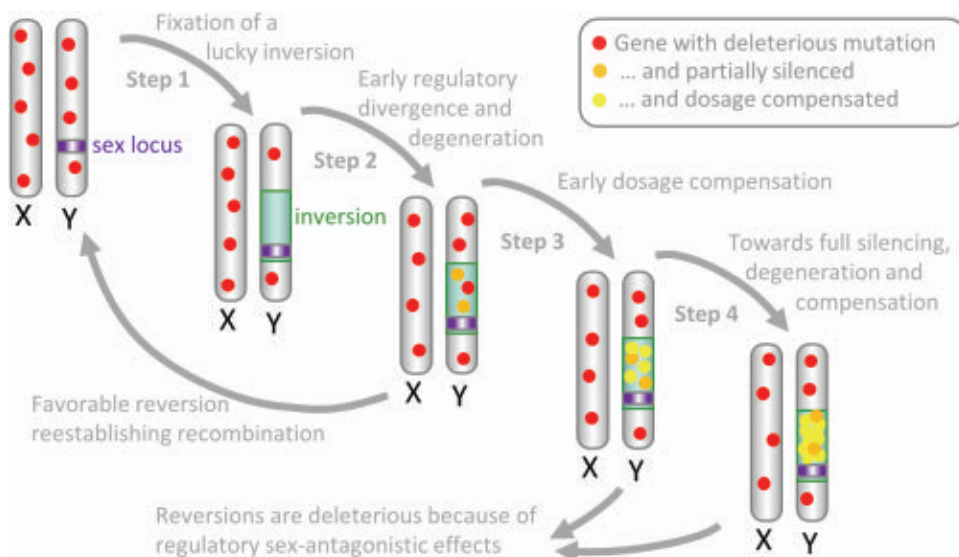
Of course, only a minority of inversions evolve this nascent dosage compensation within a fast enough time frame relative to the speed of degeneration to remain immune to reversion (meaning that they remain, at all times, unlikely to be selectively outcompeted by recombinant chromosomes arising after a reversion). However, a positive-feedback loop is also operating here. Namely, when an inversion starts evolving dosage compensation it becomes relatively immune to reversion and is maintained longer in the population, giving it more time to evolve further dosage compensation. The inversion eventually becomes completely degenerated with complete dosage compensation (for dosage-sensitive genes). This leads to very strong sexually antagonistic regulatory effects, which effectively make the inversion irreversibly immune to reversions.

In our model, recombination suppression evolves along with regulatory evolution, but paradoxically, it is opposed by selective interference. The evolution of nascent dosage compensation involves the fixation of compensatory mutations and is partly adaptive. However, if selective interference is too strong, inversions accumulate deleterious mutations too fast and are quickly replaced by reversions. Accordingly, stabilized inversions tend to be strongly biased toward small sizes, though less so when the population size is larger (fig. S2C). In large populations, recombination suppression and degeneration evolve more quickly, because more inversions occur and selective interference (the effect of which is stronger in smaller populations) is relatively less efficient at removing large inversions (fig. S2). Finally, as expected, this overall process is faster when the intensity of stabilizing selection on gene expression levels is strong. This is because selection on dosage fosters the evolution of dosage compensation and concurrently protects partially degenerated inversions from reversions (fig. S3).

Thus, our model suggests that the Y chromosome is entangled in a regulatory trap leading to recombination arrest and degeneration, even in the absence of selective pressures related to sexual dimorphism. Indeed, unlike previous theories (6–9), our model only includes genes with the same optimal expression level in males and females and deleterious mutations that have the same effect in both sexes. This process is inherently stochastic,

**Fig. 4. Steps involved in the evolution of a Y nonrecombining stratum.**

The process involves four steps, as explained in the text, and is briefly described by captions on the figure. Only the first stratum is illustrated, but steps one to four are repeated for strata extending the nonrecombining portion of the until the whole chromosome is degenerated, silenced, and dosage-compensated.



as it involves the rare stabilization of a handful of inversions and is highly variable (fig. S4). However, it works faster in larger populations, as selective interference opposes recombination arrest and the stabilization of large strata.

Our model also reverses the causality proposed by previous theories by showing that dosage compensation can cause recombination suppression, rather than being a consequence of degeneration after such suppression. Sexually antagonistic effects are involved in the evolution of suppressed recombination. However, they result from the fact that one sex is heterogametic, not from males and females having divergent sex-specific optima for reproductive traits or expression levels. All genes for which dosage affects fitness can contribute to the process, not just a subset of sexually antagonistic loci. The potential sexually antagonistic effect of dosage compensation has long been appreciated (7, 12, 28–30). However, its potential role in recombination arrest has not been previously recognized, as it is usually thought to occur late in the degeneration process. Once recombination has stopped, sexually antagonistic alleles can arise and be maintained (9, 31), but they are not required for recombination arrest, as shown here.

We showed that the emergence of non-recombining and degenerated sex chromosomes in diploid organisms requires very few ingredients: genetic sex determination, deleterious mutations, inversions, sex-specific trans regulators, and stabilizing selection on gene expression levels. This theory includes all steps (Fig. 4 and fig. S8) in a single set of assumptions and is compatible with current data on sex chromosome evolution in chiasmate species (25). It predicts the occurrence of strata,

including small ones (16) and the occurrence of early regulatory changes in young sex chromosomes (20–24). It also accounts for the lack of decisive evidence for a causal role of sexually antagonistic loci on recombination arrest (16–19). Overall, this theory explains the rapid expansion, degeneration, and dosage compensation of the nonrecombining region of sex chromosomes without requiring pre-existing selection pressures favoring sexual dimorphism.

#### REFERENCES AND NOTES

1. D. Bachtrog et al., *PLOS Biol.* **12**, e1001899 (2014).
2. D. Charlesworth, B. Charlesworth, G. Marais, *Heredity* **95**, 118–128 (2005).
3. J. K. Abbott, A. K. Nordén, B. Hansson, *Proc. Biol. Sci.* **284**, 20162806 (2017).
4. L. W. Beukeboom, N. Perrin, *The Evolution of Sex Determination* (Oxford Univ. Press, 2014).
5. D. Bachtrog, *Nat. Rev. Genet.* **14**, 113–124 (2013).
6. J. J. Bull, *Evolution of Sex Determining Mechanisms* (Benjamin Cummings, 1983).
7. B. Charlesworth, *Proc. Natl. Acad. Sci. U.S.A.* **75**, 5618–5622 (1978).
8. D. Charlesworth, B. Charlesworth, *Genet. Res.* **35**, 205–214 (1980).
9. W. R. Rice, *Evolution* **41**, 911–914 (1987).
10. B. Charlesworth, D. Charlesworth, *Philos. Trans. R. Soc. London B Biol. Sci.* **355**, 1563–1572 (2000).
11. J. Engelstädter, *Genetics* **180**, 957–967 (2008).
12. B. Charlesworth, *Curr. Biol.* **6**, 149–162 (1996).
13. L. Gu, J. R. Walters, *Genome Biol. Evol.* **9**, 2461–2476 (2017).
14. A. Muyle, R. Shearn, G. A. Marais, *Genome Biol. Evol.* **9**, 627–645 (2017).
15. J. E. Mank, *Trends Genet.* **29**, 677–683 (2013).
16. D. Charlesworth, *Evolution* **75**, 569–581 (2021).
17. D. Charlesworth, *Philos. Trans. R. Soc. Lond. B Biol. Sci.* **372**, 20160456 (2017).
18. J. E. E. Ironside, *BioEssays* **32**, 718–726 (2010).
19. S. Ponnika, H. Sigeman, J. K. Abbott, B. Hansson, *Trends Genet.* **34**, 492–503 (2018).
20. P. Veltsos et al., *Genetics* **212**, 815–835 (2019).
21. K. H. C. Wei, D. Bachtrog, *PLOS Genet.* **15**, e1008502 (2019).

22. J. Hough, J. D. Hollister, W. Wang, S. C. H. Barrett, S. I. Wright, *Proc. Natl. Acad. Sci. U.S.A.* **111**, 7713–7718 (2014).
23. H. Martin et al., *Genome Biol. Evol.* **11**, 350–361 (2019).
24. A. Muyle et al., *PLOS Biol.* **10**, e1001308 (2012).
25. See supplementary materials.
26. M. S. Hill, P. Vande Zande, P. J. Wittkopp, *Nat. Rev. Genet.* **22**, 203–215 (2021).
27. T. Lenormand, F. Fyon, E. Sun, D. Roze, Sex Chromosome Degeneration by Regulatory Evolution, *Curr. Biol.* **30**, 3001–3006.e5 (2020).
28. S. Ohno, *Sex Chromosomes and Sex-Linked Genes*, vol. 1 of Monographs on Endocrinology (Springer, 1967).
29. C. Mullon, A. E. Wright, M. Reuter, A. Pomiankowski, J. E. Mank, *Nat. Commun.* **6**, 7720 (2015).
30. J. Engelstädter, D. Haig, *Evolution* **62**, 2097–2104 (2008).
31. W. R. Rice, *Evolution* **38**, 735–742 (1984).
32. T. Lenormand, D. Roze, *Zenodo* (2021), doi:10.5281/zenodo.5504423.

#### ACKNOWLEDGMENTS

We thank D. Charlesworth, G. Marais, Y. Michalakakis, and four anonymous reviewers for comments and suggestions and K. McKean for editing. We thank the MBB cluster from Labex CEMEB, and the CNRS ABIMs cluster. **Funding:** This work was supported by grant GenAsex ANR-17-CE02-0016-01. **Author contributions:** Original idea: T.L. and D.R.; Model conception: T.L. and D.R.; Code: D.R. and T.L.; Simulations: T.L.; Data analyses: T.L.; Interpretation: T.L. and D.R.; First draft, editing and revisions: T.L. and D.R.; Project management and funding: T.L. **Competing interests:** The authors declare no conflicts of interest. **Data and materials availability:** Simulation code is available at Zenodo (32).

#### SUPPLEMENTARY MATERIALS

science.org/doi/10.1126/science.abj1813  
Materials and Methods  
Supplementary Text  
Figs. S1 to S8  
References (33–46)  
MDAR Reproducibility Checklist

26 April 2021; accepted 14 December 2021  
10.1126/science.abj1813

## CORONAVIRUS

# COVID mortality in India: National survey data and health facility deaths

Prabhat Jha<sup>1\*</sup>, Yashwant Deshmukh<sup>2</sup>, Chinmay Tumbe<sup>3</sup>, Wilson Suraweera<sup>1</sup>, Aditi Bhowmick<sup>4</sup>, Sankalp Sharma<sup>4</sup>, Paul Novosad<sup>5</sup>, Sze Hang Fu<sup>1</sup>, Leslie Newcombe<sup>1</sup>, Hellen Gelband<sup>1</sup>, Patrick Brown<sup>1</sup>

India's national COVID death totals remain undetermined. Using an independent nationally representative survey of 0.14 million (M) adults, we compared COVID mortality during the 2020 and 2021 viral waves to expected all-cause mortality. COVID constituted 29% (95% confidence interval, 28 to 31%) of deaths from June 2020 to July 2021, corresponding to 3.2 M (3.1 to 3.4) deaths, of which 2.7 M (2.6 to 2.9) occurred in April to July 2021 (when COVID doubled all-cause mortality). A subsurvey of 57,000 adults showed similar temporal increases in mortality, with COVID and non-COVID deaths peaking similarly. Two government data sources found that, when compared to prepandemic periods, all-cause mortality was 27% (23 to 32%) higher in 0.2 M health facilities and 26% (21 to 31%) higher in civil registration deaths in 10 states; both increases occurred mostly in 2021. The analyses find that India's cumulative COVID deaths by September 2021 were six to seven times higher than reported officially.

As of 1 January 2022 and prior to the current surge driven by the Omicron variant, India reported over 35 million cases of severe acute respiratory syndrome coronavirus 2 (SARS-CoV-2), second only to the United States (1). India's official cumulative COVID death count of 0.48 million implies a COVID death rate of ~345 per million population, about one-seventh of the US death rate (2). India's reported COVID death totals are widely believed to be underreports because of incomplete certification of COVID deaths and misattribution to chronic diseases and because most deaths occur in rural areas, often without medical attention (3, 4). Of India's 10 million deaths estimated by the United Nations Population Division (UNPD) in 2020, over 3 million were not registered and over 8 million did not undergo medical certification (fig. S1 and table S1).

Model-based estimates of cumulative COVID deaths through June 2021 in India range from a few hundred thousand to more than 4 million, with most suggesting a substantial official undercount (5–12) (table S2). However, models start with official reports and apply varying assumptions, leading to wide or implausible estimates. In the absence of near universal and timely death registration and the lack of release of data from India's Sample Registration System (SRS), which tracks deaths in a random sample of about 1% of Indian homes (13), alternative approaches are needed to estimate COVID deaths. Recorded increases in all-cause mortality during peak pandemic transmission

are likely nearly all caused by COVID infection (14). The World Health Organization (WHO) has recognized such counts as a crude but useful method to track the pandemic (15). Reports by journalists and nongovernmental organizations using civil registration system (CRS) data have documented a large increase in deaths from all causes compared with previous years (16). Unfortunately, CRS data are reliably available only in states that cover about half of the estimated total deaths in India and may be affected by

changes in the level of registration. Given the marked heterogeneity in the temporal patterns of confirmed COVID mortality cases and deaths across states (17), and the variable background of mortality rates from chronic diseases affected by COVID infection (3), extrapolating from selected states has its limitations.

To fill the gaps in national-level estimates, we quantified COVID mortality in India using one independent and two government data sources. The first study is mortality reported in a nationally representative telephone survey conducted by CVoter, an established, independent, private polling agency, which launched the survey on a nonprofit basis to help track the pandemic [see materials and methods, p. 2 (18)]. The COVID Tracker survey covers 0.14 million adults (including a substudy of 57,000 people in 13,500 households with more exact reporting of COVID and non-COVID deaths in immediate family members) (18, 19). In addition, we studied the Government of India's administrative data on national facility-based deaths and CRS deaths in 10 states (fig. S2).

The CVoter Tracker survey is a nationally representative, random probability-based computer-assisted telephone interview survey carried out daily to track governance, media, and other socioeconomic indicators (19). In March 2020, it began to capture COVID symptoms among adults aged 18 years or older, covering ~2100 randomly selected respondents

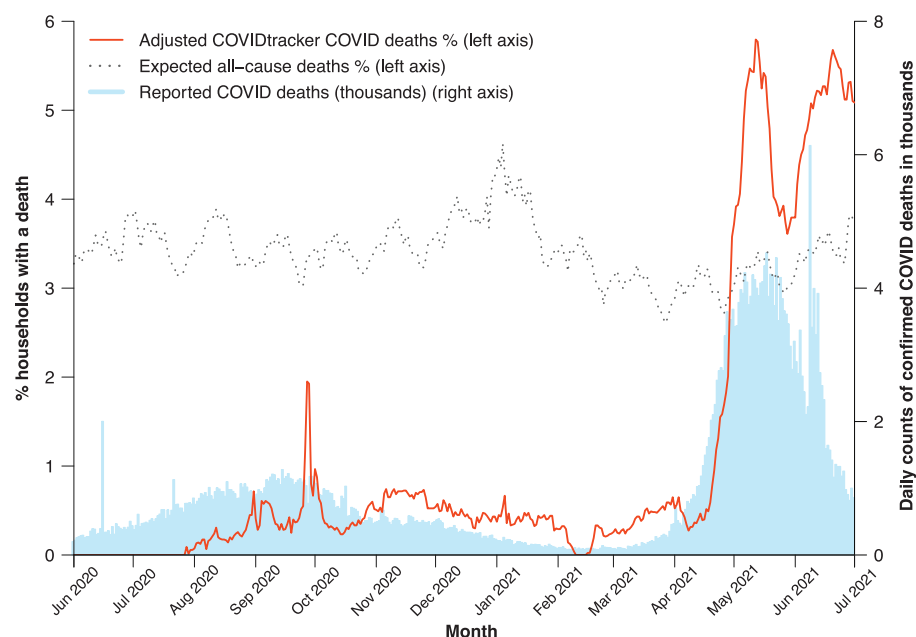


**Fig. 1. Percentages of adults reporting daily death in household, expected percentage in 2020, and daily confirmed COVID deaths in India, 1 June 2020 to 1 July 2021.** COVID Tracker deaths (red line, left vertical scale) represent COVID deaths reported daily (smoothed for rolling 7-day averages) at age 35 or older, less a subtraction value of 0.59% to represent nonhousehold reporting. Expected all-cause deaths (gray dashed line, left vertical scale) per year of 3.4% (see text), with 7-day smoothed weekly adjustment from variation observed among 480,000 deaths in the Million Death Study from 2004 to 2014. Confirmed COVID deaths (blue bars, right vertical scale) are daily reports from Covid19india.org (2).

<sup>1</sup>Centre for Global Health Research, Unity Health Toronto and Dalla Lana School of Public Health, University of Toronto, Toronto, Ontario, Canada. <sup>2</sup>Center For Voting Opinions and Trends in Election Research, Noida, Uttar Pradesh, India. <sup>3</sup>Department of Economics, Indian Institute of Management Ahmedabad, Ahmedabad, Gujarat, India. <sup>4</sup>Development Data Lab, Washington, DC, USA. <sup>5</sup>Department of Economics, Dartmouth College, Hanover, NH, USA. \*Corresponding author. Email: prabhat.jha@utoronto.ca



weekly, drawn from ~4000 local electoral areas in the whole of the country, providing a rolling 7-day average of COVID symptoms and deaths. The survey covers >98% of Indian population by geography, with interviews in 11 languages. The response rate was 55%; 137,289 respondents in all states and union territories were interviewed from March 2020 to July 2021.

Our numerator was defined as the average weekly percentages of surveyed households reporting a COVID death (defined by the household, as medical certification remains uncommon in India; fig. S1). We excluded the 16% of reported COVID deaths that were below age 35 years (confirmed COVID deaths below this age are infrequent; fig. S3) and subtracted a fixed percentage of 0.59%, which was an assumed value for reported deaths that did not occur among immediate family members. The assumed value drew on observed background rates during February–March 2021, when few COVID cases or deaths were reported in the official government data (see materials and methods, p. 3). Results using survey weights or raw proportions were similar, so we used the latter. We compared these survey-reported COVID deaths to a denominator defined as the expected weekly percentage for all-cause deaths, based on 2020 death totals from the UNPD's comprehensive demographic estimates that combine censuses, survey data, and models (20) (Fig. 1). India had about 296 million households in 2020, with an average household size of 4.6 (27). Dividing this into the 10.16 million deaths estimated by the UNPD in India in 2020 yields ~3.4% of households expected to report a death from any cause in that year (with nearly identical results for 2021). To this expected all-cause proportion, we applied the weekly variation observed in the Million Death Study, a large and representative mortality study conducted within the SRS (3).

For most of the weeks from June 2020 to March 2021, zero to 0.7% of households in the CVoter survey reported a COVID death. Even the upper value of 0.7% during some weeks corresponded to 20% of the expected annual all-cause death proportion of 3.4%. During the first viral peak, 1.2% of households reported a COVID death (or about 35% of expected all-cause deaths) over 10 days from 24 September to 4 October 2020. There was a second sharp increase in reported COVID deaths from mid-April to the end of June 2021, reaching weekly peaks close to 6% of households. From 1 April to 1 July 2021, the proportion of households reporting COVID deaths was 3.7%, which was 108% [95% lower limits (LL) and upper limits (UL), 103 to 113%] of the expected all-cause deaths of 3.4% (Table 1). The same comparison for 1 June to 31 December 2020 showed that COVID deaths were 8.1% (7.7 to 8.5%) of expected all-cause deaths.

Applying these proportions to expected overall deaths from 1 June 2020 to 1 July 2021

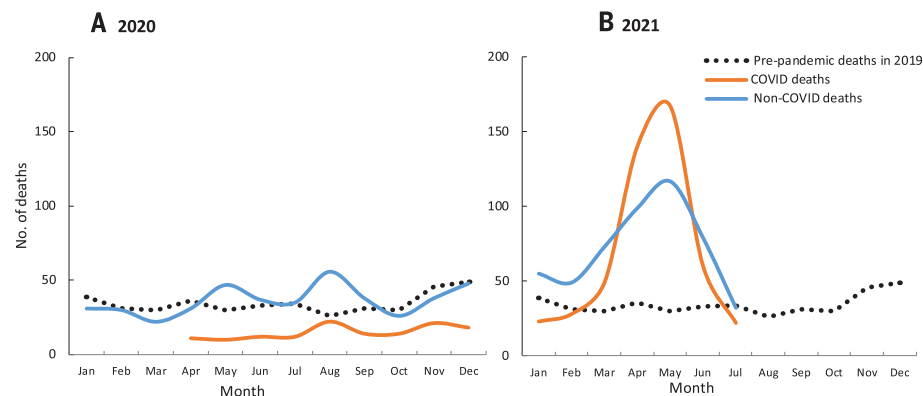


**Fig. 2. Monthly reporting of deaths as COVID (including COVID-associated) and non-COVID by month for 2019 to 2021 in a substudy of 57,000 adults in 13,500 households within the COVID Tracker survey (2).** Table S3 provides the input data. (A) 2020 deaths; (B) 2021 deaths.

yielded an estimate of 3.2 million (3.1 to 3.4) COVID deaths, or 29% (28 to 31%) of expected all-cause deaths during the 13-month period, including during the interspersed weeks of assumed lower transmission. The majority of COVID deaths that India experienced throughout the pandemic occurred from 1 April to 1 July 2021 (2.7 million; 2.6 to 2.9). Given that the subtraction value for nonhousehold reporting of COVID deaths was somewhat subjective, we ran sensitivity analyses of 50% and 150% of our baseline of 0.59%, yielding estimates ranging from 2.5 (2.4 to 2.6) to 4.0 (3.8 to 4.1) million COVID deaths.

The COVID Tracker survey's introductory question focused on flu-like symptoms among immediate family members, but the COVID question asked: "Has anyone in your family or surroundings been infected from Corona Virus?" If the self-reported answer was yes, respondents were asked whether the infected individual had died. To address a possible limitation of overreporting (i.e., COVID deaths in "surroundings" but not in the household), from 15 June to 1 Sept 2021 we implemented a substudy among a randomly selected 10% of households from the COVID Tracker Panel.

We ascertained from ~57,000 people in 13,500 households who lived in the immediate household as of 1 January 2019, who died and when, and if the respondent thought the death was due to COVID or a non-COVID cause (Fig. 2 and table S3). The criterion of "immediate household" included parents and unmarried adults. This substudy recorded 415, 618, and 1074 all-cause deaths in 2019, 2020, and 2021, respectively, corresponding to crude death rates per 1000 people of 7.2, 10.8, and 18.8, respectively [the 2019 crude death rate was similar to the UN all-cause death rate of 8.1 out of 1000 (20)]. Total COVID deaths reported in 2020 (162) and 2021 (553) corresponded to 1.2% and 4.1% of households re-

porting a COVID death, comparable to the proportions in the main COVID Tracker survey. The crude death rate in the substudy more than doubled in 2021 compared to 2019, also consistent with the increase in COVID deaths in the main survey. Compared to 2019, the increase in non-COVID deaths reported during September–October 2020 exceeded reported COVID deaths, but the reverse was true during April–June 2021. This likely reflects the misclassification of non-COVID deaths; COVID infection raises death rates not just from respiratory disease but also from vascular disease, kidney disease, and other causes (22). The Government of India's daily confirmed COVID death totals from 1 June 2020 to 1 July 2021 strongly correlated with the daily death totals in the CVoter main survey (correlation 0.88,  $p < 0.0001$ ). The government's confirmed COVID death totals for each month from 1 April 2020 to 1 July 2021 correlated with the monthly COVID deaths in the CVoter substudy (correlation 0.84,  $p < 0.001$ ; fig. S4).

We examined two government-reported data sources as comparisons to the independent CVoter survey. The first data source comprised facility-based all-cause mortality covering a nonrepresentative sample of 0.2 million public hospitals and smaller facilities nationally, more than 90% of them rural (23) (Fig. 3). Compared to 2018–2019, all-cause deaths increased 27% (23 to 32%) during 1 July 2020 to 31 May 2021, equivalent to an excess of 0.63 million deaths (0.53 to 0.73) of 2.32 million expected for the 11 months (Table 1). Much of this excess occurred in April–May 2021 (0.45 million or 71%), reaching a 120% increase over earlier year totals. The increase in facility deaths in the first viral wave was predominantly urban, but deaths in the second wave affected both urban and rural facilities (fig. S5). Compared to 2018–2019 totals, the increase in all-cause deaths in April–May 2021 varied across states, with Gujarat

reporting a 230% increase and Kerala a 37% increase. In Andhra Pradesh, which had reasonably high coverage of expected rural deaths in facilities, the major increase during April–May 2021 was for deaths of unknown cause, followed by nontuberculosis respiratory conditions, heart disease, and other chronic disease, with a small decrease in death from injuries (table S4). Analysis of increases in overall mortality may therefore better capture the diverse diseases affected by COVID infection.

The second government data source was all-cause deaths in the CRS for 10 states with 10 or more months of observations (including the interspersed periods between the two viral waves). In these states, the combined median increase, as a percentage of expected deaths based on UNPD death rates, was 26% (21 to 31%; Table 1). Total excess all-cause deaths were 1.25 million (1.00 to 1.49) for the 10 states that reported about half of national official COVID deaths (2). The median ratio of excess to confirmed COVID deaths ranged from six to seven in the two viral waves for these states (table S5).

Our national estimates of 3.1 to 3.4 million COVID deaths help fill a gap in knowledge from focal or model-based studies (table S2). During the 13 months between 1 June 2020 and 1 July 2021, the proportions of excess deaths from COVID in the national survey (28 to 31%) were comparable to the proportions from all causes in the national facility data (23 to 32%)

or the CRS data in 10 states (21 to 31%). However, the major uncertainties in these estimates are not the relatively narrow confidence intervals, but the assumptions about the nonpandemic mortality rates (24). Despite varying methodologies, each with its own limitations, our three studies and those published earlier (table S2) point to a substantial underreporting of deaths in India's official numbers. Most find a much larger excess of deaths in the second viral wave than in the first. Indeed, the COVID pandemic likely doubled the total death rate from all conditions in April–June 2021.

The estimates of 3.1 to 3.4 million deaths from the independent COVID Tracker survey represent a national COVID death rate per million population ranging from about 2300 to 2500, or approximately six- to sevenfold the officially reported rate on 1 September 2021 (7). This would put India's death rate per million population just below the range reported in Brazil (2800 per million) or Colombia (2500 per million), where registration of deaths is far more complete (15). The actual excess deaths in the facilities may be larger as the Government of India has yet to release these data from June 2021 onward. More definitive quantification of excess mortality can be expected once the Registrar General of India relaunches its SRS (13) to cover all deaths occurring in 2020 and 2021. Indeed, the extraordinary COVID death totals that we

document warrant adding a simple question on the age, sex, and date of any death (regardless of cause) occurring in 2020 or 2021 to the 2022 national census. Concurrently, India must expand and improve its death registration and medical certification system, with timelier reporting (25). Uncounted or medically uncertified deaths are not uniform, with larger gaps in the poorest states in central India and larger gaps among women than among men (fig. S1 and table S1).

Both the 2020 and 2021 viral waves were characterized by widespread (and, for 2021, mostly uncontrolled) multigenerational transmission of the virus within households, with high levels of antibodies detected (17). India's notably higher COVID death rate in 2021, compared to the lower than expected death rate in 2020, requires further research. The spread of infection to rural areas in 2021 is one factor, but there might also be differences in the pathogenicity between the original virus (Wuhan) in 2020 and the mix of Alpha and Delta variants accounting for most of the 2021 viral wave (26), or other biological predictors of severe infection that changed between these two waves. Similarly, tracking death rates will be essential to understanding the effects of the Omicron wave currently underway in India, or future viral variants.

The strengths of our study are its national representativeness and distributed sampling

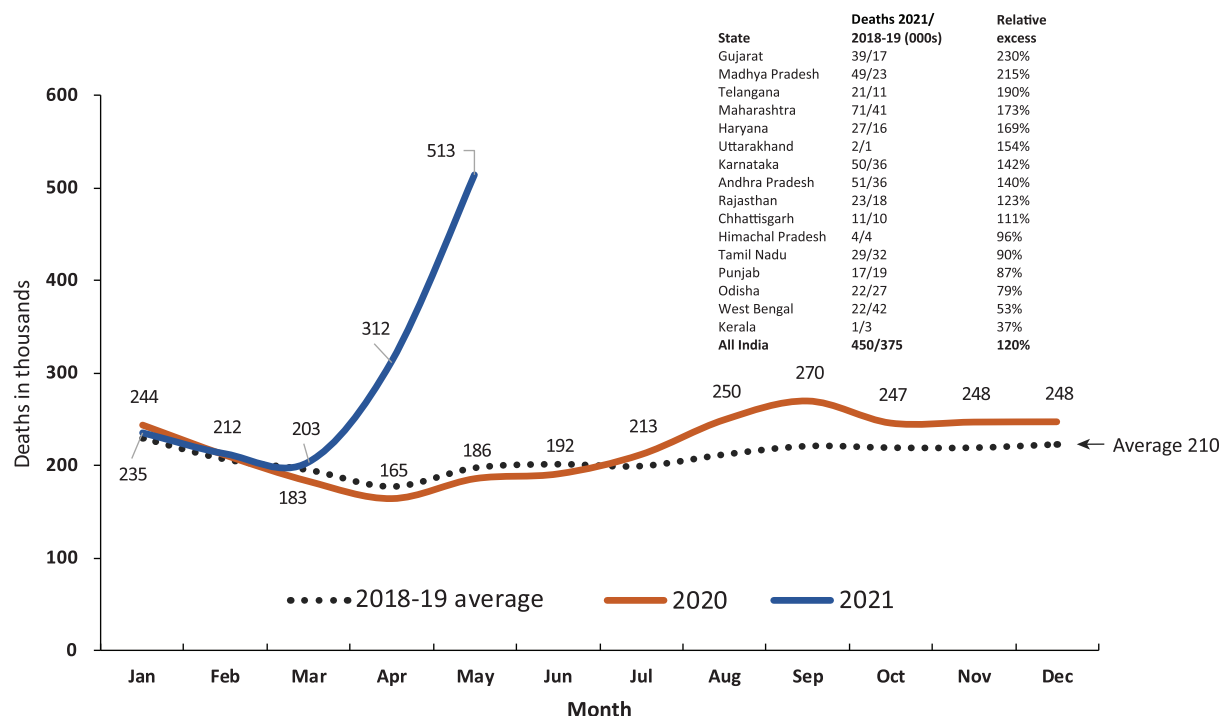


**Fig. 3. Reported deaths from all causes in India's Ministry of Health and Family Welfare Management Information System covering 0.2 million health facilities nationally, 2020 and 2021, versus average of 2018–2019, by month.** The inset shows the increases in selected states and nationally for the April–May 2021 relative to the 2018–2019 averages for the same months of comparison. Table S6 provides the input data.

**Table 1. Summary estimates of excess deaths in India nationally and for states with 10 or more months of data (including the interim weeks or months that were not pandemic).** Table S6 provides the input data.

Data source	Reference period	Months	UN-estimated deaths in reference period (thousands)	Excess deaths (LL, UL) in thousands*	Excess as percentage of UN-estimated deaths; mid (LL, UL)*
<b>Survey-based estimates, national</b>	1 June–31 Dec 2020	7	5979	486 (461, 510)	8.1 (7.7, 8.5)
	1 April–1 July 2021	3	2539	2739 (2602, 2876)	107.9 (102.5, 113.3)
	<b>1 June 2020–1 July 2021</b>	<b>13</b>	<b>10,956</b>	<b>3225 (3063, 3386)</b>	<b>29.4 (28, 30.9)</b>
<b>Facility-based deaths, national</b>	1 July–31 Dec 2020	6	1295	180 (169, 191)	13.9 (13.1, 14.8)
	1 Apr–31 May 2021	2	375	450 (362, 539)	120.2 (96.5, 143.9)
	<b>1 July 2020–31 May 2021</b>	<b>11</b>	<b>2301</b>	<b>630 (531, 730)</b>	<b>27.4 (23.1, 31.7)</b>
<b>Civil registration system deaths, selected states</b>					
Andhra Pradesh	1 July 2020–30 June 2021	12	411	207 (155, 259)	50.3 (37.7, 63)
Maharashtra	1 July 2020–31 May 2021	11	813	244 (211, 278)	45.5 (39.2, 51.8) <sup>†</sup>
Madhya Pradesh	1 July 2020–31 May 2021	11	656	205 (149, 261)	31.3 (22.8, 39.8)
Haryana	1 July 2020–31 May 2021	11	195	61 (51, 71)	31.2 (26.3, 36.2)
Karnataka	1 July 2020–30 June 2021	12	660	175 (152, 198)	26.6 (23.1, 30.1)
Himachal Pradesh	1 July 2020–31 May 2021	11	31	8 (6, 10)	25.0 (18.4, 31.6)
Tamil Nadu	1 July 2020–30 June 2021	12	619	140 (101, 179)	22.6 (16.2, 28.9)
West Bengal	1 July 2020–31 May 2021	11	626	138 (124, 152)	22.0 (19.8, 24.3)
Rajasthan	1 July 2020–31 May 2021	11	551	50 (38, 61)	17.7 (13.6, 21.8) <sup>†</sup>
Kerala	1 Aug 2020–31 May 2021	10	238	19 (15, 22)	7.8 (6.4, 9.2)
<b>Subtotals and medians</b>			<b>4801</b>	<b>1247 (1002, 1491)</b>	<b>25.8 (21.3, 30.8)</b>

\*For the independent national survey, these are COVID deaths, and for facility and civil registration deaths, these are all-cause excess deaths. †Out of the annual average of 428,000 CRS deaths for prepandemic years of Rajasthan (table S1), only 218,000 deaths (table S6) or 51% were available for our calculations. Similarly, for Maharashtra, only 66% of CRS deaths were available. Thus, we have adjusted the percentages in the last column to the available data. The lower limits (LL) and upper limits (UL) for facility-based deaths and civil registration deaths and percentages are based on the variation in monthly reporting, and those for the national survey are based on the survey margin error of  $\pm 5\%$ . See materials and methods for the calculation formulas used for absolute excess deaths and relative excess mortality for the three data sources.

for the survey, use of three data sources, and robust metrics that document increased deaths versus earlier years or expected demographic totals. Our methods are reproducible over time and avoid the limitations of model-based estimates. We focused on increased mortality only in the short time periods of pandemic peaks and assumed no excess mortality between viral peaks. COVID deaths typically are acute, occurring within weeks of infection, but the full effects of COVID infection on various underlying diseases are unknown. Thus, our results are conservative. As we had to rely on household self-reports, we adjusted for possible overreporting of deaths and ensured that denominators of CRS deaths considered the underlying deficiencies in death reporting in India. Nonetheless, we faced several limitations. We compared COVID deaths to expected all-cause mortality in the national survey, and in so doing, we might have underestimated the totals that in part arose from increases in deaths misclassified as non-COVID. The metric of excess mortality has limitations as some causes—notably road traffic accidents, non-COVID infections, or other injuries—may have decreased, particularly during COVID lockdowns (table S4). However, the nationally

representative Million Death Study, conducted within the SRS, documented that injuries constituted less than 1 in 10 of all deaths in India from 2004 to 2014 (3). By contrast, other causes, including those linked to poor mental health, may have risen, as seen in the US (22). There might also be an increase in some deaths from neglected health services, as reflected in reports that maternal mortality rose during the pandemic months (16), but these may also represent COVID infection among pregnant women (27). Changes in non-COVID causes of death are likely to be small compared with the sharp increases in COVID deaths, particularly during the second viral wave. Household self-reports of deaths likely misclassified various conditions that are in fact COVID-related (28). The COVID Tracker survey data might have overreported COVID deaths, as the questions were not restricted to immediate family members, but the sub-survey, which did not have this limitation, yielded very similar results. Rural facility death reporting may have been biased upward if more people than usual sought care during high transmission months. Delays in death registration or a backlog of deaths corrected suddenly might create a spurious peak of ex-

cess deaths. However, in the case of Andhra Pradesh, 98% of deaths registered in May 2021 took place within the previous 30 days, not earlier time periods (16).

In sum, our study finds that Indian COVID deaths are substantially greater than estimated from official reports. If our findings are confirmed, this may require substantial upward revision of WHO's estimates of cumulative global COVID mortality, which as of 1 January 2022, stood at 5.4 million (15).

## REFERENCES AND NOTES

1. "The Coronavirus App" (Scriby, Inc, 2021); <https://coronavirus.app/map>.
2. COVID-19 India Data Operations Group, "Covid19India.org" (2021); <https://www.covid19india.org/>.
3. G. R. Menon et al., *Lancet Glob. Health* **7**, e1675–e1684 (2019).
4. Office of the Registrar General, India, "Vital Statistics of India based on the Civil Registration System 2019" (2021); [https://censusindia.gov.in/2011-Common/CRS\\_2019/CRS2019\\_report.pdf](https://censusindia.gov.in/2011-Common/CRS_2019/CRS2019_report.pdf).
5. C. Z. Guilmo, Estimating the death toll of the Covid-19 pandemic in India. *medRxiv* 2021.06.29.21257965 [Preprint]. 2 July 2021. <https://www.medrxiv.org/content/10.1101/2021.06.29.21257965v1>.
6. C. T. Leffler, J. D. Lykins V, E. Yang, Preliminary Analysis of Excess Mortality in India During the Covid-19 Pandemic. *medRxiv* 2021.08.04.21261604 [Preprint]. 27 September 2021. <https://www.medrxiv.org/content/10.1101/2021.08.04.21261604v2>.



7. A. Malani, S. Ramachandran, "Using Household Rosters from Survey Data to Estimate All-cause Mortality during COVID in India" (2021); <https://www.nber.org/papers/w29192>.
8. M. Banaji, A. Gupta, Estimates of pandemic excess mortality in India based on civil registration data. *medRxiv* 2021.09.30.21264376 [Preprint]. 1 October 2021. <https://www.medrxiv.org/content/10.1101/2021.09.30.21264376v1>.
9. A. Gupta, M. Banaji, "Lessons from India's all-cause mortality data"; *The Hindu* (2021); <https://www.thehindu.com/opinion/lead/lessons-from-indias-all-cause-mortality-data/article36007188.ece>.
10. A. Anand, J. Sandefur, A. Subramanian, "Three New Estimates of India's All-Cause Excess Mortality during the COVID-19 Pandemic" (2021); <https://www.cgdev.org/publication/three-new-estimates-indias-all-cause-excess-mortality-during-covid-19-pandemic>.
11. R. J. Acosta *et al.*, All-cause excess mortality in the State of Gujarat, India, during the COVID-19 pandemic. *medRxiv* 2021.08.22.21262432 [Preprint]. 25 August 2021. <https://www.medrxiv.org/content/10.1101/2021.08.22.21262432v1>.
12. A. Bamezai *et al.*, Survey evidence of excess mortality in Bihar in the second COVID-19 surge. *SocArXiv* [Preprint]. 29 July 2021. <https://osf.io/preprints/socarxiv/zxq97/>.
13. Office of the Registrar General & Census Commissioner, India, "SRS statistical report 2018" (2020); [https://censusindia.gov.in/vital\\_statistics/SRS\\_Reports\\_2018.html](https://censusindia.gov.in/vital_statistics/SRS_Reports_2018.html).
14. P. E. Brown *et al.*, Mortality from COVID in Colombia and Peru: Analyses of Mortality Data and Statistical Forecasts. *medRxiv* 2020.08.24.20181016 [Preprint]. 16 November 2020. <https://www.medrxiv.org/content/10.1101/2020.08.24.20181016v2>.
15. World Health Organization, "The true death toll of COVID-19: estimating global excess mortality"; <https://www.who.int/data/stories/the-true-death-toll-of-covid-19-estimating-global-excess-mortality>.
16. R. S., "Deaths By 'Unknown Causes' On National Health Mission Portal 2X Official Covid Toll"; *IndiaSpend* (2021); <https://www.indiaspend.com/covid-19/deaths-unknown-causes-national-health-mission-portal-covid-toll-760219>.
17. A. Velumani *et al.*, SARS-CoV-2 Seroprevalence in 12 Cities of India from July-December 2020. *medRxiv* 2021.03.19.21253429 [Preprint]. 24 March 2021. <https://www.medrxiv.org/content/10.1101/2021.03.19.21253429v1>.
18. Team CVoter, "COVID-19 Tracker Surveys in India" (2020); [https://cvoterindia.com/wp-content/uploads/2020/Covid\\_Tracker\\_Methodology\\_Note.pdf](https://cvoterindia.com/wp-content/uploads/2020/Covid_Tracker_Methodology_Note.pdf).
19. Team CVoter, "CVoter News Services"; <https://cvoterindia.com/trackers/>.
20. United Nations, Department of Economic and Social Affairs, Population Division, "World Population Prospects 2019: Highlights" (2019); [https://population.un.org/wpp/Publications/Files/WPP2019\\_Highlights.pdf](https://population.un.org/wpp/Publications/Files/WPP2019_Highlights.pdf).
21. Population Reference Bureau, "International Indicators: Average Household Size" (2020); <https://www.prb.org/international/indicator/hh-size-av/map/country>.
22. S. H. Woolf, D. A. Chapman, R. T. Sabo, E. B. Zimmerman, *JAMA* **325**, 1786–1789 (2021).
23. Ministry of Health and Family Welfare, Government of India, "Health Management Information System" (2021); <https://hmis.nhp.gov.in/#/standardReports>.
24. M. R. Nepomuceno *et al.*, Sensitivity of excess mortality due to the COVID-19 pandemic to the choice of the mortality index, method, reference period, and the time unit of the death series. *medRxiv* 2021.07.20.21260869 [Preprint]. 23 July 2021. <https://www.medrxiv.org/content/10.1101/2021.07.20.21260869v1>.
25. P. Jha, *BMC Med.* **12**, 19 (2014).
26. C. Pattabiraman *et al.*, *Wellcome Open Res.* **6**, 110 (2021).
27. C. Meh *et al.*, *BJOG* **147**, 1471–1478 (2020).
28. P. Madhah, H. Wunsch, P. Jha, A. S. Slutsky, D. Brodie, *Lancet Respir. Med.* **9**, 322–324 (2021).
29. Centre for Global Health Research, Zenodo (2021). [https://github.com/cghr-toronto/Indian\\_Covid\\_Mortality](https://github.com/cghr-toronto/Indian_Covid_Mortality).

## ACKNOWLEDGMENTS

We thank Rukmini S. S. Ramani, V. Radhakrishnan, A. Saikia, M. Alavi, S. Das, P. Vardhan, and D. Rajendran, who were crucial in filing petitions to access the various data sources. No individual-level patient data were used in the analyses. Unity Health, St. Michael's Hospital, Toronto provided ethics approval (REB 15-231). The opinions expressed are those of the authors and not necessarily the institutions to which they are affiliated. **Funding:** Canadian Institutes of Health Research; Emergent Ventures.

**Author contributions:** P.J. conceived the study. Y.D., W.S., C.T., A.B., S.S., and S.H.F. contributed to statistical analyses. P.J., H.G., and P.N. wrote the first draft, and all authors contributed.

**Competing interests:** The authors declare no competing interests. Y.D. is the director and founding editor of CVoter. No external funding was received for the CVoter COVID Tracker survey or substudy. **Data and materials availability:** The data used for the main facility and CRS deaths are in the supplementary materials (table S6); the primary CVoter data showing daily results are available at <https://cvoterindia.com/trackers>, and the substudy data are in table S3. All input data are available at [https://github.com/cghr-toronto/Indian\\_Covid\\_Mortality](https://github.com/cghr-toronto/Indian_Covid_Mortality) (29). This work is licensed under a Creative Commons Attribution 4.0 International (CC BY 4.0) license, which permits unrestricted use, distribution, and reproduction in any medium, provided the original work is properly cited. To view a copy of this license, visit <https://creativecommons.org/licenses/by/4.0/>. This license does not apply to figures/photos/artwork or other content included in the

article that is credited to a third party; obtain authorization from the rights holder before using such material.

## SUPPLEMENTARY MATERIALS

[science.org/doi/10.1126/science.abm5154](https://science.org/doi/10.1126/science.abm5154)  
Materials and Methods  
Figs. S1 to S5  
Tables S1 to S6  
References (30–35)  
MDAR Reproducibility Checklist  
Movie S1

23 September 2021; resubmitted 18 November 2021  
Accepted 4 January 2022  
Published online 6 January 2022  
10.1126/science.abm5154

## AGING

# Caloric restriction in humans reveals immunometabolic regulators of health span

O. Spadaro<sup>1,2,3</sup>, Y. Youm<sup>1,2,3</sup>, I. Shchukina<sup>4</sup>, S. Ryu<sup>1,2,3</sup>, S. Sidorov<sup>1,2,3</sup>, A. Ravussin<sup>1,2,3</sup>, K. Nguyen<sup>1,2,3</sup>, E. Aladyeva<sup>4</sup>, A. N. Predeus<sup>5</sup>, S. R. Smith<sup>5</sup>, E. Ravussin<sup>6</sup>, C. Galban<sup>7</sup>, M. N. Artyomov<sup>4</sup>, V. D. Dixit<sup>1,2,3,8,9,\*</sup>

The extension of life span driven by 40% caloric restriction (CR) in rodents causes trade-offs in growth, reproduction, and immune defense that make it difficult to identify therapeutically relevant CR-mimetic targets. We report that about 14% CR for 2 years in healthy humans improved thymopoiesis and was correlated with mobilization of intrathymic ectopic lipid. CR-induced transcriptional reprogramming in adipose tissue implicated pathways regulating mitochondrial bioenergetics, anti-inflammatory responses, and longevity. Expression of the gene *Pla2g7* encoding platelet activating factor acetyl hydrolase (PLA2G7) is inhibited in humans undergoing CR. Deletion of *Pla2g7* in mice showed decreased thymic lipofatty, protection against age-related inflammation, lowered NLRP3 inflammasome activation, and improved metabolic health. Therefore, the reduction of PLA2G7 may mediate the immunometabolic effects of CR and could potentially be harnessed to lower inflammation and extend the health span.

**T**he beneficial effects of caloric restriction (CR) include enhanced longevity and reduced disease burden (1). However, 40% reduction of calories from a normal ad libitum state in many rodent studies showing life-span extension is associated with increased severity of viral and parasitic infections (2, 3), including mortality from polymicrobial sepsis (4). Impaired immunity may result because energetically expensive functions are dispensed with severe CR as energy resources are diverted toward somatic cell maintenance (5, 6).

In addition to host defense, the resident immune system in every organ is required for integration of cellular metabolism, tissue repair, and function. Thus immunological trade-offs may make it difficult to identify clinically relevant beneficial CR mimetics (7). Furthermore, forced extreme CR in nonconsenting animals may elicit stress responses evidenced by increased production of glucocorticoids (8), which can further compromise the immune system by causing thymocyte death and thymic involution (9). To address the relevance of CR on human physiology, the Comprehensive Assessment of Long-term Effects of Reducing Intake of Energy (CALERIE) clinical trial was designed to test the long-term effects of 2 years of moderate CR on physiology, aging biomarkers, and predictors of health span and longevity in healthy volunteers (10). The energy intake at baseline (ad libitum state) was evaluated by two consecutive 14-day measures of total daily energy expenditure (TDEE) using doubly labeled water (11). Average %CR over 6-month intervals was retrospectively calculated using the intake-balance method, which involves simultaneous

<sup>1</sup>Department of Pathology, Yale School of Medicine, New Haven, CT, USA. <sup>2</sup>Department of Immunobiology, Yale School of Medicine, New Haven, CT, USA. <sup>3</sup>Department of Comparative Medicine, Yale School of Medicine, New Haven, CT, USA. <sup>4</sup>Department of Pathology and Immunology, Washington University School of Medicine, St. Louis, MO, USA. <sup>5</sup>Translational Research Institute for Metabolism and Diabetes, AdventHealth, Orlando, FL, USA. <sup>6</sup>Pennington Biomedical Research Center, LSU, Baton Rouge, LA, USA. <sup>7</sup>Department of Radiology, Michigan Medicine, University of Michigan, Ann Arbor, MI, USA. <sup>8</sup>Yale Center for Molecular and Systems Metabolism, Yale School of Medicine, New Haven, CT, USA. <sup>9</sup>Yale Center for Research on Aging, Yale School of Medicine, New Haven, CT, USA.  
**\*Corresponding author. Email: vishwa.dixit@yale.edu**

measures of TDEE using doubly labeled water together with changes in body composition (17). This study established that in free-living conditions, humans achieve ~14% sustained CR for 2 years (10–12). This level of voluntary CR in humans in free-living conditions is much

lower than the forced 25 to 40% restriction of calories in laboratory animals and may engage unique mechanisms to maintain homeostasis.

Mice on life-long 40% CR maintain thymic lymphopoiesis into late life and have a diverse T cell receptor (TCR) diversity (13), whereas

14% CR in humans reduces the number of circulating lymphocytes and proinflammatory cytokines in the blood (14). Aging of thymus precedes aging of other organs, a process characterized by increased thymic lipid accumulation and loss of T cell production (15). We

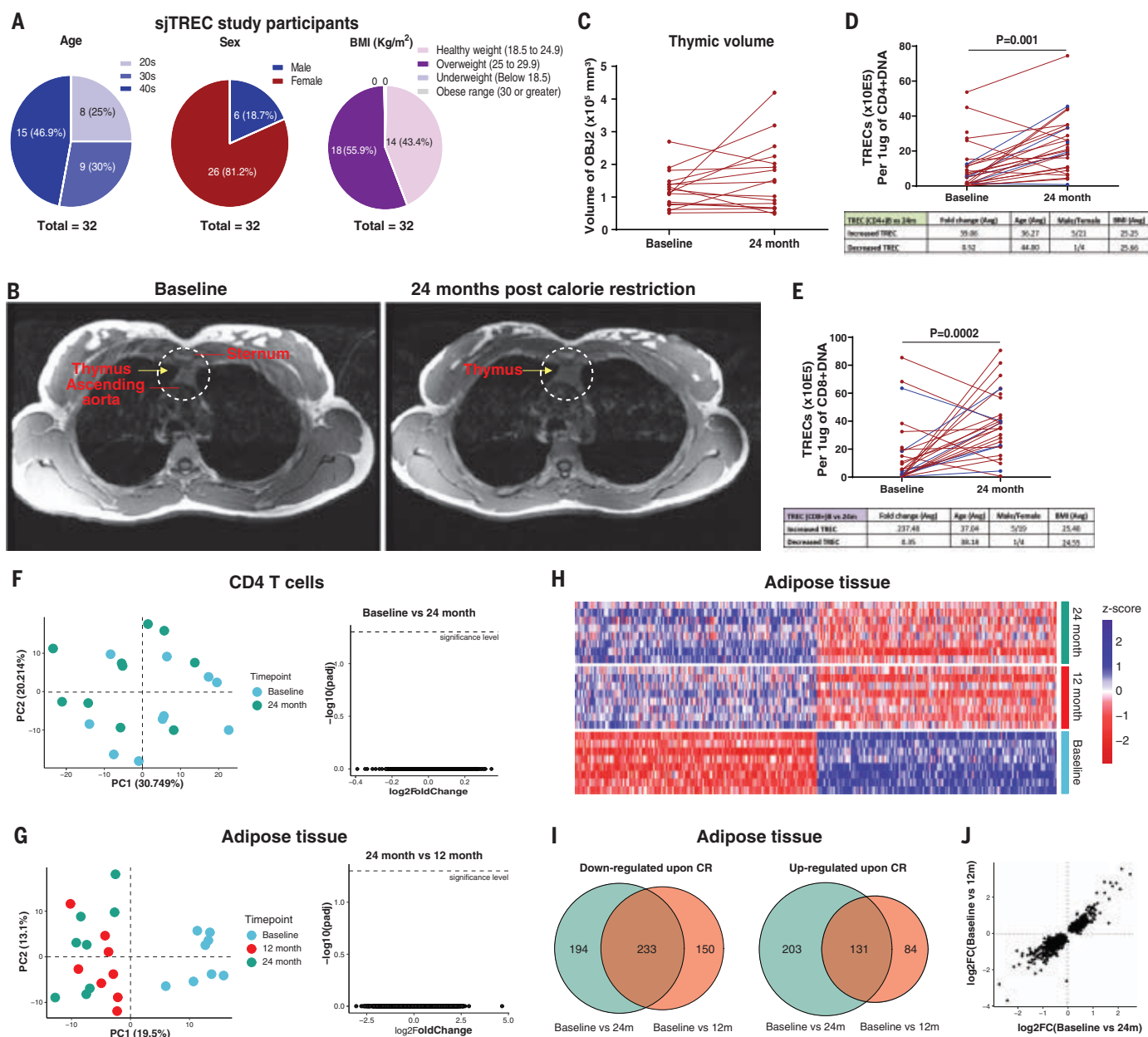


**Fig. 1. CR in humans improves thymic function and remodels adipose transcriptome.** (A) Participant information for the sjTREC study ( $n = 32$ ). (B) Representative MRI examination image of a female participant performed with the subject head first and supine in a 3 T full-body scanner at the baseline (left) and after 2 years of CR (right). The region of interest depicting the thymus is highlighted by yellow arrows in dotted circle after the fat saturation sequence was applied. (C) Thymic volume of female study participants analyzed by MRI at baseline and after 24 months of CR. (D and E) sjTREC analysis results of CD4 (D) and CD8 (E) T cells at baseline after 2 years of CR. Red line indicates TREC in females; blue line indicates TREC in males. (F) PCA of transcriptional profile of blood CD4 T cells at baseline and after 2 years of CR.

Volcano plot depicts the results of differential gene expression analysis of CD4 T cells between baseline and after 2 years of CR. (G) PCA of RNA sequencing of adipose tissue at baseline and after 1 and 2 years of CR ( $n = 8$ ). Volcano plot depicts the results of differential analysis of subcutaneous adipose tissue between 1 and 2 years of CR (right). Each dot represents a gene. (H) Heatmap of significant differentially expressed genes between baseline and either 1 or 2 years of CR in adipose tissue. (I) Venn diagram illustrating overlaps between genes found to be differential [false discovery rate (FDR), 5%] between baseline and either 1 or 2 years of CR. Overlapping area indicates the genes that are differentially expressed after both 1 and 2 years of CR. (J) Comparison of the log<sub>2</sub>-scaled fold change between baseline and 1 or 2 years of CR.

therefore investigated thymic function at baseline and after 2 years of sustained CR in middle-aged healthy CALERIE participants (Fig. 1A and fig. S1, A to C) using magnetic resonance imaging (MRI) and quantification of signal-joint T cell receptor excision circles (sjTRECs) in blood, which are episomal DNA by-products of TCR recombination and are indicators of recently produced T cells from thymus. Compared with baseline, sustained CR for 2 years significantly ( $P < 0.05$ ) increased thymic mass (Fig. 1B) as well as total thymic volume in study participants (Fig. 1C). The control participants showed no significant change in thymic volume from baseline to year two (fig. S2A). Compared with baseline, 2 years of CR significantly increased the recent thymic emigrant cells as measured by the presence of sjTRECs in CD4 (Fig. 1D) and CD8 cells (Fig. 1E) in the majority of female ( $n = 22$  and 20, respectively) and male ( $n = 5$  and 5, respectively) study participants. We conducted RNA sequencing of peripheral blood CD4 T cells from study participants to measure the transcriptional changes. However, principal component analysis (PCA) (Fig. 1F) and multidimensional scaling (MDS) analysis (fig. S2C) revealed no effect of CR on gene expression in CD4 T cells. These data may indicate that 14% CR in healthy humans activates a tissue-protective immunometabolic program that can enhance thymic function without altering the transcriptome of CD4 T cells.

Reduction in caloric intake induces a decrease in glucose utilization and a switch to fatty acid oxidation and lipolysis (16). Accordingly, the participants in the CALERIE-II study experienced reduction of fat mass (17). Given that adipose tissue also contains a resident immune system that controls inflammation (6), we measured the impact of CR on gene expression in the adipose tissue biopsies. PCA and MDS analysis of whole-transcriptome gene expression in abdominal subcutaneous adipose tissue of study participants revealed that compared with baseline, 1 year of CR altered the transcriptome, and this difference was maintained after 2 years of CR (Fig. 1G and fig. S2C). In adipose tissue after CR (Fig. 1H), 233 genes were differentially up-regulated and 131 genes were down-regulated relative to baseline at the year one and year two time points (Fig. 1I). No significant changes in gene expression were found comparing year one and year two after CR (Fig. 1G).

Adaptation to CR requires rewiring of immunometabolic inputs that control adipose tissue function, which in turn may drive systemic health span effects in humans (6). The top 20 up- and down-regulated genes in human adipose tissue after 14% CR identified transcripts previously not highlighted in rodent studies (Fig. 2A). Transcripts altered at year one of CR (*PLA2G7*, *SPARC*, *CA3*, *PLIN5*, *ACVR1C*, *CALCLRL*, *PDE3A*, *DPT*, *EGFL6*, *NAMPT*, and *PPARA*) did

not change under ad libitum fed conditions for 1 year (fig. S2B). Changes in gene expression in adipose tissue after CR were similar to those observed after bariatric surgery (fig. S3A). Similar gene expression patterns were also observed in a dataset describing twin pairs discordant for physical activity (Fig. 2B), providing an example of another lifestyle intervention that can reprogram the adipose tissue transcriptome.

We investigated whether 2 years of CR in humans regulated core pathways previously identified from model organisms that are implicated in nutrient sensing, inflammation, and longevity (1). CR (i) increased mitochondrial biogenesis and the peroxisome proliferator activated receptor (PPAR- $\alpha$ )-driven fatty acid oxidation, including increased expression of components of insulin signaling, suggesting enhanced insulin sensitivity (Fig. 2, C and D); (ii) up-regulated proton-coupled transport of monocarboxylates such as lactate, pyruvate, and ketone bodies (Fig. 2C); (iii) induced the BMAL1 clock pathway in human adipose tissue and sumoylation (Fig. 2C), which are implicated in mediating some of CR's pro-longevity effects (17, 18); (iv) decreased the expression of components of innate immune activation such as antigen-processing pathways in lysosomes, complement cascade, and noncanonical nuclear factor- $\kappa$ B signaling; (v) decreased the expression of components of extracellular matrix deposition (Fig. 2, C and D) that may reflect lower inflammation; and (vi) increased the gene expression of flavin containing dimethylaniline monooxygenase 2 (FMO-2), an enzyme for which increased activity is associated with enhanced life span in *Caenorhabditis elegans* (19). FMO proteins (E.C.1.14.13.8 FMO-1 to FMO-5) may have overlapping functions in xenobiotic metabolism, but the relevance of FMO2 to human physiology is unclear (20) (Fig. 2E). In addition, the deconvolution of RNA-sequencing data from whole adipose tissue revealed an anti-inflammatory tissue response with a reduction of macrophage-specific transcripts (Fig. 2F). These data indicate that CR in humans elicits anti-inflammatory pathways that may improve adipose tissue metabolism.

In rodents maintained at the standard sub-thermoneutral housing temperature, CR decreases core body temperature (CBT) to elicit mitochondrial uncoupling, white adipose tissue browning, and thermogenesis to defend the CBT setpoint (1). CALERIE participants in thermoneutral settings maintained their CBT within the normal physiological range (fig. S3B). CR did not affect the transcriptional signatures of adipose tissue thermogenesis (21) (fig. S3C and Fig. 2D). The CALERIE participants also did not show any change in uncoupling protein-1 (UCP1) expression in adipose tissue (fig. S3D). Although a general signature characteristic of brown adipose tissue from the Mouse Gene Atlas (21) was up-regulated in human CR samples (fig. S3E, lower panel, and Fig. 2D), this

effect was not associated with changes in classical drivers of mitochondrial uncoupling. Thus, in healthy humans, CR does not appear to trigger adaptive thermogenesis and adipose tissue browning.

CR is known to lower inflammation (1, 6, 14). We investigated the impact of CR on gene expression in myeloid cells using bioinformatic deconvolution of adipose tissue RNA-sequencing data. Several proinflammatory-like genes and many transcripts of unknown function in myeloid cells were specifically inhibited after CR (Fig. 2G). Among the top six genes inhibited at both 1 and 2 years of CR. The phospholipase belonging to group VII A platelet activating factor acetylhydrolase (PLA2G7) is secreted by macrophages (22). PLA2G7 can degrade platelet activating factor and generate lysophosphatidylcholine (LysoPC) by degrading OxpAPC (oxidized 1-palmitoyl-2-arachidonoyl-*sn*-glycero-3-phosphatidylcholine) (22). Given that CR inhibits PLA2G7 and OxpAPC regulates inflammasome activation, we tested whether depletion of PLA2G7 influences inflammation. In mice, CRISPR-mediated deletion of *Pla2g7* (fig. S4A) resulted in its efficient ablation in activated macrophages (Fig. 3A). The control and *Pla2g7* knockout (KO) mice were born at normal Mendelian frequencies and displayed similar body weight on a chow diet (Fig. 3B and fig. S4B). PLA2G7-deficient animals were partially protected from high-fat-diet (HFD)-induced weight gain and increased fat mass (Fig. 3B). In addition, compared with their littermate controls, the *Pla2g7* KO mice were partially protected from hepatic steatosis, with reduced expression of interleukin (IL)-1 $\beta$  and caspase-1, which are implicated in controlling obesity-induced lipid metabolism and liver dysfunction (23) (Fig. 3, D and E). The reduced weight gain in *Pla2g7* KO mice corresponded with increased energy expenditure (Fig. 3, F and G). Analysis of covariance (ANCOVA) further supported that the reduction in PLA2G7 increases TDEE (Fig. 3H). PLA2G7-deficient animals had increased adipose tissue lipolysis as measured by increased concentration of glycerol and free fatty acids (Fig. 3, I and J). Consistent with improved adipose tissue metabolism, the PLA2G7-deficient MI-like macrophages had lower expression of the proinflammatory cytokines IL-6, IL-12, and tumor necrosis factor  $\alpha$  (TNF $\alpha$ ) (Fig. 3K). Middle-aged PLA2G7-deficient mice had lower serum concentrations of IL-1 $\beta$  after exposure to lipopolysaccharide (LPS) (Fig. 3L).

Chronic systemic inflammation in aging and Nlrp3 inflammasome activation is associated with age-related functional decline (24). Twenty-four-month-old *Pla2g7*<sup>-/-</sup> mice had decreased circulating concentrations of TNF- $\alpha$  and IL-1 $\beta$  without any significant change in IL-6, chemokine C-X-C motif ligand -1 (CXCL1), chemokine C-C motif ligand 2 (CCL2), or C-C motif



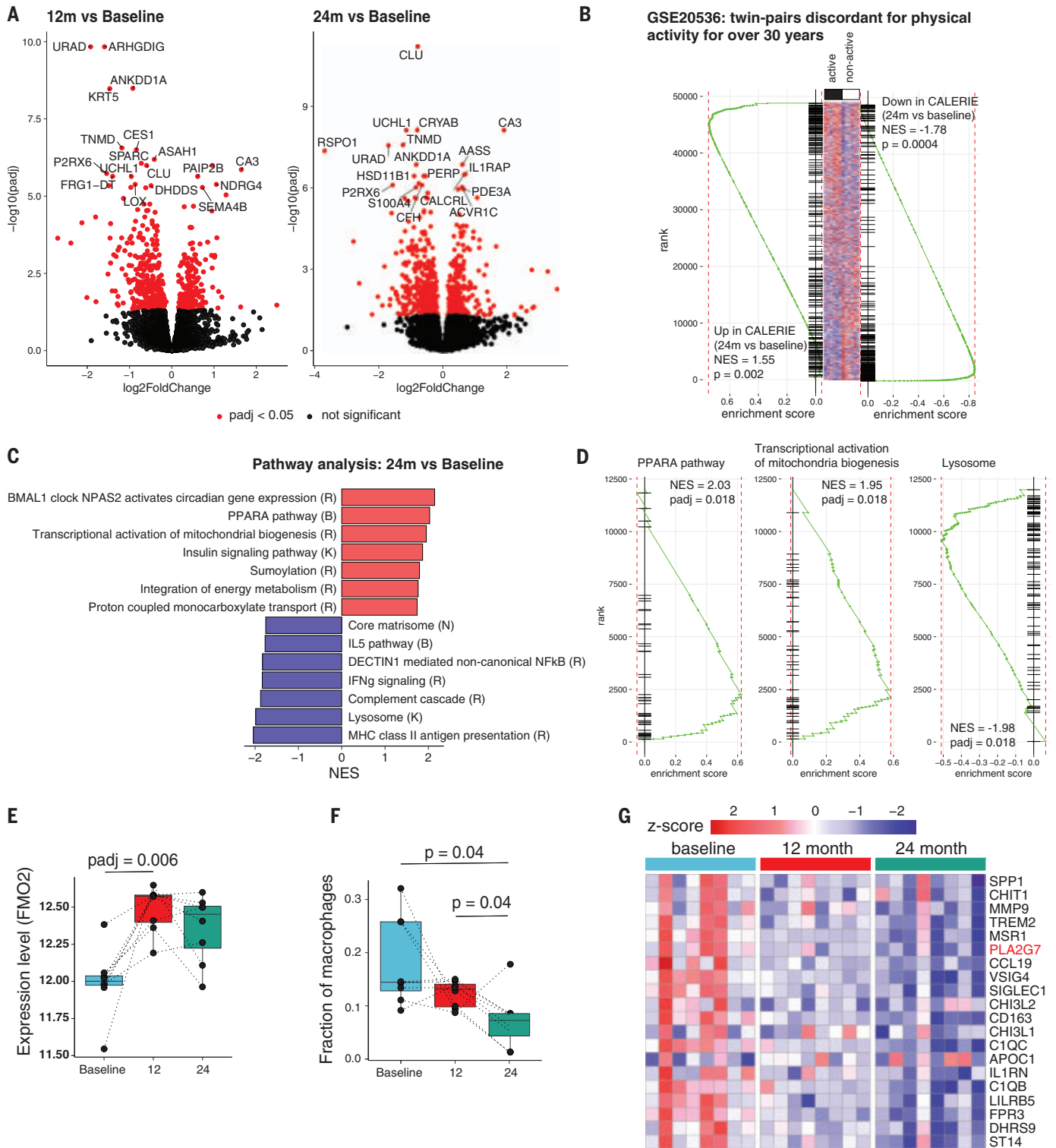


**Fig. 2. CR in humans reveals anti-aging immunometabolic checkpoints.** (A) Volcano plots depicting the results of differential gene expression analysis of adipose tissue. Each dot represents a gene. Top 18 significantly up- or down-regulated genes at 1 year (left) or 2 years (right) of CR compared with baseline ( $n = 8$ ). (B) Gene set enrichment analysis (GSEA) of genes up- and down-regulated after 2 years of CR in a signature describing differences between active and nonactive twins (GSE20536). (C) Selected pathways significantly (FDR, 5%) regulated by 2 years of CR based on GSEA. Red and blue bars indicate pathways up- and down-regulated by CR, respectively. Letters correspond to the source of

pathway gene set. K, KEGG; R, Reactome; B, BioCarta. (D) Enrichment curves for selected significantly regulated pathways. y-axis denotes rank of the gene in list ordered by log2FC. (E) Changes in the expression level of FMO-2 after CR. Adjusted  $P$  values (padj) were calculated in the differential gene expression analysis. (F) Box plots showing estimated macrophage fractions after deconvolution of adipose transcriptome in adipose tissue at baseline and 1 and 2 years after CR.  $P$  values were calculated using the paired  $t$  test. (G) Expression of genes specific to adipose tissue-resident macrophages shown at baseline and 1 and 2 years after CR. NES corresponds to the normalized enrichment score.

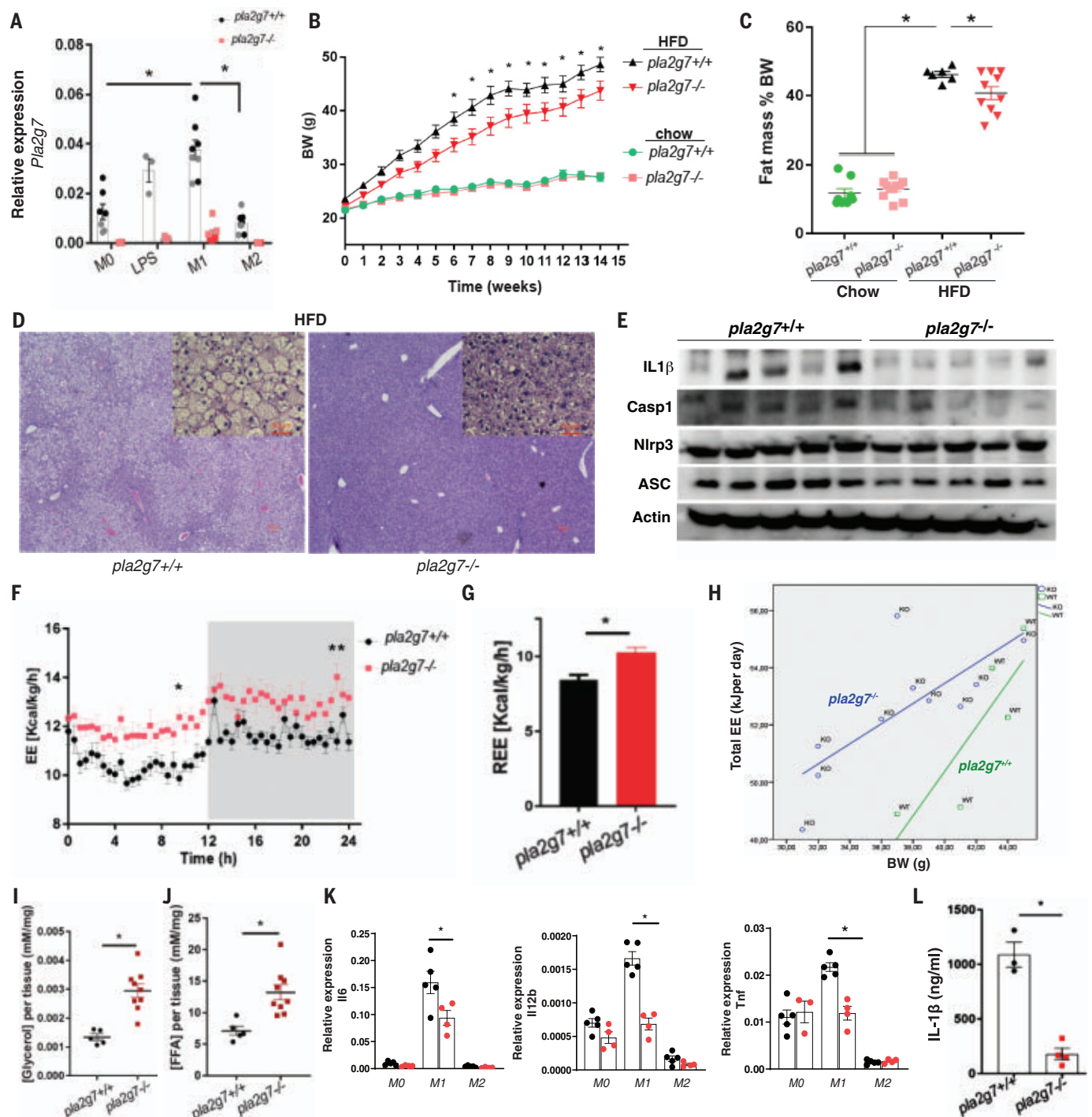


**Fig. 3. Reduction of PLA2G7 serves as anti-adiposity CR mimic.**

(A) Expression of *Pla2g7* in nonpolarized (M0) ( $n = 7$  and  $7$ , respectively), LPS-treated ( $n = 3$  and  $3$ , respectively), M1-polarized (M1) ( $n = 8$  and  $7$ , respectively), and M2-polarized (M2) ( $n = 8$  and  $7$ , respectively) bone marrow-derived macrophages (BMDMs) generated from wild-type (WT) and PLA2G7-deficient mice. (B) Body weight change of WT and PLA2G7 KO mice provided with chow diet ( $n = 8$  and  $11$ , respectively) or HFD ( $n = 8$  and  $16$ , respectively) for 14 weeks. (C) Fat composition of WT and PLA2G7 KO mice ( $n = 8$ ,  $11$ ,  $6$ , and  $10$ , respectively). (D) Representative images of livers from WT and PLA2G7 KO mice with H&E staining. Large images are  $10\times$ , small insets are  $20\times$ , and each scale bar indicates  $50\ \mu\text{m}$ . (E) Immunoblot analysis of inflammasome proteins (*IL1 $\beta$* , *Caspase 1*, *NLRP3*, and *ASC*) from livers in WT and PLA2G7-deficient mice fed with HFD. (F and G) Total daily energy expenditure (TDEE) (F) and resting energy expenditure (REE) (G) of *pla2g7<sup>+/+</sup>* and

*pla2g7<sup>-/-</sup>* mice fed with HFD ( $n = 6$  and  $10$ , respectively). (H) ANCOVA of body weight and EE of WT and PLA2G7 KO mice fed with HFD ( $n = 6$  and  $10$ , respectively). (I and J) Lipolysis assay of visceral adipose tissue from WT and PLA2G7 KO mice fed HFD to detect the release of glycerol ( $n = 5$  and  $9$ , respectively) (I) and free fatty acid ( $n = 5$  and  $9$ , respectively) (J). (K) Quantitative polymerase chain reaction (qPCR) showing the relative expression of the inflammatory genes *Il-6*, *Il-12b*, and *Tnf* to *Gapdh* in non-polarized (M0) ( $n = 5$  and  $4$ , respectively) and polarized (M1 and M2) BMDMs generated from WT and PLA2G7 KO mice. (L) Serum level of IL-1 $\beta$  in LPS-treated WT and PLA2G7 KO mice (12 months). Error bars represent the mean  $\pm$  SEM. Statistical significance was calculated by a two-tailed unpaired Student's *t* test [(G), (I), (J), and (L)] and two-way ANOVA and Holm-Sidak post hoc tests for multiple hypothesis [(A), (B), (C), and (K)]. \* $P < 0.05$ ; \*\* $P < 0.005$ ; \*\*\* $P < 0.001$ ; \*\*\*\* $P < 0.0001$ .

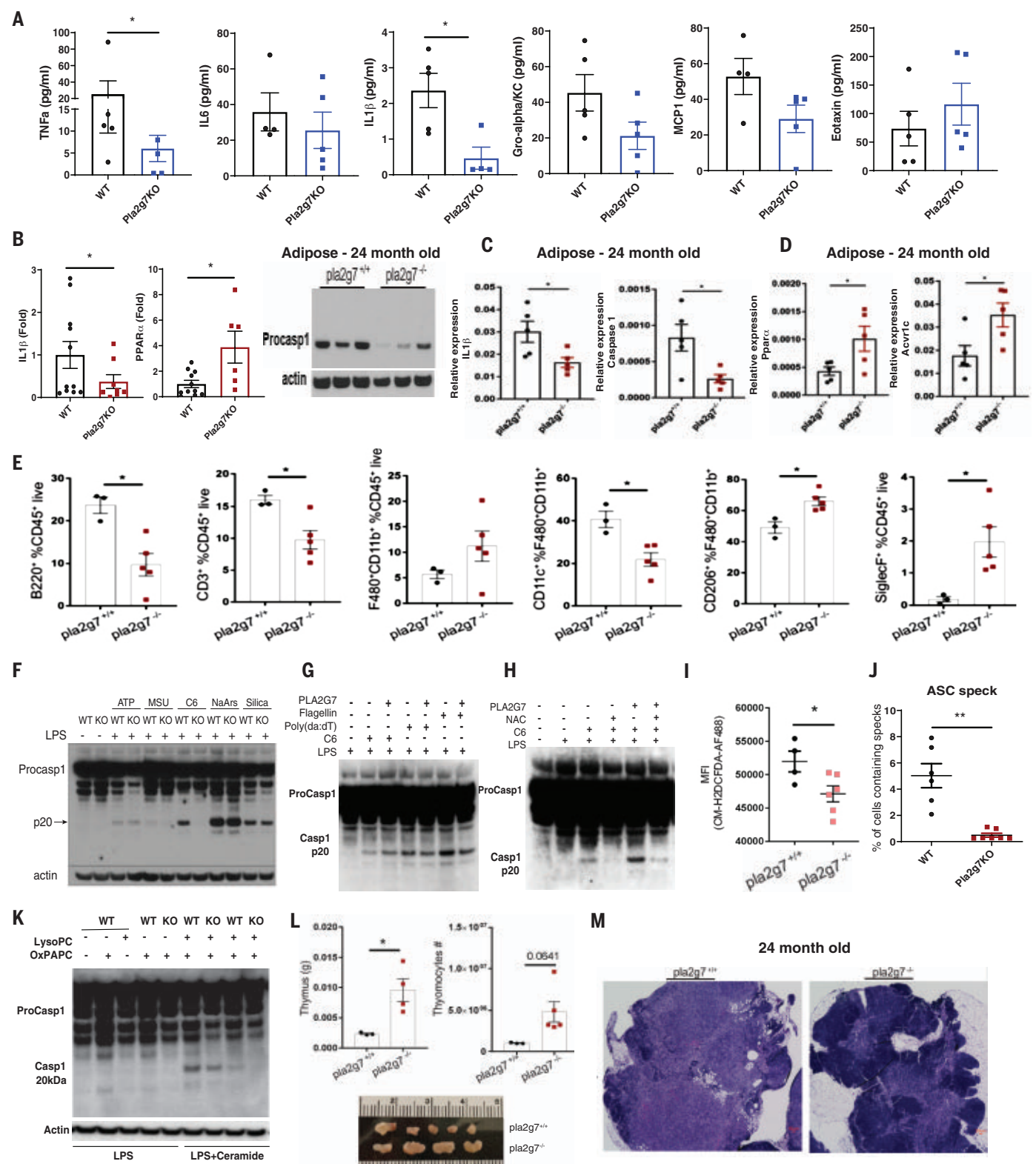


**Fig. 4. Inhibition of PLA2G7 protects against inflammaging and thymic lipodystrophy** (A) Circulating proinflammatory cytokines (TNF- $\alpha$ , IL-6, IL-1 $\beta$ , Gro- $\alpha$ /K/C, MCP-1, and Eotaxin) from serum in 24-month-old control and *Pla2g7*<sup>-/-</sup> mice (B) qPCR analysis of relative expression of *Il-1b* and *Ppara* compared with *Gapdh* in sorted F4/80<sup>+</sup> cells from visceral adipose tissues in 24-month-old control and *Pla2g7* KO mice and Caspase 1 protein expression in

the adipose tissue of 24-month-old control and *Pla2g7*<sup>-/-</sup> deficient mice ( $n = 3$  and  $3$ , respectively). (C and D) qPCR analysis of the proinflammatory genes *Il-1b* and *Casp1* in the visceral adipose tissue of control and *Pla2g7* KO mice. (C and D) The CR-regulated fatty acid oxidation inducers *Ppara* and *Acrv1c* in subcutaneous adipose tissue (SAT) of 24-month-old control (C) and *Pla2g7* KO mice ( $n = 5$ , 5) (D). (E) FACS analysis of proportions of different immune cell



populations in the adipose tissue of 24-month-old WT and *Pla2g7* KO mice.

**(F)** Representative immunoblot analysis of inflammasome activated by multiple NLRP3 activators in LPS-primed BMDMs from WT and *Pla2g7*-deficient mice. Inactive caspase-1 (48 kDa), enzymatically active caspase-1 (P20, 20kDa).

**(G)** Western blot analysis of caspase-1 in BMDMs treated with recombinant PLA2G7 (1 µg/ml) in the presence of flagellin and poly(dA:dT) to activate the NLRP3 and AIM2 inflammasomes. **(H)** Inflammasome activation measured by caspase-1 Western blot of BMDMs activated with LPS and ceramide and treated in the presence of recombinant PLA2G7 and *N*-acetyl-cysteine (NAC) (representative of three experiments).

**(I)** Mean fluorescence intensity (MFI) depicting mitochondrial ROS after ceramide-induced NLRP3 inflammasome

activation of control and *Pla2g7*-deficient BMDMs. (*n* = 4 and 6, respectively).

**(J)** Quantification of ASC speck formation in BMDMs from WT and *Pla2g7* mice activated by LPS and ceramide. **(K)** Caspase 1 expression from BMDM from control and *Pla2g7*-deficient mice activated by LPS and ceramide in the presence of OxpAPC and LysoPC. **(L)** Characterization of thymic involution of 24-month-old control WT and *Pla2g7* KO mice. Shown are thymus weight (top left) (*n* = 5), cellularity (top right) (*n* = 5), and thymic size (bottom) (*n* = 5, 4).

**(M)** H&E staining of representative thymi from 24-month-old control mice showing ectopic adipocytes and loss of corticomedullary junction in control mice and preservation of cellularity in *Pla2g7* KO mice. Error bars represent the mean ± SEM. Two-tailed unpaired *t* tests were performed for statistical analysis. \**P* < 0.05.

chemokine 11 (CCL11, also called eotaxin). Figure 4A). Furthermore, aged *Pla2g7*<sup>−/−</sup> mice displayed decreased gene expression of IL-1β, increased PPARα mRNA in adipose tissue macrophages, and reduced caspase-1 protein (Fig. 4B), with lower *Il-1b* and *Casp-1* mRNA expression in aged visceral adipose tissue (Fig. 4C). Depletion of PLA2G7 in old mice increased the expression of the *Ppara* and *Acox1c* genes (Fig. 4D), which are involved in mitochondrial fatty acid oxidation and were increased in human adipose tissue after CR. Altered abundance of visceral adipose tissue resident immune cells is implicated in inflammaging (6). Loss of PLA2G7 reduced the abundance of the B cell, T cell, and macrophage subsets (CD11c<sup>+</sup>F4/80<sup>+</sup>CD11b<sup>+</sup>), which impair adipose metabolism (6), and increased abundance of CD206<sup>+</sup>F4/80<sup>+</sup>CD11b<sup>+</sup> macrophages and eosinophils (Fig. 4E and fig. S4D), which promote tissue remodeling and responses to metabolic stresses (6).

The PLA2G7-deficient macrophages, when primed with LPS and activated by ceramides, showed reduced activation of caspase-1 (Fig. 4, F to I) and Asc speck formation (Fig. 4J and fig. S4C), which is an indicator of inflammasome assembly (23). Consistent with the role of PLA2G7 in lipid metabolism, the anti-inflammasome effects were specific to ceramides and not to other NLRP3 activators such as ATP, urate crystals, sodium arsenite, and silica particles (Fig. 4F). Neither gain of PLA2G7 (Fig. 4G) nor loss of its function in macrophages (fig. S4E) affected NLRP3 or AIM2 inflammasome activation. PLA2G7-driven ceramide-induced Nlrp3 inflammasome activation was dependent on reactive oxygen species (ROS) (Fig. 4H), and PLA2G7-deficient macrophages showed reduced ROS concentrations when activated by ceramides (Fig. 4I and fig. S4F). When exposed to oxPAPC and LysoPC and primed with LPS and ceramide, the PLA2G7-deficient macrophages showed decreased inflammasome activation (Fig. 4K). The macrophages exposed to oxPAPC or LysoPC together with recombinant PLA2G7 did not activate the inflammasome (fig. S4G). We suspect that in a tissue microenvironment such as adipose tissue, where macrophages have to process a complex mixture of lipids, PLA2G7 might be an important regu-

lator of the inflammasome. Nlrp3 inflammasome activation by ceramide is also implicated in age-related thymic involution (24). We tested whether loss of PLA2G7 mimicked the beneficial effects of CR on age-related immunological parameters such as thymic lipoatrophy. Twenty-four-month-old PLA2G7-deficient mice (analogous to ~70-year-old humans) had larger thymi and higher thymocyte abundance (Fig. 4L) and were protected from age-related thymic involution (Fig. 4M). We propose that reduction of PLA2G7 caused by CR in humans might contribute to better adipose tissue metabolism, lower inflammation, and reduced thymic lipoatrophy.

Although studies in animal models reported divergent effects on immune response, including susceptibility to infections, (2–4), the CALERIE-II analyses indicate that CR in humans over 2-year period may not decrease immunological function. Moreover, 14% sustained CR in humans reduced ectopic lipid and enhanced thymic function in a subset of healthy middle-aged humans. The data from this human study are also relevant regarding controversies emerging from animal studies that questioned CR's effects on health and inflammation (7). Collectively, our findings demonstrate that sustained CR in humans activates a core transcriptional program that promotes immune function, reduces inflammation, and reveals PLA2G7 as one of the potential mechanisms to mimic the beneficial effects of CR.

## REFERENCES AND NOTES

- R. M. Anderson, D. G. Le Couteur, R. de Cabo, *J. Gerontol. A Biol. Sci. Med. Sci.* **73**, 1–3 (2017).
- D. M. Kristan, *Aging Cell* **6**, 817–825 (2007).
- E. M. Gardner, *J. Gerontol. A Biol. Sci. Med. Sci.* **60**, 688–694 (2005).
- D. Sun, A. R. Muthukumar, R. A. Lawrence, G. Fernandes, *Clin. Diagn. Lab. Immunol.* **8**, 1003–1011 (2001).
- T. L. Kirkwood, P. Kapahi, D. P. Shanley, *J. Anat.* **197**, 587–590 (2000).
- A. H. Lee, V. D. Dixit, *Immunity* **53**, 510–523 (2020).
- J. R. Speakman, S. E. Mitchell, *Mol. Aspects Med.* **32**, 159–221 (2011).
- N. V. Patel, C. E. Finch, *Neurobiol. Aging* **23**, 707–717 (2002).
- H. L. Poetschke et al., *Carcinogenesis* **21**, 1959–1964 (2000).
- J. Rochon et al., *J. Gerontol. A Biol. Sci. Med. Sci.* **66**, 97–108 (2011).
- E. Ravussin et al., *J. Gerontol. A Biol. Sci. Med. Sci.* **70**, 1097–1104 (2015).
- W. E. Kraus et al., *Lancet Diabetes Endocrinol.* **7**, 673–683 (2019).
- H. Yang, Y. H. Youm, V. D. Dixit, *J. Immunol.* **183**, 3040–3052 (2009).

- S. N. Meydani et al., *Aging (Albany NY)* **8**, 1416–1431 (2016).
- V. D. Dixit, *Curr. Opin. Immunol.* **22**, 521–528 (2010).
- M. D. Bruss, C. F. Khambatta, M. A. Ruby, I. Aggarwal, M. K. Hellerstein, *Am. J. Physiol. Endocrinol. Metab.* **298**, E108–E116 (2010).
- S. A. Patel, A. Chaudhari, R. Gupta, N. Velingkaar, R. V. Kondratov, *FASEB J.* **30**, 1634–1642 (2016).
- L. Moll et al., *eLife* **7**, e38635 (2018).
- S. F. Leiser et al., *Science* **350**, 1375–1378 (2015).
- J. R. Cashman, J. Zhang, *Annu. Rev. Pharmacol. Toxicol.* **46**, 65–100 (2006).
- K. Shinoda et al., *Nat. Med.* **21**, 389–394 (2015).
- D. M. Stafforini, *Cardiovasc. Drugs Ther.* **23**, 73–83 (2009).
- K. V. Swanson, M. Deng, J. P. Ting, *Nat. Rev. Immunol.* **19**, 477–489 (2019).
- Y. H. Youm et al., *Cell Metab.* **18**, 519–532 (2013).

## ACKNOWLEDGMENTS

We are grateful to the study participants, investigators, and clinical support staff involved in the CALERIE study and D. K. Ingram and T. Horvath for presubmission review of this manuscript.

**Funding:** This research was supported in part by the National Institutes of Health (NIH grants AG031797, AG045712, P01AG051459, and AR070811 to V.D.D.); the Glenn Foundation for Medical Research (V.D.D.); Cure Alzheimer's Fund (V.D.D.); and the Aging Biology Foundation (M.N.A.). The CALERIE study was funded by the National Institute on Aging (grants U01AG022132, U01AG020478, U01AG020487, and U01AG020480). **Author contributions:** O.S. performed human adipose tissue and CD4 T cell RNA sequencing and all mouse experiments, analyzed data, and participated in manuscript preparation. I.S. analyzed RNA-sequencing data. Y.Y. performed experiments and data analyses for T cell TREC and the MRI study and supported the mouse phenotyping studies. S.R. performed qPCR experiments, analyzed data, and prepared the manuscript. S.S. and A.P. analyzed RNA-sequencing data. A.R. and K.N. analyzed the thymic MRI data. S.R.S. and E.R. designed the CALERIE study, were involved in experimental design and data analysis, and provided critical reviews. C.G. supervised the thymic MRI data acquisition, analysis, and interpretation. M.A. provided critical reviews and supervised the bioinformatic analyses and interpretation of the transcriptome data. All authors participated in manuscript preparation. V.D.D. conceived the project, helped with data analysis and interpretation, and wrote the manuscript. **Competing interests:** The authors declare no competing interests. **Data and materials availability:** The datasets generated in this study are available from the corresponding author on reasonable request. The RNA-sequencing data have been uploaded at SYNAPSE (www.synapse.org) with Synapse ID syn23667189.

## SUPPLEMENTARY MATERIALS

science.org/doi/10.1126/science.abg7292  
Materials and Methods  
Figs. S1 to S4  
Table S1  
References (25–32)  
MDAR Reproducibility Checklist

25 January 2021; resubmitted 30 June 2021  
Accepted 9 December 2021  
10.1126/science.abg7292

## CORONAVIRUS

# Neutralization of SARS-CoV-2 Omicron by BNT162b2 mRNA vaccine-elicited human sera

Alexander Muik<sup>1</sup>, Bonny Gaby Lui<sup>1</sup>, Ann-Kathrin Wallisch<sup>1</sup>, Maren Bacher<sup>1</sup>, Julia Mühl<sup>1</sup>, Jonas Reinholz<sup>1</sup>, Orkun Ozhelvaci<sup>1</sup>, Nina Beckmann<sup>1</sup>, Ramón de la Caridad Güimil García<sup>1</sup>, Asaf Poran<sup>2</sup>, Svetlana Shpyro<sup>1</sup>, Andrew Finlayson<sup>1</sup>, Hui Cai<sup>3</sup>, Qi Yang<sup>3</sup>, Kena A. Swanson<sup>3</sup>, Özlem Türeci<sup>1,4</sup>, Ugur Sahin<sup>1,5\*</sup>

The globally circulating severe acute respiratory syndrome coronavirus 2 (SARS-CoV-2) variant of concern Omicron (B.1.1.529) has a large number of mutations, especially in the spike protein, indicating that recognition by neutralizing antibodies may be compromised. We tested Wuhan (Wuhan-Hu-1 reference strain), Beta (B.1.351), Delta (B.1.617.2), or Omicron pseudoviruses with sera of 51 participants who received two or three doses of the messenger RNA (mRNA)-based COVID-19 vaccine BNT162b2. After two doses, Omicron-neutralizing titers were reduced >22-fold compared with Wuhan-neutralizing titers. One month after the third vaccine dose, Omicron-neutralizing titers were increased 23-fold relative to their levels after two doses and were similar to levels of Wuhan-neutralizing titers after two doses. The requirement of a third vaccine dose to effectively neutralize Omicron was confirmed with sera from a subset of participants using live SARS-CoV-2. These data suggest that three doses of the mRNA vaccine BNT162b2 may protect against Omicron-mediated COVID-19.

Since the first reports of severe acute respiratory syndrome coronavirus 2 (SARS-CoV-2) in humans in December 2019, numerous genetically distinct lineages have evolved. Among those, variants of concern (VOCs), especially the Alpha (B.1.1.7) and Delta (B.1.617.2) variants, were associated with increased viral transmissibility and sparked new waves of infection, with Delta [first designated a VOC on 11 May 2021 (1)] quickly becoming a globally dominant variant (2). On 26 November 2021, a new VOC—Omicron (B.1.1.529)—was reported by the World Health Organization (WHO) (3). Omicron is a highly divergent variant and harbors a previously unseen number of mutations in its spike (S) glycoprotein (4). Fifteen mutations are located in the receptor binding domain and another eight mutated sites are found in the N-terminal domain, both being immunodominant targets of neutralizing antibodies elicited by COVID-19 vaccines or by SARS-CoV-2 infection (5, 6). Some amino acid changes [ $\Delta$ 69/70, T95I, G142D,  $\Delta$ 145, K417N, T478K, N501Y, and P681H (T, Thr; I, Ile; G, Gly; D, Asp; K, Lys; N, Asn; Y, Tyr; P, Pro; H, His)] are shared mutations also found in the Alpha, Beta (B.1.351), Gamma (P.1), or Delta VOCs and were described to lead to increased transmissibility, as well as to a typically mild partial

escape from vaccine-induced humoral immunity (7–10).

The BNT162b2 COVID-19 mRNA vaccine contains lipid nanoparticle-formulated mRNA that encodes the SARS-CoV-2 S glycoprotein from the parental Wuhan reference strain (Wuhan-Hu-1) (11). Administration of two 30- $\mu$ g doses of BNT162b2 was shown to have 95% efficacy in a phase 3 trial (12) and to elicit strong antibody responses, effectively neutralizing the parental strain as well as diverse SARS-CoV-2 VOCs (13–15). Because neutralizing antibody titers are strongly predictive of the degree of immune protection against symptomatic SARS-CoV-2 infection (16), it is important to understand the effect of the new mutations in Omicron on recognition by neutralizing antibodies in convalescent and vaccinated individuals.

To evaluate whether BNT162b2-elicited antibodies (17) are capable of neutralizing the Omicron variant, we used two orthogonal test systems: a pseudovirus-neutralization test (pVNT) that has been shown to be in close concordance with live SARS-CoV-2-neutralization assays (17, 18), as well as a live SARS-CoV-2-neutralization test (VNT). For the former, we generated vesicular stomatitis virus (VSV)-SARS-CoV-2-S pseudoviruses bearing the S proteins of the Wuhan strain, Omicron, Beta [as a benchmark for partially reduced neutralization (7) without major impact on effectiveness (19, 20)], or Delta (the predominant strain until mid-December 2021). BNT162b2 immune sera from vaccinated individuals between 20 and 72 years of age (with more than one-third being  $\geq$ 56 years of age; table S1) were obtained from different clinical trials—the phase 1/2 trial BNT162-01 (NCT04380701), the phase 2 rollover trial BNT162-14 (NCT04949490) con-

ducted in Germany, and the global phase 2 trial BNT162-17 (NCT05004181) (see materials and methods). Neutralizing titers against VSV-SARS-CoV-2-S pseudoviruses were analyzed with serum drawn from 32 participants from the BNT162-01 trial 21 days (median of 22 days; range: 19 to 23 days) after two doses of BNT162b2 (median time from dose one to dose two: 21 days; range: 19 to 23 days; table S1) and with serum drawn from 30 participants from the BNT162-14 ( $n = 11$ ) and BNT162-17 ( $n = 19$ ) trials 1 month (median: 28 days; range: 26 to 30 days) after the third dose of BNT162b2 (median time from dose two to dose three: 219 days; range: 180 to 342 days). Eleven of the individuals in this analysis were rolled over from the BNT162-01 into the BNT162-14 trial and were included in a longitudinal analysis of neutralizing antibody responses against Wuhan or Omicron variant pseudovirus. These individuals were immunized with a third dose of BNT162b2, with sera collected (i) 21 days after the second dose (median: 21 days; range: 19 to 23 days), (ii) directly before the third dose (median: 256 days after dose two; range: 180 to 342 days), and (iii) 1 month (28 days) after the third dose.

After two doses of BNT162b2, geometric mean neutralization titers (GMTs) against Omicron pseudovirus were reduced 22.8-fold compared with those for the Wuhan reference pseudovirus (Fig. 1; GMT of 7 versus 160). Twenty of 32 immune serum specimens displayed no detectable neutralizing activity against Omicron (table S2). By contrast, the majority of sera neutralized Beta and Delta pseudoviruses with GMTs of 24 and 73, respectively. This corresponds to 6.7- and 2.2-fold reductions in neutralization activity compared with the Wuhan pseudovirus and is in line with previous reports (11, 14, 15, 21).

One month after the third BNT162b2 dose, neutralizing GMTs against the Omicron variant pseudovirus increased 23.4-fold relative to their levels 21 days after the second dose (GMT of 164 versus 7) and were comparable to neutralizing GMTs against the reference Wuhan pseudovirus at 21 days after two doses of BNT162b2 (GMT of 164 versus 160). Twenty-nine of 30 serum specimens were capable of neutralizing the Omicron pseudovirus (table S3). The third dose of BNT162b2 also increased neutralizing activity against Beta, Delta, and Wuhan pseudoviruses, with GMTs of 279, 413, and 368, respectively.

For 11 individuals included in the aforementioned analyses, a longitudinal analysis of neutralizing titers against Omicron and Wuhan pseudovirus was performed. Twenty-one days after dose two, sera exhibited a 21.4-fold reduction in GMT against the Omicron variant compared with the Wuhan reference pseudovirus (fig. S1; GMT of 7 versus 150). Before receiving the third dose of BNT162b2 (at a

<sup>1</sup>BioNTech, An der Goldgrube 12, 55131 Mainz, Germany.

<sup>2</sup>BioNTech US, 40 Erie Street, Cambridge, MA 02139, USA.

<sup>3</sup>Pfizer, 401 N Middletown Rd., Pearl River, NY 10960, USA.

<sup>4</sup>HI-TRON – Helmholtz Institute for Translational Oncology Mainz by DKFZ, Obere Zahlbacherstr. 63, 55131 Mainz, Germany.

<sup>5</sup>TRON gGmbH – Translational Oncology at the University Medical Center of the Johannes Gutenberg University, Freiligrathstraße 12, 55131 Mainz, Germany.

\*Corresponding author. Email: ugur.sahin@biontech.de

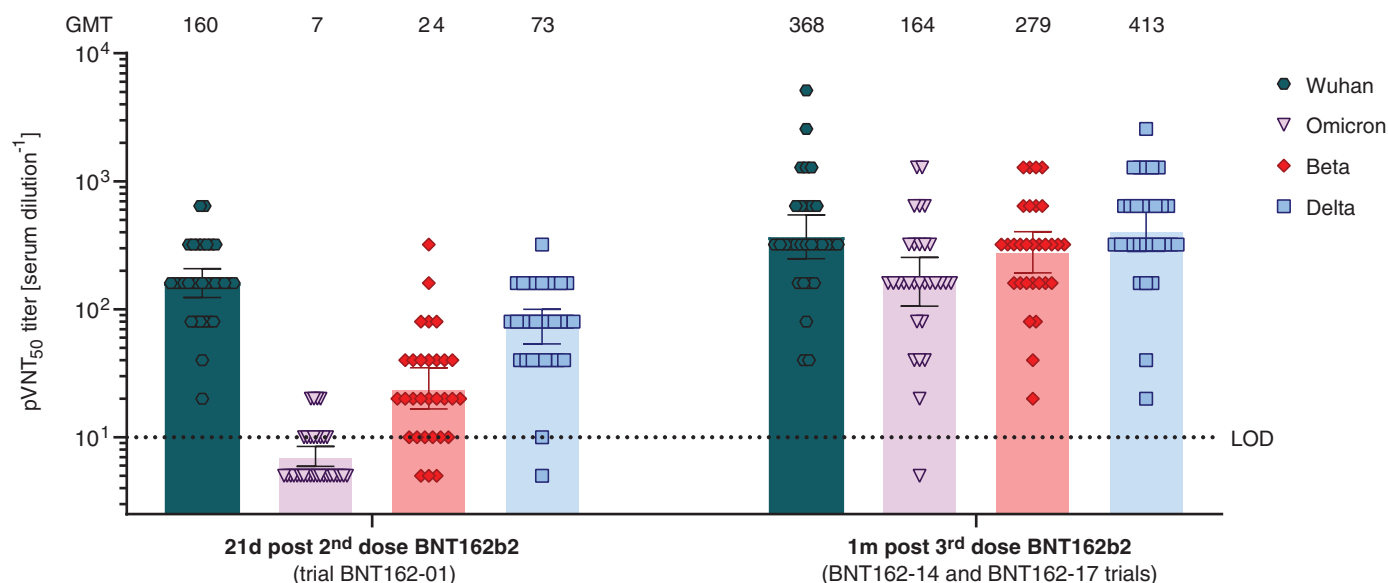
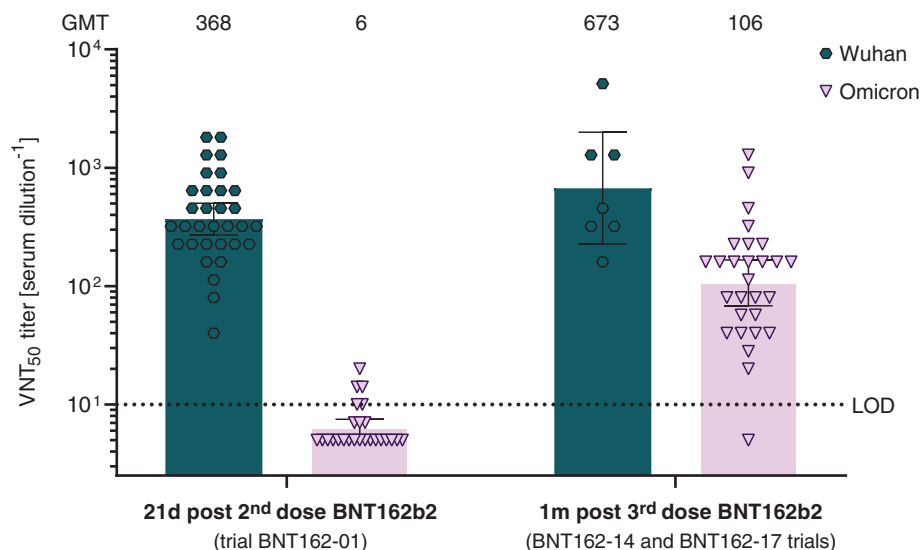


**Fig. 1. 50% pseudovirus-neutralization titers (pVNT<sub>50</sub>) of sera from vaccine recipients, collected after two or three doses of BNT162b2 against VSV-SARS-CoV-2-S pseudovirus bearing the Wuhan, Omicron, Beta, or Delta variant S protein.** *N* = 32 serum specimens from participants in trial BNT162-01, drawn 21 days after dose two, and *n* = 30 serum specimens from

participants in the BNT162-14 (*n* = 11) and BNT162-17 (*n* = 19) trials, drawn 1 month after dose three, were tested. Each specimen was tested in duplicate, and geometric mean 50% pseudovirus-neutralizing titers (GMTs) were plotted. Below the limit of detection (LOD), LOD/2 values were plotted. Group GMTs (values) and 95% confidence intervals are indicated.

**Fig. 2. 50% live SARS-CoV-2-neutralization titers (VNT<sub>50</sub>) of sera from vaccine recipients, collected after two or three doses of BNT162b2.**

Sera from participants in trial BNT162-01, drawn 21 days after dose two, were tested for neutralization against SARS-CoV-2 Wuhan (*n* = 32) and Omicron (*n* = 25), respectively. Sera from participants in the BNT162-14 and BNT162-17 trials, drawn 1 month after dose three, were tested for neutralization against SARS-CoV-2 Wuhan (*n* = 7 from BNT162-14) and Omicron (total *n* = 28: 11 from BNT162-14 and 17 from BNT162-17), respectively. Each specimen was tested in duplicate, and geometric mean 50% SARS-CoV-2-neutralizing titers (GMTs) were plotted. Below the limit of detection (LOD), LOD/2 values were plotted. Group GMTs (values) and 95% confidence intervals are indicated.



median 256 days after dose two), neutralizing titers against the Wuhan pseudovirus were considerably reduced (GMT of 13), whereas the Omicron-specific titers were below the limit of detection. Consistent with the larger serum panel, the third dose of BNT162b2 resulted in a significant increase in neutralizing titers against the Wuhan pseudovirus (GMT of 320) and a 25.8-fold increase in neutralizing titers against Omicron 1 month after dose three compared with 21 days after dose two (GMT of 181 versus 7).

Sera from a subset of trial participants were analyzed with the second neutralization assay using live SARS-CoV-2 Wuhan and Omicron virus. Serum samples from 32 and 25 participants in trial BNT162-01, drawn 21 days after dose two, and from 7 and 28 participants in the BNT162-14 (*n* = 7 and 11) and BNT162-17 (*n* = 0 and 17) trials, drawn 1 month after dose three, were tested for neutralization against SARS-CoV-2 Wuhan and Omicron, respectively. Neutralizing GMTs against live SARS-CoV-2 Omicron were reduced 61.3-fold relative

to those against the Wuhan reference strain (Fig. 2; GMT of 6 versus 368) at 21 days after two doses of BNT162b2. Seventeen of 25 serum specimens displayed no detectable neutralizing activity against Omicron (table S4). One month after the third BNT162b2 dose, neutralizing GMTs against Omicron were increased 17.6-fold compared with neutralizing GMTs at 21 days after the second dose (GMT of 106 versus 6) and were reduced 3.4-fold compared with those against the Wuhan reference at 21 days after two doses of BNT162b2



(GMT of 106 versus 368). Twenty-seven of 28 post-dose three serum specimens neutralized live SARS-CoV-2 Omicron (table S5).

The observed SARS-CoV-2-neutralizing GMTs correlated positively with the neutralizing GMTs against VSV-SARS-CoV-2-S pseudoviruses (fig. S2).

BNT162b2 vaccination induces strong poly-epitopic T cell responses, directed against multiple epitopes spanning the length of the S protein (11). To assess the risk of immune evasion of CD8<sup>+</sup> T cell responses by Omicron, we investigated a set of human leukocyte antigen class I-restricted T cell epitopes from the Wuhan S protein sequence that were reported as immunogenic in the Immune Epitope Database (IEDB) ( $n = 244$ ; see materials and methods). Despite the multitude of mutations in the Omicron S protein, 85.3% ( $n = 208$ ) of the described class I epitopes were not affected on the amino acid sequence level, indicating that the targets of most T cell responses elicited by BNT162b2 may still be conserved in the Omicron variant (fig. S3).

In summary, our data indicate that two doses of the BNT162b2 mRNA vaccine may not be sufficient to protect against infection with the Omicron variant. In both neutralization assay platforms, we observed a substantial reduction in neutralizing activity for immune sera drawn 21 days after the primary two-dose series of BNT162b2, confirming preliminary reports that describe a 20- to 40-fold reduction in titers (22, 23). Both assays also showed that a third dose of BNT162b2 boosts Omicron-neutralization capability to robust levels. In the pseudovirus assay, Omicron-neutralization titers after three doses reach a level similar to that observed for Wuhan-neutralizing titers after two doses, whereas in the live SARS-CoV-2 assay, Omicron-neutralizing GMTs after dose three were reduced 3.4-fold relative to Wuhan-neutralizing GMTs after two doses. The observed variability in specific titers and fold differences between nonreplicating pseudovirus- and replicating live virus-neutralization assay platforms as well as different SARS-CoV-2 strains are not unexpected. Notably, the overall trends are similar and demonstrate that a third dose of BNT162b2 augments antibody-based immunity against Omicron, in line with previous observations that a third vaccination broadens humoral immune responses against VOCs (24).

In the analysis presented here, we have evaluated and compared serum panels from different clinical trials with a limited sample size. For BNT162-01 trial participants, the first two doses of BNT162b2 were separated by 21 days (median: 21 days; range: 19 to 23 days), but the time elapsed between the second and third doses was not consistent across participants.

Recent reports indicate that a longer interval (>42 days) between the first and second doses improves immunogenicity, potentially resulting in a more favorable outcome (25). Future analyses are needed to evaluate antibody persistence.

Neutralizing antibodies represent a first layer of adaptive immunity against COVID-19. T cell responses play a vital role as a second layer of defense, in particular in the prevention of severe COVID-19 (26). CD8<sup>+</sup> T cell responses in individuals vaccinated with BNT162b2 are polyepitopic (11), and our analyses suggest that CD8<sup>+</sup> T cell recognition of Omicron S glycoprotein epitopes is largely preserved. Our data show that a third BNT162b2 dose effectively neutralizes Omicron at a similar order of magnitude to that observed for wild-type SARS-CoV-2 after two doses of BNT162b2. Early reports estimate moderate to high vaccine effectiveness against symptomatic Omicron infection, especially shortly after dose three: In the UK, 65 to 75% effectiveness has been reported 2 to 4 weeks after the booster dose, dropping to 55 to 70% at 5 to 9 weeks and below 55% >10 weeks after the third dose (27, 28). Further clinical trial and real-world data will soon emerge to elucidate the effectiveness of a third dose of BNT162b2 against COVID-19 caused by the Omicron variant.

## REFERENCES AND NOTES

1. WHO, Tracking SARS-CoV-2 variants; [www.who.int/en/activities/tracking-SARS-CoV-2-variants/](http://www.who.int/en/activities/tracking-SARS-CoV-2-variants/).
2. WHO, "SARS-CoV-2 Delta variant now dominant in much of European region; efforts must be reinforced to prevent transmission," warns WHO Regional Office for Europe and ECDC" (2021); [www.euro.who.int/en/media-centre/sections/press-releases/2021/sars-cov-2-delta-variant-now-dominant-in-much-of-european-region-efforts-must-be-reinforced-to-prevent-transmission,-warns-who-regional-office-for-europe-and-ecdc](http://www.euro.who.int/en/media-centre/sections/press-releases/2021/sars-cov-2-delta-variant-now-dominant-in-much-of-european-region-efforts-must-be-reinforced-to-prevent-transmission,-warns-who-regional-office-for-europe-and-ecdc).
3. WHO Technical Advisory Group on SARS-CoV-2 Virus Evolution (TAG-VE), "Classification of Omicron (B.1.1.529): SARS-CoV-2 Variant of Concern" (2021); [www.who.int/news/item/26-11-2021-classification-of-omicron-\(b.1.1.529\)-sars-cov-2-variant-of-concern](http://www.who.int/news/item/26-11-2021-classification-of-omicron-(b.1.1.529)-sars-cov-2-variant-of-concern).
4. WHO Headquarters, WHO Health Emergencies Programme, "Enhancing Readiness for Omicron (B.1.1.529): Technical Brief and Priority Actions for Member States" (2021); [www.who.int/publications/m/item/enhancing-readiness-for-omicron-\(b.1.1.529\)-technical-brief-and-priority-actions-for-member-states](http://www.who.int/publications/m/item/enhancing-readiness-for-omicron-(b.1.1.529)-technical-brief-and-priority-actions-for-member-states).
5. L. Premkumar et al., *Sci. Immunol.* **5**, eabc8413 (2020).
6. W. T. Harvey et al., *Nat. Rev. Microbiol.* **19**, 409–424 (2021).
7. P. Wang et al., *Nature* **593**, 130–135 (2021).
8. D. Planas et al., *Nature* **596**, 276–280 (2021).
9. Q. Wang et al., *iScience* **24**, 103393 (2021).
10. A. J. Greaney et al., *Cell Host Microbe* **29**, 44–57.e9 (2021).
11. U. Sahin et al., *Nature* **595**, 572–577 (2021).
12. F. P. Polack et al., *N. Engl. J. Med.* **383**, 2603–2615 (2020).
13. A. Muik et al., *Science* **371**, 1152–1153 (2021).
14. J. Liu et al., *Nature* **596**, 273–275 (2021).
15. Y. Liu et al., *N. Engl. J. Med.* **384**, 1466–1468 (2021).
16. D. S. Khoury et al., *Nat. Med.* **27**, 1205–1211 (2021).
17. J. B. Case et al., *Cell Host Microbe* **28**, 475–485.e5 (2020).
18. A. B. Vogel et al., *Nature* **592**, 283–289 (2021).

19. L. J. Abu-Raddad, H. Chemaitelly, A. A. Butt; National Study Group for COVID-19 Vaccination, *N. Engl. J. Med.* **385**, 187–189 (2021).
20. O. Mor et al., *J. Clin. Epidemiol.* **142**, 38–44 (2022).
21. A. Kuzmina et al., *iScience* **24**, 103467 (2021).
22. S. Cele et al., *medRxiv* 2021.12.08.21267417 [Preprint] (2021); <https://doi.org/10.1101/2021.12.08.21267417>.
23. A. Wilhelm et al., *medRxiv* 2021.12.07.21267432 [Preprint] (2021); <https://doi.org/10.1101/2021.12.07.21267432>.
24. A. R. Falsey et al., *N. Engl. J. Med.* **385**, 1627–1629 (2021).
25. B. Brunau et al., *JAMA* **327**, 279–281 (2022).
26. A. Bertoletti, N. Le Bert, M. Qui, A. T. Tan, *Cell. Mol. Immunol.* **18**, 2307–2312 (2021).
27. UK Health Security Agency, "SARS-CoV-2 variants of concern and variants under investigation in England - Technical briefing: Update on hospitalisation and vaccine effectiveness for Omicron VOC-21NOV-01 (B.1.1.529)" (2021); [https://assets.publishing.service.gov.uk/government/uploads/system/uploads/attachment\\_data/file/1044481/Technical-Briefing-31-Dec-2021-Omicron\\_severity\\_update.pdf](https://assets.publishing.service.gov.uk/government/uploads/system/uploads/attachment_data/file/1044481/Technical-Briefing-31-Dec-2021-Omicron_severity_update.pdf).
28. N. Ferguson et al., "Report 49: Growth, population distribution and immune escape of Omicron in England" (Imperial College London, 2021); <https://doi.org/10.25561/93038>.

## ACKNOWLEDGMENTS

We thank the BioNTech German clinical phase 1/2 trial (NCT04380701, EudraCT: 2020-001038-36), the German phase 2 rollover booster trial (NCT04949490, EudraCT: 2021-002387-50), and the global clinical phase 2 trial (NCT04380701) participants, from whom the postimmunization human sera were obtained. We thank the many colleagues at BioNTech and Pfizer who developed and produced the BNT162b2 mRNA vaccine candidate. We thank S. Jägle for logistical support; B. Huang for support in generating fig. S4; the VisMederi team for work on live virus-neutralizing antibody assays; and C. Heiser, A. Telorman, K. Krüger, C. Müller, A. Wanamaker, N. Williams, and J. VanCamp for sample demographics support. **Funding:** This work was supported by BioNTech and Pfizer. **Author contributions:** U.S., Ö.T., and A.M. conceived and conceptualized the work. A.M., B.G.L., J.R., H.C., Q.Y., K.A.S., and R.C.G.G. planned and supervised experiments. A.M., A.-K.W., B.G.L., J.M., J.R., M.B., N.B., and R.C.G.G. performed experiments. A.M., A.P., B.G.L., J.R., K.A.S., O.O., R.C.G.G., and S.S. analyzed data. U.S., Ö.T., A.M., A.F., and K.A.S. interpreted data and wrote the manuscript. All authors supported the review of the manuscript. **Competing interests:** U.S. and Ö.T. are management board members and employees at BioNTech SE. A.F., A.M., A.-K.W., B.G.L., J.M., J.R., M.B., N.B., O.O., S.S., and R.C.G.G. are employees at BioNTech SE. A.P. is an employee at BioNTech US. U.S., Ö.T., H.C., Q.Y., K.A.S., and A.M. are inventors on patents and patent applications related to RNA technology and COVID-19 vaccine. U.S., Ö.T., N.B., A.F., A.M., A.P., A.-K.W., B.G.L., J.M., O.O., J.R., S.S., and R.C.G.G. have securities from BioNTech SE; H.C., Q.Y., and K.A.S. are employees at Pfizer and may have securities from Pfizer. **Data and materials availability:** All data are available in the main manuscript or the supplementary materials. Trial participant baseline characteristics are provided in table S1. The neutralization titers are provided in tables S2 to S5. Materials are available from the authors under a material transfer agreement with BioNTech. This work is licensed under a Creative Commons Attribution 4.0 International (CC BY 4.0) license, which permits unrestricted use, distribution, and reproduction in any medium, provided the original work is properly cited. To view a copy of this license, visit <https://creativecommons.org/licenses/by/4.0/>. This license does not apply to figures/photos/artwork or other content included in the article that is credited to a third party; obtain authorization from the rights holder before using such material.

## SUPPLEMENTARY MATERIALS

[science.org/doi/10.1126/science.abn7591](https://science.org/doi/10.1126/science.abn7591)  
Materials and Methods  
Figs. S1 to S4  
Tables S1 to S5  
References (29–32)  
MDAR Reproducibility Checklist

20 December 2021; accepted 11 January 2022  
Published online 18 January 2022  
10.1126/science.abn7591

## SPATIAL EPIGENOMICS

## Spatial-CUT&amp;Tag: Spatially resolved chromatin modification profiling at the cellular level

Yanxiang Deng<sup>1,2</sup>, Marek Bartosovic<sup>3</sup>, Petra Kukanja<sup>3</sup>, Di Zhang<sup>1</sup>, Yang Liu<sup>1,2</sup>, Graham Su<sup>1,2</sup>, Archibald Enninfu<sup>1,2</sup>, Zhiliang Bai<sup>1</sup>, Gonçalo Castelo-Branco<sup>3,4</sup>, Rong Fan<sup>1,2,5\*</sup>

Spatial omics emerged as a new frontier of biological and biomedical research. Here, we present spatial-CUT&Tag for spatially resolved genome-wide profiling of histone modifications by combining in situ CUT&Tag chemistry, microfluidic deterministic barcoding, and next-generation sequencing. Spatially resolved chromatin states in mouse embryos revealed tissue-type-specific epigenetic regulations in concordance with ENCODE references and provide spatial information at tissue scale. Spatial-CUT&Tag revealed epigenetic control of the cortical layer development and spatial patterning of cell types determined by histone modification in mouse brain. Single-cell epigenomes can be derived in situ by identifying 20-micrometer pixels containing only one nucleus using immunofluorescence imaging. Spatial chromatin modification profiling in tissue may offer new opportunities to study epigenetic regulation, cell function, and fate decision in normal physiology and pathogenesis.

Chromatin state determines genome function and is regulated in a cell-type-specific manner (1, 2). Despite recent breakthroughs in single-cell sequencing (3–5) that have enabled the profiling of the epigenome in single cells (6–11), it remains challenging to integrate the spatial information of individual cells in the tissue of origin. Here, we report spatial-CUT&Tag for spatial histone modification profiling, which combines in-tissue deterministic barcoding (12, 13) with the cleavage under targets and tagmentation (CUT&Tag) chemistry (14, 15) (Fig. 1A and fig. S1). First, antibody against the target histone modification was added to a fixed tissue section, followed by a secondary antibody binding to enhance the tethering of pA-Tn5 transposome. After activating the transposome, adapters containing a ligation linker were inserted to genomic DNA at the histone mark antibody recognition sites. Next, a set of DNA barcode solutions  $A_i$  ( $i = 1$  to 50) were flowed over the tissue surface through microchannel-guided delivery to perform in situ ligation to the adapters. Next, a second set of barcodes  $B_j$  ( $j = 1$  to 50) were flowed over the same tissue surface through microchannels perpendicular to those in the first barcoding step. These barcodes were then ligated at the intersections, resulting in a two-dimensional (2D) grid of tissue pixels, each of which contains a distinct combination of barcodes  $A_i$  and  $B_j$  ( $i = 1$  to 50,  $j = 1$  to 50). The tissue

section was imaged after these steps to correlate the tissue morphology with the spatial epigenomics map. Finally, DNA fragments were collected by cross-link reversal to complete library construction (see the supplemental materials and methods).

We performed spatial-CUT&Tag with antibodies against H3K27me3 (repressing loci), H3K4me3 (activating promoters), and H3K27ac (activating enhancers and/or promoters) in embryonic day 11 (E11) mouse embryos. With 50- $\mu$ m pixel size, we obtained a median of 9788 (H3K27me3), 16,777 (H3K4me3), or 19,721 (H3K27ac) unique fragments per pixel, of which 16% (H3K27me3), 67% (H3K4me3), or 16% (H3K27ac) of fragments fell within peak regions, indicating high coverage and low background [as a reference, the fraction of reads in peaks (FRiP) of bulk CUT&Tag of E11 mouse embryo with H3K27me3 was ~24%] (Fig. 1, B and C). In addition, the proportion of mitochondrial fragments is low [a median of 0.16% (H3K27me3), 0.13% (H3K4me3), or 0.01% (H3K27ac) of fragments was from mitochondrial reads] (Fig. 1D). With a 20- $\mu$ m pixel size (cellular level), we obtained a median of 10,064 (H3K27me3), 7310 (H3K4me3), or 13,171 (H3K27ac) unique fragments per pixel, of which 20% (H3K27me3), 37% (H3K4me3), or 12% (H3K27ac) of fragments fell within peak regions (Fig. 1, B and C). The fractions of read-pairs mapping to mitochondria were 0.01% (H3K27me3), 0.02% (H3K4me3), or 0% (H3K27ac) (Fig. 1D). Additionally, the fragment length distribution was consistent with the capture of nucleosomal and subnucleosomal fragments (the subnucleosomal fragments may represent background signal from untethered Tn5) (fig. S2). To measure the extent of tagmentation by free Tn5, we compared the spatial-CUT&Tag H3K27me3 signals with reference chromatin immunoprecipitation sequencing (ChIP-seq) and assay for transposase-

accessible chromatin using sequencing (ATAC-seq) (2). The results showed that ~11.5% of peaks that did not overlap with ChIP-seq were observed in ATAC-seq (fig. S3), which may correspond to the Tn5 insertion events unrelated to the histone mark (16).

We compared spatial-CUT&Tag at the 20- $\mu$ m pixel size with published single-cell CUT&Tag (scCUT&Tag) also on mouse brain at the same sequencing depth (8) and found that spatial-CUT&Tag detected more unique fragments (H3K27me3: 9735; H3K4me3: 3686) than scCUT&Tag (H3K27me3: 682; H3K4me3: 453) (Fig. 1B). We also isolated tissue pixels containing single nuclei that showed similar unique fragment counts compared with scCUT&Tag. However, the FRiP from spatial-CUT&Tag (H3K27me3: 10%; H3K4me3: 53%) was lower than that from scCUT&Tag (H3K27me3: 24%; H3K4me3: 82%) (Fig. 1C), presumably because of the use of frozen sections, which has been reported to affect chromatin structures and generate higher background noise (17).

The Pearson correlation coefficient from different spatial-CUT&Tag experiments was >0.95 (fig. S4, A to F), demonstrating a high degree of reproducibility. Spatial-CUT&Tag also reproduced the chromatin state pattern and peaks (fig. S4, G to I). Furthermore, the peaks called from spatial-CUT&Tag aggregate data were consistent with the ENCODE ChIP-seq data (fig. S5A). Spatial-CUT&Tag also yielded high-quality profiles in the liver comparable to the reference data (fig. S5B).

Cell types were identified de novo by chromatin states. Mapping the clusters back to spatial locations identified spatially distinct patterns that agreed with the tissue histology in a hematoxylin and eosin (H&E)-stained adjacent tissue section (Fig. 1, E to G, and fig. S6). Cluster 1 of H3K27me3 and cluster 6 of H3K4me3 correspond to the heart; cluster 2 of H3K27me3 and H3K4me3 and cluster 4 of H3K27ac correspond to the liver region; cluster 8 of H3K27me3, cluster 3 of H3K4me3, and cluster 1 of H3K27ac correspond to the forebrain; cluster 9 of H3K27me3, cluster 5 of H3K4me3, and cluster 3 of H3K27ac correspond to the brainstem, including the mid-brain; and cluster 11 of H3K27me3, cluster 8 of H3K4me3, and cluster 2 of H3K27ac correspond to the more posterior regions of the central nervous system (CNS) such as the spinal cord.

To benchmark spatial-CUT&Tag, we projected the organ-specific ChIP-seq data onto our uniform manifold approximation and projection (UMAP) embedding (2, 18). Overall, cluster identification matched well with the ChIP-seq projection (Fig. 1, G and H) and distinguished major cell types in E11 mouse embryo. To identify spatial patterning during development, we examined cell-type-specific marker genes. For H3K27me3, the chromatin

<sup>1</sup>Department of Biomedical Engineering, Yale University, New Haven, CT 06520, USA. <sup>2</sup>Yale Stem Cell Center and Yale Cancer Center, Yale School of Medicine, New Haven, CT 06520, USA. <sup>3</sup>Laboratory of Molecular Neurobiology, Department of Medical Biochemistry and Biophysics, Karolinska Institutet, 17177 Stockholm, Sweden. <sup>4</sup>Ming Wai Lau Centre for Reproductive Medicine, Karolinska Institutet, 17177 Stockholm, Sweden. <sup>5</sup>Human and Translational Immunology Program, Yale School of Medicine, New Haven, CT 06520, USA.

\*Corresponding author. Email: rong.fan@yale.edu



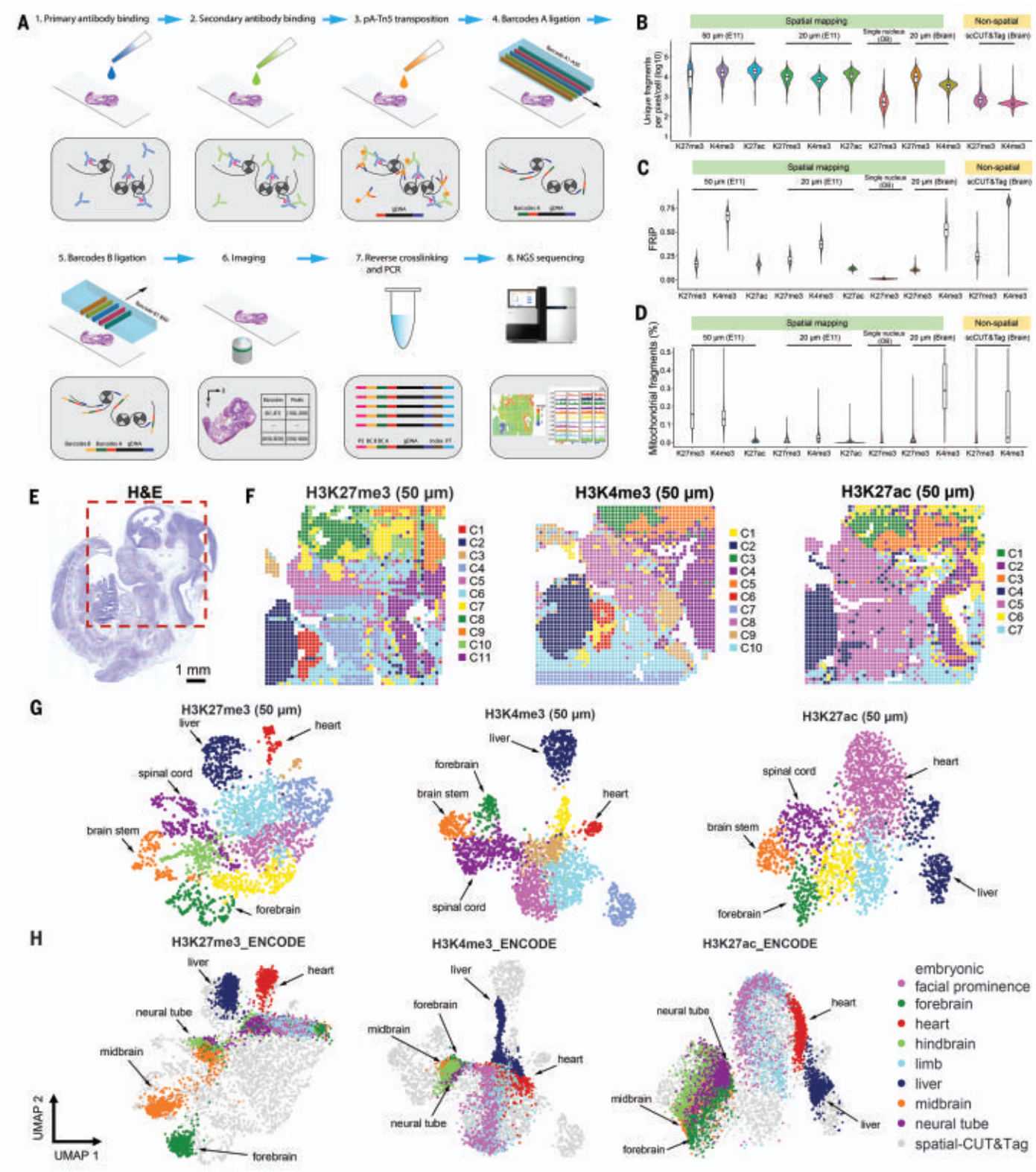


**Fig. 1. Spatial-CUT&Tag: design and validation.** (A) Schematic workflow. (B to D) Comparison of unique fragments, FRiP, and mitochondrial reads between our spatial method and other nonspatial methods. OB, olfactory bulb. (E) H&E-stained image from an adjacent tissue section of E11 mouse embryo and a region of interest for spatial mapping. (F and G) Spatial distribution (F) and UMAP (G) of unsupervised clustering analysis. (H) Projection of ENCODE ChIP-seq data onto the spatial-CUT&Tag embedding.



silencing score (CSS) was calculated to predict the gene expression (9), and active genes should have a low CSS because of the lack of an H3K27me<sub>3</sub>-repressive mark (Fig. 2A and fig. S7A). For example, *Hand2*, which is required for vascular development and plays an essential role in cardiac morphogenesis (19), showed a lack of H3K27me<sub>3</sub> enrichment in the heart (C1). For H3K4me<sub>3</sub> and H3K27ac, gene activity score (GAS) was used because they are related to active genes (Fig. 2B and figs. S8A and S10A). For example, *Nfe2l*, which is essential for regulating erythroid and hematopoietic cell maturation and differentiation (19), was active in liver and to some extent in the heart (C2 and C6 for H3K4me<sub>3</sub>). We further analyzed Gene Ontology (GO) pathways, and the results agreed with the anatomical annotation (figs. S7B, S8B, and S10B). To understand which regulatory factors are most active across clusters, we calculated transcription factor (TF) motif enrichments in

H3K4me<sub>3</sub> and H3K27ac modification loci (figs. S9 and S11). As expected, the most enriched motifs in liver correspond to GATA transcription factors including *Gata2*, whereas *Mef2a* was enriched in the heart region. To predict the gene-regulatory interactions of enhancers and their target genes across clusters, we correlated gene expression from single-cell RNA-sequencing (scRNA-seq) (5) and H3K27ac modifications at the candidate enhancers (Fig. 2C). The correlation-based map successfully predicted some enhancer-gene interactions that have been experimentally validated. For example, the predicted enhancers of *Ascl1* and *Kcnq3* were enriched in the CNS (C1, C2, C3, and C6), which is in agreement with the VISTA validated elements (20).

We then integrated scRNA-seq data (5) with spatial-CUT&Tag data to identify cell types (Fig. 2, D to H, and fig. S12). Spatial tissue pixels were found to conform well into the clusters of single-cell transcriptomes. Sev-

eral organ-specific cell types were detected (Fig. 2, E and G). For example, the definitive erythroid lineage cells were exclusively enriched in the liver, which is the major hematopoietic organ at day 11.5 (19). Cardiac muscle cell types were observed only in the heart region in agreement with the anatomical annotation. Chondrocytes and osteoblasts were observed widely in the embryonic facial prominence. Inhibitory interneurons were highly enriched in the brain stem. Postmitotic premature neurons were observed extensively in the spinal cord region. A high-resolution clustering further identified subpopulations of developing neurons with distinct spatial distributions and chromatin states (Fig. 2I and fig. S12B). For instance, the H3K27ac radial glia could be further divided to three clusters. Genes related to stem cell maintenance in the CNS (e.g., *Sox2*) had higher GAS in subcluster 2, which was enriched along the ventricles in the developing brain stem and spinal cord.

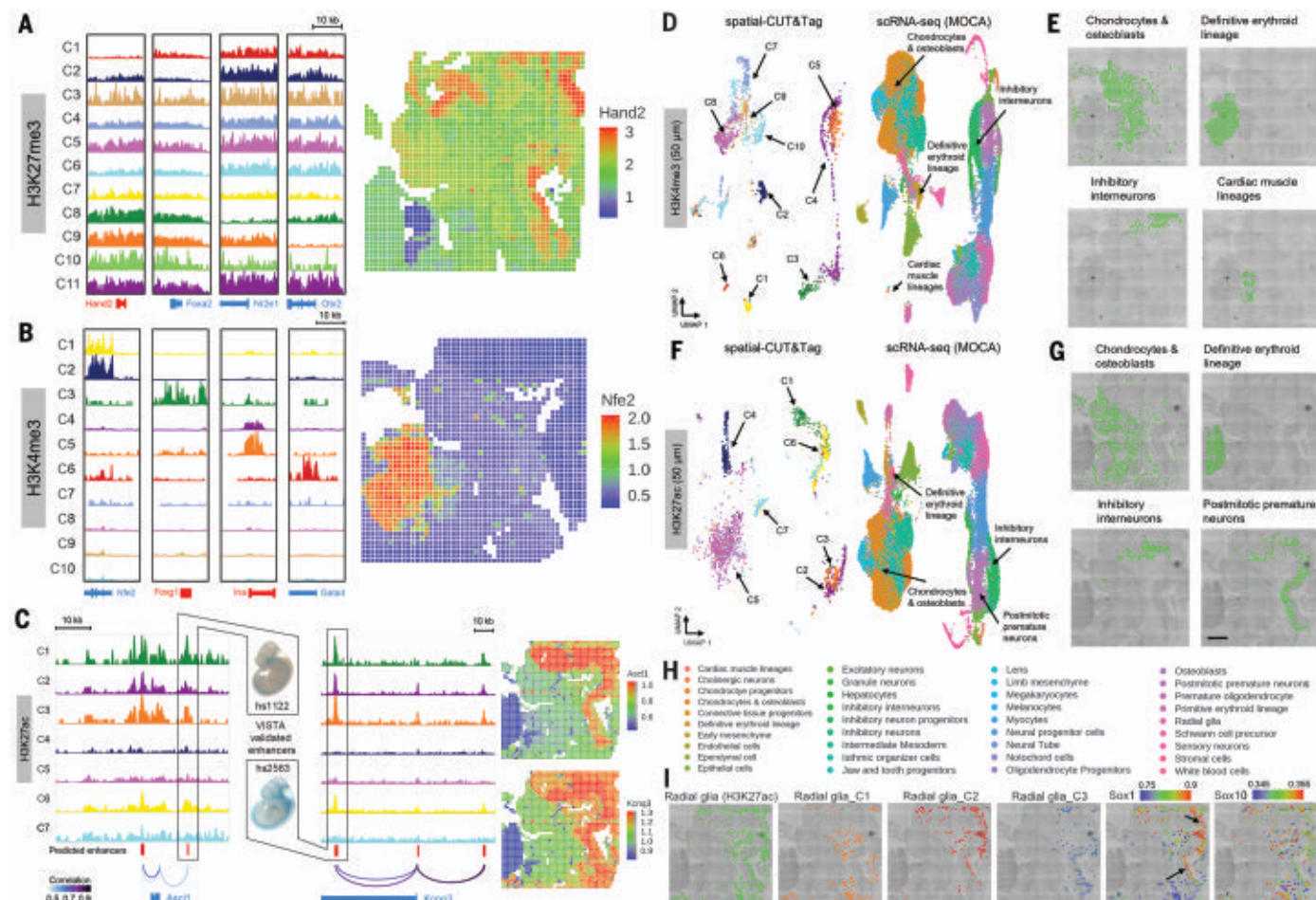


**Fig. 2. Spatial mapping and integrative analysis of mouse embryos.** (A and B) Genome browser tracks (left) and spatial mapping (right) of gene silencing by H3K27me<sub>3</sub> and gene activity by H3K4me<sub>3</sub> modification. (C) Predicted enhancers of *Ascl1* (chr10: 87,463,659 to 87,513,660; mm10) (left) and *Kcnq3* (chr15: 66,231,223 to 66,331,224; mm10) (right) from H3K27ac profiling. Cluster

of each track corresponds to Fig. 1F. Enhancers validated by in vivo reporter assays are shown between main panels. (D and F) Integration of scRNA-seq (5) and spatial-CUT&Tag data. (E and G) Spatial mapping of selected cell types identified by label transferring. (H) List of cell types in scRNA-seq. (I) Refined clustering of radial glial cells enabled identification of subpopulations. Scale bar, 1 mm.

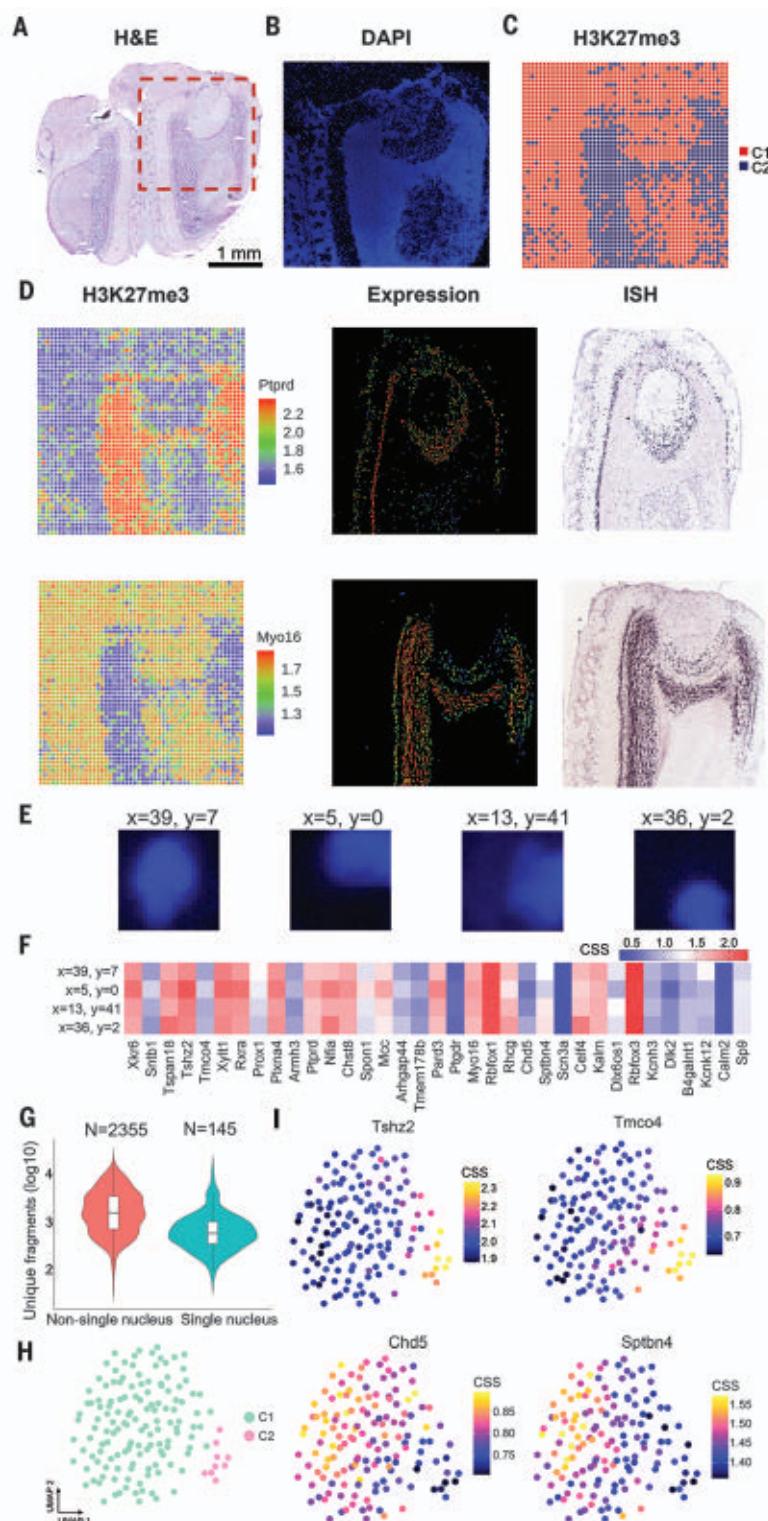


**Fig. 3. Spatial mapping of an immunofluorescence-stained mouse olfactory bulb tissue section.** (A) H&E-stained image from an adjacent tissue section and a region of interest for spatial mapping. (B) Fluorescent image of nuclear staining with DAPI. (C) Unsupervised clustering analysis and spatial distribution of each cluster (20- $\mu$ m pixel size). (D) Spatial mapping (left) of H3K27me3 modification for selected marker genes. In situ hybridization (right) and expression images (middle) of corresponding genes are from the Allen Mouse Brain Atlas. (E) Fluorescent images of selected pixels containing a single nucleus (DAPI). (F) Heatmap of chromatin silencing score of selected pixels. (G) Comparison of unique fragments in pixels with more than one nucleus and those with a single nucleus. (H and I) Unsupervised clustering of selected pixels containing single nuclei (H) and colored by CSS for selected genes (I).

By contrast, subcluster 3 cells were in the spinal cord parenchyma, whereas subcluster 1 cells were mainly outside the CNS, and thus might represent neural crest progenitors (e.g., active *Sox10*) (Fig. 2I). Additionally, two subclusters were found in the chondrocytes and osteoblasts, and the genes related to developing teeth (e.g., *Barx1*) had higher GAS in subcluster 2 (fig. S12B).

The data were further used to examine the developmental process from radial glia to excitatory neurons through postmitotic premature neurons as the immediate state and the cells were ordered in pseudotime. Spatial projection of each pixel's pseudotime revealed the spatially organized developmental trajectory (fig. S13). Cells early in differentiation were enriched around the ventricles in the developing brainstem, whereas those farther away exhibited a more differentiated phenotype (2I) (fig. S13B). We then identified changes in gene activity based on H3K4me3 across this developmental process, and many of the genes recovered are important in neuron development, including *Pou4f1* and *Car10* (19, 22) (fig. S13, C and D).

We next combined spatial-CUT&Tag with immunofluorescence staining in the same tissue section (Fig. 3). We stained an olfactory bulb with 4',6-diamidino-2-phenylindole (DAPI) for nuclear DNA (Fig. 3B) and next performed spatial-CUT&Tag against H3K27me3 with 20- $\mu$ m pixel size, which distinguished the major cell types, including the glomerular (C1) and granular (C2) layer (Fig. 3). Spatial patterns of H3K27me3 modification were validated by in situ hybridization (Fig. 3D). With DAPI staining for the nucleus, we could select the pixels of interest such as those containing a single nucleus or those showing specific histone modifications, allowing for extracting single-cell epigenome data without tissue dissociation (Fig. 3, E to I).

We also conducted spatial-CUT&Tag with 20- $\mu$ m pixel size to analyze the brain region of an E11 mouse embryo (fig. S14) and observed distinct spatial patterns. H3K27me3 yielded the most spatial clusters (fig. S14, A to C). The clusters identified agreed with the projection of ENCODE organ-specific bulk ChIP-seq data in the UMAP embedding (fig. S14, C and D). We further surveyed H3K27me3 modifications and observed distinct modification patterns across clusters (figs. S14E and S15A). *Cfap77* was repressed extensively except in a portion of the forebrain. *Six1*, which is involved in limb development, had low CSS in cluster 5. Although *Sfta3-ps* and *Rhcg* lack H3K27me3 enrichment in the forebrain, they had distinct spatial patterns. Pathway analysis of marker genes revealed that cluster 1 was involved in the forebrain development, cluster 2 corresponded to anterior/posterior pattern specification, and cluster 4 was associated with



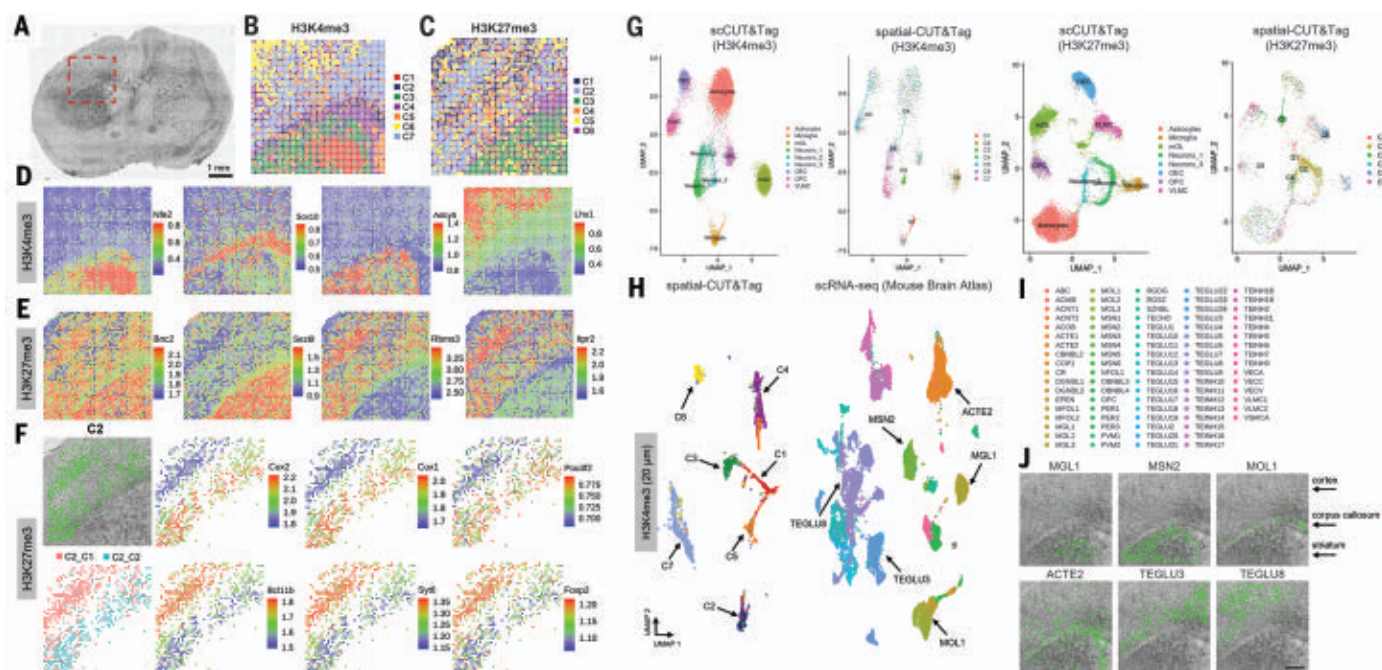


**Fig. 4. Spatial mapping and integrative analysis of mouse brain.** (A) Image of mouse brain tissue section and the region of interest for spatial mapping. (B and C) Unsupervised clustering analysis and spatial distribution of each cluster (20- $\mu$ m pixel size). (D and E) Spatial mapping of gene activity by H3K4me3 and gene silencing by H3K27me3 modification for selected marker

genes. (F) Refined clustering identified subpopulations in neurons with distinct spatial distributions and marker genes. (G and H) Integration of scCUT&Tag (8), scRNA-seq (23), and spatial-CUT&Tag data. (I) List of cell types in scRNA-seq. (J) Spatial mapping of selected cell types identified by label transferring. Scale bar, 500  $\mu$ m.

heart morphogenesis, all in agreement with anatomical annotations (figs. S14A and S15B). Next, we sought to improve the clustering resolution by integrating data across H3K4me3 and H3K27ac histone marks at gene resolution. The granularity of 2D representation of the data obtained from the integrated analysis was further improved (fig. S14F). To assign cell types to each cluster, we integrated the spatial-CUT&Tag data (H3K4me3 and H3K27ac) with the mouse embryo cell atlas from scRNA-seq (5) (fig. S14, G to K). For example, chondrocytes and osteoblasts were mainly in the embryonic facial prominence, and radial glia and inhibitory neuron progenitors were observed in the forebrain (fig. S14, H and J). Although H3K4me3 and H3K27ac had fewer clusters than H3K27me3 at the 20- $\mu$ m resolution, we found that the clusters that appeared to be homogeneous could be further deconvoluted into subpopulations.

Finally, spatial-CUT&Tag with 20- $\mu$ m pixel size was applied to the P21 mouse brains, and unsupervised clustering revealed distinct spatial features (Fig. 4, A to C). We set out to explore the spatial patterns of specific marker genes to distinguish cell types and compared them with the gene expression pattern in the single-cell transcriptomic atlas (23) (Fig. 4, D and E, and figs. S16 and S17). For example, *Sox10* showed high GAS in cluster 2 of H3K4me3, and *Itpr2* had low CSS in cluster 6

of H3K27me3, indicating that these clusters were enriched with oligodendrocyte lineage cells. Cells of these clusters were particularly enriched in a stripe-like structure that corresponds to the corpus callosum (Fig. 4, D and E). For cluster 3 of H3K4me3 and H3K27me3, *Adcy5* was activated and *Rbms3* was repressed, suggesting that medium spiny neurons were enriched in these clusters. Some clusters that appeared to be homogeneous could be further deconvoluted into subpopulations with distinct spatial distributions (Fig. 4F). For example, cluster 2 of H3K27me3 could be further divided into two clusters. *Cux2*, a marker of the superficial cortical layers 2 and 3, had lower H3K27me3 signal in subcluster 1. By contrast, *Bcl11b*, a marker of the deeper cortical layers 4 to 6 presented higher H3K27me3 signal. Although Polycomb has been previously shown to play a role in the establishment of cortical layers at embryonic stages (24, 25), our data suggest that H3K27me3 is also involved in maintaining cortical layer identities at postnatal stages. To examine the interplay between active and repressive marks and to infer the potential H3K4me3/H3K27me3 bivalency, we identified all active promoters specific to individual populations marked by H3K4me3 and plotted the signals of H3K4me3 and H3K27me3 (fig. S18). As expected, H3K27me3 signals were depleted when the promoter was enriched in H3K4me3 in the respective population. How-

ever, H3K27me3 signals were also observed around a few marker genes in oligodendrocytes and medium spiny neurons.

To further identify cell types, we integrated spatial-CUT&Tag data with the published scCUT&Tag (8) and scRNA-seq dataset (23). This revealed that microglia, mature oligodendrocytes, medium spiny neurons, astrocytes, and excitatory neurons were enriched in clusters 1, 2, 3, 4, and 7, respectively, in the H3K4me3 dataset, and subpopulations of neurons could also be identified (Fig. 4, G to J, and figs. S16 and S17). Moreover, the integration of spatial-CUT&Tag with scRNA-seq or scCUT&Tag could allow prediction of the region in which a specific cell type in scRNA-seq or scCUT&Tag is localized (Fig. 4, G to J). We identified that mature oligodendrocytes (MOL1) are abundant in the corpus callosum, whereas medium spiny neurons (MSN2) are present in the striatum, and TEGLU3 excitatory neurons are present in deeper cortical layer 6, which is in agreement with previous results (23) but was determined herein by epigenetic modification states. TEGLU8 excitatory neurons have been shown to populate cortical layer 4 (23), and indeed we observed that the corresponding epigenetic state of this neuronal population was distributed in a more superficial cortical layer than TEGLU3 (Fig. 4J). We found that a subpopulation of nonactivated microglia (MGL1)



populates the striatum but not the corpus callosum or cortex. In addition, the epigenetic state associated with protoplasmic astrocytes (ACTE2) is mainly localized in the corpus callosum, although it was also observed in the cortex and striatum at lower frequencies.

Our study demonstrates the profiling of chromatin states in situ in tissue sections with high spatial resolution. Although spatial-CUT&Tag focuses on the tissue mapping of histone modifications, integration with other assays such as transcriptome and proteins is feasible with our microfluidic in tissue bar-coding approach by combining reagents for DBiT-seq (12) and spatial-CUT&Tag to achieve spatial multi-omics profiling. Moreover, the mapping area could be further increased by using a serpentine microfluidic channel or increasing the number of barcodes (e.g., 100 × 100). Spatial-CUT&Tag is a next-generation sequencing-based approach, which is unbiased for genome-wide mapping of epigenetic mechanisms in the tissue context.

## REFERENCES AND NOTES

- G. Kelsey, O. Stegle, W. Reik, *Science* **358**, 69–75 (2017).
- D. U. Gorkin *et al.*, *Nature* **583**, 744–751 (2020).
- E. Z. Macosko *et al.*, *Cell* **161**, 1202–1214 (2015).
- A. M. Klein *et al.*, *Cell* **161**, 1187–1201 (2015).
- J. Cao *et al.*, *Nature* **566**, 496–502 (2019).
- A. Rotem *et al.*, *Nat. Biotechnol.* **33**, 1165–1172 (2015).
- K. Grosselin *et al.*, *Nat. Genet.* **51**, 1060–1066 (2019).
- M. Bartosovic, M. Kabbe, G. Castelo-Branco, *Nat. Biotechnol.* **39**, 825–835 (2021).
- S. J. Wu *et al.*, *Nat. Biotechnol.* **39**, 819–824 (2021).
- S. Ma *et al.*, *Cell* **183**, 1103–1116.e20 (2020).
- B. B. Lake *et al.*, *Nat. Biotechnol.* **36**, 70–80 (2018).
- Y. Liu *et al.*, *Cell* **183**, 1665–1681.e18 (2020).
- Y. Liu, A. Enninfu, Y. Deng, R. Fan, Spatial transcriptome sequencing of FFPE tissues at cellular level. *bioRxiv* 2020.2010.2013.338475 [Preprint] (2020); <https://doi.org/10.1101/2020.10.13.338475>.
- H. S. Kaya-Okur *et al.*, *Nat. Commun.* **10**, 1930 (2019).
- S. Henikoff, J. G. Henikoff, H. S. Kaya-Okur, K. Ahmad, *eLife* **9**, e63274 (2020).
- M. Wang, Y. Zhang, Tn5 transposase-based epigenomic profiling methods are prone to open chromatin bias. *bioRxiv* 2021.2007.2009.451758 [Preprint] (2021); <https://doi.org/10.1101/2021.07.09.451758>.
- P. Milani *et al.*, *Sci. Rep.* **6**, 25474 (2016).
- J. M. Granja *et al.*, *Nat. Genet.* **53**, 403–411 (2021).
- G. Stelzer *et al.*, *Curr. Protoc. Bioinformatics* **54**, 1.30.1–1.30.33 (2016).
- A. Visel, S. Minovitsky, I. Dubchak, L. A. Pennacchio, *Nucleic Acids Res.* **35** (Database), D88–D92 (2007).
- S. R. Srivatsan *et al.*, *Science* **373**, 111–117 (2021).
- W. Luo *et al.*, *BMC Biol.* **19**, 135 (2021).
- A. Zeisel *et al.*, *Cell* **174**, 999–1014.e22 (2018).
- Y. Hirabayashi *et al.*, *Neuron* **63**, 600–613 (2009).
- J. D. Pereira *et al.*, *Proc. Natl. Acad. Sci. U.S.A.* **107**, 15957–15962 (2010).
- Y. Deng, M. Bartosovic, G. Castelo-Branco, R. Fan, Codes for: Spatial-CUT&Tag: Spatially resolved chromatin modification profiling at the cellular level, version 1.0.0, Zenodo (2021); <https://zenodo.org/record/5797109#YenP5-rMKUK>.

## ACKNOWLEDGMENTS

We thank T. Jimenez-Beristain in the GCB laboratory for writing laboratory animal ethics permit 1995\_2019 and for assistance with animal experiments. We also thank the Yale Center for Research Computing for guidance and use of the research computing infrastructure. The molds for microfluidic chips were fabricated at the Yale University School of Engineering and Applied Science (SEAS) Nanofabrication Center. We used the service provided by the Genomics Core of Yale Cooperative Center of Excellence in Hematology (U54DK106857). Next-generation sequencing was conducted at Yale Stem Cell Center Genomics Core Facility, which was supported by the Connecticut Regenerative Medicine

Research Fund and the Li Ka Shing Foundation. **Funding:** This research was supported by a Packard Fellowship for Science and Engineering (to R.F.); a Yale Stem Cell Center Chen Innovation Award (to R.F.); and the National Institutes of Health (NIH) (grants U54CA209992, R01CA245313, UG3CA257393, and R1MH128876 to R.F.). This material is based in part upon work supported under a collaboration by Stand Up To Cancer, a program of the Entertainment Industry Foundation and the Society for Immunotherapy of Cancer (to R.F. and Y.L.). The work in G.C.-B.'s research group was supported by the Swedish Research Council (grant 2019-01360), the European Union (Horizon 2020 Research and Innovation Programme/European Research Council Consolidator EPISCOPE grant 681893), the Swedish Cancer Society (Cancerfonden grant 190394 Pj), the Knut and Alice Wallenberg Foundation (grants 2019-0107 and 2019-0089), the Swedish Society for Medical Research (grant JUB2019), the Ming Wai Lau Center for Reproductive Medicine, and the Karolinska Institutet. **Author contributions:** Conceptualization: R.F.; Data analysis: Y.D., M.B., G.C.-B., R.F.; Investigation: Y.D., P.K., and D.Z.; Methodology: Y.D., D.Z., and Y.L.; Resources: G.S., A.E., and Z.B.; Writing – original draft: Y.D. and R.F. All authors reviewed, edited, and approved the manuscript. **Competing interests:** R.F. and Y.D. are inventors of a patent application related to this work. R.F. is scientific founder and adviser for IsoPlexis, Singleron Biotechnologies, and AtlasXomics. The interests of R.F. were reviewed and managed by Yale University Provost's Office in accordance with the University's conflict of interest policies. **Data and materials availability:** The sequencing data reported in this paper are deposited in the Gene Expression Omnibus (GEO) with accession code GSE165217. Code for sequencing data analysis is available on Zenodo (26).

## SUPPLEMENTARY MATERIALS

[science.org/doi/10.1126/science.abg7216](https://science.org/doi/10.1126/science.abg7216)  
Materials and Methods  
Figs. S1 to S18  
Tables S1 to S3  
References (27–35)  
MDAR Reproducibility Checklist

23 January 2021; resubmitted 11 October 2021  
Accepted 12 January 2022  
10.1126/science.abg7216



Apply by  
March 25

# Presidential Society of STEM Post-Doctoral Fellows

Supporting the future of STEM  
by enabling post-docs in research,  
teaching, and diversity excellence

This new society is focused on excellence in  
STEM research and teaching with an emphasis  
on supporting diversity, equity, and inclusion  
within the university and community.

Become part of our inaugural cohort and advance  
your career by working with world-class faculty and  
exceptional students.

This is a guaranteed, multi-year position  
located in the heart of Cleveland's  
vibrant University Circle, a major medical,  
academic, and art hub.

**\$75,000  
salary**

UMC\_4465-01\_2022



[case.edu/provost/presidential-fellows](https://case.edu/provost/presidential-fellows)



## Postdoctoral Fellow – Cancer Research UT Health San Antonio (UT Health SA)

The Mays Cancer Center, an NCI-designated cancer center located at UT Health SA, is recruiting **postdoctoral fellows** for ongoing translational cancer research. Research at Mays Cancer Center combines the expertise of renowned cancer researchers, state-of-the-art laboratory technologies and a team approach. These capabilities fuel discovery at an accelerated pace. Our goal is to lessen cancer's impact on our community and beyond.

UT Health SA is a research-intensive institution located in San Antonio and it sits in the gateway to the picturesque Texas Hill Country. San Antonio is a vibrant, multicultural city with year-round recreational activities, affordable housing, and a high standard of living.

Individual job postings for Mays Cancer Center faculty are available through the Office of Postdoctoral Affairs: <https://opa.uthscsa.edu/position-listings/postdoctoral-position?category=Cancer#Cancer>.

All postdoctoral appointments are designated as security sensitive positions.

*UT Health SA is an Equal Opportunity/Affirmative Action Employer. All qualified applicants will receive consideration for employment without regard to sex, gender identity, sexual orientation, race, color, religion, national origin, disability, protected Veteran status, age, or any other characteristic protected by law or policy.*

Benaroya Research Institute  
Seattle, Washington

**POWERING  
POSSIBILITY™**

## WHY WORK AT BRI?

BRI has a bold mission to predict, prevent, reverse and cure diseases that impact the immune system – from autoimmune disease, to cancer to COVID-19. We study the immune system in health and disease, to understand how these conditions start and to find ways to rebalance the immune system back to health.

- Collaborative culture
- Biorepositories of samples from people with immune system diseases
- Core Labs: Tetramers, Genomics, Genotyping and Cell and Tissue Analysis

## BE PART OF THE NEXT BIG DISCOVERY

**BRI is looking for postdocs in the following areas:** immunology, molecular biology, bioinformatics, biostatistics, computational biology or related field.

## LEARN MORE AND APPLY

To learn more about available positions visit **[BenaroyaResearch.org/careers](https://BenaroyaResearch.org/careers)** today.

Equal opportunity employer, including disability/vets.



# Faculty Position in Physical Limnology

at the Ecole polytechnique fédérale de Lausanne (EPFL)

The EPFL School of Architecture, Civil and Environmental Engineering (ENAC) invites applications for a tenure track Assistant Professor of Physical Limnology in the Institute of Environmental Engineering (IIE).

The new professor will be a member of the Limnology Center (LIMNC) and the Center for Climate Impact and Action (CLIMACT), and will have access to the multi-institutional experimental platform for limnological research LÉXPLORE, located on Lake Geneva near EPFL.

We seek applicants with acknowledged research expertise on physical processes in inland surface waters and their response to natural and anthropogenic impacts. Particularly welcome are candidates with research interests that include the impacts of climate change on aquatic environments. We also encourage applications from candidates whose research vision encompasses the quantitative interdisciplinary connections between physical, chemical and biological processes that contribute to ecosystem services provided by lakes and other inland water bodies.

The appointee is expected to lead an internationally recognized research program in physical limnology that leverages the opportunities offered by EPFL. The professor will be committed to excellence in undergraduate and graduate level teaching, and will contribute to the Environmental Engineering program, which emphasizes basic and translational research as the foundation for environmental adaptation and engineering design.

EPFL, with its main campus located in Lausanne, on the shores of Lake Geneva, is a dynamically growing and well-funded institution fostering excellence and diversity. It is well equipped with experimental and computational infrastructure, and offers a fertile environment for research collaboration between various disciplines. The EPFL environment is multilingual and multicultural, with English serving as a common interface. EPFL offers internationally competitive start-up resources, salaries and benefits.

The following documents are requested in PDF format: cover letter including a statement of motivation, curriculum vitae, publication list, concise statements of research and teaching interests (up to 5 pages for each) as well as the names and contact information of three referees who are ready to supply a letter upon request. Applications should be uploaded to the EPFL recruitment web site:

<https://facultyrecruiting.epfl.ch/position/34865161>

Formal evaluation of the applications will begin on **April 1, 2022**.

Further enquiries should be made to:

**Prof. Fernando Porté-Agel**

Chair of the Search Committee

e-mail: [SearchLimnology@epfl.ch](mailto:SearchLimnology@epfl.ch)

For additional information on EPFL, please consult:

[www.epfl.ch](http://www.epfl.ch)

[www.epfl.ch/schools/enac](http://www.epfl.ch/schools/enac)

[www.epfl.ch/schools/enac/research/environmental-engineering-institute-iie](http://www.epfl.ch/schools/enac/research/environmental-engineering-institute-iie)

[www.epfl.ch/research/domains/limnc](http://www.epfl.ch/research/domains/limnc)

[www.epfl.ch/schools/enac/research/centers/climact](http://www.epfl.ch/schools/enac/research/centers/climact)

[www.epfl.ch/research/domains/limnc/projects/explore](http://www.epfl.ch/research/domains/limnc/projects/explore)

[www.epfl.ch/schools/enac/education/environmental](http://www.epfl.ch/schools/enac/education/environmental)

EPFL is an equal opportunity employer and a family friendly university, committed to increasing the diversity of its faculty, and strongly encourages women to apply.

**myIDP:**  
A career plan customized  
for you, by you.



For your career in science, there's only one Science

## Features in myIDP include:

- Exercises to help you examine your skills, interests, and values.
- A list of 20 scientific career paths with a prediction of which ones best fit your skills and interests.
- A tool for setting strategic goals for the coming year, with optional reminders to keep you on track.
- Articles and resources to guide you through the process.
- Options to save materials online and print them for further review and discussion.
- Ability to select which portion of your IDP you wish to share with advisors, mentors, or others.
- A certificate of completion for users that finish myIDP.



Visit the website and start  
planning today!

[myIDP.sciencecareers.org](http://myIDP.sciencecareers.org)



In partnership with:







On September 24, 2021, Quad partners Australia, India, Japan, and the United States announced the **Quad Fellowship: a first-of-its-kind scholarship program designed to build ties among the next generation of scientists and technologists.**

This program will sponsor 100 exceptional American, Japanese, Australian, and Indian master's and doctoral students in science, technology, engineering, and mathematics to study in the United States. The fellowship will develop a network of science and technology experts committed to advancing innovation and collaboration in the private, public, and academic sectors, in their own nations and among Quad countries.

### Benefits

#### The Quad Fellowship will:

- Provide scholarship or research funding for STEM master's and doctoral programs at leading universities in the United States
- Connect students with top scientists, technologists, and national leaders from Quad countries, providing unparalleled opportunities for networking and mentorship
- Help build a foundational understanding among Quad Fellows of one another's societies and cultures through unique travel opportunities
- Build lifelong, international networks between STEM innovators

Learn more at [www.quadfellowship.org](http://www.quadfellowship.org)

## ARE YOU THE KIND WHO WORKS TO HELP ALL HUMANKIND?



 Find your next job at [ScienceCareers.org](http://ScienceCareers.org)

**ScienceCareers**

FROM THE JOURNAL SCIENCE 



Shenzhen Institute of  
Advanced Technology  
Chinese Academy of Sciences



Established in partnership between the Chinese Academy of Sciences and the Shenzhen Municipal Government, the Shenzhen Institute of Advanced Technology (SIAT) is a newly-created university with an objective to become the world's preeminent institute for emerging science and engineering programs. SIAT is equipped with state-of-art teaching and research facilities and is dedicated to cultivating international, visionary, and interdisciplinary talents while delivering research support to pursue innovation-driven development.

SIAT is located in Shenzhen, also known as the "Silicon Valley of China," a modern, clean, and green city, well-known for its stunning architecture, vibrant economy, and its status as a leading global technology hub. SIAT is seeking applications for faculty positions of all ranks in the following academic programs: Computer Science and Engineering, Bioinformatics, Robotics, Life Sciences, Material Science and Engineering, Bio-medical Engineering, Pharmaceutical Sciences, Synthetic Biology, Neurosciences, etc. SIAT seeks individuals with a strong record of scholarship who possess the ability to develop and lead high-quality teaching and research programs. SIAT offers a comprehensive benefits package and is committed to faculty success throughout the academic career trajectory, providing support for ambitious and world-class research projects and innovative, interactive teaching methods.

Further information:

<http://english.siat.cas.cn/DP/Va/> 

By Alvina G. Lai

# Following my curiosity

I'm a lab biologist by training. I'm good at running experiments, taking care of animals, and cloning difficult genes. But as a postdoc, I started to crave a new challenge. I began to look over the shoulder of the bioinformatician whose job it was to wrangle and analyze gigabytes of genomic data that our group generated. It was complicated and challenging work that required a unique skill set, which was why we had a person dedicated entirely to the task. But after learning about his work and seeing his code and visualizations, I grew interested in learning how to do it myself. With faculty positions hard to come by in my field, I figured, "What better time to upskill than now?"

I didn't have the time or resources to enroll in a degree program. So I would need to be creative. Thankfully, my postdoc adviser agreed I could spend some time to learn bioinformatics on my own, even though he already paid someone to do that task. I persuaded him that someone with lab experience could bring new insights to the data analysis process. But I still had experiments to run and animals to care for, so I had to be strategic.

I looked over my calendar. It didn't have a lot of wiggle room; finding time to learn something new was going to be a challenge. I re-evaluated every entry and thought hard about how much time I was spending on each task.

I was attending several seminars and journal clubs each week, which were not bringing much value to my work. I was also spending way too much time preparing for lab meeting presentations, trying to perfect my slides. And I was doing tasks in the lab that I could reasonably delegate to others.

Our lab had hired a new research assistant who was working on my project. She had limited experience, but after I invested time to train her, she was able to take over many lab tasks, which freed up a lot of my time.

The next step was to sit down and learn. I began by working with a data set I'd generated in the lab—one that I would have normally passed off to the bioinformatician to analyze. I started by learning just enough to complete small tasks, writing a few lines of code before stopping to look up what I needed to do for my next step. I relied on online resources, and I asked our bioinformatician for help when I got stuck. It was a steep learning curve, but by the end, I'd completed an analysis that we included in our publication. This gave me the confidence to take my learning up a notch.



**"Coding quickly became an obsession. ... It taught me what I wanted in a career."**

Over time, as I analyzed more data sets and learned new skills, the imposter syndrome voice in my head began to diminish. Coding quickly became an obsession; I impulsively executed command after command just to see what they do.

After 3 years, I applied for a postdoc position in a lab that didn't have a bioinformatics expert on hand already. I was recruited because of my skills with large genomic data sets, and I saw the position as an opportunity to further hone those skills. It helped me do that. But more importantly, it taught me what I wanted in a career.

I was still tasked with some bench work during my second postdoc, and I often found myself frustrated that I was not able to spend 100% of my time on computational work. I started to find lab tasks monotonous

and I grew impatient during rate-limiting steps—for instance, when I was waiting for cells to grow. In contrast, when I was working on a coding problem or a data visualization challenge, my creative juices flowed. I also produced results at a faster rate, which made me feel productive. That helped me see that, going forward, I only wanted bioinformatics jobs.

I started to apply for faculty jobs and in less than 2 months I secured a position to lead a data science group. I've been in that position now for almost 3 years, and I'm happy I made the switch away from bench science. I now focus on all things data science, whether in teaching or research. And I feel free and in control of my time.

Curiosity initially enticed me to try my hand at bioinformatics. Over time, it grew into a full-fledged career. It wasn't easy to learn a new skill set while I had experiments to run and papers to write. But taking the time to do that opened doors for me and led me to a career I truly enjoy. ■

Alvina G. Lai is an associate professor at University College London.



CALL FOR PAPERS



# Ultrafast Science

 OPEN ACCESS

*Ultrafast Science* is an online-only, Open Access journal published in affiliation with **Xi'an Institute of Optics and Precision Mechanics (XIOPM)** of CAS and distributed by the **American Association for the Advancement of Science (AAAS)**. The mission of the journal is to build a platform for ultrafast scientific research; present new theories, concepts, ideas, technologies and progress in this field; publish the latest research representing the forefront of the discipline and that of international concern; and promote academic exchange and development worldwide. *Ultrafast Science* will publish high-quality original research articles, comprehensive reviews, editorials, and perspectives which feature high novelty, significance and technical quality in cutting-edge and emerging topics in ultrafast science with broad interest from scientific communities.

**Submit your research to *Ultrafast Science* today!**

Learn more at [spj.sciencemag.org/ultrafastscience](http://spj.sciencemag.org/ultrafastscience)

The Science Partner Journal (SPJ) program was established by the American Association for the Advancement of Science (AAAS), the nonprofit publisher of the *Science* family of journals. The SPJ program features high-quality, online-only, Open-Access publications produced in collaboration with international research institutions, foundations, funders and societies. Through these collaborations, AAAS furthers its mission to communicate science broadly and for the benefit of all people by providing top-tier international research organizations with the technology, visibility, and publishing expertise that AAAS is uniquely positioned to offer as the world's largest general science membership society. Visit us at [spj.sciencemag.org](http://spj.sciencemag.org)



@SPJournals

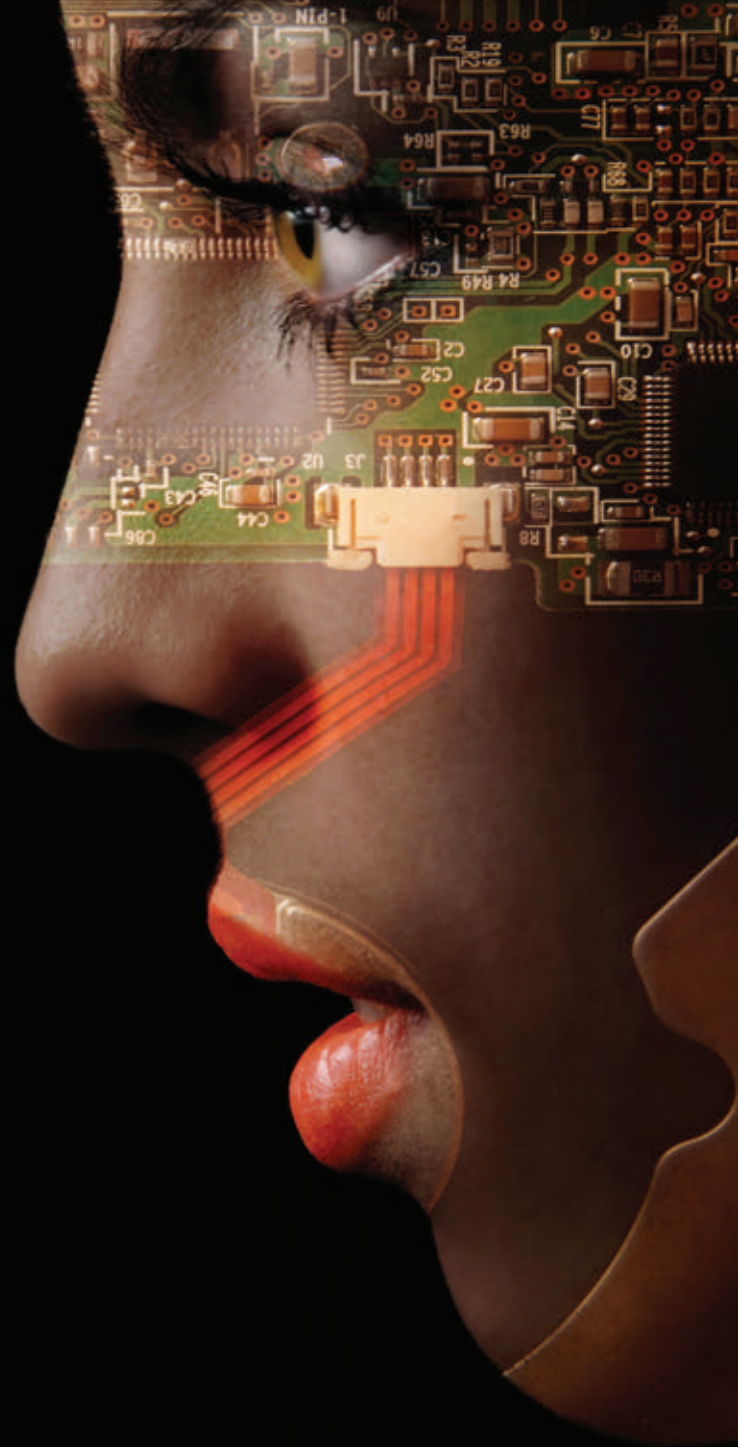


@SPJournals

ARTICLE PROCESSING CHARGES WAIVED UNTIL OCTOBER 2024




# Share Your Robotics Research with the World.



*Shaping the future of robotics with high impact research!*

As a multidisciplinary online-only journal, *Science Robotics* publishes original, peer-reviewed, research articles that advance the field of robotics. The journal provides a central forum for communication of new ideas, general principles, and original developments in research and applications of robotics for all environments.

Submit your research today. Learn more at: [science.org/journal/scirobotics](https://science.org/journal/scirobotics)

 Twitter: @SciRobotics

 Facebook: @ScienceRobotics

Science Robotics

 AAAS